Biological and Medical Physics, Biomedical Engineering

Xiang Yang Liu *Editor*

Bioinspiration

From Nano to Micro Scales

Springer

BIOLOGICAL AND MEDICAL PHYSICS, BIOMEDICAL ENGINEERING

BIOLOGICAL AND MEDICAL PHYSICS, BIOMEDICAL ENGINEERING

The fields of biological and medical physics and biomedical engineering are broad, multidisciplinary and dynamic. They lie at the crossroads of frontier research in physics, biology, chemistry, and medicine. The Biological and Medical Physics, Biomedical Engineering Series is intended to be comprehensive, covering a broad range of topics important to the study of the physical, chemical and biological sciences. Its goal is to provide scientists and engineers with textbooks, monographs, and reference works to address the growing need for information.

Books in the series emphasize established and emergent areas of science including molecular, membrane, and mathematical biophysics; photosynthetic energy harvesting and conversion; information processing; physical principles of genetics; sensory communications; automata networks, neural networks, and cellular automata. Equally important will be coverage of applied aspects of biological and medical physics and biomedical engineering such as molecular electronic components and devices, biosensors, medicine, imaging, physical principles of renewable energy production, advanced prostheses, and environmental control and engineering.

For further volumes:
http://www.springer.com/series/3740

Xiang Yang Liu
Editor

Bioinspiration

From Nano to Micro Scales

Springer

Editor
Xiang Yang Liu
College of Materials
Xiamen University
Xiamen, P.R. China

and

Department of Physics
and Department of Chemistry
Faculty of Science
National University of Singapore
Singapore

ISSN 1618-7210
ISBN 978-1-4614-5303-1 ISBN 978-1-4614-5372-7 (eBook)
DOI 10.1007/978-1-4614-5372-7
Springer New York Heidelberg Dordrecht London

Library of Congress Control Number: 2012952280

Printed on acid-free paper

Springer is part of Springer Science+Business Media (www.springer.com)

Preface

Bioinspiration, the study of the structure and function of biological systems as models for the design and engineering of materials, becomes increasingly important due to the following facts. The breakthrough of modern sciences and technologies depends to a large extent on the step advances in materials science. The research and engineering of materials have become one of the most exciting areas, across physics, chemistry, biology, and engineering. In addressing the current issues concerning health, environment, and the sustainability of development, new materials become particularly important. In this regard, the three major trends of research in materials science are summarized as follows.

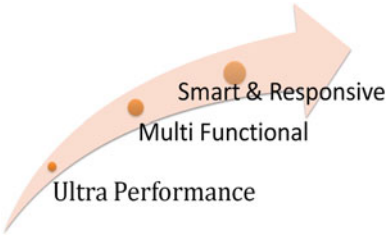

Fig. 1 Three major trends in materials science and engineering

1. *Ultra-performance materials*. The materials refer to those having some extraordinary properties. For instance, the materials entirely or partially appear to be super hard, superhydrophobic, superhydrophilic, superconducting, etc.
2. *Multifunctional materials*. As suggested by the term, the materials correspond to those having more than one major in-use properties/functions.
3. *Smart and responsive materials*. These are the materials which respond to some external stimuli, in the way that some particular properties of the materials change drastically and/or in opposite to conventional materials. Sensing materials are one of the examples. *Under some external simulating*, the color, optical properties, conductivity, etc. of the materials change correspondingly. Artificial

gecko's foot (Chap. 7) is another example where the adhesive force of the surface of the materials will be tuned with the polarity and bias voltage applied.

In this context, we notice that many biomaterials, the materials which occur in organisms, or are formed in a biological environment, fall into one of the three categories. Spider silk is considered as one of the toughest materials in terms of energy and the density. It was estimated that one pencil thick spider silk string can stop a Boeing 747 in flight. Lotus leaves turn out to be one of the common examples of superhydrophobicity, with the capability of self-cleaning. The examples are not exhausted. Therefore, taking lessons from nature becomes one of the major strategies for materials scientists and engineering.

Due to the increasing demands in the modern society and the increase of the global populations, we are now facing some serious sustainable or even survival challenges ahead. These include the impacts of the human activities on the environment and the global climate, the exhaustion of crude oil and other fossil fuels, which turn out to be the raw materials for the most synthetic materials nowadays. To address the increasing concerns about the environmental and climate changes, "sustainable materials" become more and more important. The materials, which will not cause serious environmental impacts in either production or applications and are recyclable, are one of the key focuses in materials science and engineering. Nevertheless, the materialsfalling into this category, i.e., biomaterials, etc., are of inferior properties compared with the relevant synthetic materials in some aspects. The answer to address the questions is biomimicking or bioinspiration engineering, by which we can burst up some particular functions of these materials.

We notice that methods in bioinspiration and biomimicking have been around for a long time. However, due to current advances in modern physical, biological sciences, and technologies, our understanding of the methods have evolved to a new level. This is due not only to the identification of mysterious and fascinating phenomena but also to the understandings of the correlation between the structural factors and the performance based on the latest theoretical, modeling, and experimental technologies.

This book provides readers with a broad view of the frontiers of research in the area of bioinspiration from the nano- to macroscopic scales, particularly in the areas of biomineralization, antifreeze protein/antifreeze effect. It also covers such methods as the lotus effect and superhydrophobicity, structural colors in animal kingdom and beyond, as well as behavior in ion channels. A number of international experts in related fields have contributed to this book, which offers a comprehensive and synergistic look into challenging issues such as theoretical modeling, advanced surface probing, and fabrication. In order to serve as a tutorial for the new comers to the fields, the chapters are designed to cover the basic knowledge in the related fields. Therefore, the book provides not only a link to the engineering of novel advanced materials playing an important role in advancing technologies in various fields, but also the fundamentals behind the sciences and technologies. It suits for

a broad spectrum of readers, ranging from scientists and engineers to graduate students who are prepared themselves for the new challenges in the fields of materials science.

Xiang Yang Liu

Contents

Chapter 1
Bioinspired Nanoscale Water Channel and its Potential Applications

Haiping Fang, Chunlei Wang, Rongzheng Wan, Hangjun Lu, Yusong Tu, and Peng Xiu

Abstract The dynamics of water molecules confined in nanochannels is of great importance for designing novel molecular devices/machines/sensors, which have wide applications in nanotechnology, such as water desalination, chemical separation, sensing. In this chapter, inspired by the aquaporins, which are proteins embedded in the cell membrane that regulate the flow of water but stop the protons, we will discuss the mechanism of water channel gating and water channel pumping, where water molecules form single-filed structure. The single-filed water molecules can also serve as molecular devices for signal transmission, conversion, and multiplication. Moreover, the water in the channel may have great potential applications in designing the lab-in-tube to controllable manipulation of biomolecules.

1.1 Introduction

With the development of nanoscience and nanotechnologies, particularly the successful fabrications of various nanochannels, the study of the water permeation across the nanoscale channels has become conceivable. The understanding of the

H. Fang (✉) • C. Wang • R. Wan
Shanghai Institute of Applied Physics, Chinese Academy of Sciences,
No.2019 Baojia Road, P.O. Box 800-204, Shanghai, 201800 China
e-mail: fanghaiping@sinap.ac.cn; wangchunlei@sinap.ac.cn; wanrongzheng@sinap.ac.cn

H. Lu
Department of Physics, Zhejiang Normanl University, Jinhua, 321004 China
e-mail: zjlhjun@zjnu.cn

Y. Tu
Institute of Systems Biology, Shanghai University, Shanghai, 200444 China
e-mail: tuyusong@gmail.com

P. Xiu
Bio-X Lab, Department of Physics, Zhejiang University, Hangzhou, 310027 China
e-mail: meihuazhuang@163.com

X.Y. Liu (ed.), *Bioinspiration: From Nano to Micro Scales*, Biological and Medical Physics, Biomedical Engineering, DOI 10.1007/978-1-4614-5372-7_1,

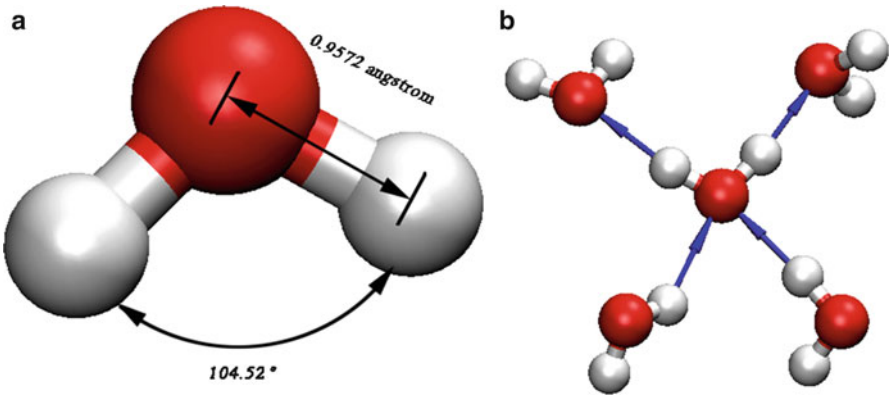

Fig. 1.1 (**a**) A water molecule, where the *red* and *gray balls* represent one oxygen atom and two hydrogen atoms. (**b**) A water molecule together with four neighboring water molecules. The *arrows* denote a hydrogen bond and the head and the end of an *arrow* shows the acceptor and the donor, respectively

dynamics of water molecules confined in nanochannels is also of great importance in designing novel molecular devices/machines/sensors, which have wide applications in nanotechnology [1–19], including lab-on-a-chip technology [20]. In this decade, the lack of clean water, particularly in developing countries, has become one of the main challenges. The desalination of seawater and filtration of polluted water [5] are regarded as two main methods to solve the clean water shortage. Considering the difficulty in the existing techniques, the nanotechnologies based on the water permeation across the nanochannels have become the most promising direction.

There have been many discussions on the water across the nanochannels [17, 21–28]. In 2001, Hummer et al., using molecular dynamics (MD) simulations, showed that water confined in very narrow nanochannels with appropriate radii displayed single-filed structure [21]. Later, Holt et al. [6] experimentally found that the water flow rate through a carbon nanotube (CNT) with a radius of 1–2 nm, a comparable radius to the CNTs used by Hummer et al. in the numerical simulations, was more than three orders of magnitude faster than the conventional nonslip hydrodynamic flow.

Biological systems always inspire us with new idea. In 1980s, Peter Agre discovered the aquaporins, which are proteins embedded in the cell membrane that regulate the flow of water but stop the protons [29, 30]. Later, the structure, the function, and the physics of aquaporins have been extensively studied both from experiments and from numerical simulations [31–39]. In 2001, Groot and Grubmuller used MD simulations to study the water permeation across the biological membrane proteins: aquaporin-1 (AQP1) and Glpf [32]. They found that the water molecules in those biological channels were single-filed. Later, Tajkhorshid et al. examined the apparently paradoxical property, facilitation of efficient permeation of water while excluding protons [34]. We note that people usually take the biological systems as

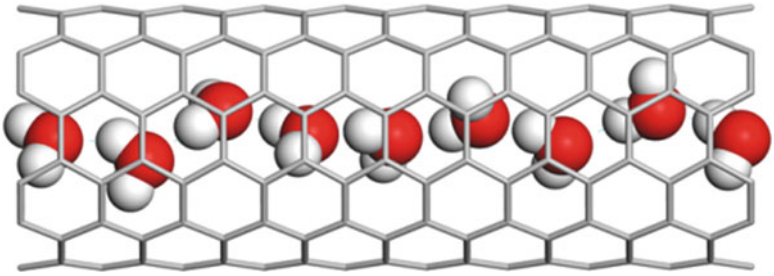

Fig. 1.2 A snapshot of water confined in a (6,6) armchair single-walled carbon nanotube. The *red* and *gray balls* represent the oxygen and hydrogen atoms, respectively. It can be seen clearly that each oxygen atom is located in the right side of the two hydrogen atoms in the same water molecule. The single-walled carbon nanotube is represented by *gray lines*

the most effective ones and can effectively shield the thermal noise and represent the useful signal. In this chapter, we will review the recent progress obtained by our group using MD simulations in the study of the water permeation across the nanoscale channels inspired by the aquaporins.

Let us first review the basic properties of water in a classical view. As is shown in Fig. 1.1, a water molecule is composed of one oxygen atom and two hydrogen atoms with the angle between OHO of about 104.52°. The water molecule is polar due to the residual charges on the oxygen atom and the hydrogen atoms. The most important thing in the water molecules is the hydrogen bonds between neighboring water molecules. Explicitly, an oxygen atom in one water molecule may have a strong interaction with a hydrogen atom in another, which is called the existence of a hydrogen bond. The strength of the hydrogen bonds, though much smaller than that of the chemical bonds, can be more than tens of $k_B T$. Thus, this bond usually plays a very important role in the system full of thermal fluctuation. It is believed that the anomalies of water mainly result from the existence of the hydrogen bonds.

1.1.1 Gating and Pumping of Nanoscale Channels

The water molecules are connected by one-dimensional hydrogen bonds as shown in Fig. 1.2 when the water molecules exhibit single-filed structure in a nanochannel. The motions of the water molecules are concerted transport through the channels. Obviously, at least one hydrogen bond should be broken if we want to stop the water flow across the nanotube. There are at least two methods to achieve this goal. One is to deform the nanotube and the other is to use external electric field to attract the water molecules.

As the model shown in Fig. 1.3, a single-walled carbon nanotube (SWNT) 13.4 Å in length and 8.1 Å in diameter is embedded in a graphite sheet as a water channel. The SWNT and the graphite are solvated in a box ($3 \times 3 \times 4$ nm) with water

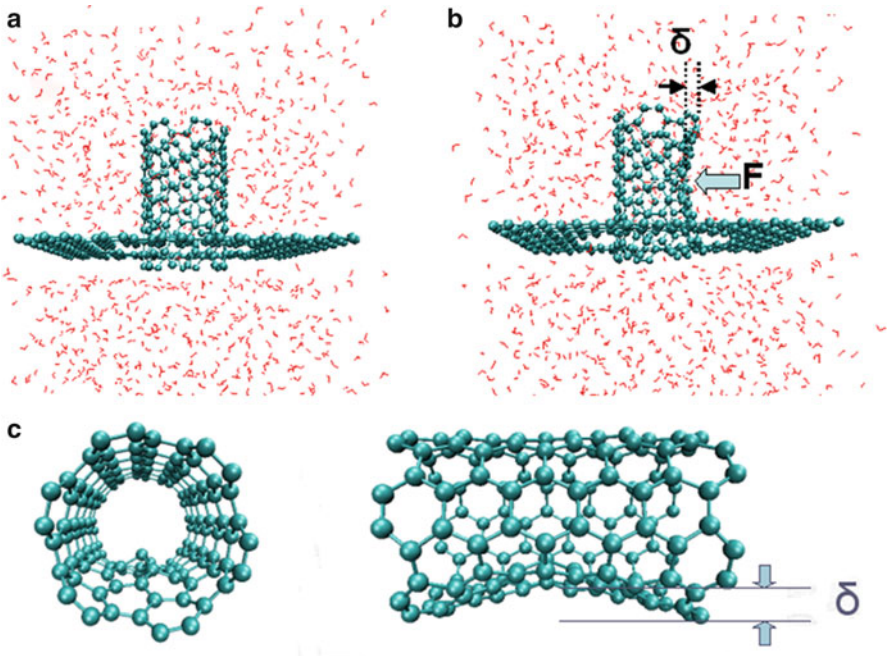

Fig. 1.3 (**a**, **b**) A snapshot of the simulation system. The single-walled carbon nanotube and the graphite sheet are solvated in a box ($3 \times 3 \times 4$ nm) with water molecules. The gap between the graphite plane and the nanotube is too small for a water molecule to penetrate. An external force, marked by "F," acts on an atom of the carbon nanotube and a deformation can be clearly seen (reprinted from [40]. Copyright 2005 American Chemical Society). (**c**) δ is the displacement of the atom directly acted by the external force from its initial equilibrium position

molecules using TIP3P water model. The SWNT can be controllably deformed by an external force F applied to one carbon atom (namely, the forced atom) in the right side of the CNT while the carbon atoms in the left half of the CNT were fixed [40]. In reality, the force can be the active force to control the flow or the perturbations from the other parts in the biological systems.

An additional acceleration of 0.1 nm ps^{-2} along the $+z$ direction is added at each atom to mimic an osmotic pressure difference of 133 MPa between two ends of the SWNT [23, 40]. The carbon atoms at the inlet, outlet, and where the external force is exerted are fixed to prevent the SWNT from being swept away in the simulation. The simulation is carried out at a constant pressure (1 bar) and temperature (300 K).

For each δ corresponding to an external force F, the time for the numerical simulation is 232 ns. The last 216 ns of the simulation are collected for analysis. Figure 1.4 displays the average number of water molecules inside the tube N, together with the net water flux averaged each 18 ns, as a function of time for each δ. For the unperturbed nanotube, the average number of water molecules inside the tube is about 5. During the entire 216 ns simulation, 1955 and 726 water molecules

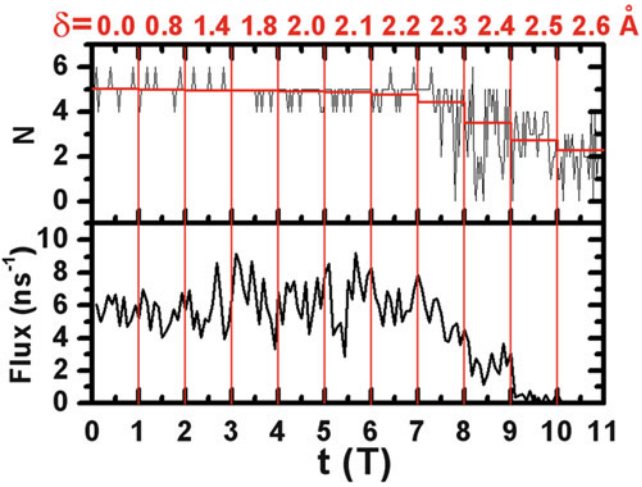

Fig. 1.4 Number of water molecules inside the nanotube (N) and the water flux (which is defined as the number of water molecules passing through the nanotube along z axis and the opposite direction per nanosecond) as a function of time for each deformation δ. The time period for each deformation δ is T, where $T = 12$ ns for N and 216 ns for the flux. The flux shown is averaged each 18 ns (reprinted from [40]. Copyright 2005 American Chemical Society)

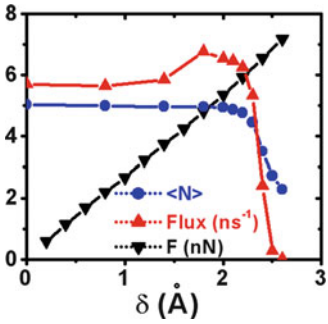

Fig. 1.5 Average number of N and the average net flux in the whole period of T, together with the force F acting on the atom, as a function of δ (reprinted from [40]. Copyright 2005 American Chemical Society)

pass through the tube along z axis and the opposite direction, respectively, resulting in a net water flux of 5.69 water molecules per nanosecond along z axis.

In macroscopy, as the force $F(t)$ increases, the flow across the nanotube decreases monotonically due to the increase in the deformation [40], which can be characterized by a parameter δ, which is the displacement of the forced-atom from its initial position in the pristine SWNT as shown in Fig. 1.3. However, in this system, the water flux and occupancy N do not decrease as expected as shown in Figs. 1.4 and 1.5 when δ increases from 0 to 2.0 Å. In the interval of 1.4 Å $< \delta < \delta_C \approx 2.0$ Å, the water flux even increases a little. Please be noted that the radius of a water molecule is only 1.4 Å. This shows that the water flux is unexpectedly stable even when the deformation of the forced-atom is larger than the

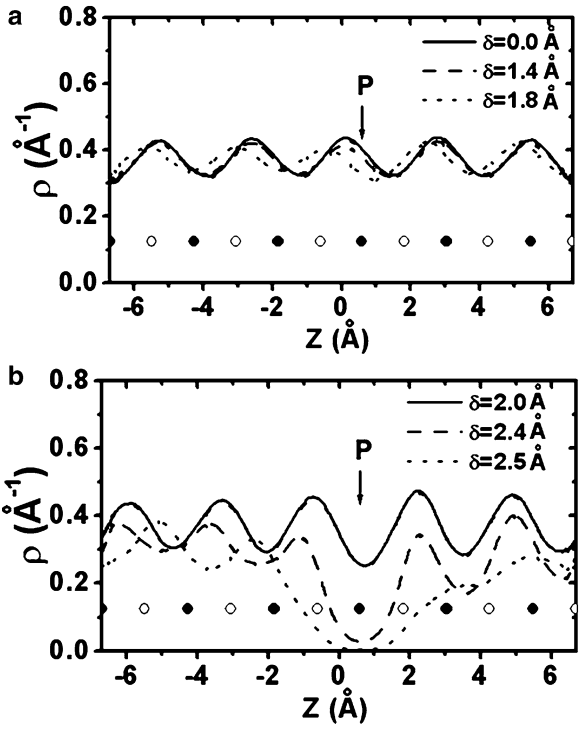

Fig. 1.6 Water distributions along z axis together with the positions of carbon atoms (the *open circles* and the *filled circles*). The *arrow*, marked by *P*, is the position of forced-atom. (**a**) $\delta = 0.0$, 1.4, 1.8 Å (**b**) $\delta = 2.0$, 2.4, 2.5 Å

radius of a water atom. Only when $\delta > \delta_C \approx 2.0$ Å, the net flux and the occupancy N decrease as δ further increases. When $\delta = 2.6$ Å, the water flux through the tube becomes a negligible value. In the total 216 ns simulation, no water molecules enter the tube from one end or leave from the other, indicating that at $\delta = 2.6$ Å, the nanotube is functionally closed. It shows that a CNT can be completely closed from an open state by moving the forced-atom by only 0.6 Å. Here, the CNT shows excellent gating behavior corresponding to external mechanical signals. On one hand, the water flux and occupancy of the CNT are extremely irrespective of external signals ($\delta < 2.0$ Å), for example, deformations due to noise. On the other hand, the water flux and occupancy of the nanotube are sensitive to further deformations. An additional increase of 0.6 Å for δ leads to an abrupt transition from an open state (flux same as an unperturbed nanotube) to a closed state (no flux).

In order to further study the physics for such gating behavior, we show the water distribution inside the CNT for different δ in Fig. 1.6. As is well known, the density of water is constant along a macroscopic channel with a uniform radius. However, for a CNT with 8.1 Å in diameter and 13.4 Å in length, the water density distribution appears in wavelike pattern. Furthermore, the gating of the water transportation through the CNT is found related to the wavelike pattern of water density distribution.

The water density distribution along the tube axis $\rho(z)$ can be calculated by

$$\rho(z) = \frac{N(z)}{N\Delta L},$$

where ΔL is the bin length and $N(z)$ is the number of water molecules appearing at the bin at z for the total of N snapshots from simulation. In order to compute the water density distribution near two openings of the CNT, we can extend the CNT from each end to bulk by 11.3 Å to construct a virtual cylinder with 8.1 Å in diameter. The whole cylinder was divided into 1,000 bins. In the case of $\delta = 0$ Å, the distribution has a wavelike structure with minimal values at the openings and five peaks, which is consistent with the average value of the water occupancy N ($N \approx 5$ for $\delta = 0$ Å from Fig. 1.5). For $0 \leq \delta < 2.0$ Å, the distribution changes gradually and the peak move leftward as δ increases, but the values of the peaks do not change much. This is conforming to the stable value of water occupancy N at the range of $0 \leq \delta < 2.0$ Å in Fig. 1.5. The water distribution at P, the location facing the forced-atom, decreases corresponding to the narrowing of the nanotube at P. When $\delta \geq 2.0$ Å, the distribution at P is smaller than that of the other dips, and the wavelike pattern is considerably deformed; the values of the peaks decrease obviously corresponding to the decrease in N in Fig. 1.5 at the same range of δ. The distribution at P is very close to zero when $\delta = 2.5$ Å. However, we still observe that about one water molecule enters from one side and leaves from the other side per nanosecond when $\delta = 2.5$ Å. Further inspection of the data shows that water molecules can pass the position of P very rapidly without staying.

The gating behavior can also be understood from the distance between the two water molecules, one left to the forced-atom and the other right to the forced-atom. As shown in Fig. 1.7, the distance almost keep the initial value without the deformation of the SWNT of 2–2.8 Å for $\delta < 2.0$ Å. Further increase in δ makes the distance increases rapidly, breaking the connection (hydrogen bonding) between those two water molecules. It is just the strong interaction of the hydrogen bonds that keeps the distance almost as a constant when $\delta < 2.0$ Å. Thus the water transportation across the nanotube stops.

As we have mentioned before, the water molecules form hydrogen bonds with neighboring water molecules, and the water molecules inside the CNT form a single hydrogen-bonded chain. The dipoles of the water molecules are nearly aligned along the nanotube axis. Due to the deformation of the nanotube, the total number of hydrogen bonds inside the nanotube decreases as δ increases (Fig. 1.8). The average number of the hydrogen bonds, denoted by N_{Hbond}, decreases very slowly in a linear fashion as $N_{\text{Hbond}} = 3.16–0.136$ Å in the range of $\delta < 2.0$ Å. In the range of $2.0 \text{ Å} \leq \delta < 2.5$ Å, N_{Hbond} decreases sharply from 2.87 to 1.43. This sharp decrease results from the decrease in the total water molecules inside the nanotube N as well as the increase in the distance between those two water molecules neighbor to the position P. The linear decrease in N_{Hbond} in the range of $\delta < 2.0$ Å mainly results from the increase in the distance between those two water molecules neighbor to the position P, for the value of N keeps stable in this range. The effect of the increase

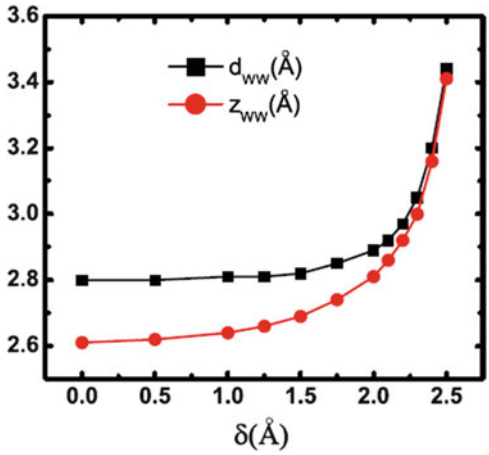

Fig. 1.7 The distance between the two water molecules near the forced-atom d_{WW} and its z-projection Z_{WW} for different δ (reprinted from [129]. Copyright 2008 American Physical Society)

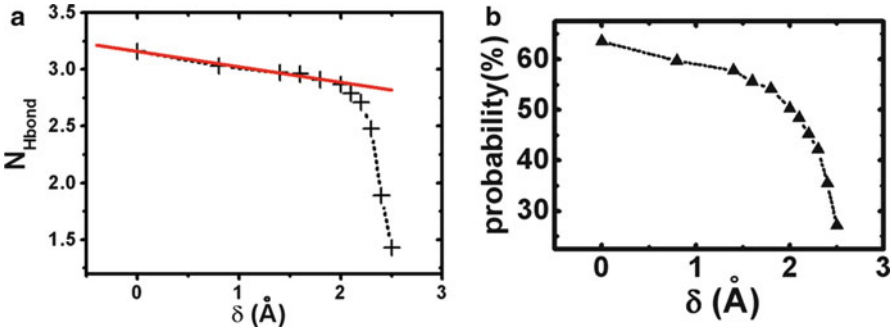

Fig. 1.8 (**a**) Average number of the hydrogen bonds inside the nanotube, the *solid line*, is a linear fit when $\delta < 2.0$ Å, and (**b**) the probability of the hydrogen bond formed by those two water molecules neighboring the forced-atom for different δ (reprinted from [40]. Copyright 2005 American Chemical Society)

in distance between two water molecules near P can be shown by the probability of the hydrogen bond formed by those two water molecules neighboring the forced-atom (Fig. 1.8). In the range of $\delta < 2.0$ Å, the deformation is not strong enough to perturb the hydrogen bonds chain inside the CNT, and the dynamics of water inside the CNT (e.g., occupancy and net flux) keeps stable in this range. When $\delta \geq 2.0$ Å, the deformation is strong enough to break the hydrogen bonds chain, resulting in a sharp decrease in water occupancy and net flux.

To explore the flipping behavior of water dipoles inside the CNT and its sensitivity to the deformation, we define ϕ as the angle between a water dipole and the nanotube axis, and $\bar{\phi}$ as the average angle of all the water molecules inside the tube. Some $\bar{\phi}$ for different δ are shown in Fig. 1.9. For the unperturbed CNT, $\bar{\phi}$ falls in two ranges $15^\circ < \bar{\phi} < 50^\circ$ and $130^\circ < \bar{\phi} < 165^\circ$ most of the time, which is

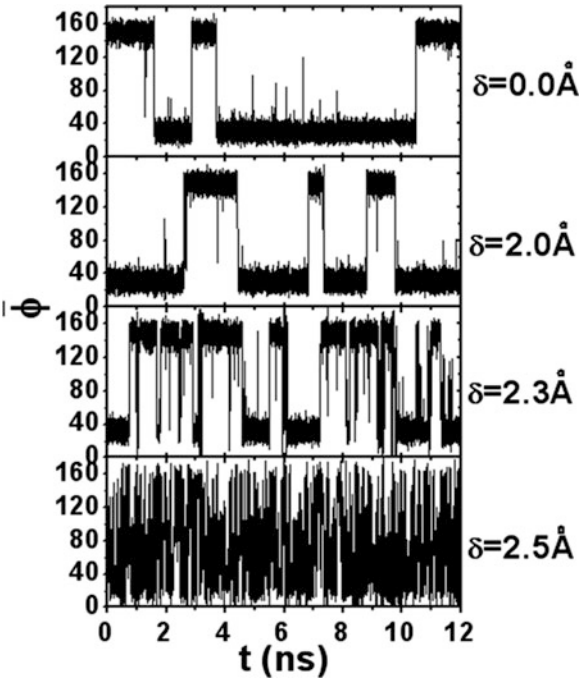

Fig. 1.9 $\bar{\phi}$ for $\delta = 0.0$, 2.0, 2.3, and 2.5 Å (reprinted from [40]. Copyright 2005 American Chemical Society)

consistent with the observation that the water molecules in CNT are nearly aligned. If we define a flip as $\bar{\phi}$ passing through 90°, we can calculate the number of flips per nanosecond, denoted by the flipping frequency f_{flip}.

The flipping frequency f_{flip} is governed by the potential barrier against flipping. And the increment of δ leads to two aspects of the potential change, decrease due to the breakage of hydrogen bonds inside the nanotube and increase due to the narrowing of the nanotube that confines water molecules to a smaller space. As is shown in Fig. 1.8, N_{Hbond} decreases very slowly with respect to δ for $\delta \leq 1.4$ Å. The confinement of water molecules is the main reason for the slow decrease in f_{flip} in this range.

As δ further increases, f_{flip} increases. The dependence of f_{flip} on N_{Hbond} is shown in Fig. 1.10. In the range of 2.0 Å $\leq \delta <$ 2.2 Å, the function

$$f_{\text{flip}} \propto \exp(-N_{\text{Hbond}} E_{\text{Hbond}} / kT)$$

can fit the data quite well, where E_{Hbond} is the average energy of a hydrogen bond in the nanotube for $\delta = 2.0$, 2.1, and 2.2 Å. Numerically, we find $E_{\text{Hbond}} = 12.96\,kT$. This exponential decay indicates that the change of the potential barrier mainly results from the decrease in the number of hydrogen bonds inside the nanotube in this parameter range. For even larger δ, say 2.5 Å, the water chain is frequently ruptured (Fig. 1.11). Only for a small period of time, $\bar{\phi}$ falls into the two parameter

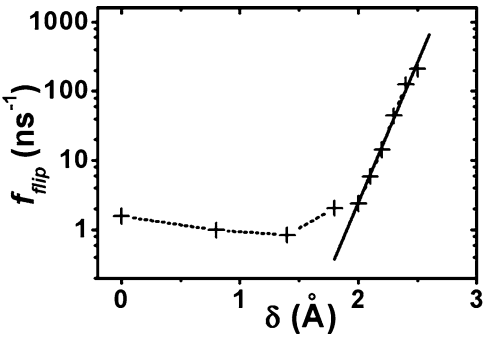

Fig. 1.10 Dependence of flipping frequency f_{flip} on the number of hydrogen bonds N_{Hbond}; the *solid line* is the fits for the exponential decay vs. N_{Hbond} (reprinted from [40]. Copyright 2005 American Chemical Society)

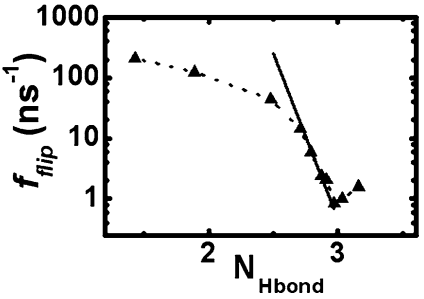

Fig. 1.11 Dependence of flipping frequency f_{flip} on δ. The *solid line* is the fit for the exponential growth vs. δ (reprinted from [40]. Copyright 2005 American Chemical Society)

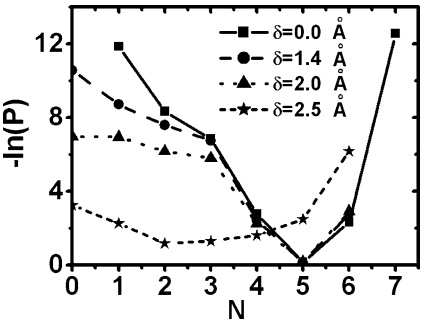

Fig. 1.12 Relative free energy depends on water occupancy, $\beta F(N) = -\ln p(N)$, for $\delta = 0.0$, 1.4, 2.0, and 2.5 Å (reprinted from [40]. Copyright 2005 American Chemical Society)

ranges, i.e., $15° < \bar{\phi} < 50°$ and $130° < \bar{\phi} < 165°$. However, in the interval of 2.0 Å $\leq \delta <$ 2.5 Å, the exponential function $f_{\text{flip}} \propto \exp(\{\delta\}/\{\tau\})$ with $\tau = 0.107$ can fit the data very well (Fig. 1.11).

In order to show the water occupancy fluctuations, the free energy depends on water occupancy N as shown in Fig. 1.12. This relative free energy can be calculated by $\beta F(N) = -\ln p(N)$, where $p(N)$ is the probability of finding exactly N water molecules inside the nanotube. To obtain good statistics, data are collected every 0.25 ps in the calculation of $p(N)$. An approximate Gaussian occupation fluctuation is found for $\delta = 0$. The free energies for $\delta = 1.4$ Å and 2.0 Å are similar to those for $\delta = 0$. However, three events have been found with $N = 7$ for $\delta = 0$ while none

for $\delta = 1.4$ Å and 2.0 Å. And for the case of $N = 0$, it occurs 11 and 388 times for $\delta = 1.4$ Å and 2.0 Å, but none for $\delta = 0$. It seems that the effect of the deformation for $\delta \leq 2.0$ Å is considerable for the possibilities of the rare events although the change of the average value of the water molecules inside is negligible.

For $\delta = 2.5$ Å, the function of free energy is somewhat flat between $N = 2$ and 4, with a minimum at $N = 2$, due to the frequently rupture of the water chain. No intermittent filling is found in the range of $0 \leq \delta \leq 2.5$ Å, consistent with that there is not any minimum at $N = 0$. Although there are many cases with $N = 0$ for $\delta = 2.5$ Å, the durations for them are short. We have not found two successive data with $N = 0$, indicating that the duration for each case with $N = 0$ is less than 0.25 ps.

In addition, in MD simulations, the update algorithm develops a very slow change in the center of mass (COM) velocity, and thus in the total kinetic energy of the system, especially when temperature coupling is used. For the systems with limited friction, if such changes are not quenched, an appreciable COM motion will be developed eventually in long runs. Thus, the method of center of mass motion removal (CMMR) is necessary. During MD simulations, the CMMR method can be applied at a certain frequency. But for the systems with pressure difference to evoke a unidirectional transportation, for example, the gating system we discussed before, the application of CMMR may reduce the effect of such equivalent pressure difference.

It is clear that this excellent gating behavior results from the one-dimensional hydrogen bonds between the neighboring water molecules, which shield the external perturbations. Thus the water permeation across the bio-mimicked nanochannel with single-filed water molecules inside the nanochannel is effectively resistant to mechanical noises and sensitive to available mechanical signals.

Further, we consider the effect of CNT length on the behavior of water molecules in the tube. The CNT we choose is 14.6 Å in length and 8.1 Å in diameter. Along the z direction, it is embedded in the center of a graphite sheet, which is similar with the system shown in Fig. 1.3. A force is also applied to one carbon atom, namely the forced-atom. Note that the number of carbon rings along the nanotube is 5.5, which is 0.5 ring longer than the CNT used in previous sections. Interestingly, our simulation results indicate that the wavelike pattern of water density distribution becomes much weaker when the length of the perfect CNT is increased to 14.6 Å (see Fig. 1.13). Especially, the wavelike pattern is quite flat near the center of the CNT for the unperturbed nanotube. Even near two openings of the CNT, the wavelike pattern is less obvious than that of the CNT that is 13.4 Å. The height between the first peak and the dip from the left opening of the CNT is only about 0.05 $Å^{-1}$, which is much smaller than the average value of 0.12 $Å^{-1}$ for the CNT of 13.4 Å.

The shape of the CNT plays a role in the structure of the water density distribution along tube axis as well. Simulation results indicate that the weak wavelike pattern of water density distribution becomes obvious and shifts slightly when the CNT is deformed by external force. For $\delta < 1.5$ Å, the amplitude of

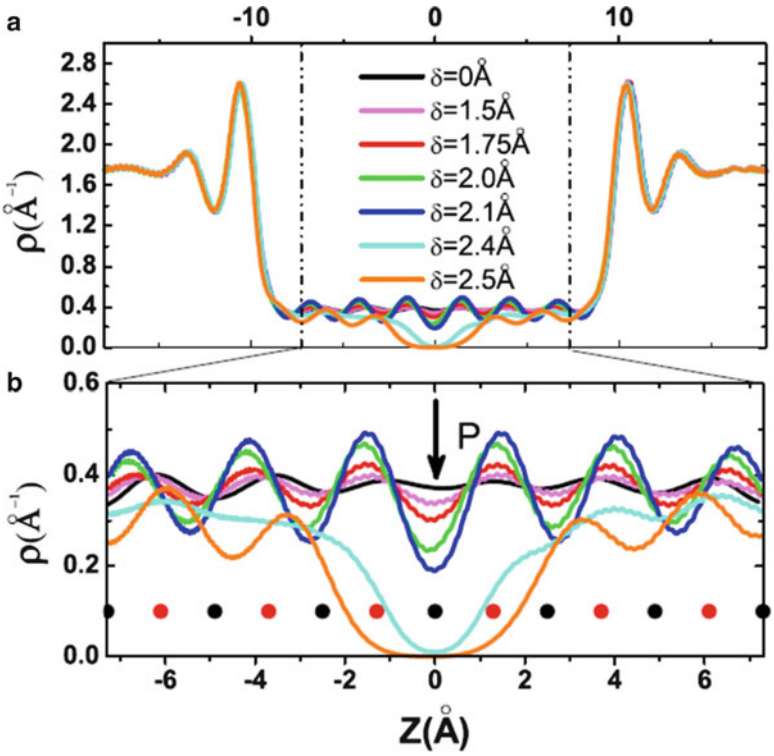

Fig. 1.13 (**a**) Water density distributions along z (carbon nanotube axis). (**b**) Water density distributions inside the nanotube together with the positions of the carbon atoms. The *red* and *black filledcircles* denote the positions of the carbon atoms. The *arrow*, marked by P, is the position of the atom affected by an external force (reprinted from [129]. Copyright 2008 American Physical Society)

wavelike pattern increases obviously, but the distances between crests and troughs change very little, almost fixed. For $1.5 < \delta \leqslant \delta_c \approx 2.0$ Å, the amplitude of the wavelike pattern increases sharply. From $\delta \approx 2.0$ Å and up, the wavelike pattern of the water density distribution was deformed and the density at P is smaller than that of the other parts. For $\delta \geqslant 2.5$ Å, the density distribution at P is very close to zero. Outside the CNT, the water density distribution is not affected by the shape of the CNT. There are two peaks near the two openings of the CNT due to the van der Waals (VDW) attraction of two graphite sheets.

The average number of water molecules inside the CNT of 13.4 Å is about five. For the CNT of 14.6 Å, the average number of water molecules inside the nanotube is about 5.5. The number of water molecules inside the CNT fluctuates with respect to time (see Fig. 1.14). There are two stable states with $N = 5$ and $N = 6$. The system switches mainly between the two states. The average durations for the states with

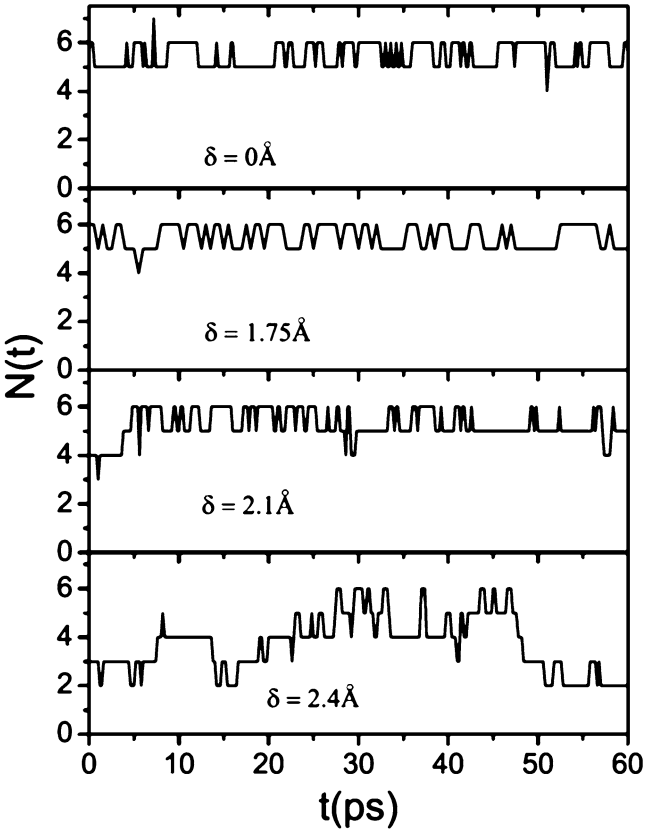

Fig. 1.14 Number of water molecules inside the carbon nanotube with respect to time in several representative systems (reprinted from [129]. Copyright 2008 American Physical Society)

$N = 5$ and $N = 6$ are 0.96 and 0.90 ps, respectively, showing similar probabilities for two states. When $\delta = 0$ Å, the total probabilities of $N = 5$, 6 are about 52 and 48%, both close to 50%.

The free energy of occupancy fluctuations $G(N)$ can be calculated by $G(N) = -k_B T \ln p(N)$, where $p(N)$ is the probability of N water molecules inside the nanotube, k_B is the Boltzmann constant, and T is the temperature.

Figure 1.15 shows that the free energy of $N = 5$ is close to the free energy of $N = 6$ for $\delta \leqslant \delta_c \approx 2.0$ Å. Profile of free energy of occupancy shows that two states of $N = 5$ and $N = 6$ are steady for $\delta \leqslant \delta_c \approx 2.0$ Å. The rapid transitions between the two states in the water permeation across the CNT are similar to those observed in the KcsA ion channel. However, for $\delta > \delta_c$, free energy of $N = 4$ is the minimum. The behavior of the single-filed water molecules inside the nanotube becomes different.

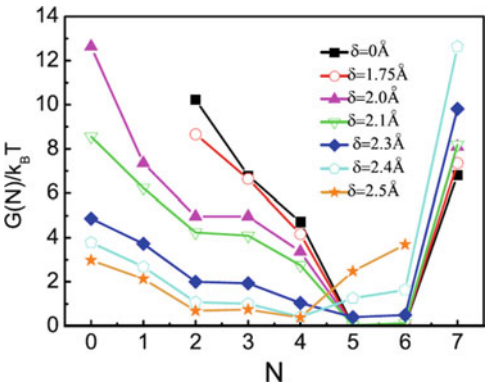

Fig. 1.15 Free energy of occupancy fluctuation for different δ (reprinted from [129]. Copyright 2008 American Physical Society)

Now, we consider the question why the water density distribution is so flat for the unperturbed nanochannel and the wavelike pattern becomes obvious as the CNT is deformed by external force.

For the unperturbed CNT with 14.6 Å in length, there are two steady states of $N = 5$ and $N = 6$. Their probabilities are both close to 50%. From Fig. 1.16, we can see that the water probability densities of $N = 5$ and $N = 6$ show obvious wavelike pattern. The average amplitude is about 0.32 $Å^{-1}$. The distance between troughs and crests of the waves is about 2.6 Å, close to the length of the hydrogen bonds between water molecules. However, the wave profiles of $N = 5$ and $N = 6$ are not in the same phase. The phase difference between them is about 1/2 period. Thus, the total water probability density becomes flat from the superposition of those two cases, especially in the middle region.

When the middle part of the CNT is pressed by the external force, the density distribution pattern changes correspondingly. It is noted that the crest of the water probability density of $N = 5$ just locates in the middle part of the CNT, while the corresponding position is the trough of the water probability density of $N = 6$. Thus, the wavelike pattern of $N = 6$ almost keeps the initial profile of $\delta = 0$ Å, while the amplitude of $N = 5$ becomes smaller. Thus, the flat profile of the total water density distribution is broken, showing a new wavelike pattern.

In the case of $\delta = 2.4$ Å, the middle portion of the CNT becomes narrower. There are clear valleys in the middle portion for all the cases of N, resulting in a big valley in the total water density distribution.

So now we know the reason why the total water density distribution in the middle part is flat and becomes wavelike pattern when the middle portion of the nanotube is narrowed. It results from the phase difference between the two states of $N = 5$ and $N = 6$, and the deformed portion just locates in the middle. But the origins of the wavelike pattern of water density distribution of $N = 5$ and $N = 6$ are still not clear.

First, we calculate the water–CNT interaction along the nanotube axis. The results are shown in Fig. 1.17.

"U"-like profile of water–CNT shows that the more middle water molecule locates in, the stronger the CNT attracts water molecules. When the middle portion

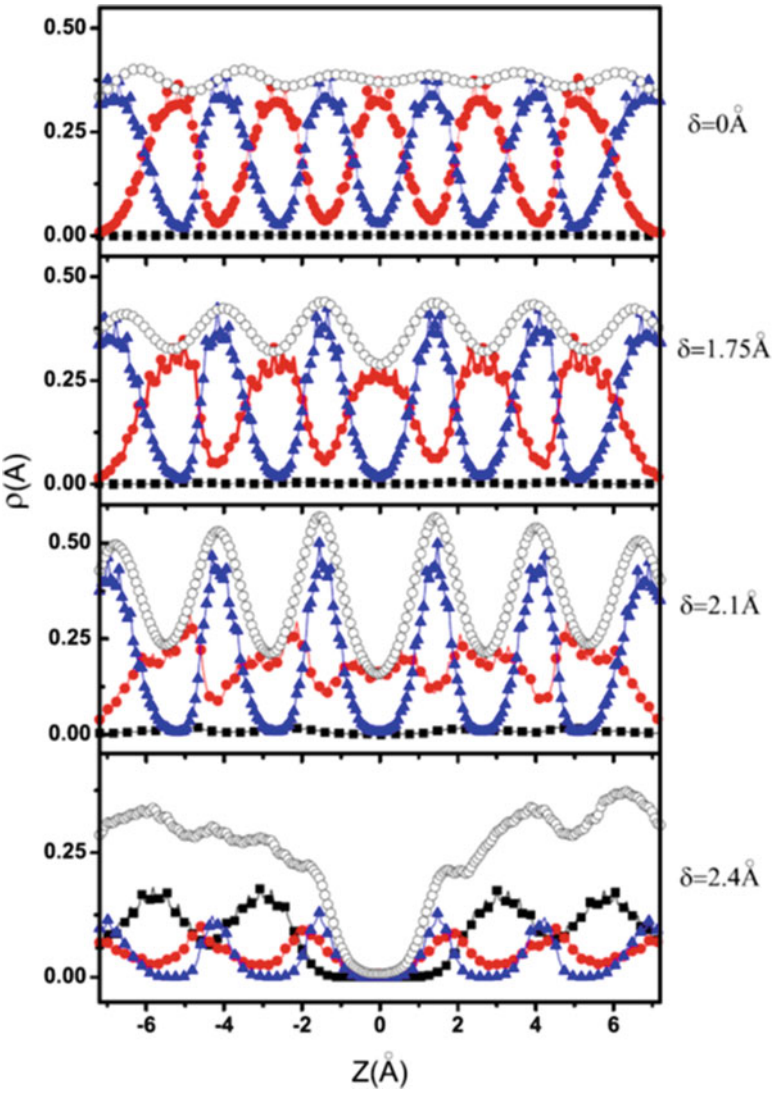

Fig. 1.16 Water probability density along the nanotube axis. *Black filledsquares* indicate the water probability density of $N = 4$, *red filledcircles* indicate the water probability density of $N = 5$, and the *open circles* indicate the total water probability density (reprinted from [129]. Copyright 2008 American Physical Society)

of the CNT is narrowed by the external force, the water–CNT interaction of a water molecule in the middle becomes positive. The profile changes from "U" shape to "W" shape. The deformed portion interrupts the single-filed water molecules inside the CNT.

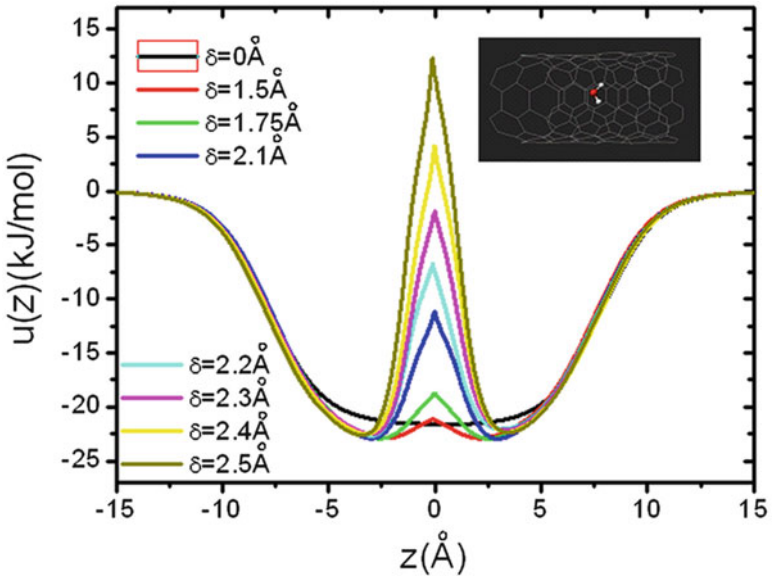

Fig. 1.17 Water–CNT interaction energy $u(z)$ of a water molecule at z with the carbon nanotube. The inset shows a water molecule locating in the center of the cross section at z of the carbon nanotube. Water–CNT interaction, $u(z)$, is calculated by $u(z) = 4\varepsilon_{CO} \sum_{i=1}^{i=156} \left[\left(\frac{\sigma_{CO}}{r_i} \right)^{12} - \left(\frac{\sigma_{CO}}{r_i} \right)^{6} \right]$, where r_i is the distance between the water molecule and ith carbon atom. In the calculation, we assume that the water molecule locates at the center of the cross section of the nanotube (reprinted from [129]. Copyright 2008 American Physical Society)

Now, we present a theoretical model to understand the origin of the wavelike pattern of water density along the nanotube axis. There are three assumptions:

1. Water molecules inside the nanotube form a single-filed chain.
2. The distance between any two neighboring water molecules inside the nanotube along the z direction is fixed, which is denoted by d.
3. The change in free energy of the single-filed water inside the nanotube mainly results from the change in water–CNT interaction energy $u(z)$ when the CNT is deformed by the external force. Water molecules inside the nanotube form a single-filed chain.

If we know the water–CNT interaction energy $u(z)$ and the distance between the two neighboring water molecules inside the CNT, according to the above three assumptions, we can calculate the water probability density along the CNT. Both the water–CNT interaction and the distance between the two neighboring water molecules can be obtained without numerical simulations. $u(z)$ is shown in Fig. 1.17. The equilibrium distance between the two water molecules is about 2.8 Å. Considering that the water molecules inside the channel are usually connected by

hydrogen bonds and appear in zigzag structure instead of a line (see Fig. 1.7), the distance between the two water molecules along the z direction is about 2.6 Å.

The total potential $U(z)$ of water molecules inside the CNT is given by

$$U(z) = \sum_{i=-\infty}^{i=+\infty} u(z + id) f(z_i), \tag{1.1}$$

where z is the coordinate of a water molecule (denoted by P_0). $i > 0$ indicates that the water molecule locates only in the right side of the $P_{0,}$ vice versa. $f(z_i)$ is a truncation function, which is given by

$$f(z_i) = \begin{cases} 1 \text{if} z_{\min} \leqslant z_i \leqslant z_{\max}, \\ 0 \text{if} z_i < z_{\min}, z_i > z_{\max}, \end{cases}$$

where $z_{\min}$ and $z_{\max}$ are the z-coordinates of the left and right ends of the CNT, respectively.

The probability density of finding water molecules at position z can be assumed as

$$\rho(z) = A \exp[-U(z)/k_B T], \tag{1.2}$$

where k_B is the Boltzmann constant, T is the temperature of the system, and A can be determined by the average number of water molecules in the CNT,

$$< N >= \int_{z_{\min}}^{z_{\max}} \rho(z) \mathrm{d}z. \tag{1.3}$$

According to (1.1) and (1.2), we can calculate the probability density of the representative systems.

Comparing between the theoretical results and the simulation results for $\delta = 0$ Å (see Fig. 1.18), we can find that the main structure of water probability density distribution is consistent. Similar to the simulation results, the curves of the theoretical result in the case of $N = 5$, 6 have five and six troughs, respectively. The peaks of the curves of the theoretical results are a little sharper than those of the simulation results, mainly results from that in the above model, the distance between water molecules inside the CNT is assumed to be a constant. In reality, the distance between neighboring water molecules fluctuates according to the interaction potential.

When the CNT is deformed by external force, the water–CNT interaction energy will increase correspondingly (see Fig. 1.17). According to (1.2), the probability of finding water molecules in the narrow portion of the CNT decreases. The deformation greatly changes the water density distribution especially for $N = 5$, while slightly for $N = 6$. The errors in the theoretical predictions increase with the deformation of CNT. The main reason is that the distance between neighboring

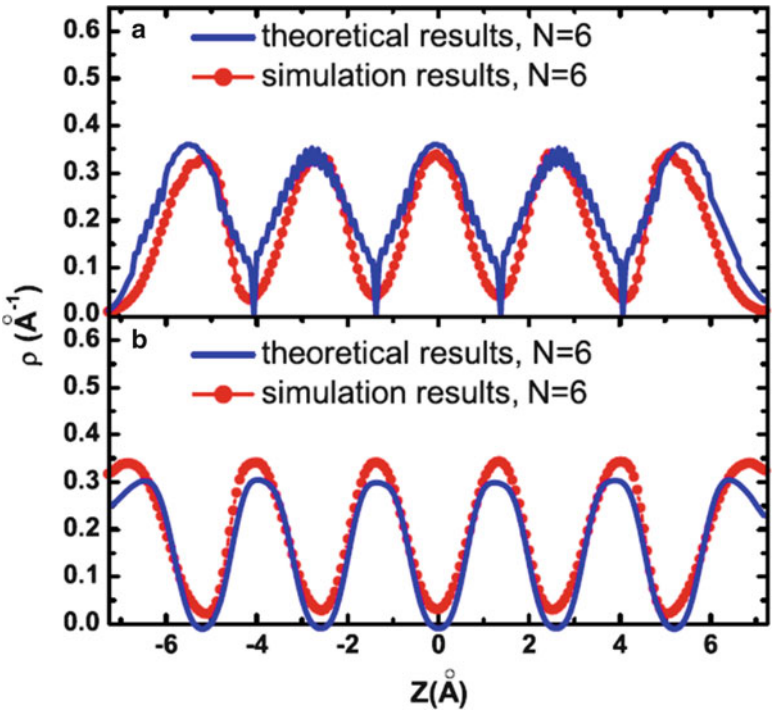

Fig. 1.18 The water probability density distributions along the nanotube axis for $\delta = 0$ Å (reprinted from [129]. Copyright 2008 American Physical Society)

water molecules located in the middle part of the nanotube increases. The distance between water molecules is not a constant in this case. But in the above model, d is assumed to be fixed. As δ further increases from δ_c, the error of the theoretical prediction increases very quickly (see Fig. 1.19).

From the theoretical model, we can understand the origin of the wavelike pattern of water density distribution inside the CNT. The wavelike pattern mainly results from the potential barriers at both ends of the nanotube together with the tight hydrogen-bonding chain inside the tube that fixes the distance between neighboring water molecules approximately.

We know, for molecular biological systems, that the external and internal fluctuations are usually nonnegligible. In this section, we will discuss the effect of the external fluctuation on water molecule transportation. Different from the above where the forced-atom is fixed, if the forced carbon atom vibrates periodically, the behavior of the single-filed water chain inside the CNT still keeps stable. The simulation framework is similar to the simulation system in Fig. 1.3. In this system, the forced-atom is forced to move according to the equation

$$x = x_0 + A\cos(\omega t + \phi),$$

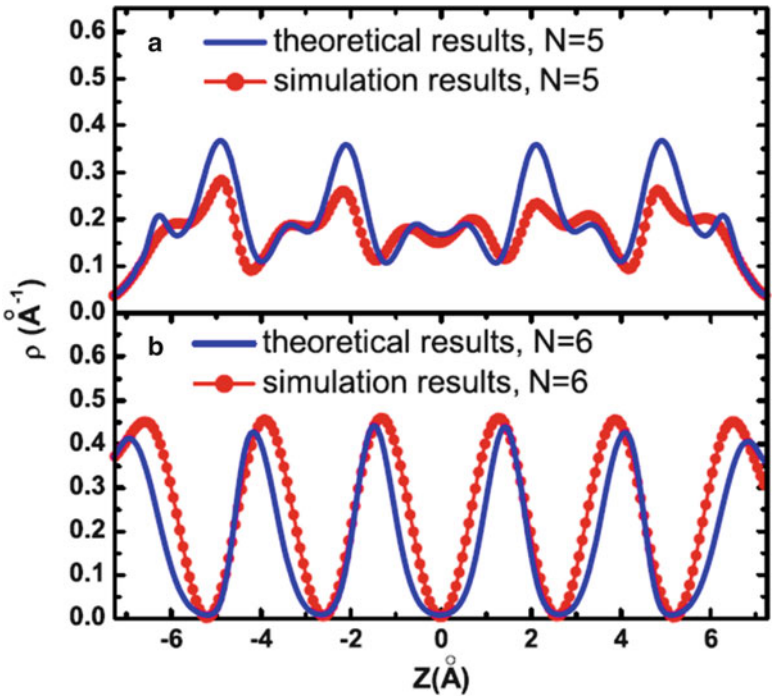

Fig. 1.19 The water probability density distributions along the nanotube axis for $\delta = 2.1$ Å (reprinted from [129]. Copyright 2008 American Physical Society)

where x_0 is the initial position of the vibrating carbon atom, A is the amplitude, ω is angular frequency, and ϕ is the initial phase. The frequency is defined as $\frac{\omega}{2\pi}$. It is found that the vibrating frequency, f, plays a role in water transportation through (6,6) CNT.

From the simulation result shown in Fig. 1.20, we can find that the water flow, net flux, and $<N>$ almost keep the value of the unperturbed system when the frequency $f < f_c \approx 1,333$ GHz. The corresponding period time is 0.75 ps and the velocity of the moving-atom under this frequency (f_c) is about 200 m/s, about half the average thermal velocity of water molecules (nearly 400 m/s) at room temperature. In real systems, it is impossible for a carbon atom in CNT to vibrate at such a high velocity and in such a large amplitude (2 Å). Thus, the permeation property of the water molecules confined in the nanochannel can be effectively shielded from strong noise.

From Fig. 1.21, we can find that the water density distribution maintains the similar wavelike pattern for $f < f_c \approx 1,333$, which leads to the invariability of the total number of water molecules inside the nanotube. The single-filed water chain connected with hydrogen bonds can accommodate the fluctuation of the CNT due to external force. For $f > f_c$, the wavelike pattern of density distribution is destroyed.

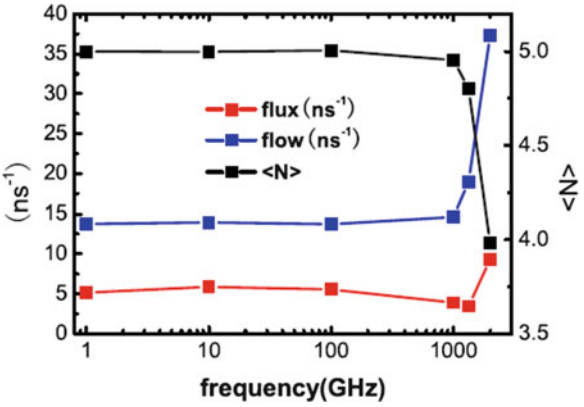

Fig. 1.20 Flux, flow, and average number of water molecules inside the CNT for different vibrating frequencies f (reprinted from [130]. Copyright 2008 Chinese Physics Society)

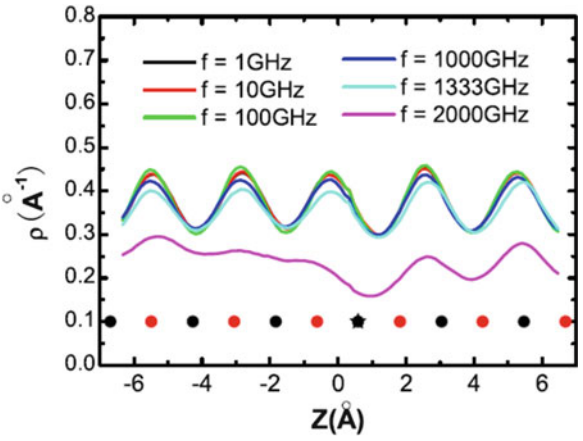

Fig. 1.21 Water density distribution along the nanotube axis. The *open* and *filled circles* denote the locations of the carbon atoms. The *asterisk* is the position of the vibrating atom affected by an external force (reprinted from [130]. Copyright 2008 Chinese Physics Society)

Fluctuations of CNT induce the number of water molecules inside the nanotube to decrease and the velocity of the transportation of water chain to increase.

Water molecules confined inside the (6,6) CNT form a single-filed chain connected by hydrogen bonds. An important feature of the hydrogen bond is that it possesses directionality (see Fig. 1.1). Molecular transport through the quasi-one-dimensional CNT is highly collective, since motion of one water molecule requires concomitant motion of all water molecules in the file. The chain rarely ruptures because of the tight hydrogen bonds in the protective environment of the CNT. Hydrogen bonds nearly align along the nanochannel axis and collectively flip in their orientations. The orientation of water chain is defined by a characteristic angle $\overline{\varphi}$ [40]. There are two stable states $15° < \overline{\varphi} < 50°$ and $130° < \overline{\varphi} < 165°$ and $\overline{\varphi}$ switches between them (see Fig. 1.22). Here we define a flip as $\overline{\varphi}$ transforms from one state to another state passing through $\overline{\varphi} = 90°$. During the flipping process, under the transition state, a hydrogen bond defect along the water chain inside the SWNT is formed. The flipping frequency f_{flip} for different vibrating frequency is shown in Fig. 1.23. Interestingly, the effect of the vibration of the CNT on the

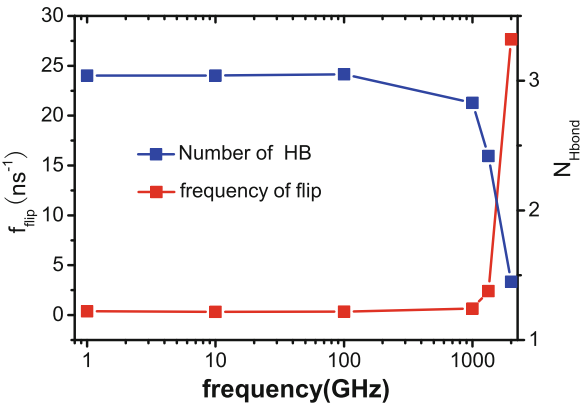

Fig. 1.22 Characteristic angle, $\overline{\varphi}$, for different vibrating frequency f (reprinted from [130]. Copyright 2008 Chinese Physics Society)

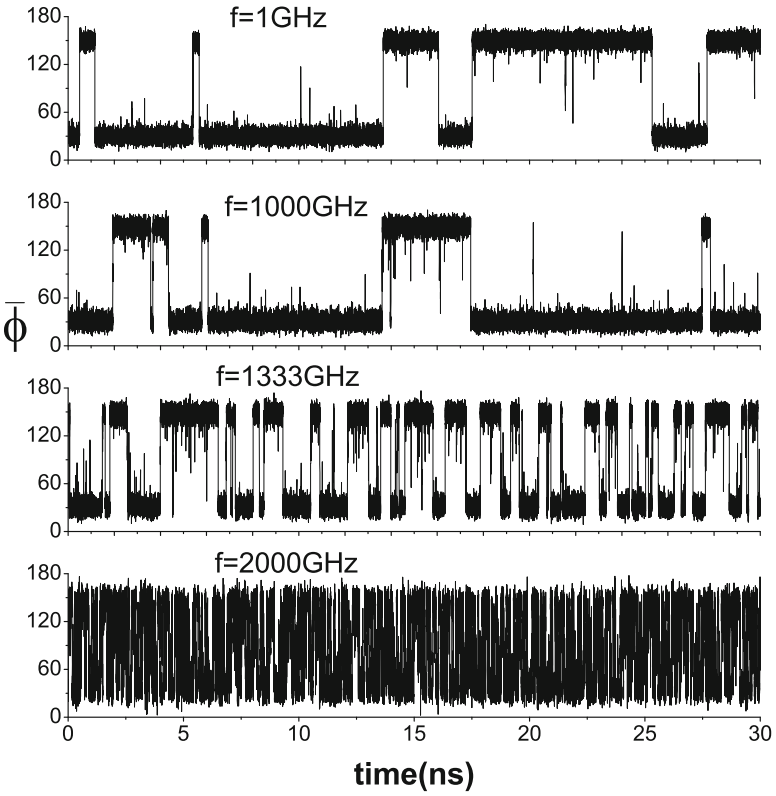

Fig. 1.23 Average number of the hydrogen bonds inside the nanotube and the flipping frequency for different vibrating frequency f (reprinted from [130]. Copyright 2008 Chinese Physics Society)

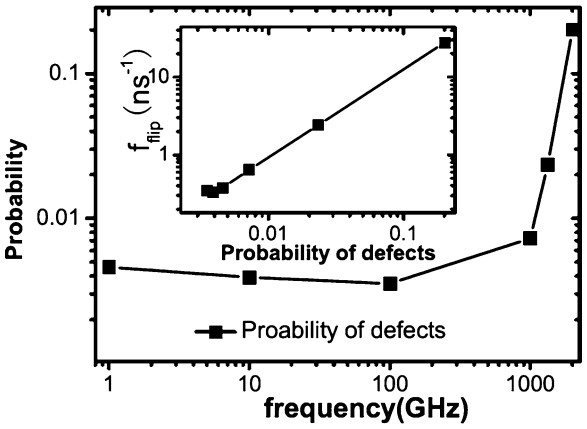

Fig. 1.24 Probabilities of defects vs. vibration frequency f and (inset) f_{flip} with respect to the probabilities of defects (reprinted from [130]. Copyright 2008 Chinese Physics Society)

frequency of flip is limited for $f < f_c$, which results from the stability of the whole water chain confined inside the CNT. As f becomes larger than f_c, the flipping frequency increases sharply. The hydrogen bond near the middle part of water chain is usually broken due to violently vibrating, which induces hydrogen bond defects in the middle portion of the CNT, not only in the inlets of the nanotube.

The dipole flip of ordered water chain inside the CNT is the process that a hydrogen-bonding defect moves through the tube. Figure 1.24 gives the probability of defects (corresponding to transition states) with respect to the vibrating frequency and the relationship between the dipole flipping frequency and the probability of defects. Similar to the above results, for $f < f_c$, the effect of the vibrating fluctuation on the formation of defects is slight. As frequency grows above f_c, the probability of defects increases dramatically. Correspondingly, the dipole flipping frequency increases sharply. From simulation results shown in the inset of Fig. 1.24, we find that the function $f_{\text{flip}} = f^0_{\text{flip}} + A * P$ can fit the data quite well, where P is the probability of defects in water chain, $f^0_{\text{flip}} = -0.36\text{ns}^{-1}$, and A is 139.47 ns^{-1}.

The above sections have discussed the effects of the geometrical shape on the transportation of water molecules through the nanochannels by deforming the CNT. Simulation results indicate that pressing the middle part of the CNT by external force can control the transportation of water chain well. Now we focus on discussing the effects of the position of the controllable region on water transportation.

The simulation framework is shown in Fig. 1.25. In order to explore the effect of the position of the narrow region on water transportation, one carbon atom (the forced-atom) is pushed away from its initial position, resulting in 2.2 Å radial displacement in each simulation system. Seven different systems are considered by choosing different forced-atoms (spheres of the nanotube shown in Fig. 1.25). For the convenience of analysis, the middle carbon atom is taken as the origin point of the z axis, and the distance between the forced-atoms and origin point is denoted by d. The positions of forced-atoms indexed from 1 to 7 are −7.4, −4.9, −2.5, 0, 2.5, 4.9 and 7.4Å, respectively.

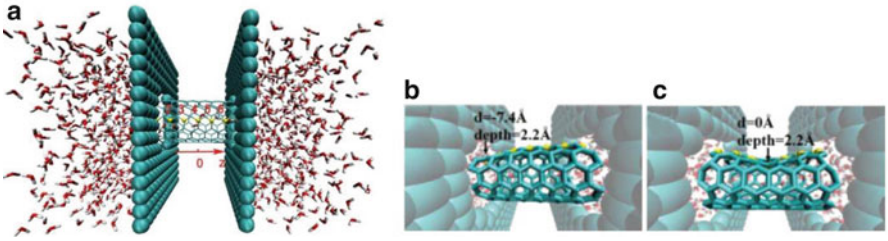

Fig. 1.25 Simulation framework. The spheres of the nanotube denote the possible forced-atoms and d is the z coordinate of the possible forced-atom (reprinted from [131]. Copyright 2011 American Physical Society)

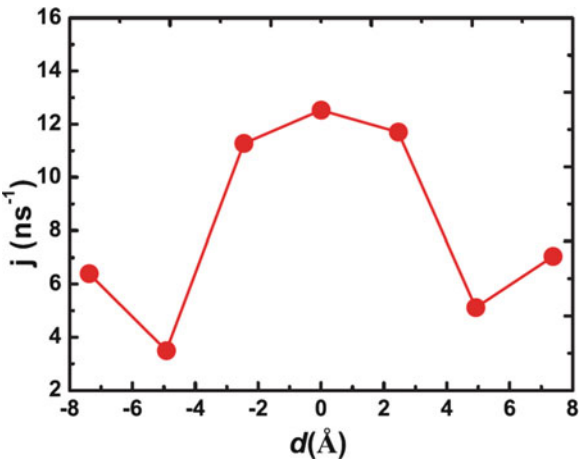

Fig. 1.26 The water flux across the carbon nanotube for different deformation positions d (reprinted from [131]. Copyright 2011 American Physical Society)

Our first observation is that the net water flux is sensitive to the position of the deformation (see Fig. 1.26). For the unperturbed CNT, the net water flux is about 14.8 ns^{-1}. The W-type profile shows that the water flux peaks at 12.5 ns^{-1} when the deformation exists in the middle region ($d = 0$ Å) of the SWNT. And it decreases sharply as long as the deformation position moves away from the middle region. Note that if the deformation position moves from $d = 0$ Å to $d = -4.9$ Å (~2.5 Å distance from the end of the nanotube), the net water flux reaches the minimum. One readily sees that the net water flux decreases dramatically when the deformation position occurs near the end of the SWNT. The flux for $d = -4.9$ Å falls to only approximately one quarter of the flux for $d = 0$ Å. In other words, the nozzle effect is very important for water permeation. Furthermore, simulation results indicate that the W-type profile is not fully symmetrical, even though the deformation positions are symmetrical at approximately $d = 0$ Å (see Figs. 1.25 and 1.26). For example, the net water flux for $d = -4.9$ Å (3.5 ns^{-1}) is obviously smaller than that for $d = 4.9$ Å (5.1 ns^{-1}). Meanwhile, the net water fluxes for $d = -7.4$ and 7.4 Å also exhibit similar behavior and their values are 6.4 and 7.0 ns^{-1}, respectively.

We now come to exploit the question why the location of the narrow portion plays a key role in water transportation through the nanotube. We have known that the transportation behavior of water molecules is mainly determined by the profile of the total interaction potential (it is denoted by the symbol P in this chapter). In this section, potential includes two parts: one is the water–water interactions (the interaction energies of the water molecule at position z inside the SWNT with its neighboring water molecules), denoted by P_{WW}, and the other part is the water–SWNT interactions (the interactions of the confined water at position z with the carbon atoms of SWNT), denoted by P_{WC}. It is consistent with the results shown in Fig. 1.17 that the potential energy curve of P_{WC} for the unperturbed SWNT has a symmetrical "U-like" shape, and the lowest is located in the middle of the SWNT (the position of $z = 0$ Å). When the SWNT is narrowed at d, the potential barrier appears at $z = d$. The profile of the curve of P_{WC} changes from a "U-like" shape into a "W-like" shape. As the location of the narrow portion moves to the ends of the nanotube, the peak of P_{WC} moves to the openings of the nanotube correspondingly, and the height of the peak increases due to a "U-like" shape of P_{WC} for the unperturbed SWNT.

Water molecules inside the CNT are connected by hydrogen bond. The strength of the energy is about $10\,k_BT$. For $|d| \leqslant 2.5$ Å, the hydrogen-bonding chain structure inside the SWNT is still perfect because the water–SWNT interaction potential P_{WC} is negligible compared to the strength of the hydrogen bond. However, if the location of the deformation moves out from the middle region, the water–SWNT interaction energy increases obviously. Thus, for $|d| \geqslant 4.9$ Å, the possibility of producing defects by breaking the hydrogen bond increases dramatically. Figure 1.27 shows that P_{WW} for $d = -4.9$ Å peaks at $z = -2.1$ Å, which is ~2.8 Å (about the size of a water molecule) away from the deformed position of $z = d = -4.9$ Å, indicating that the hydrogen bond that connects between the water molecule at $z = -2.1$ Å and its left one (the water molecule at $z = -4.9$ Å) usually is violated. Correspondingly, for $d = -4.9$ Å, the value of P_{WW} ($z = -4.9$ Å) is lower than that of P_{WW} ($z = -2.1$ Å). In fact, it results mainly from that the possibility of the water molecule located in $z = -2.1$ Å is larger than that in $z = -4.9$ Å due to P_{WC} ($z = -4.9$ Å) > P_{WC} (-2.1 Å). Certainly, the average number of the hydrogen bonds of the water molecule at $z = -2.1$ Å is larger than that of the water molecule at $z = -4.9$ Å. In other words, when there is a water molecule near $z = -4.9$ Å, usually there exist water molecules in two sides of it (near $z = -2.1$ Å and $z = -7.7$ Å), rather than vice versa. P_{WW} ($z < -4.9$ Å) is lower than P_{WW} ($z > -4.9$ Å) because the water molecules in the region of $z < -4.9$ Å are closer to the bulk water than those in the region of $z > -4.9$ Å. The same mechanism (water molecules near $z = -7.9$ Å are closer to the bulk water than those near $z = -4.9$ Å) makes the height of the peak of P_{WW} for $d = -7.4$ Å lower than that for $d = -4.9$ Å. The total interaction potential $P(z)$ is given by $P(z) = P_{WC}(z) + P_{WW}(z)$. For $d = -7.4$, -4.9, 4.9, and 7.4 Å, the distributions of $P(z)$ are lifted up. The higher the total interaction potential is, the less the water flux through the CNT is. In the case of $d = 0$ Å, the average interaction potential is lower than that in the others, which results in the largest net flux. In the cases of $d = -4.9$

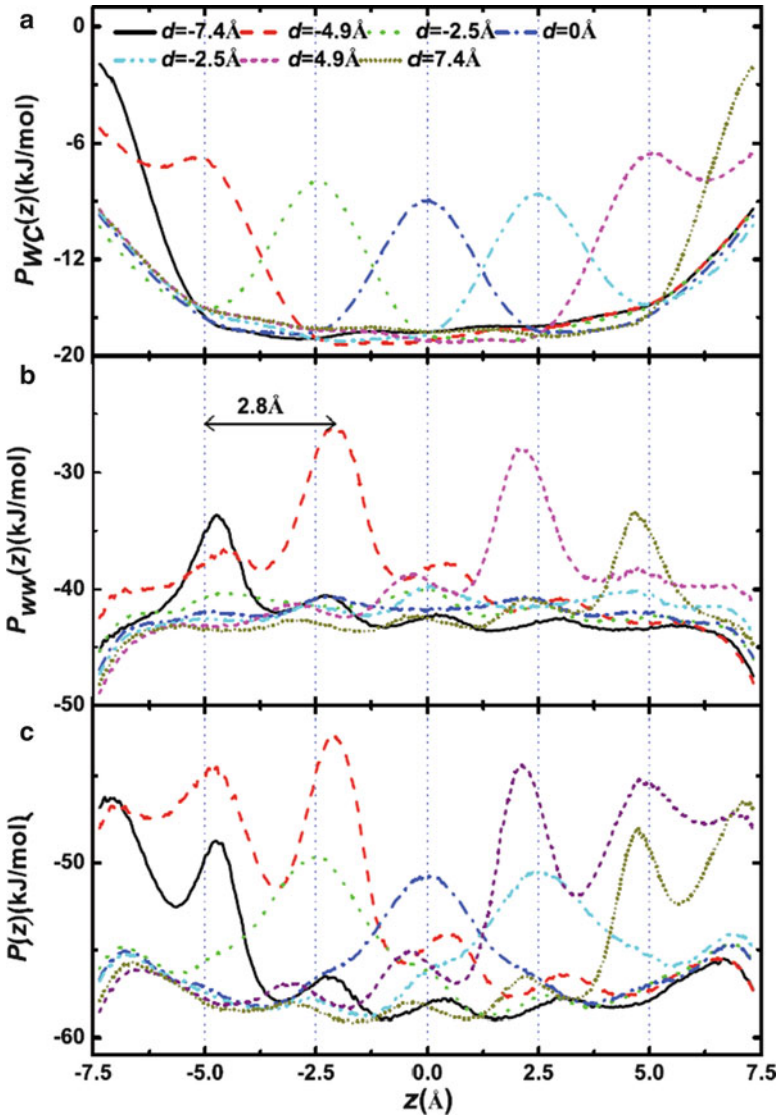

Fig. 1.27 The average water–SWNT interaction energy, water–water interaction energy, and the total interaction energy along z for different d (reprinted from [131]. Copyright 2011 American Physical Society)

and 4.9 Å, the average interaction potentials are large. Correspondingly, the net water flux in these two systems is small. The net water flux is mainly regulated by the water–water interaction and water–carbon interaction. The different position of the narrow region results in a change of the total interaction potential, meanwhile the net water flux changes.

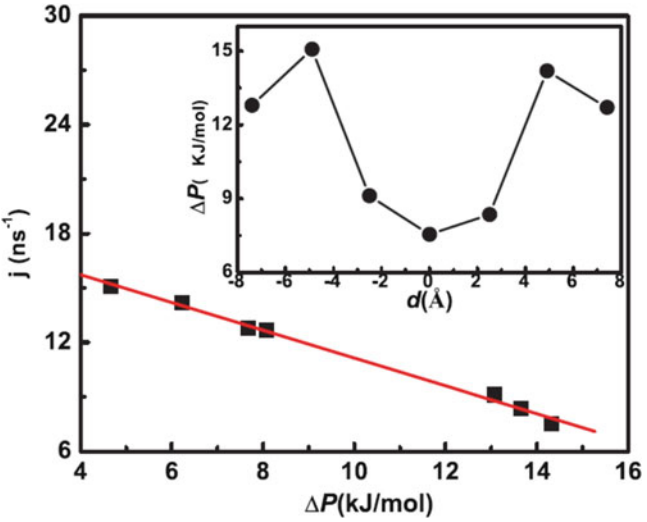

Fig. 1.28 The water flux j for different ΔP and (inset) ΔP for different d. In this figure, ΔP is the difference between the maximum and the minimum of the interaction potential, which is usually used to characterize the potential profiles (reprinted from [131]. Copyright 2011 American Physical Society)

From Fig. 1.28, we can find the M-type profile of ΔP, showing that ΔP approaches to the minimum as the narrow portion moves to the middle of the SWNT. The corresponding value of ΔP is $\sim$7.7 kJ mol^{-1}, only half of the ΔP for $d = -4.9$ or 4.9 Å. Consequently, the flux for $d = 0$ Å approaches to the maximum. From the simulation results shown in Fig. 1.28, we can find that the water flux decreases almost linearly with increasing ΔP. The data can be well fitted by the following formula:

$$j = j_0(1 - \Delta P/\varepsilon),$$

where $\varepsilon \approx 18.1$ kJ mol^{-1} and $j_0 = 21.7$ ns^{-1}. According to the above fitted formula, the net water flux would decrease to zero when $\Delta P = \varepsilon \approx 18.1$kJ mol^{-1}. To check the validity of the prediction, a system of depth = 2.3 Å and $d = -4.9$ Å was simulated, and then the simulation result shows that the net water flux is still $\sim$0.6 ns^{-1} and the matching ΔP is $\sim$22 kJ mol^{-1}, implying that the fitted linear law is a good fit only for $\Delta P < 16$kJmol^{-1}.

From the above simulation results and discussions, it is concluded that the water flux is not only sensitive to the strength of the deformation but also significantly influenced by the location of the deformation. When the deformation is just located in the middle of the nanotube, forming an hourglass-shaped region, the water flux across the nanotube reaches a maximum. Simulation results furthermore indicate that the hourglass shape is more convenient for water molecules to pass through the nanotube than a funnel shape.

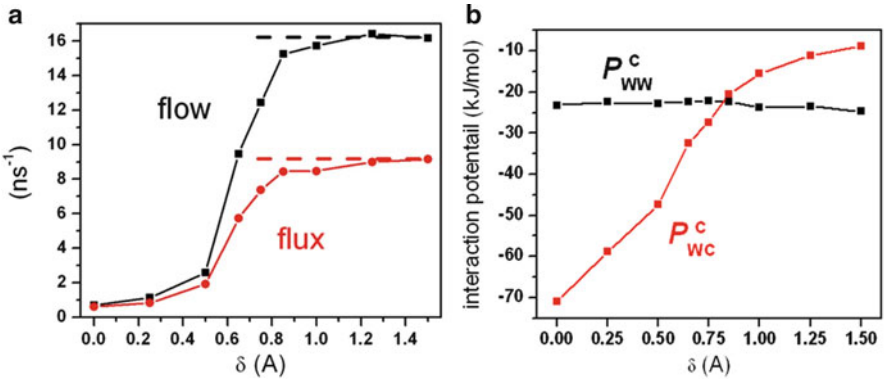

Fig. 1.29 (**a**) Averaged water flow (*black*) and net flux (*red*) through the channel with respect to δ, together with those for the system without an external charge (*dashed lines*). δ is the distance of the imposed charge to the centerline minus the radius of the single-walled carbon nanotube. (**b**) Values of P^{C}_{WC} and P^{C}_{WW}, with respect to δ. P^{C}_{WC} is the electrostatic potential between the water molecule in the middle of the nanotube with the imposed charge, and P^{C}_{WW} is the average value of the electrostatic potential between the water molecule and one of its neighboring water molecule (reprinted from [22]. Copyright 2007 National Academy of Science, USA)

Electrical field can also be used to control the channels. Electrical field can be initiated by an external charge. As is shown in Fig. 1.29, we have introduced a positive charge of quantity $1.0e$ on the plane of the graphite that divides the full space into two parts [22]. Similar to the case under the deformation of the SWNT, the average flow and net flux across the channel are approximately equal to those in the system without any charge until a value of $\delta_C = 0.85$ Å. Here, the distance of the imposed charge to the centerline minus the radius of the SWNT is also denoted by δ. Both the average flow and net flux decrease monotonically and sharply as δ further decreases. At $\delta = 0$, the channel is almost closed with the average flow below 1.0 ns^{-1}.

These behaviors result from the competitions between the water–charge interaction and the water–water interaction (mainly from the hydrogen bonds). As is shown in Fig. 1.2, all the water molecules inside the channel have orientation concerted, along or opposite to the nanotube. This orientation distribution is not easy to be changed by an external charge outside the nanotube due to the strong hydrogen bonds between the neighboring bonds. Only when the charge is close enough so that the interaction of the water and the charge is comparable to a hydrogen bond, the water chain inside the nanotube shows considerable change. In Fig. 1.29, we show the average value of the electrostatic potential between the water molecule in the middle of the nanotube with the imposed charge, P^{C}_{WC}, together with the average value of the electrostatic potential between the water molecule and one of its neighboring water molecule. It is clear that at $\delta \approx \delta_C$, $P^{C}_{WW} = P^{C}_{WC}$. Further approach of the charge makes the interaction between the water and the charge stronger, and the orientation of the water molecule facing the charge changes its

direction, becoming to point to the external charge, which makes the interaction between the water and the charge even stronger. This will result in more difficulties when water molecules move along the nanotube, thus the net flux across the nanochannel decreases.

It seems that the water permeation across the bio-mimicked nanochannel with single-filed water molecules inside the nanochannel is also effectively resistant to charge noises and sensitive to available charge signals.

Now we have come to the structure of aquaporins again. The structure of aquaporins is appropriate that the water molecules inside the pore are single filed. Moreover, compared to the CNT, aquaporins are much more complex while the functions of most of the structures are unknown. There are two impressive parts in those complex structures: the two highly conserved fingerprint Asp–Pro–Ala (NPA) motifs in the pore center are proposed to determine the selectivity of permeation for the channel, and the ar/R region near extracellular side, formed by the aromatic side chains of Phe and His, and Arg, is proposed to function as a proton filter [32]. We note that there are some important charged parts on these regions: the Arg residue on ar/R region is positively charged ($+1e$); the two Asn residues on NPA motifs can be considered to be carrying an effective charge of $+0.5e$ on each residue, since they are at the ends of two α-helixes (it is known that an α-helix has a net dipole moment whose magnitude corresponds to a charge of 0.5–0.7e at each end of the helix [41]). With further steps to understand the functions of those parts in the aquaporins and trying to design nanochannels inspired by aquaporins, we assign the charges on those parts near a CNT, as shown in Fig. 1.30.

Explicitly, an SWNT 23 Å in length and 8.1 Å in diameter is embedded along the vertical direction between two graphite sheets, and three positive charges with charge magnitudes of 1.0e, 0.5e, and 0.5e are positioned at $z = -d$, −0.7 Å, and 0.7 Å, respectively, where $z = 0$ corresponds to the center of the channel. All of the positive charges are at the same radial distance, δ, from the carbon atoms. Numerically, they have found that when $\delta \approx$ 0.5 Å, there is a considerable net flux from top to bottom.

1.1.2 Manipulating Biomolecules with Aqueous Liquids Confined Within Nanoscale Channels

One thing we are inspired from this molecular water pump is that there is a strong interaction between the charge outside the nanotube and the water molecules inside the nanotube. This is because of the ordered dipole orientations of the water molecules inside the nanotube when there is a charge outside the nanotube. It is the ordering of the water dipole orientations that makes the interaction between the charge and the water molecules strong. In Fig. 1.31, we have shown the averaged dipole orientation $<\theta>$ of water molecules when there is a charge outside the nanotube (see inset in Fig. 1.32), where r is the distance of a water molecule inside

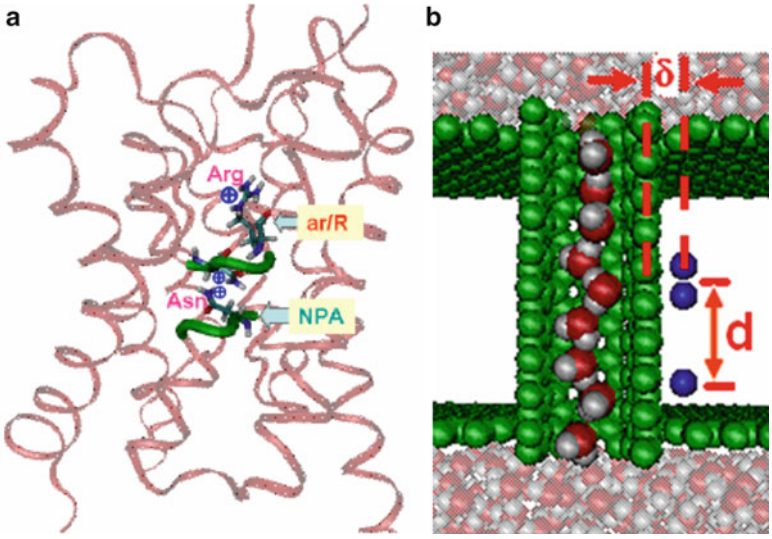

Fig. 1.30 Structure of AQP1 together with a scheme of the molecular water pump. (**a**) Ribbon diagram of the structure of AQP1. Two NPA regions are in green tube form. The ar/R region is around the Arg residue. The Arg and Asn residues are in licorice form. The Arg residue has a $+e$ net charge, and the two Asn residues on NPA motifs can be considered to carry an effective charge of $+0.5e$ on each residue (see text for details). The X-ray structure of AQP1 is obtained from Protein Data Bank (PDB) (reprinted from [18]. Copyright 2008 Institute of Physics, UK) (**b**) snapshot of the system, side view. The *green spheres* are the carbon atoms of the nanotube and the graphite sheets. The *blue points* are the positive charges. The figure is not drawn to scale that the sizes of water molecules and charges are enlarged (reprinted from [43]. Copyright 2007 Nature Publishing Group)

the nanotube and the external charge, θ, is defined as the angle between the dipole orientation of the water molecule and the line connecting the oxygen of the water molecule and the external charge. It is clear that $<\theta>$ approaches 90° when r is large enough, and the departure of $<\theta>$ from 90° shows the ordering of the water orientations. We can even predict the electrostatic interaction energy of the external charge with a water molecule at r, denoted by E_{theory}, from this $<\theta>$ distribution with the dipole moment for each water molecule ($0.489e$ Å in the TIP3P water model). As is shown in the figure (red symbols •-•), E_{theory} agrees well with the simulation result $E_{\text{simulation}}$ (the black symbols ■-■).

With this observation, we can manipulate a drop of water in the nanotube by a charge outside the nanotube. When there is a biomolecule in the water drop, we can even manipulate its position. As the charge moves along, the water–peptide mixture will follow it inside the nanotube. As the example shown in Fig. 1.32, we have shown the x-coordinate of the COM of the peptide and the peptide–water mixture as a function of time together with the x-coordinate of the external charge. We can see that the peptide–water mixture shows controllable movement by the manipulation of external charge [42]. As we know, encapsulating the molecules into

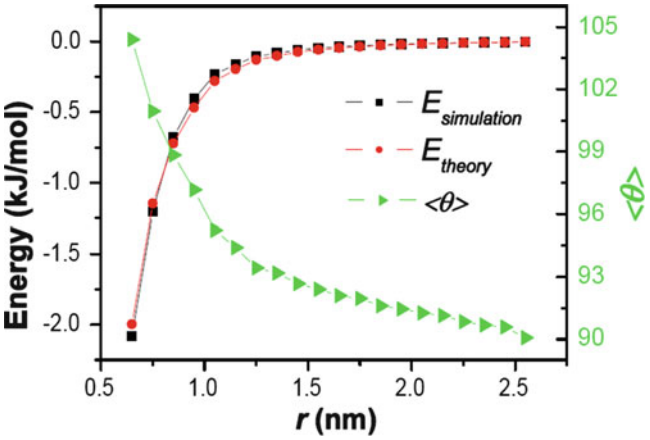

Fig. 1.31 Water–charge electrostatic interaction energy (E_{theory} *and* $E_{\text{simulation}}$) together with the averaged dipole orientation of water molecules $<\theta>$ (*green* and *right Y*-axis) with respect to the distance between a water molecule and the external charge for $q = 0.5e$. E_{theory} (*red symbols*) is computed from the $<\theta>$ distribution and $E_{\text{simulation}}$ (*black symbols*) is determined directly from numerical simulations (reprinted from [42]. Copyright 2009 American Chemical Society)

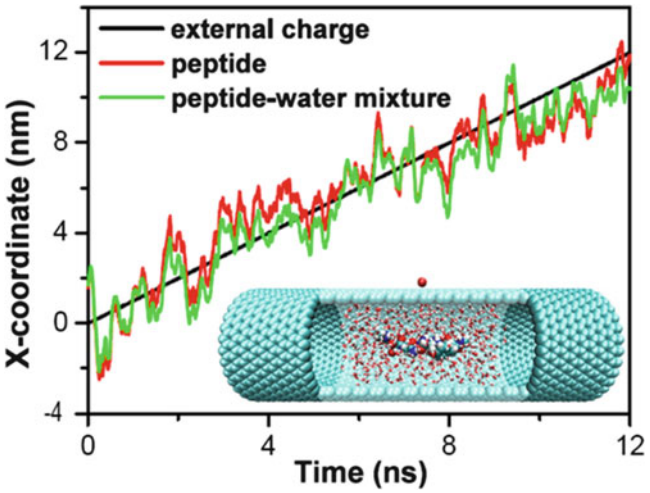

Fig. 1.32 *X*-coordinate of the center of mass of the peptide and the peptide–water mixture as a function of time, together with the *x*-coordinate of the external charge for the effective charge $q = 0.5e$. Inset: a water droplet with the peptide (GNNQQNY) in a single-walled carbon nanotube (SWNT) together with a charge (*big redsphere*) outside the tube. The *light bluespheres* represent the SWNT. Some carbon atoms of SWNT are not shown or drawn transparent for demonstration. The other colored spheres in the middle of SWNT are the atoms of the peptide

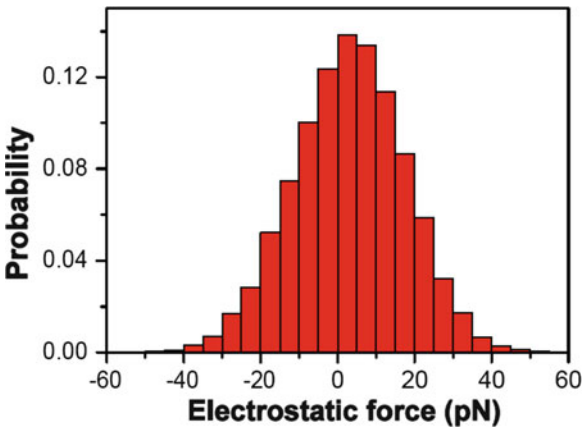

Fig. 1.33 The electrostatic forces by the external charge exerting on the peptide–water mixture along the *x*-axis for the case of System I when $q = +0.5e$. The positive direction of the force is the positive direction of the *x*-axis, and a 5 pN force interval is used (reprinted from [42]. Copyright 2009 American Chemical Society)

nanoscale pores can lead to interesting properties and behaviors that significantly differ from those of bulk systems [6, 21, 22, 32, 40, 43–59], including the enhanced catalysis [44, 45] and enhanced stability of the native structure of proteins [47], new folding mechanisms of proteins [49, 50], ordered water structure [52–54], extrafast motion of water molecules [6, 21, 46], non-Fickian-type diffusion [55], and excellent on–off gating behavior [22, 40]. Furthermore, it has been found that when the molecules are confined in nanosized water droplets [60, 61], their structures, hydrophobic and ionic interactions differ from those in bulk water [62, 63]. Manipulating the positions of the molecules encapsulated in the nanopores with respect to time is important in controlling the interactions or chemical reactions of the inner molecules. In recent years, there have been considerable efforts [14, 64–70] devoted to the study of the translocation/permeation of molecules along/through the nanochannels. Yeh and Hummer used an electric field to drive the charged macromolecules through nanopores [64]. Longhurst and Quirke made use of capillary force to draw decane molecules into an SWNT and temperature difference to drive their transport through the SWNT [67]. Zhao et al. demonstrated experimentally that a water flow can be driven by the applied current of the SWNT [14]. Král used laser to excitate an electric current in the CNT, thus resulting in a net force on ions absorbed in the nanotube [70].

We have also calculated the electrostatic force that the external charge exerts on the peptide–water mixture along the *x*-axis. The electrostatic forces dominatively range from −40 to +40 pN (see Fig. 1.33), which fall within the working ranges of many existing techniques such as STM and AFM. This result suggests that the AFM/STM tip carrying charge(s) may be able to manipulate the peptide with aqueous liquids according to the method described here.

Furthermore, on the basis of the above design, we can controllably move two biomolecule–water mixtures together conveniently for the interaction of the two biomolecules, as demonstrated in Fig. 1.34. Here, we use the same peptides used

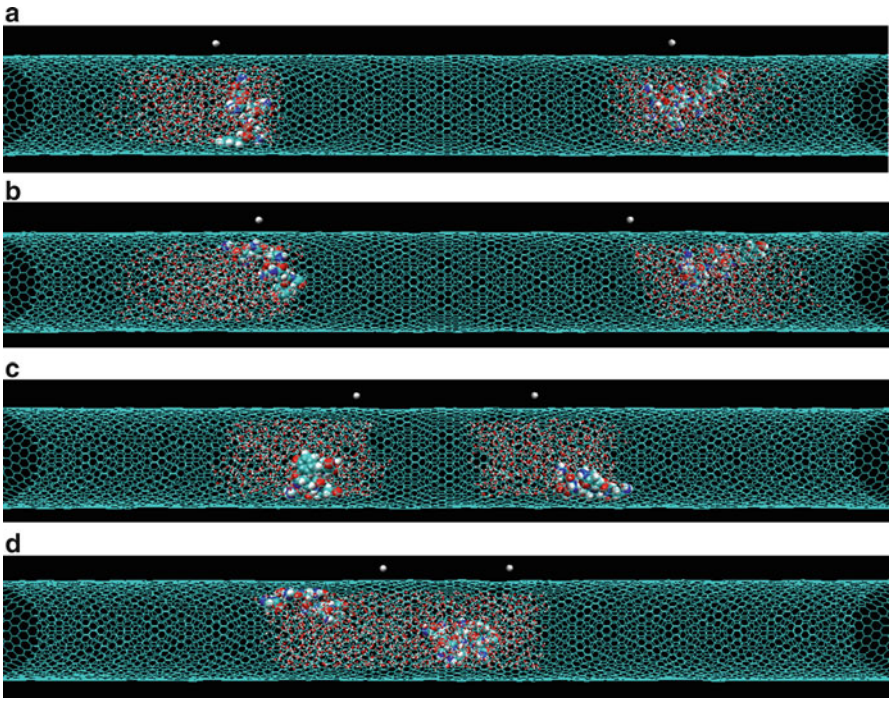

Fig. 1.34 Controllable moving of two biomolecule–water mixtures together. The *light greenlines* (linked hexagons) represent the SWNT. The colored spheres inside SWNT are the atoms of the peptide. The *white spheres* outside the SWNT are the external charges (each has a value of $+0.5e$) and the *red–white dots* are the water molecules

in the text (Ace–GNNQQNY–NMe) for demonstration. Each external charge has a value of $+0.5e$. The counterion with a value of $-1e$ is constrained at the edge of the box.

There are many factors affecting the manipulation. First, let us discuss the influence of the quantity of the external charge on the manipulation. Thermal fluctuation will sometimes make the manipulation unsuccessful, but for $q = \pm 1.0e$, this is a rare event. When $q = \pm 0.5e$, we have observed that the peptide–water mixture follows the external charge in 8 of the 11 simulations for the same systems with different initial conditions. In the cases where $q = \pm 0.33e$ and $\pm 0.25e$, the peptide–water mixture has low probabilities to follow the external charge.

Second, we have found that the speed of the external charge has a remarkable influence on the manipulation. When the speed of the external charge increases from 1 to 10 m/s, only one successful manipulation is observed in ten simulations with different initial conditions. We expect that as the speed of the external charge decreases, the probabilities for these unsuccessful cases decrease. Usually, the speed of the AFM/STM tip is within the magnitudes from 1 nm/s to 1 μm/s. Considering that the speed of the external charge in our simulation is up to 1 m/s, the rate

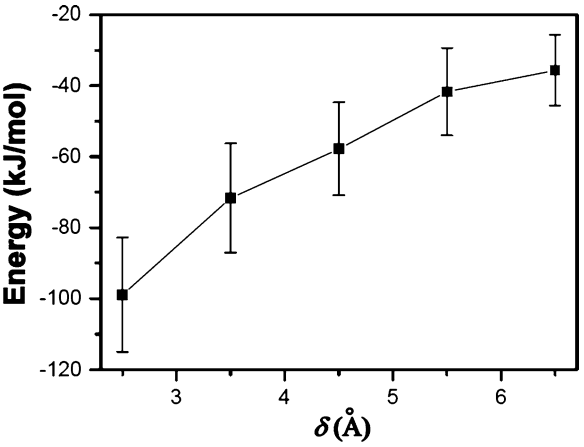

Fig. 1.35 The electrostatic interaction energies between the external charge and the water molecules with respect to the distance of the external charge from the tube wall (defined by δ) for the case of System I when $q = +1e$. The *error bars* show the fluctuations due to thermal noise (reprinted from [42]. Copyright 2009 American Chemical Society)

for a successful manipulation may even be higher for a much lower speed under experimental conditions. When the peptide is substituted by a larger molecule such as a protein, the effective value of the external charge required for successful manipulation should be larger. We note that in the case where the probability of the successful manipulations by a single charge is low, we can use a series of charges, which can greatly enhance the successful probabilities.

Third, the distance of the external charge from the tube wall (defined by δ) also influences the manipulation. For System I, as is shown in Fig. 1.35, the electrostatic interaction energy between the external charge with the effective value of $q = +1e$ and the water molecules in the peptide–water mixture increases gradually as δ increases. Numerically, our simulation shows that even when δ is up to 6.5 Å, the peptide–water mixture can also follow the external charge well. When $q = +0.5e$, we have observed two of the three cases with different initial conditions that the peptide–water mixture follows the external charge in 12 ns simulation when the distance is 5.5 Å, with an electrostatic interaction energy between the external charge and the water molecules of -10.5 ± 6.3 kJ/mol, obtained from the successful manipulation cases.

Finally, since our simulations are based on the stochastic dynamics, the damping coefficient used will influence the manipulation. For System I, when the damping coefficient $\xi = 0.01$ ps^{-1}, according to the Langevin equation, the force due to Langevin damping is $f_{\text{damping}} = M\xi v = 0.153$ pN, in which M is the mass of peptide–water mixture, if we assume that the peptide–water mixture follows the external charge extremely well with the same velocity $v = 1$ m/s. This value of f_{damping} is much smaller than the electrostatic force that the external charge exerts on the water molecules. We find that some modifications of the value of ξ do not change the results much in this chapter. Our calculation shows that when $\xi = 0.1$ ps^{-1}, the electrostatic interaction energy is -17.0 ± 8.5 kJ/mol ($q = +0.5e$), which is very close to the value of -18.5 ± 7.9 kJ/mol for $\xi = 0.01$ ps^{-1} case; moreover, the peptide–water mixture still follows the external charge well in the 12 ns simulation

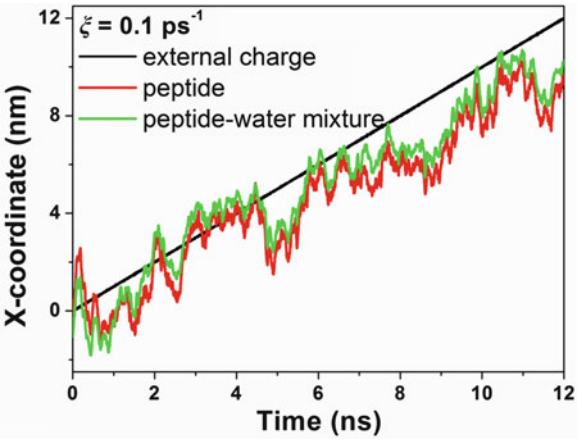

Fig. 1.36 The influence of larger damping coefficient ξ ($\xi = 0.1$ ps^{-1}) on the manipulation. *X*-coordinate of the center of mass of the GNNQQNY peptide (in *red*) and the peptide–water mixture (in *green*) vs. time, together with the *x*-coordinate of the external charge (in *black*) for the case of System I when $q = +0.5e$. As a comparison, Fig. 1.9 shows the manipulation when $\xi = 0.01$ ps^{-1}

time (see Fig. 1.36). We note that, in this case, the peptide or peptide–water mixture gets behind the external charge in most of time due to the larger Langevin damping force; in contrast, in the case of $\xi = 0.01$ ps^{-1}, the peptide or peptide–water mixture usually goes ahead of the external charge due to thermal fluctuation. Moreover, we have also carried conventional MD simulation: the controllable manipulation abilities are consistent with the results presented here.

The aforementioned design can be regarded as an "indirect" approach, which manipulates the position of biomolecule through manipulating the position of water molecules surrounding it. We also propose a "direct" approach, which can manipulate the position of biomolecule with charged residue(s) inside a water-filled nanotube directly. To demonstrate this design, we have built another system, namely, System II. It contains a peptide called Aβ_{16-22} [71] (Ace–KLVFFAE–NMe) inside a (29, 0) zigzag SWNT with dimensions of 8.33 nm in length and 2.24 nm in diameter (see Fig. 1.37). This peptide is an Alzheimer's disease-related peptide, having a lysine (K) residue with one positive charge ($+1e$) at one end and a glutamic acid (E) residue with one negative charge ($-1e$) at the other. The other space in SWNT is fully filled with water. The SWNT is aligned along the *x*-axis in a periodic box of $8.4 \times 12 \times 12$ nm^3. A group of external charges that contained 12 charges forming a 3×4 array is allocated 3.5 Å from the SWNT wall and initially above the glutamic acid residue of the peptide. The distance between the nearest adjacent charges is 2.88 Å. This charge pattern is very similar to the Au (100) crystal face. We note that other patterns of the external charge group do not change much the conclusion we have obtained here provided that the external charges are densely packed in two dimensions. The quantity of each charge is also denoted by q. The corresponding counterions are constrained at the right edge of the box to make the system neutral.

For the case of System II, Fig. 1.38 shows a typical example of the *x*-coordinate of the COM of the peptide as a function of time, together with the *x*-coordinate of the geometrical center of the external charges for $q = +0.5e$ per atom. The peptide

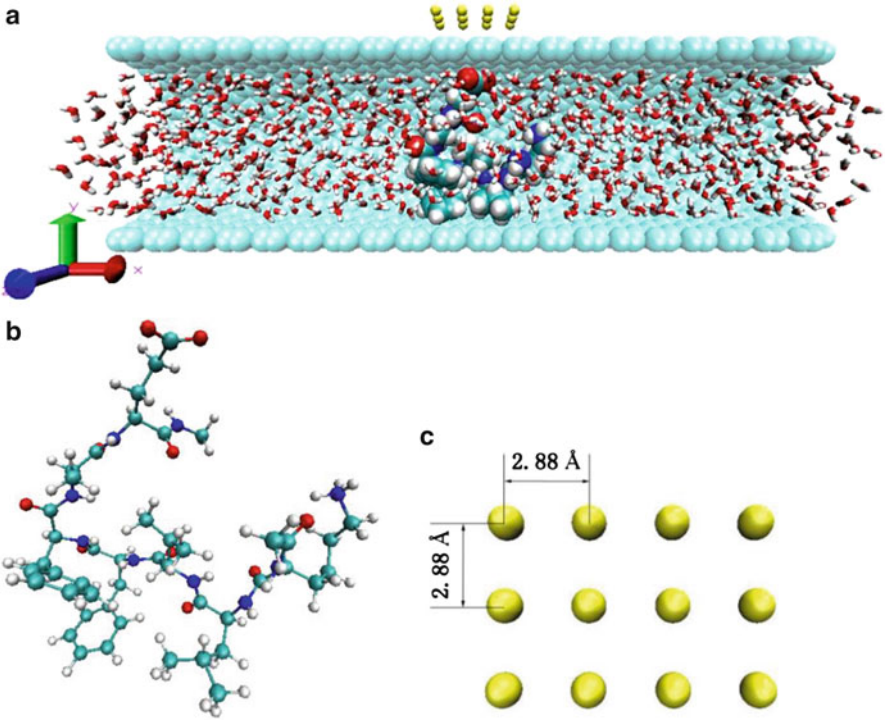

Fig. 1.37 The simulated system (System II). (**a**) Initial framework of System II. The SWNT (*light bluespheres*) is fully filled with water molecules (*red-white pillars*). Some carbon atoms of SWNT are omitted for clarity. The other colored spheres in the middle of SWNT are the atoms of the $A\beta_{16–22}$ peptide. The *yellow spheres* outside the nanotube stand for the external charges (reprinted from [42]. Copyright 2009 American Chemical Society) (**b**) initial structure of $A\beta_{16–22}$ peptide (Ace–KLVFFAE–NMe). It contains a lysine (K) residue with one positive charge ($+1e$) at one end and a glutamic acid (E) residue with one negative charge ($-1e$) at the other. (**c**) Structure of the lattice of external charges, which contains 12 charges forming a 3×4 array. The distance between the nearest adjacent charges is 2.88 Å

follows the external charges very well. In the six simulations we have performed with different initial conditions, only in one simulation the peptide does not follow the external charges.

We have computed the electrostatic interaction energy of the external charges with the peptide vs. time, shown in Fig. 1.39. The average electrostatic interaction energy (averaged over five successful manipulation cases) is -704 ± 142 kJ/mol. In all simulations, the distances between the COM of the peptide and the geometrical center of the external charges range from 1.2 to 2.6 nm with an average value of 1.6 nm. We have noted that the deprotonated carboxyl group (COO) on the glutamic acid residue of the peptide carries most ($-0.9e$) of the negative charge of the whole residue ($-1e$). Since the external charges are positive, the interaction between the peptide and the external charges is dominated by the interaction between the

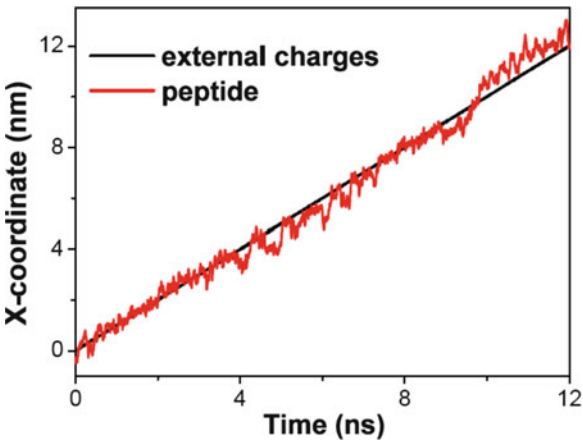

Fig. 1.38 Manipulating the peptide with charged residues inside a water-filled nanotube (i.e., System II). The x-coordinate of the center of mass of the Aβ_{16-22} peptide (*red line*) as a function of time, together with the x-coordinate of the geometrical center of the external charges (*black line*) (reprinted from [42]. Copyright 2009 American Chemical Society)

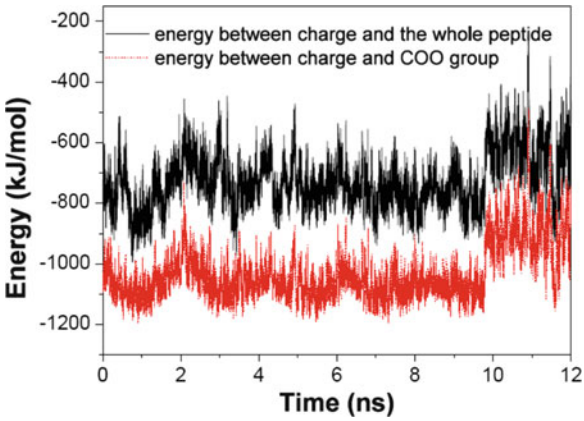

Fig. 1.39 Electrostatic interaction energy of the external charges with the Aβ_{16-22} peptide and with the deprotonated carboxyl group (COO) as a function of simulation time

COO group and the external charges. Numerically, we have found that the average electrostatic interaction energy of the external charges with the COO group is -973 ± 143 kJ/mol, quite close to the electrostatic interaction energy of the external charges with the peptide (see also Fig. 1.39). Likewise, the distances between the COM of the COO group and the geometrical center of the external charge range from 0.6 to 2.2 nm with an average value of 0.8 nm. These distances are smaller than the distances between the COM of the peptide and the geometrical center of the external charges. Consequently, the manipulation of the peptide mainly results from the tight trapping of the COO group by the external charges.

We have also calculated the electrostatic forces that the peptide and water inside the nanochannel exert on the external charges along the x-axis. The forces range from -600 to $+600$ pN (see Fig. 1.40), which also fall within the working ranges of many existing techniques such as STM and AFM.

The number of the charges in the externally charged group is important for the manipulation. We have found only one successful case in five simulations with

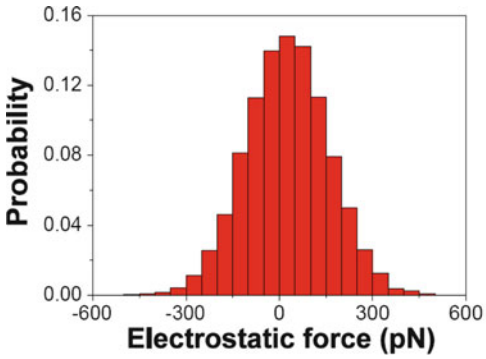

Fig. 1.40 The electrostatic forces that the peptide and water inside the nanochannel exert on the external charges along the *x*-axis for the case of System II. The positive direction of the force is the positive direction of the *x*-axis, and a 50 pN force interval is used

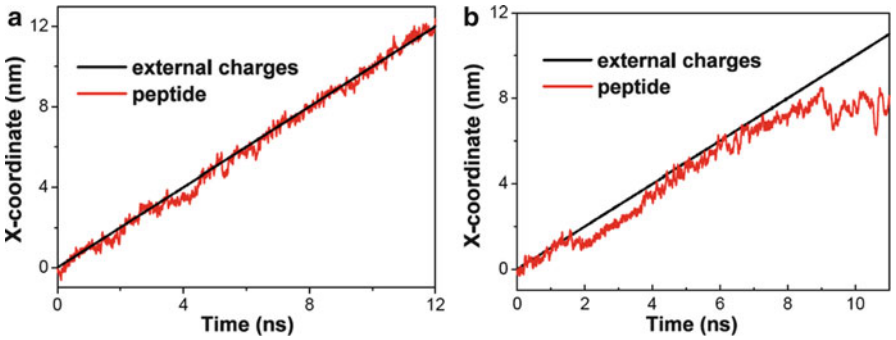

Fig. 1.41 Manipulating the peptide with charged residues inside a water-filled nanotube when the number of external charges reduces to nine (in a 3×3 array with $q = 0.5e$ per atom). *Red* and *black lines* represent the *x*-coordinate of the center of mass of the $A\beta_{16–22}$ peptide and the geometrical center of the external charges, respectively, as a function of time. Only one successful case is observed (**a**) in five simulations. (**b**) A typical unsuccessful manipulating case

different initial conditions when there are only nine charges in a 3×3 array with $q = 0.5e$ per atom (see Fig. 1.41). When the group of external charges is substituted by one externally charged atom, the minimal value of the external charge required for manipulation is around $+3e$. It seems that the manipulation of the peptide inside a water-filled SWNT is much more difficult than the manipulation of the peptide in a drop of peptide–water mixture inside an empty SWNT.

The peptide used here has only one negatively and one positively charged residue and is neutral as a whole. It should be noted that many biomolecules with highly charged fragments may not be neutral. For example, the peptide LDTGADDTVLE [72], which is the fragment 24–34 of the protease of the human immunodeficiency virus type 1, has a total of $-4e$ charges because of the presence of three aspartic acid (D) residues and one glutamic acid (E) residue, all of which are negatively charged, and the absence of positively charged residue. It could be expected that for this kind of biomolecules, the manipulation becomes more effective.

Finally, we note that we have not considered the possible metal semiconductor property of the nanotube. For those nanotubes, the screening effect should be considered, and the charges used here should be regarded as effective charges. It is interesting to note that even for the metallic nanotube, the interaction between a charge outside the single-walled nanotube and the charges inside the nanotube is still quite strong. However, insulator nanochannels may be much better in the application, which is expected to be fabricated in the future. Considering that the external charges required for these manipulations are quite small, which are still available after taking into account the screen effect of many nanotubes, our designs may serve as lab-in-nanotube for the interactions and chemical reactions of molecules especially biomolecules and hence may have wide applications in nanotechnology and biotechnology.

1.1.3 Signal Transmission, Conversion, and Multiplication with Polar Molecules Confined in Nanochannels

Another thing we are inspired from the one-dimensional hydrogen bonds chain as shown in Fig. 1.2 is that the highly stable chain can be used in the signal transmission, conversion, and multiplication at nanoscale and/or molecular scale. Nanoscale structures or molecules have been utilized as the elements in electronic devices [73–76], such as nanowires, switches, rectifiers, and logic circuits, and the integration of these molecular-based devices and other nanoscale structures has led to a number of demonstrations of new and useful applications [77, 78]. Particularly, electrical transportation [79], electrical and partity switching [73–76], and chemical and biomolecular sensors [80, 81] have been developed based on nanowires or nanotubes. Biosensors for DNA diagnostics, gene analysis, fast detection of warfare agents, and forensic applications have also been achieved by electrochemical method[14] and microarrays[17] together with the particular behavior of biomolecules in nanoscale [82].

In biology, signal representations are often related to electrical changes. For example, in central nerve systems, the most common mechanism for signaling between neurons is the neurotransmitter-releasing chemical synapse, but faster and simpler signaling can be achieved with electrical synapses, specialized junctions (gap junctions) that mediate electrical coupling between neurons [83–86]. Electrical coupling mediated by electrical synapses is an important feature of local inhibitory circuits and plays a fundamental role in the detection and promotion of synchronous activity (firing pattern) within the neocortex [87–89]. In fact, weak coupling may lead to antiphasic or asynchronous firing [83, 84, 90].

On the other hand, although it has been of great interest to study the mechanism of signal transmission, conversion, and multiplication at molecular level, molecular details in these systems remain largely unknown due to the intrinsic complexity in these molecular systems and the significant noises arising from thermal fluctuations

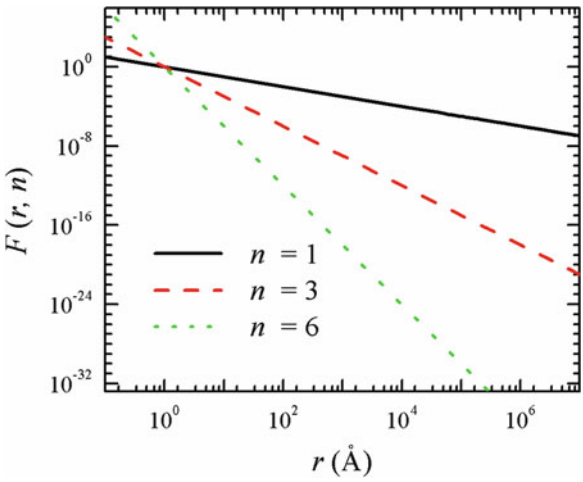

Fig. 1.42 Curves for function $F(r, n) = A_n\ (r/r_0)^{-n}$ for $r_0 = 1$ Å and $n = 1, 3, 6$, and $A_n = 1$ (reprinted from [132]. Copyright 2010 Royal Society of Chemistry)

as well as interferences between branch signals. For example, we note that the signal transmission along intercellular and intracellular pathways and between the exterior and the interior of a cell may be mediated by protein allostery [91–93], which may lead to the redistribution of the charges and the reorientations of the charge dipoles in the proteins, but the exact molecular mechanism is still unclear.

As we have known, thermal noises usually hold important interference in signal transmission, conversion, and multiplication. Particularly at the nanoscale, thermal noises often significantly reduce the signal strength during the transmission, conversion, and multiplication.

More critically, it should be noted that the interferences between signals can be very strong if the signals are transmitted by charges. In terms of Coulomb's law, the interaction potential between two charges decreases with respect to r^{-1}, where r is the distance between those two charges. At the nanoscale, this slow decay will result in strong interaction between two charges (signals). Therefore, within one nanometer's distance, although the VDW interaction almost decreases to zero with respect to r^{-6}, extremely faster than r^{-1}, the interaction cannot be neglected between two atoms yet. As a comparison in Fig. 1.42, we show a diagram of the function $F(r, n) = A_n\ (r/r_0)^{-n}$ with respect to r for $r_0 = 1$ Å and $n = 1, 3, 6$, where A_n is set as a constant 1. Therein, the dipole–dipole interaction potential just has a form of r^{-3}, decaying much faster than the charge–charge interaction (r^{-1}) with distance.

It is much worthwhile making an attempt to use the dipole to transmit a signal, due to the much faster decay of the interaction between different dipole signals. Several decades ago, one began to study the properties of electric dipoles and the applications on them. The most notable one is the Ising model [94, 95]. Recently, the behavior of one-dimensional dipole chains has been discussed, including the energy transfer in a dipole chain [96], the design of a logical AND port using dipole chains with a junction [97], and the initiation of the orientation of one-dimensional dipole chains by a local field [98].

Here, we find water, as the most important matter in the world, can be designed to become an excellent medium for the transmission of signals. Water molecules confined within nanoscale channels exhibit structures and dynamics that are very different from bulk [6, 15, 17, 22, 32, 34, 43, 52, 99–103]. Particularly, in nanochannels with suitable radii, water molecules are confined to form one-dimensional chains linked by hydrogen bonding with the "concerted" water dipole orientations [21, 22, 43, 104], which provide an excellent example for the transmission of signals due to water dipole interactions. Note that the stable water molecular chain is a prerequisite for signal transmission as a medium.

Fortunately, the reorientation of this water dipole chain has its characteristic time estimated to be in the range of 2–3 ns for CNTs with a length of 1.34 nm [21]. More remarkably, the water molecule chains in a nanotube can remain dipole-ordered up to macroscopic lengths of 0.1 mm, with durations up to 0.1 s [104].

As an example, Fig. 1.43 shows the "concerted" orientations of water molecules (water dipoles are ordered cooperatively inside the CNT) [21, 22, 40, 43, 59, 104]. If we can "tune" the orientation of one water molecule using a single charge at one end, we might be able to control the orientations of other water molecules in the same channel or other connected channels. In other words, we have a molecular level "signal transmission," i.e., converting a charge signal to water dipole orientation signal (at one end) and then transmitting the water dipole orientation signal to other ends, which might be converted back to a charge signal again. Furthermore, if we use Y-shaped nanochannels, i.e., three nanochannels connected with each other to form a Y-junction, we can even achieve a "signal multiplication," which means that a water dipole orientation signal can be multiplied into many water dipole orientation signals [59]. It is also observed that the signal transmission and multiplication, via water molecules confined in nanoscale channels, can be effectively shielded from thermal fluctuations.

We have applied MD simulations, which are widely used in nanoscale- and molecular-scale simulations for both physical and biological systems [22, 59, 105–111], to investigate this interesting phenomenon of water-mediated signal transmission. NVT ensemble simulations have been carried out at a constant temperature of 300 K using a Berendsen thermostat [105] and in constant volumes ($L_x \times L_y \times L_z = 6.01\,\text{nm} \times 6.01\,\text{nm} \times 11.00\,\text{nm}$ in SWNT systems with 12,922 water molecules using the molecular modeling package Gromacs 4.0.5 [106, 108], and more settings are referred to Ref. [59]). A typical (6, 6) uncapped armchair SWNT with a width of 0.81 nm and a length of 5.13 nm is adopted as shown in Fig. 1.43. This device is constrained at the center of the simulation boxes by using the position restraints (the whole tube length is partitioned evenly into three segments with an interval 1.71 nm, and thus the four rings of carbon atoms are constrained) solvated with water molecules with constant density. We have adopted the particle-mesh Ewald method [112] to model long-range electrostatic interactions, and we have applied periodic boundary conditions in all directions. A time step of 2 fs is used, and data are collected every 0.5 ps. In all of our simulation results, the TIP3P water model is applied and the carbon atoms are modeled as uncharged Lennard-Jones particles with a cross section of $\sigma_{CC} = 0.34\text{nm}$ and $\sigma_{CO} = 0.3275\,\text{nm}$, and a

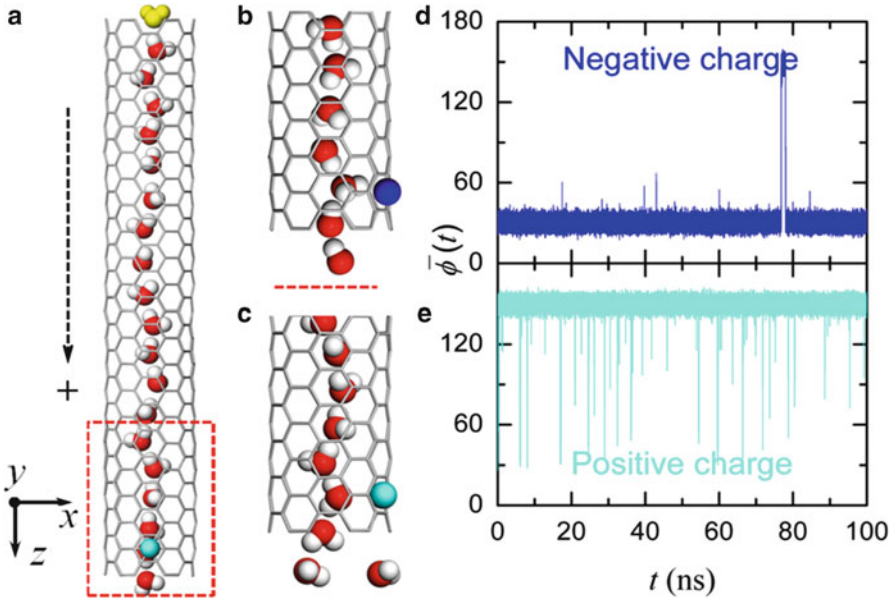

Fig. 1.43 Schematic snapshots (a, b, c) of the system with a single channel in side view (the *xz*-plane) together with the trajectories (**d**, **e**) of average dipole angle $\bar{\phi}(t)$ of the water orientations. The snapshots shown in (**b**, **c**) correspond to the *red dashed* part of the system (see subfigure a) in another side view (*yz*-plane). *Blue* and *green spheres* denote the negative charge and the positive charge, respectively, which result in different orientations of the water molecules facing the charges. The water molecule facing the external charge is named as "monitored-water." The single-walled CNT is represented by *gray lines* and its positive direction is shown by the *black dashedarrowhead*. Water molecules are shown with oxygen in *red* and hydrogen in *gray*, and the first water molecule outside the channels opposite to the charge signal input is shown in *yellow*. The dipole direction of the water molecules is not shown, which is along the midline between the two O–H chemical bonds of the water molecule. Water molecules outside the nanotubes are omitted in the figure (reprinted from [132]. Copyright 2010 Royal Society of Chemistry)

potential well depth of $\varepsilon_{CC} = 0.3612\,\mathrm{kJ \cdot mol^{-1}}$ and $\varepsilon_{CO} = 0.4802\,\mathrm{kJ \cdot mol^{-1}}$ [21]. The system is first minimized with conjugate gradient method for 10,000 steps and then equilibrated with MD for 5 ns at 300 K before data collection. An external signal charge of magnitude $1.0e$ is then introduced to the center of the second carbon ring of the main tubes (constrained by using the position restraints during the simulations), and its opposite charge for neutralization is constrained near the edge of each box at coordinates (0.00, 3.00, and 0.00 nm), which is far enough to have any meaningful influence on the signal charge (our numerical data also confirm this).

Note that at the center of a second carbon ring of the nanotube, this charge is attached in order to control the direction of the dipole orientation of the water molecule to face the charge, and we call this confined water as "monitored-water" hereafter. We have found that different signs of the charge q result in different

orientations of the monitored-water (see Fig. 1.43). Moreover, we have found that the monitored-water determined all the water orientations in the nanotube, upward or downward in concert [59]. Quantitatively, we define the water dipole orientation in the nanotube as an angle ϕ_i between the ith water molecule and the nanotube axis [59]:

$$\phi_i = \text{acos}(\vec{p}_i \cdot \hat{u}/|\vec{p}_i|),$$

where $\vec{p}_i$ is the dipole of ith water molecule and $\hat{u}$ is the axis unit vector of the nanotube. The averaged dipole angle $\bar{\phi}(t)$ is computed by

$$\bar{\phi}(t) = \sum_{i}^{N} \phi_i(t)/N(t),$$

where the average runs over all the water molecules inside a nanotube at time t, and $N(t)$ is the number of water molecules within this tube. The averaged dipole angle is used to characterize the water-mediated signal transmission. The results are shown in Fig. 1.43. It is clear that $\bar{\varphi}$ falls into very different ranges most of the time for a positive or negative signal charge: $110° < \bar{\varphi} < 170°$ for $q = +e$ and $10° < \bar{\varphi} < 70°$ for $q = -e$, indicating that the water molecules within each nanotube are well ordered (i.e., in concert). Thus, the charge ($+e$/$-e$) signal at one end of the nanotube can be readily distinguished from the dipole orientation (upward/downward) of the water molecules at the other end of the nanotube.

Next, from the aforementioned systems, the water orientation states are extracted every 10 ns after the first 30 ns of simulation time. In these states, we switch the attached charge polarity and adopt them as initial states for new next simulations. Based on these simulations with switched charge polarity, we discuss the time delay of the water orientations in response to a switch in the charge signal. Figure 1.44 display the averaged angle $\bar{\phi}(t)$ for four such scenarios. The time delay associated with the branch tubes is 3.2 ns on average, with a minimal duration of 0.04 ns (Fig. 1.44 (the last one)) and the maximal one 9.2 ns to respond to the $+e \rightarrow -e$ signal switch (which is slower) and approximately 0.07 ns only to respond to the $-e \rightarrow +e$ switch (which is much faster). This obvious disparity in the response time results from the interaction of the monitored-water with the signal charge. The negative charge attracts the two hydrogen atoms of the monitored-water and limits the mobility of the oxygen atom to a certain extent. Positive charge attracts the oxygen atom, and the two hydrogen atoms have more freedom to rotate or swing, which enables an easier switch for the configurations. This point can also be easily seen from Fig. 1.43, as we observe more fluctuations in the case with a positive signal charge. We note that the short (average 0.07–3.2 ns) response time delay implies that the signal with frequency in gigahertz range can be expected.

In response to a switch in the charge signal, it takes only tens of picoseconds for the orientation of the entire water chain to flip over inside the nanochannels. This delay time mainly results from the reorientation time of the monitored-water

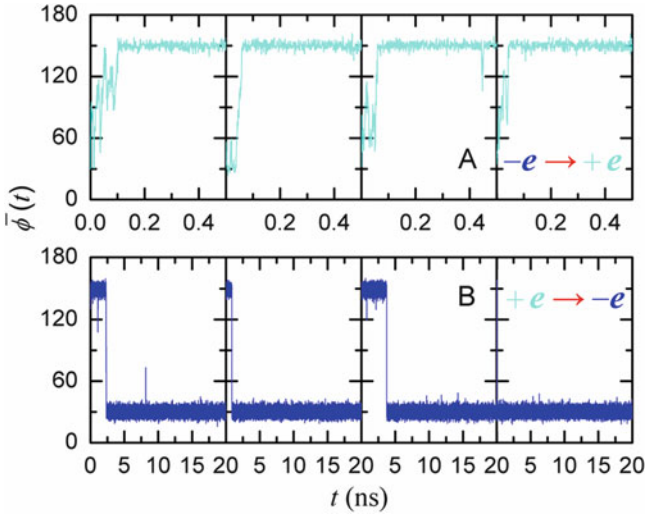

Fig. 1.44 Signal switching in an SWNT. Trajectories of the average dipole angle $\bar{\phi}(t)$ of the water orientations in an SWNT for the charge signal switch from negative to positive (*top*) and from positive to negative (*bottom*) for four typical cases with different initial states. The dipole orientations in the SWNT fully respond in approximately 0.07 ns when the charge switches from negative to positive and in 3.2 ns in the case of positive-to-negative transition (reprinted from [132]. Copyright 2010 Royal Society of Chemistry)

and its neighboring water molecules. As is shown in Fig. 1.45, a typical process displays the reorientation of water molecules in the nanochannel in response to a $+e \rightarrow -e$ signal switch. In this process, the dipoles of water chain molecules always flip over one by one, from the bottom to the top (see Fig. 1.43). In order to observe the motion of this flipping forefront point, we can trace the position of the water molecule (along the nanochannel axial direction), whose dipole angle ϕ falls into the ranges of [70°, 110°], while its two nearest neighbor molecules have their dipole angles falling into [110°, 70°] and [10°, 70°], respectively. If there is no such water molecule at any given moment, we take the position of the last-turning molecule as the current forefront. We have also plotted the value of $\bar{\varphi}$ as a function of the time. Clearly, the turning forefront is consistent with the value of $\bar{\varphi}$.

As we have seen above, charge polarity signal can transmit via the one-dimensional water dipole chain confined within nanochannels with suitable radii. More importantly, we have achieved signal multiplication at the nanoscale, making use of the Y-shaped water chain confined in the Y-shaped nanochannels.

Recently, Y-shaped nanotubes have been successfully fabricated by several different methods, including alumina templates [113], chemical vapor deposition of products generated from a pyrolysis of metallocenes [114–116], nano-welding of overlapping isolated nanotubes using high-intensity electron beams [117], and spontaneous growth of nanotube mats using Ti-doped Fe catalysts [118]. In Ref. [42], we have constructed a computational model of Y-shaped CNT, called Y-SWNT,

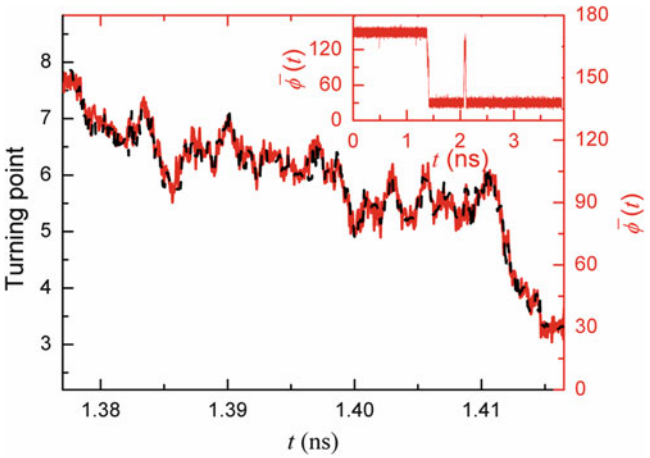

Fig. 1.45 A typical reorientation process of water molecules in nanochannel in response to a $+e \rightarrow -e$ signal switch (one data point every 50 fs). In this figure, the *red solidline* represents the detailed trajectory of the average dipole angle $\bar{\varphi}(t)$ adopting the *left* and *bottom axes* (inset shows its whole trajectory in a longer period). This trajectory indicates that the reorientation of the whole water chain is carried out by turning over the orientations of the water molecules one by one. The *black dashedline* shows this turning position in nanochannel as a time function using the *top* and *right axes* (reprinted from [132]. Copyright 2010 Royal Society of Chemistry)

as shown in Fig. 1.46. Explicitly, the Y-SWNT is obtained by joining three SWNTs symmetrically, with an angle of 120° among them. Interestingly, we have found that the behavior of the water orientations inside one branch channel can be controlled by the water orientations in another branch channel. In the following, for easy discussion, we name the three branch tubes as the main, first branch, and second branch tubes, which are denoted by MT, BT_1, and BT_2, respectively, as shown in the figure.

We still perform the MD simulations in NVT ensemble, with similar simulations methods and parameters above (all settings are referred to Ref. [59]). The Y-SWNT device is constrained by using the position restraints at the center of the simulation boxes, solvated with water molecules with constant density. An external signal charge of magnitude $1.0e$ is then introduced to the center of the second carbon ring of the main tubes (constrained by using the position restraints during the simulations), and its opposite charge for neutralization is constrained near the edge of each box at coordinates (0.00, 3.00, and 0.00 nm), which is far enough to have any meaningful influence on the signal charge (our numerical data also confirm this). These charges are introduced to the system after initial equilibration in order to observe the response time of water dipole reorientation upon the charge signal.

Obviously, a Y-shaped water chain is formed in Y-shaped nanochannels, and the water chains in different nanotubes interact with one another at the Y-junction. This usually affects the water dipole orientations in different tubes. Surprisingly, water dipoles are still in concert, just like those in the single channels. We have

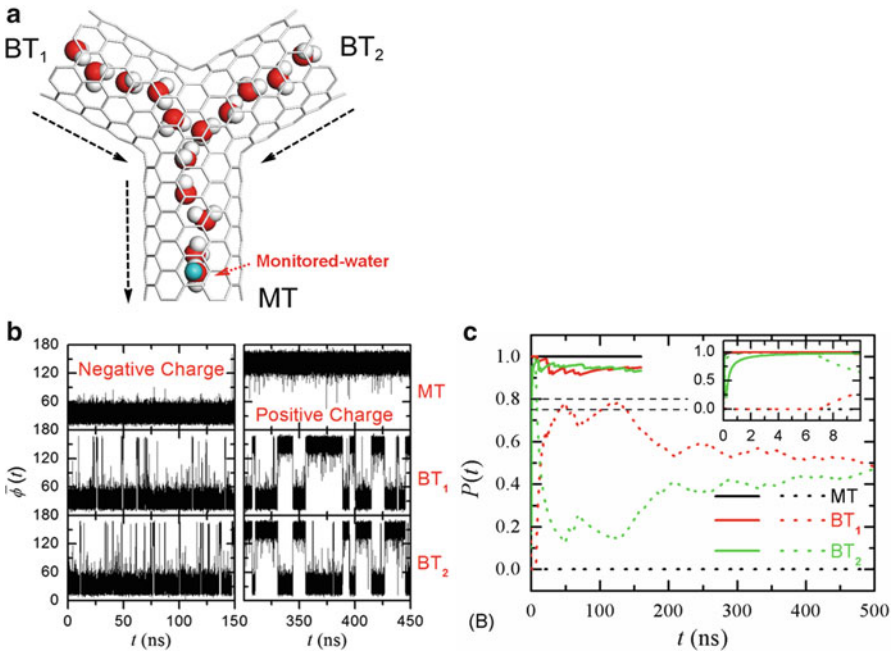

Fig. 1.46 (**a**) A schematic snapshot of the simulation system in side view (the *xz*-plane). The Y-SWNT features a main tube (MT) and two branch tubes (BT_1, BT_2) positioned in the same plane (the *xz*-plane). The angle between each two neighboring SWNTs is 120°. Small angular changes do not affect the results. The single-walled CNTs are represented by *gray lines*. Water molecules are shown with oxygen in *red* and hydrogen in *gray*. Water molecules outside the nanotubes are omitted in the figure. The *green sphere* represents the imposed charge. The lengths of MT, BT_1, and BT_2 are 1.44, 1.21, and 1.21 nm, respectively. (**b**) The average dipole angle $\bar{\varphi}(t)$ of the water orientations inside the MT, BT_1, and BT_2 for a negative charge (*left*) and a positive charge (*right*). (**c**) The probabilities of the dipole orientations $P(t)$ in different tubes for a negative charge (*solid lines*) and a positive charge (*dashed lines*). $P(t)$ for a negative charge converges to about 1.0 within a few nanoseconds (reprinted from [59]. Copyright 2009 National Academy of Science, USA)

adopted the similar approach that an external charge q is attached at the center of a second carbon ring of the MT (see Fig. 1.46) to initiate a signal of water dipole orientations. Similar to the single channels, the water molecules in the MT have the upward and downward concerted dipole orientation for $q = -e$ and $q = +e$, respectively. Remarkably, the water orientations in both the BTs follow the water orientations in the MT when water orientations in the MT are downward, while the water orientations in both the BTs fluctuate between upward and downward when the water orientations in the MT are upward. This can be seen more clearly from the time-dependent behavior of $\bar{\varphi}(t)$ as shown in Fig. 1.46. Therefore, from the water orientations in each branch tube of the Y-shaped channel, we can easily distinguish the sign of the imposed charge at the MT. In other words, the charge signal at the bottom of the MT is "converted" into water dipole signal and then transmitted to the two Y-branch tops and "multiplied" (from one signal to two).

We characterize the water-mediated signal multiplication, by computing the probability of occurrence in the range of $10° < \bar{\varphi} < 70°$, denoted by $P(t)$. We can expect that $P(t)$ approaches 1 in both BTs when the water orientations in the MT are downward (after a sufficiently long time). In contrast, $P(t)$ approaches 0.5 in both BTs when the water orientations in the MT are upward, since the water orientations in both BTs fluctuate between upward and downward with a roughly equal probability. If we set P_C as a value between 0.5 and 1, we expect that $P > P_C$ in the BTs corresponds to the downward water orientations in the MT and that $P < P_C$ in the BTs implies the upward water orientations in the MT after a sufficiently long time. Considering the rapid convergence of the case for the downward water orientations in the MT, $P_C = 0.8$ is set, which is a little larger than the average value of 0.5 and 1. From Fig. 1.46, we can see that $P > P_C$ in both BTs for any time $t > 1$ ns for the downward water orientations in the MT, while $P < P_C$ in both BTs for any time $t > 8$ ns for the upward water orientations in the MT. Thus, the charge signal at the MT can be readily distinguished from the value of $P(t)$ in each BT within a time interval of 8 ns with an appropriate threshold $P_C = 0.8$.

In the following, we further examine the water orientations inside the branched tubes (BTs). Let us first consider a single channel without any external charge. There is a hydrogen atom pointing out at the upmost (or bottommost) end when water molecules inside the channel have a concerted upward (or downward) orientation inside the single channel. One upward → downward switch of the water orientations inside the nanochannel will result in an "apparent" transportation of an upward-pointing hydrogen atom at the upmost-end of the tube to a downward-pointing hydrogen atom at its bottommost-end.

However, there is a different situation in Y-shaped nanochannels. Let us think about what happens to the water orientations inside a Y-shaped nanochannel. In the MT, there is the similar bottom → upper transportation of only one hydrogen atom, after the downward → upward switch of its concerted water orientation. But this transportation causes a different situation in the BTs. There is the transportation of only half a hydrogen atom on the average in each BT, due to the conservation of the hydrogen atom (the total number of the hydrogen transportation is also one for both BTs). Different from the above simple single-tube case, this creates asymmetry for the Y-shaped tube, since the average half hydrogen atom "transported" in BTs can be either zero or one at any moment. Thus, the situation will not be always a simple upward → downward (or downward → upward) orientation switch in each BT following that in the MT. In other words, if the water orientations in both BTs follow the *downward* water orientations as in the MT, these same water orientations in both BTs might not follow the *upward* water orientations as in the MT on the other hand.

Interestingly, our simulations exactly reproduce this situation. For example, the downward water orientations in both BTs are observed when the water orientations in the MT are downward (corresponding to a negative monitored charge), while the upward water orientation in the MT (corresponding to a positive monitored charge) results in a fluctuation of the water orientations between the downward and upward

orientations with a roughly equal probability in the BTs. This behavior can be partly explained from the interactions of water molecules at the Y-junction. When the water orientations are downward in the MT, the O atom of the uppermost water molecule in the MT attracts two H atoms from the two bottommost water molecules in the BTs; on the other hand, when the water orientations are upward in the MT, one of the H atoms of the uppermost water molecule in the MT attracts both O atoms in the bottommost water molecules in the BTs. The interaction in the former case is much stronger than interaction in the latter case. Consequently, the average value of $P(t)$ in the branch tubes is 0.5 for a concerted upward water orientation in the MT (corresponding to a positive monitored charge).

In Y-shaped nanochannels, water reorientation also holds its time delay in response to a switch in the charge signal [59]. In our simulations, the time delay associated with the BTs is found to be slow, 40 ns on average with a maximal duration of 150 ns, to respond to the downward → upward signal switch of the water orientations in the MT, but much faster, 4 ns only, to respond to the upward → downward switch of the water orientations in the MT. Clearly, the former has longer delay time than the latter. This is because that the downward water orientations in the MT (where one O atom controls two H atoms at the Y-junction) are much more stable than the case for the upward water orientations in the MT (where one H atom controls two O atoms at the Y-junction). It takes more time to shift from a more stable state to a less stable one. Compared to the time delay for switches in a single nanochannel (0.07–3.2 ns), the response times in the Y-channels are also generally longer, particularly for the downward → upward switch.

We emphasize that the stability of water chain confined in nanochannels is a guarantee to achieve water-mediated signal transmission, conversion, and multiplication. The phenomenon that we have observed is robust. First, we note that the signal multiplication capability is not very sensitive to the angles of the Y-shaped tube (the angles between SWNTs, currently at 120°, 120°, 120°). We have tried T-shaped tubes (with an angle of 90°, 90°, 180°) and other slightly different angles, and the results are more or less the same in terms of water orientation propagations.

Next, the orientation of the monitored-water and, consequently, the orientations of the all water molecules in the nanotubes can be controlled by a single charge with a quantity of one electron. This is a remarkable capability from the viewpoint of the signal transmission and conversion. Thus, what is the minimal charge needed for this capability? Numerical analysis shows that the magnitude of this signal charge needs to be larger than $0.6e$—our data using a charge from $0.6e$ to $1.0e$ indicate that the water orientations can be well controlled with such a single charge. From the previous discussion [22], it is clear that the orientation of the monitored-water can be "fixated" only when the electrostatic interaction energy between the external charge and the monitored-water is comparable to the interaction energy of the monitored-water with either side of its neighboring water molecules. Since the imposed charge is placed at the center of a second carbon ring of the nanotube, which has a distance of about 4 Å from the centerline of the nanotube (close to the distance between two water neighboring molecules), the charge required to control the orientation of the

monitored-water should probably be larger than the partial charge on each hydrogen atom (e.g., 0.417e in TIP3P water model). This is consistent with our numerical observation.

On the other hand, for the practical applications, it is very important to output the water dipole signal. As we have shown above, there is a hydrogen (oxygen) atom with a partial positive (negative) charge at the end of the nanochannel when the water dipole chain is pointing outward (inward). This partial charge can trigger (or control) a neighboring polar molecule or charge outside the channel (e.g., see Fig. 1.43, for the yellow-colored first water molecule outside the channel). Since all the water molecules share the same dipole orientation as the first water molecule inside the nanochannels, the overall water dipole moment might be large enough to be detected. This dipole moment has a value of several Debyes [59] and can interact with the electric field. We note that the semiconductor or conductor properties of some nanotubes may screen the dipole moment interacting with electric field. Insulator nanochannels, which may be fabricated in the future, might be better for this application.

Finally, via dipole–dipole interaction, with relevant interference at nanoscale, we can achieve signal transmission, conversion, and multiplication. As an important view, since water is not the only polar molecule with a dipole moment, we expect that other polar molecules, such as urea or ethanol, might have the same capability to transmit and multiply signals inside nanotubes. These small molecules, especially water, have some unusual and important physical and chemical properties, including their interactions with proteins [99,100,107,119]. In fact, as a fundamental property of all cells, cell polarity has already played a central role in signal transmission and controlled a variety of polarized cell behaviors [120–124]. Similar to the monitored charge that we have used in this chapter, a polarizing signal initiates polar distribution of signaling molecules and leads to polarity establishment and maintenance through the cytoskeleton and vesicular trafficking [121]. For example, during planar cell polarity (PCP) signaling, core PCP proteins are sorted asymmetrically along the polarization axis, where PCP refers to coordinated polarization of cells within the plane of a cell sheet. This sorting is thought to direct coordinated downstream morphogenetic changes across the entire tissue [123–126]. We also note that there have been other modes to achieve signal transmission, such as using the injection of finite-duration vibrational signals encoding information into a biomolecular wire of the polypeptide glycine1000 [127].

For this open field, there are still much more to be thought and to be done. Future directions might include, but not limited to, the following forefronts.

(1). The concerted orientations of the dipole molecule chains inside the nanochannels are maintained by the dipole–dipole interactions. It is expected that the "in phase" strength between those dipole orientations becomes weak as the number of dipole molecules increases. This is very important in the practice of the long-range transmission of the dipole signals. It has been shown that the correlation of the motion of the water molecules in a one-dimensional water chain confined

in the SWNT decays as the number of water molecules in this water chain increases [128]. How to achieve long correlation in the dipole orientation in practice is a huge challenge.

(2). Is there an energy transfer, and how does the energy transfer process work during such a dipole signal transmission, conduction, and multiplication? These questions are still unclear.

(3). Water molecules are very small. The devices and sensors based on water can be very small. However, the very small size of the water molecules can at the same time make the experimental realization and applications very difficult. The exploration of other larger polar molecules, such as urea, ethanol, and glycerol, to be used as media in the nanotubes is highly needed and desired.

(4). What other methods can ignite the initial dipole orientation of the monitored-water or some other molecules? Examples might be external electric fields and/or other polar molecules connected to this monitored-water. Finally, we should note that most of the progresses discussed in this short feature chapter are based on MD simulations so far. Experimental validations are therefore much needed.

1.2 Conclusion Remarks

Inspired by the biological channels called aquporins, the behavior of water inside the nanochannels has been extensively investigated. Particularly, the water channel with single-filed water is gated by external mechanical and electric signals; the water flow inside the nanochannel with single-filed water can be driven with biased direction by the static asymmetric electric field based on the ratchet effect; the water molecules inside the nanochannel with single-filed structure can even be used for signal transmission, conversion, and multiplication at the molecular level. When the radius of the nanochannel is larger, the channel can even serve as the lab-in-tube to controllably manipulate biomolecules for various applications, including chemical reaction.

Finally, we noted that most of the studies for the water inside nanochannels are experimental and numerical. Analytical study may better exploit the physics underlying, and we think this is an important direction.

References

1. Whitesides, G.M.: The origins and the future of microfluidics. Nature **442**(7101), 368–373 (2006)
2. Whitby, M., Quirke, N.: Fluid flow in carbon nanotubes and nanopipes. Nat. Nanotech. **2**(2), 87–94 (2007)
3. Squires, T.M., Quake, S.R.: Microfluidics: fluid physics at the nanoliter scale. Rev. Mod. Phys. **77**, 977 (2005)

4. Regan, B.C., Aloni, S., Ritchie, R.O., Dahmen, U., Zettl, A.: Carbon nanotubes as nanoscale mass conveyors. Nature **428**(6986), 924–927 (2004)
5. Service, R.F.: Desalination freshens up. Science **313**(5790), 1088–1090 (2006)
6. Holt, J.K., Park, H.G., Wang, Y.M., Stadermann, M., Artyukhin, A.B., Grigoropoulos, C.P., Noy, A., Bakajin, O.: Fast mass transport through sub-2-nanometer carbon nanotubes. Science **312**(5776), 1034–1037 (2006)
7. Bourlon, B., Wong, J., Miko, C., Forro, L., Bockrath, M.: A nanoscale probe for fluidic and ionic transport. Nat. Nanotech. **2**(2), 104–107 (2007)
8. Besteman, K., Lee, J.O., Wiertz, F.G.M., Heering, H.A., Dekker, C.: Enzyme-coated carbon nanotubes as single-molecule biosensors. Nano Lett. **3**, 727–730 (2003)
9. Ghosh, S., Sood, A.K., Kumar, N.: Carbon nanotube flow sensors. Science **299**(5609), 1042–1044 (2003)
10. Cambr, E.S., Schoeters, B., Luyckx, S., Goovaerts, E., Wenseleers, W.: Experimental observation of single-filed water filling of thin single-wall carbon nanotubes down to chiral index (5,3). Phys. Rev. Lett. **104**(20), 207401 (2010)
11. Falk, K., Sedlmeier, F., Joly, L., Netz, R.R., Bocquet, L.: Molecular origin of fast water transport in carbon nanotube membranes: superlubricity versus curvature dependent friction. Nano Lett. **10**(10), 4067–4073 (2010)
12. Liu, B., Li, X., Li, B., Xu, B., Zhao, Y.: Carbon nanotube based artificial water channel protein: membrane perturbation and water transportation. Nano Lett. **9**(4), 1386–1394 (2009)
13. Yuan, Q., Zhao, Y.-P.: Hydroelectric voltage generation based on water-filled single-walled carbon nanotubes. J. Am. Chem. Soc. **131**(18), 6374–6376 (2009)
14. Zhao, Y.C., Song, L., Deng, K., Liu, Z., Zhang, Z.X., Yang, Y.L., Wang, C., Yang, H.F., Jin, A.Z., Luo, Q., Gu, C.Z., Xie, S.S., Sun, L.F.: Individual water-filled single-walled carbon nanotubes as hydroelectric power converters. Adv. Mater. **20**(9), 1772 (2008)
15. Joseph, S., Aluru, N.R.: Why are carbon nanotubes fast transporters of water? Nano Lett. **8**(2), 452–458 (2008)
16. Wang, B., Král, P.: Coulombic dragging of molecules on surfaces induced by separately flowing liquids. J. Am. Chem. Soc. **128**(50), 15984–15985 (2006)
17. Majumder, M., Chopra, N., Andrews, R., Hinds, B.J.: Nanoscale hydrodynamics: enhanced flow in carbon nanotubes. Nature **438**(7064), 44–44 (2005)
18. Fang, H., et al.: Dynamics of single-file water chains inside nanoscale channels: physics, biological significance and applications. J. Phys. D Appl. Phys. **41**(10), 103002 (2008)
19. Wan, R., Fang, H.: Water transportation across narrow channel of nanometer dimension. Solid State Commun. **150**(21–22), 968–975 (2010)
20. Craighead, H.: Future lab-on-a-chip technologies for interrogating individual molecules. Nature **442**(7101), 387–393 (2006)
21. Hummer, G., Rasaiah, J.C., Noworyta, J.P.: Water conduction through the hydrophobic channel of a carbon nanotube. Nature **414**, 188–190 (2001)
22. Li, J.Y., Gong, X.J., Lu, H.J., Li, D., Fang, H.P., Zhou, R.H.: Electrostatic gating of a nanometer water channel. Proc. Natl. Acad. Sci. U. S. A. **104**, 3687–3692 (2007)
23. Zhu, F., Schulten, K.: Water and proton conduction through carbon nanotubes as models for biological channels. Biophys. J. **85**(1), 236–244 (2003)
24. Beckstein, O., Sansom, M.S.P.: Liquid–vapor oscillations of water in hydrophobic nanopores. Proc. Natl. Acad. Sci. U. S. A. **100**(12), 7063–7068 (2003)
25. Reiter, G., Burnham, C., Homouz, D., Platzman, P.M., Mayers, J., Abdul-Redah, T., Moravsky, A.P., Li, J.C., Loong, C.K., Kolesnikov, A.I.: Anomalous behavior of proton zero point motion in water confined in carbon nanotubes. Phys. Rev. Lett. **97**(24), 247801 (2006)
26. Sun, L., Crooks, R.M.: Single carbon nanotube membranes: a well-defined model for studying mass transport through nanoporous materials. J. Am. Chem. Soc. **122**(49), 12340–12345 (2000)
27. Tenne, R.: Inorganic nanotubes and fullerene-like nanoparticles. Nat. Nanotech. **1**(2), 103–111 (2006)

28. Joseph, S., Mashl, R.J., Jakobsson, E., Aluru, N.R.: Electrolytic transport in modified carbon nanotubes. Nano Lett. **3**(10), 1399–1403 (2003)
29. Denker, B.M., Smith, B.L., Kuhajda, F.P., Agre, P.: Identification, purification, and partial characterization of a novel Mr 28,000 integral membrane protein from erythrocytes and renal tubules. J. Biol. Chem. **263**(30), 15634–15642 (1988)
30. Zeidel, M.L., Ambudkar, S.V., Smith, B.L., Agre, P.: Reconstitution of functional water channels in liposomes containing purified red cell CHIP28 protein. Biochemistry **31**(33), 7436–7440 (1992)
31. Jensen, M.Ø., Tajkhorshid, E., Schulten, K.: Electrostatic tuning of permeation and selectivity in aquaporin water channels. Biophys. J. **85**(5), 2884–2899 (2003)
32. de Groot, B.L., Grubmuller, H.: Water permeation across biological membranes: mechanism and dynamics of aquaporin-1 and GlpF. Science **294**(5550), 2353–2357 (2001)
33. Chakrabarti, N., Tajkhorshid, E., Roux, B., Pomès, R.: Molecular basis of proton blockage in aquaporins. Structure **12**(1), 65–74 (2004)
34. Tajkhorshid, E., Nollert, P., Jensen, M.O., Miercke, L.J.W., O'Connell, J., Stroud, R.M., Schulten, K.: Control of the selectivity of the aquaporin water channel family by global orientational tuning. Science **296**(5567), 525–530 (2002)
35. Ilan, B., Tajkhorshid, E., Schulten, K., Voth, G.A.: The mechanism of proton exclusion in aquaporin channels. Proteins Struct. Funct. Bioinf. **55**(2), 223–228 (2004)
36. Burykin, A., Warshel, A.: What really prevents proton transport through aquaporin? Charge self-energy versus proton wire proposals. Biophys. J. **85**(6), 3696–3706 (2003)
37. Patargias, G., Bond, P.J., Deol, S.S., Sansom, M.S.P.: Molecular dynamics simulations of GlpF in a Micelle vs in a Bilayer: conformational dynamics of a membrane protein as a function of environment. J. Phys. Chem. B **109**(1), 575–582 (2004)
38. Vidossich, P., Cascella, M., Carloni, P.: Dynamics and energetics of water permeation through the aquaporin channel. Proteins Struct. Funct. Bioinf. **55**(4), 924–931 (2004)
39. Sui, H., Han, B.-G., Lee, J.K., Walian, P., Jap, B.K.: Structural basis of water-specific transport through the AQP1 water channel. Nature **414**(6866), 872–878 (2001)
40. Wan, R.Z., Li, J.Y., Lu, H.J., Fang, H.P.: Controllable water channel gating of nanometer dimensions. J. Am. Chem. Soc. **127**(19), 7166–7170 (2005)
41. Branden, C., Tooze, J.: Introduction to protein structure. Garland Publishing, New York and London (1991)
42. Xiu, P., Zhou, B., Qi, W.P., Lu, H.J., Tu, Y.S., Fang, H.P.: Manipulating biomolecules with aqueous liquids confined within single-walled nanotubes. J. Am. Chem. Soc. **131**(8), 2840–2845 (2009)
43. Gong, X.J., Li, J.Y., Lu, H.J., Wan, R.Z., Li, J.C., Hu, J., Fang, H.P.: A charge-driven molecular water pump. Nat. Nanotech. **2**, 709–712 (2007)
44. Pan, X.L., Fan, Z.L., Chen, W., Ding, Y.J., Luo, H.Y., Bao, X.H.: Enhanced ethanol production inside carbon-nanotube reactors containing catalytic particles. Nat. Mater. **6**(7), 507–511 (2007)
45. Yang, H.Q., Zhang, L., Zhong, L., Yang, Q.H., Li, C.: Enhanced cooperative activation effect in the hydrolytic kinetic resolution of Epoxides on [Co(salen)] catalysts confined in nanocages. Angew. Chem. Int. Ed. **46**(36), 6861–6865 (2007)
46. Won, C.Y., Aluru, N.R.: Water permeation through a subnanometer boron nitride nanotube. J. Am. Chem. Soc. **129**(10), 2748 (2007)
47. Eggers, D.K., Valentine, J.S.: Molecular confinement influences protein structure and enhances thermal protein stability. Protein Sci. **10**(2), 250–261 (2001)
48. Shin, K., Obukhov, S., Chen, J.T., Huh, J., Hwang, Y., Mok, S., Dobriyal, P., Thiyagarajan, P., Russell, T.P.: Enhanced mobility of confined polymers. Nat. Mater. **6**(12), 961–965 (2007)
49. Lucent, D., Vishal, V., Pande, V.S.: Protein folding under confinement: a role for solvent. Proc. Natl. Acad. Sci. U. S. A. **104**(25), 10430–10434 (2007)
50. Zhang, S.Q., Cheung, M.S.: Manipulating biopolymer dynamics by anisotropic nanoconfinement. Nano Lett. **7**(11), 3438–3442 (2007)

51. Sorin, E.J., Pande, V.S.: Nanotube confinement denatures protein helices. J. Am. Chem. Soc. **128**(19), 6316–6317 (2006)
52. Koga, K., Gao, G.T., Tanaka, H., Zeng, X.C.: Formation of ordered ice nanotubes inside carbon nanotubes. Nature **412**(6849), 802–805 (2001)
53. Noon, W.H., Ausman, K.D., Smalley, R.E., Ma, J.P.: Helical ice-sheets inside carbon nanotubes in the physiological condition. Chem. Phys. Lett. **355**(5–6), 445–448 (2002)
54. Mashl, R.J., Joseph, S., Aluru, N.R., Jakobsson, E.: Anomalously immobilized water: a new water phase induced by confinement in nanotubes. Nano Lett. **3**(5), 589–592 (2003)
55. Striolo, A.: The mechanism of water diffusion in narrow carbon nanotubes. Nano Lett. **6**(4), 633–639 (2006)
56. Raghavender, U.S., Kantharaju, Aravinda, S., Shamala, N., Balaram, P.: Hydrophobic peptide channels and encapsulated water wires. J. Am. Chem. Soc. **132**(3), 1075–1086 (2010)
57. Reddy, G., Straub, J.E., Thirumalai, D.: Dry amyloid fibril assembly in a yeast prion peptide is mediated by long-lived structures containing water wires. Proc. Natl. Acad. Sci. U. S. A. **107**(50), 21459–21464 (2010)
58. Xiu, P., Yang, Z.X., Zhou, B., Das, P., Fang, H.P., Zhou, R.H.: Urea-induced drying of hydrophobic nanotubes: comparison of different urea models. J. Phys. Chem. B **115**(12), 2988–2994 (2011)
59. Tu, Y., Xiu, P., Wan, R., Hu, J., Zhou, R., Fang, H.: Water-mediated signal multiplication with Y-shaped carbon nanotubes. Proc. Natl. Acad. Sci. U. S. A. **106**(43), 18120–18124 (2009)
60. Dokter, A.M., Woutersen, S., Bakker, H.J.: Anomalous slowing down of the vibrational relaxation of liquid water upon nanoscale confinement. Phys. Rev. Lett. **94**(17), 178301 (2005)
61. Ju, S.P., Yang, S.H., Liao, M.L.: Study of molecular behavior in a water nanocluster: size and temperature effect. J. Phys. Chem. B **110**(18), 9286–9290 (2006)
62. Vaitheeswaran, S., Thirumalai, D.: Hydrophobic and ionic interactions in nanosized water droplets. J. Am. Chem. Soc. **128**(41), 13490–13496 (2006)
63. Sykes, M.T., Levitt, M.: Simulations of RNA base pairs in a nanodroplet reveal solvation-dependent stability. Proc. Natl. Acad. Sci. U. S. A. **104**(30), 12336–12340 (2007)
64. Yeh, I.C., Hummer, G.: Nucleic acid transport through carbon nanotube membranes. Proc. Natl. Acad. Sci. U. S. A. **101**(33), 12177–12182 (2004)
65. Zimmerli, U., Koumoutsakos, P.: Simulations of electrophoretic RNA transport through transmembrane carbon nanotubes. Biophys. J. **94**(7), 2546–2557 (2008)
66. Insepov, Z., Wolf, D., Hassanein, A.: Nanopumping using carbon nanotubes. Nano Lett. **6**(9), 1893–1895 (2006)
67. Longhurst, M.J., Quirke, N.: Temperature-driven pumping of fluid through single-walled carbon nanotubes. Nano Lett. **7**(11), 3324–3328 (2007)
68. Wang, Z.K., Ci, L.J., Chen, L., Nayak, S., Ajayan, P.M., Koratkar, N.: Polarity-dependent electrochemically controlled transport of water through carbon nanotube membranes. Nano Lett. **7**(3), 697–702 (2007)
69. Savariar, E.N., Krishnamoorthy, K., Thayumanavan, S.: Molecular discrimination inside polymer nanotubules. Nat. Nanotech. **3**(2), 112–117 (2008)
70. Kral, P., Tomanek, D.: Laser-driven atomic pump. Phys. Rev. Lett. **82**(26), 5373–5376 (1999)
71. Balbach, J.J., Ishii, Y., Antzutkin, O.N., Leapman, R.D., Rizzo, N.W., Dyda, F., Reed, J., Tycko, R.: Amyloid fibril formation by A beta(16–22), a seven-residue fragment of the Alzheimer's beta-amyloid peptide, and structural characterization by solid state NMR. Biochemistry **39**(45), 13748–13759 (2000)
72. Bonomi, M., Gervasio, F.L., Tiana, G., Provasi, D., Broglia, R.A., Parrinello, M.: Insight into the folding inhibition of the HIV-1 protease by a small peptide. Biophys. J. **93**(8), 2813–2821 (2007)
73. Bandaru, P.R., Daraio, C., Jin, S., Rao, A.M.: Novel electrical switching behaviour and logic in carbon nanotube Y-junctions. Nat. Mater. **4**(9), 663–666 (2005)
74. Bachtold, A., Hadley, P., Nakanishi, T., Dekker, C.: Logic circuits with carbon nanotube transistors. Science **294**(5545), 1317–1320 (2001)

75. Fan, R., Yue, M., Karnik, R., Majumdar, A., Yang, P.D.: Polarity switching and transient responses in single nanotube nanofluidic transistors. Phys. Rev. Lett. **95**(8), 086607 (2005)
76. Chen, F., Hihath, J., Huang, Z., Li, X., Tao, N.J.: Measurement of single-molecule conductance. Annu. Rev. Phys. Chem. **58**(1), 535–564 (2007)
77. Heath, J.R.: Molecular electronics. Annu. Rev. Mater. Res. **39**(1), 1–23 (2009)
78. Drummond, T., Hill, M., Barton, J.: Electrochemical DNA sensors. Nat. Biotechnol. **21**(10), 1192–1199 (2003)
79. Yuan, G.D., Zhang, W.J., Jie, J.S., Fan, X., Zapien, J.A., Leung, Y.H., Luo, L.B., Wang, P.F., Lee, C.S., Lee, S.T.: p-Type ZnO nanowire arrays. Nano Lett. **8**(8), 2591–2597 (2008)
80. Kong, J., Franklin, N., Zhou, C., Chapline, M., Peng, S., Cho, K., Dai, H.: Nanotube molecular wires as chemical sensors. Science **287**(5453), 622–625 (1999)
81. Cui, Y., Wei, Q., Park, H., Lieber, C.: Nanowire nanosensors for highly sensitive and selective detection of biological and chemical species. Science **293**(5533), 1289 (2001)
82. Li, D., Song, S., Fan, C.: Target-responsive structural switching for nucleic acid-based sensors. Acc. Chem. Res. **43**(5), 631–641 (2010)
83. Bennett, M., Zukin, R.: Electrical coupling and neuronal synchronization in the mammalian brain. Neuron **41**(4), 495–511 (2004)
84. Connors, B., Long, M.: Electrical synapses in the mammalian brain. Annu. Rev. Neurosci. **27**, 393–418 (2004)
85. Bartos, M., Vida, I., Jonas, P.: Synaptic mechanisms of synchronized gamma oscillations in inhibitory interneuron networks. Nat. Rev. Neurosci. **8**(1), 45–56 (2007)
86. Söhl, G., Maxeiner, S., Willecke, K.: Expression and functions of neuronal gap junctions. Nat. Rev. Neurosci. **6**, 191 (2005)
87. Hormuzdi, S., Pais, I., LeBeau, F., Towers, S., Rozov, A., Buhl, E., Whittington, M., Monyer, H.: Impaired electrical signaling disrupts gamma frequency oscillations in Connexin 36-Deficient Mice. Neuron **31**, 487–495 (2001)
88. Amitai, Y., Gibson, J., Beierlein, M., Patrick, S., Ho, A., Connors, B., Golomb, D.: The spatial dimensions of electrically coupled networks of interneurons in the neocortex. J. Neurosci. **22**(10), 4142 (2002)
89. Zoidl, G., Dermietzel, R.: On the search for the electrical synapse: a glimpse at the future. Cell Tissue Res. **310**(2), 137–142 (2002)
90. Pfeuty, B., Mato, G., Golomb, D., Hansel, D.: Electrical synapses and synchrony: the role of intrinsic currents. J. Neurosci. **23**(15), 6280 (2003)
91. Smock, R.G., Gierasch, L.M.: Sending signals dynamically. Science **324**(5924), 198–203 (2009)
92. Tsai, C.-J., del Sol, A., Nussinov, R.: Allostery: absence of a change in shape does not imply that allostery is not at play. J. Mol. Biol. **378**(1), 1–11 (2008)
93. Tsai, C., Sol, A., Nussinov, R.: Protein allostery, signal transmission and dynamics: a classification scheme of allosteric mechanisms. Mol. Biosyst. **5**(3), 207–216 (2009)
94. Sethna, J.: Statistical mechanics: entropy, order parameters, and complexity. Oxford University Press, USA (2006)
95. Dudko, O.: Statistical mechanics: entropy, order parameters, and complexity. J. Stat. Phys. **126**(2), 429–430 (2007)
96. de Jonge, J.J., Ratner, M.A., de Leeuw, S.W., Simonis, R.O.: Molecular dipole chains III: energy transfer. J. Phys. Chem. B **108**(8), 2666–2675 (2004)
97. de Jonge, J.J., Ratner, M.A., de Leeuw, S.W., Simonis, R.O.: Controlling the energy transfer in dipole chains. J. Phys. Chem. B **110**(1), 442–446 (2005)
98. de Jonge, J.J., Ratner, M.A., de Leeuw, S.W.: Local field controlled switching in a one-dimensional dipolar array. J. Phys. Chem. C **111**(9), 3770–3777 (2007)
99. Ball, P.: Water as an active constituent in cell biology. Chem. Rev. **108**(1), 74–108 (2008)
100. Zhou, R.H., Huang, X.H., Margulis, C.J., Berne, B.J.: Hydrophobic collapse in multidomain protein folding. Science **305**(5690), 1605–1609 (2004)
101. Brewer, M.L., Schmitt, U.W., Voth, G.A.: The formation and dynamics of proton wires in channel environments. Biophys. J. **80**(4), 1691–1702 (2001)

102. Pomes, R., Roux, B.: Molecular mechanism of H+ conduction in the single-file water chain of the gramicidin channel. Biophys. J. **82**(5), 2304–2316 (2002)
103. Beckstein, O., Biggin, P.C., Sansom, M.S.P.: A hydrophobic gating mechanism for nanopores. J. Phys. Chem. B **105**(51), 12902–12905 (2001)
104. Köfinger, J., Hummer, G., Dellago, C.: Macroscopically ordered water in nanopores. Proc. Natl. Acad. Sci. U. S. A. **105**(36), 13218–13222 (2008)
105. Berendsen, H.J.C., Postma, J.P.M., van Gunsteren, W.F., DiNola, A., Haak, J.R.: Molecular dynamics with coupling to an external bath. J. Chem. Phys. **81**(8), 3684–3690 (1984)
106. Berendsen, H.J.C., van der Spoel, D., van Drunen, R.: GROMACS: a message-passing parallel molecular dynamics implementation. Comput. Phys. Commun. **91**(1–3), 43–56 (1995)
107. Hua, L., Zhou, R., Thirumalai, D., Berne, B.: Urea denaturation by stronger dispersion interactions with proteins than water implies a 2-stage unfolding. Proc. Natl. Acad. Sci. U. S. A. **105**(44), 16928 (2008)
108. Lindahl, E., Hess, B., van der Spoel, D.: GROMACS 3.0: a package for molecular simulation and trajectory analysis. J. Mol. Model. **7**(8), 306–317 (2001)
109. Zhou, R.: Exploring the protein folding free energy landscape: coupling replica exchange method with P3ME/RESPA algorithm. J. Mol. Graph. Model **22**(5), 451–463 (2004)
110. Hua, L., Huang, X., Zhou, R., Berne, B.J.: Dynamics of water confined in the interdomain region of a multidomain protein. J. Phys. Chem. B **110**(8), 3704–3711 (2006)
111. Liu, P., Huang, X., Zhou, R., Berne, B.J.: Hydrophobic aided replica exchange: an efficient algorithm for protein folding in explicit solvent. J. Phys. Chem. B **110**(38), 19018–19022 (2006)
112. Darden, T., York, D., Pedersen, L.: Particle mesh Ewald: an N [center-dot] log(N) method for Ewald sums in large systems. J. Chem. Phys. **98**(12), 10089–10092 (1993)
113. Papadopoulos, C., Rakitin, A., Li, J., Vedeneev, A.S., Xu, J.M.: Electronic transport in Y-junction carbon nanotubes. Phys. Rev. Lett. **85**(16), 3476 (2000)
114. Satishkumar, B.C., Thomas, P.J., Govindaraj, A., Rao, C.N.R.: Y-junction carbon nanotubes. Appl. Phys. Lett. **77**(16), 2530–2532 (2000)
115. Li, W.Z., Wen, J.G., Ren, Z.F.: Straight carbon nanotube Y junctions. Appl. Phys. Lett. **79**(12), 1879–1881 (2001)
116. Deepak, F.L., Govindaraj, A., Rao, C.N.R.: Synthetic strategies for Y-junction carbon nanotubes. Chem. Phys. Lett. **345**(1–2), 5–10 (2001)
117. Terrones, M., Banhart, F., Grobert, N., Charlier, J.C., Terrones, H., Ajayan, P.M.: Molecular junctions by joining single-walled carbon nanotubes. Phys. Rev. Lett. **89**(7), 075505 (2002)
118. Gothard, N., Daraio, C., Gaillard, J., Zidan, R., Jin, S., Rao, A.M.: Controlled growth of Y-junction nanotubes using Ti-Doped vapor catalyst. Nano Lett. **4**(2), 213–217 (2004)
119. Liu, P., Huang, X., Zhou, R., Berne, B.: Observation of a dewetting transition in the collapse of the melittin tetramer. Nature **437**(7055), 159–162 (2005)
120. Søgaard-Andersen, L.: Cell polarity, intercellular signalling and morphogenetic cell movements in Myxococcus xanthus. Curr. Opin. Microbiol. **7**(6), 587–593 (2004)
121. Yang, Z.: Cell polarity signaling in Arabidopsis. Annu. Rev. Cell Dev. Bi. **24**, 551–575 (2008)
122. Fuller-Espie, S., Hoffman Towler, P., Wiest, D., Tietjen, I., Spain, L.: Transmembrane polar residues of TCR beta chain are required for signal transduction. Int. Immunol. **10**(7), 923 (1998)
123. Jones, C., Roper, V.C., Foucher, I., Qian, D., Banizs, B., Petit, C., Yoder, B.K., Chen, P.: Ciliary proteins link basal body polarization to planar cell polarity regulation. Nat. Genet. **40**(1), 69–77 (2008)
124. Ganner, A., Lienkamp, S., Schäfer, T., Romaker, D., Wegierski, T., Park, T., Spreitzer, S., Simons, M., Gloy, J., Kim, E.: Regulation of ciliary polarity by the APC/C. Proc. Natl. Acad. Sci. U. S. A. **106**(42), 17799 (2009)
125. Axelrod, J.: Unipolar membrane association of Dishevelled mediates Frizzled planar cell polarity signaling. Gene. Dev. **15**(10), 1182 (2001)

126. Mitchell, B., Jacobs, R., Li, J., Chien, S., Kintner, C.: A positive feedback mechanism governs the polarity and motion of motile cilia. Nature **447**(7140), 97–101 (2007)
127. Miao, L., Seminario, J.: Molecular dynamics simulations of signal transmission through a glycine peptide chain. J. Chem. Phys. **127**, 134708 (2007)
128. Li, J.-Y., Yang, Z.-X., Fang, H.-P., Zhou, R.-H., Tang, X.-W.: Effect of the carbon-nanotube length on water permeability. Chin. Phys. Lett. **24**(9), 2710–2713 (2007)
129. Lu, H., Li, J., Gong, X., Wan, R., Zeng, L., Fang, H.: Water permeation and wavelike density distributions inside narrow nanochannels. Phys. Rev. B **77**(17), 174115 (2008)
130. Lu, H.-J., Gong, X.-J., Wang, C.-L., Fang, H.-P., Wan, R.-Z.: Effect of vibration on water transport through carbon nanotubes. Chin. Phys. Lett. **25**(3), 1145–1148 (2008)
131. Wu, L., Wu, F., Kou, J., Lu, H., Liu, Y.: Effect of the position of constriction on water permeation across a single-walled carbon nanotube. Phy. Rev. E **83**(6), 061913 (2011)
132. Tu, Y., Zhou, R., Fang, H.: Signal transmission, conversion and multiplication by polar molecules confined in nanochannels. Nanoscale **2**(8), 1976–1983 (2010)

Chapter 2
Survival from the Cold Winter: Freezing and Ice Crystallization Inhibition by Antifreeze Proteins

Ning Du, Guoyang William Toh, and Xiang Yang Liu

Abstract Antifreeze proteins (AFPs), occurring in some polar animals, plants, fungi, and other organisms, are capable of inhibiting ice freezing at subzero temperatures. The application of AFPs can be found in medicine and industry where low temperature storage is required and ice crystallization is damaging. This includes improved protection of blood platelets and human organs at low temperature, increasing the effectiveness of the destruction of malignant tumors in cryosurgery, and improvement of the smooth texture of frozen foods. In this review, the antifreeze mechanisms of AFPs are discussed, focusing on their inhibition effects on both ice nucleation and crystal growth. AFPs have been found to act in two stages. As a precursor to ice growth, ice nucleation is suppressed by the surface adsorption of AFPs to both ice nucleus and ice nucleators. At the second stage, in cases where inhibition of ice nucleation has had partial or no success, AFPs proceed to inhibit the growth of ice by adsorbing on specific surfaces of ice. Based

*The authors Ning Du, Guoyang William Toh, contributed equally to this work.

N. Du
Department of Physics and Department of Chemistry, Faculty of Science, National University of Singapore, 2 Science Drive 3, 117542, Singapore

Singapore-MIT Alliance for Research and Technology Center, Block S16, 3 Science Drive 2, Singapore, 117543 Singapore

G.W. Toh
Department of Physics and Department of Chemistry, Faculty of Science, National University of Singapore, 2 Science Drive 3, 117542, Singapore

X.Y. Liu (✉)
College of Materials, Xiamen University, 422 Si Ming Nan Road, Xiamen, 361005, P.R. China

Department of Physics and Department of Chemistry, Faculty of Science, National University of Singapore, 2 Science Drive 3, 117542, Singapore
e-mail: phyliuxy@nus.edu.sg

X.Y. Liu (ed.), *Bioinspiration: From Nano to Micro Scales*, Biological and Medical Physics, Biomedical Engineering, DOI 10.1007/978-1-4614-5372-7_2,

on the understanding of structure–activity relationship, one is able to mimic the active domain of AFGPs and synthesize antifreeze glycoproteins by using ligation and polymerization strategies. However, further optimization of the chemistry, as well as new routes to mimic AFPs and functional analogues are needed to allow the routine production of quantities of pure material on commercially relevant scales.

Keywords Ice nucleation • Ice crystal growth • Antifreeze protein • Thermal hysteresis • Heterogeneous nucleation • Nucleation kinetics • Ice nucleator • Cryoprotection • Morphological modification • AFP mimics

2.1 Introduction

2.1.1 Freezing and Antifreeze in Biological Systems

Water is the solvent of all biological systems, and the necessity of maintaining a liquid state at the cellular level for life is obvious. For poikilotherms, the limits of cellular function and life are set by the temperatures at which phase transitions of water take place. Thermodynamically, when ice becomes a stable phase, the freezing of water may occur spontaneously. Nevertheless, normally the freezing point of either water or the body fluids of the organism is lower than 0°C due to kinetic factors.

The understanding of the freezing of water in microsized water droplets is crucial in climate change, agriculture, food industries, and life sciences [1–5]. Freezing is a process of ice crystallization from supercooled water. In this process, water should undergo the stage of ice nucleation, followed by the growth of ice [6–9]. Nucleation is the key step to determine if or not ice will occur in the supercooled water, while the growth process will determine how big and what shape the ice crystallites will acquire. Actually, whether or not freezing takes place is determined to a large extent by ice nucleation. In other words, there would be no ice crystallization if ice nucleation does not occur. Therefore, to control freezing one should first control ice nucleation and the growth if nucleation control fails.

Due to the fact that ice nucleation is the initial and one of the most important steps in the freezing process, the question of whether ice crystallization is governed by homogeneous or heterogeneous nucleation bears significant implications for antifreeze, ice nucleation promotion, and freezing-related phenomena and activities. It was considered that spontaneous nucleation of ice from water, in particular below −40°C, belongs to “homogeneous nucleation” [2–5, 10, 11]. This implies that the freezing of water is considered to be clean and dusts or foreign bodies exert no influence on nucleation. The key questions to be addressed are whether the conclusion is correct, and if not, under what condition homogeneous nucleation will take place. The latest results indicate that under a well-controlled condition, the influence of dust particles on freezing is still effective below −40°C [12] or heterogeneous nucleation of ice still occurs below −40°C. According to the recent

most accurate estimation of the ice–water interfacial energy, and the homogeneous nucleation barrier, genuine homogeneous ice nucleation may hardly take place even below −80°C [12]. This implies that if we can eliminate the influence of foreign bodies, freezing may never occur [12].

As freezing is mediated by minute foreign particles, i.e., dust particles, bacterial epiphytes, which cannot be removed completely, in theory, the most effective way to block freezing is to inhibit the promoting effect of foreign bodies on nucleation. In this regard, the understanding of ice nucleation under the influence of minute foreign particles is particularly important for the identification of novel technologies in controlling freezing and antifreeze in general.

Due to the fact that crystallization involves nucleation and growth, the inhibition of the growth of ice crystallites becomes important if the nucleation inhibition fails. We notice that many antifreeze proteins (AFPs) are capable of modifying the growth habit of ice crystallites. As the habit modification is attributed to the retardation of some particular orientations in the crystal growth form [13–17], we therefore can consider the habit modification as a special case of the growth inhibition.

Many plants, fish, insects, and other organisms have evolved with unique adaptive mechanisms that allow them to survive in harsh environments at the extremes of temperature [18–21]. Scholander [22, 23] and DeVries [24, 25] were the first to investigate the mechanisms by which polar fish are able to survive. Analysis of the blood plasma of these fish showed that while the concentrations of salts and small ions in the body fluids are somewhat higher relative to fish in temperate waters, these salts are only responsible for 40–50% of the observed freezing point depression. The remainder of the protective effect was attributed to the presence of a series of relatively high molecular mass glycoproteins and proteins [26–29].

The eminent antifreeze effect results from AFPs found in the blood and tissues of organisms that live in freezing environments [2]. In these organisms, the effect of freezing proteins is retarded, or the damage incurred upon freezing and thawing is reduced [2–4]. Applications of the antifreeze effect of these AFPs, the capacity to inhibit ice crystallization, have been sought for maintaining texture in frozen foods, improving storage of blood, tissues and organs, cryosurgery, and protecting crops from freezing [4].

AFPs and antifreeze glycoproteins (AFGPs) have since been identified in the body fluids of many species of polar fish. The study of annual cycle of AFP production and secretion into the blood in polar fish such as winter flounder indicates that plasma AFP levels correlate closely with the annual cycle of seawater temperatures. AFP appears in the plasma as the water temperature declines, reaches peak levels of 10–15 mg/mL during winter, and clears from the plasma as the temperature rises above 0°C [30]. Peak levels of AFP during winter reduce the plasma freezing temperature of winter flounder to approximately −1.7°C.

In this chapter, we will review the latest works on freezing kinetics and the antifreeze mechanism of AFP and AFGPs. This includes the effect of a trace amount of foreign nanoparticles on ice nucleation in ultrapure microsized water droplets and its implications for freezing and antifreeze in general. As highlighted earlier, how AFPs change the surface characteristics of foreign bodies so as to inhibit ice

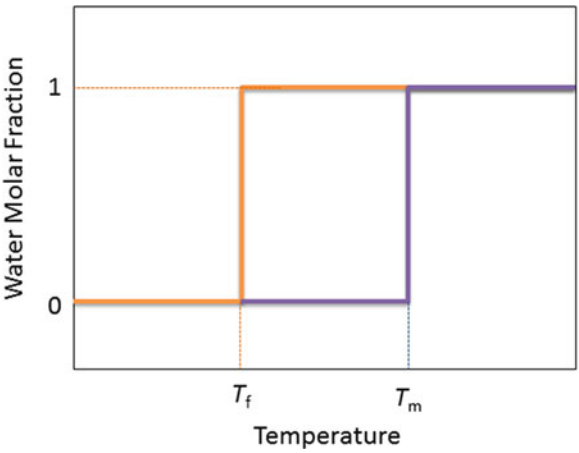

Fig. 2.1 Definition of hysteresis ($=T_m - T_f$)

nucleation will be reviewed. The inhibition of AFP and AFGPs on the growth of ice crystals will also be discussed on a surface structural analysis. We notice that although there have been a significant number of papers on AFPs, a comprehensive overview on freezing promotion and antifreeze mechanisms from a kinetic point of view has never been achieved yet. The applications of AFP and AFGPs will also be reviewed at the end. This chapter will provide a platform to review the works in this area. Hopefully, the knowledge obtained here will provide some basic ideas to mimic the antifreeze effect without AFPs.

2.1.2 Thermal Hysteresis of AFPs

There are two classes of substances that inhibit water freezing. The first class comprises those solutes that depress both freezing point and melting point. Such substances include sodium chloride, glycerol, glucose, etc. The first class is to change the equilibrium point and can be regarded as a thermodynamic approach. The second class comprises substances having the ability to depress freezing point without significantly affecting the melting point. This is attributed to the change of the freezing kinetics, mainly nucleation and growth. Therefore, the substances mainly block ice formation based on the kinetic factors.

AFPs, also known as thermal hysteresis proteins, lowering the nonequilibrium freezing point of water while not significantly affecting the melting point, belong to the second class. The difference between the freezing and melting points is termed "thermal hysteresis." The magnitude of this characteristic thermal hysteresis activity is dependent upon the specific activity and concentration of the particular AFP [25] (Fig. 2.1).

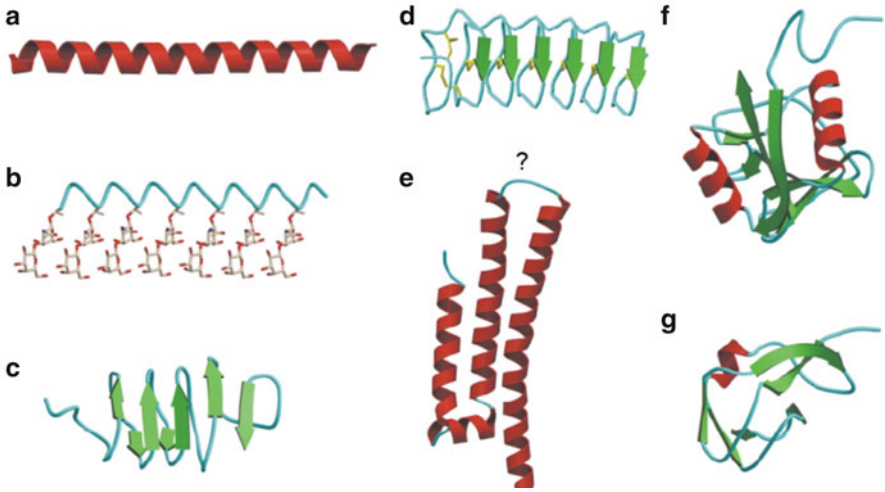

Fig. 2.2 Diversity of fish AFGPs. (**a**) Type I AFP from winter flounder. (**b**) Antifreeze glycoprotein (AFGP). (**c**) Spruce budworm AFP. (**d**) *Tenebrio molitor* AFP. (**e**) Type IV AFP. (**f**, **g**) Nonrepetitive AFPs. (**f**) Type II AFP from sea raven (2AFP). (**g**) Type III AFP from ocean pout. Reprinted with permission from ref. [31]. Copyright (2002) Elsevier

2.1.3 AFP Diversity

For over 50 years since their initial discovery, AFPs and AFGPs have been identified in the body fluids of many species of polar fish. Four classes of structurally diverse fish AFPs (cf. Fig. 2.2), classified as type I [32], type II [33], type III [34], and type IV [35], have now been identified along with a single class of glycosylated protein denoted AFGP [36].

Although AFPs were first discovered in fish, the phenomenon of thermal hysteresis was initially observed by Ramsay in larvae of the beetle *Tenebrio molitor* [37] during his classic investigation of the physiology of the cryptonephridial rectal complex. AFPs have also been identified in several other terrestrial arthropods including spiders [38], mites [39], and centipedes [40]. AFPs have been identified, often based on their thermal hysteresis activity, in over 40 species of insects (cf. Fig. 2.2). Among the insects, 65% of the known AFP-producing species are beetles [41]. AFPs have been shown to be also common in plants [42], fungi, and bacteria [19].

2.2 Ice Nucleation Inhibition by Antifreeze Proteins

2.2.1 Structure of Ice

The crystals of ice consist of a periodic 3D array of water molecules bound together by hydrogen bonds. The hydrogen bonding in water molecules is the starting point to account for the structure of ice. The basic structure of ice is well established by Pauling [43] and illustrated in Fig. 2.3. The oxygen atoms, shown by the dark balls, are arranged on a hexagonal lattice. Hexagonal ice belongs to the space group *P*63/*mmc*, $a = 4.519$ Å and $c = 7.357$ Å. The unit cell contains four water molecules, taken at the oxygen positions. The O–O bonds, having lengths $p = 2.763$ Å and $q = 2.765$ Å, are in tetrahedral coordination. Each oxygen has four bonds in the first coordination sphere. Whereas the q bonds of each oxygen are symmetrically related, the p bond is symmetrically distinct.

As indicated, in the case of freezing, i.e., ice crystallization, nucleation is the initial and one of the most important steps toward creating ice [1]. Without this step, ice will never occur in supercooled water. In order to discuss the antifreeze mechanism of AFPs, we will first review the nucleation of ice in general.

2.2.2 Ice Nucleation Kinetics

Since the nucleation phenomenon was identified and studied by Gibbs, numerous models and theories have been published. Nevertheless, the first detailed experiment monitoring nucleation from the pre-nucleation to post-nucleation stages and quantitatively comparing them with the theories was carried by Liu et al. [45]. A general picture of 3D nucleation was described in ref. [46]. The constituent atoms

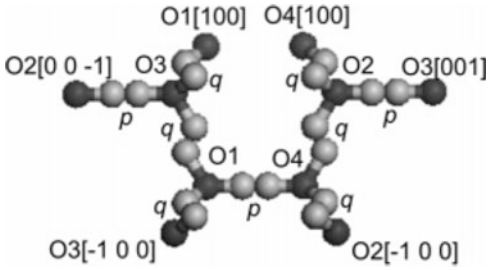

Fig. 2.3 Unit cell of hexagonal ice consisting of water molecules with oxygen atoms 1–4, projected on a plane perpendicular to the *b*-axis, and for each oxygen, the strong bonds (p, q, q, q) in the first coordination sphere. Each strong bond consists of two O–O links, mediated by two hydrogen atoms. *Dark balls* oxygen atoms; *light balls* hydrogen atoms. Reprinted with permission from ref. [44]. Copyright (2005) American Chemical Society

or molecules in the solution may, on collision, join into groups of two, three, four, or more particles, forming dimers, trimers, tetramers, etc. The kinetics of nucleation is described by the nucleation rate J, which is defined as the number of nuclei created per unit volume-time, and determined by the nucleation barrier, kink integration rate, transport, and other factors. J is an important characteristic of the process of new phase formation.

2.2.2.1 Thermodynamic Driving Force

Nucleation is the process in which the first-order phase transitions begin. The driving force for nucleation of new phases (e.g., crystals) $\Delta\mu$, which is defined as the difference between the chemical potentials of a growth unit in the mother and the crystalline, and for ice crystallization, is given according to [47]:

$$\Delta\mu = \frac{\Delta h_{\mathrm{m}} \Delta T}{T_{\mathrm{e}}}, \tag{2.1}$$

$$\Delta T = (T_{\mathrm{e}} - T), \tag{2.2}$$

where Δh_{m} is the ice enthalpy of melting per molecule, T_{e} is the equilibrium temperature (the melting temperature of ice), and ΔT is supercooling.

2.2.2.2 Nucleation Barrier

A characteristic feature of the nucleation process is that the substance with the properties of the new phase is fluctuating and localized in small nanoscale spatial regions. These are occupied by various numbers of atoms or molecules in the form of clusters. The clusters remaining at equilibrium with the surrounding mother phase are the critical nuclei, and the smaller or the larger clusters are the subnuclei or supernuclei, respectively. Only the supernuclei are the clusters that can grow spontaneously to reach macroscopic sizes. For simplicity, we call hereafter the subnuclei "clusters," and the supernuclei "nuclei" (cf. Fig. 2.4a).

The nucleation rate J describing the number of nuclei successfully generated from the population of clusters per unit time, per unit volume is determined by the height of the free energy barrier, the so-called nucleation barrier. The occurrence of a nucleation barrier is attributed to the following two opposing effects:

1. Since the crystalline phase is a stable phase, the emergence of the new phase from the mother phase will lead to a lowering of the (Gibbs) free energy of the system.

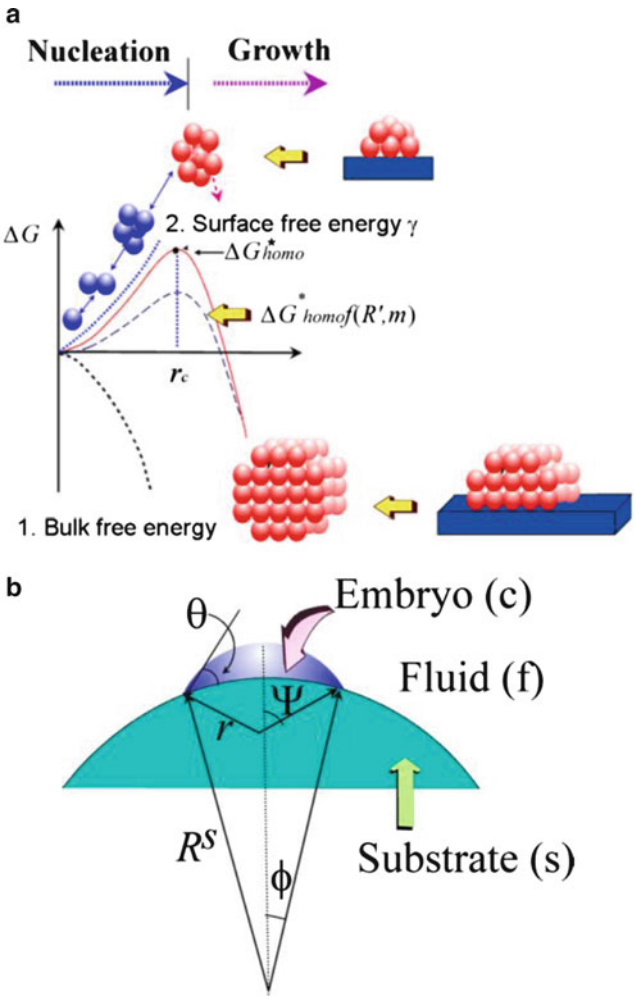

Fig. 2.4 (**a**) Crystallization normally takes place via nucleation, followed by the growth of crystals. Nucleation is a kinetic process of overcoming the nucleation barrier, which is the outcome of the occurrence of the surface free energy γ. Reprinted with permission from ref. [48]. Copyright (2012) WILEY-VCH Verlag GmbH. (**b**) Illustration of nucleation on a foreign particle. θ is the virtual contact angle between nucleating phase and substrate. Reprinted with permission from ref. [8]. Copyright (2004) Springer

2. Due to the interfacial (or surface) free energy, the increase in the size of the crystalline new phase leads to an increase in the interface (or surface) area, and consequently the interface (or surface) free energy. This will cause an increase in the Gibbs free energy of the system. The combination of these two effects results in the formation of the nucleation barrier.

The free energy change to form a cluster of $n = 1, 2, 3, \ldots$ molecules can be found by thermodynamic considerations, since it is defined as

$$\Delta G = G_{\text{fin}} - G_{\text{ini}} \tag{2.3}$$

for a system at constant pressure and temperature (G_{ini} and G_{fin} denotes the Gibbs free energies of the system in the initial and final states before and after the cluster formation, respectively).

$$\Delta G = -n\Delta\mu + \Phi_n, \tag{2.4}$$

where Φ_n is the total surface energy of the n-sized cluster.

ΔG reaches its maximum ΔG^* at $r = r_c$, or $n = n^*$. The cluster of n^* molecules is the critical nucleus, r_c is the radius of curvature of the critical nuclei, and ΔG^* is the nucleation barrier. One of the major problems in the nucleation theory is to find ΔG^*, which, physically, is the energy barrier of nucleation.

The occurrence of foreign bodies in the nucleation system normally reduces the interfacial (or surface) free energy, which therefore will also lower the nucleation barrier. Under a given condition, if the probability of creating a nucleus is homogeneous throughout the system, the nucleation is considered to be homogeneous nucleation. Otherwise, it is considered to be heterogeneous nucleation. In heterogeneous nucleation on solid or liquid surfaces, microclusters, dusts, and macromolecules, the property of these foreign bodies is an additional factor upon which this barrier and rate depend. Let ΔG^*_{homo}, be the homogeneous nucleation barrier, and $\Delta G^*_{\text{hetero}}$ be the heterogeneous nucleation barrier (the nucleation barrier in the presence of a foreign body.) We can then define here a factor describing the lowering of the nucleation barrier due to the foreign body:

$$f = \frac{\Delta G^*_{\text{heter}}}{\Delta G^*_{\text{homo}}}. \tag{2.5}$$

In the following, $\Delta G^*_{\text{heter}}$ and f are derived [49].

As shown in Fig. 2.4b, we assume that nucleation occurs at a foreign body with a radius of R^s. The mother phase is represented by subscript f, the cluster of the crystalline phase by c, and the foreign body by s. If we denote the volume by V and the surface area of the foreign body by S, then the free energy of formation of a cluster of radius r on a nucleating particle of radius R^s is given, according to (2.4), by

$$\Delta G = -\Delta\mu V_c/\Omega + \gamma_{cf} S_{cf} + (\gamma_{sf} - \gamma_{sc}) S_{sc}, \tag{2.6}$$

where γ_{ij} is the surface free energy between phases i and j and Ω is the volume per structural unit. Assume that the concept of contact angle can still be applied in this case. We have then

$$m = \frac{\gamma_{sf} - \gamma_{sc}}{\gamma_{cf}} \approx \cos\theta \quad (-1 \leqslant m \leqslant 1). \tag{2.7}$$

Referring again to Fig. 2.4, we have

$$S_{sc} = 2\pi(R^s)^2(1-\cos\varphi), \quad S_{cf} = 2\pi r^2(1-\cos\Psi),$$
$$\text{and} \quad V_c = \frac{1}{3}\pi r^3(2-3\cos\Psi+\cos^3\Psi) - \frac{1}{3}\pi(R^s)^3(2-3\cos\varphi+\cos^3\varphi), \tag{2.8}$$

$$\cos\varphi = (R^s - r\cos\theta)/l = (R^s - rm)/l, \tag{2.9}$$

$$\cos\Psi = -(r - R^s\cos\theta)/l = -(r - R^s m)/l, \tag{2.10}$$

and

$$l = [(R^s)^2 + r^2 - 2R^s rm]^{1/2}. \tag{2.11}$$

To evaluate the critical free energy ΔG^*_{heter}, we can substitute expression (2.8) into (2.6) and require that

$$\frac{\partial \Delta G}{\partial r} = 0. \tag{2.12}$$

Regarding the fact that the radius of curvature r_c of the critical nuclei is only determined by γ_{cf} and the driving force $\Delta\mu$ [49], we then have

$$r_c = \frac{2\Omega\gamma_{cf}}{\Delta\mu}. \tag{2.13}$$

We notice that in the case of epitaxial growth, some strain will develop due to the structural mismatch at the crystal–substrate interface. The strain will affect both the bulk free energy of nuclei and the interfacial free energy γ_{cf}. In this case, the occurrence of substrate affects r_c.

Now substituting expressions (2.7)–(2.13) into (2.6) and writing

$$R\prime = \frac{R^s}{r_c} = \frac{R^s\Delta\mu}{\Omega\gamma_{cf}}, \tag{2.14}$$

the free energy of formation of a critical nucleus is

$$\Delta G^*_{heter} = \Delta G^*_{homo} f \tag{2.15}$$

with

$$\Delta G^*_{homo} = \frac{16\pi\gamma_{cf}^3\Omega^2}{3kS_m^2 T\Delta T^2}, \tag{2.16}$$

$$f(m, R') = \frac{1}{2} + \frac{1}{2}\left(\frac{1 - mR'}{w}\right)^2 + \frac{1}{2}R'^3\left[2 - 3\left(\frac{R' - m}{w}\right) + \left(\frac{R' - m}{w}\right)^2\right] + \frac{3}{2}mR'^2\left(\frac{R' - m}{w} - 1\right) \tag{2.17}$$

and

$$w = (1 + (R')^2 - 2R'm)^{1/2}. \tag{2.18}$$

Here R' is actually the dimensionless radius of the curvature of the substrate with respect to the radius of the critical nuclei r_c. In other words, it only makes sense if the curvature of a foreign body or a substrate refers to the curvature of the critical nuclei.

Substituting appropriate values of R^s, m, γ_{cf}, and $\Delta\mu$ into (2.13)–(2.18), one can calculate $f(m, R')$ and ΔG^*_{heter} for any nucleation process. Note that the factor $f(m, R')$ varies from 1 to 0. Obviously, this factor plays an important role in the determination of the heterogeneous nucleation barrier ΔG^*_{heter}. One can see from (2.5) that the influence of foreign particles on the nucleation barrier can be fully characterized by f.

Figure 2.5a shows $f(m, R')$ as a function of R' for a given m. When $R' \to 0$, $f(m, R') = 1$, implying that the foreign body as a nucleating substrate will "vanish" completely. In practice, if foreign bodies are too small, i.e., clusters of several molecules, nucleation on these substrates will not be stable. Then, the foreign bodies play no role in lowering the nucleation barrier. If $R' \gg 1$, the foreign body can be treated as a flat substrate compared to the critical nuclei. In this case, $f(m, R')$ is solely a function of m (Fig. 2.5b), and the curvature of the foreign body has no effect on the nucleation kinetics. Equation (2.17) is then reduced to

$$f(m, R') = f(m) = \frac{1}{4}(2 - 3m + m^3). \tag{2.19}$$

2.2.2.3 Heterogeneous Nucleation: The Effect of Ice Nucleators

Let us recapture the picture of the heterogeneous nucleation model. On the substrate surface, some molecular processes occur due to transient visiting molecules that adsorb, form short-lived unions, break up, desorb, etc. An instantaneous census would show some distributions of subcritical nuclei (or clusters) with 1, 2, 3, ... molecules per cluster (cf. Fig. 2.6). Taking into account the effect of the substrate on both the nucleation barrier and the transport process, and the fact that the average nucleation rate in the fluid phase depends on the density and size of foreign particles present in the system, the nucleation rate is given by [50].

$$J = 4\pi a \beta_{kink}[(R^s)^2 N^o] f''(m)[f(m)]^{1/2} B \exp[-\kappa f(m)/(T\Delta T^2)] \tag{2.20}$$

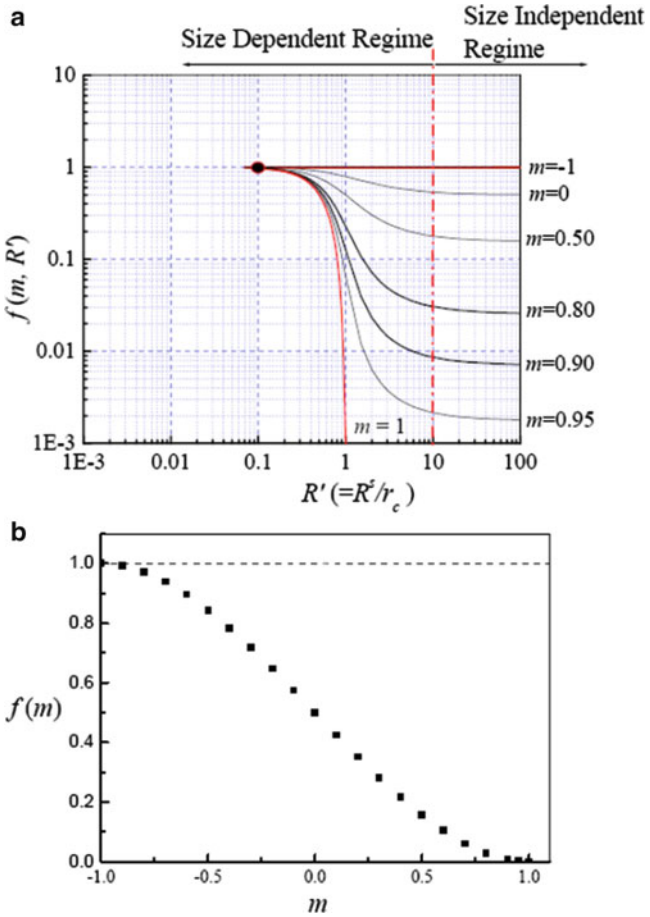

Fig. 2.5 (**a**) Dependence of the interfacial correlation function $f(m, R')$ on m and R'. (**b**) Dependence of the interfacial correlation function $f(m, R')$ on m at $R' > 10$. Reprinted with permission from ref. [8]. Copyright (2004) Springer

with

$$\kappa = \frac{16\pi\gamma_{\mathrm{cf}}^3\Omega^2}{3kS_{\mathrm{m}}^2},$$

$$B = 14\pi a^2\Omega\left(\frac{\gamma_{\mathrm{cf}}}{kT}\right)^{1/2}, \tag{2.21}$$

$$f''(m, R') = \frac{1 + (1 - R'm)/w}{2} \tag{2.22}$$

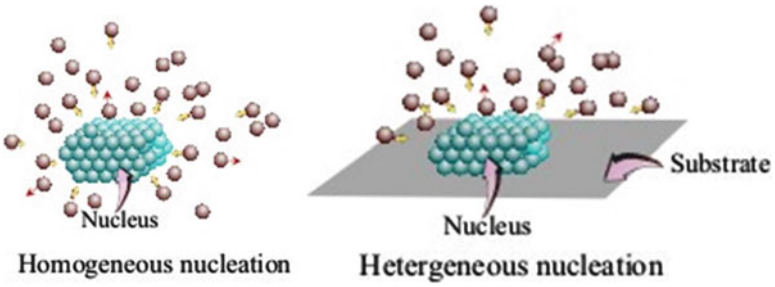

Fig. 2.6 Scheme of the shadow effect of the substrate in heterogeneous nucleation. Reprinted with permission from ref. [8]. Copyright (2004) Springer

and

$$f''(m, R') = f''(m) = \frac{1}{2}(1 - m) \text{ at } R' \gg 1, \tag{2.23}$$

where B is the kinetic constant and N° denotes the density of substrates (or "seeds"). The growth of nuclei is subject to collisions between growth units and the surfaces of the nuclei, followed by incorporation of the growth units in the nuclei (cf. Fig. 2.6). In the case of homogeneous nucleation, growth units can be incorporated into the nuclei from all directions. However, in the case of heterogeneous nucleation, the presence of substrates will block the collision of growth units with the surfaces of these nuclei. $f''(m, R')$ in the preexponential term describes the ratio between the average effective collision in the presence of substrates and that of homogeneous nucleation (no substrate).

Both $f(m, R')$ and $f''(m, R')$ are functions of m and R'. When $R' \to 0$ or $m = -1$, $f(m, R')$, $f''(m, R') = 1$. This is equivalent to the case of homogeneous nucleation. In the case where $m \to 1$ and $R \gg 1$, one has $f(m, R')$, $f''(m, R') = 0$. Normally, heterogeneous nucleation occurs when m is within the range between 1 and -1, or $f(m, R')$ is between 0 and 1, depending on the nature of the substrate surface and supersaturation.

Notice that for homogeneous nucleation, one has $f''(m, R') = f(m, R') = 1$, and $4\pi a(R^s)^2 N^o \to 1$. In this case, (2.20) is converted to:

$$J = B \exp\left[-\frac{16\pi\gamma_{cf}^3\Omega^2}{3kTS_m^2\Delta T^2}\right]. \tag{2.24}$$

This implies that (2.20) is applicable to describe both homogeneous and heterogeneous nucleation.

One of the most common ways to describe the kinetics of nucleation is to measure the induction time t_s of nucleation at different supersaturations. By definition, one has

$$J = \frac{1}{t_s V}, \tag{2.25}$$

where V is the volume of the system. It follows then from (2.20)

$$\ln(t_{\text{nucl}}V) = kf(m)/(T\Delta T^2) + \Delta G^{\#}_{\text{kink}}/kT - \ln(f''(m)(f(m))^{1/2}B') \quad (2.26)$$

with

$$\kappa = 16\pi\gamma_{\text{cf}}^3\Omega^2/3kS_{\text{m}}, \quad (2.27)$$

where $B' = B[(R^s)^2N^{\text{o}}]$. For a given system, changes in the slope and/or the intercept of the $\ln(TV) \sim 1/(T\Delta T^2)$ plot will correspond to the modifications in $f(m, R')$, $f''(m, R')$ and β_{kink}.

"Zero-Sized" Effect of Foreign Particles (Ice Nucleators)

As discussed earlier, the ice nucleation process can be regarded as a kinetic process for ice nuclei to overcome the so-called nucleation barrier ΔG^*, under a given supercooling ΔT ($\Delta T = T_{\text{m}} - T$; T and T_{m} are the actual and the melting temperatures, respectively). To obtain the ice nucleation kinetics, the correlation between the nucleation induction time T, the time required for the first nucleus to appear in the drop of water with a given volume V, and supercooling ΔT, was examined. The precise ice nucleation experiments were carried out in a cell based on the "micro water suspending" technology (cf. Fig. 2.7a) [51].

The experiments by Liu et al. [12] show that under normal crystallization conditions, it is almost impossible to eliminate the influence of dust particles. This is evidenced by the fact that the freezing temperature (for a constant droplet volume) decreases progressively as the pore size of the filters is decreased progressively from 200 nm, to 100 nm, to 20 nm (cf. Table 2.1). Actually, in most cases, the term "homogenous ice crystallization," to which most authors refer [52], is a heterogeneous ice nucleation process promoted by dust particles. This implies that the effect of the dust particles on ice crystallization is inevitable, and should be taken into account in our discussion.

Just as an ice nucleation substrate does, so do foreign bodies always lower the nucleation barrier by a factor f (cf. (2.15)). For an optimal interaction and structural match between the nucleating phase and the substrate $m \to 1$ and $f(m, R') \to 0$, meaning that the nucleation barrier is completely eliminated due to the occurrence of foreign particles. When $f(m, R') = 1$ (extremely poor structure match/interaction between ice and foreign particles), the nucleation barrier is the highest ($\sim\Delta G^*_{\text{homo}}$) under the given conditions even when the foreign particles are still present, in which case the foreign particles do not play any role in lowering the nucleation barrier.

If freezing were first controlled by heterogeneous nucleation and followed by homogeneous nucleation as ΔT increased, we would have obtained for a nucleating system pair-wise intersecting straight-line segments in the $\ln(\tau V)$ versus $1/(T\Delta T^2)$ plot (cf. Fig. 2.7b): one segment with a small slope at low ΔT (or high $1/(T\Delta T^2)$), the other segment with the largest slope at high ΔT (cf. (2.26). The slope would

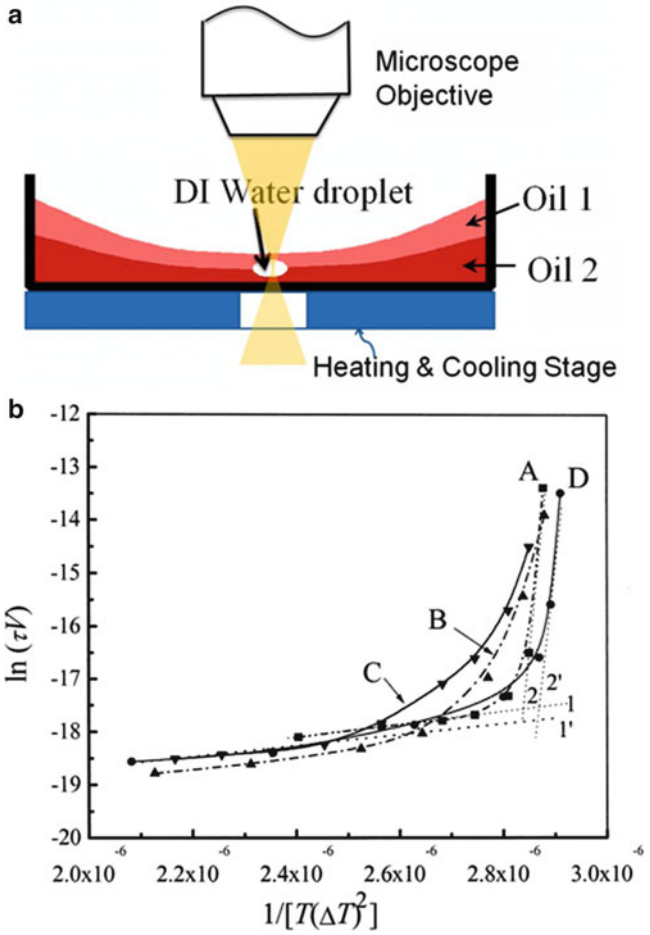

Fig. 2.7 (**a**) The "micro water suspending" technology to examine ice nucleation**.** Illustration of the sample cell and the placement of a microsized DI water drop. The density of Oil I is smaller than water, and the density of Oil II is higher than water. Before experiments, both water and oils were carefully filtrated [51]. (**b**) The correlation between $\ln(\tau V)$ and $1/T(\Delta T)^2$ for DI water filtered by a 20 nm filter (*curve A*), 0.5 mg/mL AFPIII solution filtered by a 20 nm filter (*curve B*), 2.5 mg/mL AFPIII solution filtered by a 20 nm filter (*curve C*), and DI water filtered by a 200 nm filter (*curve D*). Reprinted with permission from ref. [12]. Copyright (2004) the American Society for Biochemistry and Molecular Biology

then be $\kappa f(m, R') = \kappa$, as $f(m, R')|_{\max} = 1$). In contrast to this expectation, we obtain at low ΔT (high $1/(T\Delta T^2)$) a straight-line segment with the largest slope within the measurable range of ΔT, whereas at high ΔT (low $1/(T\Delta T^2)$) we obtain a straight-line segment with a much smaller slope, the two straight-line segments being joined by a curve (Fig. 2.7b). This implies that the nucleation barrier rises abruptly to the highest level ($\Delta G^* \approx \Delta G^*_{\text{homo}}, f(m, R') = 1$) at low supercoolings as if the foreign

Table 2.1 The freezing temperature (for a droplet of constant volume) is dependent on the number and size of dust particles

Filter pore size (nm)	200	100	20
Freezing temperature (°C)	−53	−58	−65

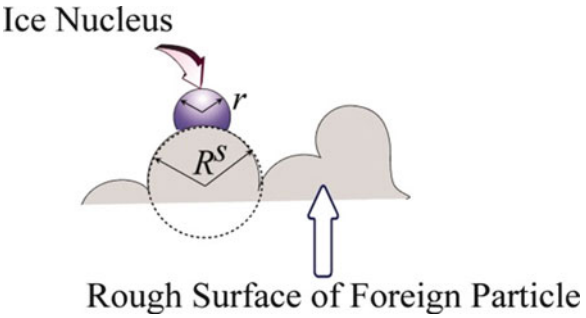

Fig. 2.8 Illustration of ice nucleation on a rough surface of a foreign (dust) particle**.** Normally, the surface of dust particles is rough. Therefore, the radius of the local curvature of the foreign particles is smaller than the size of the particles. r, the radius of the ice nucleus; R^s, the radius of the local curvature of the foreign particles. Reprinted with permission from ref. [8]. Copyright (2004) Springer

particles had "disappeared" (cf. (2.5) and (2.26)). Notice that the other three curves (B, C, D) share the similar characteristics. Such an effect on nucleation revealed by foreign particles at low supercoolings is called the "zero-sized" effect.

Effective Curvature of the Surface Roughness of Foreign Particles (Ice Nucleators)

R' is actually the ratio between the radius of the local curvature of the foreign particles (substrate) and that of the critical nuclei r_c (2.14, cf. Fig. 2.8).

For a given crystallization system, R' is proportional to ΔT (compare (2.1) and (2.14)). As shown in Fig. 2.5a, the $f(m, R')$ versus R' diagram can be divided into three regimes based on R' or ΔT. Regime I (linear regime): $R' \gg 1$ (relatively large supercoolings and/or large R^s). In comparison to the critical nuclei, the foreign particles can be treated as a flat substrate. $f(m, R')$ then attains its lowest value and becomes a constant with respect to R' (or ΔT), i.e., it assumes the form $f(m)$. According to (2.26), the plot of $\ln(\tau V)$ versus $1/(T\Delta T^2)$ is a straight line because κ is constant for a given system (compare portion 1 of curve A in Fig. 2.7b). Regime II (nonlinear regime): as ΔT deceases (or $1/(T\Delta T^2)$ increases), r_c becomes comparable with R^s ($R' \sim 1$) (compare (2.14)). The $\ln(\tau V) \sim 1/(T\Delta T^2)$ plot becomes a curve (compare the curved segment between portions 1 and 2 of curve A) as $f(m, R')$ varies with ΔT (or R'). Regime III (zero-sized regime): further lowering ΔT (or raising $1/(T\Delta T^2)$) leads to a much larger r_c than the radius R^s of the

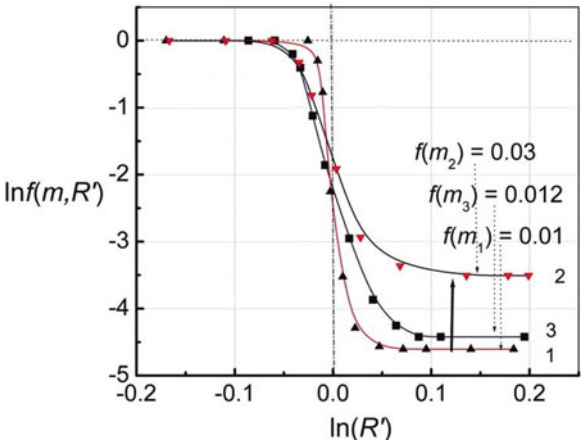

Fig. 2.9 Experimental $f(m, R') \sim R'$ for the four different systems: DI water filtered by a 200 nm filter (*curve 1*), 2.5 mg/mL AFPIII DI water solution filtered by a 20 nm filter (*curve 2*), DI water filtered by a 20 nm filter (*curve 3*). The curves were obtained based on the data given in Fig. 2.7b (R' is obtained based on (2.1) and (2.4)). The entropy of melting per molecule $\Delta S_m \sim 3.67 \times 10^{-23}$ JK^{-1}; the volume per molecule $\Omega \sim 32.53 \times 10^{-30}$ m^3. Reprinted with permission from ref. [12]. Copyright (2004) the American Society for Biochemistry and Molecular Biology

foreign particles or $R' \to 0$. In the case $f(m, R')_{max} = 1$, one has a straight line with the largest slope (line 2 of curve A in Fig. 2.7b). In this regime, as suggested by the zero-sized effect, the particles behave as if they had "vanished," although they are still physically present in water. According (2.15), the occurrence of the particles does not lower the nucleation barrier with respect to that of genuine homogeneous nucleation. Notice that the nucleation in Regime III is still not genuine homogeneous nucleation. In the case of genuine homogeneous nucleation, one has $f"(m, R') = f(m, R') = 1$ and $\ln(f"(m, R')(f(m, R'))^{1/2} BN^o) =$ constant for the same system, meaning that only one $\ln(\tau V)$ versus $1/(T\Delta T^2)$ plot can be identified in this case for the same system, such as DI water filtrated by a 20 nm filter (Fig. 2.7b, curve A) and DI water filtrated by a 200 nm filter (Fig. 2.7b, curve D). Nevertheless, in comparison to segment 2 in curve A and segment $2'$ in curve D, one has two parallel straight lines instead of a single straight line. This means that the nucleation occurring at the "zero-sized" regime (Regime III) is still not genuine homogeneous nucleation, although the height of the nucleation barrier is equivalent to that of homogeneous nucleation. This result is attributed to the fact that the probability of nucleation around the foreign particles may still be higher than elsewhere within the water droplet because of the particle-induced molecular preordering. Based on the fact that this homogeneous-like nucleation occurs at low supercoolings rather than at high supercoolings as expected previously [53], this type of nucleation is then referred to as inverse homogeneous-like nucleation.

Figure 2.7b was converted into $f(m, R') \sim R'$ as given in Fig. 2.9. According to (2.26), the slope of the $\ln(\tau V) \sim 1/(T\Delta T^2)$ plot is $\kappa f(m, R')$. If the inverse

Table 2.2 The measured transition temperature $(\Delta T)_{\text{mid}}$ and the radius of the local curvature of foreign particles for different systems

	$(\Delta T)_{\text{mid}}$ (K)	$(r_c)_{\text{mid}}$ $(=R^s)$ (nm)
DI water (20 nm filter)	39.1	2.28
DI water (200 nm filter)	33.9	2.54
AFP III 2.5 mg/mL (20 nm filter)	40.3	1.42

homogeneous-like nucleation takes place (Regime III, $f(m, R') = 1$), one then has $\kappa f(m, R') = \kappa$. It follows that the experimental $f(m, R') \sim \Delta T$ curve can be obtained from the ratio between the slope of the $\ln(\tau V) \sim 1/T(\Delta T)^2$ plot and the corresponding κ at different ΔT. Because r_c can be obtained from (2.1) and (2.13) and κ, one of the most challenging and important steps in obtaining $f(m, R') \sim R'$ is to estimate the average local radius R^s of the rough surface of the foreign particles (compare (2.14) and Fig. 2.7b). As illustrated by Fig. 2.5a (e.g., $m = 0.8$), one has approximately $R' \approx 1$ or $(r_c)_{\text{mid}} \approx R^s$ at the midpoint of the $\ln(f(m, R')) \sim \ln(R')$ curve $(-\ln(f(m))/2)$, enabling one to estimate, according to (2.14), R^s from $(r_c)_{\text{mid}}$, which can be obtained from $(\Delta T)_{\text{mid}}$ (compare (2.13) and (2.1); $(\Delta T)_{\text{mid}}$ is the supercooling of the midpoint $(-\ln(f(m))/2)$ of the $\ln(f(m, R')) \sim \ln(\Delta T)$ plot). The values of R^s for various systems are listed in Table 2.2.

Interfacial Correlation between Foreign Particles and Nucleating Phase

As shown by Fig. 2.5a, in the case of $R' \gg 1$, the substrate can be regarded as being essentially flat, and $f(m, R')$ is then solely dependent on m. This implies that $f(m, R') = f(m)$ is independent of the supersaturation. According to (2.26), the plot of $\ln(\tau V) \sim 1/(T\Delta T^2)$ should give rise to a straight line whose slope is determined by κ and $f(m)$. Obviously, for a given system (κ, $B' = \text{const.}$), the slope of the straight line will change according to $f(m)$. In this sense, the slope of the $\ln(\tau V) \sim 1/(T\Delta T^2)$ plot gives the relative $f(m)$ for the given system. One can analyze the change of the correlation between the substrate and the crystalline phase in terms of the variation of the slope.

As given by (2.7), m is directly associated with γ_{cs}, which is determined by the interaction and/or structural match between the crystalline phase and the substrate. For a given crystalline phase and a substrate, an optimal structural match is the crystallographic orientation $\{hkl\}$, corresponding to the strongest average interaction or the lowest interfacial energy difference between the crystalline phase and the substrate between the two phases. This orientation corresponds to the (minimal) cusp at the γ-plot (Fig. 2.10a).

As the structural match varies from a perfect to a poor match, m decreases from 1 to 0, -1. The extreme case will be $m \to -1$, corresponding to the situation where no crystal–substrate correlation exits. This is the case when substrates exert almost no influence on nucleation, and nucleation is controlled by homogeneous nucleation kinetics. The nuclei emerging in this case are completely disordered, bearing no correlation to the substrate. One has then $f(m, R') = 1$.

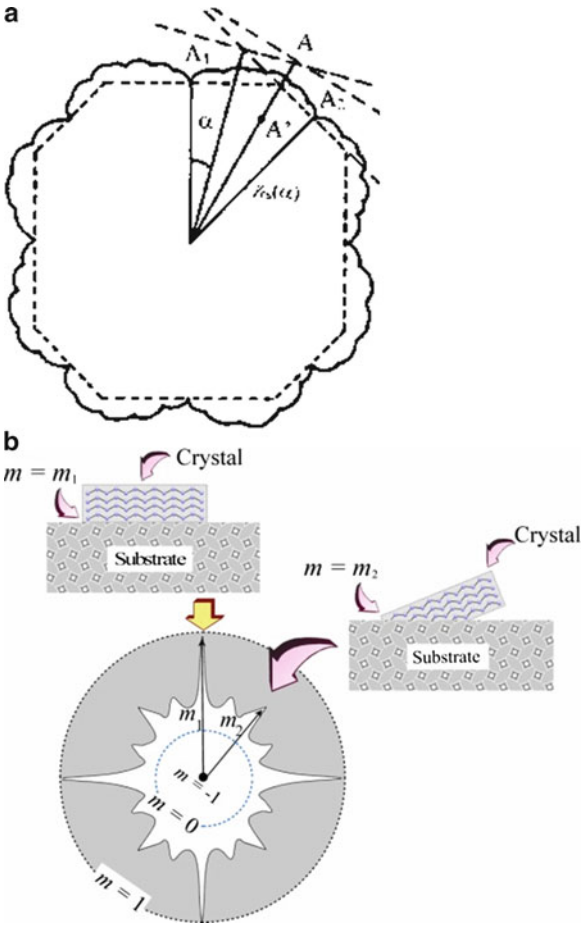

Fig. 2.10 (**a**) $\gamma_{cs}(\alpha)$ plot in two dimensions. (**b**) Illustration of m as a function of crystallographic orientation. The structural match between nucleus and substrate and the corresponding m. Reprinted with permission from ref. [8]. Copyright (2004) Springer

In general, as $f(m, R')$ varies from 0 to 1 (or m from 1 to -1), the interfacial structure correlation between the nucleating phase and the substrate changes from a completely correlated and ordered state to a completely uncorrelated and disordered state.

Due to the anisotropy of the crystalline phase, the deviations from the optimal structural match position toward the secondary optimal structural match (the second lowest $\gamma_{cs}(\alpha)$, Fig. 2.10b) will adopt discrete values rather than exhibit a continuous change, which is the second lowest minimum of γ_{cs} in the orientation of $\{h'k'l'\}$. A similar principle holds for further deviations. Therefore, the deviations from the optimal structural match reflect the transition of m from m_1 to lower and discrete values $m = m_2, m_3$, etc. (cf. Fig. 2.10b).

In the case of nucleation promotion, the adsorption of additives on foreign particles will improve the interaction and/or the structural match between the substrate (foreign particles) and the nucleating phase. This will then result in $m \to 1$

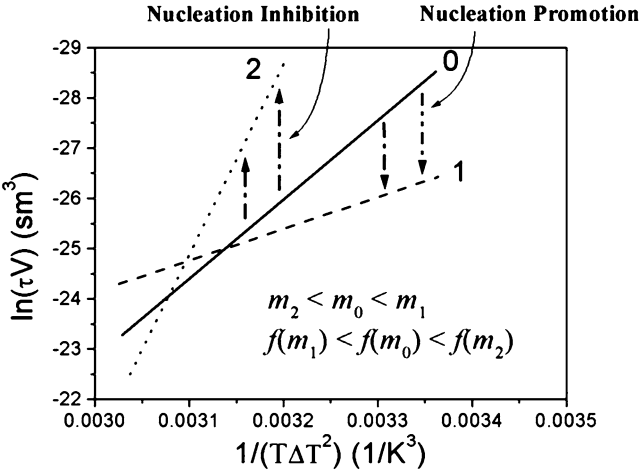

Fig. 2.11 Illustration of the effect of m on the nucleation kinetics. The increase of m will lower the interfacial effect parameter f and the slope of $\ln(\tau V) \sim 1/(T\Delta T^2)$ and vice versa. Reprinted with permission from ref. [54]. Copyright (2003) the American Society for Biochemistry and Molecular Biology

and $f \to 0$. Since for a given nucleation system, K is constant under a given condition (see (2.26) and (2.27)), such a change can then be identified from the lowering of the slope and the increase of the intercept of $\ln(\tau V) \sim 1/(T\Delta T^2)$ plot (cf. (2.26)). The shift from curve 0 to curve 1 in Fig. 2.11 illustrates this change. Conversely, if the adsorption of additives leads to a stronger repulsion and an interfacial structure mismatch between the substrate and the nucleating phase, one has then $m \to -1$ and $f \to 1$. This corresponds to an increase in the nucleation barrier (cf. (2.15)). The effect can be identified from the increase in the slope $f(m)$ of $\ln(\tau V) \sim 1/(T\Delta T^2)$ and the decrease of the intercept (from line 0 to line 2 in Fig. 2.11).

2.2.2.4 Surface Kinetics on Ice Nuclei

Apart from overcoming the nucleation barrier, the nucleation of ice is also affected by the incorporation of H_2O molecules onto the surface of ice nuclei at the kink sites. The rate of kink kinetics is described by β_{kink}. β_{kink} is associated with $\Delta^{\#}_{\text{kink}}$, the energy barrier to be overcome in order to remove other molecules adsorbed at the kink sites, and is given by

$$\beta_{\text{kink}} \sim \exp(-\Delta G^{\#}_{\text{kink}}/kT). \tag{2.28}$$

Obviously, the adsorption of additives on the surface of ice, in particular at the kink sites, will enhance $\Delta^{\#}_{\text{kink}}$ by $\Delta(\Delta G^{\#}_{\text{kink}}) = \Delta G^{\#\prime}_{\text{kink}} - \Delta G^{\#}_{\text{kink}}$. $\Delta G^{\#\prime}_{\text{kink}}$ denotes the kink kinetics barrier attributed to the adsorption of impurities/additives on the

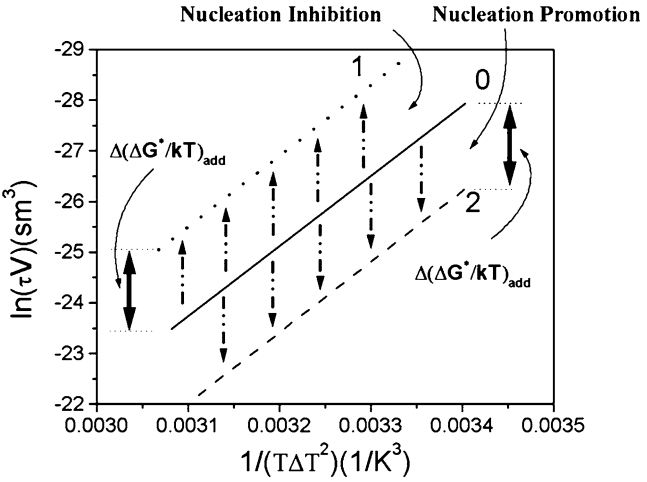

Fig. 2.12 Illustration of the change in kink kinetics and the corresponding shift in the $\ln(\tau V) \sim 1/(T\Delta T^2)$ plot. The change in the kink kinetic coefficient β_{kink} or the kink integration barrier will cause a parallel shift upward or downward, depending on whether there is nucleation inhibition or promotion. Reprinted with permission from ref. [54]. Copyright (2003) the American Society for Biochemistry and Molecular Biology

surface (cf. Fig. 2.12). Consequently, the integration of H_2O units in the ice crystal structure will be significantly slowed down or even stopped due to a very low β_{kink} (or high $\Delta G^{\#}_{\text{kink}}$) (cf. (2.28)).

It follows from (2.26) that for ice nucleation, the plot $\ln(\tau V) \sim 1/(T\Delta T^2)$ will give rise to a straight line for a given $f(m)$ (and $f''(m)$). The slope and intercept of the line can be utilized to derive the key parameters associated with the kinetics of ice nucleation.

2.2.3 *Ice Nucleation Inhibition by AFPs*

As mentioned earlier, the adsorption of AFP III on the ice nucleators and the impact on nucleation can be quantified from the $\ln(\tau V) \sim 1/(T\Delta T^2)$ plot. The plots obtained in the aforementioned experiments, using the plots of deionized (DI) water without and with AFP III are given in Fig. 2.13. The slopes and intercepts resulting from the linear regression for these systems are listed in Table 2.3. It follows that ice nucleation is inhibited by AFP III (longer induction time) at the two concentrations. The two effects can be quantified by the changes in the slopes and the intercepts compared with the DI water within the range of supercoolings.

The adsorption of AFP III molecules on ice nucleators turns out to strongly disturb the structural match between the nucleating ice and the dust particles (cf. Fig. 2.13 and Table 2.3). This can be identified from the variation of m (or $f(m)$),

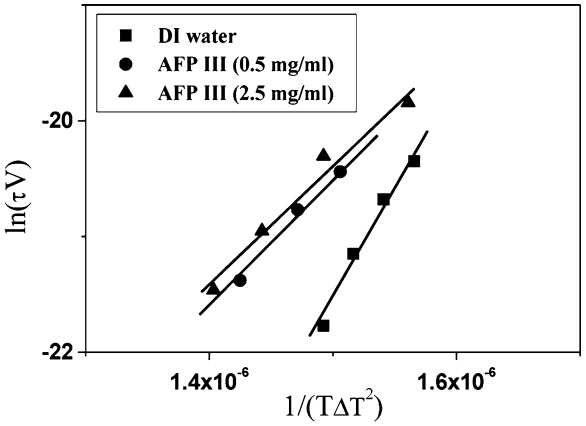

Fig. 2.13 The effect of AFP III on the ice nucleation kinetics and the corresponding shift in the $\ln(\tau V) \sim 1/(T\Delta T^2)$ plot. Reprinted with permission from ref. [54]. Copyright (2003) the American Society for Biochemistry and Molecular Biology

Table 2.3 Effect of AFP III on the interfacial effect parameter and kink kinetic energy barrier for the nucleation of ice

Curve	κ	$f(m)$	$\Delta G^*/\Delta G^*_{\text{DIwater}}$ [a]	m	$\Delta(\Delta G^{\#}_{\text{kink}}/kT)_{\text{add}}$
DI water[b]	1.21×10^8	0.2	1	0.43	–
AFP III(0.5 mg/mL)	0.39×10^8	0.35	1.75	0.20	↑ 13.7
AFPIII (2.5 mg/mL)	0.32×10^8	0.45	2.25	0.07	↑ 13.9

[a] $\Delta G^*/\Delta G^*_{\text{DIwater}} = f(m)_{\text{AFPIII}}/f(m)_{\text{DIwater}}$ [b] DI water: deionized water

which decreases from 0.43 to 0.2 and 0.07 and the enhancement of the nucleation barrier by a factor 1.75 and 2.25, for a 0.05 wt% and 0.25 wt% solution, respectively.

The results given in Fig. 2.13 and Table 2.3 show that AFP III will also adsorb onto the growing ice nuclei. This can be seen from the increase in the desolvation kink kinetics barrier $\Delta G^{\#}_{\text{kink}}$ ($13.7kT$ for 0.05 wt% solution, $13.9kT$ for 0.25 wt% solution, cf. Table 2.3).

It is worth noting that the presence of the AFP III molecules on the surface of the embryos causes the interfacial free energy γ_{cf} between the crystalline phase c and mother phase f to decrease. Based on (2.27), this change will lower κ and induce nucleation promotion. However, the aforementioned analysis shows that this promotion effect is not dominant compared to the other two inhibition effects of AFP III.

2.3 Ice Crystal Growth Inhibition by Antifreeze Proteins

2.3.1 Ice Crystal Growth Inhibition

As ice crystallization includes both nucleation and growth, once the inhibition of ice nucleation fails, AFPs should proceed to inhibit the growth of ice.

The growth of crystals occurs at the boundaries/interfaces between the crystal phase and the fluid phase when the boundaries move toward the fluid phase. In this sense, the configuration of crystal surfaces will to a large extent determine the growth kinetics of crystal faces [55–68]. We normally have two types of crystal surfaces: the surfaces with an essentially flat configuration—*so-called flat crystal surfaces*, or with a rough configuration—*so-called roughened crystal surfaces* (Fig. 2.14a). The growth of crystals will therefore be in one of the two modes: (1) faceted growth or layer-by-layer growth mode or (2) roughened growth or normal growth mode, respectively [60–65]. A faceted crystal surface will have a transition from the flat mode to the rough mode at the temperature higher than the critical temperature, so-called roughening temperature T^{R} [55–58, 66].

In general, the growth of crystals can be regarded as a process of delivering growth units from the bulk to the crystal surface and incorporating these units into the kinks (cf. Fig. 2.14b). In the case of faceted growth, the crystal face is atomically smooth and the kinks occur only at the steps. In this case, the steps can be regarded as "sinks" for growth units to enter the crystals [8]. As shown in Fig. 2.14b, each advancing step will disappear when it spreads over the surface and reaches the edge of the surface. In order to continue the growth of the crystal surface, a subsequent crystal layer needs to be generated on the existing crystal surface. Therefore, the step source for the creation of new layers will determine the growth rate of the crystal surface. Due to the presence of a step free energy, the creation of a new layer on the existing layer of the crystal surface requires overcoming that free energy barrier, which is the so-called 2D nucleation barrier [67]. Normally, for the growth of flat or faceted crystal surfaces, the screw dislocations occurring on the surface will provide uninterrupted step sources for a layer-by-layer growth [68], and in such cases the growth is controlled by screw dislocation mechanisms [68].

The growth of crystals that are free from screw dislocations is governed by the so-called 2D nucleation growth mechanism [67]. This implies that the crystal faces grow by depositing one crystal layer on top of the previous layer [67].

Ice crystal growth inhibition is attained by reduction of the growth rates of all crystal faces occurring on the ice crystallites. One of the mechanisms is to "pin" the growing steps by adsorbing additive (i.e., AFPs) molecules onto the surfaces (cf. Fig. 2.14c). This happens only when the crystal surfaces are flat. The basic mechanism is that when the average distance between the molecules is smaller than $2r_{\mathrm{c}}^{2\mathrm{D}}$ ($r_{\mathrm{c}}^{2\mathrm{D}}$: critical radius of 2D nucleation [67]), the movement of the steps on the crystal surface will be blocked. Another mechanism is that the additives are adsorbed at the kink sites so that the kink desolvation free energy barrier is greatly enhanced (cf. Fig. 2.14d). Based on (2.30), the kink integration coefficient β_{kink} will be significantly reduced [61, 62]. The second mechanism is applied to both flat and rough crystal surfaces.

Note that a substantial curtailment of the growth of ice would amount to a substantial reduction of the absolute size of the ice crystallites. This is a commonly occurring phenomenon, as evidenced by the relatively small sizes of the ice crystals found in the bellies of fish in subzero environments. If all facets are inhibited by

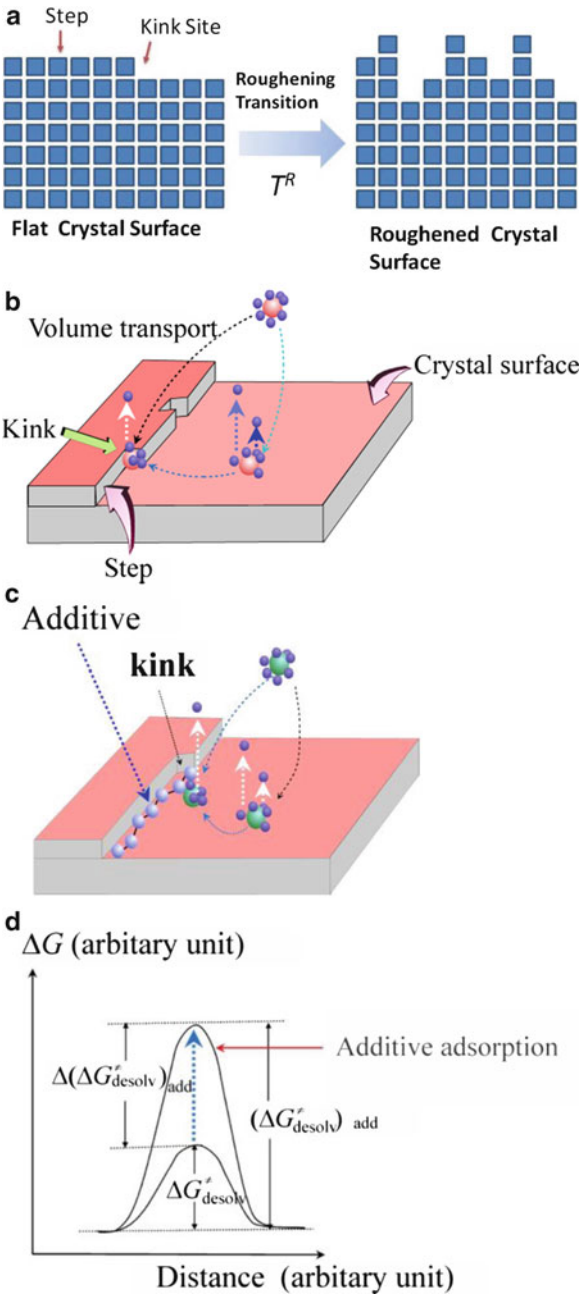

Fig. 2.14 (**a**) Schematic illustration of flat and roughened crystal surfaces [55–58, 66]. Normally, flat crystal surfaces will grow slower than roughened crystal surfaces and dominate the crystal morphology. (**b**) Schematic illustration of the surface integration occurring on the surface of a cluster. Reproduced with permission from ref. [69]. Copyright (2001) American Chemical Society. (**c**) Schematic illustration of the adsorption of additives at a kink site and (**d**) the enhancement of the kink desolvation free energy barrier. Reprinted with permission from ref. [8]. Copyright (2004) Springer

equal proportions, then the crystallites will be smaller but will retain the same shape; however, preferential inhibition of some surfaces over others will lead to both smaller crystallites and a modified shape. In this section, the AFP-induced ice morphological modification is discussed, focusing on a comparison of various ice morphologies produced by different types of AFPs.

2.3.2 AFP-Induced Morphological Modification

Crystals, including ice crystals, are bounded by the faces of the lowest growth rate. Therefore, the morphology of crystals is determined by these crystal faces. In general, crystals are bounded by faceted faces as these are the slow growth faces. For a given crystalline material, i.e., ice, if the ratio of the growth rates of these faces remains unchanged, the morphology of the crystals will be identical. Nevertheless, once the growth rates of some particular surfaces are reduced due to the selective adsorption of additives (i.e., AFPs or AFGPs), the shape or morphology of crystals will be modified (cf. Fig. 2.15).

Given a crystal system, the prediction of the growth morphology of crystals is equivalent to the prediction of relative growth rate in different crystallographic orientations. The primary surfaces can be used to derive the structural morphology [70–72]. The simplest one is the Bravais–Friedel–Donnay–Harker law [73]. Whether or not a primary surface will actually appear on the growth form, and to what extent it will dominate the morphology, depends on the relative growth rates of the neighboring surfaces. According to the BFDH theory, the relative growth rate of the crystal face (*hkl*) R_{hkl} can be predicted by

$$R_{hkl} \propto \frac{1}{d_{hkl}}, \tag{2.29}$$

where d_{hkl} denotes the lattice spacing of (*hkl*) corrected by the extension condition (cf. Fig. 2.16). The physics consideration of this model is that the interaction between the growth units in the adjacent lattice planes will decrease with the

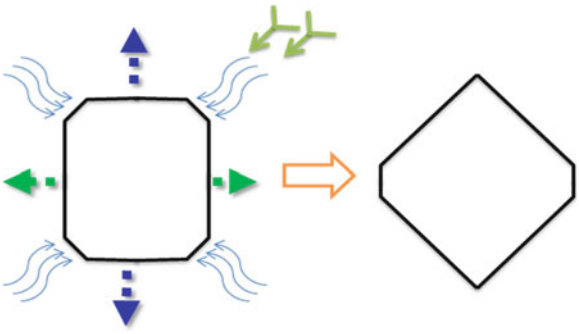

Fig. 2.15 Illustration of crystal growth habit modification

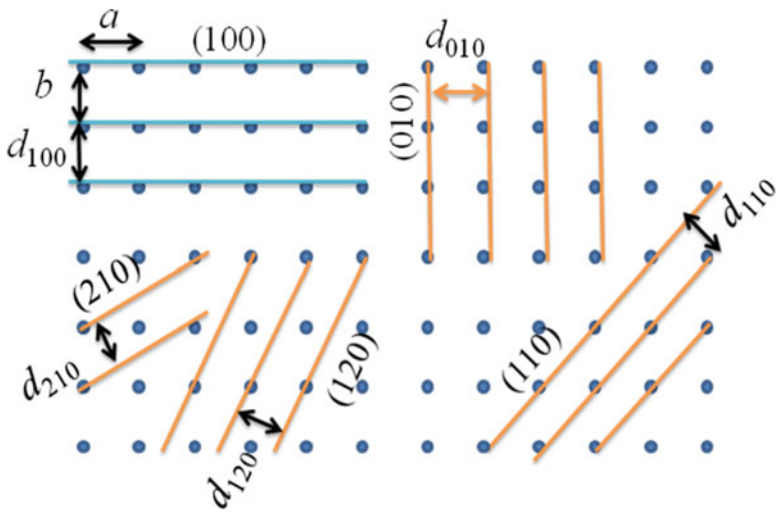

Fig. 2.16 An orthorhombic lattice projected along the *c* axis. The projections of (100), (010), (110), (120), and (210) lattice plans and the corresponding spacings

increase of the spacing. Then the growth rate in the same orientation will decrease correspondingly.

The structure of the morphology of crystals can be plotted by the Gubbs-Wulff plot [13] based on (2.29) and the symmetry of the crystals.

One of the most popular theories is the Hartman–Perdok theory or the periodic bond chain (PBC) theory, which was first published by Hartman and Perdok [13, 74–77]. The key points of the PBC theory can be summarized as follows:

1. In a crystal structure, one can always identify some *uninterrupted* periodic *strong* bond chains (PBCs), running through the crystal structure.
2. A PBC along the direction of [*uvw*] should have the basic crystallographic period in the given direction.
3. If one PBC period consists of different types of bonds, the strength of PBC will be determined by the weakest bond.
4. The important crystallographic directions must be in line with the strong PBCs.

An example of PBC analysis is given by Fig. 2.17. In the bond structure given, three PBCs can be identified: PBC[*uvw*], PBC[$u_1v_1w_1$], PBC[$u_2v_2w_2$]. If the rank of the bond strength is given as strong bond 1 > strong bond 2 ≫ weak bond 1 > weak bond 2, one has then PBC[*uvw*] > PBC[$u_1v_1w_1$] > PBC[$u_2v_2w_2$].

Based on the concept of PBC, the crystal faces can be classified into three types: F-face, S-face, and K-face (cf. Fig. 2.18).

- F-face: Flat face—more than two nonparallel PBCs in parallel to the surface are identified.

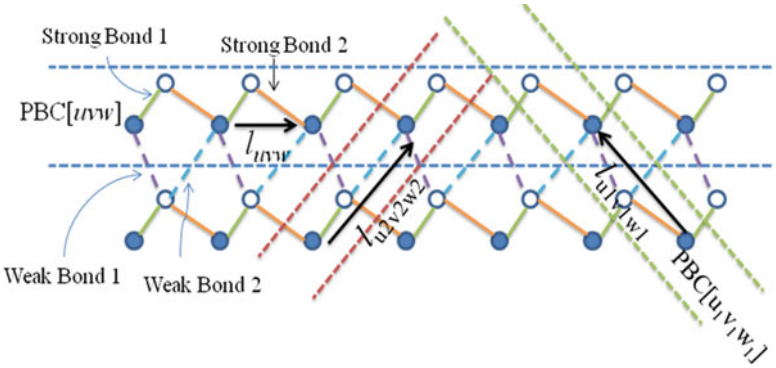

Fig. 2.17 A crystal bond network and the identification of three PBCs

Fig. 2.18 Illustration of F, S, and K faces of crystals [74–77]

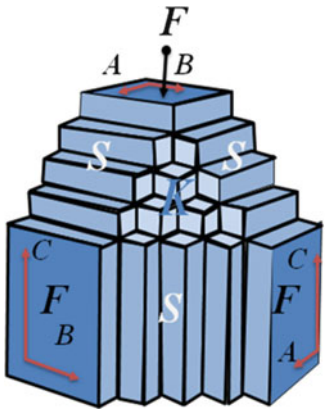

- S-face: Stepped face (roughened face)—one PBC in parallel to the surface is identified.
- K-face: Kink face (roughened face)—no PBC in parallel to the surface is identified.

According to Hartman [74–77], crystals are bounded by F faces. Here, F faces correspond to the faceted or flat faces while S and K faces are the roughened faces. According to definition of F face, there should be an *interconnected* bond network parallel to an F face (cf. Fig. 2.17). It follows from the modern statistic physics [78] that there will be a nonzero roughening temperature. For S and K faces, since no *connected* bond network occurs in parallel to the faces, the faces are roughened all the time. In summary, the PBC analysis includes the following key steps:

1. Calculate/identify various bonds/interactions connecting the neighboring structural units. (Only the bonds established in the crystallization will be considered.)
2. Indentify the bond structure of the crystals.
3. Identify PBCs and the networks in all directions.
4. Identify F faces.

In corresponding to the Bravais–Friedel–Donnay–Harker law, in the Hartman–Perdok theory, the growth rate of F-faces is taken proportional to the attachment energy E_{att}

$$R_{hkl} \propto E_{hkl}^{\text{att}}, \tag{2.30}$$

$$E_{\text{latt}} = E_{hkl}^{\text{att}} + E_{hkl}^{\text{slice}}, \tag{2.31}$$

where E_{latt} denotes the lattice energy of crystals, E_{hkl}^{slice} is the slice energy or 2D lattice energy of face (*hkl*). The slice energy refers to the amount of energy contained in that growth layer and E_{att}, the attachment energy, refers to the quantity of energy released when a new growth layer becomes attached to the crystal. According to (2.30), the most favorable molecular composition of a primary surface is the one with the smallest attachment energy [70–72]. The implication of (2.30) and (2.31) is that the larger the slice energy (equivalent to smaller attachment energy), the smaller the growth rate and the more crucial the face [71, 72].

The PBC theory precisely identified the mechanisms by which AFPs alter the ice morphology as reported by Strom et al. [44, 79, 80]. These works overcome the drawback of most other studies in which randomly obtained planar cut surfaces are selected. In fact, crystallographically valid flat surfaces need not be planar cut slices of the structure. Both the AFP–ice interaction and the molecular equilibrium distribution in the AFP–ice–water system depend crucially on the detailed definition of the simulated ice crystal substrates.

The morphological modification caused by external factors can be assessed from knowledge of the growth conditions, that is, usually the surrounding liquid, often containing influential molecular species. Such species may exert an even stronger morphological effect than the liquid itself, as is the case with the AFP (cf. Fig. 2.15).

The slice energies of the low index (*hk*0) and (*h*0*l*) secondary surfaces are characterized by relatively high slice energies, comparable to those of the primary surfaces. The main impediment to the appearance of some secondary prismatic and pyramidal facets on the growth form of ice would not likely arise from a modest deficit in the energy of the surface bonding pattern. That impediment is rather due to the lack of bonding in a second lattice direction transverse to the single existing one.

As mentioned before, crystals are only bounded by F faces, not by S or K faces. It is surprising to see some S faces can occur on the morphology of ice crystals when some AFPs and AFGPs are added [31]. It was found that these AFPs and AFGPs can turn the S faces into pseudo “F” faces surface bridging. According to the work by Strom et al. [44], the fish-type ice binding surface stabilizes a secondary surface by introducing effectively a second strong-bonding direction to intersect with the existing one. This is schematically illustrated in Fig. 2.18. Some of the surface molecular compositions available for engagement will offer a better match than others to the ice binding surface structure. The selection of the face indices of the reconstructed surface occurs by identifying the particular surface molecular composition that offers the best structural match or the strongest interaction with

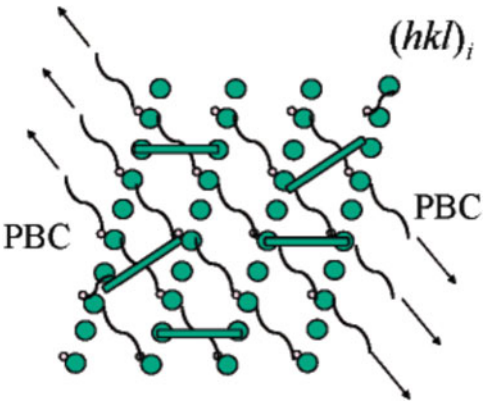

Fig. 2.19 Schematic illustration of a statistical distribution of fish-type ice binding surfaces on a low-index secondary surface, inducing a surface-reconstruction-type effect while selecting the face indices $(hkl)i$. Reprinted with permission from ref. [44]. Copyright (2005) American Chemical Society

a fish-type ice binding surface. By providing supplementary bonding in various directions transverse to the existing strong bonding direction, the ice binding surface modifies the surface orientation. Out of the numerous possibilities available for the surface orientations parallel to the PBC, the specific face indices $(hkl)_i$ are selected in Fig. 2.19. Therefore, the indices of the observed ice facets are expected to vary according to the specific properties of the ice binding surface of the AFP and according to the changes in the ice binding surface caused by the experimental conditions.

The available experimental results show that the morphological modification mechanism of surface reconstruction is triggered by two variants of the fish-type ice binding surface. The "one-dimensional" ice binding surface variant found in fish-type I AFPs and AFGPs is characterized by one or more linearly extended helices, having regularly spaced binding intervals in only one direction. It can align its helix/helices along any one of several alternative lattice translations transverse to the existing strong bonding direction, thus mimicking a second intersecting strong bonding direction that is absent from the crystal structure. The bridged distances are lattice periods between adjacent parallel PBCs. Therefore, surface reconstruction through "supplementary inter*chain* bonding" is triggered by the 1D ice binding surface variant. In globular type II and III AFPs, however, the "irregular" ice binding surface variant consists of mixed α and β structures that are not 1D. It need not either be planar or exhibit any spacing regularity in its binding sites in order to function. It can align itself along numerous shorter distances in various directions. It bridges intermolecular distances that need not be lattice translations, by linking oxygen–oxygen pairs on adjacent parallel PBCs. So the irregular ice binding surface variant can trigger surface reconstruction through "supplementary inter*molecular* bonding."

It has been noted [44] that the geometrical differences between prismatic and pyramidal faces become significant in comparing theoretical prediction against experimental observation. The prism is an open form, implying that it can appear on the crystal habit in combination with other forms but not by itself, for example,

basal plane and/or pyramid. A hexagonal prism seen in isolation cannot be distinguished from another differently oriented hexagonal prism. In contrast, a hexagonal bipyramid is a closed form that can appear on the growth form by itself; however, it can also appear in combination with the basal face and/or various prisms. Visual inspections of the crystallite shape using the height-to-baseline ratio or the apical angle can readily distinguished bipyramids from other differently oriented bipyramids. For that reason, the broad range within which the experimentally observed pyramidal facets differ is directly observable on the obtained images reported in the literature.

Strom et al. [44] have noticed that the fish-type ice binding surface enhances the growth rate along the [001] direction, which is part of the secondary prismatic surfaces (*hk*0). Their face indices, as observed experimentally [81–84], vary from (110) up to (410); (110) is the most frequently reported secondary prismatic form. The identification of the (110) secondary prism in ice grown in the presence of sculpin AFP is reported [81]. The sculpin AFP is responsible for the growth of prismatic (2 –1 0) ice crystals, where (2 –1 0) is symmetrically identical to (110) [5, 85]. Combinations of secondary prisms with primary (and other secondary) forms are not ruled out theoretically. Indeed, ice crystallites grown out of a solution with AFGPs exhibit (*hk*0) surfaces [86], sometimes in combination with the primary surface (100) [87]. It is easier to observe the difference of secondary face orientations in the case of bipyramids. PBC in [010] is the most strongly bonded PBC contained in the secondary pyramidal surfaces (*h*0*l*). A large variety in secondary pyramidal shapes has been observed in terms of height-to-baseline ratios or apical angles (cf. Fig. 2.20). The experimentally observed variety of secondary pyramidal surfaces activated by the fish-type ice binding surface [84] ranges from (302) to higher than (401). Among others, (201) is the most common secondary pyramid triggered by the wild-type sculpin AFP [83] and by the winter flounder AFP type I[88, 89]. However, no explanation has been given for the specific occurrence of (201) [83]. In line with the theoretical formulation, none of the pyramids produced by the fish-type ice binding surface, matches in shape the primary pyramid (101) illustrated in Fig. 2.20. As predicted, secondary pyramids appear in combination with primary (and other secondary) forms; the bipyramidal crystals depicted in the observations [84] are combined with the basal face (001) and also some unidentified prismatic facets. The theoretically admissible occurrence of combinations of secondary and primary surfaces can be verified in the experimental images. For example, a combination of (201) and (001) is observed [83].

AFPs of the sculpin engage secondary prisms such as (2 –1 0), while AFPs of the winter flounder later engage the secondary pyramid (201) even though both families have closely related and largely hydrophobic ice binding surfaces [83]. The explanation provided in ref. [83] was that although both ice binding surfaces were indeed hydrophobic, they differed in their structure properties, such as the arrangement of their binding intervals. It is reported [83] that the wild type and few sculpin AFP variants produce secondary pyramids with different degrees of activity even though most sculpin AFPs produce prismatic ice crystals. In addition, the origin of the explanation could be due to the ice binding surface structural

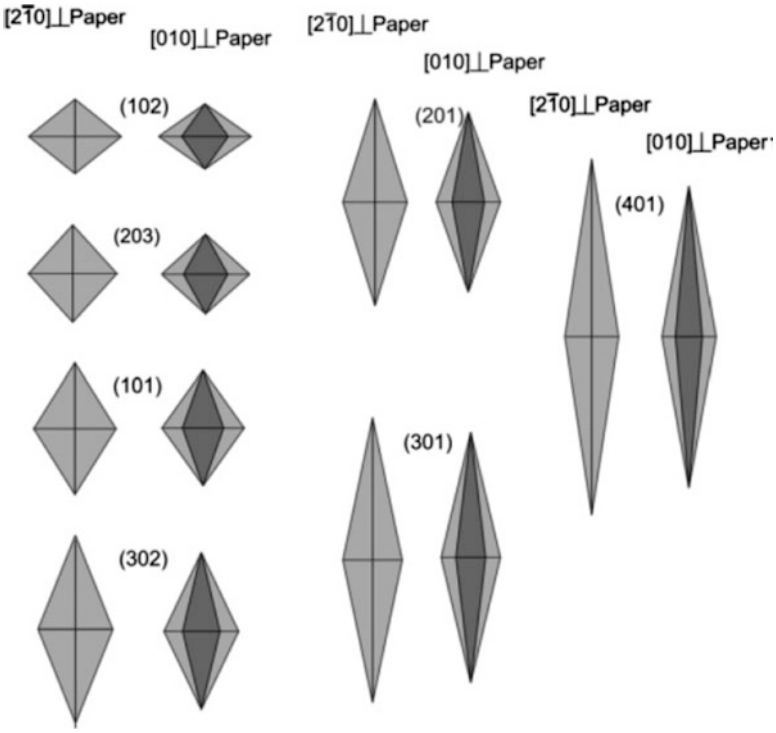

Fig. 2.20 Outlines of ice pyramidal faces (*h*0*l*) encountered in a broad range of pyramid-shaped ice crystallites under the influence of (mostly) fish AFPs (absolute size is not to scale). [The ice pyramid face labeled (101) resembles those triggered by the insect TmAFP.] Reprinted with permission from ref. [44]. Copyright (2005) American Chemical Society

aspects. In the work of ref. [90], the addition of divalent ions changes the ice binding surface of the AFP so radically as to transform the crystal shape from secondary to primary facets and vice versa. Moreover, the report on the action of dimer, trimer, and tetramer of type III AFP on ice crystals [91] states that each multimer "changes the morphology of a single ice crystal into a unique shape that is similar but not identical to the ordinary hexagonal bipyramid." The ice binding surface of type III AFP belongs to the irregular globular ice binding surface type. A significant change in the ice binding surface was noted to cause a radical conversion between pyramidal (Fig. 2.2a of ref. [91]) and prismatic (Fig. 2.2c of ref. [91]) forms, leading to a strong, direct correlation between ice binding surface structure and morphology.

It has long been recognized in the literature [5] that the insect AFP's capacity to suppress freezing is because of its capacity to grip firmly on the ice lattice via its 2D periodic binding intervals attuned to the ice lattice constants. Take the primary prism (100) (cf. Fig. 2.21) as an example, the spruce budworm AFP producing the hexagonal disk type [92] morphology (Fig. 2.21b) has regular binding intervals in two directions equal to ∼4.5 and 7.5 Å, matching the periods of the strong bonding

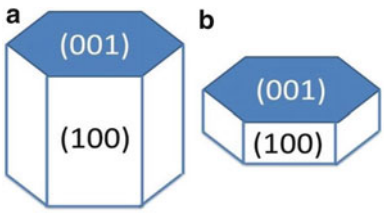

Fig. 2.21 Structural morphology of hexagonal ice

directions [010] and [001]. The characteristic morphology of ice grown from most insect AFP solutions is hexagonal plates [5, 92]. In contrast to the structural or the natural morphology, these ice crystallites reveal a strongly pronounced basal face (001) and a morphologically much weakened primary prism (100). In all ice crystallites grown as basal and primary prismatic forms, resulting from layer-by-layer growth, triggered, e.g., by the spruce budworm AFP, no deviation from the {001} and {100} indices has been observed under all experimental conditions. One presumed exception to the hexagonal disk form is found in the action of the TmAFP, the presence of which gives rise to a pyramidal ice habit. It is traditionally held that the action of the insect TmAFP is deviant in causing a pyramidal rather than a disk-shaped morphological modification, whereas all other known insect AFPs cause a hexagonal plate habit. The question arises in the case of the TmAFP as to whether the mechanism of morphological modification is exceptional; that means, whether the ice binding surface of the TmAFP acts on secondary ice surfaces by an exceptional mechanism or on primary ice surfaces by surface pinning through 2D PBC matching, just like the remaining insect-type ice binding surfaces. What this question amounts to is whether the pyramidal ice form observed in the presence of the TmAFP is one of the secondary pyramids with variable indices ($h0l$) or the primary pyramid (101). It is found that the ice bipyramid triggered by the TmAFP [93] has consistently a stubby lemon shape, showing no variation in the apical angle, so that the TmAFP gives rise to a pyramid of fixed indices. The lemon-shaped ice bipyramid produced by the TmAFP is not elongated like the predominant (201) or higher-indexed pyramids observed in connection with the fish AFPs. From the assortment of pyramidal shapes, it can be seen that this bipyramid matches well the primary surface (101). Also in all ice crystallites grown as primary pyramidal forms triggered by the TmAFP, resulting from layer-by-layer growth, no deviation from the {101} indices has been observed under all experimental conditions. Thus, the TmAFP action is by no means exceptional. According to Liou et al. [94], the TmAFP has a high tendency to form hydrogen bonds with an ice surface. This result agrees with the theoretical observation that there are 30% more unbonded hydrogen atoms on the (101) than in the other primary surfaces, pointing to an increased interaction between the ice binding surface of the TmAFP and the (101) primary pyramid [80].

Lastly, it is worth mentioning that although freezing inhibition is always accompanied by a modification of the morphology of the ice crystallites, the converse does not hold true: a morphological modification of ice does not necessarily imply that

the freezing point has been depressed [44]. This is because a change in morphology can have different causes and can be accompanied by total protein inactivity [5, 84, 95]. The particular ice morphology observed is a direct consequence of the structural details related to the adsorption mechanism of the AFP on the ice surfaces, such that different modes of adsorption trigger different crystal habits consistently and predictably.

2.4 Applications of AFPs

Any organic compound with the ability to inhibit the growth of ice has many potential medical, industrial, and commercial applications. Although AFPs have potential uses in all of these areas, this review highlights the medical [96, 97] and food [98] applications of AFPs.

2.4.1 Cryoprotection

Many complex processes occur when the cell ambient temperature is lowered near to or below that of the freezing point. Physical cell rupture, necrosis, and cold-induced apoptosis are presently the three distinct modes of cell death that occur upon freezing [99]. Although all three processes are significant, the most common form of cell death associated with cryopreservation is cell rupture owing to fluctuating cell volumes and intracellular ice formation [100–104] and, consequently, in this section cell damage will be emphasized because of membrane rupture followed by intracellular ice formation.

Much effort has been dedicated to developing enhanced cryoprotectants and preservation techniques after an accidental discovery that glycerol enabled fowl spermatozoa to survive freezing at −70°C. All cells are regarded as compartmentalized systems and the probability of ice nucleation is directly proportional to the degree of supercooling and volume. Consequently, as the temperature is lowered, ice nucleation is more likely to occur outside of the cell since the volume is greater and the concentration of colligatively acting substances (salts, proteins, and so forth) is lower than inside the cell. After nucleation occurs, extracellular ice growth results in an increase in solute concentration in the diminishing extracellular volume. As the concentration of these solutes increases, extracellular osmotic pressure increases. The rate at which osmotic pressure increase occurs is directly proportional to the rate of supercooling and this osmotic flux is compensated by the cell through the regulation in the flow of water through the semipermeable cell membrane. Fracturing of the cell membrane is possible when the rate of extracellular ice growth is rapid. Upon the occurrence of the fracture, intracellular ice formation occurs leading to the destruction of the cell. Debates have been going on by researchers as

to whether the ice or elevated salt concentration is the cause for damage during the progressive freezing of cells. The effect of the cooling rate on water transport during progressive cooling was demonstrated by Mazur et al. [105] and they correlated this with cell survival. This eventually leads to a "two factor hypothesis," which states that solute damage occurs at low cooling rates where extracellular ice formation is innocuous to the cells. On the contrary, at high cooling rates, intracellular ice formation is generally lethal. Cryoprotectant is correlated with an optimum cooling rate since there is a dramatic variation in the membrane permeability of each cell type.

The issues surrounding the cryopreservation of multicellular systems, such as tissues and organs, are infinitely more complex given that many cell types exist and each will differ in the requirements for optimal preservation. The most considerable obstacle to the cryopreservation of multicellular systems is likely to be extracellular ice formation, which leads to the focus on the use of various cryoprotectants that possess the ability to regulate the formation of extracellular ice. Thus, effective cryopreservation of such systems would be expected to occur through an "ice-free" cooling or vitrification process even though this necessitates a high concentration of cryoprotectant. The issue of toxicity arises due to the greatly limited concentration that a tissue can tolerate before freezing. In addition, an osmotic imbalance is inevitable as cryoprotectants penetrate the cell membrane more slowly than water. Thus, cell volume must be regulated carefully during the addition and removal of cryoprotectants.

Vitrification is a common technique employed for the freezing of cells and tissues to avoid cell damage from ice formation. During this process, the solution transforms into a "glass-like" solid enabling the sample to be frozen under "ice-free" conditions. Despite the attractive features of vitrification, it does possess some limitations. For instance, when dealing with larger volumes the heat transfer in cells, tissues, and organs does not permit vitrification without the risk of crystallization. Consequently, a slow freezing process (0.5–100°C/min cooling rate) is often applied for preservation of large volumes. However, in the vitrification process, a very rapid cooling rate (24–130,000°C/min [106]) is applied, resulting in a glassy or vitreous state, which is dependent on the concentration, viscosity, volume, and cooling rate of the process. Although this high cooling rate minimizes cellular damage, recrystallization can still occur during warming. To avoid the risk of recrystallization, rapid and uniform warming can be achieved using microwaves [107–109].

Two problems unique to vitrification are encountered when using the methodologies outlined earlier. First, the necessary cryoprotectant concentration is very high and is sometimes too toxic for the cell. Although the process is feasible with lower concentrations of cryoprotectants, a higher cooling rate must be used to achieve a vitrified state. Second, some fractionation of the glassy state still occurs. The extent to which this occurs is dependent on the volume and the cooling rate and such relationships have been examined in detail [106]. Vitrification works well with small volumes (i.e., <1 μL) even though it is not useful for large volumes. However,

each protocol must be optimized and various cryoprotectants must be used. Some of the most promising cryoprotectant solutions incorporate AFGPs. Not only do they inhibit ice formation at any subzero temperature but they also interact with the cell membrane during the thermotropic phase transition state to avoid leakage, thereby addressing two issues at once. (The second effect will be discussed in Sect. 2.4.2.) Numerous factors that influence the success of post-thaw revival include the nature, the temperature, the concentration of the cryoprotectant, the rate of cooling and warming, the storage temperature, and the speed at which the cryoprotectant is added and removed. AFGPs from Antarctic nototheniid fishes were discovered to have special cryoprotective properties that significantly improve morphological integrity upon cooling. Since, the idea of using AFGP additives was then explored in the directional cooling for the preservation of pig oocytes [110]. Vitrified oocytes were observed not be able to survive the cooling/warming cycle. The primary site of damage was to the oolemma. It was subsequently hypothesized that the oolemma was acting as a site for ice nucleation, although the sample was successfully vitrified. A mixture of AFGP 1–8 was added to the sample in an attempt to overcome this problem. This solution resulted in an 82% survival rate of the oocytes as determined by each oocyte reaching the MI or MII stage during incubation. An explanation based on viscosity was proposed by Rubinsky and Eto [111] to explain why AFGP enhanced oocyte viability. They speculated that AFGPs increased solution viscosity and augmented the probability of an "ice-free" state without nucleation. This is a feasible explanation given that the probability for ice nucleation in aqueous solutions is inversely proportional to solution viscosity [112]. The viscosity of solutions containing varying amounts of AFGP was examined in a comprehensive study on AFGP properties and it was reported that as little as 1 mg/mL of AFGP in solutions caused significant increases in solution viscosity with saturation taking place at 20 mg/mL. The viscosity of an aqueous solution of BSA was measured and compared to that of AFGP of comparable weight and reported that solutions of AFGP were slightly more viscous than solutions of BSA. Similar measurements showed that a 20 mg/mL solution of AFGP is 0.005 M, which was equally effective compared to a 1 M solution of dimethyl sulfoxide (DMSO) a commonly used cryoprotectant for vitrification. Subsequently, by using AFGP solutions that are 200 times less concentrated to produce the same effect, the toxic effects of concentrated DMSO solutions maybe eliminated. This observation implies that AFGP might work well as an effective substitute during cryopreservation by vitrification. It is particularly difficult to cryopreserve mammalian oocytes because low temperatures will disrupt the cytoskeleton [113–115] and harden the zona pellucida [116], causing difficulties for sperm to penetrate and fertilize the oocyte. Limited success has been achieved using murine oocytes with both fast and slow cooling protocols. Although vitrication has been achieved with several species of embryos, variable results are often obtained and reproducibility is a problem. It has been speculated that this variability is a result of devitrification of the sample. DeVries and coworkers [115] studied the vitrification of mouse oocytes using a mixture of 6 M DMSO containing 0.1- and 1-mg/mL solution of AFGP [115]. It was demonstrated by them that cryopreservation using 6 M DMSO supplemented with 1 mg/mL of AFGP resulted in low variation and high survival rates.

2.4.2 Lipid Membrane Stabilization

It was [117, 118] observed by Rubinsky and coworkers that the external cell membrane integrity was enhanced during cooling, and protection against rupture by AFGP and AFP occurred [119]. They suggested that the enhancement of the membrane integrity was due to the blocking of ion fluxes across the membrane by AFGP. Biological antifreezes were then inferred to be directly interacting with membrane-bound ion channels. However, the suggestion has met with some disagreement [119–121]. It was confirmed a few years later by Hayes et al. [122] that AFGP/AFP enhanced membrane integrity during cooling, but they suggest an alternate mechanism consistent with a nonspecific interaction with the liposome membrane. In this work, four different types of phospholipids which were all phosphatidylcholine derived that contained carboxyfluorescein (CF) probes were used to prepare liposomes. Liposomes were observed to leak up to 50% of the trapped marker as they were cooled through the thermotropic phase transition in the absence of AFGP. During this transition state (typically between 12 and 41°C), both gel and liquid crystalline states of the lipid membrane coexist [122–124], provoking a mismatch of the hydrocarbon chains and ultimately facilitating leakage of the lipid membrane. In the presence of less than 1 mg/mL of AFGP, no leakage was observed during cooling or warming through the thermotropic phase transition. Other proteins were also shown to inhibit leakage. The study by Hayes et al. was further expanded by Wu and Fletcher [125] and they examined interactions of AFGP, AFP type 1–3, and albumin interactions with liposomes as model cell membranes. Because most cell membranes are more complex than a phosphatidylcholine (PC) liposome, they prepared liposomes derived from dielaidoylphosphatidylethanolamine and dielaidoylphosphatidylglycerol. Complex AFGP was found to be extremely effective at preventing leakage from the liposomes as each was cooled through its respective thermotropic phase transition. These researchers concluded that AFGP may interact with the lipid bilayer in one of two ways. NMR studies have suggested that AFGP adopts a threefold left-handed helical conformation. The carbohydrate moieties line up on one side of the helix while the hydrophobic alanine residues line up on the other [126, 127]. With this given arrangement, the hydrophilic carbohydrate moieties might interact with the polar head groups of the lipid bilayer, while the hydrophobic backbone of AFGP was hypothesized to be partially immersed in the lipid bilayer and that this may be sufficient to prevent disruption of the bilayer.

The only AFP I that has been studied with liposomes is the naturally occurring protein TTTT. A concentration of 5 mg/mL of TTTT was found to be able to completely inhibit the leakage of the fluorophore carboxyfluorescein from the center of the liposomes as the liposomes were chilled through their thermotropic phase transition temperature. In contrast, this protection against leakage was not observed when the same experiments were performed with low-molecular-weight fractions of AFGPs. Independent experiments indicated that significant amounts of TTTT remained associated with the lipid portions of the bilayer even after

rewarming of the bilayers after they had been cooled through their Tm. These results, which suggest hydrophobic interactions in the stabilization mechanism, are interesting, as hydrophobicity has also been identified as a key property required for thermal hysteresis. Studies using the synthetic derivatives XXXX2KE with different lipid mixtures have been recently reported to clarify the mechanism by which TTTT interacts with membranes [128]. The study showed that the overall charge and mutations in XXXX (X = T, A, V, I) had a profound effect on the ability of the peptide to stabilize membranes. While TTTT stabilized the model membranes to leakage, all four peptides XXXX2KE destabilized the membranes to leakage. TTTT2KE and AAAA2KE interacted preferentially with the DGDG in the lipid mixture, while VVVV2KE showed no preference for either lipid. The results are consistent with interactions involving the hydrophobic face of AFP I and the model bilayers, which is the same face of the protein that is responsible for antifreeze properties. The different effects correlate with the helicity of the peptides, suggesting that the solution conformation of the peptides has a significant role in determining the effects of the peptides on thermotropic phase transitions of the membrane.

AFGPs was proposed by Tomczak and Crowe [129] to form a monolayer coverage of the surface of the membrane to prevent leakage from phospholipid membranes, blocking transient leakage across the membrane as it is cooled through its thermal phase transition (T_m). In contrast, direct interactions between the α-helical AFP I, TTTT, and liposomes containing plant lipid bilayers (that alter the order of the alkyl chains in the hydrophobic core) were proposed as a mechanism for stabilization, via partial insertion of the N-terminal residues of the peptide into the membrane during chilling.

The proposed role of the hydrophobic residues in the four synthetic analogues (XXXX2KE X = T, A, I, V) in interactions with lipids [130] is consistent with the ice growth inhibition properties of these compounds. This ice growth inhibition is directly correlated to the hydrophobic face of the helix being oriented toward the ice at the ice/water interface [131]. However, the results with XXXX2KE [86] and liposomes are also informative in terms of the design of synthetic helical AFPs. While TTTT2KE and VVVV2KE retain antifreeze properties (i.e., thermal hysteresis and modification of ice crystal growth) comparable to the native winter flounder AFP TTTT, the introduction of the additional salt bridges in XXXX2KE leads to a destabilization of membranes, clearly an undesirable property when the goal is enhancement of stabilization of membranes to leakage. Further experiments are required to establish whether the destabilization is due to the large size of the additional 2KE side chains, or the increased hydrophilicity of one face of the helix.

2.4.3 Food Technology

Ice crystal morphology plays an important role in the textural and physical properties of frozen and frozen-thawed foods and in processes such as freeze

drying, freeze concentration, and freeze texturization [98]. Size and location of ice crystals are major factors in the quality of thawed tissue products. Smaller ice crystals are preferred in ice cream since large crystals will results in an icy texture. In freeze drying, ice morphology influences the rate of sublimation and several morphological characteristics of the freeze-dried matrix as well as the biological activity of components (e.g., in pharmaceuticals).

Nucleation is the most critical step to control the crystal size distribution during crystallization [132]. The freezing (cooling) rate is usually the parameter used for controlling the size and size distribution of ice crystals in frozen and partly frozen systems. Recently, the use of nucleation agents, AFPs, ultrasound, and pressure freezing methods, known by the generic name of "freezing assisting techniques," have been proposed to control nucleation and ice morphology [133].

Several potential applications for AFPs have been envisaged in foods [98]. In ice cream manufacture, AFPs have been used to fabricate smaller ice crystals compared to a control [134]. In meat products, ice crystal size are reduced by soaking bovine and ovine muscle in a aqueous solution up to 1 mg/mL of AFP prior to freezing at −20°C [135]. Preslaughter administration of AFP intravenous injectation to lambs reduced ice crystal size and drip loss after thawing [136]. The gel-forming functionality of surimi in both chilled and frozen conditions is also preserved by AFPs. In contrast to conventional cryoprotectants such as sucrose–sorbitol mixtures, AFPs remarkably preserved Ca^{2+} ATPase activity of actiomyosin during storage and provided better protection [137].

Fungal hydrophobin AFPs repressed ice crystal growth during frozen storage, i.e., ice recrystallization, and modified ice crystal shape in aerated and nonaerated frozen food products as suggested by Unilever patent [138]. Although commercial AFPs are currently available, they are mainly for research or special uses because of their high price. Chemical synthesis and genetic engineering may be a solution to produce cost-effective AFPs, hence the need to promote their applications in frozen food products [139].

2.5 AFPs Synthesis and Mimics

2.5.1 Antifreeze Glycoproteins Synthesis and Mimics

The synthesis of AFGPs as pure glycoforms has been achieved through using ligation and polymerization strategies, and key structure–activity studies that are essential to inform the design of functional mimics have been reported [140–142].

The AFGPs isolated from fish blood plasma range in molecular mass from approximately 33 kDa (50 repeating units) to 2.6 kDa (four repeating units). They consist of repeating tripeptide units $(Ala\text{-}Thr\text{-}Ala)_n$ with a disaccharide moiety (Galb1-3GalNAca1-) attached to each threonyl residue [25]. Nishimura and colleagues reported the first synthesis of AFGPs in the form of pure glycoforms in

2004 [140], in a landmark paper that also reported the first structure–activity studies on AFGPs, and thus provided data that are essential to understanding the mechanism of action and to guiding the design of AFGP mimics. It was reported in an earlier communication polymeric AFGP of molecular weight (M_W) = 6–7 k could be efficiently synthesized by simple polymerization of the repeating glycopeptides unit of AFGP with diphenylphosphoryl azide (DPPA) as a promoter [141]. In the presence of the unprotected hydroxyl groups in the sugars, DPPA selectively activates the peptide carboxylic acid and by using this method, glycopeptides polymers of different ranges of molecular weight were produced. Through optimization of the chemistry, polymerization occurs most efficiently when using the glycoside of Ala-Thr-Ala; steric effects are minimized in the polymerization reaction compared with Ala-Ala-Thr with a glycoside C terminus [143]. Additional sugars were also appended enzymatically to the disaccharides [143].

The details of the overall synthesis is described in reference [140]. Low-molecular-weight fractions containing between two and eight repeating units (syAFGP2–syAFGP8) were obtained using a lower temperature and shorter reaction times. Consistent fractions of precise chain lengths containing up to seven repeating units were achieved by using recycling preparative size-exclusion chromatography. The effectiveness of 1-isobutoxycarbonyl-2-isobutoxy-1,2-dihydroquinoline (IIDQ) and 4-(4,6-dimethoxy-1,3,5-triazin-2-yl)-4 methylmorpholinium chloride (DMTMM) versus DPPA was also assessed as promoters for the formation of the glycopolymers [33]. DMT-MM-mediated condensation reactions proceeded smoothly, even though the average molecular weights of the polymers obtained with IIDQ were lower than those obtained with DPPA, and therefore provides a more general reagent for the synthesis of AFGP analogues consisting base-labile functional groups.

The recent NMR solution structure of syAFGP3 showed a significant population of a folded conformation with hydrophilic and hydrophobic faces [140]. This solution structure, and clear evidence for the important role of hydrophobic interactions in the interactions of several classes of AFPs with ice [44, 131, 144, 145] has refocused attention on understanding the possible role of hydrophobicity in the mechanism of action of AFGPs. Of particular note is the high prevalence of Ala and Thr residues in both type I AFPs [145] and AFGPs. It should be noted that AFGP8 at high concentrations (20–40 mM) exists predominately as dimer aggregates with higher thermal hysteresis activity as shown through dynamic light scattering and CD studies [44]. Overall solution conformation does not appear to be affected by these aggregates, and diffusion NMR studies of AFGP8 revealed no evidence for aggregation in solution at biologically relevant conditions [97]. In light of these structural studies, recent solution studies by a variety of techniques have looked for any proof for a preferred conformation of AFGPs at close to 0°C, or a rise in population of folded conformers that might be important in the interaction with the ice/water interfaces. The dynamics, structure, and conformational free energy of AFGP8, the smallest 14-residue AFGP containing two Pro residues, were studied by molecular dynamics [146]. The results confirmed that N-acetyl group plays an important role, with hydrogen bonding between the N-acetyl group and

the peptide backbone detected approximately 43% of the time. It was concluded from the study that AFGP8 has numerous structurally distinct degenerate minima, and this set of low-energy minima was proposed to be important for antifreeze activity. In particular, interconversion among multiple minima of AFGP8 can act as a thermal reservoir that will retard the growth rate of the ice crystal locally where it accumulates on the ice surface. This study overall suggests that conformational flexibility to access a variety of low-energy minima states is critical for antifreeze activity even though the Pro residues have an important role in stabilizing the conformations adopted by the AFGP.

The self-diffusion of AFGP8 as a function of temperature was monitored by NMR spectroscopy (243–303 K) in an independent study to evaluate if AFGPs undergo any global structural rearrangements in the supercooled regime that could be the cause for their function [65]. These results suggested that AFGP is more hydrated (ca. 30% increase in the bead radius) than other globular proteins, but showed no evidence for any major structural reorganization in order to function. Nishiumra et al. have also detected the presence of hydrated forms of syAFGP3 with water molecules by using cold spray ionization time-of-flight mass spectrometry [140]. The involvement of the Thr residue in the hydration of AFGPs is supported by recent studies that have demonstrated that the Thr g-methyl group is an important determinant of both the carbohydrate orientation and the degree of hydration [147]. Substituting d-GalNAcThr with d-GalNAcSer affects the strength of hydrogen bond involving the N-acetyl group and results in a significant increase in conformational degrees of freedom as well as the orientation of the neighboring water molecules. Consequently, the evolution of AFGPs with Thr in their structure, rather than Ser, may be attributed to the contribution of Thr to hydrophobicity and hydration effects, as well as the restricted conformational space of Thr glycosides compared with Ser glycosides [142].

The helical content of AFGP in the liquid, supercooled and frozen states of the solution film have been compared by attenuated total reflection (ATR)-FTIR spectroscopy [148]. The results showed that the AFGP molecules do not show any large conformational changes during supercooling whereas they change their conformation and become significantly helical upon freezing. It was proposed that the increase in helicity was to allow the AFGPs to increase the number of adsorption sites and maximize the interaction with ice crystals.

A number of studies on the interaction of AFGPs with surfaces have been carried out to probe the contributions of hydrophobic and hydrophilic interactions to adsorption. These studies are not of direct relevance to the biological mechanism of action of AFGPs, as these surfaces are models for an ice/vacuum interaction. However, such models can provide insights into surface properties such as nucleation events and surface roughening, and have been useful in the delineation of the features required for the assembly and development of functional materials. Sarno et al. examined the adsorption of AFGP8 onto mica and highly ordered pyrolytic graphite (HOPG), which contains both hydrophilic and hydrophobic binding sites (step edges or planes) [149]. The results showed that AFGP8 binds preferentially to the hydrophilic step edges of the surface. It was further shown that AFGP8 deposited

on mica by the solution droplet evaporation technique resulted in patterned surfaces formed by a single layer of protein [150] and that AFGP aggregates prior to deposition. Raman spectroscopy has also been used to monitor the interaction of AFGP8 on HOPG and Ag-coated glass-ceramic surfaces [151, 152].

A novel attempt to mimic the active domain of AFGPs in a simple monolayer is achieved by Hederos et al. A disaccharide-functionalized alkyl thiol chain was co-adsorbed with C2H5OC2H4NHCOC15H30SH to form statistically mixing self-assembled monolayers on gold [153]. Ice crystallization was examined by optical microscopy as the surface was cooled under an atmosphere of constant relative humidity. Water molecules appeared to organize and nucleate onto the self-assembled monolayer surface with high disaccharide content (>30%, i.e., the same ratio as AFGP) with behavior consistent with the absorption–inhibition model of AFGPs. Nonetheless, any direct comparison between the results with this system and native AFGPs is not yet possible as noted by the authors.

2.5.2 Protein-Based Anti-Ice Coating

The described features of AFPs are very interesting for nano(bio)technological applications, and the feasibility of both anti-ice and ice nucleation coatings has been demonstrated in proof-of-concept studies [154]. Wierzbicki et al. [155] described the structure–function relationship of a de novo synthesized 43-residue alanine–lysine-rich antifreeze polypeptide that is able to bind to designated ice planes along a specific direction [155]. A new protein-based ice-nucleating coating containing locally isolated nucleation points in a low surface energy matrix was synthesized by Zwieg et al. [156] using a sol–gel method. In addition to ice nucleation, this coating also displayed improved ice-repellent properties compared with commercial coatings. In addition, inspired by the sacred lotus leaf, anti-icing of surfaces has been performed with superhydrophobic coatings [157].

A feasibility study to modify lacquer surfaces with AFPs was conducted at the Fraunhofer IFAM, Germany [158]. Winter flounder and the European fir budworm were chosen as suitable AFP model organisms. Defined peptide sequences were produced by solid-phase peptide synthesis on a laboratory scale. Three different strategies were used to achieve the bonding of the artificial AFP residues to commercially available lacquer systems. The first approach consists of spraying an aqueous protein solution onto the lacquer by means of an ultrasound nebulizer. The coating system contained epoxy resin and a polyamine hardener. The epoxide groups on the lacquer surface reacted with the amino groups of the proteins and the protein became incorporated into the polymer. The second approach involves integrating photochemically active molecule into the lacquer system and AFPs were attached by photochemical means. The third approach consists of attaching the peptides to the lacquer via linker molecules, thus displaying the AFP residues on the surface. Among the three approaches, the third approach proved to be very promising. Control tests were carried out with various coating setups in a frosting chamber

at controlled airflow temperatures. Considerably less ice formed on the AFP-functionalized surfaces in contrast to the control, while a nonuniform coating also resulted in nonuniform frosting patterns. The results demonstrate both the feasibility and the enormous potential of biomimetic antifreeze coatings based on AFPs.

2.6 Conclusions and Outlook

The strategies employed by diverse organisms to cope with the cold provide fascinating insights into the adaptability of life on Earth. Continuing research into the molecular mechanisms of cold adaptation and freezing survival offer valuable insights into the molecular mechanisms of structure–function relationships, such as the case of what people have found about AFPs. Furthermore, these studies provide unique opportunities to identify new key applications for biotechnology advancement, such as improved freeze tolerance in plants and cold hardiness in animals, organ cryopreservation, and the destruction of malignant tumors in cryosurgery in medicine.

References

1. Mutaftschiev, B.: In: Hurle, D.T.J. (ed.) Handbook of Crystal Growth. North-Holland, Amsterdam, The Netherlands (1993)
2. Davies, P.L., Sykes, B.D.: Antifreeze proteins. Curr. Opin. Struct. Biol. **7**, 828–834 (1997)
3. Davies, P.L., Hew, C.L.: Biochemistry of fish antifreeze proteins. FASEB J. **4**, 2460–2468 (1990)
4. Knight, C.A.: Adding to the antifreeze agenda. Nature **406**, 249–251 (2000)
5. Jia, Z.C., Davies, P.L.: Antifreeze proteins: an unusual receptor-ligand interaction. Trends Biochem. Sci. **27**, 101–106 (2002)
6. Liu, X.Y.: Simulating 'atomic' processes of crystallization via controlled colloidal assembly. In: Wang, M., Tsukamoto, K., Wu, D. (eds.) Selected Topics on Crystal Growth: 14th International Summer School on Crystal Growth, pp. 173–220. American Institute of Physics, Dalian (2010)
7. Liu, X.Y.: From templated nucleation to functional materials engineering. In: Skowronski, M., DeYoreo, J.J., Wang, C.A. (eds.) Perspectives on Inorganic, Organic and Biological Crystal Growth: from Fundamentals to Applications, pp. 439–465. American Institute of Physics, Park City, UT (2007)
8. Liu, X.Y.: From molecular structure of solid–fluid interfaces to nucleation kinetics: implications for nanostructure engineering. In: De Yoreo, J., Liu, X.Y. (eds.) Nanoscale Structure and Assembly at Solid–Fluid Interfaces. **1**, Springer (2004)
9. Liu, X.Y.: Generic mechanism of heterogeneous nucleation and molecular interfacial effects. In: Sato, K., Nakajima, K., Furukawa, Y. (eds.) Advances in Crystal Growth Research, pp. 42–61. Elsevier Science B.V., Amsterdam (2001)
10. Koop, T., et al.: A new optical technique to study aerosol phase transitions: the nucleation of ice from H_2SO_4 aerosols. J. Phys. Chem. A **102**(45), 8924–8931 (1998)
11. Hare, D.E., Sorensen, C.M.: The density of supercooled water. II. Bulk samples cooled to the homogeneous nucleation limit. J. Chem. Phys. **87**(8), 4840–4845 (1987)

12. Liu, X.Y., Du, N.: Zero-sized effect of nano-particles and inverse homogeneous nucleation: principles of freezing and antifreeze. J. Biol. Chem. **279**, 6124–6131 (2004)
13. Liu, X.Y., et al.: Prediction of crystal growth morphology based on structural analysis of the solid–fluid interface. Nature **374**(6520), 342–345 (1995)
14. Liu, X.-Y., Bennema, P.: Morphology of crystals: internal and external controlling factors. Phys. Rev. B **49**(2), 765–775 (1994)
15. Liu, X.Y., et al.: Analysis of morphology of crystals based on identification of interfacial structure. J. Chem. Phys. **103**(9), 3747–3754 (1995)
16. Liu, X.-Y., Bennema, P.: Theoretical consideration of the growth morphology of crystals. Phys. Rev. B **53**(5), 2314–2325 (1996)
17. Liu, X.Y.: Modeling of the fluid-phase interfacial effect on the growth morphology of crystals. Phys. Rev. B **60**(4), 2810–2817 (1999)
18. DeVries, A.L.: *Survival at freezing temperatures*. In: Sargent, J.M., Malins, D.C. (eds.) Biochemical and Biophysical Perspectives in Marine Biology, pp. 289–330. Academic Press, London (1974)
19. Duman, J.G., Olsen, T.M.: Thermal hysteresis protein activity in bacteria, fungi, and phylogenetically diverse plants. Cryobiology **30**, 322–328 (1993)
20. Yeh, Y., Feeney, R.E.: Antifreeze proteins-structures and mechanisms of function. Chem. Rev. **96**, 601–617 (1996)
21. Graham, L.A., Liou, Y.-C., Walker, V.K., Davies, P.L.: Hyperactive antifreeze protein from beetles. Nature **388**, 727–728 (1997)
22. Scholander, P.F., Dam, L.V., Kanwisher, J., Hammel, T., Gordon, M.S.: Supercooling and osmoregulation in Arctic fish. J. Cell. Comp. Physiol. **49**, 5–24 (1957)
23. Gordon, M.S., Amdur, B.H., Scholander, P.F.: Freezing resistance in some northern fishes. Biol. Bull. **122**, 52–62 (1962)
24. DeVries, A.L.: Freezing resistance in some Antarctic fishes. Science **163**, 1073–1075 (1969)
25. DeVries, A.L., Komatsu, S.K., Feeney, R.E.: Chemical and physical properties of freezing point-depressing glycoproteins from Antarctic fishes. J. Biol. Chem. **245**, 2901–2908 (1970)
26. Duman, J.G., DeVries, A.L.: Freezing behaviour of aqueous solutions of glycoproteins from the blood of an Antarctic fish. Cryobiology **9**, 469–472 (1972)
27. Lin, Y., Duman, J.G., DeVries, A.L.: Studies on the structure and activity of lowmolecular weight glycoproteins from an Antarctic fish. Biochem. Biophys. Res. Commun. **46**, 87–92 (1972)
28. Raymond, J.A., DeVries, A.L.: Freezing behaviour of fish blood glycoproteins with antifreeze properties. Cryobiology **9**, 541–547 (1972)
29. Scholander, P.F., Maggert, J.E.: Supercooling and ice propagation in blood from Arctic fishes. Cryobiology **8**, 371–374 (1971)
30. Fletcher, G.L., Hew, C.L., Davies, P.L.: Antifreeze proteins of Teleost fishes. Annu. Rev. Physiol. **63**, 359–390 (2001)
31. Jia, Z., Davies, P.L.: Antifreeze proteins: an unusual receptor–ligand interaction. Trends Biochem. Sci. **2**, 101–106 (2002)
32. Duman, J.G., DeVries, A.L.: Freezing resistance in winter flounder *Pseudopleuronectus americanus*. Nature **247**, 237–238 (1974)
33. Ng, N.F., Trinh, K.-Y., Hew, C.L.: Structure of an antifreeze polypeptide precursor from the sea raven, *Hemitripterus americanus*. J. Biol. Chem. **261**, 15690–15695 (1986)
34. Jia, Z.C., Deluca, C.I., Davies, P.L.: Crystallization and preliminary X-ray crystallographic studies on type III antifreeze protein. Protein Sci. **4**, 1236–1238 (1995)
35. Deng, G.J., Andrews, D.W., Laursen, R.A.: Amino acid sequence of a new type of antifreeze protein—from the longhorn sculpin Myoxocephalus octodecimspinosis. FEBS Lett. **402**, 17–20 (1997)
36. DeVries, A.L.: Glycoproteins as biological antifreeze agents in Antarctic fishes. Science **172**, 1152–1155 (1971)
37. Ramsay, R.A.: The rectal complex of the mealworm (*Tenebrio molitor* L. *Coleoptera, Tenebrionidae*). Philos. Trans. R. Soc. London Ser. B **248**, 279–314 (1964)

38. Duman, J.G.: Subzero temperature tolerance in spiders: the role of thermal hysteresis factors. J. Comp. Physiol. **131**, 347–352 (1979)
39. Block, W., Duman, J.G.: Presence of thermal hysteresis producing antifreeze proteins in the Antarctic mite Alaskozetes antarcticus. J. Exp. Zool. **250**, 229–231 (1989)
40. Tursman, D., Duman, J.G., Knight, C.A.: Freeze tolerance adaptations in the centipede Lithobius forficatus. J. Exp. Zool. **268**, 347–353 (1994)
41. Duman, J.G.: Antifreeze and ice nucleator proteins in terrestrial arthropods. Annu. Rev. Physiol. **63**, 327–357 (2001)
42. Urrutia, M.E., Duman, J.G., Knight, C.A.: Plant thermal hysteresis proteins. Biochim. Biophys. Acta **1121**, 199–206 (1992)
43. Pauling, L.: The structure and entropy of ice and of other crystals with some randomness of atomic arrangement. J. Am. Chem. Soc. **57**, 2680–2684 (1935)
44. Strom, C.S., Liu, X.Y., Jia, Z.: Ice surface reconstruction as antifreeze protein-induced morphological modification mechanism. J. Am. Chem. Soc. **127**, 428–440 (2005)
45. Zhang, K.-Q., Liu, X.Y.: In situ observation of colloidal monolayer nucleation driven by an alternating electric field. Nature **429**(6993), 739–743 (2004)
46. Liu, X.Y.: From molecular structure of solid-fluid interfaces to nucleation kinetics: implications for nanostructure engineering. In Nanoscale structure and assembly at solid-fluid interfaces, edited by X.Y. Liu, and James J. De Yoreo, Springer, London, Vol.I, p. 109–175 (2004)
47. Fowler, R., Giggenhein, E.A.: Statistical Thermoddynamics. Cambrideg University, London (1960)
48. Diao, Y.Y., Liu, X.Y.: Controlled colloidal assembly: experimental modeling of general crystallization and biomimicking of structural color. Adv. Funct. Mater. **22**(7), 1354–1375 (2012)
49. Liu, X.Y.: Generic mechanism of heterogeneous nucleation and molecular interfacial effects. In Advances in Crystal Growth Research, edited by K.Sato, K.Nakajima and Y. Furukawa ELSEVIER SCIENCE B.V., Amsterdam, 42–61 (2001)
50. Liu, X.Y.: A new kinetic model for 3D heterogeneous nucleation, compared with experiments. J. Chem. Phys. **111**, 1628–1635 (1999)
51. Du, N., Liu, X.Y.: Controlled ice nucleation in microsized water droplet. Appl. Phys. Lett. **81**, 445–447 (2002)
52. Rasmussen, D.H.: Thermodynamics and nucleation phenomena—a set of experimental observations. J. Cryst. Growth **56**, 56–66 (1982)
53. Mullin, J.W.: Crystallization, pp. 182–194. Butterworth-Heinemann, Oxford (1997)
54. Du, N., Liu, X.Y.: Ice nucleation inhibition: mechanism of antifreeze by antifreeze protein. J. Biol. Chem. **278**, 36000–36004 (2003)
55. Liu, X.-Y., Bennema, P., van der Eerden, J.P.: Rough-flat-rough transition of crystal surfaces. Nature **356**(6372), 778–780 (1992)
56. Liu, X.-Y., van Hoof, P., Bennema, P.: Surface roughening of normal alkane crystals: solvent dependent critical behavior. Phys. Rev. Lett. **71**(1), 109–112 (1993)
57. Liu, X.-Y., Bennema, P.: The equilibrium state of solid–liquid interfaces of aliphatic compounds. J. Chem. Phys. **97**(5), 3600–3609 (1992)
58. Liu, X.-Y.: First-order thermal roughening of normal alkane crystals. Phys. Rev. B **48**(3), 1825–1829 (1993)
59. Liu, X.-Y., Bennema, P.: Self-consistent-field calculation of structures and static properties of the solid–fluid interface: paraffinlike molecule systems. Phys. Rev. E **48**(3), 2006–2015 (1993)
60. Liu, X.-Y., Bennema, P.: The relation between macroscopic quantities and the solid–fluid interfacial structure. J. Chem. Phys. **98**(7), 5863–5872 (1993)
61. Xiang-Yang, L.: The solid–fluid interface: a comparison and further description using the layer model. Surf. Sci. **290**(3), 403–412 (1993)
62. Liu, X.-Y.: Properties and structure of crystal-solution interfaces of normal alkane crystals: influence of solvents. J. Chem. Phys. **102**(3), 1373–1384 (1995)

63. Liu, X.Y., et al.: Can a foreign particle cause surface instability? J. Phys. Chem. B **104**(50), 11942–11949 (2000)
64. Liu, X.Y.: Effect of foreign particles on the growth of faceted crystal faces. J. Chem. Phys. **113**(19), 8807–8816 (2000)
65. Liu, X.Y., Bennema, P.: Foreign body induced kinetic roughening: kinetics and observations. J. Chem. Phys. **115**(9), 4268–4274 (2001)
66. Zhang, K.-Q., Liu, X.Y.: Two scenarios for colloidal phase transitions. Phys. Rev. Lett. **96**(10), 105701 (2006)
67. Liu, X.Y., Maiwa, K., Tsukamoto, K.: Heterogeneous two-dimensional nucleation and growth kinetics. J. Chem. Phys. **106**(5), 1870–1879 (1997)
68. Chernov, A.A.: Modern Crystallography III Crystal Growth. Springer Verlag, Berlin (1984)
69. Liu, X.Y.: Interfacial effect of molecules on nucleation kinetics. J. Phys. Chem. B **105**(47), 11550–11558 (2001)
70. Strom, C. S.: Graph-theoretic construction of Periodic Bond Chains I, General Case. Z. Kristallogr. **153**, 99–113 (1980)
71. Hartman, P.: The dependence of crystal morphology on crystal structure. In: Sheftal, N.N. (ed.) Growth of Crystals, pp. 3–18. Consultants Bureau, New York (1969)
72. Strom, C.S.: Ionic crystals. In: Myerson, A.S. (ed.) Molecular Modeling Applications in Crystallization, pp. 228–312. Cambridge University Press, New York (1999)
73. Donnay, J.D.H.: Spherical Trigonometry after the Cesàro Method. Interscience Publishers, Inc., New York, NY (1945)
74. Hartman, P., Perdok, W.G.: On the relations between structure and morphology of crystals. II. Acta Crystallogr. **8**(9), 521–524 (1955)
75. Hartman, P., Perdok, W.G.: On the relations between structure and morphology of crystals. III. Acta Crystallogr. **8**(9), 525–529 (1955)
76. Hartman, P., Perdok, W.G.: On the relations between structure and morphology of crystals. I. Acta Crystallogr. **8**(1), 49–52 (1955)
77. Hartman, P., Bennema, P.: The attachment energy as a habit controlling factor: I. Theoretical considerations. J. Cryst. Growth **49**(1), 145–156 (1980)
78. Bennema, P.: Thermodynamics and kinetics. In: Hurle, D.T.J. (ed.) Handbook of Crystal Growth 1a Fundamentals, pp. 477–581. Elsevier, Amsterdam (1993)
79. Strom, C.S., Liu, X.Y., Jia, Z.: Antifreeze protein-induced morphological modification mechanisms linked to ice binding surface. J. Biol. Chem. **279**, 32407–32417 (2004)
80. Strom, C.S., Liu, X.Y., Jia, Z.: Why does insect antifreeze protein from Tenebrio molitor produce pyramidal ice crystallites? Biophys. J. **89**, 2618–2627 (2005)
81. Baardsnes J., Jelokhani-Niaraki, M., Kondejewski, L.H., Kuiper, M.J., Kay, C.M., Hodges, R.S., Davies, P.L. Antifreeze protein from shorthorn sculpin: identification of the ice-binding surface. Protein Sci. **10**, 2566–2576 (2001)
82. Zhang, W.L.: Artificial antifreeze polypeptides: α-helical peptides with KAAK motifs have antifreeze and ice crystal morphology modifying properties. FEBS Lett. **455**, 372–376 (1999)
83. Fairley, K., Westman, B.J., Pham, L.H., Haymet, A.D. J., Harding, M.M., Mackay, J.P. Type I shorthorn sculpin antifreeze protein - Recombinant synthesis, solution conformation, and ice growth inhibition studies. J. Biol. Chem. **277**, 24073–24080 (2002).
84. Houston, M.E., Chao, H., Hodges, R.S., Sykes, B.D., Kay, C.M., Sonnichsen, F.D., Loewen, M.C., Davies, P.L.: Binding of an oligopeptide to a specific plane of ice. J. Biol. Chem. **273**, 11714–11718 (1998)
85. Wierzbicki, A., Taylor, M.S., Knight, C.A., Madura, J.D., Harrington, J.P., Sikes, C.S.: Analysis of shorthorn sculpin antifreeze protein stereospecific binding to (2–10) faces of ice. Biophys. J. **71**, 8–18 (1996)
86. Harding, M.M., Anderberg, P.I., Haymet, A.D.J.: 'Antifreeze' glycoproteins from polar fish. Eur. J. Biochem. **270**(7), 1381–1392 (2003)
87. Wilson, P.W., Gould, M., Devries, A.L. Hexagonal shaped ice spicules in frozen antifreeze protein solutions. Cryobiology **44**, 240–250 (2002)

88. Harding, M.M., Ward, L.G., Haymet, A.D. Type I 'antifreeze' proteins. Structure-activity studies and mechanisms of ice growth inhibition. Eur J Biochem, **264**, 653–665 (1999).
89. Haymet, A.D., Ward, L.G., Harding, M.M., Knight, C.A.: Valine substituted winter flounder 'antifreeze': preservation of ice growth hysteresis. FEBS Lett. **430**, 301–306 (1998)
90. Ewart, K.V., Yang, D.S.C., Ananthanarayanan, V.S., Fletcher, G.L., Hew, C.L.: Ca2+-dependent antifreeze proteins modulation of conformation and activity by divalent ions. J. Biol. Chem. **271**, 16627–16632 (1996)
91. Nishimiya, Y., Ohgiya, S., Tsuda, S. : Artificial Multimers of The Type III Antifreeze Protein: Effects on Thermal Hysteresis and Ice Crystal Morphology. J. Biol. Chem., **278**, 32307–32312 (2003).
92. Graether, S.P., Kuiper, M.J., Gagn, S.M., Walker, V.K., Jia, Z., Sykes, B.D., Davies, P.L.: β-Helix structure and ice-binding properties of a hyperactive antifreeze protein from an insect. Nature **406**, 325–328 (2000)
93. Wathen, B., Kuiper, M., Walker, V., Jia, Z. A new model for simulating 3D crystal growth and its application to the study of antifreeze proteins. J. Am. Chem. Soc. **125**, 729–737 (2003).
94. Liou, Y.-C., Tocilj, A., Davies, P.L., Jia, Z.: Mimicry of ice structure by surface hydroxyls and water of a β-helix antifreeze protein. Nature **406**, 322–324 (2000)
95. Baardsnes, J., Kondejewski, L.H., Hodges, R.S., Chao, H., Kay, C., Davies, P.L.: New ice-binding face for type I antifreeze protein. FEBS Lett. **463**, 87–91 (1999)
96. Bouvet, V., Ben, R.N.: Antifreeze glycoproteins structure, conformation, and biological applications. Cell Biochem. Biophys. **39**, 133–144 (2003)
97. Inglis, S.R., Turner, J.J., Harding, M.M.: Applications of type I antifreeze proteins: studies with model membranes & cryoprotectant properties. Curr. Protein Pept. Sci. **7**, 509–522 (2006)
98. Aguilera, G.P.J.M.: Ice morphology: fundamentals and technological applications in foods. Food Biophys. **4**, 378–396 (2009)
99. Baust, J.M.: Molecular mechanisms of cellular demise associated with cryopreservation failure. Cell Preserv. Technol. **1**, 17–31 (2002)
100. Glander, A.J., Schaller, J.: Binding of annexin V to plasma membranes of human spermatozoa: a rapid assay for detection of membrane changes after cryostorage. Mol. Hum. Reprod. **5**, 109–115 (1999)
101. Baust, J.M., Van Buskirk, R.G., Baust, J.G.: Cell viability improves following inhibition of cryopreservation-induced apoptosis. In Vitro Cell. Dev. Biol. Anim. **36**, 262–270 (2000)
102. Fowke, K.R., Behnke, J., Hanson, C., Shea, K., Cosentino, M.: Apoptosis: a method for evaluating the cryopreservation of whole blood mononuclear cells. J. Immunol. Methods **244**, 139–144 (2000)
103. Hilbert, S.L., Luna, R.E., Zhang, J., Wang, Y., Hopkins, R.A., Yu, Z.X., Ferran, V.T.: Allograft heart valves: the role of apoptosismediated cell loss. J. Thorac. Cardiovasc. Surg. **117**, 454–462 (1999)
104. Villalba, R., Pena, J., Luque, E., Gomez-Villagran, J.L.: Characterization of ultrastructural damage of valves cryopreserved under standard conditions. Cryobiology **43**, 81–84 (2001)
105. Mazur, P.: Kinetic of water loss from cells at subzero temperatures and the likelihood of intracellular freezing. J. Gen. Physiol. **47**, 347–369 (1963)
106. Arav, A., Yavin, S., Zeron, Y., Natan, D., Dekel, I., Gacitua, H.: New trends in gamete's cryopreservation. Mol. Cell. Endocrinol. **187**, 77–81 (2002)
107. Marsland, T.P., Evans, S., Pegg, D.E.: Dielectric measurements for design of an electromagnetic rewarming system. Cryobiology **24**, 311–323 (1981)
108. Robinson, M.P., Pegg, D.E.: Rapid electromagnetic warming of cells and tissues. IEEE Trans. Biomed. Eng. **46**, 1413–1425 (1999)
109. Pegg, D.E.: The history and principles of cryopreservation. Semin. Reprod. Med. **20**, 5–13 (2002)
110. Rubinsky, B., Arav, A., Devries, A.L.: Cryopreservation of oocytes using directional cooling and antifreeze glycoproteins. Cryo Lett. **12**, 93–106 (1991)

111. Eto, T.K., Rubinsky, B.: Antifreeze glycoproteins increase solution viscosity. Biochem. Biophys. Res. Commun. **197**, 927–931 (1993)
112. Wu, Y., Banoub, J., Goddard, S.V., Kao, M.H., Fletcher, G.L.: Antifreeze glycoproteins: relationship between molecular weight, thermal hysteresis and the inhibition of leakage from liposomes during thermotropic phase transition. Comp. Biochem. Physiol. B **128**, 265–273 (2001)
113. Pickering, S.J., Braude, P.R., Johnson, M.H., Can, A., Currie, J.: Transient cooling to room temperature can cause irreversible disruption of the meiotic spindle in the human oocyte. Fertil. Steril. **54**, 102–108 (1990)
114. Pickering, S.J., Johnson, M.H.: The influence of cooling on the organization of the meiotic spindle of the mouse oocyte. Hum. Reprod. **2**, 207–216 (1987)
115. O'Neil, L., Paynter, S.J., Fuller, B.J., Shaw, R.W., DeVries, A.L.: Vitrification of mature mouse oocytes in a 6 M Me2SO solution supplemented with antifreeze glycoproteins: The effect of temperature. Cryobiology **37**, 59–66 (1998)
116. Vincent, C., Johnson, M.H.: Cooling, cryoprotectants, and the cytoskeleton of the mammalian oocyte. Oxford Rev. Reprod. Biol. **14**, 73–100 (1992)
117. Rubinsky, B., Arav, A., Devries, A.L.: The cryoprotective effect of antifreeze glycopeptides from Antarctic fishes. Cryobiology **29**, 69–79 (1992)
118. Storey, K.B., Bischof, J., Rubinsky, B.: Cryomicroscopic analysis of freezing in liver of the freeze tolerant wood frog. Am. J. Physiol. **263**, R185–R194 (1992)
119. Hincha, D.K., Devries, A.L., Schmitt, J.M.: Cryotoxicity of antifreeze proteins and glycoproteins to spinach thylakoid membranes—comparison with cryotoxic sugar acids. Biochim. Biophys. Acta **1146**, 258–264 (1993)
120. Cheng, C., Devries, A.L.: Do antifreeze proteins have a role in maintenance of ion gradients across cell membranes in polar fishes and invertebrates? Cryobiology **29**, 783 (1992)
121. Payne, S.R., Oliver, J.E., Upreti, G.C.: Effect of antifreeze proteins on the motility of ram spermatozoa. Cryobiology **31**, 180–184 (1994)
122. Hays, L., Feeney, R.E., Crowe, L.M., Crowe, J.H., Oliver, A.E.: Antifreeze glycoproteins inhibit leakage from liposomes during thermotropic phase transitions. Proc. Natl. Acad. Sci. U.S.A. **93**, 6835–6840 (1996)
123. Quinn, P.J.: A liquid-phase separation model of low temperature damage to biological membranes. Cryobiology **22**, 128–146 (1995)
124. Clerc, S.G., Thompson, T.G.: Permeability of dimyristoyl phosphatidylcholine/dipalmitoyl phosphatidylcholine bilayer-membranes with coexisting gel and liquid-crystalline phases. Biophys. J. **68**, 2333–2341 (1995)
125. Wu, Y., Fletcher, G.L.: Efficacy of antifreeze protein types in protecting liposome membrane integrity depends on phospholipid class. Biochim. Biophys. Acta **1524**, 11–16 (2000)
126. Knight, C.A., Driggers, E., Devries, A.L.: Adsorption to ice of fish antifreeze glycopeptide-7 and glycopeptide-8. Biophys. J. **64**, 252–259 (1993)
127. Franks, F., Morris, E.R.: Blood glycoprotein from Antarctic fish. Possible conformational origins of antifreeze activity. Biochem. Biophys. Acta **540**, 346–356 (1978)
128. Tomczak, M.M., Hincha, D.K., Estrada, S.D., Wolkers, W.F., Crowe, L.M., Feeney, R.E., Tablin, F., Crowe, J.H.: A mechanism for stabilization of membranes at low temperatures by an antifreeze protein. Biophys. J. **82**, 874–881 (2002)
129. Tomczak, M.A.C.: In: Ewart, K.V., Hew, C.L. (eds.) Fish Antifreeze Proteins. World Scientific Publishing, Singapore, pp. 187–212 (2002)
130. Tomczak, M.M., Hincha, D.K., Crowe, J.H., Harding, M.M., Haymet, A.D.J., Ward, L.G., Harding, M.M.: The effect of hydrophobic analogues of the type I winter flounder antifreeze protein on lipid bilayers. FEBS Lett. **551**, 13–19 (2003)
131. Haymet, A.D.J., Ward, L.G., Harding, M.M.: winter flounder antifreeze proteins: synthesis and ice growth inhibition of analogues that probe the relative importance of hydrophobic and hydrogen bonding interactions. J. Am. Chem. Soc. **121**, 941–948 (1999)
132. Hartel, R.W.: Crystallization in Foods. Aspen, Gaithersburg (2001)

133. Li, B., Sun, D.-W.: Novel method for rapid freezing and thawing of foods—a review. J. Food Eng. **54**, 175–182 (2002)
134. Warren, G.J., Mueller, G.M., McKown, R.L.: Ice crystal growth suppression polypeptides and method of making. US Patent (1992)
135. Payne, S.R., Sandford, D., Harris, A., Young, O.A.: The effects of antifreeze proteins on chilled and frozen meats. Meat Sci. **37**, 429–438 (1994)
136. Payne, S.R., Young, O.A.: Effects of pre-slaughter administration of antifreeze proteins on frozen meat quality. Meat Sci. **41**, 147–155 (1995)
137. Boonsupthip, W., Lee, T.-C.: Application of antifreeze protein for food preservation: effect of type III antifreeze protein for preservation of gel forming of frozen and chilled actomyosin. Food Sci. **68**, 1804–1809 (2003)
138. Aldred, D.L., Berry, M.J., Cebula, D.J., Cox, A.R., Golding, M.D., Golding, S., Keenan, R.D., Malone, M.E., Twigg, S.: Frozen products. US Patent (2006)
139. Sun, D.-W., Zheng, L.: Innovations in freezing process. In: Sun, D.-W. (ed.) Handbook of Frozen Food Processing and Packaging, pp. 175–195. CRC Press, Boca Raton (2006)
140. Tachibana, Y., Fletcher, G.L., Fujitani, N., Tsuda, S., Monde, K., Nishimura, S.: Antifreeze glycoproteins: elucidation of the structural motifs that are essential for antifreeze activity. Angew. Chem. Int. Ed. **43**, 856–862 (2004)
141. Tsuda, T., Nishimura, S.I.: Synthesis of an antifreeze glycoprotein analogue: Efficient preparation of sequential glycopolymers. Chem. Commun. **24**, 2779–2780 (1996)
142. Harding, M.M., Garner, J.: Design and synthesis of antifreeze glycoproteins and mimics. ChemBioChem **11**, 2489–2498 (2010)
143. Tachibana, Y., Matsubara, N., Nakajima, F., Tsuda, T., Tsuda, S., Monde, K., Nishimura, S.-I.: Efficient and versatile synthesis of mucin-like glycoprotein mimics. Tetrahedron **58**, 10213–10224 (2002)
144. Wierzbicki, A., Dalal, P., Cheatham III, T.E., Knickelbein, J.E., Haymet, A.D.J., Madura, J.D.: Antifreeze proteins at the ice/water interface: three calculated discriminating properties for orientation of type I proteins. Biophys. J. **93**, 1442–1451 (2007)
145. Harding, M.M., Ward, L.G., Haymet, A.D.J.: Type I 'antifreeze' proteins. Structure-activity studies and mechanisms of ice growth inhibition. Eur. J. Biochem. **264**, 653–665 (1999)
146. Nguyen, D.H., Colvin, M.E., Yeh, Y., Feeney, R.E., Fink, W.H.: The dynamics, structure, and conformational free energy of proline-containing antifreeze glycoprotein. Biophys. J. **82**, 2892–2905 (2002)
147. Corzana, F., Busto, J.H., Jimenez-Oses, G., Garcia de Luis, M., Asensio, J.L., Jimenez-Barbero, J., Peregrina, J.M., Avenoza, A.: Serine versus threonine glycosylation: the methyl group causes a drastic alteration on the carbohydrate orientation and on the surrounding water shell. J. Am. Chem. Soc. **129**, 9458–9467 (2007)
148. Uda, Y., Zepeda, S., Kaneko, F., Matsuura, Y., Furukawa, Y.: Adsorption-induced conformational changes of antifreeze glycoproteins at the ice/water interface. J. Phys. Chem. B **111**, 14355–14361 (2007)
149. Sarno, D.M., Murphy, A.V., DiVirgilio, E.S., Jones Jr., W.E., Ben, R.N.: Direct observation of antifreeze glycoprotein-fraction 8 on hydrophobic and hydrophilic interfaces using atomic force microscopy. Langmuir **19**, 4740–4744 (2003)
150. Younes-Metzler, O., Ben, R.N., Giorgi, J.B.: Pattern formation of antifreeze glycoproteins via solvent evaporation. Langmuir **23**, 11355–11359 (2007)
151. Cui, Y., Turner, G., Roy, U.N., Guo, M., Pan, Z., Morgan, S., Burger, A., Yeh, Y.: Raman spectroscopy shows antifreeze glycoproteins interact with highly oriented pyrolytic graphite. J. Raman Spectrosc. **36**, 1113–1117 (2005)
152. Pan, Z., Morgan, S.H., Ueda, A., Mu, R., Cui, Y., Guo, M., Burger, A., Yeh, Y.: Surface-enhanced Raman probing of biomolecules using Ag-coated porous glass-ceramic substrates. J. Raman Spectrosc. **36**, 1082–1087 (2005)
153. Hederos, M., Konradsson, P., Borgh, A., Liedberg, B.: Mimicking the properties of antifreeze glycoproteins: synthesis and characterization of a model system for ice nucleation and antifreeze studies. J. Phys. Chem. B **109**, 15849–15859 (2005)

154. Garner, J., Harding, M.M.: Design and synthesis of alpha-helical peptides and mimetics. Org. Biomol. Chem. **5**, 3577–3585 (2007)
155. Wierzbicki, A., Knight, C.A., Rutland, T.J., Muccio, D.D., Pybus, B.S., Sikes, C.S.: Structure-function relationship in the antifreeze activity of synthetic alanine-lysine antifreeze polypeptides. Biomacromolecules **1**, 268–274 (2000)
156. Zwieg, T., Cucarella, V., Kauffeld, M.: Novel biomimetically based ice-nucleating coatings. Int. J. Mater. Res. **98**, 597–602 (2007)
157. Solga, A., Cerman, Z., Striffler, B.F., Spaeth, M., Barthlott, W.: The dream of staying clean: lotus and biomimetic surfaces. Bioinspir. Biomim. **2**, 126–134 (2007)
158. Grunwald, I., Rischka, K.: Prevention of ice adhesion and ice growth on surfaces: one problem, two prospective solutions. Annual report 2007/08, Fraunhofer IFAM, pp. 66–68 (2008)

Chapter 3
Biomineralization: Mechanisms of Hydroxyapatite Crystal Growth

Kazuo Onuma, Toru Tsuji, and Mayumi Iijima

Abstract Progress in the investigation of the growth mechanism of hydroxyapatite, the most important biomineral, is described in relation to observation and measurement techniques of crystals growing in aqueous solutions. Optical interferometry, especially phase-shift interferometry, can measure the apatite growth rate precisely and facilitates estimates of several growth parameters necessary to analyze the growth mechanism of apatite. The data strongly suggest that the growth unit of apatite takes the form of energetically stable clusters. Apatite growth proceeds via accumulation of clusters, resembling the growth of macromolecular protein crystals, although conventional spiral or two-dimensional nucleation growth occurs on the surface, as in the case of protein crystals. Phase transformation of amorphous calcium phosphate into apatite proceeds via direct structure reconstruction of aggregates with clusters as the minimum unit. These cluster-based transformation and growth phenomena are not specific to apatite: they also occur in other biominerals, such as calcium carbonates.

Keywords Biomineralization • Hydroxyapatite • Growth mechanism • Phase-shift interferometry • Cluster

K. Onuma (✉)
National Institute of Advanced Industrial Science & Technology, Central 6, 1-1-1 Higashi, Tsukuba, Ibaraki, 305-8566, Japan
e-mail: k.onuma@aist.go.jp

T. Tsuji
Advanced Research Centers, Keio University, 3-14-1, Hiyoshi, Kohoku-ku, Yokohama, 223-8522, Japan
e-mail: toruts2002@yahoo.co.jp

M. Iijima
Asahi University School of Dentistry, Oral Functional Science and Rehabilitation, Dental Materials Science, 1851-1 Hozumi, Mizuho, Gifu, 501-0296, Japan
e-mail: iijima@dent.asahi-u.ac.jp

X.Y. Liu (ed.), *Bioinspiration: From Nano to Micro Scales*, Biological and Medical Physics, Biomedical Engineering, DOI 10.1007/978-1-4614-5372-7_3,

3.1 Introduction

The production of crystals or amorphous materials resulting from the interactions of organic and inorganic substances that accompany biological activity within living organisms is known as biomineralization. These living organisms can be both lower and higher organisms, including humans. The production of calcium salt crystals (calcium oxalate) within plants was first described in the 1600s. Therefore, viewed from a historical perspective, biomineralization is an academic field with an extremely long life span.

Narrowly defined, biomineralization is the process by which inorganic substances are produced on organic templates within an organism. Representative examples include the formation of bone and teeth within the human body and the formation of sea urchin spines and shells. Single crystals of apatite, a calcium phosphate, are arranged in human bone possesses an organization in which single crystals of apatite, a species of calcium phosphate with their crystal orientations aligned. This arrangement produces a fine structure possessing both strength and flexibility. Teeth are also assemblies of single apatite crystals, and enamel in particular is a high-hardness tissue comprised of densely packed fine apatite with an extremely high degree of crystallinity. Another example of biomineralization is the pearl layer of the Akoya pearl oyster, in which single crystals of aragonite, a calcium carbonate, are packed in an orderly fashion within a microscopic space. The proteins that fill in the surrounding gaps contribute to the creation of a beautiful sheen.

While biomineralization can occur in mild environments under normal temperatures and pressures, it is difficult to directly form the groups of inorganic crystals seen in hard tissues such as teeth, bone, and shells from simple solutions under normal temperature and pressure while maintaining high crystallinity. The mechanism used by organisms to build the tissues necessary for survival—the use of organic substances as templates—enables crystallization with lower activation energy. The application of this mechanism to industrial crystallization, which is totally unrelated to living organisms, is a promising area of research. Crystallization that utilizes organic–inorganic interaction processes in a mild environmental field not related to living organisms is commonly called “biomineralization-mimicking” or “biomineralization-based” crystallization.

Although biomineralization beneficially forms tissues necessary for maintaining normal organism function, it also produces substances that adversely affect organism health. For example, (broadly defined) biomineralization can cause gout, gallstones, kidney stones, urinary tract stones, vein wall deposit, and cholesterol accumulation in humans. Stones contain organic substances such as uric acid and urate salts, in addition to inorganic substances such as calcium phosphate and calcium oxalate salts. A cholesterol crystal, for example, is a natural organic substance. This means that the production of organic crystals on organic substance templates can be regarded as a type of biomineralization. Many of the crystals formed by biomineralization inside organisms, especially within the human body,

are calcium salts, so their formation can be generically classified as calcification. Representative examples of beneficial calcification include the formation of teeth and bone, while harmful calcification includes, in addition to stone formation, the buildup of atherosclerotic plaques, the calcification of brain tissue, and the accumulation of fine calcium salt crystals that often accompanies the presence of cancerous tissues.

Among the calcium salts formed by biomineralization, calcium phosphates, represented by apatite, have by far received the most attention and in-depth study. This is probably because calcium phosphate salts are not only integral to tissue formation but are also believed to be very deeply involved in life processes and in the evolution of species [1]. While there have been many debates on this topic, a consensus of opinions has not yet been reached. For instance, one enduring question is why vertebrates, as represented by humans, use apatite (a calcium phosphate salt) to produce hard tissues in the body while invertebrates such as shellfish use calcium carbonate salts such as aragonite and calcite to produce hard tissues. One explanation is that invertebrates have a unique immune mechanism. And while there are intriguing theories related to apatite and the origins of life, the supporting evidence is inconclusive. For example, the surface of apatite has extremely strong affinity for the substances constituting living organisms such as amino acids, proteins, sugars, and lipids. Moreover, amino acids arrange themselves with high regularity on apatite surfaces and are able to initiate condensation reactions, a key factor in the origin of life [2].

Biomineralization is a typical interdisciplinary topic that is related to physics, chemistry, and biology (including medical science), and the subject of interest depends on the perspective taken. When considered from the viewpoint of crystal growth, the important points are likely to include the growth mechanisms of biominerals themselves, the actual nature of the organic–inorganic interactions that are the essence of the biomineralization process, and the products in the environment with a complex chemical composition such as organisms.

As an example of biomineralization, these sections will describe and explain calcium phosphate salts—the most important biominerals in humans—with particular focus on apatite. In this chapter, the mechanisms of apatite crystal growth will be introduced. Apatite will be considered as purely an inorganic material, and developments in the understanding of crystal growth mechanisms in simple solution systems will be reviewed. In Chap. 4, examples of research focusing on the relationship between proteins and apatite will be described from the perspective of organic–inorganic interactions. The process used by proteins to control the formation of minerals will be explained, and the control of biomineralization using protein engineering will be described. In Chap. 5, the current state of research on the tooth enamel, as a representative example of biomineralization within an organism, will be reviewed. The relationship between the concept of apatite formation mechanisms with clusters as growth units (described in this chapter) and the roles of amorphous calcium phosphate (ACP) and octacalcium phosphate in the formation of enamel, which is attracting much attention, will be described.

3.2 Types and Solubilities of Calcium Phosphates

Phosphate ions, which comprise a phosphorous ion with a charge of +5 and an oxygen ion with a charge of −2, are grouped on the basis of their chemical composition into orthophosphates, metaphosphates, pyrophosphates, and polyphosphates. The phosphate ions described in the present chapter belong to the orthophosphate group. Orthophosphate ions, which have the chemical composition PO_4^{3-}, are a component of all the calcium phosphates that are described.

One of the characteristics of biomineralization is the variety of chemical compositions and crystal structures of the substances produced. Calcium phosphate is considered to be a representative biomineralization compound. Primary substances that are a calcium phosphate with a known chemical composition and structure and which can be precipitated as crystals between room temperature (about 25°C) and human body temperature (about 37°C) are dicalcium phosphate dyhydrite (DCPD: $CaHPO_4{\cdot}2H_2O$), dicalcium phosphate anhydrous (DCPA: $CaHPO_4$), β-tricalcium phosphate (β-TCP: β-$Ca_3(PO_4)_2$), octacalcium phosphate (OCP: $Ca_8(HPO_4)_2(PO_4)_4{\cdot}5H_2O$), and hydroxyapatite (HAP: $Ca_{10}(PO_4)_6(OH)_2$) [3,4]. In addition, while it does not itself form a crystal structure, one of the main precipitates is ACP. The following two paragraphs will briefly explain HAP and ACP, which are covered primarily in the present chapter, as well as the solubility of calcium phosphate salts. A recent detailed review of ACP can be found elsewhere [5].

In some instances, the crystal structure of HAP takes on the monoclinic system ($P2_1/b$) [6], while in others it takes on the hexagonal system ($P6_3/m$) [7]. The monoclinic structure is considered to be stable; however, the HAP in organisms has a hexagonal structure. The unit cell constants of HAP with hexagonal system are $a = b = 0.94302$, $c = 0.68911$ nm, and $\gamma = 120°$, while the monoclinic HAP has a symmetry in which the length of the *b*-axis is twice that of the *a*-axis, with $a = 0.98421$, $b = 2a$, $c = 0.68814$ nm, and $\gamma = 120°$ [8]. Structural analysis using synchrotron radiation has shown that the *b*-axis is slightly longer than $2a$ [9]. Although the stoichiometric composition of HAP is $Ca_{10}(PO_4)_6(OH)_2$, hexagonal HAP with this composition is not found in the human body. HAP substitutes various ions within its core structure, so its chemical composition varies widely (for example, [3]). The CO_3^{2-} can substitute for PO_4^{3-} and a proportion of the OH^- groups, and F^- and Cl^- can substitute for a proportion of the OH^- groups. The substitution of CO_3^{2-} in HAP, which constitutes bone and teeth, is particularly common. It is generally thought that HAP in bone and teeth contains 4–5 wt.% and 3–5 wt.% carbon dioxide, respectively [10,11]; this HAP is sometimes referred to as carbonate-containing HAP. The columns created by Ca^{2+} in a crystal structure form a channel parallel to the *c*-axis, and the separation of ions from the channel and substitution of different ionic species readily occur. Instances are known in which gaps created by the separation of Ca^{2+} are replaced by cations such as Na^+, Sr^{2+}, and Mg^{2+}. In these cases, a large stoichiometric discrepancy occurs, resulting in Ca-deficient HAP. The HAP in bone is a classic Ca-deficient HAP in which the Ca/P ratio does not attain the stoichiometric 1.67 value. When the calcium content

is the lowest, the Ca/P ratio may on occasion fall to around 1.50. In this chapter, the various species of HAP, including those with modified chemical compositions, are generically referred to as HAP unless otherwise noted.

Although ACP and amorphous HAP are clearly distinguishable, their structures have many similar features [12]. ACP readily forms under high-pH and high-supersaturation conditions, and its component ratios of calcium and phosphate vary over a range wider than that of HAP, depending on the environmental conditions and post-precipitation treatment. Early studies showed the Ca/P ratio to be 1.50 (with $Ca_3(PO_4)_2xH_2O$ as a representative formula) [12–14]. Subsequent studies showed that the Ca/P ratio can be changed from 1.18 to 1.50 by varying the pH range from 6.6 to 10.6 and that sufficient rinsing after precipitation stabilizes the ratio at 1.50 [15]. Instances have been reported in which the Ca/P ratio was increased to 2.50 by using an even higher pH (∼11.7) [16]. There are also reports describing ACP species with the same chemical composition that can exist in two phases (ACP1 and ACP2) differing in solubility [17,18]. ACP1 is regarded as closer to a crystalline state than ACP2, and while both phases are amorphous, this may contrast with differences in the crystals' polymorphic structure. Within its structure, ACP contains 10–20 wt. % water molecules, which separate from the structure due to an increase in temperature. ACP has an essentially "loose" structure; however, the arrangement of constituent ions is not completely random. Nano-sized orderly structures (clusters) are linked with one another through weak bonds. The Posner cluster, $Ca_9(PO_4)_6$, is a representative example of this model [19]. Water molecules fill the gaps between these clusters. The result of ^{31}P nuclear magnetic resonance (NMR) measurements of ACP indicated that the strength of the ACP sidebands is a characteristic structural distortion of unprotonated phosphate (not of a mixture of it and protonated phosphates) [20]. X-ray diffraction analysis of ACP revealed that it has amorphous properties (broad diffraction patterns). However, extended X-ray adsorption fine structure (EXAFS) analysis showed that its structure is characterized by a short-range order similar to that of HAP [21–23]. These results suggest that ACP and HAP essentially have a common minimal structural unit. Observations of the phase transformation process from ACP to HAP using time-resolved static light scattering have shown that ACP can structurally transform directly into HAP without dissolution [24]. Assuming no similarities between the minimal structural units of ACP and HAP, the energy needed for directly transforming one structure into the other should be extraordinarily large. It is natural, therefore, to consider that ACP and HAP share a common structural unit.

Figure 3.1a shows the solubility curve (37°C) of each calcium phosphate salt in the $Ca(OH)_2$-H_3PO_4-H_2O system. The solubility product of each calcium phosphate was presented in a review article [4]. Since the standard pH of human body fluid is 7.2–7.4, HAP has the lowest solubility and the most stable phase under physiological conditions. This means that metastable calcium phosphates other than HAP that precipitate in an aqueous solution with a near-neutral pH are likely to transform into HAP in a time-dependent manner unless the solution pH changes. The solubility of HAP fluctuates with the ionic species in its structure. In particular, the substitution of CO_3^{2-} increases the HAP solubility although a consensus has not

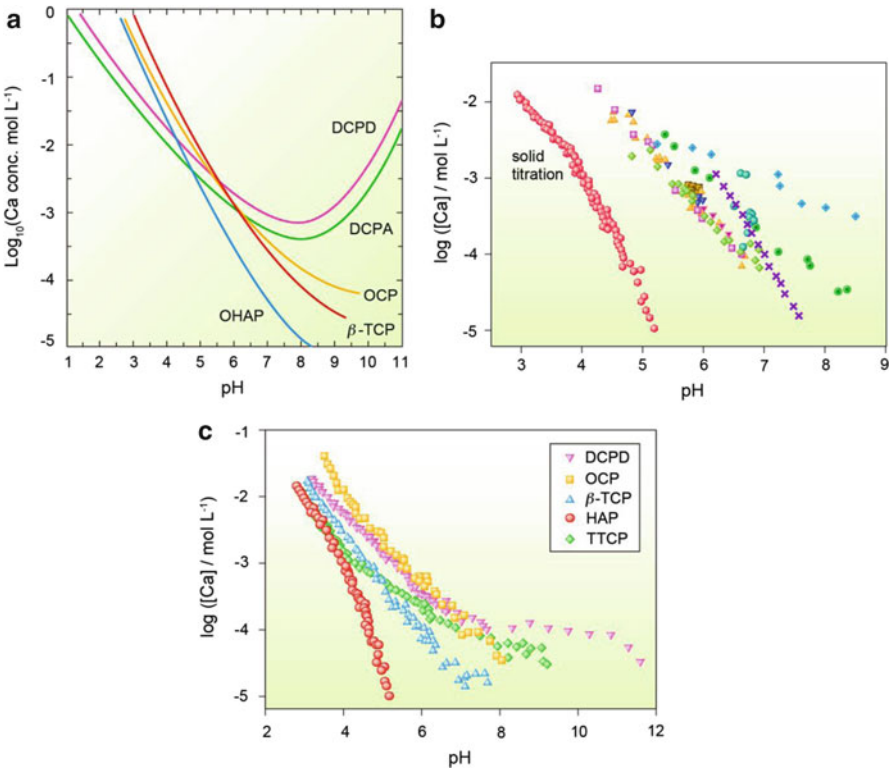

Fig. 3.1 (**a**) Solubility isotherms of calcium phosphate minerals in the system $Ca(OH)_2$-H_3PO_4-H_2O at 37°C (reproduced with permission from [3]) (copyright 1994, Elsevier). (**b**) Solubility of HAP by solid titration method compared with conventional excess-solid method. References of data in conventional method can be seen in original article [25]. (**c**) Solid titration isotherms for calcium phosphates salts (reproduced with permission from ref. [25]) (copyright 2009, American Chemical Society)

been reached regarding changes in the solubility product. One reason for this may be that solubility measurements are not performed under standardized conditions since the solubility of the solid phase is affected by the strain introduced into the structure by ionic substitution and the CO_3^{2-} content in the environmental field (solution phase). The concentrations of calcium and phosphate ions contained in human body fluid are naturally in a supersaturated state with respect to HAP. Nonetheless, indiscriminate precipitation of HAP does not occur in the human body. One reason for this is that high concentrations of CO_2 dissolve into the body fluids and become a carbonate buffer, thereby raising the solubility of HAP.

The solubility of fluorapatite ($Ca_{10}(PO_4)_6F_2$), in which the OH^- of HAP is completely replaced by F^-, is lower than that of HAP. Within the HAP structure, there is a column of OH^- groups parallel to the *c*-axis. However, since the position of each OH^- is slightly staggered relative to the others, there is strain in the

structure. Replacing the OH^- with F^- is thought to release the strain so that the subsequent stabilization of the crystal structure reduces the solubility of the solid phase. Another likely cause of structural stabilization is that the replacement of the polar group OH^- by the nonpolar group F^- affects the local charge balance. The solubility of ACP is not shown in Fig. 3.1a. However, as mentioned above, the phase transformation from ACP to HAP has been observed. Therefore, at least near a neutral pH, ACP has a higher solubility than HAP. Although the solubility of all calcium phosphates rapidly increases with decreasing pH, the rate of increase differs greatly depending on the type of salt. Compared to HAP, OCP, and TCP, the pH-dependence of solubility for DCPA and DCPD is relatively small. For this reason, the solubility of HAP exceeds that of DCPA at $pH \leq 4.5$, and DCPA becomes the most stable phase. The form of the solubility curves for each calcium phosphate in Fig. 3.1a, as well as the pH at which DCPA becomes the most stable phase, vary to some extent when there are ionic species other than calcium and phosphoric acid in the solution. However, it is thought that HAP is the most stable at a near-neutral pH and that DCPA or DCPD is the most stable at a low pH. However, questions have been raised that challenge this idea [25].

The conventional method for measuring solubility is to inject an excess amount of the solid phase of the target calcium phosphate salt into solution, and after sufficient stirring, measure the ionic concentrations and calculate the equilibrium concentrations. Pan and Darvell pointed out a shortcoming in this method—solid calcium phosphate in solution undergoes incongruent dissolution, which in turn triggers a phase transformation that results in large errors in the calculated equilibrium concentrations. They measured the solubility of HAP using a unique solid-titration method and found that it was considerably lower than conventionally reported values (Fig. 3.1b). They also measured the solubility of other calcium phosphate salts using the solid-titration method and compared the results. They concluded that HAP represented the most stable phase for $pH \leq 4.2$ and not DCPD, as was generally believed (Fig. 3.1c). In explaining why DCPD was believed to be the most stable phase, they mentioned the stability of DCPD and the nucleation frequency and concluded that DCPD is far more likely to nucleate than HAP at low pH. In titration experiments using solid DCPD, the only phase observed at a pH of 3.60 or 4.50 was DCPD; however, when a minute amount of HAP was added to this equilibrium state, the DCPD disappeared and highly crystalline HAP formed at a pH of 3.30, 3.60, and 4.47.

3.3 Crystal Growth Mechanisms in an Aqueous Solution System: Historical Review

Given that the growth of HAP occurs in an aqueous solution environment, the history of research on the mechanisms of crystal growth in aqueous solutions will be reviewed before the growth mechanisms of HAP are discussed.

Theoretical treatment of crystal growth mechanisms in dilute environments at the atomic scale was given in the form of the Burton-Cabrera-Frank (BCF) model in 1951 [26]. The growth rate of crystal face R in which the growth unit goes through the surface diffusion before incorporating in the growth step is expressed as a function of the driving force of growth (supersaturation, σ):

$$R = C\frac{\sigma^2}{\sigma_1}\tanh\frac{\sigma_1}{\sigma}, \tag{3.1}$$

where C and σ_1 are constants determined by the growth conditions. A characteristic of this formula is that it is possible to approximate $R \sim \sigma^2$ at low supersaturation and $R \sim \sigma$ at high supersaturation, which was frequently used for discussing the growth mechanisms.

The research conducted on $NaClO_3$ is an example in which detailed analysis of growth mechanism using the BCF model was performed on crystal grown from aqueous solution [27]. The relationship between the face growth rates and supersaturation was investigated with precise temperature control ($<$1/100°C of fluctuation) at low supersaturation ($\leq$1%), and the data were analyzed using (3.1). It was concluded that spiral growth via surface diffusion occurred. This was the first time that spiral growth via surface diffusion in aqueous solution was quantitatively shown. Denk and Botsaris performed the measurements of potassium alum (K-Alum) under high-supersaturation conditions and concluded that the data could be interpreted by considering the combination of spiral growth and two-dimensional nucleation [28]. Subsequently, growth mechanisms approximated using face growth rate data and growth theory equations became widely used, and the growth mechanisms of numerous aqueous inorganic and organic crystals were elucidated (for example, [29]).

These studies focused on two important topics. The first was the growth mode in an aqueous solution system (spiral or two-dimensional nucleation growth), and the second was the investigation of the rate-limiting process of growth, in which emphasis was placed on the assertion that the importance of surface diffusion that had originally been applied to crystals grown in the gas system also holds for aqueous solution systems. Chernov proposed a model in which the growth unit is directly incorporated from the environmental phase into growth steps [30]. This model showed that the surface diffusion of the growth unit is not important in a solution system, particularly an aqueous solution system.

Following the tests of the spiral growth model by measuring the crystal growth rate, attempts to obtain direct evidence for spiral growth from surface observations were actively conducted from the 1970s onward, even for aqueous solution crystals. Examples include the observations of NaCl and KCl [31], K-Alum [32], potassium hydrogen phthalate (KAP) [33], and $NiSO_4{\cdot}6H_2O$ [34].

In a study of crystal growth mechanisms, van Erk et al. vividly showed the importance of surface observations although not in regard to crystals grown in aqueous solutions. They measured the growth rate of garnet crystals grown by liquid phase epitaxy and concluded that spiral growth through surface diffusion had

occurred [35]. Using surface observations conducted, and after performing detailed measurement of the slope of the growth hillock formed by spiral steps, together with face growth rate data, they indirectly calculated the step velocity. It disagreed with the linear dependence on supersaturation predicted by the BCF model. They explained this contradiction by arguing that the step velocity increased non-linearly due to two-dimensional nucleation occurring at the terraces between steps.

With spiral growth, the original BCF model described the face growth rate on the basis of the behavior of the growth steps at a single growth center on the crystal surface. However, there are multiple growth centers on a crystal surface, and the ones that control the growth rate undergo changes as a result of alterations in their relative activity that are associated with supersaturation. Efforts to resolve this problem and conduct measurements near the theoretically assumed growth conditions were carried out vigorously from the late 1980s to the early 1990s using in situ optical interferometry. This method was applied to ADP and KDP crystals [36,37] and subsequently led to studies on $Ba(NO_3)_2$ [38] and on K-Alum [39].

The use of interferometry for studying various soluble inorganic crystals has clarified many phenomena. For example, observations of KDP and K-Alum confirmed the nonlinear dependence of the step velocity on supersaturation, which was the similar with that reported by van Erk et al. for the garnet crystal. However, it was shown that this nonlinear dependence is not due to two-dimensional nucleation at the terraces but rather to a decrease in velocity caused by adsorption of impurities on the step front at low supersaturation and a rapid increase in velocity caused by less adsorption of impurities with an increase in supersaturation. It was also showed that step behavior, which differs from that predicted by the BCF model, greatly affects the dependence of the face growth rate on the supersaturation. For example, even when spiral growth occurs on a crystal surface, the relationship between the growth rate and supersaturation could suggest growth by two-dimensional nucleation. These findings revealed the danger inherent in the simplistic fitting of growth rate data to a model.

The rate-limiting process of growth has also been investigated using interferometry. In early research on KDP and ADP, surface diffusion was thought to be unimportant, as it was for research on $Ba(NO_3)_2$ and K-Alum. For crystal growth in an aqueous solution system, the consensus was that surface diffusion did not play a major role, and even if it were present, the diffusion length would be minimal. Vekilov et al. investigated the previously unobserved faces of ADP crystals and, after performing detailed comparison of data using growth models, concluded that growth progressed via surface diffusion and that a surface kinetic process including surface diffusion was rate-limiting [40]. It is currently understood that, even in the same crystal, the optimal growth model depends on the relative importance of each elemental process for each crystal face.

Observations using interferometry of two-dimensional nucleation of ADP have been performed [41]. The observations and subsequent quantitative analysis revealed that impurities reduce the activation energy needed for nucleation at low supersaturation and are active sites for heterogeneous nucleation. Homogeneous nucleation takes place only at high supersaturation. This has been verified by the

finding that the edge free energy required for nucleation is discontinuously smaller at low supersaturation. As will be discussed later, even for HAP growth, there are cases in which discrepancies between edge-free-energy data sets can be explained by considering a heterogeneous nucleation model.

3.4 HAP Crystal Growth Mechanisms

3.4.1 Driving Force for Growth

In a two-component simple aqueous solution system of soluble salts, supersaturation—the thermodynamic driving force for growth—is determined by the solubility curve of the solid phase. This method is sufficiently useful as an approximation; there are no significant problems even when interpreting data on growth rate versus supersaturation and in calculating physical constants related to growth. However, in the case of insoluble calcium phosphate salts, including HAP, there are three problems in particular: the possibility of multistep dissociation equilibrium of the phosphate group in solution, the possibility of ion pair formation between calcium and phosphate ions, and the possibility that the solutions in which the crystals are grown contains cations and anions other than calcium and phosphate. For these reasons, the driving force is normally defined using the ion product I_P—defined as the ionic strength I calculated from the concentration and the total charge of each ion in the solution—and the solubility product of the solid phase K_{sp} (solely a function of temperature).

Let a_i and c_i be the activity and concentration, respectively, of the ith ion contained in the solution.

$$a_i = f_{\pm} c_i, \tag{3.2}$$

where $f_{\pm}$ is the mean activity coefficient, which, from the Debye–Hückel approximation, is expressed by the following equations using ionic strength I:

$$\log f_{\pm} = \frac{-A z_i{}^2 \sqrt{I}}{1 + B r_i \sqrt{I}} \tag{3.3}$$

$$I = 0.5 \sum c_i z_i{}^2. \tag{3.4}$$

The z_i is the charge of the ith ion, r_i is the effective radius of each ion, and A and B are theoretical coefficients determined by the specific permittivity of solvent ε_r and absolute temperature T, commonly using

$$A = \frac{1.8246 \times 10^6}{(\varepsilon_r T)^{3/2}} \tag{3.5}$$

$$B = \frac{50.29 \times 10^8}{(\varepsilon_r T)^{1/2}}. \tag{3.6}$$

The driving force for growth, i.e., the chemical potential difference between the solid phase and liquid phase $\Delta\mu$, is

$$\frac{\Delta\mu}{kT} = \ln\frac{a_i}{a_{\mathrm{ei}}} = \ln\frac{I_{\mathrm{P}}}{K_{\mathrm{sp}}}, \tag{3.7}$$

where a_{ei} is the ionic activity at equilibrium. Between $\Delta\mu$ and supersaturation σ, the relationship $\Delta\mu/kT = \ln(1+\sigma)$ holds. Therefore,

$$\sigma = \frac{I_{\mathrm{P}}}{K_{\mathrm{sp}}} - 1. \tag{3.8}$$

However, to enable comparisons under a consistent supersaturation, even between solid phases that have naturally different stoichiometric ratios, an equation standardized by N, the sum of the valences for each ion comprising the solid phase, is used [42]:

$$\sigma = \left(\frac{I_{\mathrm{P}}}{K_{\mathrm{sp}}}\right)^{1/N} - 1. \tag{3.9}$$

For $Ca_{10}(PO_4)_6(OH)_2$, which is the stoichiometric composition of HAP, N is 18. In the form of (3.9), a constant supersaturation is applied even if the descriptive formula for the chemical composition of the target solid phase differs. For HAP, K_{sp} is occasionally defined on the basis of its half-unit cell $Ca_5(PO_4)_3OH$. However, this value turns out to be approximately the square root of the K_{sp} value for $Ca_{10}(PO_4)_6(OH)_2$, the corresponding full-unit cell. Therefore, supersaturation calculated using (3.9) is the same value independent of the definition of the unit cell.

Equation (3.9) includes an ionic product term. For this reason, even if the calcium or phosphate concentrations are constant, the supersaturation greatly varies depending on the background salt concentration, and this affects the conditions for growth and phase transformation. For example, the structural reconstruction-type phase transformation of ACP to HAP, which is described elsewhere [24], occurs when only calcium and phosphate ions (excluding hydrogen and hydroxide ions) are contained in the solution. When the supersaturation is raised by adding 10 mM of KCl to this solution, the phase transformation switches to a heterogeneous-type nucleation in which HAP forms around ACP as the nucleus (or template).

3.4.2 Biological HAP Formation Model

The HAP growth mechanisms, including nucleation, differ considerably depending on whether they are viewed from a biological or a physicochemical perspective.

With HAP, which forms bone tissue in the human body, a number of formation theories were proposed many years ago. For example, Robinson theorized that HAP nucleation occurs as a result of a localized increase in the phosphate ion concentration due to hydrolysis of the organic phosphate ester substrate by the enzyme alkaline phosphatase [43]. Newman and Newman theorized that the molecular chains on the collagen surfaces behave as effective sites of HAP nucleation [1]. Brighton and Hunt theorized which that once the fine HAP nuclei formed from the calcium and phosphate ions in a matrix vesicle grow to a certain size, they break through and arrange themselves on the collagen fibers [44]. Newman and Newman's epitaxial theory leads to the contemporary notion of biomineralization. With the matrix vesicle theory, the amount of HAP that can be formed in the bone is much greater than the amount that can be formed in the matrix vesicles. In other words, in addition to the HAP that is formed within the matrix vesicles, there is a need for HAP formation to occur directly from the body fluids onto collagen fibers.

Each of these theories focuses on HAP nucleation. The growth and dissolution behavior of HAP in formed bone tissue has led to a biological consensus on the concept of remodeling [45]: the renewal over time of bone tissue occurs through the growth and dissolution of HAP. It involves competition between osteoclasts, which dissolve bone, and osteoblasts, which create bone.

3.4.3 Constant Composition Method

Consideration of HAP as a pure inorganic compound in an attempt to understand its mechanisms of growth and dissolution physicochemically would not reveal the essence of these mechanisms due to the complex systems—including cells—that are involved. Even considering that various types of cells play a primary role in bone tissue formation within the organism, the phenomenon that consequently occurs at the interface between HAP and the environmental phase (body fluid) is ultimately crystal growth of inorganic salts. Therefore, illustration of the HAP formation mechanisms within the organism requires first conducting studies in simple cell-free aqueous solution systems. Researchers investigating the HAP growth mechanisms have mainly been doing this since the 1970s.

Early studies were done using Bennema's procedure: estimate the dependence of the HAP growth rate on supersaturation and compare the data with growth theories such as the BCF model to elucidate the growth mechanisms. In a growth experiment using highly crystalline synthetic HAP polycrystals as seeds [46], the growth rate and chemical composition of HAP were obtained by measuring the solution pH as well as the calcium and phosphate ion concentrations accompanying growth. The growth rate was estimated from the change in solution composition, which was derived from HAP surface area. The growth rate data had a relationship of $R \sim \sigma^2$, and it was concluded that spiral growth, which could be expected in solutions with low supersaturation, took place. Since the measurements were in a closed system, the change in the chemical composition of the solution associated with HAP growth would lead to a change in supersaturation. In addition, it could not be conclusively

stated that the chemical composition of the formed HAP was constant throughout, and it was necessary to carefully analyze errors in the rate data since the amount of growth was small. Nonetheless, this study showed the possibility of investigating growth mechanisms even for insoluble salts using a method similar to that used for soluble salts.

Development of the constant composition (CC) method [47] ultimately resolved the technical problems of the experiment discussed above. In this method, real-time measurements of the pH and chemical composition of the growth solution are taken with a glass electrode. The composition of the mixture is maintained by automatically supplementing the solution with drops containing calcium or phosphate ions. In order to maintain the lowered pH at its original value during growth, a solution containing hydroxide ions is added. The growth rate is calculated from the surface area of the seed crystal and the drip rate. The CC method has three particular advantages: (1) more accurate growth rate data can be obtained since it is possible to sufficiently grow the crystals with respect to the seeds, (2) the amount of growth can be measured even in solutions with a relatively low supersaturation since the measurement of the pH and chemical composition with the glass electrode is highly sensitive, and (3) the metastable phase that forms during HAP growth can be estimated by tracking changes in the solution composition. The CC method has been used to not only measure the growth rate but also the dissolution rate and nucleation induction time.

In the CC method, the relationship between the growth rate and supersaturation is approximated by the following simple equation, and the growth mechanisms are discussed in terms of n:

$$R = C\sigma^n \quad (C \text{ is the reaction constant} : n \text{ is the reaction order.}) \tag{3.10}$$

Koutsoukos et al. grew HAP to an amount several times that of the seed crystal using the CC method and obtained the relationship $R \sim \sigma$ [48]. From this result they concluded that spiral growth is involved in HAP growth. A similar conclusion was reached in other studies [49]. In contrast, Arends et al. obtained the relationship $R \sim \sigma^{2.9-3.2}$, and postulated that growth involved multiple two-dimensional nucleation [50]. Christoffersen and Christoffersen used various growth theory equations to analyze HAP growth rate data obtained with the CC method. They concluded that while growth rate equation that takes multiple two-dimensional nucleation into account is optimal, spiral growth occurring simultaneously with two-dimensional nucleation would be possible [51,52]. Although debates on growth mechanisms are common, with the CC method, there are also debates ranging from the reaction orders to growth path (via surface diffusion or not).

3.4.4 Synthesis of HAP Single Crystal

Although it is desirable to conduct growth rate measurements for each crystal face using a single crystal when investigating crystal growth mechanisms in relation to

theory, this type of research for HAP is uncommon. This is not due to technical hurdles that prevent the growth of a single crystal to a size suitable for handling. Indeed, in the 1950s and 1960s, there were numerous investigations of the synthesis of HAP single crystals using the hydrothermal method. With early hydrothermal synthesis methods, the starting material was placed in a sealed container, and synthesis was performed across several days at a temperature of 300–700°C under high pressure (8.6–200 MPa). The type of starting material and synthesis steps varied widely. The approaches included recrystallizing HAP polycrystal in NaOH solution [53,54], hydrolysizing calcium phosphate salts [55], mixing CaO and β-$Ca_2P_2O_7$ stoichiometrically and reacting them in an aqueous solution [56], and using reactions in a $Ca(NO_3)_2$-KH_2PO_4-NaOH-H_2O system [57]. In later studies, simple methods of recrystallizing HAP polycrystal in pure water [58], as well as methods using reactions in an H_3PO_4-$Ca(NO_3)_2$-H_2O system [59], were used. One successful example of promoting the growth of HAP single crystals by hydrothermal synthesis resulted in synthesis of a giant crystal ($7 \times 3 \times 3$ mm) [60].

Synthesis of HAP using a chemical composition containing CO_3^{2-}, similar to that found in organisms, has also been carried out. Studies using recrystallization of HAP polycrystal have produced HAP single crystals about 0.5 mm in length after 3 months under conditions of 300°C and a CO_2 partial pressure of 16.7 MPa [61]. This single crystal had a hexagonal columnar morphology consisting of a $(10\bar{1}0)$ prism face (*a*-face), a $(10\bar{1}1)$ face, and a (0001) basal face (*c*-face). When the CO_3^{2-} group was substituted for the OH^- group and the CO_3^{2-} content was increased slightly to above 0.1 wt.%, the *c*-face incidence increased. An experiment using hydrolysis of $CaHPO_4$ in the presence of CO_2 gas resulted in a giant HAP single crystal (length of 12 mm (*c*-axis direction) and width of 0.2 mm) [62]. In this experiment, dry ice was added to the aqueous solution as a CO_3^{2-} source, and a top-down temperature gradient was applied using long cylindrical synthesis container to generate convections. HAP single crystals nucleated on the sintered bodies of synthetic HAP suspended in the solution, taking the morphology of a hexagonal column with a large aspect ratio consisting of *a*- and *c*-faces. As in the previous case, the CO_3^{2-} group was substituted for the OH group, and its content was 0.09–0.65 wt.%. The Ca/P ratio of the grown HAP crystals was 1.60–1.67.

Large crystals are easier to obtain with the flux method than with the hydrothermal synthesis method. In one experiment, for example, cooling a flux in which TCP was dissolved in a $Ca(OH)_2$ melt resulted in the growth of a HAP crystal 4–8 mm long in the *c*-axis direction and 0.5 mm wide [63]. In this experiment, 10 wt.% TCP and 90 wt.% $Ca(OH)_2$ were used. The flux was maintained at 925°C for 24 h, and then the crystal was grown by gradually cooling the flux over several days to 775°C, followed by rapid cooling to room temperature. The obtained crystal was a monoclinic HAP. Observations of cross-sections cut perpendicular to the *c*-axis revealed a morphology approximating that of a twin crystal. Synthesis in which deuterium was substituted for the hydrogen in $Ca(OH)_2$ was also performed and the resulting HAP crystals contained deuterium rather than hydrogen. A HAP crystal 8 mm long and 0.5 mm wide was also obtained using a similar method in which 25 wt.% water was added to the flux (hydrothermal flux) and the temperature was increased from 750 to 880°C to suppress unnecessary nucleation [64].

3.4.5 *Real-Time Phase-Shift Interferometry for Observation of Biomineral Growth*

Although it is possible in principle to obtain large HAP crystals that can be used for observation, the rate of growth for each face is not performed using a single HAP crystal due to the slowness of the growth. The growth rate of a soluble inorganic crystal depends on the type of crystal and crystal face. It typically ranges from 10 to 100 nm/s even when the supersaturation is a few percent. The growth rate of a HAP crystal is thought to be 2–4 orders of magnitude lower than this value. The simplest way to measure the growth rate using a single crystal is to measure the amount of normal growth of the target face. However, an excessively low growth rate markedly decreases the time resolution for the growth amount, and precise data to compare with theory cannot be obtained. Although optical interferometry can measure growth rates far more rapidly than simply measuring the normal growth of the crystal face, the technique is extremely sensitive to temperature changes in the vicinity of the equipment and to external disturbances such as vibration. It is therefore not well suited to measurements of long duration. For this reason, optical interferometry has not been applied to the measurement of HAP growth rates. However, real-time phase-shift interferometry has helped to resolve the problem of external disturbances [65].

Although real-time phase-shift interferometry is essentially a type of optical interferometry, in contrast to conventional interferometry, which produces only an interference image of the crystal surface, it simultaneously (or nearly simultaneously) obtains multiple interference images that are slightly phase shifted from each other. This method markedly improves the height resolution because it includes calculation of the two-dimensional intensity-distribution profile using multiple interference images. This enables the increments in the height direction to be observed within a short time. Since low-frequency external disturbances are the primary factor that causes artifactual changes in interference fringes, the phase-shift method can greatly reduce the effects of these disturbances. While the height resolution depends on the number of interference images used, phase-shift interferometry can increase the height resolution to more than 100 times that of conventional two-beam interferometry, which is comparable to the resolution achieved using atomic force microscopy (AFM).

The first application of phase-shift interferometry to biominerals was to calcite [66]. With natural calcite crystals as the seed, the dissolution rate in aqueous solution was measured in situ. Maruyama et al. elucidated the growth process of calcite [67]. Their research included detailed investigation of how the chirality of amino acids (asparagines), included as an impurity, affected the step velocity. The calcite growth rate was estimated with good precision by taking measurements over approximately 20 min.

HAP growth rate measurements using the phase-shift method were first reported for the *c*-face of HAP [68]. An example of *c*-face observation using real-time phase-shift interferometry is shown in Fig.3.2. In this research using large HAP single crystals obtained from hydrothermal synthesis as seeds, a pseudo body fluid

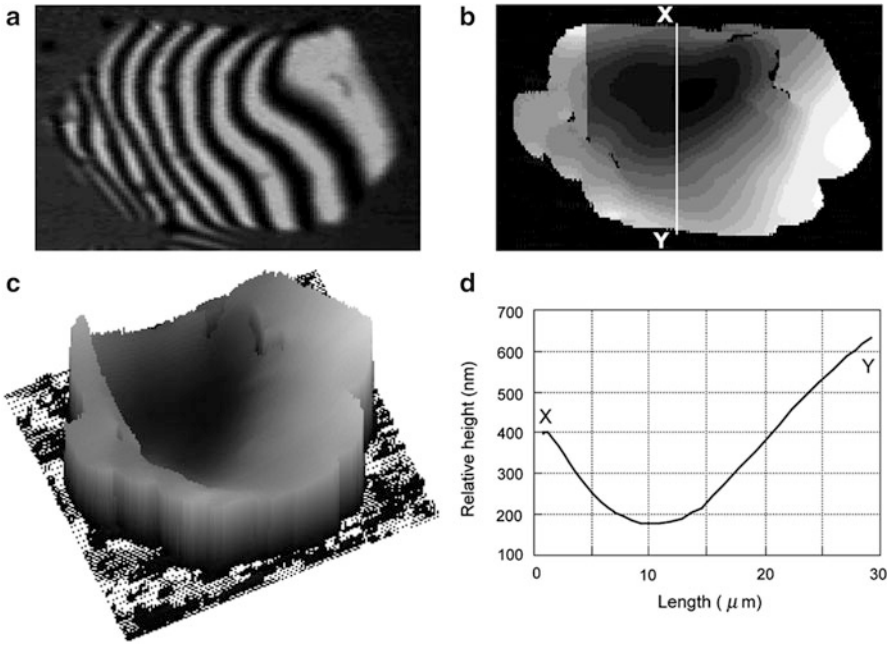

Fig. 3.2 Observation of HAP *c*-face using Moire phase-shift interferometry. (**a**) Original interferogram of *c*-face. (**b**) Two-dimensional phase distribution profile produced using three interferograms with phase-shifted 90° each other. (**c**) Three-dimensional surface image created using (**b**). (**d**) Section profile between X and Y in (**b**) (reproduced with permission from [68]) (copyright 1998, American Chemical Society)

mimicking the components of human body fluid was used as the supersaturated solution in which the HAP was grown. The concentrations of NaCl, calcium ion, and phosphate ion, as well as the pH, of the pseudo body fluid were adjusted to simulate those found in human body fluid. Several unique contrivances were devised for the interferometers used for the growth rate measurements. For example, to completely exclude fluctuations in the interference fringes due to external disturbances, a "common-path" interferometer was constructed using a Nomarski prism in which the test and reference optical paths in the interferometer pass through nearly identical paths. In principle, a common-path type interferometer is completely unaffected by disturbances since any disturbance acts identically on the test and reference optical paths. However, fluctuations in the interference fringes due to movement of the crystal itself cannot be removed. Even if the crystal is immobilized using an adhesive agent with a low expansion rate, the position of the crystal undergoes very slight irregular fluctuations over an extended period of time. Therefore, for the *a*-face, for which the growth rate is more than an order of magnitude lower than that for the *c*-face, growth rate measurements even with phase-shift interferometry have not succeeded.

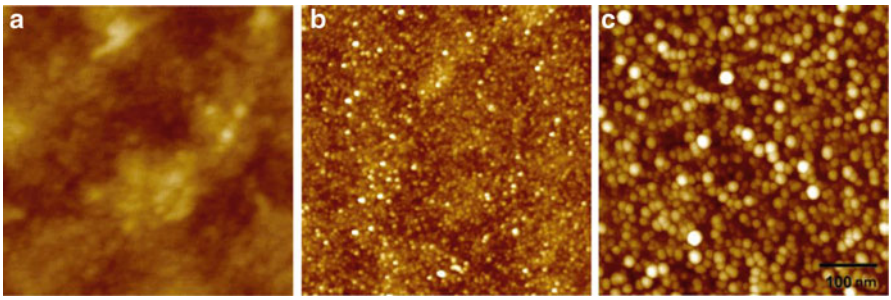

Fig. 3.3 AFM images of HAP *c*-face growing in pseudo-body fluid. (**a**) Original seed surface. (**b**) Surface after 5 min of growth. Many small islands grew. (**c**) Surface after 2 h of growth. Number and size of islands increased. Growth proceeded by multiple two-dimensional nucleation (reproduced with permission from [69]) (copyright 1998, American Chemical Society)

3.4.6 Analysis of Growth Features and Growth Rate Data of HAP c-face

The importance of surface observations in the investigation of growth mechanisms was described above. While surface observation is clearly possible with phase-shift interferometry, the resolution in the within-plane horizontal direction is limited to that at the normal optical microscopic level although that in the height direction is superior. For this reason, detailed surface observations of the HAP *c*-face using AFM were performed in combination with the growth rate measurements using the phase-shift interferometry. While AFM observations are not in situ, they are able to give a clear picture of the growth mode of the *c*-face in pseudo-body fluid.

Results of such observations are shown in Fig. 3.3, [69]. The crystal was grown for 5 min in pseudo body fluid followed by removal and observation with AFM (Fig. 3.3b). Innumerable small islands had formed on the surface. After observation, the crystal was returned to the pseudo body fluid and grown for an additional 2 h. The number and the size of the islands greatly increased, as shown in Fig. 3.3c. The growth of the *c*-face therefore proceeds in a multiple two-dimensional nucleation mode. In this study, the lowest supersaturation in which growth was confirmed by AFM was $\sigma = 0.85$. However, growth was multiple two-dimensional nucleation even in this supersaturation, and no spiral growth was observed. The face growth rate via multiple two-dimensional nucleation is expressed by the formula below, with h as the height of the formed two-dimensional nucleus, v as the step velocity of the two-dimensional nucleus, and J as the frequency of two-dimensional nucleation [70]:

$$R = h(\pi v^2 J/3)^{1/3} \tag{3.11}$$

$$v = \varpi C_e \beta \sigma \tag{3.12}$$

$$J = B\exp(-\pi\alpha^2\varpi h/k_B T\Delta\mu) = B\exp\{-\pi\alpha^2\varpi h/(k_B T)^2\ln(1+\sigma)\}. \tag{3.13}$$

The β in (3.12) is a physical quantity known as the step kinetic coefficient. It corresponds to the rate coefficient when a growth unit is incorporated into a step and is expressed as $\beta \sim \exp(-E/k_{\mathrm{B}}T)$ using activation energy E for growth unit incorporation. The C_{e} is the equilibrium concentration. The α in (3.13) is the surface energy and is related to edge free energy γ on the step front: $\gamma = \alpha(h\varpi)^{1/2}$. The ϖ is the molecular volume of the crystal. Factor B is given by

$$B = Z(2\pi NC\varpi\gamma/\Delta\mu)v\exp(-E/k_{\mathrm{B}}T). \tag{3.14}$$

where Z is the Zeldovich factor, and N and C are constants. Since $Z = (\Delta\mu)^{3/2}/4\pi\gamma(k_{\mathrm{B}}T)^{1/2}$,

$$B = 0.5N\varpi Cv\exp(-E/k_{\mathrm{B}}T)(1+\sigma)\{\ln(1+\sigma)\}^{1/2} \exp\{-\pi\gamma^2/(k_{\mathrm{B}}T)^2\ln(1+\sigma)\}, \tag{3.15}$$

and ultimately the growth rate is given as

$$R = K\sigma^{2/3}(1+\sigma)^{1/3}\{\ln(1+\sigma)\}^{1/6}\exp[-\pi\gamma^2/\{3(k_{\mathrm{B}}T)^2\ln(1+\sigma)\}]. \tag{3.16}$$

Here, K is a constant that includes E. Taking the logarithms on both sides of (3.16) gives

$$\ln[R/[\sigma^{2/3}(1+\sigma)^{1/3}\{\ln(1+\sigma)\}^{1/6}]] = \ln K - \{\pi\gamma^2/3(k_{\mathrm{B}}T)^2\} \times 1/\ln(1+\sigma). \tag{3.17}$$

Calculating the left side from the measured growth rate and plotting it against $1/\ln(1+\sigma)$ gives the most important parameter for two-dimensional nucleation, γ. The value of γ for the c-face of the HAP crystal was determined to be $3.3\,k_{\mathrm{B}}T$. When surface energy α, calculated from growth rate measurements based on the CC method, is converted to γ, its value is estimated as $\gamma = 1.1 - 2.0\,k_{\mathrm{B}}T$, which is considerably smaller than $3.3\,k_{\mathrm{B}}T$. In the CC method, the growth crystal face is not specified; hence, there are problems with direct comparisons between the two values. However, assuming that the results of the CC method are representative of the γ value of the c-face makes it possible to explain the differences between the two in terms of the nucleation mode.

The growth rate has been measured using the phase-shift method for supersaturation ranging from 9.8 to 22.0. Although measurements have been performed below this range, the results were deemed unusable because of the large distribution of the data. In contrast, the supersaturation range used for measurements with the CC method was set to 0.4–7.0, which is considerably lower than for the phase-shift method. As seen in the two-dimensional nucleation of soluble inorganic crystals, heterogeneous nucleation with impurities as active sites is more likely to occur at low supersaturation, and the apparent γ markedly decreases. With HAP as well, for which heterogeneous nucleation occurs at low supersaturation and homogeneous

nucleation occurs at high supersaturation, it is possible to explain the above results. In fact, for measurements based on the phase-shift method, the growth rate data in the low supersaturation range (while highly variable) does not lie on the expected curve extrapolated from that in the high supersaturation range.

The effects of adding zinc or magnesium ions to the pseudo-body fluid have also been investigated for growth rate measurements of the *c*-face [71, 72]. Although both elements are essential for organisms, they are thought to be impurities for HAP growth [73–75]. AFM observations of *c*-face growth in a system containing 0.03–1.5 mM of magnesium ions or 0.3–7.5 μM of zinc ions added to pseudo-body fluid with $\sigma = 22.0$ revealed that they strongly inhibit the growth of the two-dimensional nucleus. The effect of zinc ions in particular is more pronounced than that of magnesium ions. The effects of magnesium and zinc ions on γ from data on growth rate measurements are carried out at various levels of supersaturation with their concentrations fixed at 0.06 mM and 0.75 μM, respectively. Liu et al. has formalized the growth rate for heterogeneous nucleation mode when impurities are present [76]:

$$R = C_2\beta\sigma^{2/3}(1+\sigma)^{1/3}\{\ln(1+\sigma)\}^{1/6}\exp\left[-\pi{\gamma_0}^2 f/\left\{3(k_\mathrm{B}T)^2\ln(1+\sigma)\right\}\right]\delta^{1/3} \tag{3.18}$$

$$\ln[R/[\sigma^{2/3}(1+\sigma)^{1/3}\{\ln(1+\sigma)\}^{1/6}]] = \ln C_2 + \ln\beta - \{\pi{\gamma_0}^2 f/3(k_\mathrm{B}T)^2\} \times 1/\ln(1+\sigma) + \ln\delta^{1/3}. \tag{3.19}$$

In (3.18), C_2 is a constant, and γ_0 is the edge free energy of a two-dimensional nucleus in a system in which impurities are absent. In (3.19), f and δ are physical quantities unique to heterogeneous nucleation: the former is the ratio of the radii of the critical two-dimensional nucleus to that of the impurity particles, and the latter is the contact angle between the two-dimensional nucleus and the impurity particles. Both f and δ have a range of $0 < f, \delta \leqslant 1$, and when $f = \delta = 1$, (3.18) coincides with (3.16), which indicates homogeneous nucleation. The function $\gamma_i = \gamma_0 \times f^{1/2}$ (i = impurity type) relates γ_0 to γ_i, the edge-free energy in the presence of impurities. Finally, $\gamma_0 = 3.3k_\mathrm{B}T$, $\gamma_\mathrm{Mg} = 3.0k_\mathrm{B}T$, and $\gamma_\mathrm{Zn} = 3.4k_\mathrm{B}T$, and $f_\mathrm{Mg} = 0.8$ and $f_\mathrm{Zn} = 1.1$ were obtained. On the basis of the permissible range for f and the measurement error for γ, f_Zn can be regarded to be 1.0, meaning that the addition of zinc does not affect γ. Although the difference between the measured γ and that obtained in a pure solution was somewhat larger than the measurement error for magnesium, it is difficult to determine conclusively whether this difference alone affects γ. Therefore, the rate of reduction in the growth rate and the rate of change in β were carefully estimated against various combinations of f and δ in the presence of magnesium. The result led to the conclusion that, in the case of magnesium, the difference between the γ values is not significant.

Therefore, while zinc and magnesium reduce the face growth rate by reducing the step velocity of the formed two-dimensional nucleus, it is thought that they do

not affect the edge free energy. This implies that both impurities have almost no effect on the nucleation frequency (at least for the range of concentrations tested). This conclusion is consistent with the morphology of HAP seen in bone tissue. If zinc and magnesium do not affect the nucleation frequency of HAP crystals but rather only suppress the growth of precipitated crystals, likely result is the formation of numerous nano-sized HAP crystals, as seen in human bone. If zinc and magnesium had no evident impurity effect for growth, HAP crystals would easily become enlarged, and the combined strength and flexibility originally possessed by bone might be lost.

In growth rate measurement experiments in the presence of impurities using the phase-shift method, investigations have been carried out on adsorption mechanism using Langmuir and Temkin isotherms as well as on the chemical morphologies of adsorbed zinc and magnesium [71]. A Langmuir-type adsorption model for kinks was determined to be appropriate on the basis of model fitting in which impurities adsorb onto the kink sites in the step front and onto the terraces between steps.

In contrast to detailed growth rate measurements for the *c*-face, there are no reports on the growth rate of the *a*-face. As mentioned previously, the reason for this is the lack of reliable data due the fact that the growth rate of the *a*-face is more than 1 order of magnitude lower than that of the *c*-face. Observations based on AFM have been reported for the growth mode of the *a*-face [77]. Under similar experimental conditions as those for the *c*-face (growth in pseudo body fluid), growth by step movement occurs on the *a*-face. Although it has not been directly proven that this step originates from spiral dislocation, spiral growth probably occurs because the growth proceeds with the filling of etch pits on the surface. The dependence of the step velocity on the supersaturation, as well as changes in velocity associated with changes in the step spacing, has been measured, and the surface diffusion length was concluded to be only a few nanometers.

3.4.7 Discussion of HAP Growth Unit

In discussing crystal growth mechanisms, the growth unit (that which serves as the minimal unit of growth) is generally considered to be an atom or molecule. In this model, growth of soluble inorganic salts is assumed to proceed as a result of positive or negative ions being incorporated into the crystal lattice. However, depending on the type and growth environment of the crystals, there are instances in which the experimental data are better explained by considering the growth unit as a far larger assembly than an atom or molecule [78–80]. Such a cluster is composed of aggregates of atoms or molecules and has a defined structure, unlike random aggregates.

The concept of the cluster itself is very old. For example, even when the term cluster was not in widespread use, there had been attempts to explain the mosaic structure displayed by NaCl crystals growing in aqueous solution with a growth model incorporating units called block nuclei. Biominerals, including HAP, are

examples for which growth models with clusters as units are thought to fit the data well. Viewed qualitatively, a number of reasons for this may be offered. Examples include (1) an extremely low growth rate despite the high supersaturation, (2) difficulty growing giant crystals that retain high crystallinity under normal temperature and pressure, and (3) ease of producing an amorphous phase. These characteristics reflect phenomena observed in the growth of protein crystals. In proteins, in which growth proceeds as a result of the aggregation of giant molecules, two types of growth driving forces need to be considered: supersaturation, which is determined thermodynamically, and intermolecular interactions. The latter factor is normally not considered in the growth of ionic crystals. If we imagine the simplest situation, intermolecular interactions are determined by the competition of repulsive forces due to the average charge of the molecular surface and the van der Waals attraction force between molecules. When intermolecular interactions are involved, complex phenomena arise. For example, even under conditions of very high concentrations of the solute itself, the growth rate becomes extremely low when very weak attractive interaction operates, and sometimes no crystal growth occurs and only an amorphous phase precipitates due to the solubility difference between crystal and amorphous phases. Therefore, if biomineral growth proceeds in a manner similar to that of protein crystal growth, the growth unit should be considered as an aggregate (a cluster) and there is intermolecular interaction between units.

Two lines of circumstantial evidence can be offered for the suggestion that the growth unit for HAP (at least in environments resembling those within the human body) takes the form of a cluster. The first involves the physical constants related to growth. The values for the edge free energy and the step kinetic coefficients diverge widely from typical values for soluble inorganic crystals and, in fact, are closer to those of protein crystals [77]. The second is that dynamic light-scattering measurements of pseudo-body fluid show the existence of aggregates with a hydrodynamic radius of about 0.5 nm [81,82]. Since these aggregates disappear when calcium or phosphate ions are removed from the solution, it is highly likely that they are calcium phosphate clusters. Initially, these clusters were thought to be Posner clusters ($Ca_9(PO_4)_6$), and a crystal growth model based on the simple aggregation of clusters was proposed.

When assuming the presence of Posner clusters within the HAP crystal structure, it is possible to define two types of chiral clusters. The two types correspond to the L- and D-forms of amino acids and comprise structures with threefold symmetry in which six phosphate ions are arranged around the calcium ion at the center of the cluster. An ab initio calculation was performed to estimate whether or not a structure with the chemical composition $Ca_9(PO_4)_6$ could exist in a stable form. In this calculation, the relative energies of clusters were compared by obtaining stable structures of $Ca_3(PO_4)_2$ [83], and then combining up to four of these structures [84–86]. First, energy calculations were performed for $Ca_3(PO_4)_2$ (corresponding to the monomer), taking into consideration the spatial arrangements (three types) that could be assumed given a pair of calcium and phosphate ions. Ten types of isomers with a local energy minimum were defined. Among these, an isomer with D_{3h} symmetry and basket-like morphology was overwhelmingly stable compared

to the others, so this isomer was established as the monomer. After two, three, and four of these monomers were combined in simple combinations, the cluster energy decreased monotonically with the number of monomers. However, comparison of the energies for structures with the most compact morphology at each number combination showed that the minimum energy was attained with a $Ca_9(PO_4)_6$ trimer. The structure of $Ca_9(PO_4)_6$ in this case has a T_h symmetry, and, when refined to take up the minimum energy structure on the potential energy surface (PES), it shows an S_6 symmetry.

Although 24 types of isomers with a local energy minimum appear on the $Ca_9(PO_4)_6$ PES, among these, S_6 is a special structure that has nearly the lowest energy despite its extremely high symmetry. From these results, it was determined that if clusters are considered as the growth units for HAP, S_6 is the most appropriate structure. It has sixfold symmetry, and the crystal structure of HAP cannot be constructed by aggregating these clusters. However, simply by slightly rotating the surrounding phosphate ions relative to the calcium ion at the center of the cluster, the cluster can be changed into a Posner cluster with threefold symmetry. Depending on whether the direction of rotation is clockwise or counterclockwise, it is possible to bestow chirality to the cluster as well. The energy required for this rotation is 10 kcal or less and is not a barrier to structural conversion. The above-mentioned calculation results all presume treatment in vacuum, and no conclusions have yet been reached on whether or not the S_6 structure stably exists in actual solutions.

Highly intriguing research results have been reported for the growth units of biominerals, including HAP [87]. In this research, a diluted solution of calcium chloride was gradually added to a diluted carbonate buffer solution under constant pH conditions and changes in the solution concentration of calcium ions were measured using a calcium ion electrode. Even when the solution condition was undersaturated for calcium carbonate salts (such as calcite), the rate of increase in free calcium ions was considerably lower than the value calculated from the amount of calcium ions added (Fig. 3.4a). In other words, many of the added calcium ions were in a bound state and were consumed by the formation of some sort of assembly. A further important point is that the rate of increase in free calcium ions was nearly constant as the solution transitioned from an undersaturated state to a supersaturated state as a result of calcium ion addition until immediately before nucleation occurred. These results indicate that calcium carbonate clusters in solution are already in the undersaturated state and that their aggregation (or an increase in their size) causes nucleation. Although the appearance of metastable clusters during the course of nucleation is also considered in classical nucleation models, unlike these types, the above-mentioned clusters are energetically stable (in local energy-minimum state).

In this research, attempts were made to measure the size of the clusters using analytical ultracentrifugation. This method measures the diffusion coefficients from the precipitation rate of the clusters formed by centrifugation. Like the dynamic light-scattering method, the measured diffusion coefficients are converted into a hydrodynamic radius in accordance with the Stokes–Einstein equation. In an undersaturated solution, clusters were not detected because of the low concentration;

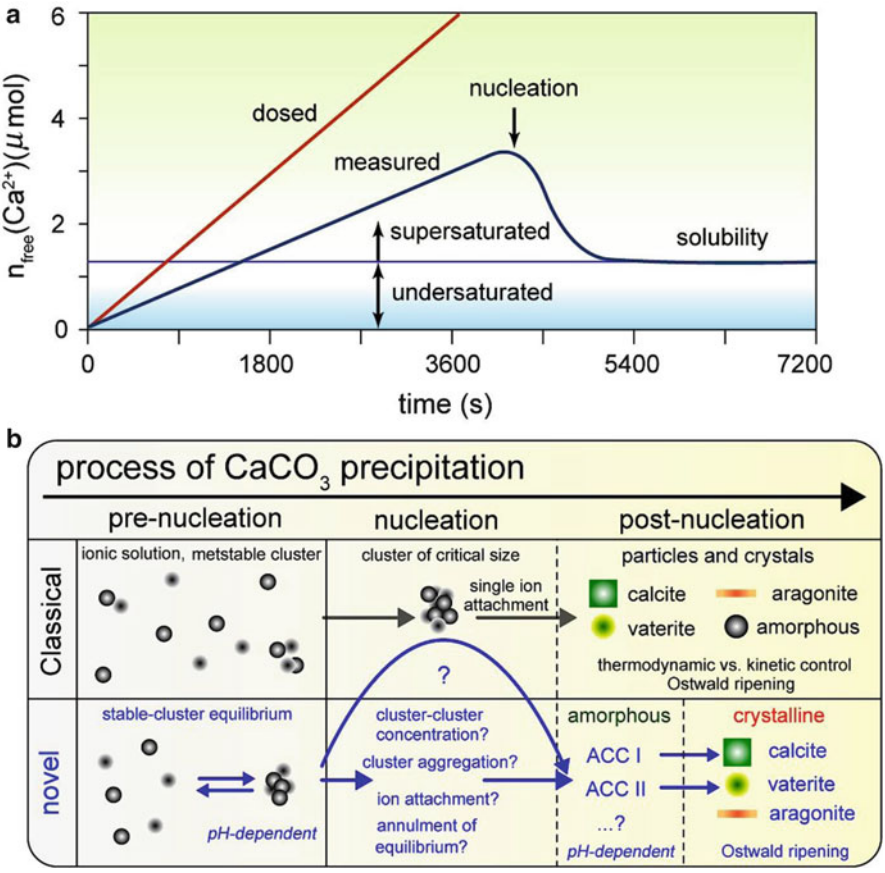

Fig. 3.4 (**a**) Time-dependent amount of free calcium ions measured in the solution (*blue*) using calcium ion selective electrode in comparison with dosed amount of calcium ions (*red*). (**b**) Schematic image of novel nucleation process through thermodynamically stable calcium carbonate clusters in comparison with classical nucleation process (reproduced with permission from [87]) (copyright 2008, American Association of Advancement of Science)

however, in a supersaturated solution, immediately before nucleation, clusters with a radius of 1 nm were detected. Furthermore, while the incidence was low, the existence of clusters with a radius of about 2 nm was also suggested.

Immediately after nucleation, the clusters further increased in size. There was variation in the structure of the clusters, meaning that it was possible that these different clusters ultimately formed different polymorphs of calcium carbonate—i.e., calcite, vaterite, and aragonite—through the formation of amorphous phases differing in structure (Fig. 3.4b). This idea clearly differs from classical models, which assume that the final crystal polymorph types are determined after nucleation.

In terms of the association between the macroscopic morphology of the produced crystal and the growth unit, Banfield et al. suggested that natural biomineralization

processes proceed in an aggregation-based manner and result in the construction of characteristic fine structures [88]. Gebauer et al., using methods similar to those mentioned above, conducted measurements on calcium phosphate solutions and have confirmed the presence of clusters in this case as well. Given the various lines of experimental evidence presented in recent years, it appears almost certain that clusters are involved in some way in the growth of insoluble biominerals.

3.5 Future Perspectives

The crystal growth of HAP does not qualitatively differ from that of either soluble inorganic crystals or organic crystals. In other words, spiral growth mediated by dislocation having spiral components or growth by two-dimensional nucleation occurs. This is supported by surface observations of growing crystals. Regarding the rate-limiting process of growth, although incorporation of a growth unit into the crystal requires the highest energy, whether or not this incorporation proceeds through surface diffusion is unclear. The diffusion length is probably minimal. The important point is not in the growth mode but that classical growth models—i.e., models in which growth proceeds as a result of ionic bonds—may not be applicable. This is a problem that is not limited to HAP but also applies to biominerals in general. In the aforementioned cases where growth occurred with cluster units, how the driving force of growth is defined is very important. Depending on the definition, the values for the various physical constants involved in growth, which have been reported in studies to date, may change substantially. Furthermore, it is likely that the problem of how to quantify the intermolecular interactions between clusters and then relate them to growth features will become an issue as well. As mentioned above, the crystallization process for proteins is qualitatively the same as for soluble salts but the growth features are complex because intermolecular interactions are included as a growth factor. With intermolecular interactions, the magnitude of the Hamaker constant (a constant indicative of the van der Waals attraction force) of a molecule has a powerful effect. In biomineral growth as well, it will likely be necessary to conduct tests on the Hamaker constant for each cluster in order to understand the growth mechanisms completely and to clarify the relationship between the final product and the growth unit.

References

1. Newman, W.F., Newman, M.W.: The chemical dynamics of bone mineral. University Chicago Press, Chicago (1958)
2. Aoki, H.: Kyoi no Seitai Busshitsu Apatite (in Japanese). Ishiyaku Publishers Inc., Tokyo (1999)
3. Elliot, J.C.: Structure and chemistry of the apatites and other calcium orthophosphates. Elsevier, Amsterdam (1994)

4. Wang, L., Nancollas, G.H.: Calcium orthophosphates: crystallization and dissolution. Chem. Rev. **108**, 4628–4669 (2008)
5. Combes, C., Rey, C.: Amorphous calcium phosphates: synthesis, properties and uses in biomaterials. Acta Biomaterialia **6**(9), 3362–3378 (2010)
6. Elliot, J.C.: Monoclinic space group of hydroxyapatite. Nature **230**, 72 (1971)
7. Posner, A.S., Perloff, A., Diorio, A.F.: Refinement of the hydroxyapatite structure. Acta. Cryst. **11**, 308–309 (1958)
8. Elliot, J.C., Mackie, P.E., Young, R.A.: Monoclinic hydroxyapatite. Science **180**, 1055–1057 (1973)
9. Bauer, M.: Röntgenographische und Dielektrische Untersuchungen an Apatiten. Dissertation, Fakultät für Physik, Universität Karlsruhe (1991)
10. Dallemagne, M.J., Richelle, L.J.: Inorganic chemistry of bone. Biological mineralization, pp. 23–42. Wiley, New York (1973)
11. Weatherell, J.A., Robinson, C.: The inorganic composition of teeth. Biological mineralization, pp. 43–74. Wiley, New York (1973)
12. Bienenstock, A., Posner, A.S.: Calculations of the X-ray intensities from arrays of small crystallites of hydroxyapatite. Arch. Biochem. Biophys. **124**, 604–607 (1968)
13. Eanes, E.D., Gillessen, I.H., Posner, A.S.: Intermediate states in the precipitation of hydroxyapatite. Nature **208**, 365–367 (1965)
14. Termine, J.D., Posner, A.S.: Calcium phosphate formation in vitro. I. Factors affecting initial phase separation. Arch. Biochem. Biophys. **140**, 307–317 (1970)
15. Termine, J.D., Eanes, E.D.: Comparative chemistry of amorphous and apatitic calcium phosphate preparations. Calcif. Tissue. Res. **10**, 171–197 (1972)
16. Dorozhkin, S.V., Epple, M.: Biological and medical significance of calcium phosphates. Angew. Chem. Int. Ed. **41**, 3130–3146 (2002)
17. Christofferesen, J., Christofferesen, M.R., Kibalczyc, W., Andersen, A.: A contribution of understanding of the formation of calcium phosphates. J. Cryst. Growth **94**, 767–777 (1989)
18. Christofferesen, J., Christofferesen, M.R., Kibalczyc, W.: Apparent solubilities of two amorphous calcium phosphates and of octacalcium phosphate in the temperature range 30-42°C. J. Cryst. Growth **106**, 349–354 (1990)
19. Posner, A.S., Betts, F.: Synthetic amorphous calcium phosphate and its relation to bone mineral. Accounts Chem. Res. **8**, 273–281 (1975)
20. Tropp, J., Blumenthal, N.C., Waugh, J.S.: Phosphorous NMR study of solid amorphous calcium phosphate. J. Am. Chem. Soc. **105**, 22–26 (1983)
21. Harries, J.E., Hukins, D.W.L., Hasnain, S.S.: Analysis of the EXAFS spectrum of hydroxyapatite. Mater. Res. Bull. **9**, 353–360 (1986)
22. Harries, J.E., Hukins, D.W.L., Holt, C., Hasnain, S.S.: Conversion of amorphous calcium phosphate into hydroxyapatite investigated by EXAFS spectroscopy. J. Cryst. Growth **84**, 563–570 (1987)
23. Peters, F., Schwarz, K., Epple, M.: The structure of bone studied with synchrotron X-ray diffraction, X-ray absorption spectroscopy and thermal analysis. Thermochim. Acta. **361**, 131–138 (2000)
24. Onuma, K., Oyane, A., Tsutsui, K., Tanaka, K., Treboux, G., Kanzaki, N., Ito, A.: Precipitation kinetics of hydroxyapatite revealed by the continuous-angle laser light-scattering technique. J. Phys. Chem. B **104**, 10563–10568 (2000)
25. Pan, H.-B., Darvell, B.W.: Calcium phosphate solubility: the need for re-evaluation. Cryst. Growth & Des. **9**, 639–645 (2009)
26. Burton, W.K., Cabrera, N., Frank, F.C.: The growth of crystals and the equilibrium structure of their surfaces. Phil. Trans. Roy. Soc. London **A234**, 299–358 (1951)
27. Bennema, P.: Crystal growth measurements on potassium aluminium alum and sodium chlorate from slightly supersaturated solutions. Phy. Stat. Solidi. **17**, 563–570 (1966)
28. Denk Jr., E.G., Botsaris, G.D.: Mechanisms of potassium alum crystal growth from solution. J. Cryst. Growth **6**, 241–244 (1970)

29. Gilmer, G.H., Ghez, R., Cabrera, N.: An analysis of combined surface and volume diffusion processes in crystal growth. J. Cryst. Growth **8**, 79–93 (1971)
30. Chernov, A.A.: The spiral growth of crystals. Sov. Phys. Usp. **4**, 116–148 (1961)
31. Sunagawa, I., Tsukamoto, K.: Growth spirals on NaCl and KCl crystals growth from solution phase. J. Cryst. Growth **15**, 73–78 (1972)
32. Van Enckevort, W.J.P., Bennema, P., van der Linden, W.H.: On the observation of growth spirals with very low step heights on potassium alum single crystals. Z. Phys. Chem. **124**, 171–191 (1981)
33. Jetten, L.A.M.J., van der Hoek, B., van Enckevort, W.J.P.: In situ observations of the growth behavior of the {010} face of potassium hydrogen phthalate. J. Cryst. Growth **62**, 593–611 (1983)
34. Van Enckevort, W.J.P., Klapper, H.: Observation of growth steps with full and half unit cell heights on the {011} faces of $NiSO_4 \cdot 6H_2O$ in relation to the defect structure. J. Cryst. Growth **80**, 91–103 (1987)
35. Van Erk, W., van Hoek-Martens, H.J.G.J., Bartels, G.: The effect of substrate orientation on the growth kinetics of garnet liquid phase epitaxy. J. Cryst. Growth **48**, 621–634 (1980)
36. Chernov, A.A., Rashkovich, L.N., Mkrtchan, A.A.: Solution growth kinetics and mechanism: prismatic face of ADP. J. Cryst. Growth **74**, 101–112 (1986)
37. Chernov, A.A., Rashkovich, L.N.: Spiral crystal growth with nonlinear dependence of step growth rate on supersaturation; the {110} faces of KH_2PO_4 crystals in aqueous solution. J. Cryst. Growth **84**, 389–393 (1987)
38. Maiwa, K., Tsukamoto, K., Sunagawa, I.: Activities of spiral growth hillocks on the (111) faces of barium nitrate crystals growing in an aqueous solution. J. Cryst. Growth **102**, 43–53 (1990)
39. Onuma, K., Tsukamoto, K., Sunagawa, I.: Growth kinetics of K-Alum crystal in relation to the surface supersaturations. J. Cryst. Growth **100**, 125–132 (1990)
40. Vekilov, P.G., Kuznetsov, Y.G., Chernov, A.A.: Interstep interaction in solution growth; (101) ADP face. J. Cryst. Growth **121**, 643–655 (1992)
41. Malkin, A.I., Chernov, A.A., Alexeev, I.V.: Growth of dipyramidal face of dislocation-free ADP crystals; free energy of steps. J. Cryst. Growth **97**, 765–769 (1989)
42. Mullin, J.W.: Crystallization, 4th edn, p. 130. Butterworth-Heinemann, Oxford (2001)
43. Robinson, R.: The significance of phosphate esters in metabolism. New York University Press, New York (1932)
44. Brighton, C.T., Hunt, R.M.: Mitchodrial calcium and its role in calcification. Histochemical localization of calcium in electron micrographs of the epiphyseal growth plate with K-pyroantimonate. Clin. Orthop. **100**, 406–416 (1974)
45. Farley, J.R., Baylink, D.J.: Purification of skeletal growth factor from human bone. Biochemistry **21**, 3205–3207 (1982)
46. Moreno, E.C., Zahradnik, R.T., Glazman, A., Hwu, R.: Precipitation of hydroxyapatite from dilute solutions upon seeding. Calcif. Tissue Res. **24**, 47–57 (1977)
47. Tomson, M.B., Nancollas, G.H.: Mineralization kinetics: a constant composition approach. Science **200**, 1059–1060 (1978)
48. Koutsoukos, P., Amjad, Z., Tomson, M.B., Nancollas, G.H.: Crystallization of calcium phosphate. A constant composition study. J. Am. Chem. Soc. **102**, 1553–1557 (1980)
49. Moreno, E.C., Varughese, K.: Crystal growth of calcium apatites from dilute solutions. J. Cryst. Growth **53**, 20–30 (1981)
50. Arends, J., Christoffersen, J., Christofferesen, M.R., Eckert, H., Fowler, B.O., Heughebaert, J.C., Nancollas, G.H., Yesinowski, J.P., Zawacki, S.J.: A calcium hydroxyapatite precipitated from an aqueous solution: an international multimethod analysis. J. Cryst. Growth **84**, 515–532 (1987)
51. Christoffersen, M.R., Christoffersen, J.: A revised theory for the growth of crystals by surface nucleation. J. Cryst. Growth **121**, 608–616 (1992)
52. Christoffersen, M.R., Christoffersen, J.: Possible mechanism for the growth of the biomaterial, hydroxyapatite microcrystals. J. Cryst. Growth **121**, 617–630 (1992)

53. Hayek, E., Lechleitner, J., Böhler, W.: Hydrothermalsynthese von Hydroxylapatit. Angew. Chem. **67**, 326 (1955)
54. Hayek, E., Böhler, W., Lechleitner, J.: Hydrothermalsynthese von Calsium-Apatiten. Z. Anorg. Allg. Chem. **295**, 241–246 (1958)
55. Perloff, A., Posner, A.S.: Preparation of pure hydroxyapatite crystals. Science **124**, 583–584 (1956)
56. Simpson, D.R.: Carbonate in hydroxyapatite. Science **147**, 501–502 (1965)
57. Jullman, H., Mosebach, R.: Zur Synthese, Licht- und Doppelbrechung des Hydroxylapatits. Z. Naturf. **21**, 493–494 (1966)
58. Blakeslee, K.C., Condrate, R.A.: Vibration spectra of hydrothermally prepared hydroxyapatite. J. Am. Ceram. Soc. **54**, 559–563 (1971)
59. Baumer, A., Argiolas, R.: Synthèses hydrothermals et déterminations RX d'apatites chlorée, fluoree ou hydroxylée. Neues Jb. Miner. Mh. 344–348 (1981)
60. Mengeot, M., Harvill, M.L., Gilliam, O.R.: Hydrothermal growth of calcium hydroxyapatite single crystals. J. Cryst. Growth **19**, 199–203 (1973)
61. Arends, J., Schthof, J., van der Linden, W.H., Bennema, P., van den Berg, P.J.: Preparation of pure hydroxyapatite single crystals by hydrothermal recrystallization. J. Cryst. Growth **46**, 213–220 (1979)
62. Ito, A., Nakamura, S., Aoki, H., Akao, M., Teraoka, K., Tsutsumi, S., Onuma, K., Tateishi, T.: Hydrothermal growth of carbonate-containing hydroxyapatite single crystals. J. Cryst. Growth **163**, 311–317 (1996)
63. Mengeot, M.: Hydrothermal growth and electron-spin-resonance investigations of calcium hydroxyapatite single crystals. PhD Thesis, University of Connecticut (1975)
64. Eysel, W., Roy, D.M.: Hydrothermal flux growth of hydroxyapatites by temperature oscillation. J. Cryst. Growth **20**, 245–250 (1973)
65. Nakadate, S., Yamaguchi, I:. Japanese patent laid-open. H02-287107, (1990)
66. MacInnis, I., Onuma, K., Tsukamoto, K.: In situ study of dissolution kinetics of calcite crystal using phase shift interferometry. In: Proceedings Sixth Topical Meeting on Crystal Growth Mechanism, pp. 233–238 (1993)
67. Maruyama, M., Tsukamoto, K., Sazaki, G., Nishimura, Y., Vekilov, P.: Chiral and achiral mechanisms of regulation of calcite crystallization. Cryst. Growth & Des. **9**, 127–135 (2009)
68. Kanzaki, N., Onuma, K., Ito, A., Teraoka, K., Tateishi, T., Tsutsumi, S.: Direct growth rate measurement of hydroxyapatite single crystal by Moire phase shift interferometry. J. Phys. Chem. B **102**, 6471–6476 (1998)
69. Onuma, K., Kanzaki, N., Ito, A., Tateishi, T.: Growth kinetics of hydroxyapatite (0001) face revealed by phase shift interferometry and atomic force microscopy. J. Phys. Chem. B **102**, 7833–7838 (1998)
70. Markov, I.V.: Crystal growth for beginners: fundamental of nucleation, crystal growth and epitaxy. World Scientific Publishing, Singapore (1995)
71. Kanzaki, N., Onuma, K., Treboux, G., Tsutsumi, S., Ito, A.: Inhibitory effect of magnesium and zinc on crystallization kinetics of hydroxyapatite (0001) face. J. Phys. Chem. B **104**, 4189–4194 (2000)
72. Kanzaki, N., Onuma, K., Treboux, G., Tsutsumi, S., Ito, A.: Effect of impurity on two-dimensional nucleation kinetics: case studies of magnesium and zinc on hydroxyapatite (0001) face. J. Phys. Chem. B **105**, 1991–1994 (2001)
73. Amjad, Z., Koutsoukos, P., Nancollas, G.H.: The crystallization of hydroxyapatite and fluorapatite in the presence of magnesium ions. J. Colloid Interface Sci. **101**, 250–256 (1984)
74. Dalpi, M., Karayianni, E., Koutsoukos, P.: Inhibition of hydroxyapatite formation in aqueous solutions by zinc and 1,2-dihydroxy-1,2-bis(dihydroxyphosphonyl)ethane J. Chem. Soc. Faraday Trans. **89**, 965–969 (1993)
75. Fuierer, T.A., LoRe, M., Puckett, S.A., Nancollas, G.H.: A mineralization adsorption and mobility study of hydroxyapatite surfaces in the presence of zinc and magnesium. Langmuir **10**, 4721–4725 (1994)

76. Liu, X.Y., Maiwa, K., Tsukamoto, K.: Heterogeneous two-dimensional nucleation and growth kinetics. J. Chem. Phys. **106**, 1870–1879 (1997)
77. Onuma, K., Ito, A., Tateishi, T., Kameyama, T.: Growth kinetics of hydroxyapatite revealed by atomic force microscopy. J. Cryst. Growth **154**, 118–125 (1995)
78. Horn, D., Rieger, J.: Organic nanoparticles in the aqueous phase—theory, experiment, and use. Angew. Chem. Int. ed. **40**, 4330–4361 (2001)
79. Furrer, G., Phillips, B.L., Ulrich, K.U., Pothig, R., Casey, W.H.: The origin of aluminum flocs in polluted streams. Science **297**, 2245–2247 (2002)
80. Navrotsky, A.: Energetic clues to pathways to biomineralization: precursors, clusters, and nanoparticles. Proc. Natl. Acad. Sci. U. S. A. **101**, 12096–12101 (2004)
81. Onuma, K., Ito, A.: Cluster growth model for hydroxyapatite. Chem. Mat. **10**, 3346–3351 (1998)
82. Oyane, A., Onuma, K., Kokubo, T., Ito, A.: Clustering of calcium phosphate in the system $CaCl_2$-H_3PO_4-KCl-H_2O. J. Phys. Chem. B **103**, 8230–8235 (1999)
83. Treboux, G., Kanzaki, N., Onuma, K., Ito, A.: Energy-preeminent isomer of the $Ca_3(PO_4)_2$ cluster. J. Phys. Chem. A **103**, 8118–8120 (1999)
84. Treboux, G., Layrolle, P., Kanzaki, N., Onuma, K., Ito, A.: Existence of Posner's cluster in vacuum. J. Phys. Chem. A **104**, 5111–5114 (2000)
85. Treboux, G., Layrolle, P., Kanzaki, N., Onuma, K., Ito, A.: Symmetry of Posner's cluster. J. Am. Chem. Soc. **122**, 8323–8324 (2000)
86. Kanzaki, N., Treboux, G., Onuma, K., Tsutsumi, S., Ito, A.: Calcium phosphate clusters. Biomaterials **22**, 2921–2929 (2001)
87. Gebauer, D., Völkel, A., Cölfen, H.: Stable prenucleation calcium carbonate clusters. Science **322**, 1819–1822 (2008)
88. Banfield, J.F., Welch, S.A., Zhang, H., Ebert, T.T., Penn, R.L.: Aggregation-based crystal growth and microstructure development in natural iron oxyhydroxide biomineralization products. Science **289**, 751–754 (2000)

Chapter 4
Biomineralization: Apatite Protein Interaction

Toru Tsuji, Mayumi Iijima, and Kazuo Onuma

Abstract The evolution of recombinant DNA techniques and protein engineering has accelerated the growth in biomineralization studies over the last decade. In this chapter, we discuss recently published work focusing on the structure and function of proteins that are involved in HAP crystal formation in the body. The proteins we focus on in this review are amelogenin and dentin matrix protein 1 (DMP1). The roles of other proteins, for example, SIBLING family members, which are supposed to play significant roles in HAP crystal formation, are also described. These proteins would be involved in different steps of HAP crystal formation, that is, nucleation, growth, and transformation. We also summarize the challenges of regulating crystal growth and elucidating the mechanisms of crystal formation using artificial proteins, which are not attained by using only naturally occurring proteins.

Keywords biomineralization • amorphous calcium phosphate • transformation • hydroxyapatite • biomineralization proteins

T. Tsuji (✉)
Advanced Research Centers, Keio University, 3-14-1, Hiyoshi, Kohoku-ku, Yokohama, 223-8522, Japan
e-mail: toruts2002@yahoo.co.jp

M. Iijima
Asahi University School of Dentistry, Oral Functional Science and Rehabilitation, Dental Materials Science, 1851-1 Hozumi, Mizuho, Gifu, 501-0296, Japan
e-mail: iijima@dent.asahi-u.ac.jp

K. Onuma
National Institute of Advanced Industrial Science & Technology, Central 6, 1-1-1 Higashi, Tsukuba, Ibaraki, 305-8566, Japan
e-mail: k.onuma@aist.go.jp

X.Y. Liu (ed.), *Bioinspiration: From Nano to Micro Scales*, Biological and Medical Physics, Biomedical Engineering, DOI 10.1007/978-1-4614-5372-7_4,

4.1 Overview of Bone and Teeth Biomineralization

The crystalline phase of calcium phosphate that participates in bone formation is the hydroxyapatite (HAP) phase, the most stable calcium phosphate phase under physiological conditions. Bone contains collagen—an organic substance—at a dry weight content of 30–40%. Bone is thus an inorganic-organic hybrid material and is characterized by great elasticity and strength compared to pure inorganic substances. Bone HAP nanocrystals measure 30–50 nm in length, 10–50 nm in width, and 3–5 nm in thickness. HAP crystallizes on the collagen fibrils along the direction in which they extend [1].

Bone is synthesized by osteoblasts, which secrete type I collagen into the extracellular matrix. Collagen molecules self-assemble into insoluble fibers through multiple processes. Since biological fluid is supersaturated with respect to HAP, it is not surprising that calcification occurs ubiquitously in the human body [2]. When calcification first begins, minerals are formed specifically on the collagen fibrils. Two mechanisms have been proposed to explain this phenomenon. The first is that some molecules in biological fluid inhibit non-specific mineral deposition. It has been shown that acidic molecules containing carboxyl, phosphate, or sulfate groups inhibit deposition of calcium phosphate in vitro. The second mechanism is owing to the acidic proteins that possess affinity to collagen. Osteoblasts secrete several types of proteins in addition to collagen. Some are acidic, containing many acidic residues such as aspartic acid (Asp), glutamic acid (Glu), and phosphorylated serine, and have the ability to bind to collagen. The binding of acidic proteins to collagen apparently concentrates the calcium ions by using negatively charged groups, which elevates the degree of supersaturation around collagen. This induces calcium phosphate precipitation on the collagen molecules. These processes occur in the early stages of biomineralization during bone formation. As calcification progresses, osteoblasts are buried in the surrounding minerals. Cells imbedded in the minerals no longer secrete proteins and become osteocytes.

Since the details of tooth formation are discussed in Chap. 5, the process is summarized only briefly here. A tooth consists of three layers of mineralized tissue. Enamel forms the outer layer, dentin forms the middle layer, and cementum forms the inner layer, and they are synthesized by ameloblasts, odontoblasts, and cementoblasts, respectively. Tooth calcification is regulated by proteins secreted into the extracellular matrices. Like osteoblasts, odontoblasts and cementoblasts secrete type I collagen, while ameloblasts secrete mainly amelogenin, but not collagen. More than 90% of the organic phase of enamel consists of amelogenin. Amelogenin is believed to regulate the formation of enamel HAP crystals and their assembly into highly organized structures [3].

Enamel HAP crystals differ from those found in bone, dentin, and cementum in their morphology and size. Enamel HAP crystals do not have a platelet structure but rather forms needle-shaped crystals that extend along the *c*-axis. Enamel HAP crystals are much larger than bone ones, measuring 100–1,000 nm in length, 30–60 nm in width, and 10–30 nm in thickness. Enamel HAP crystals have a

higher crystallinity than bone ones and show a sharp peak when measured by XRD analysis. Enamel is formed from large and highly crystallized HAP crystals that are densely packed.

Enamel has a low organic content. In the early stage of enamel formation, the enamel consists of 30% mineral and 20% organic matrix, primarily amelogenin, while the remaining 50% consists of water. During the maturation process, the amelogenin is degraded by proteolytic enzymes and disappears from the enamel. This results in a final enamel composition of 95–97% inorganic content and less than 1% organic content [4]. Thus, enamel is an extremely hard tissue that consists almost entirely of inorganic substances (the elastic modulus of enamel is 80 GPa, [5] whereas that of bone is 10 GPa [6]). However, enamel does not possess as much flexibility as bone (the tensile strengths of enamel are 10 or 40 MPa according to direction [7], whereas that of bone is 100 MPa [8]).

The proteins secreted into the extracellular matrices play a key role in the mineralization of bone and teeth. Recent observations have shown that, in the early development of both bone and enamel, the minerals comprising them consist of a large amount of amorphous calcium phosphate (ACP) [9–11]. Eventually, HAP crystals form from the ACP and assemble into aggregates, which have structures specific to bone and teeth functions. Therefore, to understand the biomineralization of bone and teeth, it is necessary to know how proteins in the extracellular matrices are involved in the deposition of ACP, the nucleation of nanocrystals, and in the growth, transformation, and formation of hierarchical structures made by comprising aggregates of nanocrystals.

In this chapter, we introduce results from recently published work focusing on the structure and function of proteins that are involved in HAP crystal formation in the body. We also summarize the challenges to regulating crystal growth and elucidating the mechanisms of crystal formation using artificial proteins, which are not attained by using only naturally occurring proteins.

4.2 Proteins Involved in HAP Crystal Formation

The proteins involved in HAP crystal formation can be categorized into three groups on the basis of their functions. Those in one group form the insoluble organic matrix and determine the contours of the hard tissues. Type 1 collagen is the organic matrix for bone, dentin, and cementum, while amelogenin is the matrix for enamel. Those in the second group produce mineral deposits in specific areas. They bind to collagen and accelerate HAP crystallization. Those in the third group inhibit deposition of minerals in inappropriate areas. Since biological fluid is supersaturated with respect to HAP, it is not surprising that depositions take place ubiquitously in the body. Proteins with inhibitory function against non-specific deposition are therefore important for normal tissue formation.

4.2.1 Role of Collagen in Forming Insoluble Matrix

Type 1 collagen determines the shape of bone, dentin, and cementum. Collagen consists of polypeptides known as α-chains. One α-chain consists of approximately 1,000 amino acids, each with a molecular weight (M_w) of about 100,000. Collagen has a high glycine content, which makes up approximately one third of the total amino acid content. Following glycine is proline, which comprises one fifth of the total amino acid content. Some proline and lysine residues are hydroxylated after translation and exist as hydroxyl-proline and hydroxyl-lysine, which are specific for collagen. Each α-chain forms a left handed polyproline II type (PPII) helical coil, and further associates to form right handed triple helix. Each α-chain has a repetitive motif consisting of $(Gly\text{-}X\text{-}Y)_n$ in which glycine repeats at every third amino acid. The structure of the triple helix is maintained by glycine, which has a small side chain, placed inside the helix. The linkage of adjacent α-chains is stabilized through hydrogen bonds linking the amino and carboxyl groups of the backbone of the polypeptides [12, 13].

The collagen is secreted into the extracellular matrix as a protocollagen strand containing propeptides at its N- and C-termini. The strand associates to form procollagen triple helix after post-translation modification of lysine and proline residues. The propeptide domains are cleaved by proteases, producing tropocollagen triple helix, which self-assembles into collagen microfibiril. The microfibiril assembles to be an insoluble collagen fiber. Examination of collagen fibers under an electron microscope reveals striped patterns at 67 nm intervals. Each interval is called a "D-period" and arises from the staggered arrangement of the triple helices. Each space created by this arrangement is called a "gap zone," and this is the area in which mineral deposition occurs. It is believed that extracellular matrix proteins bind to this gap zone and induce mineral deposition [2].

4.2.2 Role of Amelogenin in Forming Insoluble Matrix

Although the amino acid sequence of human amelogenin is known, amelogenin from bovine, porcine, and mouse are primarily used for research purposes. Among these, bovine amelogenin is the longest, with 197 amino acid residues, while porcine amelogenin is the shortest, with 173 amino acid residues [14]. The molecular weight of amelogenin estimated from the amino acid sequence is 20–22 kDa, with an isoelectric point of 6.5. Amelogenin can be divided into three domains on the basis of the properties of the amino acid sequence. The N-terminal domain consists of 45 amino acid residues, and is known as TRAP (tyrosine-rich amelogenin peptide). Serine residues that eventually become phosphorylated are also located in this domain. The proline-rich and hydrophobic middle-core domain has been reported to be responsible for the formation of the PPII structure [15]. The PPII structure is a mild helix structure that can also be seen in collagen, and is often

seen in proteins that do not undergo folding. The C-terminal domain consists of only 11 amino acids, which are charged and hydrophilic. Although amelogenin is an intrinsically disordered (natively unfolded) protein that does not have a defined three-dimensional structure, it self-assembles and forms a β-sheet structure at high concentrations [16]. Details concerning intrinsically disordered proteins are discussed later in this chapter. Although the amelogenin molecule is highly hydrophobic overall, due to the hydrophilic nature of the C-terminal region, it forms an amphiphilic structure and self-assembles into nanospheres with a hydrodynamic radius of 5–50 nm [14]. The nanospheres further aggregate and form a ribbon-like structure on a micrometer scale [17]. It is of great interest to know what role this high level of protein organization plays in the enamel formation process.

4.2.3 Role of SIBLING Protein Family in Extracellular Matrices

The genes for the proteins involved in the crystallization of HAP are clustered on human chromosome 4 [18]. They include dentin sialophosphoprotein (DSPP), dentin matrix protein 1 (DMP1), bovine sialoprotein (BSP), matrix extracellular phosphoglycoprotein (MEPE), osteopontin (OPN), enamelin (ENAM), ameloblastin (AMBN), statherin (STATH), histatin (HYN), proline-rich proteins (PROL), and caseins (CSN). DSPP, DMP1, BSP, MEPE, and OPN are expressed in bone and dentin. These proteins belong to the small integrin-binding ligand N-linked glycoprotein (SIBLING) family since they contain an integrin-binding motif (Arg-Gly-Asp), are small, and are glycosylated [19]. Integrins are receptor proteins on the cell surface that regulate intracellular signaling through the binding of ligands. SIBLING proteins are believed to be involved in mineralization through their interaction with calcium phosphates. They may also be involved in cell signaling through interaction with integrins and other receptor proteins. These proteins may play a role in cancer development [20].

Although their expression level is low, both ENAM and AMBN can be found in enamel, together with amelogenin. STATH, HYN, and PROL are expressed in saliva, while CSN is expressed in milk. The similarity of the exon and intron organization and the repetitive sequences of the genes of these proteins imply that they evolved from a common ancestor protein [21, 22].

Among the SIBLING proteins, DMP1, BSP, and OPN can bind to collagen. DSPP is proteolytically cleaved, resulting in DSP (dentin sialoprotein) and DPP (dentin phosphoprotein or phosphophoryn) products. Among these proteins, DPP is able to bind to collagen. Experiments on HAP crystal formation in the presence of DMP1, BSP, OPN, and DPP showed that these proteins induce crystallization. They most likely have the ability to bind to the collagen gap zone (See note above) and form HAP crystals on collagen fibrils [2].

4.2.4 Structure and Function of Biomineralization Proteins

Ever since the discovery of the DNA double helix structure by Watson and Crick, structural biology has made great contributions to progress in the life sciences. This is because the functions of biopolymers can be inferred from their static structures. In many cases, protein function mechanisms can be understood by revealing their tertiary structures. If a protein does not have such a structure, it is impossible to determine that structure by any means. Many proteins involved in biomineralization do not have such a stable structure, making it difficult to determine a static tertiary structure using X-ray crystallography or nuclear magnetic resonance (NMR) analysis. Proteins that cannot fold into a stable structure are called "intrinsically disordered proteins" or "natively unfolded proteins" [23]. There are about 20,000 genes in the human genome, and approximately 100,000 proteins are synthesized from the genes through mechanisms including alternative splicing, which increase protein diversity. It is suggested that 33% of eukaryotic proteins contain unfolded regions lacking a stable structure [24, 25]. Proteins with unfolded regions are considered advantageous for binding multiple targets or for binding tightly to target compounds [26, 27].

The "lock and key" and the "induced-fit" models were proposed to explain how proteins recognize their substrates. In the "lock and key" model, the protein already has a structure complementary to its substrate. In the "induced fit model," the protein does not have a complementary structure, but formation of one is induced by interaction with the substrate. Common to both models is that the protein itself has a clear stable structure regardless of the experimental conditions, including the presence or absence of a substrate.

In contrast, it has been suggested that natively unfolded proteins can bind to substrates through a mechanism called "conformational selection" [28]. That is, a protein has multiple metastable conformations in the absence of a substrate and fluctuates continuously between the conformations. In the presence of a substrate, a metastable conformation complementary to the substrate is selected, and a complex is formed. The selected conformation becomes the most stable conformation. For example, the ubiquitin polypeptide, consisting of 76 amino acid residues, can form complexes with many different proteins; a total of 46 crystal structures have been reported to date. Analysis of the dynamics of ubiquitin in solution by NMR revealed a group of structures including the 46 crystal structures, thereby validating the concept of "conformational selection" [29].

For proteins involved in biomineralization, one report on statherin is noteworthy. Statherin is a small 43-amino acid protein found in saliva that inhibits the formation and growth of HAP crystals. The C-terminus of statherin does not have an ordered conformation in solution; however, structural analysis using solid-state NMR indicated that the C-terminal domain forms an α-helix upon binding to HAP [30]. The binding of statherin to HAP occurs mainly through charged amino acids at the N-terminus [31, 32], and the interaction of the C-terminus with HAP is not tight

[33]. It is unclear how this structural change in statherin induced by HAP binding can influence affects crystal growth. Schwartz reported that the C-terminal domain of statherin contributes to the inhibition of HAP precipitation [34].

4.3 Controlling Calcium Phosphate Precipitation

Mahamid et al. demonstrated the existence of a large amount of ACP in the early stage of bone formation by analyzing the mineral phase of fin bone formation in zebrafish [10]. Beniash et al. demonstrated the existence of ACP in the early stage of mouse incisor enamel formation [11]. These findings indicate that the first calcium phosphate that appears in bone and enamel is ACP. The hierarchical complex structures seen in bone and enamel are thus initially formed by ACP as a building block, and are organized in a spatiotemporal manner by the aid of proteins in extracellular matrices produced by osteoblasts or ameloblasts. Interaction between the ACP and biomolecules is discussed in this chapter.

As described above, since extracellular fluid is supersaturated with respect to HAP, it is not surprising that deposition takes place ubiquitously in the human body. However deposition in unsuitable areas is strictly controlled so that hard tissues are formed properly. For example, acidic biomolecules inhibit deposition of calcium phosphate in vitro. Acidic functional groups such as phosphoryl, carboxyl, and sulfate groups bind and chelate calcium ions, which reduce the concentration of calcium ions and the degree of supersaturation in body fluids. For example, the C-terminus of amelogenin, which is expressed in the early stage of enamel development, is proteolytically cleaved resulting in a P148 protein consisting of 148 amino acid residues [35, 36]. P148 is a major component of the organic matrix in enamel; it inhibits the deposition of ACP when it is phosphorylated [37].

One detailed mechanism of the inhibitory effects of the deposition of calcium phosphate has been proposed. DMP1, an acidic protein with a molecular weight of 50,000, is a SIBLING protein. Like many other proteins involved in biomineralization, DMP1 does not have an ordered backbone conformation [38]. However, in the presence of Ca^{2+}, a secondary structure suitable for self-assembly is formed. In this formation, the proteins aggregate into microfibrils [39]. Atomic force microscope (AFM) and transmission electron microscope (TEM) measurements revealed that complexes were formed by the combining of DMP1 oligomers and calcium phosphate particles. DMP1 oligomers were shown to inhibit mineral deposition, apparently by binding to the mineral particles and sequestering them from the external solution [40]. DMP1 has the ability to bind collagen, and, in the presence of collagen, accelerates HAP crystal formation [41]. On the basis of several observations, He et al. proposed a model in which DMP1 oligomers bind to calcium phosphate particles, thereby preventing nonspecific deposition. DMP1 binds to suitable areas of the collagen fiber in the extracellular matrix and induces calcification at specific sites (Fig. 4.1, [40]).

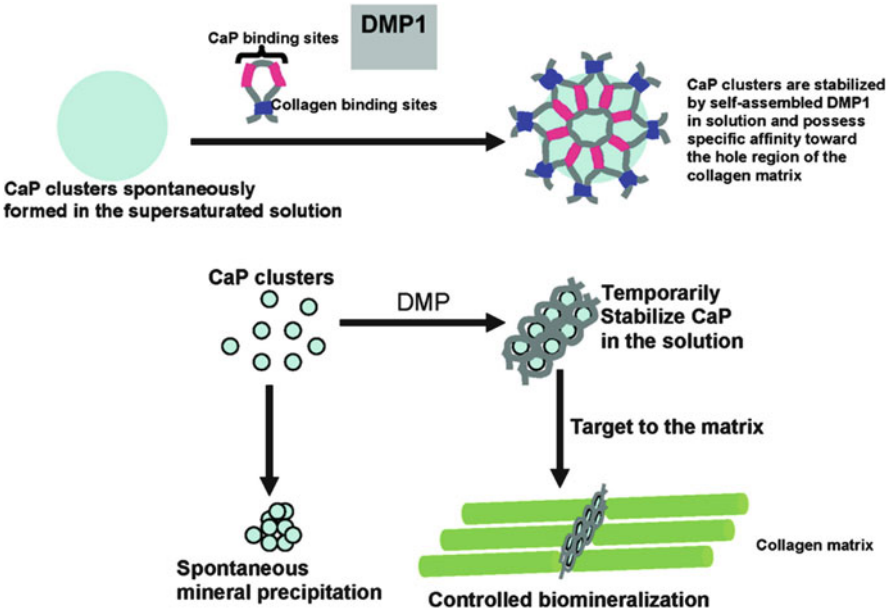

Fig. 4.1 Proposed function of DMP1. DMP1 self-assembles to the oligomeric state and inhibits spontaneous precipitation by sequestering calcium phosphate clusters from external solution. Binding of the protein to collagen fibers promotes nucleation of apatite in the matrix. Reprinted with permission from [40]. (Copyright 2005, American Chemical Society)

In addition to hard tissues such as bone and teeth, body fluids including saliva, milk, and urine are supersaturated with respect to HAP. When calcification occurs in blood vessels, it causes arteriosclerosis. Therefore, a mechanism to prevent calcium phosphate deposition in body fluid is needed for soft tissues. Fetuin forms a complex with calcium phosphate, which prevents mineral deposition [42, 43]. In milk, casein and osteopontin form a complex with calcium phosphate and further form micelles, resulting in prevention of mineral deposition in serum. In vitro experiments using a phosphorylated form of a 25 amino acid peptide, derived from the casein sequence, showed that ACP clusters with a radius of 2.4 nm were covered by peptide molecules with a thickness of 1.6 nm [44, 45]. A phosphorylated form of an osteopontin-derived peptide also binds to ACP clusters, forming a complex that prevents calcium phosphate precipitation [46].

In some cases, deposition of ACP is promoted. Poly-lysine and poly-glutamic acid (basic and acidic polymers with an isoelectric point (p*I*) of 10.5 and 4.9, respectively) were added to a calcium phosphate solution supersaturated with respect to ACP. Deposition of ACP was accelerated at a low concentration of either polymer, and deposition was delayed at a high concentration. Although the detailed molecular mechanisms of this acceleration and inhibition is are unknown, it was found that, regardless of negative or positive charge, mineral deposition is either accelerated or inhibited in a dose-dependent manner regardless of the polymer's charge [47].

4.4 Controlling Nucleation and Aggregation of HAP or OCP

Mouse amelogenin (composed of 179 amino acids), which is involved in enamel formation, was expressed in *Escherichia coli* using a recombinant DNA technique. When recombinant mouse amelogenin (rM179) was mixed in a calcium phosphate solution, which is supersaturated with respect to HAP and OCP, OCP formation was accelerated [48]. Nucleation of crystals occurs when the thermodynamic driving force of the crystal phase overcomes the negative effect of the surface free energy of small particles. If a part of the atomic arrangement of rM179 is complementary to the OCP crystal faces, the binding of rM179 to calcium phosphate particles reduces the surface free energy of the particles, which induces heterogeneous nucleation of the OCP. This heterogeneous nucleation apparently accelerates OCP precipitation. The amount of OCP precipitated depends on the rM179 concentration. The maximum amount of OCP was precipitated at an rM179 concentration of 6.5 μg/mL, and OCP deposition decreased as the rM179 concentration was increased. This was explained as follows: an increased amount of rM179 results in more binding of calcium and phosphate ions to the protein, which reduces the degree of solution supersaturation.

Moreover, rM179 not only accelerates nucleation but also regulates the assembly of HAP crystals. To investigate the function of the charged C-terminal domain of amelogenin, Beniash et al. generated rM166, which lacks the C-terminal domain of rM179. Crystallization experiments were performed in the presence of these proteins, and the properties of the resultant crystals were compared [49]. The HAP crystals that formed in the presence of rM179 were bundle-like aggregates aligned with the *c*-axis and were organized in a manner similar to the HAP in enamel. Those that formed in the presence of rM166 assembled into aggregates with a random orientation. This indicates that the C-terminal domain of amelogenin is essential for ordered assembly of HAP crystals. When pre-aggregated amelogenin was added to supersaturated solution, The HAP crystals aggregated with a random orientation, and aggregates aligned along the *c*-axis were not obtained. This suggests that the self-assembly of amelogenin and the organization of HAP crystals proceed in a cooperative manner.

Wang et al. expressed full-length recombinant porcine amelogenin (rP172) in *E. coli* and investigated the effect of the protein on crystallization and crystalline calcium phosphate aggregation. Spherical aggregates of OCP crystals were formed in the absence of rP172, and HAP crystal aggregates aligned along the *c*-axis formed in its presence. The induction time for nucleation decreased as the concentration of amelogenin was increased (measured in the concentration range of 0.5–5.0 μg/mL; maximum acceleration took place at 5 μg/mL).

In addition to the decreased induction time for nucleation, HAP and not OCP was obtained, suggesting the presence of structural matching at the interface between atomic arrangements of the amelogenin surface and HAP crystal faces ([50]; A role of amelogenin proposed by Wang et al. was also described in Sect. 5.4.4 in Chap. 5). This suggestion is based on the theory that the nucleation energy barrier decreases

and the HAP nucleation rate increases when structural matching between HAP and amelogenin takes place. It has been proposed that aligned crystals tend to be formed more often at a lower degree of supersaturation [51, 52].

A future objective is to elucidate the effect of amelogenin on the aggregation of HAP crystals aligned along the *c*-axis. Yang et al. proposed a model regarding the interaction between amelogenin and nanoclusters of calcium phosphate [53]. This model will be described in detail in Chap. 5.

As described above, Tarasevich et al. accelerated OCP deposition using mouse amelogenin, while Wang et al. formed HAP using porcine amelogenin under supersaturated conditions with respect to both HAP and OCP. In both cases, amelogenin-induced heterogeneous nucleation accelerated crystallization. Does mouse amelogenin structurally match OCP, whereas porcine amelogenin structurally matches HAP? Why did porcine amelogenin fail to form HAP deposits? And why did mouse amelogenin fail to form OCP deposits? To understand the template effect of the proteins, it is necessary to analyze the effect of various protein templates under uniform experimental conditions.

4.5 Controlling Crystal Growth

As described in Chap. 3, by analyzing step velocities on the growing crystal face in the presence or absence of different proteins, the effect of these proteins on crystal growth can be quantitatively evaluated. However, such an attempt has not been achieved with HAP. In this section, we describe the effect of amino acids, peptides, and proteins on the growth of calcite, one of the crystal phases of calcium carbonate.

In general, when an impurity adsorbs to a crystal surface, the incorporation of the crystal unit at the kinked site is inhibited, and the growth of the crystal face is slowed. It was found, however, that acidic proteins extracted from pearl layers of abalone, APα and APβ, accelerated crystal growth. Although these proteins were originally extracted from aragonite layers, their effects on the crystal growth were investigated using calcite (104) surface [54].

Elhadj et al. focused on aspartic acid residues in acidic proteins, and quantitatively analyzed the effects of aspartic acid polypeptides (monomers to hexamers (Asp1, Asp2, Asp3, Asp4, Asp5, Asp6)) on crystal growth of the calcite surface by using AFM [55]. The calcite (104) surface consisted of an acute step and an obtuse step, and the step velocities were increased in the presence of peptides. Peptides containing a large number of aspartic acid residues resulted in increased acceleration of crystal growth, and the effect was dose dependent. All peptides accelerated crystal growth at a concentration of less than 1 μM, and inhibited growth at high concentrations. Interestingly, each peptide exhibited step specificity for the acceleration. The growth of the acute step was affected by Asp1 and Asp2, and that of the obtuse step was affected by Asp3 to Asp6. The interaction between calcium atoms and peptides on the calcite surface indicates that the interaction between Asp3

to Asp6 and the acute step is strong, so these peptides should accelerate the velocity of the acute step preferentially. However, when the crystal unit is incorporated into the crystal surface, the structured water that binds to the crystal surface and crystal unit must be removed. Calculations using a semi-empirical quantum mechanical model revealed that when Asp3 to Asp6 is used, more water molecules on the crystal surface at the acute step must be removed**.** This indicates that they more effectively accelerate growth in the obtuse step.

Elhadj et al. also analyzed the effect of various Asp-containing peptides and proteins on the step velocity of a growing calcite face (104) [56]. Growth was accelerated with all molecules at low concentrations (Fig. 4.2). Examination of the acceleration rate and net molecular charge of the individual peptides revealed a clear correlation between the degree of net molecular charge and the crystal growth rate; however, the correlation was not perfect. For example, the AP7-N (aragonitic protein N-terminal domain molecular weight 7 kDa; [57]), which contains many hydrophobic amino acids, deviates from this correlation. This indicates that, in addition to the net molecular charge, the degree of hydrophilicity and hydrophobicity of the additives also affects the crystal growth rate. In fact, when the hydrophilicity–hydrophobicity of peptides used for the experiment was measured and compared with the crystal growth rate, a clear correlation was obtained. The hydrophilic molecules apparently enhanced the dehydration of the crystal face and crystal unit and thereby accelerated crystal growth.

Osteopontin is involved in the crystal growth of calcium oxalate monohydrate (COM) as well as of HAP [58]. COM is a component of kidney stones. Since urine is supersaturated with respect to COM, kidney stones are formed if COM deposition and kidney stone growth are not regulated. Osteopontin is one of the proteins that possess this inhibitory function. Grohe et al. derived peptide-containing phosphorylated serines and acidic amino acids (pSHEpSTEQSDAIDpSAEK) from the osteopontin sequence and prepared three synthetic peptides—one with three phosphates (P3), one with one phosphate (P1), and one with no phosphates (P0)—and investigated their interaction with COM [59]. All three peptides adsorbed to the COM (100) surface and inhibited crystal growth, with stronger inhibitory effects seen as the number of phosphates increased. Simulation using molecular dynamics showed that the binding to the (100) surface was achieved in the order of P3, P1, and P0. The Asp-12 and Glu-15 of the C-terminus of the P0 peptide were separated from the crystal surface upon binding. The P1 peptide as a whole was close to the crystal surface; however, amino acids from Gln-7 to Asp-12 in the middle of the peptide were slightly distant from the surface. All amino acids in the P3 peptide were close to the crystal surface. The amino acids in the P1 and P3 peptides closest to the crystal surface were aspartic acids and glutamic acids, but not phosphorylated serines. Grohe et al. suggested that the phosphate group has the ability to stabilize the interaction of crystals and peptides by drawing entire peptide molecules to the crystal surface [59]. When crystals were grown in the presence of P3 and P1 peptides, the COM crystal morphology was transformed into a dumbbell shape. P0 does not affect the morphology [60].

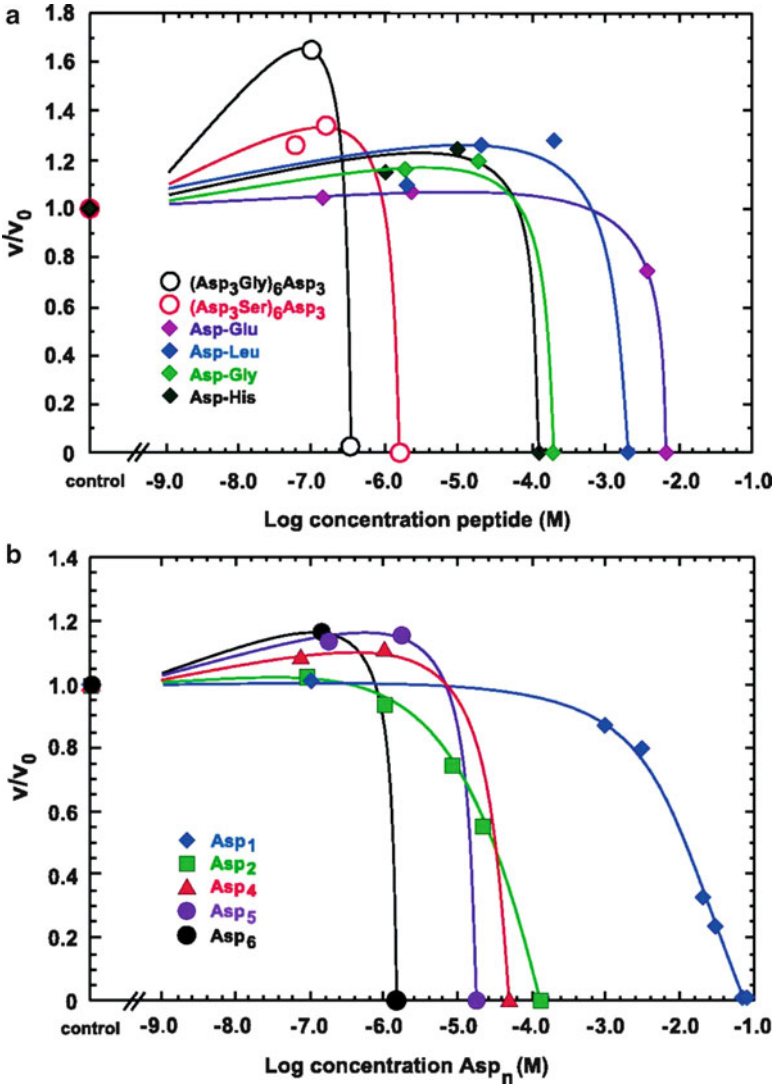

Fig. 4.2 Effects of Asp-containing peptides at different concentrations on obtuse step velocity on calcite (104) face. Dipeptides and 27-mer peptides (a) and aspartic acids of increasing molecular size (b) were used. v and v0 are step velocities in presence and absence of peptides, respectively. Reprinted with permission from [56]. (Copyright 2006, National Academy of Sciences of the United States of America)

Analysis of the interaction of COM and full length osteopontin was also performed [61]. Osteopontin obtained from cow's milk (mOPN) contains 25 phosphorylated residues, whereas osteopontin from rat's bone (bOPN) contains 10 phosphorylated residues. The binding effects to COM of these phosphorylated

proteins, as well as recombinant rat osteopontin (rOPN) lacking phosphate residues, were compared. All three OPN proteins adsorbed to the edge of the (100) and (121) surfaces of the COM crystals. However, only the mOPN and bOPN changed the crystal morphology to a dumbbell shape. The rOPN lacked this morphological transforming ability.

The attachment of mOPN and bOPN to the COM crystal surface was investigated in detail [62]. The adsorption of mOPN was more specific to the (100) surface. Since the (100) surface of COM is the richest surface in terms of calcium atoms [63], Langdon concluded, on the basis of the electrostatic interaction between phosphate residues of OPN and calcium ions on the crystal surface, that the adsorption of phosphorylated OPN is not due to the specific structure defined by the amino acid sequence but to a non-specific interaction [62].

The interaction of amelogenin to a specific crystal surface of OCP has been studied [64, 65] and is described in Chap. 5.

4.6 Controlling Transformation

He et al. examined the change in the mineral phase during HAP formation with DMP1 and identified the peptide sequences in DMP1 particularly important for HAP crystal formation. When DMP1 adsorbed to a glass plate was placed in a calcium phosphate solution, ACP precipitated on the glass plate and then transformed into HAP. In a control experiment with bovine serum albumin adsorbed to the glass plate, HAP crystal formation was not observed under the same conditions although a small amount of ACP precipitated. He et al. further found that HAP crystal formation accelerated when two peptides derived from DMP1 (ESQES and QESQSEQDS) were adsorbed to the glass plate, as seen with DMP1 [39]. However, the mechanism of HAP crystal formation promoted by the protein or peptides was not determined. Tsuji et al. used the same two peptides and applied the experiments to elucidate the mechanism of HAP crystal formation promoted by proteins containing the peptide sequences [66].

The time-resolved static light scattering (TR-SLS) measurement technique developed by Onuma et al. is an excellent method for analyzing the crystallization of small particles freely diffused in solution [67]. This technique enables real-time analysis of the apparent molecular mass, gyration radius, and fractal dimension (an index of the inner structure ordering) of calcium phosphate particles. However, although DMP1 and peptides ESQES and QESQSEQDS accelerate crystal formation when they are adsorbed to insoluble matrices such as collagen or a glass plate [38, 39], they do not accelerate crystal formation when they are present in a free form [40]. Thus, the mechanism of HAP crystal formation induced by DMP1 and these peptides cannot be analyzed using TR-SLS measurement.

Therefore, an attempt was made to synthesize proteins that can accelerate HAP crystal formation without immobilization. In general, there are strict limitations on the design and production of proteins with a desired function using only

knowledge of the structure–function relationship. Since current knowledge on the structure–function relationship of proteins is incomplete, it is more practical to take a combinatorial approach [68–70]. Using a motif programming method [71], Tsuji et al. generated a combinatorial library of proteins containing peptides ESQES and QESQSEQDS in various numbers and different orders. Eighteen genes were synthesized in vitro, expressed in *E. coli*, and purified using affinity chromatography. Proteins with the ability to accelerate HAP crystal formation without immobilization were then identified. A calcium phosphate solution with an adjusted pH of 7.4 did not produce deposits within a 10-day reaction time. Adding 1.6 μg/mL of artificial protein (#64) led to the formation of spherical aggregates of OCP within 5 days. In crystallization experiments using supersaturated solution with a high pH (8.0), #64 protein accelerated HAP crystal formation. The process of HAP crystal formation in the presence of #64 protein was analyzed using TR-SLS measurements [66].

As a control, a crystallization experiment was performed in the absence of the protein. Upon mixing of phosphate and calcium solutions, particles with a gyration radius of 350 nm soon formed. The fractal dimension of the initial phase was small (1.8). TEM analysis showed that the particles had a rounded morphology, and only a diffusive ring was observed by selected area electron diffraction (SAED), indicating that the initial particles were ACP. The initial state was maintained for 90 min. After additional time had elapsed, the apparent molecular mass, gyration radius, and fractal dimension increased simultaneously, and HAP crystal formation occurred. In the presence of protein #64 (1 μg/mL), the initial particles were ACP with a gyration radius of 350 nm, similar to that of those obtained in the absence of the protein. In contrast to a situation on a control experiment, the apparent molecular mass and fractal dimension increased after 80 min, and HAP crystal formation was achieved.

It is important to note the differences in the transformation mechanisms. While the apparent molecular mass, gyration radius, and fractal dimension increased simultaneously in the absence of the protein, only the apparent molecular mass and fractal dimension increased and the gyration radius remained unchanged in the presence of the protein (Fig. 4.3). This indicates that, in the presence of the protein, ACP particles are transformed into crystals without a change in their size. In other words, the rearrangement of atoms or clusters takes place within the ACP particles during their transformation to HAP crystals. This transformation mechanism is known as direct transformation [67]. During the transformation process of ACP to HAP, artificial proteins containing peptide sequences derived from DMP1, as designed by the motif programming method, accelerate HAP crystal formation by altering the mode of the transformation to direct transformation [66].

Is direct transformation actually taking place inside the body? Beniash et al. studied enamel formation in mouse incisor [11]. They found that different developmental stages exist in different areas simultaneously, so it is suitable to identify the mineral phase at each developmental stage. When enamel was stained with toluidine blue dye, the staining pattern of the immature outer enamel differed

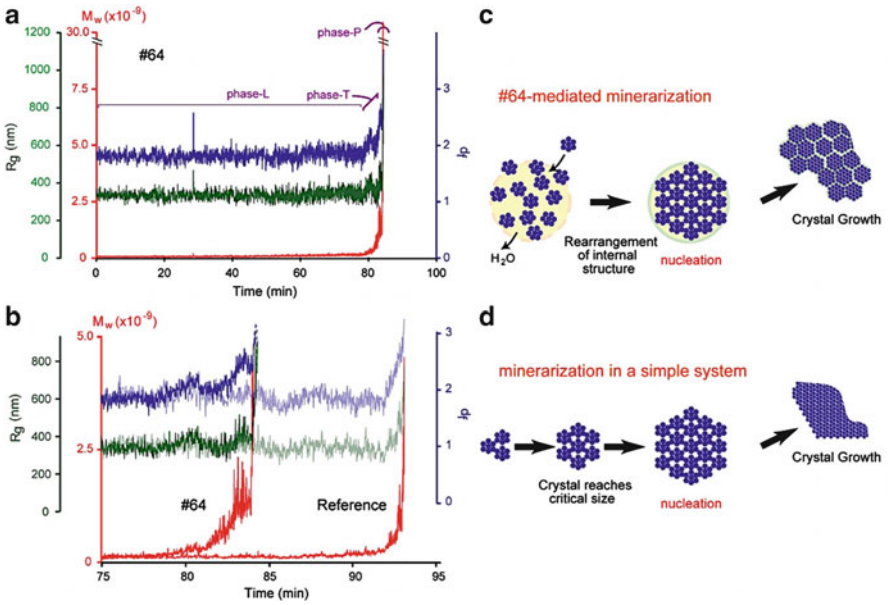

Fig. 4.3 Results of TR-SLS measurement of calcium phosphate formation. (a) Time-dependent changes in calculated apparent molecular mass (M_w, red), gyration radius (R_g, green), and fractal dimension (d_f, blue) of calcium phosphate in presence of artificial protein (#64, 1 μg/mL). Phase L (latency) was followed by phase T (transformation), and phase P (precipitation). (b) Enlargement corresponding to 75–95 min in (a). For comparison, the data obtained in the absence of #64 are shown in light colors. (c and d) Schematic representations of HAP mineralization via direct transformation mediated by a protein (c) and in a simple system (d). Reprinted with permission from [66]. (Copyright 2008, National Academy of Sciences of the United States of America)

from that of the mature inner enamel. This was attributed to the compositional differences between the organic substances in the various areas resulting from protein degradation during the enamel maturation process [72].

Observation of these areas using polarizing microscopy revealed birefringence only in the inner area. In other words, immature outer enamel does not contain crystals. Observation of sections from these areas by TEM revealed needle-shaped mineral crystallites arranged in parallel arrays, the typical morphology of enamel. The crystallites were several nm thick, 20 nm wide, and several hundred nm long, and there was no significant variation in their shape or size. There was, however, a significant difference in their patterns of electron diffraction. Those in the inner area showed 002, 004, 112, and 311 diffraction patterns, which are characteristic for HAP, whereas those in the outer area exhibited a broad ring, which is a typical pattern for ACP. In other words, the degree of crystallization differed between the inner and outer areas although the sizes and morphologies of the crystallites were similar. This suggests that transformation from ACP to HAP is not caused

by the growth of particles. Rather, the inner area minerals were crystallized by rearrangement of the atoms or clusters inside the particles [11]. This means that the apatite of enamel is formed from ACP by direct transformation.

The artificial protein used in the TR-SLS experiment by Tsuji et al. contained peptide motifs derived from DMP1. These motifs are expressed in bone and dentin but not in enamel. It would be of interest to examine the mode of crystallization by using the TR-SLS measurement technique and an enamel-specific protein such as amelogenin. As described in the previous section, amelogenin, unlike DMP1, induces HAP deposits without immobilization. This means that it can be simply applied to SLS measurements. It would also be worthwhile to obtain information on the crystallization of bone and dentin through in vivo observations.

An important study by Beniash et al. found that, not only the size and shape, but also a high level of structural organization is formed before the phase transformation from ACP to HAP [11]. This suggests that the body possesses mechanisms for constructing hierarchical structures by controlling the organization of ACP particles.

Tao et al. observed that organic molecules can control the hierarchical assembly of HAP by using ACP particles as building blocks [73]. HAP is formed by mixing calcium and phosphate ions in the presence of poly(acrylic acid) (PAA). Under these conditions, HAP spheres measuring 5 nm in diameter were formed. The PAA enables apatite spheres to stably exist without growing or assembling. High-resolution transmission electron microscope (TR-TEM) observation revealed that these particles consist of a 5 nm HAP core and an ACP shell. When the PAA was removed, the HAP particles formed colloidal aggregates. Even under colloidal conditions, the layered structure of the HAP core and ACP shell was maintained, and the particles were linked via ACP regions. SAED showed diffraction rings, meaning that the particles were nanocrystalline aggregates packed with a random orientation. The aggregates were 30 nm in size. When colloidal particles were dispersed in water in the presence of biological additives, they re-assembled into highly ordered structures. Needle-shaped single crystals and plate-like single crystals formed in the presence of Gly (glycine) and Glu (glutamic acid), respectively.

These structures are formed in the following manner. In the presence of Gly, core-shell aggregates line up. These aggregates are connected by ACP. At this stage, the direction of the HAP core of each aggregate is random. Since ACP is unstable and is transformed into HAP, the structures of connected regions of the aggregates shift from HAP-ACP-HAP to HAP-HAP-HAP. Since ACP has a fluid-like character, the HAP core within the ACP shell can rotate into the most stable orientation. Simultaneous rotation of the HAP core and transformation from ACP to HAP at the junction site results in alignment of adjacent HAP, which stabilizes the overall structure. Aggregates of nanospheres with the same orientation are thereby formed and become needle-like single crystals of HAP. This formation of needle-like single crystals takes approximately 10 days. Because the crystals are still surrounded by an ACP shell, they aggregate further. Thus, micrometer-sized HAP crystals resembling enamel HAP crystals are formed. The formation of the HAP crystals takes approximately 2 months.

A similar high level of organization was seen in the presence of amelogenin as well. Surprisingly, while 2 months were required to form this high level of organization in the presence of Gly, the process completed in only 3 days in the presence of amelogenin. This accelerated formation of needle-like aggregates of HAP crystals parallel to the *c*-axis mediated by amelogenin was reported by several groups [49, 50, 53]. This characteristic of amelogenin was confirmed in an experiment using HAP core-ACP shell particles.

On the other hand, in the presence of a Glu, HAP core—ACP shell particles were seen to reorganize into a different type of hierarchical structure and form a plate-like single crystal with a large surface (0001), which resembled the HAP crystals found in bone. In a control experiment, no highly organized structure was formed even with the addition of Glu, Gly, or amelogenin when pure HAP crystal particles without an ACP shell were used.

Although several experiments showed crystal formation due to the aggregation of nanocrystals [73, 74], the one by Tao et al. showed something particularly important: ACP connects HAP at the different crystal surfaces and forms various hierarchical structures depending on the condition of various biomolecules. Biomolecules added to the reaction determine the assembly orientation of the nanocrystals and accelerate the aggregation and transformation.

The role of Gly and Glu in the control of the morphology of nanocrystal aggregates was clarified using molecular dynamics simulation. The interfacial energies of the (0001) face and the $(1\bar{1}00)$ face of HAP in water are similar. The effects of Gly and Glu adsorption on these faces on their interfacial energies were examined. Adding Gly markedly raised the energy of the (0001) face and slightly reduced that of the $(1\bar{1}00)$ one. Thus, HAP (0001) faces become unstable in Gly solution, resulting in packing on the (0001) face and formation of a hierarchical structure along the *c*-axis. In contrast, simulation showed that the (0001) face is significantly stabilized by Glu while the $(1\bar{1}00)$ face is not affected. This indicates that packing takes place at the $(1\bar{1}00)$ face, resulting in aggregation along the axis vertical to the *c*-axis, with preferential formation of a plate-like superstructure. The simulation results explain the experimental observations, i.e., formation of needle-like HAP crystals and plate-like HAP crystals with Gly and Glu, respectively (Fig. 4.4).

4.7 Controlling Mineralization with Artificial Proteins and Peptides

An important molecular biological method is display technology. Typical display technologies include phage display [75], cell surface display [76], ribosome display [77], and mRNA display [78, 79]. Among these, phage display and cell surface display have been widely used and have been applied to inorganic materials [80]. A phage is a virus that infects *E. coli* and has a structure in which its genome is

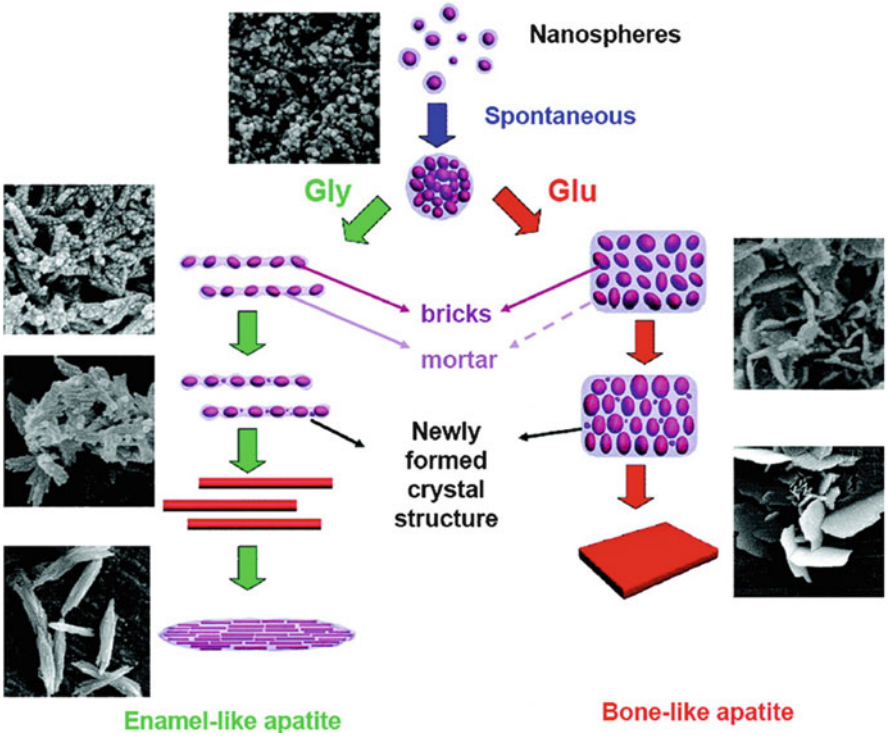

Fig. 4.4 Model of hierarchical assembly of apatite nanocrystals mediated by glycine and glutamic acid. Nanocrystals consisting of HAP core (purple) and ACP shell (light blue) aggregated spontaneously and were dispersed in water. In the presence of indicated amino acids, nanocrystals reassembled into different hierarchical structures. One-dimensional linear assemblies and two-dimensional plate-like structures were formed in the presence of Gly and Glu, respectively. Nanocrystals were connected by ACP surrounding HAP core. ACP transformed into thermodynamically stable HAP, and, at the same time, HAP core rotated to the most stable orientation. As a result, each HAP domain had the same crystallographic orientation and fused into single crystals. Reprinted with permission from [73]. (Copyright 2007, American Chemical Society)

encapsulated within a membrane consisting of proteins. When a gene encoding an artificial peptide is inserted into a gene encoding a membrane protein using recombinant DNA technology, a chimeric protein consisting of the membrane protein and the peptide is synthesized and displayed on the surface of the phage. If the artificial peptide has the ability to bind to the target compound, the phage will also be able to bind to that compound.

DNA sequences encoding 12–16 amino acids are usually inserted into a membrane protein gene. In a typical experiment, up to 10^9 phages displaying 10^9 different peptide sequences can be used. First, 10^9 phages and the target compound are mixed together. Phages that have affinity to the target compound are recovered using an affinity chromatography-like technique. The recovered phages are infected

with *E. coli* and propagated. Their DNA and peptide sequences are then determined. The concept of cell surface display is essentially the same. Cells bound to the target compound are collected and propagated, and genes encoding the peptides with binding activity are obtained.

Although display technology is commonly used in the molecular biological field for identifying the interaction of biomacromolecules such as proteins and/or peptides, it has also been used to recover peptides that bind to gold. Brown, for example, used cell surface display to recover peptides that bind to gold and showed that such peptides can be used to control gold crystal formation [81, 82]. Since then, display technology has been applied to research in the field of material science and used to synthesize semiconductor crystals [80, 83–85]. Mao et al. successfully fabricate zinc blende and Wurtzite ZnS crystal systems using two kinds of artificial peptides. The zinc blends structure was obtained in the presence of a peptide, and the Wurtzite ZnS structure was obtained in the presence of another peptide.

Peptides that bind to HAP have been isolated using phage display. Gungormus et al. used it for crystallization experiments in which two artificial peptides, a HAP strong-binding peptide (HABP1, CMLPHHGAC) and a HAP weak-binding peptide (HABP2, CNPGFAQAC), were added to supersaturated solutions with respect to HAP and OCP. Only OCP was obtained in the presence of both peptides. Both peptides delayed OCP formation, with more drastic effects seen in the presence of HABP1. The OCP crystals obtained in the presence of HABP1 were significantly larger than those obtained in the presence of HABP2 [86].

Roy et al. used phage display to isolate a peptide that binds to HAP [87]. The peptide contained the amino acid sequence SVSVGMKPSPRP. It bound efficiently to HAP, but did not bind to ACP or calcium carbonate, indicating that the peptide recognize HAP-specific atomic sequences, and not calcium or phosphate ion ones. Roy et al. showed that the peptide modified with fluorescent dye can be used for imaging teeth. The use of this technology should make it possible to analyze the processes of bone and teeth development with high sensitivity in vivo.

A peptide that can bind to titanium, commonly used for artificial bone, was isolated using phage display [88]. Although titanium has good biocompatibility, it does not bind to bone directly. Therefore, patients receiving a titanium implant are generally obliged to restrict mastication for several weeks until tight adhesion between the implant and surrounding bone is established. To overcome this problem, methods to accelerate the adhesion process have been investigated. Bone is synthesized by osteoblasts, and bone morphological protein 2 (BMP2) induces differentiation of premyoblastic cells into the osteoblastic state. Therefore, it may be possible that BMP2 immobilized on a titanium substrate induces cell differentiation into osteoblastic state, which promotes tight adhesion between the titanium substrate and surrounding bone. However, when BMP2 is directly attached to a titanium surface, it becomes inactivate due to inappropriate interaction between the protein and titanium surface. To overcome this problem, an artificial protein that binds tightly to titanium was constructed using the titanium binding peptide as a building block. The artificial protein was fused to BMP2, and the BMP2 was attached to a

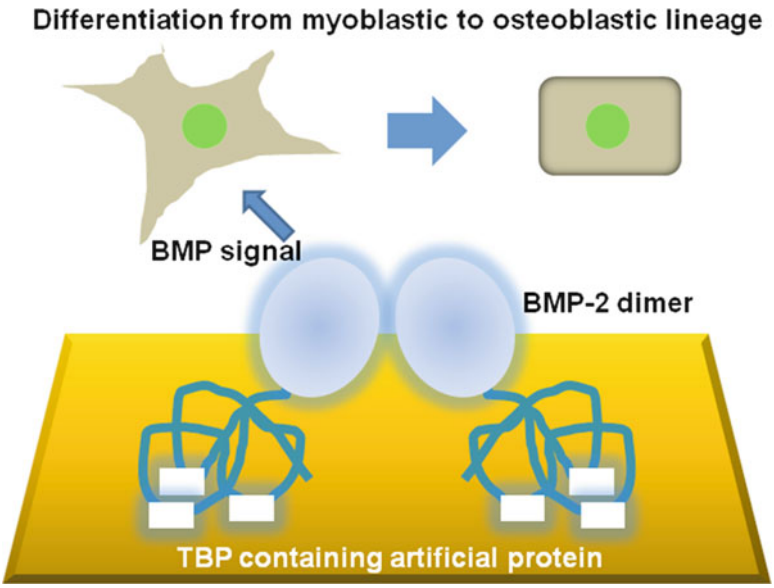

Fig. 4.5 BMP2 fused to artificial proteins containing titanium binding peptides were immobilized on titanium surface. Artificial proteins could associate with titanium surface in a reversible manner, enabling them to be BMP2 with an active state. Reprinted with permission from [89]. (Copyright 2009, Elsevier)

titanium surface using the artificial protein. Indeed, Kashiwagi et al. observed BMP-induced differentiation of osteoblastic cells when myoblastic cells were cultivated on a BMP2-modified titanium surface (Fig. 4.5, [89]).

Tsuji et al. created an artificial protein by combining DMP1-derived peptides and a titanium-binding peptide. The resulting protein showed bifunctionality—titanium binding activity and nucleation activity of crystalline calcium phosphate-, and could be used for coating of a titanium surface with OCP film under biologically relevant conditions [90]. The use of OCP coated titanium for implants would accelerate adhesion between the implants and surrounding bone.

4.8 Closing Remarks

In this chapter, we summarized the results of various research studies pertaining to biomineralization related to HAP crystal formation from the viewpoint of protein science and protein engineering. The utilization of protein and peptide engineering technology should make it possible to control biomineralization at the molecular as well as at the cellular level. Additional proteins with the capability of controlling or affecting biomineralization will likely be constructed. Understanding

the mechanisms of such proteins in detail is important for using them to produce structures with a higher level of organization. Combining technologies for protein structure and dynamics analysis, protein and peptide engineering, and crystal growth analysis will deepen our understanding of biomineralization.

References

1. LeGeros, R.Z.: Calcium phosphate-based osteoinductive materials. Chem. Rev. **108**, 4742–4753 (2008)
2. George, A., Veis, A.: Phosphorylated proteins and control over apatite nucleation, crystal growth, and inhibition. Chem. Rev. **108**, 4670–4693 (2008)
3. Fincham, A.G., Moradian-Oldak, J., Simmer, J.P.: The structural biology of the developing dental enamel matrix. J. Struct. Biol. **126**, 270–299 (1999)
4. Smith, C.E.: Cellular and chemical events during enamel maturation. Crit. Rev. Oral Biol. Med. **9**, 128–161 (1998)
5. Habelitz, S., Marshall, S.J., Marshall Jr., G.W., Balooch, M.: Mechanical properties of human dental enamel on the nanometer scale. Arch. Oral Biol. **46**, 173–183 (2001)
6. Rho, J.-Y., Tsui, T.Y., Pharr, G.M.: Elastic properties of human cortical and trabecular lamellar bone measured by nanoindentation. Biomaterials **18**, 1325–1330 (1997)
7. Giannini, M., Soares, C.J., de Carvalho, R.M.: Ultimate tensile strength of tooth structures. Dent. Mater. **20**, 322–329 (2004)
8. Bayraktar, H.H., Morgan, E.F., Niebur, G.L., Morris, G.E., Wong, E.K., Keaveny, T.M.: Comparison of the elastic and yield properties of human femoral trabecular and cortical bone tissue. J. Biomech. **37**, 27–35 (2004)
9. Gower, L.B.: Biomimetic model system for investigating the amorphous precursor pathway and its role in biomineralization. Chem. Rev. **108**, 4551–4627 (2008)
10. Mahamid, J., Sharir, A., Addadi, L., Weiner, S.: Amorphous calcium phosphate is a major component of the forming fin bones of zebrafish: Indications for an amorphous precursor phase. Proc. Natl. Acad. Sci. U.S.A. **105**, 12748–12753 (2008)
11. Beniash, E., Metzler, R.A., Lam, R.S., Gilbert, P.U.: Transient amorphous calcium phosphate in forming enamel. J. Struct. Biol. **166**, 133–143 (2009)
12. Kadler, K.E., Holmes, D.F., Trotter, J.A., Chapman, J.A.: Collagen fibril formation. Biochem. J. **316**, 1–11 (1996)
13. Shoulders, M.D., Raines, R.T.: Collagen structure and stability. Annu. Rev. Biochem. **78**, 929–958 (2009)
14. Margolis, H.C., Beniash, E., Fowler, C.E.: Role of macromolecular assembly of enamel matrix proteins in enamel formation. J. Dent. Res. **85**, 775–793 (2006)
15. Delak, K., Harcup, C., Lakshminarayanan, R., Sun, Z., Fan, Y., Moradian-Oldak, J., Evans, J.S.: The tooth enamel protein, porcine amelogenin, is an intrinsically disordered protein with an extended molecular configuration in the monomeric form. Biochemistry **48**, 2272–2281 (2009)
16. Lakshminarayanan, R., Yoon, I., Hegde, B.G., Fan, D., Du, C., Moradian-Oldak, J.: Analysis of secondary structure and self-assembly of amelogenin by variable temperature circular dichroism and isothermal titration calorimetry. Proteins **76**, 560–569 (2009)
17. Moradian-Oldak, J., Du, C., Falini, G.: On the formation of amelogenin microribbons. Eur. J. Oral Sci. **114**, 289–296 (2006)
18. Huq, N.L., Cross, K.J., Ung, M., Reynolds, E.C.: A review of protein structure and gene organisation for proteins associated with mineralised tissue and calcium phosphate stabilisation encoded on human chromosome 4. Arch. Oral Biol. **50**, 599–609 (2005)

19. Fisher, L.W., Torchia, D.A., Fohr, B., Young, M.F., Fedarko, N.S.: Flexible structures of SIBLING proteins, bone sialoprotein, and osteopontin. Biochem. Biophys. Res. Commun. **280**, 460–465 (2001)
20. Bellahcène, A., Castronovo, V., Ogbureke, K.U., Fisher, L.W., Fedarko, N.S.: Small integrin-binding ligand N-linked glycoproteins (SIBLINGs): multifunctional proteins in cancer. Nat. Rev. Cancer **8**, 212–226 (2008)
21. Kawasaki, K., Weiss, K.M.: Mineralized tissue and vertebrate evolution: the secretory calcium-binding phosphoprotein gene cluster. Proc. Natl. Acad. Sci. U.S.A. **100**, 4060–4065 (2003)
22. Fisher, L.W., Fedarko, N.S.: Six genes expressed in bones and teeth encode the current members of the SIBLING family of proteins. Connect. Tissue Res. **44**(Suppl 1), 33–40 (2003)
23. Wright, P.E., Dyson, H.J.: Intrinsically unstructured proteins: re-assessing the protein structure-function paradigm. J. Mol. Biol. **293**, 321–331 (1999)
24. Ward, J.J., Sodhi, J.S., McGuffin, L.J., Buxton, B.F., Jones, D.T.: Prediction and functional analysis of native disorder in proteins from the three kingdoms of life. J. Mol. Biol. **337**, 635–645 (2004)
25. Radivojac, P., Iakoucheva, L.M., Oldfield, C.J., Obradovic, Z., Uversky, V.N., Dunker, A.K.: Intrinsic disorder and functional proteomics. Biophys. J. **92**, 1439–1456 (2007)
26. Romero, P.R., Zaidi, S., Fang, Y.Y., Uversky, V.N., Radivojac, P., Oldfield, C.J., Cortese, M.S., Sickmeier, M., LeGall, T., Obradovic, Z., Dunker, A.K.: Alternative splicing in concert with protein intrinsic disorder enables increased functional diversity in multicellular organisms. Proc. Natl. Acad. Sci. U.S.A. **103**, 8390–8395 (2006)
27. Liu, J., Faeder, J.R., Camacho, C.J.: Toward a quantitative theory of intrinsically disordered proteins and their function. Proc. Natl. Acad. Sci. U.S.A. **106**, 19819–19823 (2009)
28. Boehr, D.D., Nussinov, R., Wright, P.E.: The role of dynamic conformational ensembles in biomolecular recognition. Nat. Chem. Biol. **5**, 789–796 (2009)
29. Lange, O.F., Lakomek, N.A., Farès, C., Schröder, G.F., Walter, K.F., Becker, S., Meiler, J., Grubmüller, H., Griesinger, C., de Groot, B.L.: Recognition dynamics up to microseconds revealed from an RDC-derived ubiquitin ensemble in solution. Science **320**, 1471–1475 (2008)
30. Goobes, G., Goobes, R., Schueler-Furman, O., Baker, D., Stayton, P.S., Drobny, G.P.: Folding of the C-terminal bacterial binding domain in statherin upon adsorption onto hydroxyapatite crystals. Proc. Natl. Acad. Sci. U.S.A. **103**, 16083–16088 (2006)
31. Long, J.R., Dindot, J.L., Zebroski, H., Kiihne, S., Clark, R.H., Campbell, A.A., Stayton, P.S., Drobny, G.P.: A peptide that inhibits hydroxyapatite growth is in an extended conformation on the crystal surface. Proc. Natl. Acad. Sci. U.S.A. **95**, 12083–12087 (1998)
32. Goobes, R., Goobes, G., Shaw, W.J., Drobny, G.P., Campbell, C.T., Stayton, P.S.: Thermodynamic roles of basic amino acids in statherin recognition of hydroxyapatite. Biochemistry **46**, 4725–4733 (2007)
33. Long, J.R., Shaw, W.J., Stayton, P.S., Drobny, G.P.: Structure and dynamics of hydrated statherin on hydroxyapatite as determined by solid-state NMR. Biochemistry **40**, 15451–15455 (2001)
34. Schwartz, S.S., Hay, D.I., Schluckebier, S.K.: Inhibition of calcium phosphate precipitation by human salivary statherin: structure-activity relationships. Calcif. Tissue Int. **50**, 511–517 (1992)
35. Tanabe, T., Fukae, M., Uchida, T., Shimizu, M.: The localization and characterization of proteinases for the initial cleavage of porcine amelogenin. Calcif. Tissue Int. **51**, 213–217 (1992)
36. Yamakoshi, Y., Tanabe, T., Fukae, M., Shimizu, M.: Porcine amelogenins. Calcif. Tissue Int. **54**, 69–75 (1994)
37. Kwak, S.Y., Wiedemann-Bidlack, F.B., Beniash, E., Yamakoshi, Y., Simmer, J.P., Litman, A., Margolis, H.C.: Role of 20-kDa amelogenin (P148) phosphorylation in calcium phosphate formation in vitro. J. Biol. Chem. **284**, 18972–18979 (2009)
38. He, G., Dahl, T., Veis, A., George, A.: Dentin matrix protein 1 initiates hydroxyapatite formation in vitro. Connect. Tissue Res. **44**(Suppl 1), 240–245 (2003)
39. He, G., Dahl, T., Veis, A., George, A.: Nucleation of apatite crystals in vitro by self-assembled dentin matrix protein 1. Nat. Mater. **2**, 552–558 (2003)

40. He, G., Gajjeraman, S., Schultz, D., Cookson, D., Qin, C., Butler, W.T., Hao, J., George, A.: Spatially and temporally controlled biomineralization is facilitated by interaction between self-assembled dentin matrix protein 1 and calcium phosphate nuclei in solution. Biochemistry **44**, 16140–16148 (2005)
41. Gajjeraman, S., Narayanan, K., Hao, J., Qin, C., George, A.: Matrix macromolecules in hard tissues control the nucleation and hierarchical assembly of hydroxyapatite. J. Biol. Chem. **282**, 1193–1204 (2007)
42. Price, P.A., Lim, J.E.: The inhibition of calcium phosphate precipitation by fetuin is accompanied by the formation of a fetuin-mineral complex. J. Biol. Chem. **278**, 22144–22152 (2003)
43. Schafer, C., Heiss, A., Schwarz, A., Westenfeld, R., Ketteler, M., Floege, J., Muller-Esterl, W., Schinke, T., Jahnen-Dechent, W.: The serum protein alpha 2-Heremans-Schmid glycoprotein/fetuin-A is a systemically acting inhibitor of ectopic calcification. J. Clin. Invest. **112**, 357–366 (2003)
44. Holt, C., Wahlgren, N.M., Drakenberg, T.: Ability of a beta-casein phosphopeptide to modulate the precipitation of calcium phosphate by forming amorphous dicalcium phosphate nanoclusters. Biochem. J. **314**, 1035–1039 (1996)
45. Holt, C., Timmins, P.A., Errington, N., Leaver, J.: A core-shell model of calcium phosphate nanoclusters stabilized by beta-casein phosphopeptides, derived from sedimentation equilibrium and small-angle X-ray and neutron-scattering measurements. Eur. J. Biochem. **252**, 73–78 (1998)
46. Holt, C., Sørensen, E.S., Clegg, R.A.: Role of calcium phosphate nanoclusters in the control of calcification. FEBS J. **276**, 2308–2323 (2009)
47. Bar-Yosef Ofir, P., Govrin-Lippman, R., Garti, N., Furedi-Milhofer, H.: The influence of polyelectrolytes on the formation and phase transformation of amorphous calcium phosphate. Cryst. Growth Des. **4**, 177–183 (2004)
48. Tarasevich, B.J., Howarda, C.J., Larsona, J.L., Sneadb, M.L., Simmerc, J.P., Paineb, M., Shawa, W.J.: The nucleation and growth of calcium phosphate by amelogenin. J. Cryst. Growth **304**, 407–415 (2007)
49. Beniash, E., Simmer, J.P., Margolis, H.C.: The effect of recombinant mouse amelogenins on the formation and organization of hydroxyapatite crystals in vitro. J. Struct. Biol. **149**, 182–190 (2005)
50. Wang, L., Guan, X., Du, C., Moradian-Oldak, J., Nancollas, G.H.: Amelogenin promotes the formation of elongated apatite microstructures in a controlled crystallization system. J. Phys. Chem. C, Nanomater Interfaces **111**, 6398–6404 (2007)
51. Liu, X.Y., Lim, S.W.: Templating and supersaturation-driven anti-templating: principles of biomineral architecture. J. Am. Chem. Soc. **125**, 888–895 (2003)
52. Jiang, H., Liu, X.Y., Zhang, G., Li, Y.: Kinetics and template nucleation of self-assembled hydroxyapatite nanocrystallites by chondroitin sulfate. J. Biol. Chem. **280**, 42061–42066 (2005)
53. Yang, X., Wang, L., Qin, Y., Sun, Z., Henneman, Z.J., Moradian-Oldak, J., Nancollas, G.H.: How amelogenin orchestrates the organization of hierarchical elongated microstructures of apatite. J. Phys. Chem. B **114**, 2293–2300 (2010)
54. Fu, G., Qiu, S.R., Orme, C.A., Morse, D.E., De Yoreo, J.J.: Acceleration of calcite kinetics by abalone nacre proteins. Adv. Mater. **17**, 2678–2683 (2005)
55. Elhadj, S., Salter, E.A., Wierzbicki, A., De Yoreo, A.A., Han, N., Dove, P.M.: Peptide controls on calcite mineralization: polyaspartate chain length affects growth kinetics and acts as a stereochemical switch on morphology. Cryst. Growth Des. **6**, 197–201 (2006)
56. Elhadj, S., De Yoreo, J.J., Hoyer, J.R., Dove, P.M.: Role of molecular charge and hydrophilicity in regulating the kinetics of crystal growth. Proc. Natl. Acad. Sci. U.S.A. **103**, 19237–19242 (2006)
57. Michenfelder, M., Fu, G., Lawrence, C., Weaver, J.C., Wustman, B.A., Taranto, L., Evans, J.S., Morse, D.E.: Characterization of two molluscan crystal-modulating biomineralization proteins and identification of putative mineral binding domains. Biopolymers **70**, 522–533 (2003)

58. Qiu, S.R., Wierzbicki, A., Orme, C.A., Cody, A.M., Hoyer, J.R., Nancollas, G.H., Zepeda, S., De Yoreo, J.J.: Molecular modulation of calcium oxalate crystallization by osteopontin and citrate. Proc. Natl. Acad. Sci. U.S.A. **101**, 1811–1815 (2004)
59. Grohe, B., O'Young, J., Ionescu, D.A., Lajoie, G., Rogers, K.A., Karttunen, M., Goldberg, H.A., Hunter, G.K.: Control of calcium oxalate crystal growth by face-specific adsorption of an osteopontin phosphopeptide. J. Am. Chem. Soc. **129**, 14946–14951 (2007)
60. O'Young, J., Chirico, S., Al Tarhuni, N., Grohe, B., Karttunen, M., Goldberg, H.A., Hunter, G.K.: Phosphorylation of osteopontin peptides mediates adsorption to and incorporation into calcium oxalate crystals. Cells Tissues Organs **189**, 51–55 (2009)
61. Hunter, G.K., Grohe, B., Jeffrey, S., O'Young, J., Sørensen, E.S., Goldberg, H.A.: Role of phosphate groups in inhibition of calcium oxalate crystal growth by osteopontin. Cells Tissues Organs **189**, 44–50 (2009)
62. Langdon, A., Wignall, G.R., Rogers, K., Sørensen, E.S., Denstedt, J., Grohe, B., Goldberg, H.A., Hunter, G.K.: Kinetics of calcium oxalate crystal growth in the presence of osteopontin isoforms: an analysis by scanning confocal interference microcopy. Calcif. Tissue Int. **84**, 240–248 (2009)
63. Jung, T., Sheng, X., Choi, C.K., Kim, W.S., Wesson, J.A., Ward, M.D.: Probing crystallization of calcium oxalate monohydrate and the role of macromolecule additives with in situ atomic force microscopy. Langmuir **20**, 8587–8596 (2004)
64. Iijima, M., Moradian-Oldak, J.: Interactions of amelogenins with octacalcium phosphate crystal faces are dose dependent. Calcif. Tissue Int. **74**, 522–531 (2004)
65. Iijima, M., Moradian-Oldak, J.: Control of octacalcium phosphate and apatite crystal growth by amelogenin matrices. J. Mater. Chem. **14**, 2189–2199 (2004)
66. Tsuji, T., Onuma, K., Yamamoto, A., Iijima, M., Shiba, K.: Direct transformation from amorphous to crystalline calcium phosphate facilitated by motif-programmed artificial proteins. Proc. Natl. Acad. Sci. U.S.A. **105**, 16866–16870 (2008)
67. Onuma, K., Oyane, A., Tsutsui, K., Tanaka, K., Treboux, G., Kanzaki, N., Ito, A.: Precipitation kinetics of hydroxyapatite revealed by the continuous-angle laser light-scattering technique. J. Phys. Chem. B **104**, 10563–10568 (2000)
68. Tsuji, T., Onimaru, M., Yanagawa, H.: Towards the creation of novel proteins by block shuffling. Comb. Chem. High Throughput Screen. **9**, 259–269 (2006)
69. Shiba, K.: Molcraft a hierarchical approach to the synthesis of artificial proteins. J. Mol. Catal. B. **28**, 145–153 (2004)
70. Shiba, K.: Natural and artificial peptide motifs: their origins and the application of motif-programming. Chem. Soc. Rev. **39**, 117–126 (2009)
71. Saito, H., Honma, T., Minamisawa, T., Yamazaki, K., Noda, T., Yamori, T., Shiba, K.: Synthesis of functional proteins by mixing peptide motifs. Chem. Biol. **11**, 765–773 (2004)
72. Simmer, J.P., Hu, J.C.: Expression, structure, and function of enamel proteinases. Connect. Tissue Res. **43**, 441–449 (2002)
73. Tao, J., Pan, H., Zeng, Y., Xu, X., Tang, R.: Roles of amorphous calcium phosphate and biological additives in the assembly of hydroxyapatite nanoparticles. J. Phys. Chem. B **111**, 13410–13418 (2007)
74. Banfield, J.F., Welch, S.A., Zhang, H., Ebert, T.T., Penn, R.L.: Aggregation-based crystal growth and microstructure development in natural iron oxyhydroxide biomineralization products. Science **289**, 751–754 (2000)
75. Scott, J.K., Smith, G.P.: Searching for peptide ligands with an epitope library. Science **249**, 386–390 (1990)
76. Boder, E.T., Wittrup, K.D.: Yeast surface display for screening combinatorial polypeptide libraries. Nat. Biotechnol. **15**, 553–557 (1997)
77. Hanes, J., Plückthun, A.: In vitro selection and evolution of functional proteins by using ribosome display. Proc. Natl. Acad. Sci. U.S.A. **94**, 4937–4942 (1997)
78. Keefe, A.D., Szostak, J.W.: Functional proteins from a random-sequence library. Nature **410**, 715–718 (2001)

79. Tsuji, T., Onimaru, M., Doi, N., Miyamoto-Sato, E., Takashima, H., Yanagawa, H.: In vitro selection of GTP-binding proteins by block shuffling of estrogen-receptor fragments. Biochem. Biophys. Res. Commun. **390**, 689–693 (2009)
80. Sarikaya, M., Tamerler, C., Jen, A.K., Schulten, K., Baneyx, F.: Molecular biomimetics: nanotechnology through biology. Nat. Mater. **2**, 577–585 (2003)
81. Brown, S.: Metal-recognition by repeating polypeptides. Nat. Biotechnol. **15**, 269–272 (1997)
82. Brown, S., Sarikaya, M., Johnson, E.: A genetic analysis of crystal growth. J. Mol. Biol. **299**, 725–735 (2000)
83. Whaley, S.R., English, D.S., Hu, E.L., Barbara, P.F., Belcher, A.M.: Selection of peptides with semiconductor binding specificity for directed nanocrystal assembly. Nature **405**, 665–668 (2000)
84. Mao, C., Flynn, C.E., Hayhurst, A., Sweeney, R., Qi, J., Georgiou, G., Iverson, B., Belcher, A.M.: Viral assembly of oriented quantum dot nanowires. Proc. Natl. Acad. Sci. U.S.A. **100**, 6946–6951 (2003)
85. Lee, Y.J., Yi, H., Kim, W.J., Kang, K., Yun, D.S., Strano, M.S., Ceder, G., Belcher, A.M.: Fabricating genetically engineered high-power lithium-ion batteries using multiple virus genes. Science **324**, 1051–1055 (2009)
86. Gungormus, M., Fong, H., Kim, I.W., Evans, J.S., Tamerler, C., Sarikaya, M.: Regulation of in vitro calcium phosphate mineralization by combinatorially selected hydroxyapatite-binding peptides. Biomacromolecules **9**, 966–973 (2008)
87. Roy, M.D., Stanley, S.K., Amis, E.J., Becker, M.L.: Identification of a highly specific hydroxyapatite-binding peptide using phage display. Adv. Mater. **20**, 1830–1836 (2008)
88. Sano, K., Shiba, K.: A hexapeptide motif that electrostatically binds to the surface of titanium. J. Am. Chem. Soc. **125**, 14234–14235 (2003)
89. Kashiwagi, K., Tsuji, T., Shiba, K.: Directional BMP-2 for functionalization of titanium surfaces. Biomaterials **30**, 1166–1175 (2009)
90. Tsuji, T., Oaki, Y., Yoshinari, M., Kato, T., Shiba, K.: Motif-programmed artificial proteins mediated nucleation of octacalcium phosphate on the titanium substrates. Chem. Commun. **46**, 6675–6677 (2010)

Chapter 5
Biomineralization: Tooth Enamel Formation

Mayumi Iijima, Kazuo Onuma, and Toru Tsuji

Abstract Tooth enamel is composed of well-crystallized apatite that elongates in the c-axis direction with a highly organized orientation. How do these crystals form? It is still an unanswered question, despite enormous efforts made on answering it.

Chapter 5 briefly reviews the physicochemical studies on clarifying the mechanism of enamel apatite formation. These studies revealed that enamel apatite crystals are formed in a fluid with discrete inorganic and organic compositions. The activity of inorganic ions changes dynamically during the formation process under strict cellular control, and it provides an adequate driving force for nucleation and successive growth. These processes include a dynamic equilibrium of inorganic ions and a transition of unstable intermediates to more stable phases. The composition and solubility of the forming enamel crystals also change dynamically. Because of this complex situation, several formation mechanisms of enamel apatite crystals have been proposed, and researchers have yet to reach a consensus on the subject. Crystal formation takes place in a gel-like enamel matrix, composed of spherical aggregates of amelogenin molecules. Amelogenin is a major component of the enamel matrix and regulates crystal formation by cooperating with enameline (minor matrix protein) and inorganic fluid components. Once enamel formation is

M. Iijima (✉)
Asahi University School of Dentistry, Oral Functional Science and Rehabilitation, Dental Materials Science, 1851-1 Hozumi, Mizuho, Gifu, 501-0296, Japan
e-mail: iijima@dent.asahi-u.ac.jp

K. Onuma
National Institute of Advanced Industrial Science & Technology, Central 6, 1-1-1 Higashi, Tsukuba, Ibaraki, 305-8566, Japan
e-mail: k.onuma@aist.go.jp

T. Tsuji
Advanced Research Centers, Keio University, 3-14-1, Hiyoshi, Kohoku-ku, Yokohama, 223-8522, Japan
e-mail: toruts2002@yahoo.co.jp

X.Y. Liu (ed.), *Bioinspiration: From Nano to Micro Scales*, Biological and Medical Physics, Biomedical Engineering, DOI 10.1007/978-1-4614-5372-7_5,

initiated, these proteins are degraded into smaller fractions, change the interaction with forming crystals and inorganic ions, and are gradually removed from the matrix, providing space for enamel crystals to grow. The chapter ends with a discussion of unique hard tissues with unusual mineral phases in vertebrate and invertebrates.

Keywords Tooth enamel • Apatite • Octacalcium phosphate • Amorphous calcium phosphate • Amelogenin

5.1 Introduction

Tooth enamel, the hardest tissue found in animals, has extremely long crystals with high crystallinity in parallel alignment. How the crystals are formed has been a controversial issue since the 1960s. In this chapter, enamel crystals and their surrounding environment are overviewed, and work aimed at clarifying the mechanism of tooth enamel biomineralization is discussed.

Abbreviations used for apatite-type compounds are:

Calcium hydroxyapatite: H-Ap
Calcium chlorapatite: Cl-Ap
Calcium fluorapatite: F-Ap
Carbonate-containing calcium hydroxyapatite: CO_3-HAp
Fluoride-containing calcium hydroxyapatite: F-HAp
CO_3, F, Cl-containing calcium apatite: CO_3, F, Cl-Ap
Biological apatite and calcium hydroxyapatite containing impurity ions, vacancies, and structural water: HAP

5.2 Enamel Crystals and Surrounding Environment

5.2.1 Overview of Tooth Enamel and its Formation

Tooth enamel is a highly mineralized tissue, with a composition approximately 95% HAP. Enamel crystals have an extremely elongated morphology from the dentin-enamel junction (DEJ) to the tooth surface, and they align parallel to each other (Fig. 5.1). The crystallinity of enamel HAP is almost equivalent to that of mineral apatites. An apatite with properties comparable to those of enamel HAP has not been obtained in vitro under physiological conditions.

Tooth enamel is formed by ameloblasts, which secrete an enamel matrix composed of water, proteins, and inorganic components. After the first layer of dentin has formed, the ameloblasts enter their formative stage. Moving away from

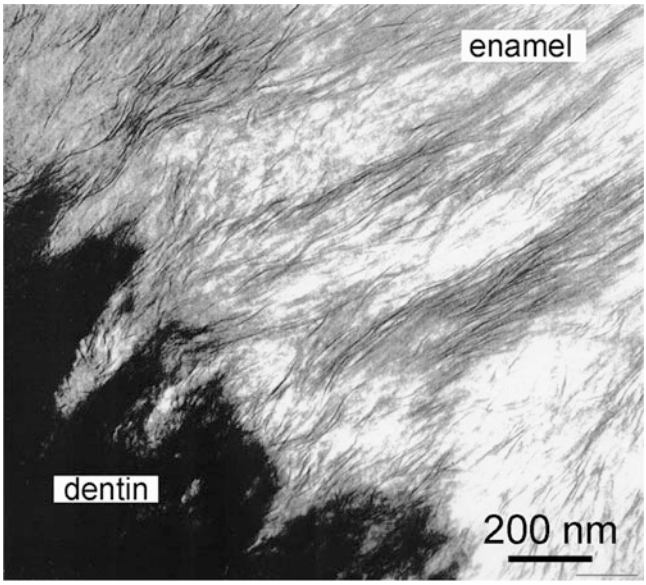

Fig. 5.1 TEM image of enamel in early stage of formation at dentin-enamel junction. In enamel, thin and ribbon-like crystals grow parallel to each other, while in dentin, tiny granules deposit in collagenous matrix. (Reproduced with permission from ref. [90]) (Copyright 1995, Springer)

the DEJ, they produce an enamel matrix in which enamel crystals grow. The enamel formation process is conventionally considered to occur in two stages [1]: organic matrix secretion and enamel crystal formation. In the first stage, enamel proteins secreted by ameloblasts form an enamel matrix [2], and the matrix partially mineralizes (to about 30% mineralization). In the second stage, the full thickness of the partially mineralized matrix is formed, and the degree of mineralization increases. The thickness of the enamel is specific to the animal species and tooth type. At a certain point in the secretory (first) stage, the matrix consists of 54% water, 31% proteins, and 15% mineral (by volume), with a density of 1.39 $g\,cm^{-3}$ [3]. In the maturation (second) stage, the enamel proteins are degraded by enzymes [4]. The degraded protein fractions and water are rapidly removed from the matrix by the ruffle-ended ameloblasts (RAs). At the same time, the RAs actively transport Ca^{2+} and PO_4^{3-} ions into the enamel matrix [5–10], enabling the crystal to increase in thickness. Thus, the water, organic, and mineral contents change during enamel formation [11, 12]. Mature human enamel contains about 1.8 wt% protein and has a density of about 2.9 $g\,cm^{-3}$[13]. Some proteins remain on the surface of the enamel crystals after most of the proteins have been removed from the matrix. As a result, the mineral content of the mature enamel is more than 95%. In contrast, degradation and removal of the structural matrix protein (collagen) does not occur in the mineralization of dentin and cementum.

5.2.2 Components and Characteristics of Enamel Matrix Proteins

The enamel matrix proteins consist of amelogenin, enamelin, sheathlin, and proteinases. Amelogenins account for about 90% of the enamel protein in the early stage of enamel formation. The 25 kDa amelogenins in porcine enamel matrix are cleaved almost immediately after being secreted and split into two fragments, a hydrophilic C-terminal region and a hydrophobic 20 kDa fragment, which is further cleaved into 13, 11, and 6 kDa fragments. The amino acid composition was initially characterized by enrichment in proline, glutamic acid, leucine, and histidine [14]. Since amelogenin has a highly aggregative property and multiple amelogenin genes, its characterization was a complicated puzzle [15]. The amino acid sequences of amelogenin were determined directly [16] or derived from the sequence of amelogenin cDNA [17]. It was a decade after the name "amelogenin" was bestowed by Eastoe [14]. After amelogenin was successfully expressed in an *Escherichia coli* system [18], investigation of amelogenin proceeded. The physicochemical properties are described in detail elsewhere, for example, solubility [19], aggregation [20–22], and interaction with HAP [23–25]. Proteomic and genetic of amelogenon are also studied [26–28]. The biology and physicochemical properties of amelogenin are reviewed by several authors [29, 30].

About 2% of the enamel protein is enamelin, which has a strong affinity for enamel crystal [31, 32]. It is also processed immediately following secretion producing intermediate fragments. Enamelin was isolated, purified, and characterized as an acidic glycoprotein enriched with aspartic acid, glutamic acid, serine, and glycine [33]. More detailed characterization then followed. Enamelin, like amelogenin, is processed immediately after secretion. Porcine intact enamelin (186 kDa) produces intermediate products (155, 145, 89, and 32 kDa) that are not stable, except the 32 kDa fragment [34–38].

The third minor component of the enamel matrix proteins is sheathlin, which has a distinctive amino acid composition, different from that of amelogenin and enamelin [39, 40]. Sheathlin distributes in the sheath (or interprismatic space) that partially separates the rod and inter-rod enamel [41].

The enamel matrix is characterized by two specific properties, which are mainly due to amelogenin: (1) the component changes during enamel formation as both amelogenin and enamelin degrade into several smaller fragments that are removed from the matrix; (2) the solubility, aggregation, and interaction with the mineral phase depend on the molecular weight, pH, temperature, and amelogenin and inorganic ion concentrations. Amelogenin and enamelin are now known to regulate enamel crystal formation.

5.2.3 *Enamel HAP Formation*

In the early stage of enamel formation, fine granules have been observed as an initial cell product [42, 43]. The process of thin ribbon-like crystallite formation from the granules comprises five main steps [42]: (1) deposition of granules (5–7 nm diameter) with low electron scattering; (2) linear assembly of granules into fibers (5–10 nm × 0.1–1.0 μm) with 5–7 nm periodicity and much greater electron scattering; (3) arrangement of fibers into parallel rows; (4) cross-linking of fibers by joining of electron-dense granules, resulting in a ladder-like appearance; and (5) deposition of many tiny crystallites, leading to the formation of ribbon-like crystals. Except for the initial granules with low electron scattering, all the electron-dense materials exhibit an apatitic electron diffraction pattern. This postulated process is related to the HAP formation mechanisms described by Beniash *et al*. [44]. Briefly, they observed that ACP particles form initially and that they assemble step-by-step into thin plates and eventually transform into HAP crystallites. They propose that the enamel proteins control the organized assemble of ACP particles and that the transition starts with proper ionic alignments within the ACP, which could dictate the direction of assembly. For details, see Chap. 4.6. Other candidates suggested as the initial enamel mineral phases are octacalcium phosphate (OCP) [45, 46], non-apatitic calcium phosphate [47], and ACP [48].

The ribbon-like enamel crystals align with their c-axes parallel to each other [49–51] (Fig. 5.1). The thickness was measured to be larger than 2 nm with distribution maxima at 2.5, 3, and 3.7 nm (newborn cat and 5-month-old human fetuses) [52]. The crystal length, obtained from enamel with a density less than 1.8 g cm^{-3}, is at least 100 μm, and the crystals are probably continuous from the DEJ to Tomes' processes [53]. In the maturation stage, the crystals increase mainly in thickness. As they do, they form plates characterized by flattened hexagonal cross-sections (Fig. 5.4c2). The thickening continues until the lateral faces of the crystals fuse to each other. Mature human enamel crystal has a mean width of 68 nm and a mean thickness of 26 nm [54]. Some researchers consider that the crystal length reaches, at most, the thickness of the enamel matrix [1].

5.2.4 *Microstructure of Enamel Matrix and Conformation of Amelogenin*

The morphological entities of the enamel matrix in the early formation stage have been variously described as fibrillar, compartmental or tubule, helical, and lamellar. These are reviewed by Nylen [55]. It is now generally accepted that amelogenin molecules assemble into spheres of nanometer size, which were initially identified as spherules with 15–20 nm diameter [20, 21], and that these nanospheres are the basic structural units of the enamel matrix (Fig. 5.2a). Further studies have shown that (1) the $–NH_2$ and –COOH groups [56] and hydrophobic regions [57] of the

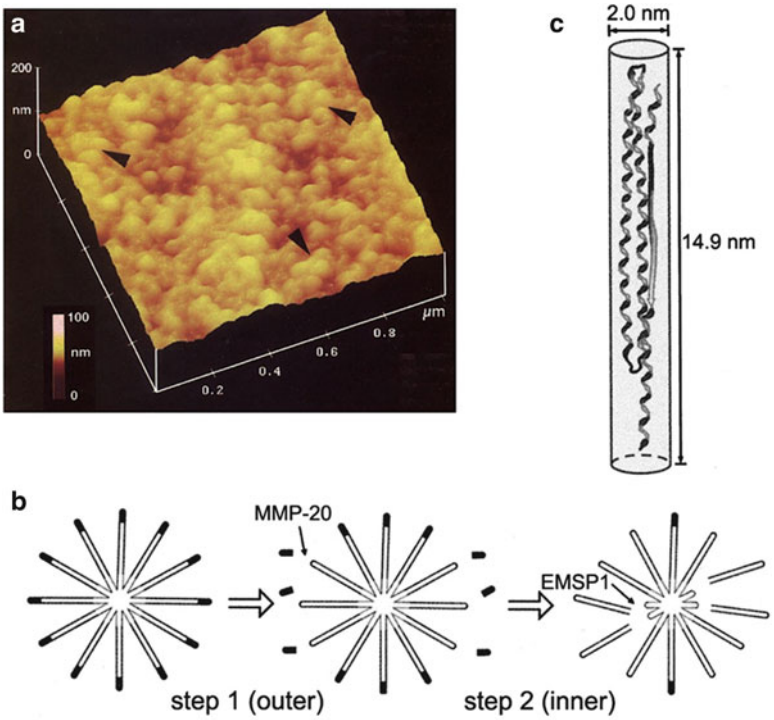

Fig. 5.2 (**a**) AFM image of porcine amelogenin gel (25 kDa (7.4%), 23 kDa (10.7%), and 20 kDa (49.6%) amelogenins and smaller peptides (32.4%)) formed at 4°C. Amelogenins assemble into nanospherules 8–20 nm in diameter. (Reproduced with permission from ref. [58]) (Copyright 1999, Elsevier) (**b**) Micelle model of 25 kDa amelogenin aggregate and proposed degradation by two-step cleavage that provides space for crystal growth: (step 1) hydrophilic C-terminal domain is cleaved by protease MMP-20; (step 2) cleavage by protease EMSP-1 releases 13 kDa fragments, leaving behind smaller micelles containing 6 kDa fragments. (Reproduced with permission from ref. [64]) (Copyright 2007, Sage Publication) (c) Model structure of amelogenin molecule (porcine, 20 kDa fragments) with three characteristic domains: β-sheet, polyproline, and random coil. (Reproduced with permission from ref. [77]) (Copyright 2009, Wakaba Publishing Inc.)

amelogenin distribute outer surface of the nanospheres; (2) the nanospheres vary in size depending on the molecular weight of the amelogenin and the pH, temperature, and protein concentration of the solution [22, 58, 59]; and (3) the nanospheres tend to form chains, which assemble into higher order structures, "microribbon," in vitro [60]. Structure of amelogenin is reviewed by several authors [61–63], and also described in 2.2 of Chap. 4.

Another model structure based on the behavior of amelogenin in solution has been proposed (Fig. 5.2b) [64]. In this micelle model, the surfaces of the 25 kDa amelogenin micelles have a highly hydrophilic C-terminal domain, which has a pattern of positive and negative charges. The micelles aggregate by ionic interaction. Micelles of 20 kDa amelogenin without the C-terminus aggregate

through hydrophobic bonds. The size of the micelles decreases as the C-terminal and 13 kDa regions are sequentially cleaved by MMP-20 [65] and EMSP-1 [66] (step 1 and step 2, respectively; Fig. 5.2b). The C-terminal and 13 kDa regions are removed from the micelles, leaving behind smaller micelles comprised of 6 kDa fragments. This provides growth space for enamel crystal.

The conformation of amelogenin molecules in solution was determined using circular dichroism (CD) and small-angle X-ray scattering (SAXS). These studies revealed that amelogenin molecules, which consist of some 180 amino acid residues, do not behave like a globular protein in solution. Porcine amelogenin molecules (20 kDa) consist of discrete folding units in the N-terminal, central, and C-terminal regions and have a β-sheet structure, a polyproline structure, and a random coil structure, respectively [67]. In 0.1–0.3 μg protein/ml 2% (v/v) acetic acid solution (pH5.3, 25°C), 20 kDa amelogenin forms an elongated bundle structure and assumes a monomeric form [67], while in 10 μg protein/mL 2% (v/v) acetic acid solution (pH < 5.3, 5°C), 20 kDa amelogenin (length of 15 nm and diameter of 2 nm) (Fig. 5.2c) assumes a dimmer form and exhibits an overall radius of gyration of 4.4 nm [68]. When rodlike molecules with both hydrophobic and hydrophilic terminals aggregate, formation of a micelle structure cannot be ruled out.

5.2.5 Ionic Composition and pH of Enamel Fluid

Separation of the enamel fluid from the secretory stage of the matrix enabled the ionic composition to be measured and the degree of saturation of the enamel fluid to be calculated with respect to the enamel HAP and related calcium phosphate [69, 70]. The water content in the secretory stage was around 30–40% of the wet weight [12]. The average composition of the enamel fluid during the secretory stage was total [Ca^{2+}] 0.5 mM, total [P] 3.9 mM, [Mg^{2+}] 0.8 mM, [Na^{+}] 140 mM, [K^{+}] 20 mM, [Cl^{-}] 150 mM, [F^{-}] 5×10^{-3} mM, and total [HCO_3^{-}] 9.74 mM. The pH, the ionic strength, and the osmolarity were 7.26, 165 mM, and 312 mosmol/kg H_2O, respectively. The pH was measured under a constant CO_2 partial pressure. The concentration of free Ca^{2+} ions (0.15 mM) was about 30% of the total Ca^{2+} concentration; the remaining 70% were bound with other inorganic ions and proteins. The total concentration of Ca^{2+} was about half that in the predentin (1.0 mM) and in the fluid of enamel organ tissue surrounding the developing teeth (1.3 mM) and was much lower than that in the blood plasma (2.5 mM). On the other hand, the PO_4^{3-}concentration of the enamel fluid (3.5 mM) was about three times that in the blood plasma (1.1 mM). The activity of Ca^{2+}, (a_{Ca}), calculated taking into account the thermodynamic factors, was 0.053 mM. The calculated free HCO_3^{-} concentration in enamel fluid was around 10 mM, lower than that of the blood plasma CO_3^{2-} concentration (about 22 mM). The calculated degree of supersaturation with respect to H-Ap, OCP, and enamel HAP suggests that the enamel fluid was supersaturated with H-Ap, undersaturated with OCP, undersaturated with enamel HAP at a pH lower than 7.1, and supersaturated with

enamel HAP at a pH higher than 7.1. Thus, the compositions of the enamel fluid and enamel crystal change during enamel formation. Direct staining of developing bovine enamel with pH indicators demonstrated that the enamel matrix has alternate acidic (pH5.8–6.0) and neutral (pH7.0–7.2) areas [71] at certain locations and times during enamel HAP formation.

During enamel HAP formation, Ca^{2+} ions are actively transported from the ameloblasts into the enamel matrix, and the amount and timing of the Ca^{2+} inflow are strictly controlled by the ameloblasts (2.2). The inflow of the Ca^{2+} increases rapidly during the maturation stage [10]. This could increase the total Ca^{2+} concentration in the matrix. However, the a_{Ca} is decreased due to the chemical equilibrium of the ionic components in the enamel fluid. These components include lactate, $H_2PO_4^-$, HPO_4^{2-}, PO_4^{3-}, HCO_3^-, and CO_3^{2-}.

The a_{Ca} is also controlled by the surrounding amelogenins. The 25 kDa amelogenins are cleaved by enzymes step-by-step during enamel formation, forming 20, 13, 11, and 6 kDa fragments. The cleaved fragments show different binding abilities with Ca^{2+} and the developing crystal. The concentration of 13 and 11 kDa fragments is 2.8 w/v% in the secretory stage of porcine enamel matrix [23]. This corresponds to a 2 mM protein concentration when calculated using a molecular weight of 13 kDa. This is several times higher than the concentration of Ca^{2+} in the enamel fluid (0.3–0.5 mM). The binding coefficient of the proteins and Ca^{2+} ions is of the order of 10^4 M [72], strongly suggesting that the fragments work as a Ca^{2+} reserve.

5.3 Mineral Component of Tooth Enamel

5.3.1 Composition and Solubility of Enamel HAP

Enamel HAP contains several impurity ions, vacancies, and structural water [73]. The chemical composition solubility of porcine enamel in the early and late secretory stage and maturation stage has been determined [74, 75]. The chemical formula for the thin ribbon-like crystals in the early stage of maturation is $(Ca)_{4.155}(Mg)_{0.034}(Na)_{0.191}(K)_{0.004}(HPO_4)_{0.35}(CO_3)_{0.357}(PO_4)_{2.384}(OH)_{0\cdot007}$.

That for erupted mature enamel is $(Ca)_{4.568}(Mg)_{0.032}(Na)_{0.11}(K)_{0.002}(HPO_4)_{0.143}(CO_3)_{0.256}(PO_4)_{2.712}(OH)_{0.378}$.

The relatively large decrease in HPO_4 during enamel formation is ascribed to the OCP-to-HAP phase transition [76]. The amount of Mg^{2+} substituted for the Ca^{2+} is almost constant, 0.7–0.8% of the Ca^{2+}, among developing enamel crystals.

The solubility products (K_{sp}) of developing enamel crystals at different stages were determined on the basis of the chemical composition $(Ca)_{5-x}(Mg)_q(Na)_u(HPO_4)_v(CO_3)_w(PO_4)_{3-y}(OH)_{1-z}$. The average ion activity product $(I_{APeq})^{1/N}$ (N is the sum of the valences for each ion comprising the solid phase; for details, see 1.3.1) had a level of 4.41×10^{-6} in the early secretory stage, 1.80×10^{-6} in the

early maturation stage, and 1.45×10^{-6} in erupted enamel [77]. Thus, the solubility of the enamel crystals decreases as maturation proceeds; in other words, the stability of enamel crystals increases with maturation.

The solubility of F-HAp with different F^- contents is minimum (6.55×10^{-63}) when almost half the OH^- has been replaced with F^- ($Ca_5(PO_4)_3(OH)_{0.43}F_{0.57}$) [78]. The relationship between the F^- content in enamel and HAP stability gives important information about the formation and prevention of caries and the remineralization of tooth enamel. Much information about the composition of apatites and their properties is readily available (for example, [79–81]).

5.3.2 CO_3-HAp and Properties of CO_3^{2-} in CO_3-HAp

The mineral component of mammalian tooth enamel is generally described as CO_3-HAp. The CO_3^{2-} is an important lattice component because it regulates the solubility, morphology, and size of biological HAP [82, 83]. Whether CO_3^{2-} can replace OH^- in the HAP lattice was a controversial issue because of the geometric restrictions caused by the form and size of PO_4^{3-} (regular tetrahedron), CO_3^{2-} (equilateral triangles), and OH^- (linear). Strict analysis of CO_3-HAp ($Ca_{10}(PO_4)_{5.99}(CO_3)_{0.86}(PO_4)_{2.384}(OH)_{0.26}O_{0.02}$) showed that one CO_3^{2-} replaces two OH^- and the plane of CO_3^{2-} triangles is almost parallel to the *c*-axis [81]. This parallel orientation creates much less steric interference than the perpendicular orientation. When CO_3^{2-} has replaced OH^-, it is defined as A-type CO_3; when it has replaced PO_4^{3-}, it is B-type CO_3; and when it has replaced OH^- and PO_4^{3-}, it is AB-type CO_3.

In developing enamel HAP, not only the CO_3^{2-} content, but also the ratio of the replacement sites, i.e., PO_4^{3-} or OH^-, changes during maturation [74]. In young and immature enamel HAP, substitution for PO_4^{3-} is favored, and then, as maturation progresses, substitution for OH^- is increasingly favored. Incorporation of CO_3^{2-} in HAP increases with an increase in the CO_3^{2-} concentration of the surrounding fluid, and substitution for PO_4^{3-} is favored under neutral pH conditions [84]. Such diversity in substitution and site occupancy of CO_3^{2-} in enamel crystal has been ascribed to changes in the enamel fluid composition and the pH conditions during the formation process.

5.3.3 Crystal Structure of HAP

The crystal structure of synthesized H-Ap was described initially as an F-Ap type, e.g., hexagonal, $P6_3/m$, with the O of the OH^- at (0,0,0.25) [85]. Later analysis using mineral H-Ap (Holly Spring, United States) by both X-ray and neutron diffraction technique [86] showed that the O is at (0,0,0.201) and that the H is at

(0,0,0.062). Because the OH^- is slightly displaced from the mirror plane ($z = 0.25$ and 0.75), the stability of H-Ap is slightly lower than that of F-Ap [87]. The crystal structure of human enamel was determined using the powdered enamel fraction with a density higher than 2.95 g cm^{-3} and the Rietveld method [88]. Enamel HAP has almost the same structure as H-Ap and structural water, and Cl^- (about 0.3 wt%) is located on the hexagonal axis between $z = 0.11$ and 0.14. Structural water is defined as water in the lattice that is removed by heating at 400°C. The lattice dimensions are $a = 0.9441(2)$ and $c = 0.6878(1)$ nm. The loss of water from enamel HAP decreases the a-axial dimension by 0.02 nm [89]. Structural aspects of HAP are also described in Chap. 3.2.

As described in Chap. 3.2, H-Ap has two possible symmetries, hexagonal and monoclinic. It has been noted that a small number of impurity ions, e.g., F^-, stabilizes the hexagonal structure [90]. Therefore, strictly speaking, any HAP, including enamel HAP, that contains impurity ions is not genuinely hexagonal but pseudohexagonal with its hexagonal symmetry stabilized by the ions.

5.4 Mechanisms of Enamel Crystal Formation

5.4.1 Regulatory Roles of Amelogenin and Enamelin

How does enamel crystal formation start? Dentin at the DEJ was once thought to be the nucleation site on the basis of transmission electron microscopy (TEM) observations of the dentin and enamel crystallites at the DEJ [91]. However, there is little other evidence supporting the nucleation of enamel crystal on dentin crystal at the DEJ. Direct epitaxial growth of enamel crystals onto dentin crystallites has not been observed [42, 92]. Along with ultrastructural studies of developing enamel crystals, in vitro HAP formation studies have shown that amelogenin accelerates the nucleation kinetics and controls the crystal morphology, indicating that the crystal formation mechanism involves amelogenin [93–96]. Nuclear magnetic resonance (NMR) studies showed that the C-terminus of amelogenin, with four $–COO^-$ groups and three $-NH^+$ groups, directly binds with the HAP crystal surface [97]. In vitro nucleation and growth of OCP are promoted by recombinant amelogenin (rP179) with the C-terminus [98]. Promotion of OCP nucleation is ascribed to the $–NH^+$ and $–COO^-$ groups in the charged C-terminal region exposed on the surface, which could reduce the nucleation energy. A role of rP179 in the OCP formation is also discussed in Chap. 4.4.

The adsorption behavior varies with the molecular weight [24]. Intact amelogenin (25 kDa for porcine) adsorbs strongly on HAP while the 20 kDa fragments adsorb less strongly [23]. The 13 kDa fragments adsorb less than the nascent 25 kDa amelogenin molecules. Ultrastructural studies of developing enamel crystals have shown that amelogenin nanospheres are on and between the developing enamel crystals [61]. Chemical force microscopy observations [99] demonstrated

that amelogenin nanospheres preferentially bind to positively charged domains of enamel crystal. Thus, functional control of crystal size, morphology, orientation, and growth rate has been ascribed to amelogenin.

Since enamelin has a strong affinity for enamel crystal (2.2), it is considered to induce nucleation and to regulate the growth rate through interaction with the crystal. The 32 kDa fragment, one of the series of cleavage products, is the most stable one. It has been shown to promote nucleation of apatite [100] and to change its conformation from α-helix to β-sheet, which interacts with Ca^{2+} in HAP, depending on the Ca^{2+} concentration [101].

Cooperative regulation of enamelin and amelogenin through their interaction has been suggested [102]. The hypothesis that amelogenin and enamelin jointly control the elongated crystal growth of OCP was examined [103] using a dual membrane experimental device in which a cation-selective membrane and a dialysis membrane form a tiny reaction chamber, and Ca^{2+} and PO_4^{3-} ions flow into the chamber in a controlled manner. OCP was chosen as a model crystal for the post-secretory growth on the basis of the evidence described in 4.6 and 4.7. A mixture of 10w/v% recombinant porcine amelogenin (rP148) and 32 kDa porcine enamelin fragments was used as a crystal growth medium at 37°C and a pH of 6.5. The aspect ratio of the OCP crystals was substantially higher at a certain ratio of amelogenin to enamelin. Thus, the co-assembly of amelogenin and 32 kDa enamelin was suggested as a mechanism regulating the morphology of OCP crystal.

5.4.2 ACP Formation and Stability in Enamel Fluid

As described in Chap. 3.2, there is no general agreement yet on the solubility product of ACP, which is required to evaluate the driving force ($\Delta\mu$) needed to precipitate ACP. Several solubility products, ranging from 24.8 to 28.3, have been proposed for ACP and amorphous tricalcium phosphate (ATCP). ACP slurry (for which a large solid/solution ratio is the best experimental approach) has a nearly constant I_{AP} of 1.6×10^{-25} in the pH range 7.4–9.25 when the formula is given as $Ca_3(PO_4)_{1.87}(HPO_4)_{0.2}$ [104]. Accordingly, "the minimum I_{AP} needed to form ACP de novo in physiological solution at pH7.4 is considerably greater than that calculated for serum" [105]. In general, the spontaneous formation of ACP is attained by mixing Ca^{2+} and PO_4^{3-} solutions with rather high concentrations of Ca^{2+} and PO_4^{3-}. The Ca^{2+} and PO_4^{3-} immediately co-aggregate into clusters large enough to be separated from the solution. However, the Ca^{2+} and PO_4^{3-} concentrations of the enamel fluid are too low to form ACP spontaneously (2.5, 3.1). Therefore, "it would appear unlikely that ACP could form in vivo" [105] without a mechanism to increase the local Ca^{2+} and PO_4^{3-} concentrations or a reasonable process to form nuclei. As described in 4.4, the mechanism could be the stepwise construction of growth units by amelogenin and pre-nucleated CaP clusters.

Although ACP is not very stable and transforms into crystalline phase in pure calcium phosphate solution, in vitro studies have shown that CO_3^{2-}, Mg^{2+}, F^-,

and $P_2O_7^{4-}$ stabilize ACP [83, 106, 107]. The potential role of a PO_4^{3-} group of amelogenin in ACP stabilization was demonstrated: P148 with a PO_4^{3-} group on serine-16 stabilized ACP for more than one day while non-phosphorylated rP172 did not [108]. ACP, once formed, could be stabilized in the enamel matrix for some period.

5.4.3 Organization of ACP into Crystals

Supramolecules composed of amelogenin and ACP have been formed in vitro [51]. The unanswered question is, "what controls the arrangement and fusion of the supramolecules and transformation into crystallines with their c-axes parallel to each other?" Since there are charged domains on developing enamel crystal surfaces [99], the domain structure of the enamel crystals is thought to be formed by the organized fusion of the crystallites in the c-axis direction. HAP crystal formation by stepwise fusion of the protein/mineral nanoparticles into long crystals was proposed [109]: initially formed fine granules align in rows and form chains by fusion; the chains fuse into plates, and the plates fuse along the c-axis direction, forming long crystals.

In the absence of a structural framework or functional materials, it would be hard to control the assembly of ACP and the final morphology of the crystalline phase derived from ACP. ACP particles formed in solution frequently aggregate into irregularly shaped branching clusters, and de novo crystallization yields crystals with a rectilinear morphology [105]. Since a spherical-shaped ACP particle has no long-range order in its structure, there must be mechanisms that organize the assembly of ACP particles and their successive growth into crystals with morphology specific to the hard tissue. Beniash *et al*. noted that partially ordered structure formed in ACP particle could dictate the direction of assembly [44].

5.4.4 CaP-Cluster Models

The formation models postulated by Wang *et al*. and Yang *et al*. ascribe this function to amelogenin and explain the process specifically [95, 96]. Both of them studied the effect of amelogenin (rP172) on nucleation and growth of HAP under strict control of the degree of supersaturation with respect to the precipitating phases using a constant composition technique [110].

Wang *et al.* used solutions supersaturated with respect to OCP ($\sigma_{OCP} = 1.45$ and 2.32) with pH 6.8 and 37°C to examine whether enamel HAP forms with OCP as an intermediate phase [95]. Figure 5.3 illustrates the step-by-step mechanism of the assembly of CaP clusters and amelogenin nanospheres into HAP crystal. In the presence of amelogenin, the induction time is less. Nucleation clusters

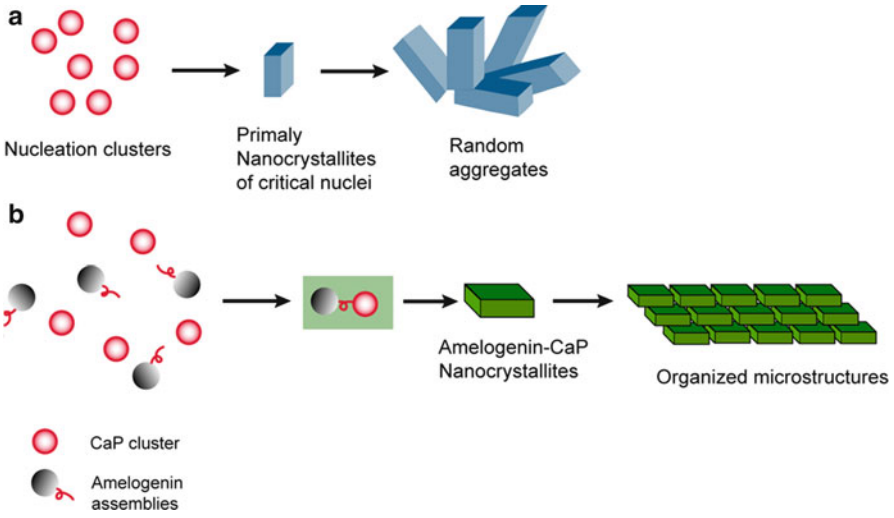

Fig. 5.3 Model of crystal formation in solution supersaturated with OCP: (a) without amelogenin, random aggregates of OCP form. (b) With amelogenin, organized microstructures form: (1) assembly of CaP clusters (red balls) and amelogenin oligomers (small nanospheres, gray ball); (2) formation of amelogenin-CaP nanocrystallites as building units; (3) organized assembly of building units into HAP nanocrystallites. (Reproduced with permission from ref. [95]) (Copyright 2007, American Chemical Society)

(CaP clusters) bind with amelogenin nanospheres and form amelogenin (amel)-CaP clusters as basic building units. These clusters form amel-CaP nanocrystallites, which subsequently assemble and form HAP nanocrystallites. The specific binding is ascribed to the charged COOH-terminal region. An important point is that amel-CaP nanocrystallites find the low-energy configurations needed to bind with the adjacent crystallite. An NMR study revealed a direct amelogenin-HAP interaction through the C-terminal region that oriented the C-terminal region on the HAP crystal [97]. Without amelogenin, spherical aggregates of OCP nanocrystallite formed.

Yang *et al*. used a solution with H-Ap stoichiometry and undersaturated with respect to OCP to analyze the nucleation process: $\sigma_{HAP} = 15.1$, pH 7.4, 37 °C, ionic strength = 0.15 M, with rP172 of 25 μg/mL [96]. The reactions in solution with lower supersaturation revealed the initial nucleation process. The newly observed crystal formation process comprises five steps: (1) CaP clusters pre-nucleate with a diameter of less than 1 nm. (2) The pre-nucleated clusters are captured by amelogenin, causing them to form amel-nano-CaP clusters, 2–10 nm in size, which in turn form nanoparticles, 30–50 nm in size. The amel-CaP nanocluster composites transform into amel-ACP nanospherical building blocks. (3) The amel-ACP nanospherules gradually assemble into nanochains. (4) The nanochains co-assemble into nanorods or nanoribbons. (5) Ostwald ripening leads to elongated HAP.

Without amelogenin, random-sized CaP clusters formed and assembled into globular ACP with an irregular size distribution. This globular ACP aggregated

and partially transformed into crystalline HAP although remaining ACP in the final product. In this process, the induction time is reduced by the amelogenin, indicating that amelogenin promotes the formation of pre-nucleated CaP and amel-CaP clusters. The postulated roles of amelogenin are (1) capturing and stabilizing the pre-nucleated CaP clusters, (2) controlling the aggregation of primary-composite nanoclusters into the initial building blocks, and (3) controlling the sequential assembly of the building blocks in the post-nucleation crystal growth stage.

Thus, the size of the initial CaP clusters and the growth unit are determined at the atomic level by amelogenin and the solution conditions. The spherules formed in the Ca-PO_4 solution with rP172 were mainly 0.8–1.4 nm, while the rP172 spherules were larger than 10 nm. This strongly suggests that the initially formed phase is CaP clusters (pre-nucleated), which are stabilized by rP172 [108], enabling them to serve as building blocks for the nanocluster composites. Note that the size of 0.8–1.4 nm is comparable to a hydrodynamic radius of aggregates (about 0.5 nm) detected in pseudo-body fluid [111, 112] (see 3.4.7 in Chap. 3).

5.4.5 Transformation from ACP to HAP and Intermediate OCP

The phase transformation from ACP to HAP was extensively investigated by thermodynamic analysis in the 1970s [113–115]. These studies postulated that the transition involves OCP and the transition usually starts before all the ACP has transformed into OCP because OCP is a very unstable intermediate of H-Ap. The lifetime of OCP is remarkably reduced in the presence of a small amount of F^-, in a basic solution, and at a higher Ca/PO_4 molar ratio. This makes it difficult to detect the intermediate phase. Therefore, OCP has been recognized as a labile intermediate. However, even when OCP was not detected as an identifiable solid phase, solution chemistry has shown that when OCP is forming in solution, the I_{AP} of the solution is larger than the solubility product of OCP [115]. This is thermodynamic evidence for the existence of OCP. For detail in this area, review is available [116].

In the transformation from ACP to HAP, OCP is usually observed as the first crystal in close contact with the surfaces of ACP particles [117, 118]. The subsequent transformation from OCP to H-Ap appears to be in situ, whereby the OCP undergoes a solid-state rearrangement into an H-Ap structure [45]. The first crystalline phase detected usually gives an apatitic X-ray diffraction (XRD) pattern with the a-axial dimension larger than that of HAP. This indicates that there is an OCP-like structure in the crystal [119]. For the transformation from ACP to H-Ap, review is available [105].

5.4.6 *Possibility of OCP Involvement in Enamel HAP Formation*

In the mechanisms of extremely long and well-crystallized enamel crystal formation, Brown *et al.* recognized the importance of OCP and theorized that OCP is a precursor of enamel HAP [45, 119]. They considered it to be a precursor because (1) OCP has a thin and platy morphology, while HAP has a hexagonal one; (2) OCP grows more rapidly than HAP; (3) OCP is a metastable phase of HAP; (4) unstable OCP readily transforms into stable-phase HAP, and (5) OCP is structurally similar to HAP. HAP formation via OCP occurs in three stages: (1) nucleus formation, (2) two-dimensional growth of OCP into a single unit-cell thickness of OCP, and (3) precipitation of a unit-cell thickness of OCP on the two-dimensional crystal and its hydrolysis. Since the transformation from OCP to HAP is topotaxial, the crystallographic axes of the OCP are preserved after the transformation. The phase transformation from OCP to HAP has been proposed as the mechanism incorporating impurity ions, water, and vacancies into HAP [119]. Although many HRTEM studies of enamel in the early formation stage caught images of OCP in the first-formed enamel crystals [52, 120–122], Brown *et al.*'s OCP precursor theory has not been generally accepted due to the difficulty of detecting a transient mineral phase.

HPO_4^{2-} is another indicator that supports the involvement of the acidic precursor phase [79, 123]. As described in 3.1, HPO_4^{2-} is a substantial lattice component of developing enamel crystals. Fourier transform infrared spectroscopy (FTIR) studies have shown that the HPO_4^{2-} group is a lattice component of the enamel crystals [74]. The amount of HPO_4^{2-} decreases with the progress of crystal maturation [76]. The higher content of HPO_4^{2-} in the early secretory enamel is consistent with the formation of an OCP-like phase.

Micro-Raman spectroscopy, which is very sensitive to the atomic order of the phase, revealed the presence of OCP in living murine calvarial tissue [124]. This was the first direct evidence without the artifact of dehydration. Moreover, there was an indication that ACP may form prior to OCP. Thus, in the case of murine calvarial tissue, bone HAP formation could include the transition of ACP to OCP.

5.4.7 *Epitaxial Overgrowth of Apatite on OCP Template*

CO_3-HAp crystals with central planar defects were synthesized for the first time by Nelson *et al*. (Fig. 5.4a1) [125]. The cross-sectional HRTEM images of the crystals resemble those of enamel HAP crystals with a central dark line (CDL) [50, 126, 127]. Fourier filtering analysis of lattice images of the CO_3-HAp crystals showed that the defects were a one- or two-unit cell thickness of two-dimensional OCP (Fig. 5.4a2) [128]. The two-dimensional OCP was parallel to the (100) plane of the CO_3-HAp. A growth model, epitaxial overgrowth of apatite on the OCP template,

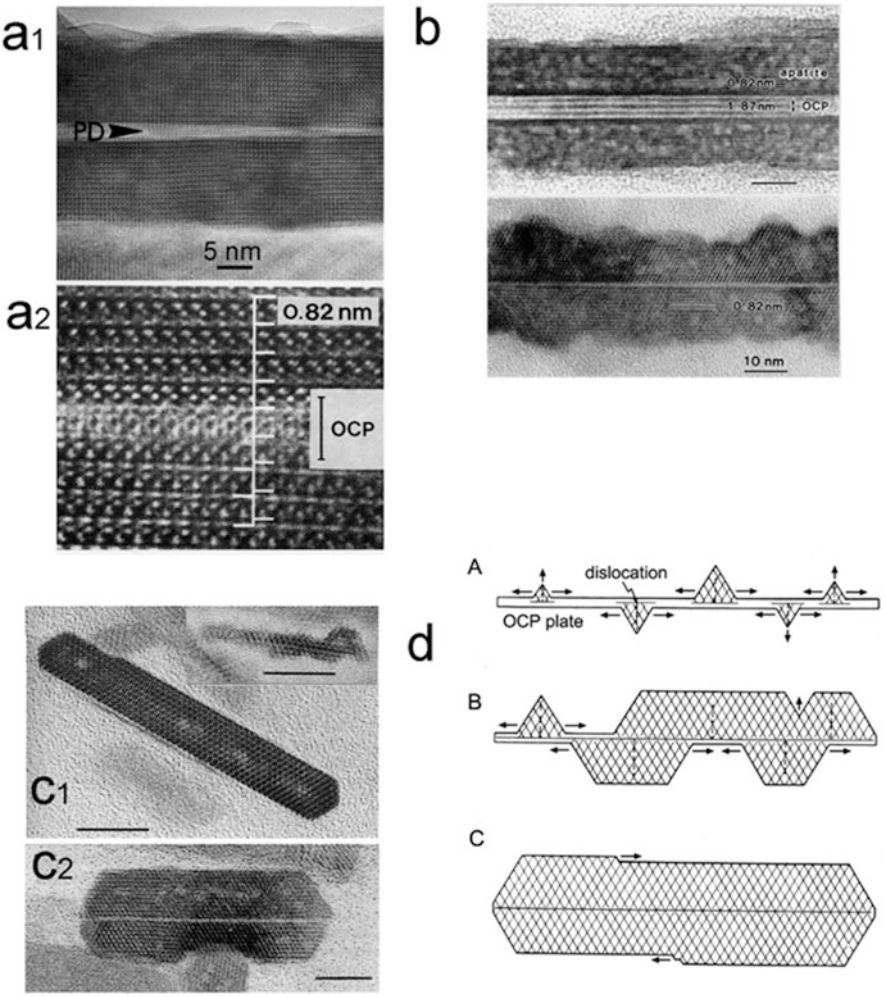

Fig. 5.4 (a1) Cross-sectional lattice image of synthesized CO_3-HAp crystal with central planar defect; (a2) higher magnification image of defect region. Central, one-unit-cell-thick OCP region is labeled; white markings show expansion of apatite lattice across defect. (Reproduced with permission from ref. [128]) (Copyright 1989, John Wiley and Sons) (b) Ap/OCP/Ap lamellar mixed crystals grown on a cation-selective membrane in the presence of 1 ppm F. (Reproduced with permission from ref. [135]) (Copyright 2001, S. Karger AG) (c1) Puffer enamel crystals in early overgrowth stage. (Reproduced with permission from ref. [130]) (Copyright 1991, Springer) (c2) Carp enameloid crystal in maturation stage. (Reproduced with permission from ref. [131]) (Copyright 1991, Springer) Horizontal bar corresponds to 10 nm. (d) Model of lateral epitaxial overgrowth of enamel crystals: (A) epitaxial growth of apatite on OCP template with one-unit-cell thickness; (B) lateral growth of isolated apatite units on template and fusion of neighboring units; (C) thickening of apatite crystals by acquisition of apatite unit cells on their prism plane. (Reproduced with permission from ref. [120]) (Copyright 1993, Springer)

was postulated to explain the central planar inclusion. Briefly, a primordial thin plate of OCP crystal works as a template for successive epitaxial growth of HAP on the (100) face, with the template embedded at the center of the HAP crystal. This model well explains the formation mechanism of the CDL, which is observed in the cross-section of enamel HAP.

A series of Ap/OCP/Ap lamella mixed crystals ([129a]) (Fig. 5.4b), developing porcine enamel crystals [120], puffer enamel HAP [130] (Fig. 5.4c1), and carp enameloid HAP [131] (Fig. 5.4c2) ensure HAP overgrowth on an OCP template in vivo and in vitro. In the Ap/OCP/Ap mixed crystals, the thickness of the OCP at the center decreased while that of the apatite overgrowth increased with an increase in the concentration of F^- from 0.1 to 1 ppm. In the presence of 1 ppm F^-, HAP with a central planar defect was obtained; cross-sectional HRTEM images of these Ap/OCP/Ap lamella mixed crystals (Fig. 5.4b) were similar to those of Nelson's CO_3-HAp crystal, carp enameloid crystals [131] and of porcine enamel crystals [120]. TEM observation has shown that the OCP template grew to its critical size, and then HAP overgrowth on the template crystal commenced [129b]. The critical size of the template depended on the solution conditions (pH, ion concentration, etc.). Interestingly, crystals with the Ap/OCP/Ap structure have been found in human dental calculus [132].

On the basis of HRTEM observation of developing fish enameloid, porcine enamel HAP, and synthesized CO_3-HAp crystals, the epitaxial overgrowth mechanism was modeled at the atomic level [120] (Fig. 5.4d): (1) two-dimensional growth of an OCP-like precursor with a one- or two-unit cell thickness and a ribbon-like morphology; (2) epitaxial overgrowth of apatite on the thin ribbon in which small, regular triangles and trapezoid crystals form as building units and are deposited on screw dislocations of the precursor crystal; (3) lateral growth of the small triangles on the template and fusion of the neighboring units; and (4) thickening of the template crystal by two-dimensional growth on the prism plane. Screw dislocations, which initiate HAP overgrowth, have been observed in both synthetic CO_3-HAp [125] and human fetal enamel crystals [127].

5.4.8 *Control of Morphology and Orientation by One-Directional Ca^{2+} Diffusion*

The ameloblasts secrete enamel precursor materials in the direction of their long axis. Osborn suggested that the crystal orientation is controlled by the secretory force generated by the ameloblasts [133]. This suggestion led to the supposition that one-directional Ca^{2+} ion supply from the ameloblasts causes the lengthwise and oriented growth during the initial crystalline phase, which was assumed to be OCP [134]. A model system constructed for this uses a cation-selective membrane to create one-directional diffusion of Ca^{2+} ions, thereby simulating the flow of Ca^{2+} ions in the enamel matrix. OCP crystals elongated in the c-axis direction grow on the membrane with the c-axes parallel to each other. Details are reviewed by Iijima [135].

The formation of OCP usually starts with deposition of granules about 100 nm in size on a membrane [136]. These granules do not show any distinctive XRD reflection, suggesting that they are ACP-like precipitates. They deposit on the membrane and assemble into irregularly shaped branching clusters, which subsequently grow into bank-like structures and then flake-like crystals. The flake-like crystals increase in height perpendicular to the membrane and eventually grow into OCP crystals elongated in the *c*-axis direction. The transition from amorphous to crystalline phase is speculated to be a de novo rearrangement of the internal structures.

5.4.9 *Correlated Interaction of F^-, Amelogenin, and Ca^{2+} in HAP Growth*

The effects of F^- on the formation and properties of HAP crystals are well known. F^- (1) increases the growth rate, (2) accelerates the hydrolysis of OCP to HAP, (3) improves the crystallinity, (4) increases the crystal size, and (5) reduces the solubility. In the combination of F^- and amelogenin, the F^- induces and precedes F-HAp formation, and the amelogenin disturbs this reaction. Amelogenin adsorption on the F-HAp crystals increases with the F^- content. F-HAp adsorbs more amelogenin than H-Ap. Since the F^- in F-HAp interferes with protease activity, the amelogenin on crystals is less degradable, so it is retained on the F-HAp longer [137].

In addition, Ca^{2+} is related to the adsorption of amelogenin on the crystals. The higher the Ca^{2+} concentration, the more rapidly the amelogenin is degraded and removed from the crystal. A higher Ca^{2+} concentration also promotes F-mediated conversion of OCP to HAP in vitro [137]. In the secretory stage, when Ca^{2+} transport is limited, degradation of amelogenin progresses slowly, while early in the maturation stage, when Ca^{2+} transport increases dramatically, the transition from OCP to HAP, the degradation of amelogenin, and the removal of the degraded fractions are accelerated. The removal of the fractions enables the F^- to adsorb on the crystal, leading to formation of F-HAp. Since F-HAp enhances amelogenin adsorption, there is an amelogenin reaction that disturbs crystal growth. Thus, F^-, Ca^{2+}, and amelogenin interact with enamel HAP in a coordinated manner.

5.4.10 *Regulation of OCP and HAP Formation by Amelogenin and F^-*

Considering OCP to be another transient phase for enamel crystals, Iijima *et al*. investigated the growth mechanism of elongated OCP crystals using a dual membrane experimental device [138–140]. OCP crystals preferentially grew in the c-axis direction on the membrane regardless of the presence of amelogenin. Amelogenin decreased the OCP crystal size. The degree of decrease was in the

order width < length < thickness. In other words, the degree of interaction of amelogenin with the OCP crystal faces was in the order (010) > (001) > (100), meaning that the interaction with the (010) face was the strongest. Thus, the aspect ratio was increased by preferential interaction of the amelogenin with the side faces of the OCP crystals. This was observed regardless of the presence of the hydrophilic C-terminus and the type of amelogenin used. Therefore, the interaction between OCP and amelogenin was ascribed to the hydrophobic core part of amelogenin. Fluoride (1 ppm) changed the mineral phase from OCP to HAP, yielding oriented prism-like HAP crystals with a large aspect ratio [139]. It is possible to incorporate F^- into the lattice to enhance the interaction between the amelogenin and crystal [137].

5.4.11 *Cooperative Regulation of HAP Growth by Amelogenin, Ca^{2+}, and Mg^{2+}*

Analysis of the adsorption of amelogenin, Ca^{2+}, and Mg^{2+} on growing enamel crystals [137] revealed that amelogenins adsorb on enamel crystals more preferentially than Mg^{2+}. In the maturation stage, as the proteolytic cleaving of amelogenin proceeds, amelogenin fragments are removed from the crystals while Mg^{2+} adsorption increases. Since Mg^{2+} adsorption is suppressed by amelogenins, the removal of amelogenin enables Mg^{2+} to adsorb. The adsorption ability of Mg^{2+} is about one-third that of Ca^{2+}, and the adsorption of Mg^{2+} decreases with the activity ratio $(a_{Mg})/(a_{Ca})$. This means that Ca^{2+} reduces the inhibitory effect of Mg^{2+}. The Mg^{2+} adsorption rate is determined by the $(a_{Mg})/(a_{Ca})$ ratio. An increase in a_{Ca} facilitates the growth of HAP crystals with less disturbance of the amelogenin and Mg.

Enamel fluid contains about 0.8 mM Mg^{2+} and 10 mM CO_3^{2-}. The Mg^{2+} inhibits the growth of HAP [79, 83], and the degree of inhibition is synergistically increased by CO_3^{2-} [83, 135]. Nevertheless, enamel crystal has good crystallinity. This can be ascribed in part to the cooperative regulation by amelogenin, Ca^{2+}, and Mg^{2+}, maintaining an a_{Ca} level suitable for growing HAP with good quality.

5.5 Evolution and Adopted Mineral Phase in Hard Tissue

In the evolution of animals, *Lingula unguis* (Brachiopoda, Inarticulata) appeared some 500 million years ago in the Ordovician period as an ancestor of animals with hard tissue [141]. *Lingula* still exists and is known as a living fossil. It has a pair of shells that cover its soft body like a bivalve. The shell is composed of apatite and β-chitin [142] instead of the typical $CaCO_3$ composition of Articulata (Brachiopoda) and Mollusca shells. Not only did species with an apatite shell appear prior to those

with a $CaCO_3$ shell, the *c*-axis of the HAP and the fiber axis of the β-chitin are parallel to each other [143, 144]. This orientation relationship between the HAP and organic matrix component indicates that a mechanism that organizes mineral crystal growth is inherent in animals with hard tissues.

HAP in a dense fraction (2.5–2.7 $g\,cm^{-3}$) of *Lingula* shell contains CO_3^{2-} (2.5 ± 0.2 wt%), F^- (2.0 ± 0.04 wt%), and Mg^{2+} (0.98 ± 0.01 wt%) with Cl^- as a minor component and structural water. Hydroxyl was not detected by FTIR analysis. *Lingula* shell HAP was identified as CO_3, F, Cl-Ap [145]. TEM [146] and SAXS [147] studies of the shell demonstrated that mineral granules (about 50 nm in diameter) were distributed in the marginal part of the shell, i.e., the newly formed part. After calcination at 1,000 °C, *Lingula* shell HAP produced β-TCP (about 30%) along with HAP with improved crystallinity. Since ACP transforms into β-TCP after being calcined [148], the existence of ACP in *Lingula* shell HAP is highly probable.

Chimaera phantasma (Holocephali), a relative of the shark, has a unique dental tissue "tooth plate" instead of sharp, marginal teeth like a shark. The tooth plate is composed of pleromin and osteodentin. The mineral phase of pleromin is whitlockite [149], and that of osteodentin is HAP. The whitlockite crystallizes in an oval shape, has high crystallinity, and deposits without orientation. *Chimaera* is a living fossil that appeared some 400 million years ago in the Devonian period. The lungfish (*Protopterus*) also has tooth plates; however, the mineral phase is HAP [150]. Thus, only *Chimaera phantasma* has dental tissue composed of whitlockite.

Recently, Bentov et al. [151] reported coexistence of calcium carbonates and calcium phosphate in the mandibles of a freshwater crayfish (the arthropod *Cherax quadricarinatus*): Amorphous calcium carbonate (ACC) and ACP located in the base of the mandible, F-Ap crystals covered the amorphose minerals, forming an enamel-like coating, and calcite located in the incisor. The use of both carbonates and phosphates as component of a functioning hard tissue was found, probably, for the first time in an evolution of biominerals.

"What determines the phase and organization of mineral in hard tissues" is an unanswered question. The higher level organizing system is thought to control the cells so that they provide a medium in which appropriate mineral can form. Recent advances in gene analysis and cloning techniques have made it possible to investigate the evolution of enamel proteins. The amino acid sequences of amelogenin have a striking level of homology among species [152, 153]. Further progress in this field could help answer the question above.

5.6 Concluding Remarks

Nucleation and growth of enamel HAP crystal proceed in an enamel matrix, which acts as a functional medium that changes the composition continuously, thereby providing an optimal environment for crystal formation. The formation process is determined by the local environment, which is determined by the tissue-specific cells. Analyses of developing enamel HAP crystal and of the components and

properties of the enamel matrix, along with in vitro evidence provided by advanced technologies, have been improving our understanding of tooth enamel formation. Further in vitro studies should enable us to better explain the mechanisms and fine-tune the formation scenario and new findings, like the coexistence of phosphates and carbonates in the crayfish mandibles, might require reconstruction of a phylogenic perspective of biominerals.

References

1. Nanci, A.: TenCate's oral histology: histology development, & function. Chapter 7, pp. 138–179. Mosby Inc., (2003)
2. Watson, M.L.: The extracellular nature of enamel in the rat. J Biophys Biochem Cytol **23**, 447–497 (1960)
3. Fukae, M., Shimizu, M.: Studies on the proteins of developing bovine enamel. Arch Oral Biol **19**, 381–386 (1974)
4. Glimcher, M.J., Mechanis, G.L., Friberg, U.A.: The amino acid composition of the organic matrix and the neutral soluble and acid soluble components of embrionic bovine enamel. Biochem J **93**, 198–202 (1964)
5. Robinson, C., Hiller, C.R., Weatherell, J.A.: Uptake of ^{32}P-labelled phosphate into developing rat incisor enamel. Calcf. Tissue. Res. **15**, 143–152 (1974)
6. Bawden, J.W., Merritt, D.H., Deaton, T.G.: In vitro study of calcium-45 and phosphorus-32 uptake in developing rat molar enamel using quantitative methods. Arch Oral Biol **26**, 477–482 (1981)
7. Takano, Y., Crenshaw, M.A., Bawden, J.W., Hammarstrom, L., Lindskog, S.: The Visualization of the patterns of ameloblast modulation by the glyoxal bis(2-hydroxyanil) staining method. J Dent Res **61**, 1580–1586 (1982)
8. Takano, Y., Crenshaw, M.A., Reith, E.J.: Correlarion of ^{45}Ca incorporation with maturation ameloblast morphology in the rat incisor. Calcif Tissue Int **34**, 211–213 (1982)
9. Kawamoto, T., Shimidzu, M.: Changes in the mode of calcium and phosphate transport during rat incisal enamel formation. Calcif Tissue Int **46**, 406–414 (1990)
10. Kawamoto, T., Shimidzu, M.: Changes of the ratio of calcium to phosphate transported into the mineralizing enamel, dentin, and bone. Jpn J Oral Biol **36**, 365–382 (1994)
11. Deakins, M.: Changes in the ash, water, and organic content of pig enamel during calcification. J Dent Res **21**, 429–435 (1942)
12. Robinson, C., Briggs, H.D., Atkinson, P.J., Weatherell, J.A.: Matrix and mineral changes in developing enamel. J Dent Res **58**, 871–880 (1984)
13. Weidmann, S.M., Weatherell, J.A., Hamm, S.: Variations of enamel density in sections of human teeth. Arch Oral Biol **12**, 85–97 (1967)
14. Eastoe, J.E.: The amino acid composition of proteins from the oral tissue-II. The matrix proteins in dentine and enamel from developing human deciduous teeth. Arch Oral Biol **8**, 633–652 (1963)
15. Fincham, A.G.: The amelogenin problem; A comparison of purified enamel matrix proteins. Calcif Tissue Int **26**, 65–73 (1979)
16. Takagi, T., Sasaki, S., Baba, T.: Complete amino acid sequence of amelogenin in developing bovine enamel. Biochem Biophys Res Commun **121**, 592–597 (1984)
17. Snead, M.L., Lau, E.C., Zeichner-David, M., Fincham, A.G., Woo, S.L.C., Slavkin, H.C.: DNA sequence for cloned cDNA for murine amelogenin reveal the amino acid sequence for enamel-specific protein. Biochem Biophys Res Commun **129**, 812–818 (1985)
18. Simmer, J.P., Lau, E.C., Hu, C.C., Aoba, T., Lacey, M., Nelson, D., Zeichner-David, M., Snead, M.L., Slavkin, H.C., Fincham, A.G.: Isolation and characterization of a mouse amelogenin expressed in *Escherichia coli*. Calcif Tissue Int **54**, 312–319 (1994)

19. Tan, J., Leung, W., Moradian-Oldak, J., Zeichner-David, M., Fincham, A.G.: Quantitative analysis of amelogenin solubility. J Dent Res **77**, 1388–1396 (1998)
20. Fincham, A.G., Moradian-Oldak, J., Simmer, J.P., Sarte, P.E., Lau, E.C., Diekwisch, T.G.H., Slavkin, H.C.: Self-assembly of a recombinant amelogenin protein generates supra-molecule structures. J Struct Biol **112**, 103–109 (1994)
21. Moradian-Oldak, J., Simmer, J.P., Lau, E.C., Sarte, P.E., Slavkin, H.C., Fincham, A.G.: Detection of monodisperse aggregates of a recombinant amelogenin by dynamic light scattering. Biopolymers **34**, 1339–1347 (1994)
22. Moradian-Oldak, J., Leung, W., Fincham, A.G.: Temperature and pH-dependent supramolecular self-assembly of amelogenin molecules: A dynamic light-scattering analysis. J Struct Biol **122**, 320–327 (1998)
23. Aoba, T., Fukae, M., Tanabe, T., Shimizu, M., Moreno, E.C.: Selective adsorption of porcine amelogenins onto hydroxyapatite and their Inhibitory activity on hydroxyapatite growth in supersaturated solutions. Calcif Tissue Int **41**, 281–289 (1987)
24. Moradian-Oldak, J., Leung, W., Tan, J., Fincham, A.G.: Interaction of amelogenin with hydroxyapatite crystals: An adherence effect through amelogenin molecular self-association. Bioploymers **46**, 225–238 (1998)
25. Ryu, O.H., Hu, C.C., Simmer, J.P.: Biochemical characterization of recombinant mouse amelogenin: protein quantitation, proton absorption, and relative affinity for enamel crystals. Connect Tissue Res **38**, 207–214 (1998)
26. Gibson, C.W., Golub, E., Abrams, W.R., Shen, G., Ding, W., Rosenbloom, J.: Bovine amelogenin message heterogeneity: alternative splicing and Y-chromosomal gene transcription. Biochemistry **31**, 8384–8388 (1992)
27. Simmer, J.P., Hu, C.C., Lau, E.C., Sarte, P.E., Moradian-Oldak, J., Slavkin, H.C., Fincham, A.G.: Alternative splicing of the mouse amelogenin primary RNA transcript. Calcif Tissue Int **55**, 302–310 (1994)
28. Hu, C.C., Yamakoshi, Y., Yamakoshi, F., Krebsbach, P.H., Simmer, J.P.: Proteomic and genetic of dental enamel. Cells Tissue Organ **181**, 219–231 (2005)
29. Brookers, S.J., Robinson, C., Kirkham, J., Bonass, W.A.: Biochemistry and molecular biology of amelogenin proteins of developing dental enamel. Arch Oral Biol **40**, 1–14 (1995)
30. Fincham, A.G., Moradian-Oldak, J., Simmer, J.P.: The structural biology of the developing dental enamel matrix. J Struct Biol **126**, 270–299 (1999)
31. Yanagisawa, T., Nylen, M.U., Termine, J.D.: Distribution of matrix components in hamster enamel. Electron microscopic study. J Dent Res **60**(A), 558 (1981)
32. Yamakoshi, Y.: Carbohydrate moieties of porcine 32 kDa enamelin. Calcif Tissue Int **56**, 323–330 (1995)
33. Termine, J.D., Belcourt, A.B., Christner, P.J., Conn, K.M., Nylen, M.U.: Properties of dissociatively extracted fetal tooth matrix proteins. 1. Principle molecular species in developing bovine enamel. J Biol Chem **255**, 9760–9768 (1980)
34. Tanabe, T., Aoba, T., Moreno, E.C., Fukae, M., Shimizu, M.: Properties of phosphrylated 32 kDa nonamelogenin proteins isolated from porcine secretory enamel. Calcif Tissue Int **46**, 205–215 (1990)
35. Deutsch, D., Palmon, A., Fisher, L., Termine, J.D., Young, M.: Sequencing of bovine enamelin ('Tuftelin'), A novel acidic enamel protein. J Biol Chem **266**, 16021–16028 (1991)
36. Fukae, M., Tanabe, T., Uchida, T., Yamakoshi, Y., Shimizu, M.: Enamelins in the newly formed bovine enamel. Calcif Tissue Int **53**, 257–261 (1993)
37. Hu, C.C., Fukae, M., Uchida, T., Qian, Q., Zhang, C.H., Ryu, O.H., Tanabe, T., Yamakoshi, Y., Murakami, C., Dohi, N., Shimizu, M., Simmer, J.P.: Cloning, and characterization of porcine enamelin mRNAs. J Dent Res **76**, 1720–1729 (1997)
38. Yamakoshi, Y., Pinheiro, F.H., Tanabe, T., Fukae, M., Shimizu, M.: Sites of asparagine-linked oligosaccharides in porcine 32 kDa enamelin. Connect Tissue Res **39**, 39–46 (1998)
39. Fukae, M., Tanabe, T.: Non-amelogenin components of porcine enamel in the protein fraction from enamel crystals. Calcif Tissue Int **40**, 286–293 (1987)

40. Uchida, T., Fukae, M., Tanabe, T., Yamakoshi, Y., Satoda, T., Murakami, C., Takahashi, O., Shimizu, M.: Immnolchemical and immnocytochemical study of a 15 kDa non-amelogenin and related proteins in the porcine immature enamel: Proposal of a new group of enamel proteins sheath proteins. Biomed Res **16**, 131–140 (1995)
41. Hu, C.C., Fukae, M., Uchida, T., Qian, Q., Zhang, C.H., Ryu, O.H., Tanabe, T., Yamakoshi, Y., Murakami, C., Dohi, N., Shimizu, M., Simmer, J.P. : Sheathlin cloning, cDNA/polypeptide sequences, and immunolocalization of porcine enamel sheath proteins. J Dent Res **76**, 648–657 (1997)
42. Fearnhead, R.W.: Mineralization of rat enamel. Nature **188**, 509–600 (1960)
43. Reith, E.J.: The early stage of amelogenesis as observed in molar teeth of young rats. J Ultrastruct Res **17**, 503–526 (1967)
44. Beniash, E., Metzler, R.A., Lam, R.S.K., Gilbert, P.U.P.A.: Transient amorphous calcium phosphate in forming enamel. J Struct Biol **166**, 133–143 (2009)
45. Brown, W.E., Lehr, J.R., Smith, J.P., Frazier, A.W.: Octacalcium phosphate and hydroxyapatite. Nature **196**, 1048–1055 (1962)
46. Brown, W.E.: Crystal Growth of bone mineral. Clin. Orthop. **44**, 205–220 (1966)
47. Cuisinier, F.J.G., Steuer, P., Senger, B., Vogel, J.C., Frank, R.M.: Human amelogenesis—high resolution electron microscopy of nanometer sized particles. Cell Tissue Res **273**, 175–182 (1993)
48. Bodier-Houlle, P., Steuer, P., Meyer, J.M., Bigeard, L., Cuisinier, F.J.G.: High resolution electron microscopic study of the relationship between human enamel and dentin crystals at the dentimo-enamel junction. Cell Tissue Res **301**, 389–395 (2000)
49. Rönnholm, E.: The amelogenesis of human teeth as revealed by electron microscopy. (II) The development of the enamel crystallites. J Ultrastruct Res **6**, 249–303 (1962)
50. Nylen, M.U., Eanes, E.D., Omnell, K.A.: Crystal growth in rat enamel. J Cell Biol **18**, 109–123 (1963)
51. Travis, D.F., Glimcher, M.J.: The structure and organization of, and the relationship between the organic matrix and the inorganic crystals of embryonic bovine enamel. J Cell Biol **23**, 447–497 (1964)
52. Weiss, M.P., Vogel, J.C., Frank, R.M.: Enamel crystallite growth: width and thickness study related to the possible presence of octacalcium phosphate during amelogenesis. J Ultrastruct Res **76**, 286–292 (1981)
53. Daculci, G., Menanteau, J., Kerevel, L.M., Mitre, D.: Enamel crystals: size Shape, length and growing process; High resolution TEM and biochemical study. In: Fearnhead, R.W., Suga, S. (eds.) Tooth Enamel IV, pp. 14–23. Elsevier Sci. Pub, Amsterdam (1984)
54. Kerebel, B., Daculsi, G., Kerebel, L.M.: Ultrastructural studies of enamel crystallites. J Dent Res **58**, 844–850 (1979)
55. Nylen, M.U.: Matrix-mineral relationships—a morphologist's viewpoint. J Dent Res **58**(B), 922–926 (1979)
56. Pain, M.L., Snead, M.L.: Protein interactions during assembly of the enamel organic extracellular matrix. J Bone Miner Res **12**, 221–227 (1997)
57. Lakshminarayanan, R., Fan, D., Du, C., Moradian-Oldak, J.: The role of secondary structre in the entropically driven amelogenin self-assembly. Biophys J **93**, 3664–3674 (2007)
58. Wen, H.B., Moradian-Oldak, J., Leung, W., Bringas Jr., P., Fincham, A.G.: Microstructures of an amelogenin gel matrix. J Struct Biol **126**, 42–51 (1999)
59. Wiedemann-Bidlack, F.B., Beniash, E., Yamakoshi, Y., Simmer, J.P., Margolis, H.C.: PH triggered self-assembly of native and recombinant amelogenins under physiological pH and temperature. J Struct Biol **160**, 57–69 (2007)
60. Moradian-Oldak, J., Du, C., Falini, G.: On the formation of amelogenin Microribbons. Eur J Oral Sci **114**, 289–296 (2006)
61. Fincham, A.G., Moradian-Oldak, J., Diekwisch, T.G.H., Lyaruu, D.M., Wright, J.T., Bringas Jr., P., Slavkin, H.C.: Evidence for amelogenin "nanospheres" as functional components of secretory-stage enamel matrix. J Struct Biol **115**, 50–59 (1995)

62. Moradian-Oldak, J., Lau, E.C., Diekwisch, T.G.H., Slavkin, H.C., Fincham, A.G.: A review of the aggregation properties of a recombinant amelogenin. Connect Tissue Res **32**, 125–130 (1995)
63. Margoris, H.C., Beniash, E., Fowler, E.C.: Role of macromolecular assembly of enamel matrix proteins in enamel formation. J Dent Res **85**, 775–793 (2006)
64. Fukae, M., Yamamoto, R., Karakido, T., Shimoda, S., Tanabe, T.: Micelle structure of amelogenin in porcine secretory enamel. J Dent Res **86**(8), 758–763 (2007)
65. Bartlett, J.D., Simmer, J.P.: Proteinases in developing dental enamel. Crit Rev Oral Biol Med **10**, 425–441 (1999)
66. Simmer, J.P., Fukae, M., Tanabe, T., Ymakoshi, Y., Uchida, T., Xue, J.: Purification, characterization, and cloning of enamel matrix serine protease 1. J Dent Res **77**, 377–386 (1998)
67. Goto, Y., Kogure, E., Takagi, T., Aimoto, S., Aoba, T.: Molecular conformation of porcine amelogenin in solution: three folding units at the N-terminal, central, and C-terminal regions. J Biochem **113**, 55–60 (1993)
68. Matsushima, N., Izumi, Y., Aoba, T.: Small-angle X-Ray scattering and computer-Aided molecular modeling studies of 20 kDa fragment of porcine amelogenin: Does amelogenin adopt an elongated bundle structure? J Biochem **123**, 150–156 (1998)
69. Aoba, T., Moreno, E.C.: The enamel fluid in the early secretory stage of porcine amelogenesis: chemical composition and saturation with respect to enamel mineral. Calcif Tissue Int **41**, 86–94 (1987)
70. Amano, T., Sato, K., Aoba, T.: Soluble constituents in the fluid environment of pig and rat developing enamel and their relevance to the regulation of mineralization. Jpn J Oral Biol **43**, 257–267 (2001)
71. Sasaki, S., Takagi, T., Suzuki, M.: Cyclic changes in pH in bovine developing enamel as sequential bands. Arch Oral Biol **36**, 227–231 (1991)
72. Moreno, E.C., Aoba, T.: Comparative solubility study of human dental enamel, dentin, and hydroxyapatite. Calcif Tissue Int **49**, 6–13 (1991)
73. McConnel, D.: Recent advance in the investigation of the crystal chemistry of dental enamel. Arch Oral Biol **3**, 28–34 (1960)
74. Aoba, T., Moreno, E.C.: Changes in the nature and composition of enamel mineral during porcine amelogenesis. Calcif Tissue Int **47**, 356–364 (1990)
75. Aoba, T., Moreno, E.C.: Changes in the solubility of enamel mineral at various stages of porcine amelogenesis. Calcif Tissue Int **50**, 266–272 (1992)
76. Shimoda, S., Aoba, T., Moreno, E.C.: Acid-phosphate contents in porcine enamel mineral at various stages of amelogenesis. J Dent Res **70**, 1516–1523 (1991)
77. Aoba, T., Sato, K.: Mechanism of developmental enamel mineralization: enamel fluid, crystals, and organic matrix. In Tooth Ename, (Association for Comparative Biology of Tooth Enamel), pp.67–81. Wakaba Pub. Inc., Japan (2009)
78. Moreno, E.C., Kresak, M., Zahradnik, R.T.: Fluoridated hydroxyapatite solubility and caries formation. Nature **247**, 64–65 (1974)
79. Brown, W.E., Mathew, M., Tung, M.S.: Crystal chemistry of octacalcium phosphate. In: Pamplin, B.R. (ed.) Progress in crystal growth and characterization, vol. 4, pp. 59–87. Pergamon Press Ltd., Great Britain (1981)
80. LeGeroe, R.Z.: Calcium phosphate in oral biology and medicine. Karger, Baskel (1991)
81. Elliott, J.C.: Structure and chemistry of the apatites and other calcium orthophosphates, vol. 18. Studies in inorganic chemistry, Elsevier, London (1994)
82. Chickerur, N.S., Tung, M.S., Brown, W.E.: A mechanism for incorporation of carbonate into apatite. Calcif Tissue Int **32**, 55–62 (1980)
83. LeGeroe, R.Z.: Apatites in biological systems. In: Pamplin, B.R. (ed.) Progress in crystal growth and characterization, vol. 4, pp. 1–45. Pergamon Press Ltd., Great Britain (1981)
84. Shimoda, S., Aoba, T., Moreno, E.C., Miake, Y.: Effect of solution composition on morphological and structural feature of carbonated calcium apatites. J Dent Res **69**, 1731–1740 (1990)

85. Posner, A.S., Perloff, A., Diorio, A.F.: Refinement of the hydroxyapatite structure. Acta Cryst **11**, 308–309 (1958)
86. Kay, M.I., Young, R.A., Posner, A.S.: Crystal structure of hydroxyapatite. Nature **204**, 1050–1052 (1964)
87. Young, R.A., Elliott, J.C.: Atomic-scale bases for several properties of apatites. Arch Oral Biol **11**, 699–707 (1966)
88. Young, R.A., Mackie, P.E.: Crystallography of human tooth enamel: initial structure refinement. Mater Res Bull **15**, 17–29 (1980)
89. Young, R.A.: Implication of atomic substitutions and other structural details in apatites. J Dent Res **53**, 193–203 (1974)
90. Hagen, A.R.: Structural features of biologicaly involved phosphates. Acta Odontol Scand **31**, 149–173 (1973)
91. Arsenault, A.L., Robinson, B.W.: The Dentino-enamel junction: a structural and microanalytical study of early mineralization. Calcif Tissue Int **45**, 111–121 (1989)
92. Diekwisch, T.G.H., Berman, B.J., Gentner, S., Slavkin, H.C.: Initial enamel crystals are not spatially associated with mineralized dentin. Cell Tissue Res **279**, 149–167 (1995)
93. Beniash, E., Simmer, J.P., Margoris, H.C.: The Effect of recombinant mouse amelogeneses nn the formation and organization of hydroxyapatite crystals in vitro. J Struct Biol **149**, 182–190 (2005)
94. Tao, J., Pan, H., Zeng, Y., Xu, X., Tang, R.: Roles of Amorphous calcium phosphate and biological additives in the assembly of hydroxyapatite nanoparticles. J Phys Chem **111**, 13410–13418 (2007)
95. Wang, L., Guan, X., Chang, D., Moradian-Oldak, J., Nancollas, G.H.: Amelogenin promotes the formation of elongated apatite microstructures in a controlled crystallization system. J Phys Chem **111**, 6398–6404 (2007)
96. Yang, X., Wang, L., Qin, Y., Sun, Z., Henneman, Z.J., Moradian-Oldak, J., Nancollas, G.H.: How amelogenin orchestrates the organization of hierarchical elongated microstructures of apatite. J Phys Chem **114**(6), 22293–22300 (2010)
97. Shaw, W.J., Campbell, A.A., Pain, M., Snead, M.L.: The COOH terminus of the amelogenin, LRAP, is oriented next to hydroxyapatite surface. J Biol Chem **279**, 40263–40266 (2004)
98. Tarasevich, B.J., Howard, C.J., Larson, J.L., Snead, M.L., Simmer, J.P., Pain, M., Shaw, W.J.: The nucleation and growth of calcium phosphate by amelogenin. J Cryst Growth **304**, 407–415 (2007)
99. Kirkham, J., Zhang, J., Brookes, S.J., Shore, R.C., Ryu, O.H., Wood, S.R., Smith, D.A., Wallwork, M.L., Robinson, C.: Evidence for charge domains on developing enamel crystal surfaces. J Dent Res **79**, 1943–1947 (2000)
100. Bouropoulos, N., Moradian-Oldak, J.: Induction of apatite by the cooperative effect of amelogenin and 32 kDa enamelin. J Dent Res **83**, 278–282 (2004)
101. Fan, D., Lakshminarayanan, R., Moradian-Oldak, J.: The 32 kDa enamelin undergoes conformational transitions upon calcium binding. J Struct Biol **163**, 109–115 (2008)
102. Fan, D., Chan, D., Sun, Z., Lakshminarayanan, R., Moradian-Oldak, J.: In vitro study on the interaction between the 32 kDa enamelin and amelogenin. J Struct Biol **166**, 88–94 (2009)
103. Iijima, M., Fan, D., Bromly, K. M., Sun, Z., Moradian-Oldak, J.: The 32 kDa enamelin undergoes conformational transitions upon calcium binding. Crystal Growth. Design, (under review). (2010)
104. Combes, C., Rey, C.: Amorphous calcium phosphates synthesis, properties and uses in biomaterials. Acta Biomaterialia. **6**(9), 3362–3378 (2010)
105. Eanes, D.E.: Amorphous calcium phosphate. In: Chow, L.C., Eanes, E.D. (eds.) Octacalcium phosphate, vol. 18, pp. 130–147. Monograp. Oral Sci, Basel, Karger (2001)
106. Eanes, E.D., Posner, A.S.: Intermediate phases in the basic solution preparation of alkaline earth phosphates. Calcif Tissue Res **2**, 38–48 (1968)
107. Termin, J.D., Peckauskas, R.A., Ponser, A.S.: Calcium phosphate formation in vitro. II. Effects of environment on amorphous-crystalline transition. Arch. Biochem. Biophys. **140**, 318–325 (1970)

108. Kwack, S.Y., Wiedemann-Bidlack, F.B., Beniash, E., Yamakoshi, Y., Simmer, J.P., Litman, A., Margolis, H.C.: Role of 20 kDa amelogenin (P148) phosphorylation in calcium phosphate formation in vitro. J Biol Chem **284**(28), 18972–18979 (2009)
109. Robinson, C., Shore, R.C., Wood, S.R., Brookes, S.J., Smith, D.A.M., Wright, J.T., Connell, S., Kirlkham, J.: Subunit structures in hydroxyapatite crystal development in enamel: implication for amelogenesis imperfecta. Connect Tissue Res **44**, 65–71 (2003)
110. Tomson, M.B., Nancollas, G.H.: Mineralization kinetics: a constant composition approach. Science **200**, 1059–1060 (1978)
111. Onuma, K., Ito, A.: Cluster growth model for hydroxyapatite. Chem Mat **10**, 3346–3351 (1998)
112. Oyane, A., Onuma, K., Kokubo, T., Ito, A.: Clustering of calcium phosphate in the system $CaCl_2$-H_3PO_4-KCl-H_2O. J Phys Chem B **103**, 8230–8235 (1999)
113. Eanes, E.D., Gillssen, I.H., Posner, A.S.: Intermediate states in the precipitation of hydroxyapatite. Nature **208**, 365 (1965)
114. Termine, J.D., Eanes, E.D.: Comparative chemistry of amorphous and apatitic calcium phosphate preparations. Calcif Tissue Res **10**, 171–197 (1972)
115. Eanes, E.D., Meyer, J.L.: The Maturation of crystalline calcium phosphates in aqueous suspensions at physiologic pH. Calcif Tissue Res **23**, 259–269 (1977)
116. Eanes, E.D.: Crystal growth of mineral phases in skeletal tissues. In: Pamplin, B.R. (ed.) Progress in crystal growth and characterization, vol. 3, pp. 3–15. Pergamon Press Ltd, Great Britain (1981)
117. Eanes, E.D., Termine, J.D., Nylen, M.U.: An electron microscopic study of the formation of amorphous calcium phosphate and its transition to crystalline apatite. Calcif Tissue Res **12**, 143–158 (1973)
118. Meyer, J.L.: Phase transformation in the spontaneous precipitation of calcium phosphate. Croat Chem Acta **56**, 753–767 (1983)
119. Brown, W.E., Schroeder, L.W., Ferris, J.S.: Interlayering of crystalline octacalcium phosphate and hydroxyapatite. J Phys Chem **83**, 1385–1388 (1979)
120. Miake, Y., Shimoda, S., Fukae, M., Aoba, T.: Epitaxial overgrowth of apatite crystals on the thin-ribbon precursor at early stages of porcine enamel mineralization. Calcif Tissue Int **53**, 249–256 (1993)
121. Tohda, H., Yamada, M., Yamaguchi, Y., Yanagisawa, T.: High-resolution electron microscopical observations of initial enamel crystals. J Electron Microsc **1**, 97–101 (1997)
122. Arnord, S., Plate, U., Wiesmann, H.P., Stratmann, U., Kohl, H., Holing, H.J.: Quantitative analyses of the biomineralization of different hard tissue. J Microsc **202**, 488–494 (2001)
123. Arends, J., Davidson, C.L.: HPO_4 contents in enamel and artificial carious lesions. Calcif Tissue Res **18**, 65–79 (1975)
124. Crane, N.J., Popescu, V., Morris, M.D., Steenhuis, P., Ignelzi Jr., M.A.: Raman spectroscopic evidence for octacalcium phosphate and other transient mineral species deposited during intramembranous mineralization. Bone **39**, 434–442 (2006)
125. Nelson, D.G.A., Wood, G.J., Barry, J.C., Featherstone, J.D.B.: The structure of (100) defects in carbonated apatite crystallites: A high resolution electron microscopy study. Ultramicroscopy **19**, 253–266 (1986)
126. Nakahara, H., Kakei, M.: Central dark line and carbonic anhydrase: Problems relating to crystal nucleation in enamel. In: Fearnhead, R. W., Suga, S. (eds.) Tooth Enamel IV. pp. 42–46, 82. Elsevier Sci. Pub., Amsterdam (1984)
127. Cuisinier, F.J.G., Steuer, P., Senger, B., Vogel, J.C., Frank, R.M.: Human amelogenesis I: High resolution electron microscopy study of ribbon-like crystals. Calcif Tissue Int **51**, 259–268 (1992)
128. Nelson, D.G.A., Barry, J.C.: High resolution electron microscopy of nonstichometric apatite crystals. Anat Rec **224**, 265–276 (1989)
129a. Iijima, M., Tohda, H., Moriwaki, Y.: Growth and structure of lamellar mixed crystals of octacalcium phosphate and apatite in a model system of enamel formation. J Cryst Growth **116**, 319–326 (1992)

129b. Iijima, M., Tohda, H., Suzuki H., Yanagisawa T., Moriwaki, Y.: Effect of F on apatite octacalcium phosphate intergrowth and morphology in a model system of tooth enamel formation. Calcif. Tiss. Int. **50**, 357–361 (1992)
130. Aoba, T., Miake, Y., Shimoda, S., Prostak, K., Moreno, E.C., Suga, S.: Dental apatites in vertebrates species: morphology and chemical properties. In: Nakahara, H., Suga, S. (eds.) Mechanisms and phylogeny of mineralization in biological systems, pp. 459–463. Springer-Verlag, Tokyo (1991)
131. Miake, Y., Aoba, T., Moreno, E.C., Shimoda, S., Prostak, K., Suga, S.: Ultrastructural studies on crystal growth of enameloid minerals in elasmobranch and teleost fish. Calcif Tissue Int **48**, 204–217 (1991)
132. Kakei, M., Sakae, T., Yoshikawa, M.: Electron microscopy of octacalcium phosphate in the dental calculus. J Electron Microsc **58**(6), 393–398 (2010)
133. Osborn, J.W.: The mechanism of prism formation in teeth: a hypothesis. Calcif Tissue Int **5**, 115–132 (1970)
134. Moriwaki, Y., Doi, Y., Kani, T., Aoba, T., Takahashi, J., Okazaki, M.: Synthesis of enamel-like apatite at physiological temperature and pH using ion-selective membranes. In: Suga, S. (ed.) Mechanism of tooth enamel formation, pp. 239–256. Quintessence, Tokyo (1983)
135. Iijima, M.: Formation of octacalcium phosphate in vitro. In: Chow, L.C., Eanes, E.D. (eds.) Octacalcium phosphate, vol. 18, pp. 17–49. Karger, Monograp. Oral Sci. (2001)
136. Hata, M., Moriwaki, Y., Doi, Y., Goto, T., Wakamatu, N., Kamemizu, H.: Oriented growth of octacalcium phosphate on cation selective membrane (in Japanese). Jpn J Crystal Growth **12**, 91–99 (1985)
137. Aoba, T., Fejerskov, O.: Dental fluorosis: chemistry and biology. Crit Rev Oral Biol Med **13**(2), 155–170 (2002)
138. Iijima, M., Moriwaki, Y., Takgi, T., Moradian-Oldak, J.: Effects of bovine amelogenins on the crystal morphology of octacalcium phosphae in a model system of tooth enamel formation. J Cryst Growths **222**, 615–626 (2001)
139. Iijima, M., Moradian-Oldak, J.: Control of octacalcium phosphae and apatite growth by amelogenin matrices. J Mater Chem **14**, 2189–2199 (2004)
140. Iijima, M., Moradian-Oldak, J.: Control of apatite crystal growth in a fluoride containing amelogenin-rich matrix. Biomaterials **26**, 1595–1603 (2005)
141. Chapman, F.: Notes on shell-structure in the genus *Lingula*, Recent and Fossil. J R Micro Soc **5**, 28–31 (1914)
142. Klement, R.: Die anorganshe skeletsubstantz. Ihre zusammensetzung, naturlichs unt kunstliche bildung. Naturewissenshaften **26**, 145–152 (1938)
143. Kelly, P. G., Oliver, P. T. P., Pautard, F. G. E.: The shell of Lingula unguis. Proc. 2nd. Eur. Symp. Calcif. Tissue. 337-345. (1965)
144. Iijima, M., Moriwaki, Y.: Orientation of apatite and organic matrix in *Lingula unguis* shell. Calcif Tissue Int **47**, 237–242 (1990)
145. Iijima, M., Kamemizu, H., Wakamatu, N., Goto, T., Moriwaki, Y.: Thermal decomposition of Lingula shell apatite. Calcif Tissue Int **49**, 128–133 (1991)
146. Iwata, K.: Ultrastructure and calcification of the shells in inarticulate Brachiopods. I. Ultrastructure of Lingula unguis (LINNAEUS). J Geol Soc Jpn **87**, 405–415 (1981)
147. Iijima, M., Moriwaki, Y., Gyotoku, T., Hayashi, K., Imura, S.: Small angle X-ray scattering study of Lingula unguis shell. Jpn J Oral Biolt **31**, 308–316 (1989)
148. Eanes, E.D.: Thermodynamical studies on amorphous calcium phosphate. Calcif Tissue Res **5**, 133–145 (1970)
149. Ishiyama, M., Sasagawa, I., Akai, J.: The inorganic content of pleromin in tooth plates of the living Holocephalan consists of a crystalline calcium phosphate known as ß-$Ca_3(PO_4)_2$ (whitlockite). Arch Histol Jpn **47**, 89–94 (1984)
150. Ishiyama, M., Teraki, Y.: The fine structure and formation of hypermineralized petrodentine in tooth plate of extant Lungfish. Arch Histol Cytol **53**, 307–321 (1990)

151. Bentov, S., Zaslansky, P., Sawalmih, A.A., Masic, A., Fratzl, P., Sagi, A., Berman, A., Aichmayer, B.: Enamel-like apatite crown covering amorphous mineral in a crayfish mandible. Nat Commun **3**, 839 (2012). doi:10.1038/ncomms1839
152. Bonass, W.A., Robinson, P.A., Kirkham, J., Shore, R.C., Robinson, C.: Molecular cloning and DNA sequence of Rat amelogenin and a comparative analysis of mammalian amelogenin protein sequence divergence. Biochem Biophys Res Commun **198**, 755–763 (1994)
153. Toyosawa, S., O'hUign, C., Figueroa, F., Tichy, H., Klein, J.: Identification and characterization of amelogenin genes in monotremes, reptiles and amphibians. Proc Natl Acad Sci U S A **95**, 13056–13061 (1998)

Chapter 6
Amorphous Calcium Carbonate: Synthesis and Transformation

Jun Jiang, Min-Rui Gao, Yun-Fei Xu, and Shu-Hong Yu

Abstract In this chapter, we discuss in detail about the syntheses and transformation of amorphous calcium carbonate (ACC). The aim of the present chapter is to present an overview on the synthetic strategies and crystallization of ACC reported till now. It should be noticed that the synthesis strategies and crystallization of ACC have achieved great progress. The main preparation methods for ACC include the direct-mixing method, gas diffusion technique, hydrolysis of carbonate source method and Kitano method, which have been fully discussed. A general review on the crystallization of ACC has been discussed. It is demonstrated that the transformation of ACC plays an important role in biomineralization. Several important transformation routes of ACC are selected for more detailed discussion. Current progress in this field demonstrates that there are a number of potential opportunities for both syntheses and transformation of ACC, and $CaCO_3$ crystals with different morphologies, structural features, and functionalities. In future, it is dramatically needed to find a reasonable way to prepare new composite materials using ACC or their transformed calcium carbonate crystals as one component, making ACC more useful for practical applications.

6.1 Introduction

Recently, material synthesis that simulates biomineralization in organic systems such as calcium carbonate, magnetic iron oxide, and amorphous silica of exquisite morphology, has attracted increasing interest because of their structural and functional value [1–11]. For example, the mechanical properties of bone and the optical

J. Jiang • M.-R. Gao • Y.-F. Xu • S.-H. Yu (✉)
Division of Nanomaterials and Chemistry, Department of Chemistry, Hefei National Laboratory for Physical Sciences at Microscale, University of Science and Technology of China, Hefei, 230026, People's Republic of China
e-mail: jiang123@mail.ustc.edu.cn; gmr@mail.ustc.edu.cn; babyxyf@mail.ustc.edu.cn; shyu@ustc.edu.cn

X.Y. Liu (ed.), *Bioinspiration: From Nano to Micro Scales*, Biological and Medical Physics, Biomedical Engineering, DOI 10.1007/978-1-4614-5372-7_6,

properties of pearls have many advantages over corresponding synthetic crystals [12, 13]. The formation of biominerals is complicated in nature, and organic templates are believed to be crucial to their crystallization and final morphologies and functions [14]. Inspired by the natural biomineralization procedure, researchers in the fields of material science and chemistry are attempting to repeat such control in lab. However, no synthetic materials have until now shown properties that can compete with those of their natural counterparts. So, many of the secrets of biomineralization need to be studied and understood.

$CaCO_3$ is one of the standard model systems for studying biomineralization because of its abundance in nature and important industrial applications (use as filler in plastic, paper, and in decorative paints) [15]. In parallel, calcium carbonate has been widely used as a model mineral in biomimetic research, leading to increased understanding of biogenic control over mineral orientation, morphology, and polymorph [16]. The polymorphs of calcium carbonate include three anhydrous crystalline phases (calcite, aragonite and vaterite), two hydrated ones (monohydrate and hexahydrate), and amorphous calcium carbonate (ACC) [17–22]. Calcite and aragonite are by far the most common and stable forms, whereas ACC, a least stable polymorph from the viewpoint of thermodynamics.

ACC has been widely found in biological organisms, where it plays an important role in the biomineraization of $CaCO_3$ [23–25]. It is generally accepted that biogenic ACC can be broadly as one of two forms: stable or transient. While the stable form remains non-crystalline, the transient phase can act as a precursor to either calcite [26, 27] or aragonite [28, 29] (calcite and aragonite are by far the most common in biological and geological samples). It is found in various organisms like Mollusk shells, American lobsters, ascidian skeletons, plant cystoliths, and so forth [30–34]. In addition, evidence has been found to suggest that calcific biominerals, such as the mollusk nacre and the urchin spine, are formed from an amorphous precursor [35–37]. The stable ACC is also formed by organisms and used as a skeletal material. Interestingly, ACC contains various amounts of water, which makes its density lower than other forms of calcium carbonate [38, 39].

Calcium carbonate crystallization in biological organisms often occurs through the transformation from the amorphous precursor [40]. Due to that the ACC is not a stable phase from the viewpoint of thermodynamics, the temporal stabilization was achieved by the incorporation of organic molecules and magnesium ions in both biological and synthetic systems [41–43]. It is believed that the ACC could be temporarily stabilized and stored, until its templated transition to the crystalline form is induced [44]. Biomimetic syntheses of crystalline calcium carbonate thin films and particles via transient ACC have been reported by many researchers [45–48].

This chapter will discuss in detail about the syntheses and transformation of ACC. The aim of the present chapter is to review the synthetic strategies and crystallization of ACC reported till date. Firstly, a general overview on the synthesis of ACC will be given. The direct-mixing method, gas diffusion technique, hydrolysis of carbonate source method and Kitano method will be introduced and discussed. Subsequently, a general overview on the crystallization of ACC will be discussed. Finally, the summary and perspectives on this field will be given.

6.2 Synthetic Strategies for Amorphous Calcium Carbonate

Calcium carbonate is one of the most important biological and industrial materials because of its abundance in nature and its wide applications in industry. The polymorphs of calcium carbonate include three anhydrous crystalline phases (aragonite, vaterite, and calcite) and three metastable forms (monohydrate, hexahydrate and ACC), in which ACC is the least stable polymorph and has been widely found in organisms. The stabilization of ACC was commonly achieved by using various additives, including biological macromolecules [49], magnesium [50], and synthetic polymers [51]. It is well known that ACC has important functions in biominerals and biomineralization processes. For example, it can be used as structural skeletal elements and temporary storage deposits. Moreover, a variety of calcium carbonate biominerals are now thought to be crystallized via an amorphous precursor pathway. Therefore, the ACC plays a key role in the biomineralization of $CaCO_3$ and how to synthesize the ACC in the lab is emerging as a hot research field.

In this chapter, we select several typical synthetic approaches commonly used to synthesize ACC to give facilities for readers to grasp the various strategies reported so far.

6.2.1 Direct-Mixing Method

6.2.1.1 The Na_2CO_3-NaOH-$CaCl_2$ Aqueous Reaction System

Amorphous precipitates of $CaCO_3$ were prepared by reaction in a mixed solution of Na_2CO_3-NaOH with a $CaCl_2$ solution within pH value in the range of $11.2 \leq pH \leq 13.0$ at an ambient temperature of 278 K [52]. Equivolumes of aqueous solutions of NaOH (0.2 mol L^{-1}) and Na_2CO_3 (0.1 mol L^{-1}) were mixed with mechanical stirring, to obtain mixed solutions. The mixed solutions and an aqueous solution of $CaCl_2$ (0.1 mol L^{-1}) were kept in a refrigerator at 278 K for 1 h. Equimolar $CaCl_2$ solution with respect CO_3^{2-} in the mixed solutions was added rapidly to the mixed solutions with mechanical stirring at an ambient temperature of 278 K. The obtained product was filtered immediately and washed with acetone. The precipitates were dried in a vacuum desiccator for 1 day. On heating, the obtained ACC loses the absorbed water until ca. 530 K and subsequent crystallization to calcite (Fig. 6.1).

6.2.1.2 The Na_2CO_3-$MgCl_2$-$CaCl_2$ Aqueous Reaction System

Magnesium can certainly be expected to influence the biogenic $CaCO_3$, such as incorporating into the calcite lattice, inducing the formation of aragonite, stabilizing the ACC and so on. Interestingly, we have come to learn that all known biogenic

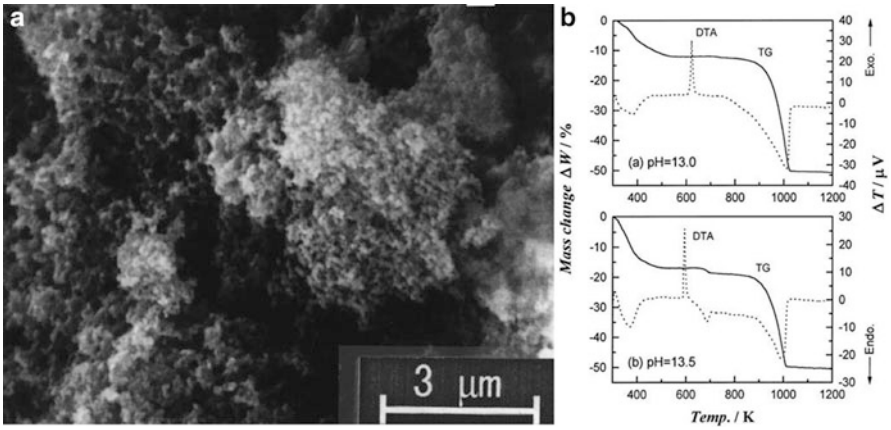

Fig. 6.1 (**a**) A typical SEM image of dehydrated ACC. (**b**) Typical TG-DTA curves for ACC. (Reproduced from [52], Copyright © 1998, Elsevier)

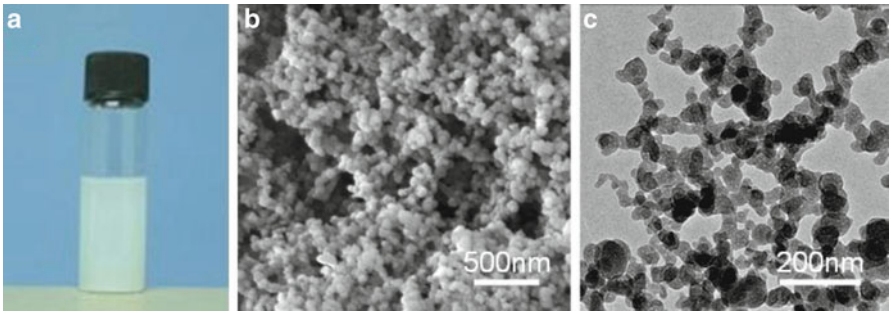

Fig. 6.2 Magnesium amorphous calcium carbonate (Mg-ACC) obtained by rapid mixing of the solutions ($CaCl_2$, Na_2CO_3, and $MgCl_2$). (**a**) the Mg-ACC powder dispersed in ethanol homogeneously, (**b**) Scanning electron microscopy (SEM) images of the obtained Mg-ACC, (**c**) Transmission electron microscopy (TEM) images of the obtained Mg-ACC. (Reproduced from [53], Copyright © 2010, Royal Society of Chemistry)

ACC almost contains magnesium, which is presented in large quantities in seawater (about 50–60 mM Mg^{2+}, relative to the 12 mM Ca^{2+}). Therefore, The Mg-ACC plays a key role in the biomineralization of $CaCO_3$.

In a typical experimental procedure, $CaCl_2$ (0.1 mol L^{-1}, 25 mL) and $MgCl_2{\cdot}6H_2O$ (0.5 mol L^{-1}, 5 mL) were mixed with mechanical stirring to obtain mixed solutions. Then, a Na_2CO_3 solution (0.1 mol L^{-1}, 25 mL) was added rapidly to the mixed solutions with mechanical stirring at an ambient temperature of 25 °C. The precipitated colloidal phase was filtered immediately and washed with ethanol. The precipitates were dried in a vacuum desiccator for 1 day (Fig. 6.2) [53].

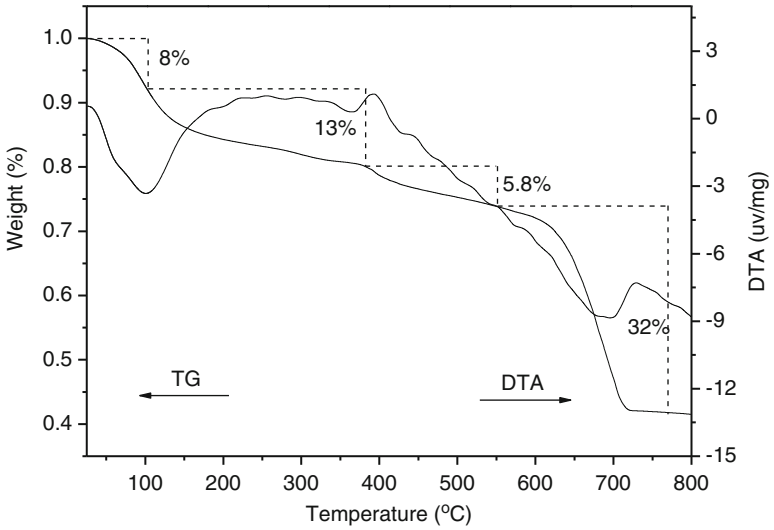

Fig. 6.3 Thermogravimetric and differential thermal curves of magnesium amorphous calcium carbonate (Mg-ACC) powder. (Reproduced from [53], Copyright © 2010, Royal Society of Chemistry)

The possible structure of the obtained Mg-ACC can be defined as $Mg_{0.15}Ca_{0.85}CO_3H_2O_{0.85}$ (Fig. 6.3). The molar ratio of Mg^{2+}:Ca^{2+}:CO_3^{2-} and the concentration ($CaCl_2$, Na_2CO_3, and $MgCl_2$) play important role in the Mg/Ca molar ratio of the obtained Mg-ACC. In particular, the Mg-ACC can be preserved for over one year without crystallization by either storing its dry powder at −5 °C or storing it in ethanol at 5 °C. The access of Mg-ACC nanoparticles in large scale would be useful for further biomineralization study and industry applications.

6.2.1.3 The Na_2CO_3-PAA-$CaCl_2$ Aqueous Reaction System

The nanosegregated amorphous composites consisting of $CaCO_3$ and an organic polymer can be prepared by this method (Fig. 6.4) [54]. The thin and bulk film of the amorphous composites possessed stability and transparency. The amorphous composite in the bulk state was formed by mixing the two solutions. The Na_2CO_3 (0.1 M) solution was poured into the precursor solution containing polyacrylic acid (PAA) (0.1 M) and $CaCl_2$ (0.1 M) at room temperature. A white precipitate gradually appeared upon mixing of these solutions. The obtained product was collected after 1–2 h by centrifugation and then the paste-like translucent material was dried at room temperature. When the reaction took place without the PAA, the ACC can also be obtained [55].

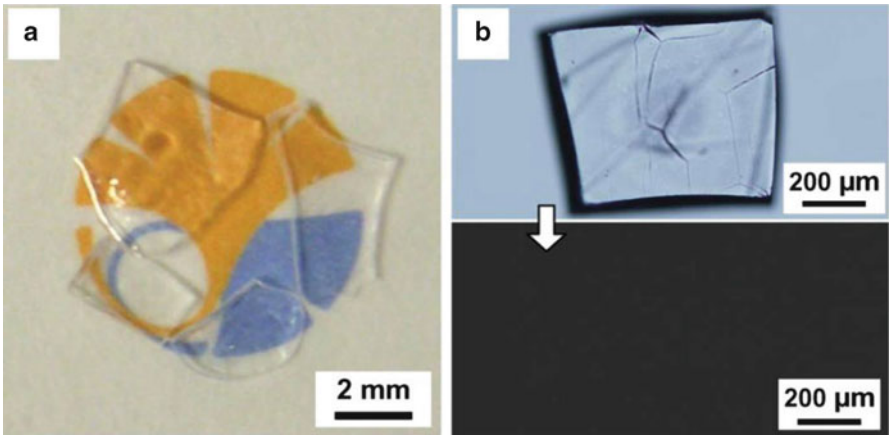

Fig. 6.4 Optical properties of the composite consisting of $CaCO_3$ and PAA in the bulk state. (**a**) Macroscopic appearance of the bulk state. (**b**) Optical microscopy (upper) and its cross-polarized optical microscopy (lower) images, respectively. (Reproduced from [54], Copyright © 2008, Wiley VCH)

6.2.2 Gas Diffusion Technique

The ACC can be obtained by using ethanolic $CaCl_2$ and ammonium carbonate as the sources of calcium and carbon dioxide, respectively [56]. Other additives or any elaborating pH control are not necessary to form the precursor of ACC. Ethanol itself inhibits the dissolution of ACC so that the solution mediated phase transition of ACC to calcite or vaterite can barely take place. The calcium carbonate precipitate (CCP) was synthesized in 10 mM ethanolic $CaCl_2$ solution by allowing the diffusion of CO_2 vapor from $(NH_4)_2CO_3$ into the solution; the whole reaction vessel was kept at 293 K using a water-circulating temperature controller. When the reaction is carried out, the solution phase became milky-white and then a white gel-like precipitate was deposited at the bottom. After 1 day, the reaction finished and the gel-like precipitate was filtered out. The obtained precipitate is called CCP. When the CCP is heated to 373 K for 24 h in a N_2 atmosphere flowing at 110 mL min^{-1}, the ACC is obtained (Fig. 6.5) [56].

Interestingly, Gower and co-workers reported that the polyaspartic acid is important for the formation of the ACC phase [57]. Furthermore, the PILP (polymer-induced liquid- precursor) process results in the formation of an amorphous phase which is induced and stabilized by a polymeric additive. The subsequent crystallization of the deposited film produces calcitic tablets similar in shape to the nacreous tablets. This PILP process was used elsewhere to grow a calcium carbonate amorphous film at a fatty acid monolayer located at an air–water interface. The vapor diffusion method that we commonly use to form the PILP droplets was scaled up to generate sufficient phase for compositional analysis. The experimental

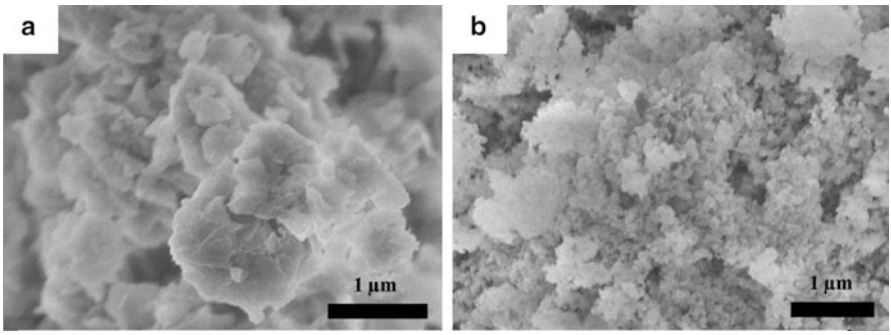

Fig. 6.5 (**a**) FE-SEM image of CCP in as-prepared state and (**b**) that after heating at 373 K for 24 h; the latter in fact corresponds to ACC. (Reproduced from [56], Copyright © 2005, Elsevier)

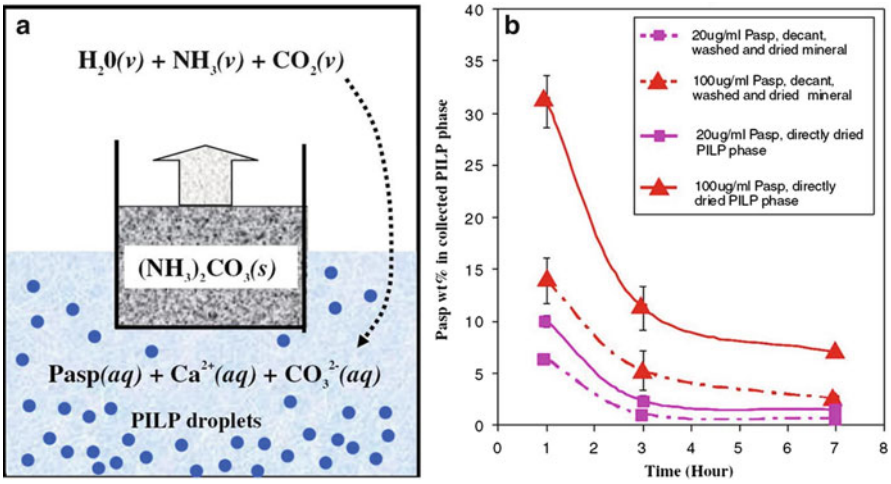

Fig. 6.6 (**a**) Schematic illustration of the experimental setup. A 150-mL glass beaker containing crushed ammonium carbonate powder was placed in a 500-mL glass beaker containing 250 mL of a 20 mM $CaCl_2$ solution with a variable amount of polyaspartate (Pasp). (**b**) Pasp weight percentage in PILP phase that was collected by centrifugation and dried for elemental analysis, versus Pasp percentage in PILP phase that was collected by centrifugation, filtered and washed, and then dried for elemental analysis. Note that the Pasp was distributed both in the mineral and in the loosely bound water of the PILP phase, and the Pasp percentage of the PILP phase decreased more significantly during the 1–3 h period. (Reproduced from [57], Copyright © 2008, Elsevier)

setup is showed in Fig. 6.6 [57]. The $(NH_4)_2CO_3$ in a 150-mL glass beaker was diffused into 250 mL of 20 Mm $CaCl_2$ solution containing polyaspartate (Pasp). When the reaction finished, the solution was centrifuged at 6500 r/min for 300 s and the precursor product was then collected and dried at 473 K. By using this approach, the weight fraction of calcium ions and carbonate ions can be estimated, which was further used to calculate the ratio of carbonate to calcium.

Moreover, Chu et al. [58] have studied the synthesis of ACC films using an acid polysaccharide as an additive by using the gas diffusion method. The thin ACC film is formed directly onto TEM grids by floating the grids onto a crystallization solution because of the rapid transformation of ACC into its crystalline phase. Thus, they have successfully used TEM in combination with SAED to characterize the mesostructure of the formed ACC films. Meldrum and co-workers [59] also demonstrated that synthetic ACC can be produced with different short-range structures by using the gas diffusion method, according to the solution additives used. Their data suggested that the influence of these additives (Pasp or Mg) on ACC formation can be apparent even in the structure of the first-formed precursor phase. It would be useful to investigate the interplay of different additives in stabilizing and directing the crystallization of synthetic ACC.

6.2.3 Hydrolysis of Carbonate Source Method

Faatz and co-workers reported a method in which the release of carbon dioxide by hydrolysis of the carbonate source (dialkyl carbonate) [60]. When dialkyl carbonates are hydrolyzed isothermally at a settled pH in an aqueous solution of calcium chloride, $CaCO_3$ is precipitated slowly, on a timescale of minutes to hours. The experiment was carried out starting with dilute solutions of calcium chloride (0.01 M) in water and an excess of dimethyl carbonate. When the solution of sodium hydroxide (0.5 M) was added, the solution started to become turbid after 90 s at 298 K. After 150 s, the precipitate was removed from the reaction mixture by centrifugation, then washed with acetone and dried under vacuum. This result demonstrates that ACC can be synthesized at room temperature in aqueous media without any additives such as polyphosphonate or magnesium salts that can prevent crystallization [60].

The size of the ACC particles can be controlled by using this method when a double hydrophilic block copolymer (DHBC) was added in the reaction [61], which is composed of blocks of polyethylene oxide and PAA. The optimally designed DHBCs can control the particle size of ACC at concentrations corresponding to a monolayer coverage of the liquid precursor droplets. The optimal concentration in DHBC was found to be between 3 and 10 ppm, and ACC nanoparticles of 60–100 nm in diameter could be formed.

In addition, the decomposition of urea by catalytically active Canavalia ensiformis urease in a solution of magnesium and calcium salts can be used to precipitate uniform nanostructured ACC particles [62]. The reaction solutions containing magnesium, calcium chloride, and urea were kept in tightly stoppered Erlenmeyer flasks and saturated with nitrogen before a measured amount of urease solution was injected. Then, the mixtures were kept at room temperature 2 min with gentle stirring. The obtained ACC were sequentially filtered and washed with deionized water to remove the excess of magnesium and calcium salts and urease. This procedure prevents the formation of a new solid phase.

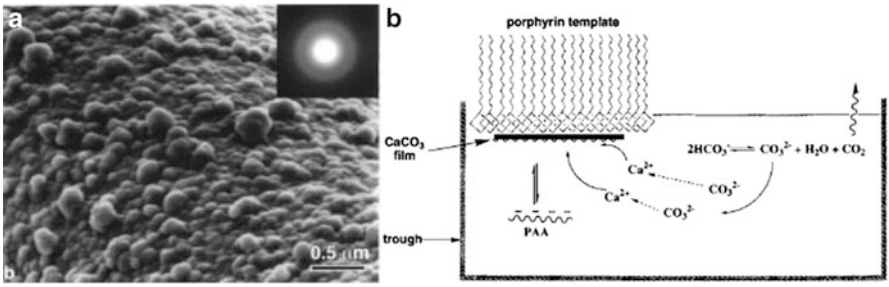

Fig. 6.7 (**a**) High magnification SEM image of the film showing the rough side that faced the subphase. The inset shows the electron diffraction pattern of the film by TEM. (**b**) A schematic representation of the experimental setup for preparing $CaCO_3$ thin films at the interface of the air/aqueous subphase. (Reproduced from [64], Copyright ©1998, American Chemical Society)

Furthermore, Wegner and co-workers investigated that the photochemical decomposition of pyruvic acid, 4-benzoylphenyl acetic acid and 2-nitro-phenylacetic gave ill-defined morphologies of calcium carbonate contaminated by organic by-products [63]. Alkaline hydrolysis of dimethyl- and diethyl-carbonate can yield ACC in form of nanospheres with narrow distribution of radius. The formation of spherical ACC particles is rationalized in terms of a liquid–liquid phase separation followed by rapid gelation of the droplet phase of high concentration of $CaCO_3$. A lower critical solution temperature is necessary and its value can be estimated as 283 K.

6.2.4 The Kitano Method

Xu and co-workers described a strategy in which the slow release of carbon dioxide by the unstable calcium bicarbonate [64]. They have synthesized continuous and macroscopic calcium carbonate thin films with a thickness ranging from 400 to 600 nm. The thin films were synthesized at air/subphase interfaces by promoting mineral deposition with amphiphilic porphyrin templates, coupled with growth inhibition by the use of poly (acrylic acid) as a soluble inhibitor. Films obtained in the early stage of formation at lower temperature (277 K) revealed characteristics of a single amorphous phase. The results provide new insights into the biomineral-inhibitor-template interaction and a new mechanism for synthesizing ACC. The experimental setup for preparing the amorphous thin film is showed in Fig. 6.7 [64]. The Ca $(HCO_3)_2$ subphase was prepared by bubbling CO_2 gas into Milli-Q deionized water in the presence of $CaCO_3$ for 2 h. Excess solid $CaCO_3$ was removed by filtering, and the filtrate was purged with CO_2 for another hour. The freshly synthesized Ca $(HCO_3)_2$ was immediately mixed with sodium polyacrylate solution to reach a final polymer concentration in the range of 10–40 ppm. Then, a porphyrin monolayer was deposited onto the surface of the subphase from a

chloroform solution, which served as a template for the $CaCO_3$ film formation. The setup was kept in a "cold" room in which the temperature was maintained at 277 K.

Furthermore, Epple and co-workers reported a facile approach to precipitate large quantities of ACC which is stable over a long time with and without additives by using the Kitano method [65]. The pure ACC was obtained by bubbling CO_2 through a saturated calcium hydroxide solution at 273 K. The precipitation was stopped when the pH reached 8 and the precipitate was filtered and rinsed with cold acetone. The product was dried under high vacuum at 273 K for 36 h and stored under P_2O_5 in a desiccator.

6.2.5 Stabilizing Effect of Additives on Amorphous Calcium Carbonate in Organisms

ACC is the most unstable form of calcium carbonate, it transforms quickly into more stable crystalline forms under ambient conditions, such as calcite and vaterite. Analyses of biogenic calcium carbonates have identified the presence of magnesium, phosphate anions and silicate, which were associated with ACC and poorly ordered calcite [66]. These additives are thought to be able to prevent crystal nucleation and growth by interfering with the formation of an ordered crystalline structure of $CaCO_3$ [67]. Moreover, heating ACC is one method to measure its stability [68]. The ACC loses bound water when it is heated, and ACC crystallizes to calcite (the thermodynamically stable polymorph) when the temperature is high enough to overcome the kinetic energy barrier.

Addadi et al. found that cystoliths with a high concentration of silicate ions in the ACC phase are more stable than the cystoliths devoid of silicate [69]. A potential mechanism for stabilization of ACC by the silicate may be the destabilization of calcite by "geometric frustration" of the crystal lattice (incorporating the planar carbonate ions) [70]. The presence of the large tetrahedral silicate ions with four negative charges in the ACC may conceivably destabilize calcite both by perturbing the charge equilibrium and preventing regular packing. On the other hand, many biogenic ACC examples contain large amounts of phosphate. The phosphate ion has a tetrahedral structure too and has been suggested to stabilize ACC in the lobster carapace by a mechanism similar to silicate ion.

6.3 Transformation of Amorphous Calcium Carbonate

Thanks to the ACC is not a stable phase from the viewpoint of thermodynamics, the temporal stabilization was achieved by the incorporation of organic molecules and magnesium ions in both biological and synthetic systems. It has been demonstrated that the ACC could be temporarily stabilized and stored, until its templated

transition to the crystalline form is induced and biomimetic syntheses of crystalline calcium carbonate thin films and particles via transient ACC have been widely investigated by many researchers.

6.3.1 *Crystallization of Amorphous Calcium Carbonate in Biomineralization*

Addadi et al. [71] pointed out that the first suggestion of a transient ACC precursor in mollusk biominerals by Hamilton and Towe, who back in 1968 observed hollow "crystals" in the developing nacre of the bivalve, and found that "a possibility exists that the incipient calcification is not in the form of aragonite but rather in some other phases". To our knowledge, the first paper to describe a transitory ACC in biominerals was that by Beniash et al. in 1997 [72], who observed spicule formation in sea urchin larvae. The spicules are comprised of single-crystalline calcite, but upon finding the presence of an additional ACC phase which transformed into calcite with time. This group also shows ex vivo evidence of an amorphous precursor in the regeneration of the adult urchin spine, as well as the teeth of sea urchins. In addition, it has been demonstrated that organisms may use ACC as a metastable precursor to form single crystals with complex shapes. Interestingly, Addadi et al. [73] found that sea urchin spine regeneration proceeds via the initial deposition of ACC. Most echinoderms probably all use this same mechanism because they produce the same type of skeletal material.

Therefore, sea urchin larval spicules have long served for the investigation of $CaCO_3$ biomineralization procedure as a model system. The mature larval spicule is composed of a single crystal of calcite [74, 75]. Furthermore, the study result showed that even at early stages, when the $CaCO_3$ is still predominantly amorphous, it already has a nascent short-range order around the calcium ions similar to that in calcite. Politi et al. used X-ray photoelectron emission spectromicroscopy with probing size of 40–200 nm to investigate the transformation mechanism of ACC into calcite in the sea urchin larval spicule [76]. They resolved three distinct mineral phases: an initial short-lived hydrated ACC phase, followed by an intermediate transient form of ACC, and the biogenic calcite phase. A secondary nucleation mechanism was proposed to explain the transformation of ACC into calcite in the sea urchin larval spicule. Based on the obtained experiment results, they proposed that a transformation from type 2 amorphous to type 3 crystalline phase propagates through the spicule via secondary nucleation, in which the crystallization of one amorphous unit promoted the transformation of the domains in contact with it. In addition, the propagation pathway through the spicule is inferred to be tortuous and complex, implying that the transformation rate depends on the size and interface structure of the amorphous domains.

In order to understand the mechanism of the crystallization, Tremel et al. reported a time-resolved investigation of the contact-free homogeneous formation and

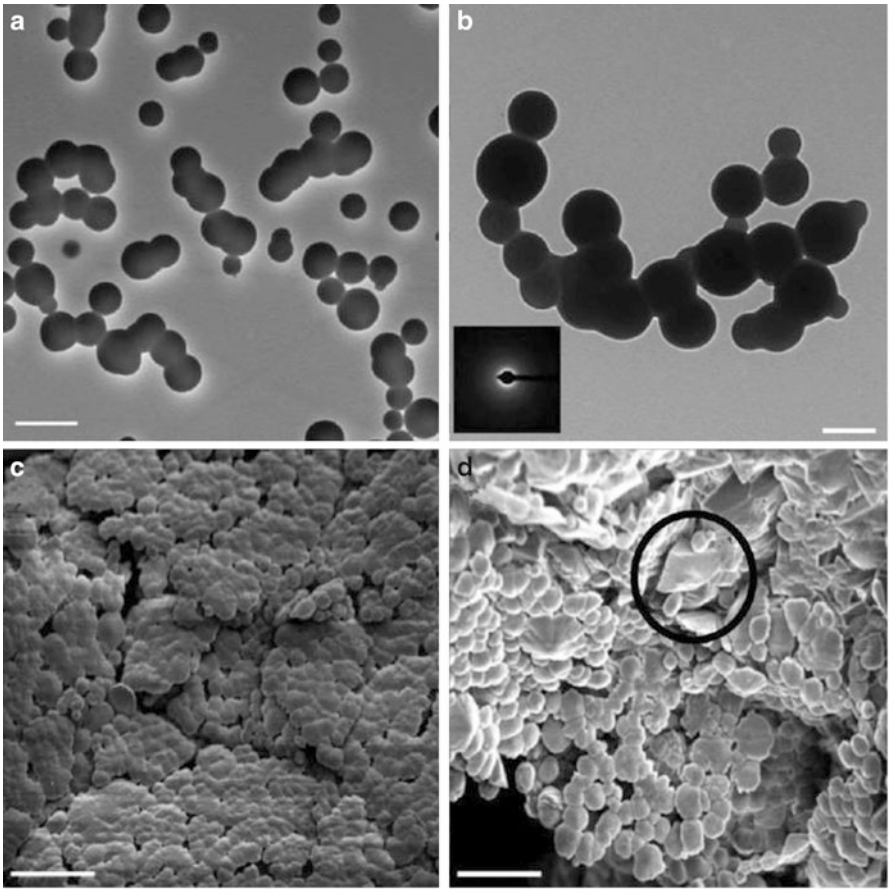

Fig. 6.8 Calcium carbonate particles obtained after 400 s (TEM: **a**, **b**). The low contrast variation within the particles indicates their liquid character. After complete evaporation, SEM revealed that spherical solid particles are present along with rhombohedral calcite crystals (**c**, **d**). Scale bars: (**a**) 500 nm, (**b**) 200 nm, (**c**) 20 μm, and (**d**) 10 μm. On the basis of the morphology of the calcite particles, the transition to the crystalline phase is assumed to take place through recrystallization. One rhomboidal calcite crystal is marked by a circle in (**d**). (Reproduced from [77], Copyright © 2008, American Chemical Society)

growth of $CaCO_3$ in levitated droplets studied from undersaturated to supersaturated concentrations in a single experiment (Fig. 6.8) [77]. This amorphous polymorph formed in the absence of additives at neutral pH. The presence of various species such as bicarbonate, carbonate, and nondissociated carbonic acid may play an important role in the stability of ACC. The crystallization procedure of $CaCO_3$ was monitored by in situ WAXS experiments performed at a synchrotron microspot beamline equipped with an ultrasonic levitator. They found that the polymorph transformation process from ACC to calcite started at the droplet surface and thus

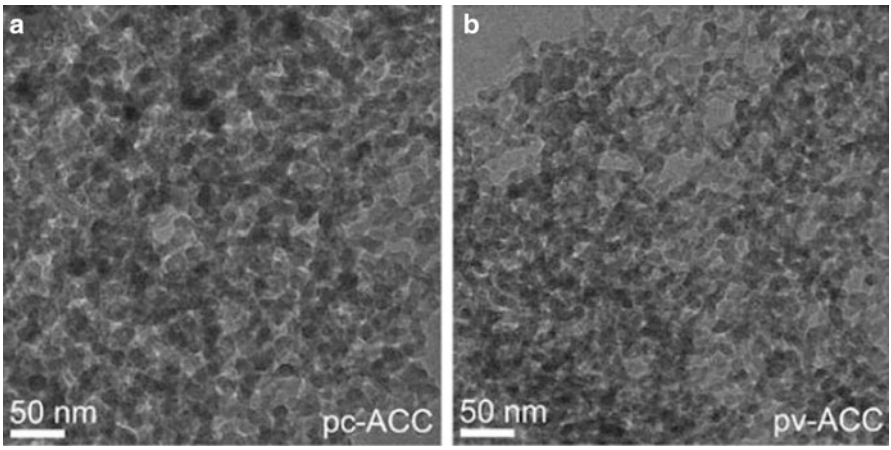

Fig. 6.9 TEM images of pc-ACC and pv-ACC. (Reproduced from [80], Copyright © 2010, Wiley)

clearly differs from the crystallization within the droplets. The crystallization was carried out homogenously by using the Kitano method. These results show that the ultrasonic trap may be a powerful tool for a real-time analysis of nucleation, crystal growth, and phase separation processes.

Moreover, a fresh picture of the crystallization of $CaCO_3$ is emerging, which involves transformations of clusters to ACC and eventually to crystalline phases [78, 79]. Hedin and co-workers studied proto-crystalline features of two amorphous intermediates, ACCI and ACCII, and discussed their relation for crystallization of $CaCO_3$ (Fig. 6.9) [80]. They rationalized the identification of ACCI with proto-calcite ACC and ACCII with proto-vaterite ACC, respectively. These ACCs were obtained from metastable solutions of $CaCO_3$ at different pH values by destabilization in excess ethanol. Interestingly, they found that structural water in proto-vaterite ACC and proto-calcite ACC as an explanation of the low coordination numbers for calcium and deviations from certain symmetries. Therefore, proto-crystalline order is intrinsic to these ACCs and only one factor influencing crystallization. Additive-free proto-crystalline ACCs play key roles in the further analyses of the processes involved in crystallization of calcium carbonate.

6.3.2 Single Crystals Formed via an Amorphous Precursor Phase

As well-known, calcium carbonate often shows complex single-crystalline structures, such as the three-dimensionally sculpted conformations of the calcite skeletal plates of coccoliths and echinoderms [81]. Meldrum and co-workers [82, 83] reported the control of calcium carbonate morphologies and demonstrates that

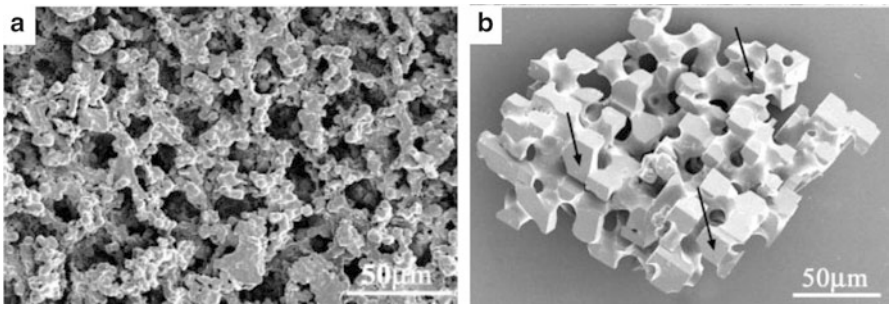

Fig. 6.10 Calcium carbonate precipitated in the polymer membrane. (**a**) Polycrystalline particle precipitated from 0.4 M reagents, (**b**) templated single crystal of calcite precipitated from 0.02 M solutions. (Reproduced from [82], Copyright © 2002, Wiley)

single crystals with complex form can be produced without using additives, by external imposition of morphology (Fig. 6.10). Calcium carbonate was obtained in a polymer membrane, which had a same morphology to a sea urchin skeletal plate. The polymer membrane was templated by a sea urchin plate and was produced by dipping a plate in a polymer monomer solution, curing the polymer, and finally dissolving away the calcium carbonate to obtain the polymer replica. Precipitation of $CaCO_3$ in the membrane was received by placing the membrane between two half U-tube arms, and filling them with Na_2CO_3 and $CaCl_2$ solutions respectively [82]. After a designated time, the membranes were removed from the U-tube set-up, washed with water, and allowed to dry at room temperature for 1 day. Removal of the membrane by heating (at 773 K for 45 min) yielded the particles of calcium carbonate that had been precipitated in the membrane [82]. The experimental results demonstrate that the single crystals of calcite with sponge-like morphologies were readily produced by precipitation within a suitable constrained volume under controlled nucleation and growth conditions. They also investigated the morphological control of single crystals by using the biological mechanisms as inspiration [84]. Calcite was obtained within the cylindrical pores of track-etch membranes via an ACC precursor.

Mosaic single-crystal $CaCO_3$ thin films can be obtained on modified poly(ethylene terephthalate) (PET) templates [85]. The thin films can be fabricated on chemically modified PET template surfaces by the process of transformation of ACC film into a crystalline phase in air. The experimental results confirmed that single-crystal $CaCO_3$ growth patterns are dependent on the surface characteristics of the PET template. Therefore, the nucleation and growth of ceramic films on polymeric templates can be controlled by chemical modification of the polymeric template surface, and by subsequent attachment of ionic polyelectrolytes.

Qi et al. reported a novel approach to obtain three-dimensional ordered macroporous (3DOM) calcite single crystals by combining the amorphous-to-crystalline strategy with the use of colloidal crystals as 3D templates [86]. The results demonstrated that that it is feasible for ACC to form single calcite with a

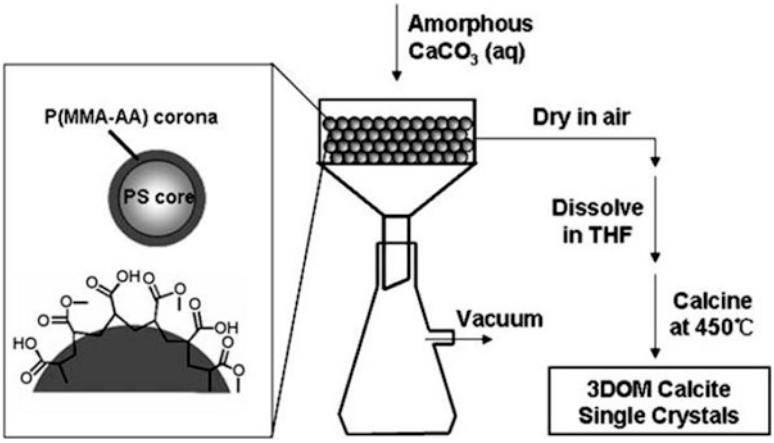

Fig. 6.11 Fabrication of 3DOM calcite single crystals by templating colloidal crystals of P(St-MMA-AA) spheres carrying a carboxylate corona. (Reproduced from [86], Copyright © 2008, Wiley)

well-defined 3DOM structure and controlled crystal orientation via specific surface functionalization of the colloidal crystal template. Based on the experimental results, they found that the calcite single crystals that formed in the colloidal crystal template evolved form small patches to large symmetric dendrites up to several tens of micrometers in size as the amount of ACC was enhanced. In particular, two factors play key roles in the formation of the calcite single crystals, that is, the vacuum-assisted filtration process which induces the filling of ACC in the interstices of the template, and the surface-functionalized template which provided the affinity to ACC [86]. In a typical experimental procedure, the 3D calcite single crystals were achieved by infiltration of the ACC precursor into polymer colloidal crystals with subsequent drying, dissolving in THF, and heated at 723 K as shown in Fig. 6.11 [86]. Monodisperse poly-(styrene-methyl methacrylate-acrylic acid) (P(St-MMA-AA)) colloidal spheres, which have a polystyrene (PS) core and a carboxylate corona [87], were assembled into 3D colloidal crystal on a filter membrane. Then, a freshly obtained ACC dispersion was added dropwise to the colloidal crystal film mounted under vacuum, leading to the deposition and crystallization of ACC within the interstices of the colloidal crystals. These experimental results suggest a general strategy for the design and fabrication of functional single-crystalline materials with desired shapes, orientations, and nanopatterns.

Moreover, single crystals of calcite with regular patterned surfaces comprising close-packed arrays of hemispherical cavities ordomes can be prepared by crystallization on colloidal monolayers or polydimethylsiloxane replicas of these monolayers, respectively [88]. This study demonstrates that crystallization within a mould provides a general route to produce single crystals with unusual morphologies and curved surfaces.

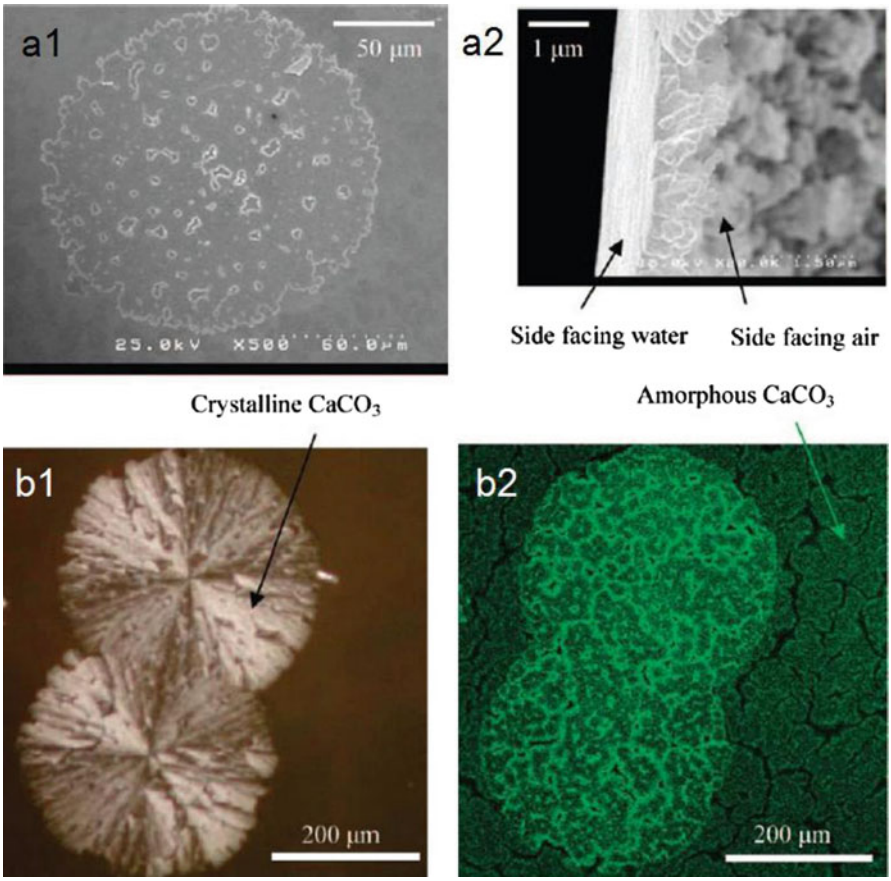

Fig. 6.12 (**a1**–**a2**) SEM images of vaterite islands. (**b**) In situ photographs of vaterite island domains formed at the liquid-air interface with $[CaCO_3] = 10$ mM, [PAA] = 40 ppm, mineralization time = 48 h: (**b1**) under crossed polarizers, (**b2**) using fluorescence confocal microscope. (Reproduced from [89], Copyright © 2009, American Chemical Society)

6.3.3 Transformation of Amorphous Calcium Carbonate Films

In biomimetic approach, calcium carbonate thin film has been obtained using cooperative interactions between natural/synthetic substrates (collagenous/polyamides eggshell membrane) and soluble polymeric additives. Aizenberg et al. previously suggested that the ACC film crystallization process occurs by mass transport between the amorphous and crystalline [49].

The micron-thick crystalline calcium carbonate continuous films can be obtained by using a simple interfacial configuration based on PAA adsorption at an air–water interface (Fig. 6.12) [89]. In this system, the formation of large partially oriented vaterite crystalline domains at the interface is shown to rely on the early

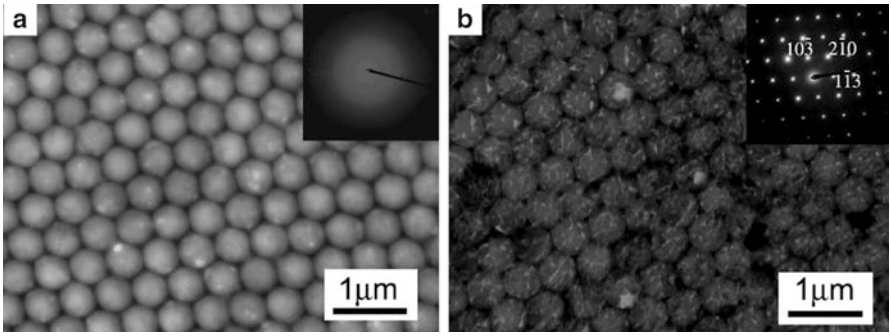

Fig. 6.13 TEM images of amorphous (**a**) and crystalline (**b**) HP-$CaCO_3$ films. Insets show the corresponding SAED patterns. (Reproduced from [90], Copyright © 2010, American Chemical Society)

precipitation of ACC microdomains. The PAA was introduced to obtain the unstable crystalline polymorph of vaterite at an air–water interface. The so-called Kitano method was used to prepare highly supersaturated $CaCO_3$ solutions. Moreover, due to the possible polymorph selection, the mineral is precipitated out of vaterite instead of the most stable calcite polymorph. The air–water interface in the presence of PAA is certainly one of the simplest biomimetic systems, which can be used for easy deposition on a positively charged substrate for further use.

The strategy of colloidal lithography can also be used to obtain the honeycomb-patterned thin films of ACC and mosaic calcite at the solution surface. The honeycomb-patterned ACC (HP-ACC) thin films were obtained by a polymer-induced ACC coating of the monolayer colloidal crystal (MCC) template at the air/water interface (Fig. 6.13) [90]. Moreover, the honeycomb-patterned, mosaic calcite thin films composed of single-crystalline calcite plates could form when the amorphous films is heated at 673 K. In a typical experimental procedure, a piece of MCC film with an area of 1 cm^2 that was deposited on a silicon substrate and then was transferred on to the surface of the $CaCl_2$ solution and PAA. The vessel holding both the precursor solution, and the floating MCC film was covered with Parafilm punched with one small aperture and put inside a closed desiccator with 2 g of $(NH_4)_2CO_3$ powder located at its bottom. The coating process lasted for 6 h at 298 K. The MCC template was then removed by dissolving the product in dichloromethane to obtain intact HP-ACC thin films. When the sample was heated at 673 K in air and then the mosaic calcite thin films composed of single-crystalline calcite plates was obtained. The very high temperature was applied to enhance the crystallization process of the ACC. Therefore, the controlled crystallization of ACC with retained patterns and shapes represents an alternative route to patterned crystalline thin films.

Moreover, Xu et al. observed two modes of transformation of ACC in air into ordered structures solid–solid phase and dissolution-recrystallization transition by using the large-area ACC films [91]. They found that oriented large-area calcite films could be prepared by controlling the transformation of an ACC film by

varying the temperature conditions in air and air humidity, without the aid of a functional template. At high temperatures, ACC is transformed into the crystalline form via a solid–solid transition, whereas under conditions of high humidity, ACC tends to dissolve and recrystallize. The crystallization mechanism is expected to be determined by the increased thermal energy when the ACC film is heated to high temperature [91]. The high temperature will promote the transformation of ACC by supplying more energy, which will allow the ionic species in ACC to cross the energy barrier for realignment. On the other hand, the rate of ACC crystallization increases with increasing relative humidity.

Gower and co-workers reported that a PILP mineralization process may play an important role in biomineralization [92]. The PILP process is induced with polyanionic polypeptides to produce colloids of an amorphous mineral that are so highly hydrated that they coalesce into smooth mineral films. Transition bars have been monitored in situ during the crystallization of ACC films deposited under Langmuir monolayers and on glass slides via the PILP process. In addition, optical microscopy was used to observe the amorphous-to-crystalline transformation in situ. The crystallographic anisotropy of the polymer occlusions and sectorization of tablets in the PILP system may help to explain some of the crystal textures found by ex vivo analysis of biominerals (e.g., seminacre and nacre).

In addition, the ACC precipitates are initially formed from highly supersaturated solutions, which then deposit as films through the cooperation between a soluble inhibitor and an insoluble matrix [93]. The inhibitor and matrix are also found to affect the morphology, growth, and structure of $CaCO_3$ crystals by influencing the transformation of ACC into crystalline forms. The generation of patterned $CaCO_3$ films with dimensions of several hundreds of micrometers using the photolithographic properties of an amphiphilic ABA block copolymer and the possibility to shape $CaCO_3$ in its amorphous state has also been reported [94]. Furthermore, Klok et al. [95] demonstrated the use of brushes to act as ionotropic matrices for the directed synthesis of microstructured calcite thin films. The acidic macromolecules are used to form an ionotropic gel, which can stabilize and host a transient ACC phase and serve to direct crystal growth into geometries defined by the macromolecular matrix. The effect of chain mobility and functionality of selected polymer substrates has been investigated by Cho and co-workers [96]. It was found that how the chain mobility and functionality of selected polymer substrates with ester groups in either the backbone or side chains affect the crystallization of ACC films fabricated through biomimetic methods. Micropatterned calcium carbonate films consisted of regularly aligned calcite oriented along the (104) direction can be selectively obtained on the patterned NDR/PAA multilayer film [97].

6.3.4 Crystallization of Precursor on Monolayer

The Langmuir monolayer is widely utilized for investigating biomineralization on biological membranes. The crystallization process of $CaCO_3$ on a stearic acid

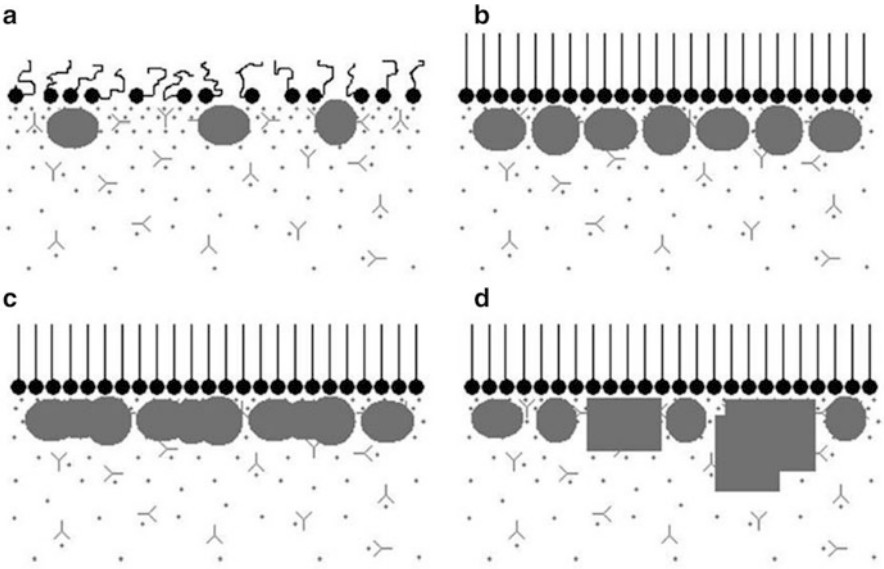

Fig. 6.14 Schematic graph showing the formation of $CaCO_3$ under the SA monolayer: (**a**) isolated ACC particles are formed during the initial compression, (**b**) the primary ACC particles grow in number density and remain stable during the continuous compression, (**c**) with prolongation of the reaction time, the ACC particles continue to nucleate and grow and tend to aggregate together, (**d**) when the reaction time is further increased, the ACC particles and the aggregates gradually transform into calcite. (Reproduced from [98], Copyright © 2009, American Chemical Society)

monolayer at the air–water interface has been studied by Yang and co-workers [98]. It is found that the final calcium carbonate crystals are transformed from ACC rather than directly from the solvated ions under the compressed stearic acid monolayer. The precursors, which are uniform spherical particles with sizes smaller than 100 nm, are produced in an early stage of mineralization and can be stabilized for at least 0.5 h. Subsequently, the ACC particles tend to aggregate and are eventually transformed into the calcite phase with the elapse of time. In addition, the Kitano method is used to form the ACC. Furthermore, the observation of the crystallization of ACC is important to the understanding of the detailed biomineralization mechanisms of cell membranes. According to the experiment results, the crystallization process of calcium carbonate under the SA monolayer can be illustrated as in Fig. 6.14 [98].

Moreover, the ACC can be obtained on a self-assembled monolayer (SAM) of hydroxyl-terminated alkanethiols on a gold surface [99]. Then, it can be stored in a dry atmosphere as a reservoir for ions and be induced to crystallize by water and a secondary surface that is functionalized with carboxylic acid-terminated SAM. This secondary surface is the template for oriented and patterned nucleation of $CaCO_3$. Using this method, various oriented crystalline arrays and micropatterned films are formed (Fig. 6.15) [99]. Foreign ions and molecules can be doped

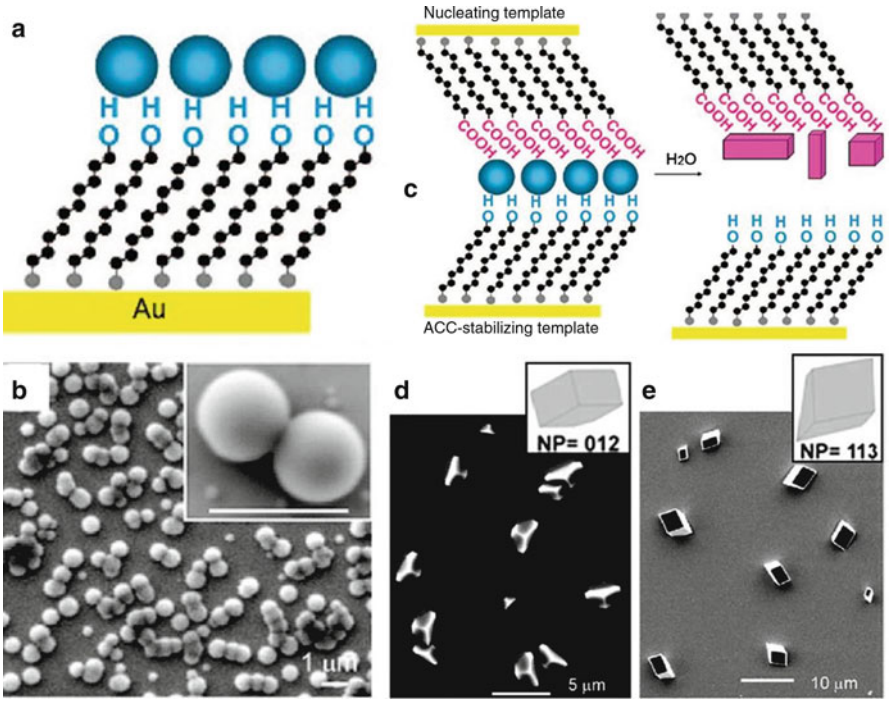

Fig. 6.15 (**a**) Schematic illustration of the ACC formation on a Au-OH SAM. (**b**) SEM of the ACC spheres removed from the solution after 45 min. Inset: high-magnification image. (**c**) Schematic presentation of the process. (**d**) SEM of the oriented calcite crystals formed on a secondary nucleating template of Au-C15-COOH. The inset shows a computer simulation of the crystal nucleated from the (012) nucleation plane (NP). (**e**) SEM of the oriented calcite crystals formed on a secondary nucleating template of Au-C10-COOH. The inset shows a computer simulation of the crystal nucleated from the (113) NP. (Reproduced from [99], Copyright © 2008, American Chemical Society)

into synthetic ACC particles and further participate in the crystallization process. This strategy opens the way to use a stabilized ACC as a versatile reservoir that can be converted in a highly controlled fashion to a crystalline form upon contacting a specially designed nucleating template in water. ACC was deposited by immersing the hydroxyl-terminated template in $CaCl_2$ solutions through the gas diffusion technique. The obtained ACC on templates was rinsed with acetone and dried under N_2. Then, a carboxylic acid-functionalized template was brought in direct contact with ACC for inducing crystallization of ACC. One milliliter water was placed in between the two substrates to initiate the crystallization process.

It is well-known that phospholipids as the important membrane constituents of biological vesicles are commonly involved in delineating reaction compartments for the crystallization of biominerals, such as magnetosomes in magnetotactic

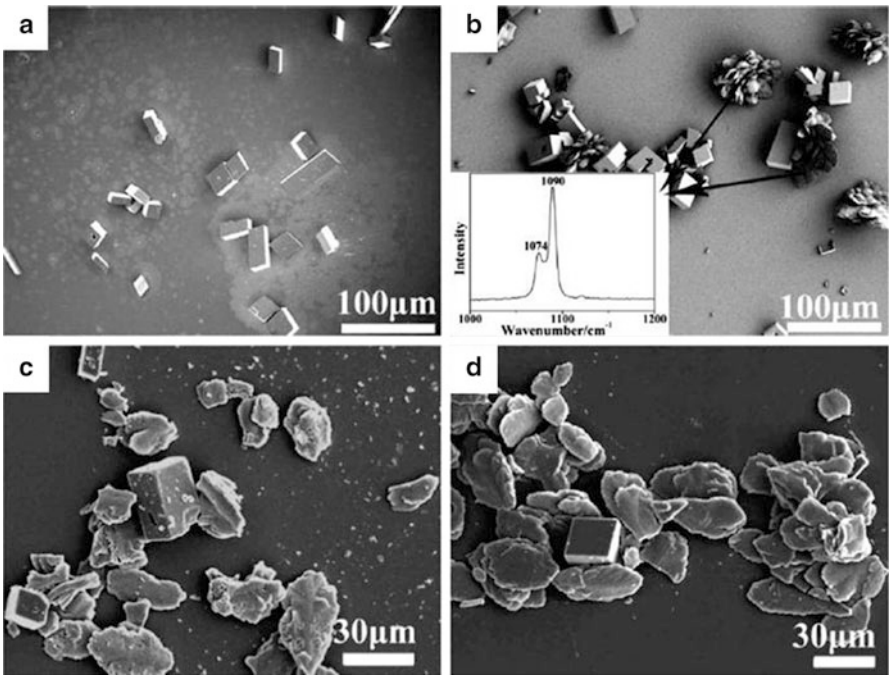

Fig. 6.16 SEM images of the $CaCO_3$ particles collected under a DPPC monolayer at different surface pressures after 9 h of reaction: (**a**) 0, (**b**) 2 (the inset displays a Raman spectrum of the floret-like crystals), (**c**) 25, and (**d**) 40 mN/m. The irregularly shaped crystals in (**c**) and d are the same as the floret-like crystals in b except that the petal-like crystals have been detached via sonication. The very small debris arising from the detachment process can be clearly seen in (**c**). (Reproduced from [104], Copyright © 2010, American Chemical Society)

bacteria [100] and the mineralizing tissues of vertebrates [101–103]. Yang and co-workers reported the mineralization processes of calcium carbonate under a phospholipid monolayer at the air–water interface (Fig. 6.16) [104]. The ACC precursor was obtained by the Kitano method. It was unstable and thus transformed into the inter-mediate vaterite. Then, the vaterite was transformed into the most thermodynamically stable calcite crystals eventually. This experiment result can be explained by the empirical Ostwald-Lussac law, which may reflect the biomineralization processes of cellular membranes. Furthermore, the spontaneity of the transformation from vaterite to calcite was found to depend sensitively on the degree of monolayer compression instead of the escape rate of the CO_2, implying that surface tension is a dominant factor in the transformation. This work has clarified the crystallization procedure of calcium carbonate under phospholipid monolayer and thus may further the understanding of the biomineralization processes induced by cellular membranes.

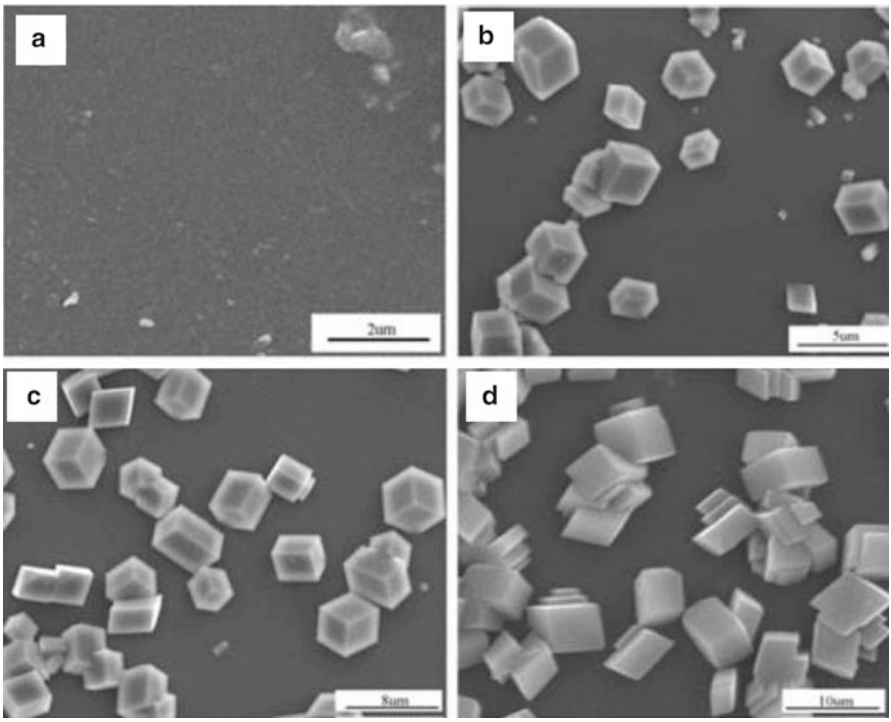

Fig. 6.17 SEM images of $CaCO_3$ films crystallized from ACC films on SAFs in the environment with the desired density of anhydrous ethanol: (**a**) as-deposited, (**b**) 1 h, (**c**) 2.5 h, (**d**) 4 h. (Reproduced from [105], Copyright © 2009, Wiley)

6.3.5 The Role of Solvent during Transformation Process

Shen and co-workers demonstrated that organic solvent has profound influence on transformation of ACC thin films (Fig. 6.17) [106]. It is a simple method to prepare polymorphic $CaCO_3$ crystal from the ACC by controlling the crystallization process. The model organic templates are introduced to obtain the ACC thin films and the organic media is used to control the transformation of $CaCO_3$. Interestingly, using anhydrous ethanol as media, ACC quickly transformed, probably by dissolving and recrystallizing, to calcite and vaterite after maturing. The experiment results indicated that the medium anhydrous ethanol facilitated the transformation of ACC and had an obvious effect on the morphology of the $CaCO_3$ crystals. Their results point out that a metastable ACC thin film was a precursor to the two polymorphs, calcite and vaterite, when organic solvent ethanol was used as media. During the process, the interactions between the surface of ACC film and ethanol molecule is exist. And the ethanol molecules are preferential to combine water molecule of calcium-enriched surfaces of the film to trigger the transformation.

Interestingly, Xu and co-workers reported two different transformations via thermal and solution pathways [107]. They found that water was released from the ACC samples when the temperature was above 373 K and the $CaCO_3$ began to crystallize at around 543–673 K, which resulted in the formation of the calcite crystals. When ACC is heated, the water molecules involved in the ACC can be released and ACC will transform into the crystal phases. On the other hand, the other metastable polymorphs of $CaCO_3$, i.e., aragonite and vaterite, were readily to be induced during the solution transformation of ACC when the low water amounts were used. Nevertheless, water could still make them turn into the stable calcite phase as the experimental time period goes on. Based on the experimental results, the roles of water and anionic polyelectrolytes in the phase transformation of ACC were confirmed. Water could promote the transformation and crystallization of ACC. Anionic polyelectrolytes, poly sodium styrenesulfonate (PSS) and PAA, inhibited the crystallization process and the crystallization temperature increased to the higher values.

Mann and co-workers [108] also found that the transformation pathways are determined by extent of water penetration into the ACC cores and electrostatic interactions at the mineral-surfactant interface. It indicated that the complex hybrid nanostructures can be assembled in situ when these processes are coupled synergistically at mesoscopic level.

6.3.6 The Role of Additive during Crystallization of Amorphous Calcium Carbonate

Magnesium can certainly be expected to influence the biogenic $CaCO_3$, such as stabilizing the ACC, incorporating into the calcite lattice [105, 109–113], inducing the formation of the aragonite [114, 115], and so on. Interestingly, almost all known biogenic ACC contains magnesium, which is presented in large quantities in seawater (around 50–60 mM Mg^{2+}, relative to the 12 mM Ca^{2+}) [116]. More recently, it has been known that the organism magnesium calcite is often produced through the magnesium amorphous precursor pathway. Yu et al. reported a facile confined crystallization method for incorporation of high content Mg in calcite by crystallization of compact tablet of Mg-ACC in water without using any organic additives [117]. In a typical experimental procedure, calcium chloride (0.15 mol dm^{-3}, 50 mL) and magnesium chloride hexahydrate (1.5225 g) were mixed with mechanical stirring to obtain a mixed solution. Then, an anhydrous sodium carbonate solution (0.15 mol dm^{-3}, 50 mL) was added rapidly to the mixed solution with mechanical stirring at an ambient temperature of 25 °C. The precipitated colloidal phase was filtered immediately and washed with ethanol. The precipitates were dried in a vacuum desiccator for 1 day. Then, the flake of Mg-ACC powder or Mg-ACC powder (about 0.25 g) was put into 500 mL double-distilled water at 25 °C for 2 days (Fig. 6.18). Around 20.90 mol% Mg was

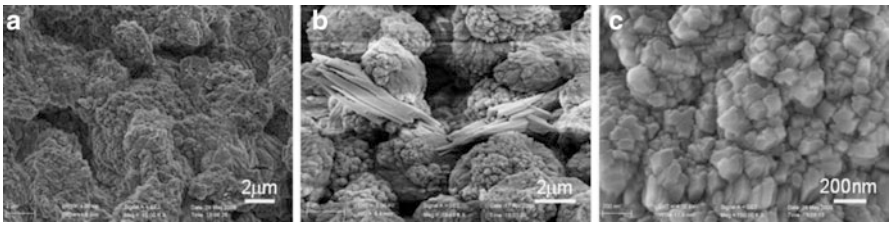

Fig. 6.18 Typical scanning electron microscopy (SEM) images of the fracture surface of the crystalline tablet obtained after mineralization reaction (**a**) low magnification view, (**b**) high magnification image, (**c**) view of higher local magnification of the Mg-calcite. The compact tablet of Mg-ACC powder is put into 500 mL double-distilled water at 25 °C for 2 days. (Reproduced from [117], Copyright © 2011, Royal Society of Chemistry)

found to be incorporated into the calcite lattice. Moreover, according to the ICP-AES, the Mg/Ca molar ratio of the crystalline flake is 1:4.3. Therefore, the mass fractions of the obtained Mg-calcite and aragonite are 89.88 wt% and 10.12 wt%, respectively. It has been demonstrated that the confined crystallization plays a key role in preventing the escape of Mg^{2+} and incorporation of magnesium in the calcite lattice, which may suggest that similar roles of confined environment in the formation of biological magnesian calcite [117]. In addition, some intermediate states can be captured in this special confined crystallization process of the compact tablet of magnesian ACC nanoparticles.

Furthermore, peanut-shaped $CaCO_3$ aggregates consisting of two dandelion-like heads have been obtained via a facile precipitation reaction between Na_2CO_3 and $CaCl_2$ at room temperature in the presence of ethanol solvent and magnesium ions [118]. The polymorph transformation of ACC to calcite and aragonite was observed in the growth process. In this experiment, a high concentration of ethanol solvent and magnesium ions played key roles in the formation of the unusual peanut-like $CaCO_3$ aggregates. The ethanol solvent increases the influence of magnesium ions on the morphology of $CaCO_3$ due to dehydrated magnesium ions are more readily adsorbed on the certain surfaces of calcite and thus affect the morphology [119]. On the other hand, the adsorption of Mg ions onto the specific growing crystal surfaces leaded to the morphological change of calcium carbonate.

Tang et al. found that the poly(4-sodium styrene sulfonate)-stabilized amorphous calcium carbonate (PSS-ACC) particles use themselves as the templates to form the new crystallized shells. It is a simple and new way for preparation of hollow calcium carbonate nanospheres under mild conditions [120]. The hollow-structured $CaCO_3$ can be utilized as drug deliverers and diagnostic markers since it provides an excellent biocompatibility. The hydrolysis of carbonate source method is used to obtain the PSS-ACC precursors. Fifteen milligram of PSS-ACC was dispersed in 10 mL of anhydrous ethanol in the presence of an ultrasonic treatment for 1 h. Then, water was added into the slurry to induce crystallization of ACC. The solids were separated by centrifugation and were washed using anhydrous ethanol. It has been demonstrated that the hollow vaterite nanospheres can be obtained by water-induced

phase transformation of PSS-ACC in water-ethanol solution at room temperature [120]. The higher PSS content and lower water amounts are two key factors to improve the formation of a large amount of hollow nanospheres with different sizes. The higher content of PSS promotes the formation of hollow vaterite nanospheres with smaller sizes. On the other hand, an increasing of water amount would result in a formation of less vaterite nanospheres. Interestingly, the formation of hollow vaterite nanospheres is self-templated by original PSS-ACC precursors.

Furthermore, Yu and co-workers found that 1,3-diamino-2-hydroxypropane-*N*,*N*,*N*′,*N*′-tetraacetic acid (H_4dhpta), a low molecule weight organic molecule with carboxyl functional groups, could stabilize ACC [121]. By interrupting the reaction at different time intervals, a whole crystallization process was successfully observed. It is found that the first formed ACC has two forms. One exists in solution and conglomerates into sphere-like precipitates. The other forms a close packed film on the substrate. The film is easily ignored as it is so dense and flat that it could be recognized as a background of the precipitate just like substrates, also for its disappearance after the crystallization finishes. However, this film is the key to inducing heterogeneous nucleation, as precipitated ACC conglomerates dissolve during the crystallization process. As various ACC films have been found, we suggest that the nucleation on ACC films may be the common behavior for heterogeneous nucleation. Thus, it is possible to combine dissolution–recrystallization [122] and the substrate physical change theory [123] into one mineralization system. After the nucleation, the intermediates at different crystallization stages were also captured. These intermediates were found to be composed of fibres. A rod–dumbell–sphere transformation phenomenon was observed (Fig. 6.19) [121]. It is believed that these are frameworks for the final crystal formation. In situ transformation of each fibre is brought forward to explain the formation of the final similar calcite hierarchical structures. As H_4dhpta here could both serve as ACC stabilizer and crystallization controller, it is expected to act as the ideal molecule for studying the way to stabilize ACC, and the crystallization and transformation process of ACC.

6.4 Summary and Outlook

In summary, this chapter provides a general overview on syntheses and transformation of ACC. It should be noticed that the synthetic strategies and crystallization of ACC have achieved great progress till now. The main preparation methods for ACC including the direct-mixing method, gas diffusion technique, hydrolysis of carbonate source method and Kitano method, have been discussed. Subsequently, crystallization of ACC in different environments has been discussed, demonstrating that the transformation of ACC plays an important role in biomineralization. Several important transformation routes of ACC are selected for more detailed discussion. Current progress in this field demonstrates that there are a number of potential opportunities for both syntheses and transformation of ACC, and $CaCO_3$ crystals with different morphologies, structural features, and functionalities. In future, it is

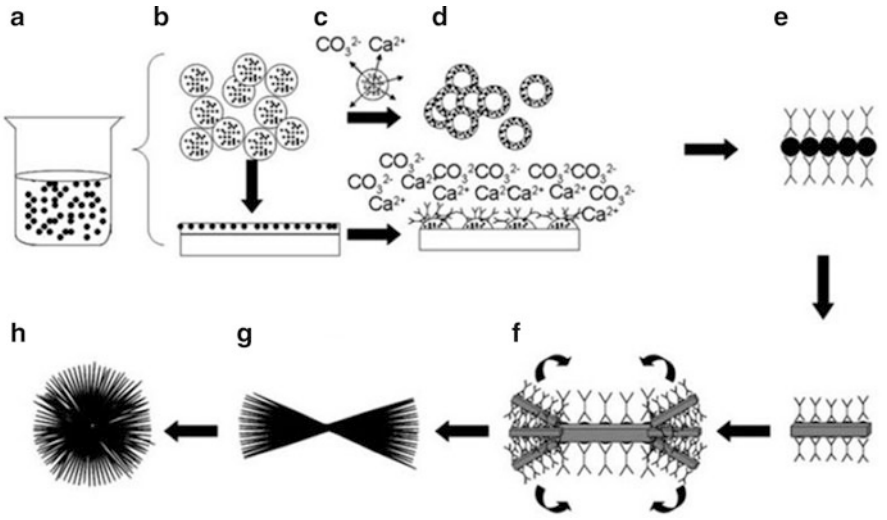

Fig. 6.19 Schematic illustrations of the transition process from ACC to hierarchical crystals. (Reproduced from [121], Copyright © 2010, Royal Society of Chemistry)

dramatically needed to find a reasonable way to prepare new composite materials using ACC or their transformed crystalline calcium carbonate crystals as one component, making ACC more useful for practical applications.

Acknowledgements We acknowledge the funding support from the National Basic Research Program of China (Grant 2010CB934700), the National Natural Science Foundation of China (Grants 91022032, 50732006), the Chinese Academy of Sciences (Grant KJZDEW-M01-1), and International Science & Technology Cooperation Program of China (the Chinese Academy of Sciences (Grant 2010DFA41170), the Principle Investigator Award by the National Synchrotron Radiation Laboratory at the University of Science and Technology of China.

References

1. Young, J.R., Davis, S.A., Bown, P.R., Mann, S.: Coccoliths ultrastructure and biomineralization. J. Struct. Boil. **126**, 195–215 (1999)
2. Mann, S.: The chemistry of form. Angew. Chem. Int. Ed. **39**, 3392–3406 (2000)
3. Ozin, G.A.: Morphogenesis of biomineral and morphosynthesis of biomimetic forms. Acc. Chem. Res. **30**, 17–27 (1997)
4. Weiner, S.W., Addadi, L.: Design strategies in mineralized biological materials. J. Mater. Chem. **7**, 689–701 (1997)
5. Estroff, L.A., Hamilton, A.D.: At the interface of organic and inorganic chemistry: bioinspired synthesis of composite materials. Chem. Mater. **13**, 3227–3235 (2001)
6. Kato, T., Sugawara, A., Hosoda, N.: Calcium carbonate–organic hybrid materials. Adv. Mater. **14**, 869–877 (2002)

7. Colfen, H., Mann, S.: Higher-order organization by mesoscale self-assembly and transformation of hybrid nanostructures. Angew. Chem. Int. Ed. **42**, 2350–2365 (2003)
8. Meldrum, F.C.: Calcium carbonate in biomineralization and biomimetic chemistry. Int. Mater. Rev. **48**, 187–224 (2003)
9. Yu, S.H., Colfen, H.: Bio-inspired crytstal morphogenesis by hydrophilic polymers. J. Mater. Chem. **14**, 2124–2147 (2004)
10. Mann, S.: Molecular tectonics in biomineralization and biomimetic materials chemistry. Nature **365**, 499–505 (1993)
11. Colfen, H.: Precipitation of carbonates: recent progress in controlled production of complex shapes. Curr. Opin. Colloid Interface Sci. **8**, 23–31 (2003)
12. Lowenstam, H.A., Weiner, S.: On Biomineralization. Oxford Universtity Press, Oxford (1989)
13. Mann, S.: Biomineralization-Principles and Concepts in Bioinorganic Materials Chemistry. Oxford University Press, Oxford (2001)
14. Mann, S., Webb, J., Williams, R.J.P.: Biomineralization. Wiley-VCH, Weinheim (1989)
15. Dalas, E., Klepetsanis, P., Koutsoukos, P.G.: The overgrowth of calcium carbonate on poly(vinyl chloride-co-vinylacetate-co-maleic acid). Langmuir **15**, 8322–8327 (1999)
16. Meldrum, F.C., Cölfen, H.: Controlling mineral morphologies and structures in biological and synthetic systems. Chem. Rev. **108**, 4332–4432 (2008)
17. Lippmann, F.: Sedimentary Carbonate Minerals. Springer, Berlin (1973)
18. Reeder, R. J.: Crystal chemistry of the rhombohedral carbonates. Reviews in Mineralogy and Geochemistry. **11**, 1–47 (1983)
19. Speer, J. A.: Crystal chemistry and phase relations of orthorhombic carbonates. Reviews in Mineralogy and Geochemistry. **11**, 145–190 (1983)
20. Wenk, H. R., Barber, D. J., Reeder, R. J.: Microstructures in carbonates. Reviews in Mineralogy and Geochemistry. **11**, 301–367 (1983)
21. Abdel-Aal, N., Satoh, K., Sawada, K.: Study of the adhension mechanism of CaCO3 using a combined buck chemisty/QCM Technique. Journal of Crystal Growth. **245**, 87-100 (2002)
22. Levi-Kalisman, Y., Raz, S., Weiner, S., Addadi, L., Sagi, I.: Structural differences between biogenic amorphous calcium carbonate phases using x-ray absorption spectroscopy. Adv. Funct. Mater. **12**, 43–48 (2002)
23. Raz, S., Hamilton, P.C., Wilt, F.H., Weiner, S., Addadi, L.: The transient phase of amorphous calcium carbonate in sea urchin larval spicules: the involvement of proteins and magnesium ions in its formation and stabilization. Adv. Funct. Mater. **13**, 480–486 (2003)
24. Aizenberg, J., Muller, D.A., Grazul, J.L., Hamann, D.R.: Direct fabrication of large micropatterned single crystals. Science **299**, 1205–1208 (2003)
25. Loste, E., Meldrum, F.: Control of calcium carbonate morphology by transformation of an amorphous precursor in a constrained volume. Chem. Commun. 901–902 (2001)
26. Beniash, E., Addadi, L., Weiner, S.: Cellular control over spicule formation in sea urchin embryos: a structural approach. J. Struct. Biol. **125**, 50–62 (1999)
27. Politi, Y., Levi-Kalisman, Y., Raz, S., Wilt, F., Addadi, L., Weiner, S., Sagi, I.: Structural characterization of the transient amorphous calcium carbonate precursor phase in sea urchin embryos. Adv. Funct. Mater. **16**, 1289–1298 (2006)
28. Weiss, I.M., Tuross, N., Addadi, L., Weiner, S.: Mollusc larval shell formation: amorphous calcium carbonate is a precursor phase for aragonite. J. Exp. Zool. B **293**, 478–491 (2002)
29. Hasse, B., Ehrenberg, H., Marxen, J.C., Becker, W., Epple, M.: Calcium carbonate modifications in the mineralized shell of the freshwater snail biomphalaria glabrata. Chem. Eur. J. **6**, 3679–3685 (2000)
30. Nassif, N., Pinna, N., Gehrke, N., Antonietti, M., Jager, C., Colfen, H.: Amorphous layer around aragonite platelets in nacre. Proc. Natl. Acad. Sci. U.S.A. **102**, 12653–12655 (2005)
31. Jager, C., Colfen, H.: Fine structure of nacre revealed by solid state ^{13}C and $^{1}HNMR$. CrystEngComm **9**, 1237–1244 (2007)
32. Travis, D.F.: Structural features of mineralization from tissue to macromolecular levels of organization in the decapod Crustacea. Ann. N.Y. Acad. Sci. **109**, 177–245 (1963)

33. Sugawara, A., Nishimura, T., Yamamoto, Y., Inoue, H., Nagasawa, H., Kato, T.: Self-organization of oriented calcium carbonate/polymer composite: effects of a matrix peptide isolated from the exoskeleton of a crayfish. Angew. Chem. Int. Ed. **45**, 2876–2879 (2006)
34. Taylor, M.G., Simkiss, K., Greaves, G.N., Okazaki, M., Mann, S.: An X-ray absorption spectroscopy study of the structure and transformation of amorphous calcium carbonate plant cystoliths. Proc. R. Soc. Lond. Ser. B **252**, 75–80 (1993)
35. Addadi, L., Raz, S., Weiner, S.: Taking advantage of disorder: amorphous calcium carbonate and its roles in biomineralization. Adv. Mat. **15**, 959–970 (2003)
36. Raz, S., Weiner, S., Addadi, L.: Formation of high magnesian calcites via an amorphous precursor phase—possible biological implications. Adv. Mater. **12**, 38–42 (2000)
37. Weiner, S., Levi-Kalisman, Y., Raz, S., Addadi, L.: Biologically formed amorphous calcium carbonate. Connect. Tissue Res. **44**, 214–218 (2003)
38. Bolz, J., Peng, B., Dingenouts, N., Panine, P., Narayanan, T., Ballauff, M.: Formation and growth of amorphous colloidal $CaCO_3$ precursor particles as detected by time-resolved SAXS. Langmuir **18**, 8364–8369 (2002)
39. Colfen, H., Volkel, A.: Application of the density variation method on calcium carbonate nanoparticles. Prog. Colloid Polym. Sci. **131**, 126–128 (2006)
40. Raz, S., Testeniere, O., Hecker, A.: Stable amorphous calcium carbonate is the main component of the calcium storage structures of the crustacean orchestia cavimana. Biol. Bull. **203**, 269–274 (2002)
41. Loste, E., Wilson, R.M., Seshadri, R., Meldrum, F.C.: The role of magnesium in stabilising amorphous calcium carbonate and controlling calcite morphologies. J. Cryst. Growth **254**, 206–218 (2003)
42. Donners, J.J.J.M., Heywood, B.R., Meijer, E.W., Nolte, R.J.M., Roman, C., Schenning, A.P.H.J., Sommerdijk, N.A.J.M.: Amorphous calcium carbonate stabilized by poly(propylene imine) dendrimers. Chem. Commun. **19**, 1937–1938 (2000)
43. Xu, A.W., Yu, Q., Dong, W.F., Antonietti, M., Colfen, H.: Stable amorphous $CaCO_3$ microparticles with hollow spherical superstructures stabilized by phytic acid. Adv. Mater. **17**, 2217–2221 (2005)
44. Ma, Y., Weiner, S., Addadi, L.: Mineral deposition and crystal growth in the continuously forming teeth of sea urchins. Adv. Funct. Mater. **17**, 2693–2700 (2007)
45. Fricke, M., Volkmer, D., Harms, M., Gower, L., Ziegler, A.: Morphosynthesis of nacre-type laminated $CaCO_3$ thin films and coatings. Angew. Chem. Int. Ed. **44**, 639–644 (2005)
46. Amos, F.F., Sharbaugh, D.M., Talham, D.R., Gower, L.B.: Formation of single-crystalline aragonite tablets/films via an amorphous precursor. Langmuir **23**, 1988–1994 (2007)
47. Sommerdijk, N.A.J.M., van Leeuwen, E.N.M., Vos, M.R.J., Janse, J.A.: Calcium carbonate thin films as biomaterial coatings using DNA as crystallization inhibitor. CrystEngComm **9**, 1209–1214 (2007)
48. Gehrke, N., Nassif, N., Pinna, N., Antonietti, M., Gupta, H.S., Colfen, H.: Retrosynthesis of nacre via amorphous precursor particles. Chem. Mater. **17**, 6514–6516 (2005)
49. Aizenberg, J., Lambert, G., Weiner, S., Addadi, L.: Factors involved in the formation of amorphous and crystalline calcium carbonate: a study of an ascidian skeleton. J. Am. Chem. Soc. **124**, 32–39 (2002)
50. Ajikumar, P.K., Wong, L.G., Subramanyam, G., Lakshminarayanan, R., Valiyaveettil, S.: Synthesis and characterization of monodispersed spheres of amorphous calcium carbonate and calcite spherules. Cryst. Growth Des. **5**, 1129–1134 (2005)
51. Donners, J.J.J.M., Heywood, B.R., Meijer, E.W., Nolte, R.J.M., Sommerdijk, N.A.J.M.: Control over calcium carbonate phase formation by dendrimer/surfactant templates. Chem. Eur. J. **8**, 2561–2567 (2002)
52. Koga, N., Nakagoe, Y.Z., Tanaka, H.: Crystallization of amorphous calcium carbonate. Thermochim. Acta **318**, 239–244 (1998)
53. Jiang, J., Gao, M.R., Qiu, Y.H., Yu, S.H.: Gram-scale, low cost, rapid synthesis of highly stable Mg-ACC nanoparticles and their long-term preservation. Nanoscale **2**, 2358–2361 (2010)

54. Oaki, Y., Kajiyama, S., Nishimura, T., Imai, H., Kato, T.: Nanosegregated amorphous composites of calcium carbonate and an organic polymer. Adv. Mater. **20**, 3633–3637 (2008)
55. Shen, Q., Wei, H., Zhou, Y., Huang, Y.P., Yang, H.R., Wang, D.J., Xu, D.F.: Properties of amorphous calcium carbonate and the template action of vaterite spheres. J. Phys. Chem. B **10**, 2994–3000 (2006)
56. Lee, H.S., Ha, T.H., Kim, K.: Fabrication of unusually stable amorphous calcium carbonate in an ethanol medium. Mater. Chem. Phys. **93**, 376–382 (2005)
57. Dai, L., Douglas, E.P., Gower, L.B.: Compositional analysis of a polymer-induced liquid-precursor (PIPL) amorphous $CaCO_3$ phase. J. Non-Cryst. Solids **354**, 1845–1854 (2008)
58. Zhong, C., Chu, C.C.: Acid polysaccharide-induced amorphous calcium carbonate (ACC) films: colloidal nanoparticle self-organization process. Langmuir **25**, 3045–3049 (2009)
59. Lam, R.S.K., Charnock, J.M., Lennie, A., Meldrum, F.C.: Synthesis-dependant structural variations in amorphous calcium carbonate. CrystEngComm **9**, 1226–1236 (2007)
60. Faatz, M., Grohn, F., Wegner, G.: Amorphous calcium carbonate: synthesis and potential internediate in biomineralization. Adv. Mater. **16**, 996–1000 (2004)
61. Guillemet, B., Faatz, M., Grohn, F., Wegner, G., Gnanou, Y.: Nanosized amorphous calcium carbonate stablized by poly(ethylene oxide)-b-poly(acrylic acid) block copolymers. Langmuir **22**, 1875–1879 (2006)
62. Sondi, I., Skapin, S.D., Salopek-Sondi, B.: Biomimetic precipitation of nanostructured colloidal calcite particles by enzyme-catalyzed reaction in the presence of magnesium ions. Cryst. Growth Des. **8**, 435–441 (2008)
63. Faatz, M., Grohn, F., Wegner, G.: Mineralization of calcium carbonate by controlled release of carbonate in aqueous solution. Mater. Sci. Eng. C **25**, 153–159 (2005)
64. Xu, G.F., Yao, N., Aksay, I.A., Groves, J.T.: Biomimetic synthesis of macroscopic-scale $CaCO_3$ thin films-evidence for a multistep assembly process. J. Am. Chem. Soc. **120**, 11977–11985 (1998)
65. Gunther, C., Becker, A., Wolf, G., Epple, M., Anorg, Z.: In vitro synthesis and structural characterization of amorphous calcium carbonate. Z. Anorg. Allg. Chem. **631**, 2830–2835 (2005)
66. Becker, A., Ziegler, A., Epple, M.: The mineral phase in the cuticles of two species of crustacean consists of magnesium calcite, amorphous calcium carbonate, and amorphous calcium phosphate. Dalton Trans. **10**, 1814–1820 (2005)
67. Davis, K.J., Dove, P.M., De Yoreo, J.J.: The role of Mg2+ as an impurity in calcite growth. Science **290**, 1134–1137 (2000)
68. Al-Sawalmih, A., Li, C.H., Siegel, S., Fratzl, P., Paris, O.: On the stability of amorphous minerals in lobster cuticle. Adv. Mater. **21**, 4011–4015 (2009)
69. Gal, A., Weiner, S., Addadi, L.: The stabilizing effect of silicate on biogenic and synthetic amorphous calcium carbonate. J. Am. Chem. Soc. **132**, 13208–13211 (2010)
70. Ramirez, A.P.: Geometric frustration: magic moments. Nature **421**, 483–486 (2003)
71. Addadi, L., Joester, D., Nudelman, F., Weiner, S.: Mollusk shell formation: a source of new concepts for understanding biomineralization processes. Chem. Eur. J. **12**, 980–987 (2006)
72. Beniash, E., Aizenberg, J., Addadi, L., Weiner, S.: Amorphous calcium carbonate transforms into calcite during sea urchin larval spicule growth. Proc. R. Soc. Lond. Ser. B **264**, 461–465 (1997)
73. Politi, Y., Arad, T., Klein, E., Weiner, S., Addadi, L.: Sea urchin spine calcite forms via a transient amorphous calcium carbonate phase. Science **306**, 1161–1164 (2004)
74. Okazaki, K., Dillaman, R.M., Wilbur, K.M.: Crystalline axes of the spine and test of the sea urchin Strongylocentrotus purpuratus: determination by crystal etching and decoration. Biol. Bull. **161**, 402–415 (1981)
75. Theel, H.: On the development of Ehinocyamus pusillus. Nova Acta Res. Soc. Sci. Upsala **15**, 1–57 (1892)
76. Politi, Y., Metzler, R.A., Abrecht, M., Gilbert, B., Wilt, F.H., Sagi, I., Addadi, L., Weiner, S., Gilbert, P.U.P.A.: Transformation mechanism of amorphous calcium carbonate into calcite in the sea urchin larval spicule. PNAS **105**, 17362–17366 (2008)

77. Wolf, S.E., Leiterer, J., Kappl, M., Emmerling, F., Tremel, W.: Early homogenous amorphous precursor stages of calcium carbonate and subsequent crystal growth in levitated droplets. J. Am. Chem. Soc. **130**, 12342–12347 (2008)
78. Pouget, E.M., Bomans, P.H.H., Goos, J.A.C.M., Frederik, P.M., deWith, G., Sommerdijk, N.A.J.M.: The initial stages of template-controlled $CaCO_3$ formation revealed by cryo-TEM. Science **323**, 1455–1458 (2009)
79. Gebauer, D., Volkel, A., Colfen, H.: Stable prenucleation calcium carbonate clusters. Science **322**, 1819–1822 (2008)
80. Gebauer, D., Gunawidjaja, P.N., Ko, J.Y.P., Bacsik, Z., Aziz, B., Liu, L., Hu, Y.F., Bergstrom, L., Tai, C.W., Sham, T.K., Eden, M., Hedin, N.: Proto-calcite and proto-vaterite in amorphous calcium carbonate. Angew. Chem. Int. Ed. **49**, 8889–8891 (2010)
81. Aizenberg, J., Tkachenko, A., Weiner, S., Addadi, L.: Calcitic microlenses as part of the photoreceptor system in brittlestars. Nature **412**, 819–822 (2001)
82. Park, R.J., Meldrum, F.C.: Synthesis of single crystals of calcite with complex morphologies. Adv. Mater. **14**, 1167–1169 (2002)
83. Park, R.J., Meldrum, F.C.: Shape-constraint as a route to calcite single crystals with complex morphologies. J. Mater. Chem. **14**, 2291–2296 (2004)
84. Loste, E., Park, R.J., Warren, J., Meldrum, F.C.: Precipitation of calcium carbonate in confinement. Adv. Funct. Mater. **14**, 1211–1220 (2004)
85. Han, J.T., Xu, X.R., Kim, D.H., Cho, K.: Mosaic, single-crystal $CaCO_3$ thin films fabricated on modified polymer templates. Adv. Funct. Mater. **15**, 475–480 (2005)
86. Li, C., Qi, L.M.: Bioinspired fabrication of 3D orderd macroporous single crystals of calcite from a transient amorphous phase. Angew. Chem. Int. Ed. **47**, 2388–2393 (2008)
87. Cong, H., Cao, W.: Colloidal crystallization induced by capillary force. Langmuir **19**, 8177–8181 (2003)
88. Hetherington, N.B.J., Kulak, A.N., Sheard, K., Meldrum, F.C.: Crystallization on surfaces of well-defined-topography. Langmuir **22**, 1955–1958 (2006)
89. Pecher, J., Guenoun, P., Chevallard, C.: Crystalline calcium carbonate thin film formation through interfacial growth and crystallization of amorphous microdomains. Cryst. Growth Des. **9**, 1306–1311 (2009)
90. Li, C., Hong, G., Yu, H., Qi, L.: Facile fabrication of honeycomb patterned thin films of amorphous calcium carbonate and mosaic calcite. Chem. Mater. **22**, 3206–3211 (2010)
91. Xu, X., Han, J.T., Kim, D.H., Cho, K.: Two modes of transformation of amorphous calcium carbonate films in air. J. Phys. Chem. B **110**, 2764–2770 (2006)
92. Dai, L., Cheng, X., Gower, L.B.: Transition bars during transformation of an amorphous calcium carbonate precursor. Chem. Mater. **20**, 6917–6928 (2008)
93. Xu, X.R., Han, J.T., Cho, K.: Two modes of transformation of amorphous calcium carbonate films in air. Chem. Mater. **16**, 1740–1746 (2004)
94. Popescu, D.C., van Leeuwen, E.N.M., Rossi, N.A.A., Holder, S.J., Jansen, J.A., Sommerdijk, N.A.J.M.: Shaping amorphous calcium carbonate films into 2D model substrates for bone cell culture. Angew. Chem. Int. Ed. **45**, 1762–1767 (2006)
95. Tugulu, S., Harms, M., Fricke, M., Volkmer, D., Klok, H.A.: Polymer brushes as lonotropic matrices for the directed fabrication of microstructured calcite thin films. Angew. Chem. Int. Ed. **45**, 7458–7461 (2006)
96. Han, J.T., Xu, X.R., Kim, D.H., Cho, K.: Two modes of transformation of amorphous calcium carbonate films in air. Chem. Mater. **17**, 136–141 (2005)
97. Lu, C.H., Qi, L.M., Ma, J.M., Cheng, H.M., Zhang, M.F., Cao, W.X.: Controlled growth of micropatterned, oriented calcite films on a self-assembled multilayer film. Langmuir **20**, 7378–7380 (2004)
98. Chen, Y., Xiao, J., Wang, Z., Yang, S.: Observation of an amorphous calcium carbonate precursor on a stearic acid monolayer formed during the biomimetic mineralization of $CaCO_3$. Langmuir **25**, 1054–1059 (2009)
99. Han, T.Y.J., Aizenberg, J.: Calcium carbonate storage in amorphous form and its template-induced crystallization. Chem. Mater. **20**, 1064–1068 (2008)

100. Anderson, H.C., Hsu, H.H.T., Raval, P., Hunt, T.R., Schwappach, J.R., Morris, D.C., Schneider, D.J.: The Mechanism of Bone Induction and Bone Healing by Human Osteosarcoma Cell-Extracts. Springer, Heidelberg, Germany (1995)
101. Mann, S., Frankel, R.B., Blakemore, R.P.: Structure, morphology and crystal growth of bacterial magnetite. Nature **310**, 405–407 (1984)
102. Mann, S., Sparks, N.H.C., Frankel, R.B., Bazylinski, D.A., Jannasch, H.W.: Biomineralization of ferrimagnetic greigite (Fe_3S_4) and iron pyrite (FeS_2) in a magnetotactic bacterium. Nature **343**, 258–261 (1990)
103. Bazylinski, D.A., Heywood, B.R., Mann, S., Frankel, R.B.: Fe_3O_4 and Fe_3S_4 in a bacterium. Nature **366**, 218 (1993). 218
104. Xiao, J., Wang, Z., Tang, Y., Yang, S.: Biomimetic mineralization of $CaCO_3$ on a phospholipid monolayer: from an amorphous calcium carbonate precursor to calcite via vaterite. Langmuir **26**, 4977–4983 (2010)
105. Meldrum, F.C., Hyde, S.T.: Morphological influence of magnesium and organic additives on the precipitation of calcite. J. Cryst. Growth **231**, 544–558 (2001)
106. Huang, F., Shen, Y., Xie, A., Zhang, X., Cai, Y., Wu, W.: Controlled deposition and transformation of amorphous calcium carbonate thin films. Cryst. Res. Technol. **44**, 818–822 (2009)
107. Xu, X.R., Cai, A.H., Liu, R., Pan, H.H., Tang, R.K., Cho, K.: The roles of water and polyelectrolytes in the phase transformation of amorphous calcium carbonate. J. Cryst. Growth **310**, 3779–3787 (2008)
108. Li, M., Mann, S.: Emergent nanostructures: water-induced mesoscale transformation of surfactant-stabilized amorphous calcium carbonate nanoparticles in reverse microemulsions. Adv. Funct. Mater. **12**, 773–779 (2002)
109. Cheng, X.G., Varona, P.L., Olszta, M.J., Gower, L.B.: Biomimetic synthesis of calcite films by a polymer-induced liquid-precursor (PILP) process 1. Influence and incorporation of magnesium. J. Cryst. Growth **307**, 395–404 (2007)
110. Goldsmith, J.R., Graf, D.L., Heard, H.C.: Lattice constants of the calcium–magnesium carbonate. Am. Mineral. **46**, 453–457 (1961)
111. Finch, A.A., Allison, N.: Coordination of Sr and Mg in calcite and aragonite. Mineral. Mag. **71**, 539–552 (2007)
112. Cusack, M., Perez-Huerta, A., Janousch, M., Finch, A.A.: Magnesium in the lattice of calcite-shelled brachiopods. Chem. Geol. **257**, 59–64 (2008)
113. Perez-Huerta, A., Cusack, M., Janousch, M., Finch, A.A.: Influence of crystallographic orientation of biogenic calcite on in situ Mg XANES analyses. J. Synchrotron Radiat. **15**, 572–575 (2008)
114. Lippman, F.: Versuche zur aufklarung der bildungsbedingungen von calcit und aragonit. Fortschr. Mineral. **38**, 156–161 (1960)
115. Folk, R.L.: The nature history of crystalline calcium carbonate: effect of magnesium content and salinity. J. Sediment. Petrol. **44**, 40–53 (1974)
116. Gower, L.B.: Biomimetic model systems for investigating the amorphous precursor pathway and its role in biomineralization. Chem. Rev. **108**, 4551–4627 (2008)
117. Jiang, J., Gao, M.R., Qiu, Y.H., Wang, G.S., Liu, L., Cai, G.B., Yu, S.H.: Confined crystallization of high-magnesian calcite from compact Mg-ACC precursor tablets and its biological implications. CrystEngComm **13**, 952–956 (2011)
118. Tang, H., Yu, J., Zhao, X.: Controlled synthesis of crystalline calcium carbonate aggregates with unusual morphologies involving the phase transformation from amorphous calcium carbonate. Mater. Res. Bull **44**, 831–835 (2009)
119. Dickinson, S.R., McGrath, K.M.: Switching between kinetic and thermodynamic control: calcium carbonate in the presence of a simple alcohol. J. Mater. Chem. **13**, 928–933 (2003)
120. Cai, A., Xu, X., Pan, H., Tao, J., Liu, R., Tang, R., Cho, K.: Direct synthesis of hollow vaterite nanospheres from amorphous calcium carbonate nanoparticles via phase transformation. J. Phys. Chem. C **112**, 11324–11330 (2008)

121. Cai, G.B., Chen, S.F., Liu, L., Jiang, J., Yao, H.B., Xu, A.W., Yu, S.H.: 1,3-diamino-2-hydroxypropane-N, N, N, N-tetraacetic acid stabilized amorphous calcium carbonate: nucleation, transformation and crystal growth. CrystEngComm **12**, 234–241 (2010)
122. Rieger, J., Frechen, T., Cox, G., Heckmann, W., Schmidt, C., Thieme, J.: Precursor structures in the crystallization/precipitation processes of $CaCO_3$ and control of particle formation by polyelectrolytes. Faraday Discuss. **136**, 265–277 (2007)
123. Sethmann, I., Putnis, A., Grassmann, O., Lobmann, P.: Observation of nano-clustered calcite growth via a transient phase mediated by organic polyanions: a close match for biomineralization. Am. Mineral. **90**, 1213–1217 (2005)

Chapter 7
Modeling of Biomineralization and Structural Color Biomimetics by Controlled Colloidal Assembly

Xiang Yang Liu and Ying Ying Diao

Abstract This chapter aims to give an overview on the recent progress of the electrically controlled colloidal assembly, as an experimental modeling system to study the crystallization-related biomineralization processes. The controlled colloidal assembly allows us not only to visualize some "atomic" details of the nucleation and surface process of crystallization, but also to treat quantitatively the previous models to such an extent that has never been achieved before by other approaches. As such, the crystallization processes were quantitatively examined at the single particle level, and the related kinetics, i.e., the kinetics of nucleation, multistep crystallization, supersaturation-driven structural mismatch nucleation, etc., can be verified from the single particle level. The results acquired can transfer our knowledge on biomineralization to a new phase. Apart from the fundamental aspects, the controlled colloidal crystallization has been attracted significant attention in many applications. In this concern, the application of colloidal crystallization to the fabrication of photonic crystals and the biomimetics of natural structural colors will be discussed.

Keywords Biomineralization • Assembly of biominerals • Supersaturation • Nucleation • homogeneous nucleation • heterogeneous nucleation • Supersaturation-driven interfacial structural mismatch • Shadow effect • Colloidal assembly • Photonic crystal • Structural color • Biomimetics • Double reflection • Silk fabrics • Multistep crystallization

X.Y. Liu (✉)
College of Materials, Xiamen University, 422 Si Ming Nan Road, 361005 Xiamen, P.R. China
e-mail: phyliuxy@nus.edu.sg

Department of Physics and Department of Chemistry, Faculty of Science, National University of Singapore, 2 Science Drive 3 117542, Singapore

Y.Y. Diao
College of Materials, Xiamen University, 422 Si Ming Nan Road, 361005 Xiamen, P.R. China

X.Y. Liu (ed.), *Bioinspiration: From Nano to Micro Scales*, Biological and Medical Physics, Biomedical Engineering, DOI 10.1007/978-1-4614-5372-7_7,

7.1 Introduction

Crystallization plays a crucial role in biomineralization, the preparation of functional materials [1–4], the structural characterization of natural and synthetic molecules [5, 6], and the development of advanced technologies [7, 8]. Nowadays, many nanomaterials are crystalline phases, and the essential structures and utmost important properties of the systems are determined by nucleation and the correlation between the nucleating nanophase and the substrate, etc. The control of crystallization is directly related to some soft materials and nanophase formation [9].

Up to now, crystallization is still considered as art other than science, mainly because there is not sufficient knowledge on its critical early stages and the atomic processes. In this regard, the kinetics of the transition from the metastable structure to the stable structure has so far been open to question. The key challenge is the in situ imaging of the atomic/molecular dynamic process, which is limited by both the spatial and the temporal definitions of current technologies and the absence of the direct observation on the transition process in real space, except for some local events of crystallization/quasicrystallization of large species, namely proteins [10] and colloidal particles [11]. Notice that computer simulations have been applied to acquire the information [12]. Nevertheless, due to the constraint of computation power and the methodologies, the knowledge obtained is still limited. It is therefore of critical importance to develop a new methodology to "simulate" or "monitor" the atomic/molecular dynamic process of the nucleation and growth of crystals [13].

Colloids, the dispersions of nano/microsized particles in a fluid background solvent, range from ink, milk, mayonnaise, paint, and smoke and have many practical applications [14–16]. Nowadays, colloids have been employed as a model system to study phase transitions [17–22]. In this regard, these nano/microsized colloids provide an important platform for sampling the aggregation and assembly at the single particle level because of its visible size, tractable dynamics, and tunable interparticle interactions [12–16, 23–25]. In addition, colloidal particles in solutions behave like big "atoms" [19, 20], and the phase behavior of colloidal suspensions is similar to that of atomic and molecular systems [21]. Therefore, from the point of view of crystallization modeling, the growth units are colloidal particles, and thus the crystallization process can be observed directly by a normal optical microscope. Furthermore, the interaction among colloidal particles can be turned by the adjustment of the ionic strength, pH of solutions/suspensions, and the applied electric field strength and frequency; therefore, the thermodynamic driving force for the crystallization can be controlled precisely in such a system. This allows the quantitative measurement and the data interpretation similar to computer experiments [20, 21]. Besides, proteins and viruses are in the colloidal domain. Any advantage in the understanding of colloidal crystallization will exert a direct impact on the control of proteins and biomacromolecule crystallization. Apart from modeling, from the technological point of view, the knowledge of nucleation, growth, and defect generation is very important in identifying robust technologies in electronic, photonic, and life sciences and technologies.

In practice, controlling the colloidal assembly could be employed to define a template for creating two-dimensional (2D)/three-dimensional (3D) periodic structures for applications in photonic devices [26, 27], biological and chemical sensors [28], and tunable lasers [29]. Recently, the controlled colloidal assembly has been utilized to mimic the structural color created by animals, i.e., butterfly wings, etc. [30, 31].

The purpose of this chapter is to provide an overview on the recent progress in the experimental simulations of crystallization processes, in particular biomineralization processes, by controlled colloidal assembly. Our attention will be focused on the following two aspects: the electrically controlled colloidal crystallization as a well-controlled and quantitative modeling system to simulate the kinetics of crystallization, i.e., biomineralization, and structural color biomimetics. As the thermodynamic driving force in crystallization can be tuned directly from altering the strength and/or frequency of the applied electric field, some most essential issues in biomineralization, i.e., nucleation kinetics, the multistep/phase crystallization, the ordered crystallites assembly, etc., which are often observed in hard tissues, can be examined quantitatively by the electrically controlled colloidal assembly in a combination of microscopic visualization. The results obtained will provide the most up-to-date knowledge on crystallization at the individual growth unit level. On the other hand, we will also review that, practically, the controlled colloidal assembly can be adopted to produce templates in engineering photonic crystals in mimicking structural colors from the animal kingdom. In this regard, some examples of structural color biomimetics and the application to textiles will be given. This may pave the new silk road in the years to come.

7.2 Thermodynamic Driving Force of Colloidal Crystallization and Assembly

As crystallization in most cases is a first-order phase transition, without thermodynamic driving force, crystallization (including biomineralization) will not take place. Therefore, to examine the kinetics of crystallization (including biomineralization) in a quantitative way, the well-controlled thermodynamic driving force is the precondition. Furthermore, exercising the control of crystallization should demonstrate the capability of controlling the thermodynamic driving force for the theoretical analysis. Regarding the colloidal crystallization, the interactions among colloidal particles play a key role in this analysis. The most general equation of the total free-energy difference (ΔG) between particles at a separation H is obtained by adding these contributions:

$$\Delta G = \Delta G^{\mathrm{att}}(\mathrm{vanderWaals}) + \Delta G^{\mathrm{rep}}(\mathrm{shortrange}) + \Delta G^{\mathrm{rep}}(\mathrm{electrostatic}) + \Delta G^{\mathrm{rep}}(\mathrm{steric}) + \Delta G(\mathrm{othereffects}) \tag{7.1}$$

where superscripts "att" and "rep" denote attraction and repulsion respectively. The consideration for the overall interactions mentioned above has been treated by the Deryagin–Landau–Verwey–Overbeek theory [32]. In practice, it is not necessary to consider all these contributions simultaneously. One shall here deal with *two simpler situations* where the long-range potential arises from electrostatic *and/or* from steric repulsion contributions. Notice that the double-layer repulsion depends on the ionic strength of the medium: the curves may show a high repulsive barrier at low ionic strengths, a so-called secondary minimum at intermediate ionic strengths, and a negligibly small barrier, or none at all, at higher ionic strengths. In the same way, the form of the steric repulsion is determined by the nature of the interactions between the adsorbed polymer chains and the solvent. A repulsive barrier of variable range and a minimum of variable depth can result, depending on the solvent and the temperature. The interaction between colloidal particles can be turned by changing the ionic strength, pH of solutions, or adding polymers. This implies that the "phase behavior" of such systems can be tuned by altering the above parameters.

Apart from the above-mentioned forces, the recent researches indicate that the interaction between colloidal particles can be induced and controlled by an alternating electric field (AEF) [13, 31, 33–46]. One can tune the interaction by altering the frequency and/or the strength of the applied field. This effect can be captured by ΔG(other effects) in (7.1). In comparison with other stimuli, the electric stimulus can be applied and switched off instantly without disturbing the original solutions. Although the interactions between colloidal particles can be of many kinds, they are basically functions of $1/r_{eq}$ (r_{eq} denotes the equilibrium distance between two neighboring particles). This implies that for a given colloidal system, the interaction between two adjacent particles is fixed once r_{eq} is constant. In other words, the change of r_{eq} can reflect directly the change of interparticle interactions.

As tuning the frequency and field strength of an AC field is much easier to achieve than other means, the following discussion will be mainly focused on the control of the colloidal crystallization under an AC field (i.e., Fig. 7.1) [35, 37, 39]. Nevertheless, not all ranges of frequency and intensity of the AC field can produce a crystalline assembly of particles. There exists a finite frequency range with well-defined lower and upper cut-off values of particle size, charge, ionic strength of the solution, pH, etc., in which the effective control can be implemented (i.e., Fig. 7.1).

The formation of various patterns is subject to the balance of the attractive and repulsive forces. Here, the attractive force that can overcome the interparticle electrostatic repulsion and enable 2D colloidal aggregation is suggested to be attributed to electrohydrodynamic flow [47, 48]. Fluid motion is set up by the interaction between this free charge and the lateral electric field, which is caused by the distortion of the applied field by the colloidal particles. A "phase diagram" of the electrically controlled colloidal assembly under a constant temperature is given in Fig. 7.1.

The thermodynamic driving force for the phase transition (including biomineralization and general crystallization) can be defined by $\Delta\mu$, referring to the difference

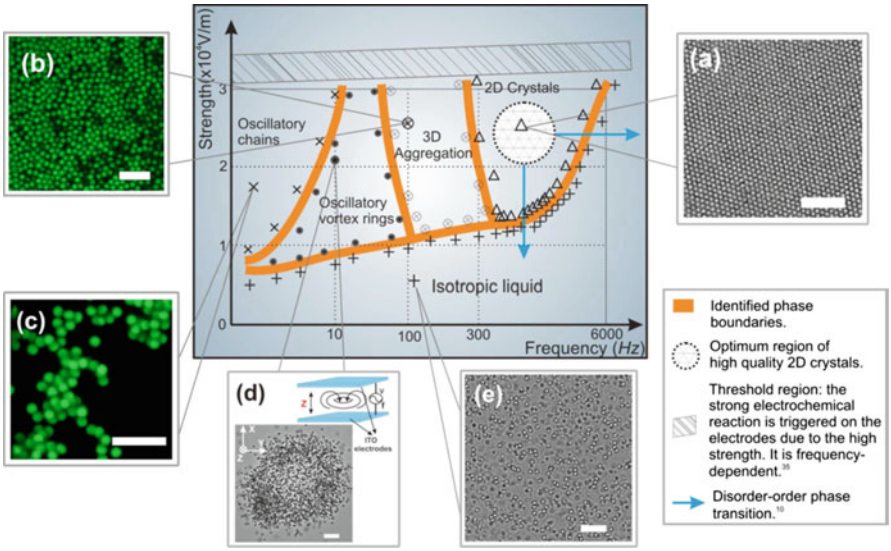

Fig. 7.1 The diagram of electrically controlled colloidal assembly. The phase diagram and typical colloidal patterns induced by an AEF at room temperature. (**a**) A 2D colloidal crystal at field strength $\sigma_E = 2.6\times10^4$ V/m and $f = 800$ Hz. (**b**) 3D aggregation of colloidal particles, as captured by the LCSM at $\sigma_E = 2.4\times10^4$ V/m and $f = 100$ Hz. (**c**) Static snapshot of colloidal chains by the LCSM at $\sigma_E = 1.8\times10^4$ V/m and $f = 0.1$ Hz. (**d**) Snapshot of oscillatory vortex rings at 2.3×10^4 V/m and $f = 1$ Hz. (**e**) The isotropic liquid state of colloidal suspension. Scale bars in (**b**) and (**c**) represent 5 μm, and in (**a**), (**d**), and (**e**) represent 10 μm. Colloidal suspension (0.1% in volume fraction) of monodisperse charged polystyrene spheres (1 μm in diameter) is confined to a horizontal layer between two conductive glass microscope slides. Glass spacers set the layer thickness in the cells at $2H = 120 \pm 5$ μm across the 1.5 cm × 1.5 cm observation area. The AEF was supplied by a waveform generator. The motions of the colloidal particles are recorded with a computer-driven digital CCD camera. Reprinted with permission from Ref. [45] ©2009 American Institute of Physics

between the chemical potentials of a growth unit in the ambient phase μ_i^{ambient} and in the crystalline phase μ_{crystal}:

$$\Delta\mu = \mu_i{}^{\text{ambient}} - \mu_{\text{crystal}} \tag{7.2}$$

where subscript i denotes the solute in the ambient phase. When $\Delta\mu > 0$, the system is said to be supersaturated. This is the thermodynamic precondition for crystallization. Conversely, when $\Delta\mu < 0$, the system is undersaturated. Under such a condition, crystals will dissolve. When $\Delta\mu = 0$, the ambient phase is in equilibrium with the crystalline phase. As for temperature T and pressure P, one has $(\mu_i^{\text{ambient}})_{\text{eq}} = \mu_{\text{crystal}}$, where $(\mu_i^{\text{ambient}})_{\text{eq}}$ is the chemical potential of a solute molecule in a state of phase equilibrium. Then for crystallization from solutions, the chemical potential of species i is given by [49, 50]

$$\mu_i = \mu_i^0 + kT \ln a_i \approx \mu_i^0 + kT \ln C_i \tag{7.3}$$

where a_i, and C_i denote the activity and concentration of species i, respectively, and μ_i^0 denotes the standard state ($a_i = 1$) of the chemical potential of species i. This then gives rise to the thermodynamic driving force

$$\frac{\Delta\mu}{kT} = \ln\frac{a_i}{a_i^{\mathrm{eq}}} \approx \ln\frac{C_i}{C_i^{\mathrm{eq}}} \tag{7.4}$$

where $a_i^{\mathrm{eq}}, C_i^{\mathrm{eq}}$ are, respectively, the equilibrium activity and concentration of species i. If we define the supersaturation for crystallization as

$$\sigma = (a_i - a_i^{\mathrm{eq}})/a_i^{\mathrm{eq}} \approx (C_i - C_i^{\mathrm{eq}})/C_i^{\mathrm{eq}} \tag{7.5}$$

(7.4) can then be rewritten as

$$\frac{\Delta\mu}{kT} = \ln(1+\sigma) \cong \sigma(\text{if } \sigma << 1) \tag{7.6}$$

For colloidal crystallization, the similar relationship can be found. If the interaction between the particles in the crystal phase remains constant at different field strength and frequencies, the supersaturation can be given by (7.6) $\sigma = (\phi - \phi_m)/\phi_m$ (ϕ and ϕ_m represent the actual concentration and the equilibrium concentration of the solute, respectively). For more precise definition of supersaturation in biomineralization, refer to Chap. 3.

7.3 Simulations of Nucleation and Crystal Growth in Biomineralization

Similar to the crystallization of other materials, 3D crystallization of biominerals occurs via (1) *the nucleation*, followed by (2) *the growth* of crystals. Nucleation will determine whether and when a mineral (crystalline) phase will occur and the correlation with its surroundings. It will also determine the total number and the average size of crystalline particles occurring in the system eventually. On the other hand, the growth of crystals will to a large extent determine the size, morphology, and perfection of crystals. Therefore, the understanding of the governing mechanism will allow us to acquire the knowledge on how organisms can exercise the effective control and on the engineering of biomineral crystalline materials. In this regard, how the colloidal crystallization can be controlled electrically can be applied to model the general process of nucleation and biomineralization-related phenomena, i.e., multistep/phase crystallization, anti-templating effect, etc.

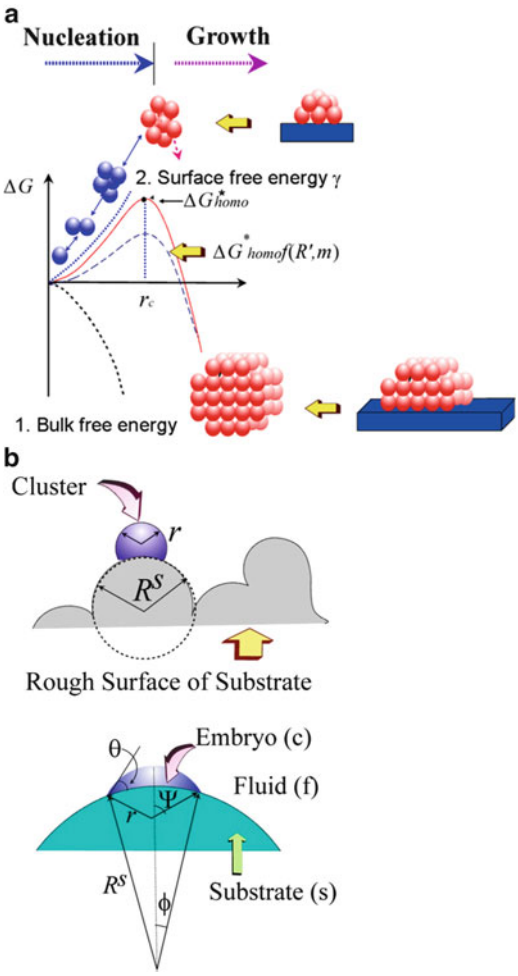

Fig. 7.2 (**a**) Crystallization normally takes place via nucleation, followed by the growth of crystals. Nucleation is a kinetic process of overcoming the nucleation barrier, which is the outcome of the occurrence of the surface free energy γ. (**b**) Illustration of nucleation on a rough substrate. Reprinted with permission from Ref. [9], ©2004 Springer

7.3.1 Nucleation Barrier

Nucleation can be regarded as a process of creating "baby crystallites" in the mother (or ambient) phase. The key step is to overcome a so-called nucleation barrier in the clustering process, which determines the rate of generating "mature" crystals in the unit volume of the ambient phase. Under the condition of crystallization, the crystal phase is the thermodynamically stable phase. As shown in Fig. 7.2, the occurrence of nucleation barrier is subject to the occurrence of the interfacial energy between the crystal phase and the ambient phase. In other words, if there is no interfacial energy between the ambient and the crystal phases, there will not be any nucleation barrier.

During nucleation, if the probability of creating critical nuclei is uniform throughout the system, nucleation is defined as *homogeneous nucleation*. Otherwise, it is defined as *heterogeneous nucleation*. Notice that what has been mentioned above is normally referred to as 3D nucleation. During crystal growth, the so-called 2D nucleation will take place at the growing crystal surfaces in order to create new growing layers. When the growth of a crystal surface occurs under its critical roughening temperature, there will be a non-zero free energy in correspondence to the interfacial free energy in 3D. The so-called step free energy is associated with the creation of a step of unit length at the surface. Such a crystal face has atomically a smooth surface. Due to the step free energy, the creation of a new layer on the existing layer of the crystal surface should overcome a free energy barrier, similar to 3D nucleation barrier. If the crystals are free of screw or mixed dislocations, they grow by the mechanism of 2D nucleation [16] and the growth rate R_g is largely determined by the 2D nucleation rate. Although they are not exactly the same, both 3D and 2D nucleation share many common features in almost all aspects [50, 51] Therefore, the analysis on 2D nucleation can be applicable to 3D nucleation, and vice versa.

As one of the most important factors, the nucleation rate J is determined by the height of the free energy barrier, the so-called nucleation barrier. The free energy change associated with the formation of a cluster of molecules can be found from thermodynamic considerations, since it is defined as

$$\Delta G = G_{\text{fin}} - G_{\text{ini}} \tag{7.7}$$

for a system at constant pressure and temperature (G_{ini} and G_{fin} denotes the Gibbs free energies of the system in the initial and final states before and after cluster formation, respectively). If M is the number of solute molecules in the system, one has then

$$\Delta G = -n\Delta\mu + \Phi_n \tag{7.8}$$

where Φ_n is the total surface energy of the n-sized cluster (except for the nucleation of bubbles when Φ_n contains also pressure–volume terms).The function ΔG reaches its maximum ΔG^* at $r = r_c$ or $n = n^*$ (r and r_c are the radius and the critical radius of the cluster, respectively). A cluster of n^* molecules is a critical nucleus, r_c is the radius of curvature of that critical nucleus, and ΔG^* is the nucleation barrier.

The occurrence of a foreign body in the system normally reduces the interfacial (or surface) free energy between the substrate and the nucleating phase; it will then lower the nucleation barrier according to (7.8). Given ΔG^*_{homo}, the homogeneous nucleation barrier, and $\Delta G^*_{\text{heter}}$, the heterogeneous nucleation barrier, we can define an interfacial correlation factor f, describing the reduction of the nucleation barrier due to the occurrence of foreign body as

$$f = \frac{\Delta G^*_{\text{heter}}}{\Delta G^*_{\text{homo}}} \tag{7.9}$$

As shown in Fig. 7.2b, we assume that nucleation occurs on a rough substrate or foreign body with a radius of curvature R^{s}. The fluid phase is denoted by the subscript f, the crystalline phase by c, and the foreign body by s. If we denote the volume by V and the surface area of the foreign body by S, then the free energy of formation of a cluster of radius r on a foreign particle of radius R^{s} is given, according to (7.8), by

$$\Delta G = -\frac{\Delta\mu V_{\text{c}}}{\Omega} + \gamma_{\text{cf}} S_{\text{cf}} + (\gamma_{\text{sf}} - \gamma_{\text{sc}}) S_{\text{sc}} \tag{7.10}$$

where γ_{ij} is the surface free energy between phases i and j, and Ω is the volume per structural unit. We have then

$$m = \frac{(\gamma_{\text{sf}} - \gamma_{\text{sc}})}{\gamma_{\text{cf}}} \approx \cos\theta \quad (-1 \leqslant m \leqslant 1) \tag{7.11}$$

To evaluate the critical free energy $\Delta G^*_{\text{heter}}$, we can substitute (7.11) and the expressions of V_{c}, S_{cf}, and S_{sc} into (7.10) and require that

$$\frac{\partial \Delta G}{\partial r} = 0 \tag{7.12}$$

Solving (7.12) should, in principle, give the value of the critical radius. Nevertheless, it will involve a complicated and tedious treatment. On the other hand, a much simpler approach based on the thermodynamics principles can be adopted: it is known that a critical nucleus is a stable nucleus with the maximum curvature for a given thermodynamic condition. Under such an experimental condition, the size of the critical nucleus is the same for homogeneous and heterogeneous nucleation due to the Gibbs–Thomson effect [52–55]. We have then [54, 56] the radius of critical nuclei,

$$r_{\text{c}} = \frac{2\Omega\gamma_{\text{cf}}}{\Delta\mu} \tag{7.13}$$

Referring to Fig. 7.2c and taking

$$R' = \frac{R^{\text{s}}}{r_{\text{c}}} = \frac{R^{\text{s}}\Delta\mu}{\Omega\gamma_{\text{cf}}} = \frac{R^{\text{s}} kT \ln(1+\sigma)}{\Omega\gamma_{\text{cf}}}, \tag{7.14}$$

the free energy of formation of a critical nucleus is given according to (7.9) by

$$\Delta G^*_{\text{heter}} = \Delta G^*_{\text{homo}} f(m, R') \tag{7.15}$$

with

$$\Delta G^*_{\text{homo}} = \frac{16\pi\gamma_{\text{cf}}^3\Omega^2}{3[kT\ln(1+\sigma)]^2} \tag{7.16}$$

$$f(m,R') = \frac{1}{2} + \frac{1}{2}\left(\frac{1-mR'}{w}\right)^2 + \frac{1}{2}R'^3\left[2-3\left(\frac{R'-m}{w}\right)+\left(\frac{R'-m}{w}\right)^2\right] + \frac{3}{2}mR'^2\left(\frac{R'-m}{w}-1\right) \tag{7.17}$$

and

$$w = \left[1+\left(R'\right)^2 - -2R'm\right]^{1/2}. \tag{7.18}$$

Here R' is actually the dimensionless radius of curvature of the substrate with reference to the radius of the critical nucleus r_c. Note that the factor $f(m,R')$ varies from 1 to 0. To acquire the details of (7.17,7.18), see Chap. 2 in this book or Refs. [54, 56]. Obviously, this factor plays an important role in the determination of the heterogeneous nucleation barrier $\Delta G^*_{\text{heter}}$. One can see from (7.9) that the influence of foreign particles on the nucleation barrier can be fully characterized by this factor.

Figure 7.3a shows that $f(m,R')$ is a function of R' for a given m. When $R' \to 0$, $f(m,R') = 1$, implying that the foreign body "vanishes" completely as a nucleating substrate. In practice, if foreign bodies are too small, e.g., clusters of several molecules, nucleation on these substrates will not be stable. Then, they play no role in lowering the nucleation barrier. On the other hand, if $R' \gg 1$, the foreign body can be treated as a flat substrate with respect to the critical nuclei. In this case, $f(m,R') = f(m)$ is solely a function of m, and (7.17) is then reduced to

$$f(m,R') = f(m) = \frac{1}{4}(2-3m+m^3) \tag{7.19}$$

$f(m)$ as a function of m is given in Fig. 7.3b.

7.3.2 Kinetics of Nucleation

The commonly accepted nucleation processes can be regarded as follows: on the substrate surface, some molecular processes occur due to transient visiting molecules that adsorb, form short-lived unions, break up, desorb, etc. An instantaneous census would show some distributions of subcritical nuclei (or clusters) with 1, 2, 3, ... molecules per cluster as,

$$\text{Monomer} \rightleftharpoons \text{Dimer} \rightleftharpoons (n--1)\text{mer} \rightleftharpoons n\text{–mer} \rightleftharpoons (n+1)\text{mer} \tag{7.20}$$

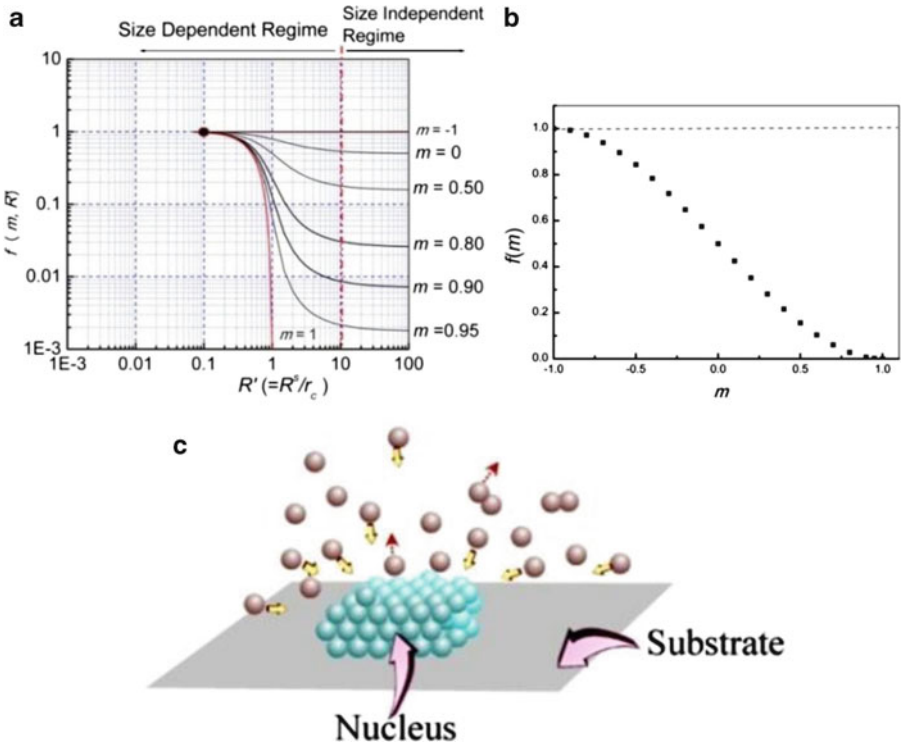

Fig. 7.3 (**a**) Dependence of the interfacial correlation function $f(m,R')$ on m and R'. (b) Measured $f(m,R')$ in ice nucleation [55–57]. (**b**) Dependence of the interfacial correlation function $f(m,R') = f(m)$ on m at $R' \gg 10$. (**c**) Schematic illustration of *the shadow effect* of the substrate in heterogeneous nucleation. The presence of the substrate blocks the collision of growth units onto the surface of the nucleus. Reprinted with permission from Ref. [9] ©2004 Springer

Although many theories have been put forward, the "atomic" process has never been visualized and treated in a quantitative way until recently when a 2D nucleation process was monitored in the system of charged PS spheres driven by the alternating field with a fixed field strength and a frequency (i.e., Fig. 7.1) [13, 57]. A typical process of nucleation has been presented in Fig. 7.4. On the electrode surfaces, the concentration of particles was supersaturated and the particles started to form the nuclei (Fig. 7.4a, b, where we represented crystal-like particles as blue spheres). The nucleus in red circle kept growing whatever its state was pre- or post-nucleation; the nucleus in green circle shrank far more frequently than they grow (Fig. 7.4c–e). In Fig. 7.4f, the plots reflected the evolution of size of two adjacent nuclei during the process of pre-nucleation. One nucleus was growing larger and larger when its size is larger than the critical size. Moreover, the other nucleus was shrinking before reaching the critical size. This implies that nucleation is a number of simultaneous fluctuating assembly–disassembly events. A successful nucleation process corresponds to one of such events that can survive till the nucleus reaches critical size [53].

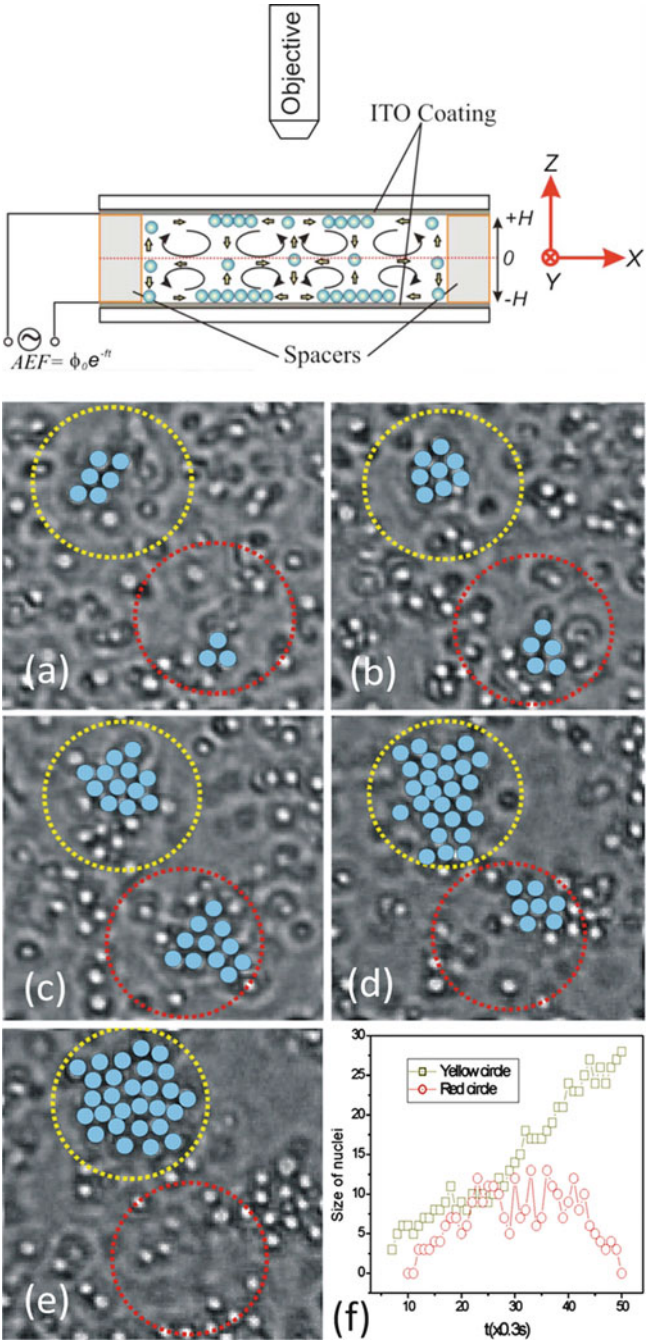

Fig. 7.4 *The top schema*: the experimental setup. The colloidal suspension is sandwiched between two ITO-coated glass plates separated by insulating spacers. Snapshots of pre-nucleation process below: (**a**) Time $t = 10t_0$ (t_0 is the timing interval of images, 0.3 s), (**b**) $20\,t_0$, (**c**) $30\,t_0$, (**d**) $40\,t_0$, (**e**) $50\,t_0$, (**f**). The evolution of size of two nuclei. The *yellow curve* represents the increasing size of nucleus in the *yellow circle*; the *red curve* represents the shrinkage of nucleus in the *red circle*. ($\sigma_E = 2.6\times10^4$ V/m, $f = 600$ Hz) (From [13]). Reprinted with permission from Ref. [13] © 2004 Nature Publishing Group

In the case of the 2D nucleation of crystals with n^* molecules, the homogeneous nucleation energy $[\Delta G^*_{\text{homo}}]_{2D}$ and the radius of critical size $(r_c)_{2D}$ are expressed by (7.21,7.22), respectively [13],

$$[\Delta G^*{}_{\text{homo}}]_{2D} = \frac{\pi \Omega (\gamma_{\text{step}})^2}{\Delta \mu} \tag{7.21}$$

$$[r_c]_{2D} = \frac{\Omega \gamma_{\text{step}}}{\Delta \mu} \tag{7.22}$$

where γ_{step} is the crystal–liquid interfacial edge free energy.

The widely accepted kinetic model of nucleation (within the cluster approach) was used first by Farkas [3] in 1927. It is based on the Szilard scheme of successive "chain reaction" between monomer molecules and n-sized clusters as shown by (7.20).

A master equation for the concentration $Z_n(t)$ of the n-sized clusters at time t is written in the form of a continuity equation [56, 58, 59]

$$\frac{dZ_n}{dt} = J_{n-1} - J_n, \tag{7.23}$$

where J_n is the flux through point n on the size axis. Thus in this formulation, J is the flux through the nucleus size n^*, i.e., $J \sim J_{n*}(t)$, so that a time dependence is introduced in the nucleation rate.

The basic problem in the nucleation kinetics is to solve the master (7.20) in the unknown cluster size distribution $Zn(t)$, as knowledge on $Zn(t)$ will allow the acquirement of the nucleation rate. In this concern, three physically distinct states of the nucleating system require a special attention: *the equilibrium*, *the stationary* (*or steady*), and *the nonstationary states*. In the following, we will brief the equilibrium and the nonstationary states and focus more on the steady state, which is more relevant in the most nucleation events.

7.3.2.1 Equilibrium State

As nucleation is a dynamic process other than that at equilibrium, this state is conceptual and never occurs in practices. Introducing this state is (1) to make a reference for other states and (2) to help in the treatment of the stationary state mathematically.

Based on the thermodynamic statistical principles, in equilibrium, $dZ_n/dt = 0$ and $J_n = 0$. Then $Z_n = C_n$ is the equilibrium cluster size distribution. (C_n is the equilibrium concentration of n-sized clusters.) According to the Boltzmann law, one can easily obtain

$$(C_n/Z) = (C_1/\sum)^n \exp(-\Delta G_n/kT) \tag{7.24}$$

(for all n; $n = 2,3,4,\ldots$) with the effective total number of "molecules" per unit volume:

Let κ_n be the rate of molecule addition. That is,

$$\kappa_n = \beta_{\text{kink}} K_n \tag{7.25}$$

where K_n denotes the collision rate of monomers with an n-sized cluster and β_{kink} is the conversion probability . Also let κ'_n be the rate at which the cluster loses molecules. Obviously, at the equilibrium state, one has the detailed balance between the growth and disintegration of clusters,

$$\kappa_n C_n - \kappa'_{n+1} C_{n+1} = 0. \tag{7.26}$$

Since $\Delta G^*_{\text{heter}}(\Delta\mu)$ has a maximum at $n = n^*$, C_n displays a minimum at the critical nucleus size. The increasing nonphysical branch of C_n at $n > n^*$ reflects the fact that the mother phase is saturated.

7.3.2.2 Stationary (or Steady) State

The stationary state is a state at which the cluster size distribution does not change with time. Normally, this state is so far the most important state and occurs in the middle stage of nucleation and can be treated quantitatively. In the stationary state, $dZ_n/dt = 0$. Because $J_n = \text{constant} = J_{n^*} = J$, $Z_n \sim Z'_n$ is the steady-state cluster size distribution. The stationary nucleation rate for homogeneous nucleation is given by the Becker–Doering formula [56]

$$J = \frac{zK^*}{v_m} \exp\left(-\frac{\Delta G^*_{\text{homo}}}{kT}\right) \tag{7.27}$$

with

$$z = \frac{Z'_{n^*}}{C_{n^*}} - \frac{Z'_{n^*+1}}{C_{n^*+1}} \tag{7.28}$$

where z is the so-called Zeldovich factor [48, 59], $K^* = K_{n^*}$ is the frequency of monomer attachment to the critical nucleus, v_m denotes the average volume of structural units in the ambient phase, and C_n is the equilibrium concentration of n-sized clusters given by[49],

$$C_n \cong C_1 \exp(-\Delta G_n / kT) \tag{7.29}$$

Based on the definition of J_n, one has

$$J_n = k_n Z'_n \tag{7.30}$$

At the steady state, J', that is the formation rate of critical nuclei per unit volume per unit time around a foreign particle is equal to the steady-state growth of clusters on the surface of the particle. The nucleation rate can then be given in terms of

$$J' = J_{n*} = J_n = \text{constant} = \text{criticalsizednucleiformed/unitvolume} - \text{time} \equiv \ldots$$
$$= k_n Z'_n - -k_{n+1} Z'_{n+1} = \text{constant}. \tag{7.31}$$

Regarding the effect of the substrate on both the nucleation barrier and the transport process, and the fact that the average nucleation rate in the fluid phase depends on the density and size of the foreign particles present in the system, the nucleation rate is given by [49, 56, 58]

$$J = 4\pi a (R^s)^2 N^{\circ} f''(m, R')[f(m, R')]^{1/2}$$
$$\times B \exp\left[-\frac{16\pi \gamma_{cf}^3 \Omega^2}{3kT[kT\ln(1+\sigma)]^2} f(m, R')\right] \tag{7.32}$$

with

$$B = (C_1)^2 4D\beta_{\text{kink}}\Omega\left(\frac{\gamma_{cf}}{kT}\right)^{1/2} \tag{7.33}$$

$$f''(m, R') = \frac{1 + (1 - R'm)/w}{2} \tag{7.34}$$

and

$$f''(m, R') = f''(m) = \frac{1}{2}(1 - m) \text{ at } R' >> 1 \tag{7.35}$$

where B is the kinetic constant and N° denotes the number density of the substrates (or "seeds"). The growth of nuclei is subject to the effective collision and incorporation of growth units into the surfaces of the nuclei (cf. Fig. 7.3c). In the case of homogeneous nucleation, the growth units can be incorporated into the nuclei from all directions. However, for heterogeneous nucleation, the presence of the substrate will block the collision path of the growth units to the surfaces of these nuclei from the side of the substrate (cf. Fig. 7.3c). This is comparable to the "shadow" of the substrate cast on the surface of nuclei. $f''(m,R')$ in the pre-exponential factor, which is the ratio between the average effective collision in the presence of substrates and that of homogeneous nucleation (i.e., in the absence of a substrate), describes this effect.

Both $f(m,R')$ and $f''(m,R')$ are functions of m and R'. When $R' \to 0$ or $m \to$ -1, $f(m,R')$, $f''(m,R') = 1$. This is equivalent to the case of homogeneous nucleation. In the case where $m \to 1$ and $R \gg 1$, one has $f(m,R')$, $f''(m,R') = 0$. Normally,

heterogeneous nucleation occurs in the range between 1 and -1, or $f(m,R')$ between 0 and 1, depending on the nature of the substrate surface and the supersaturation.

Note that for homogeneous nucleation, one has $f\prime\prime(m,R') = f(m,R') = 1$ and $4\pi a(R^s)^2 N^o \to 1$. In this case, (7.32) is converted to

$$J = B \exp\left[-\frac{16\pi\gamma_{cf}^3\Omega^2}{3kT[kT\ln(1+\sigma)]^2}\right]. \tag{7.36}$$

This implies that (7.29) is applicable to both homogeneous and heterogeneous nucleation.

Similar to 3D nucleation, 2D nucleation can also adopt a similar form [49]:

$$J_{2D} = \left\{\frac{2D_s C_1^2}{\pi}\left[\frac{\Omega\ln(1+\sigma)}{h}\right]^{1/2} \exp\left(-\frac{\Omega(\gamma_{cf}^{\text{step}})^2\pi h}{(kT)^2\ln(1+\sigma)} f_{2D}(m_{2D}, R'_{2D})\right)\right\}$$
$$\times \beta_{kink}\delta\left(m_{2D}, R'_{2D}, R^s, N^o\right) \tag{7.37}$$

with

$$\delta(m_{2D}, R'_{2D}, R^s, N^o) = \left\{\frac{\psi}{\pi} N^o \pi a R'_{2D}\left[f_{2D}(m_{2D}, R'_{2D},)\right]^{1/2}\right\} \tag{7.38}$$

where D_s denotes the surface diffusivity. In the case of 2D homogeneous nucleation, one has $\delta(m_{2D}, R'_{2D}, R^s, N^o) = f_{2D}(m_{2D}, R'_{2D})$, and (7.37) can be simplified as follows:

$$J_{2D} = \left\{\frac{2D_s n_1^2}{\pi}\left[\frac{\Omega\ln(1+\sigma)}{h}\right]^{1/2} \exp\left(-\frac{\pi\Omega h\gamma^2}{(kT)^2\ln(1+\sigma)}\right)\right\} \beta'_{\text{kink}} \tag{7.39}$$

Here n_1 is the number of single particles (monomers), and β_{kink} is the sticking possibility.

7.3.2.3 Nonstationary (or Nonsteady) State

From the initiation of nucleation ($t = 0$) to the stationary/steady state, there must be a transit state where the size distribution of clusters will change with time. This state is known as the nonstationary (or nonsteady) state. Similarly, when nucleation comes to the end, we will also experience this state. When the nucleation is nonstationary, $dZ_n/dt \neq 0$, and flux J_n is a function of both n and t. The nucleation rate is then time dependent and this nonstationary nucleation rate $J_{\text{nonst}}(t) = J_{n^*}(t)$. In other word, $J_{\text{nonst}}(t)$ will change with time.

7.3.2.4 Experimental Verification of Nucleation Kinetics Based on Colloidal Crystallization

Although theoretical analysis on the above states of nucleation has been published for long time, experimental verification, in particular, the direct measurement for the distribution of subcritical nuclei had never been achieved till recently when the electrically controlled 2D colloidal nucleation was carried out [13]. By measuring the size distribution of subcritical nuclei on the surface of flat electrode, we observed the evolution among the different kinetics: nonstationary, stationary, and equilibrium states [49] in the process of pre-nucleation. Figure 7.5a presented a typical distribution at different time. Once the driving force is applied, the small nuclei are formed. Subsequently, the cluster size exceeded the critical size of nuclei, and the nuclei were growing to the crystallites gradually. Figure 7.5a reflected this image of nucleation kinetics. Here we defined a transient point $n^*(t)$, where the size distribution approached to a steady number of clusters in the nucleation (see Fig. 7.5a, inset).

It follows from Fig. 7.5 that, first, the system starts from a nonstationary state ($t = 3.2$ s) at the beginning and gradually approaches toward the stationary state ($t > 20$ s) in which the distribution of nucleating clusters Z_n is independent of time. Second, a nucleation event is successful once the distribution of nucleating clusters $Z_{n^*} = 1$ in any time. Therefore, the cluster size at $Z_n = 1$ can be defined as the critical size of nucleation n^*.

Before reaching the stationary state, n^* is time dependent. Only after reaching the stationary state, the critical size of nucleus n^* can acquire a constant value (Fig. 7.5b). In other words, it makes sense to discuss the critical size of nucleus only at the stationary state.

In Fig. 7.5c, the average nucleation rate in the unit area of surface according to the fitting slope of curves was measured. Figure 7.5d presents the nucleation rate density under different driving forces. The linear fitting of the plot of $\ln(J)$ $1/\ln(1+\sigma)$ indicates that (7.39) can be applied to quantify the nucleation kinetics of 2D nucleation.

7.3.3 Initial Stage of Nucleation: Is Classical Nucleation Theory Accurate?

Although the basic treatments of classical nucleation theories (CNTs) have been approved to be correct as shown in Sect. 7.3.2.3, some aspects of nucleation remain unclear. In the analysis of nucleation kinetics in Sect. 7.3.2, the structure of crystal nuclei is supposed to be identical to the bulk crystals. Is this assumption correct? If not, what are the consequences? In the following, we will describe the interfacial structural evolution during nucleation, the impact of the interfacial structure of nucleating clusters on the nucleation energy barrier, in terms of 2D colloidal crystallization model system.

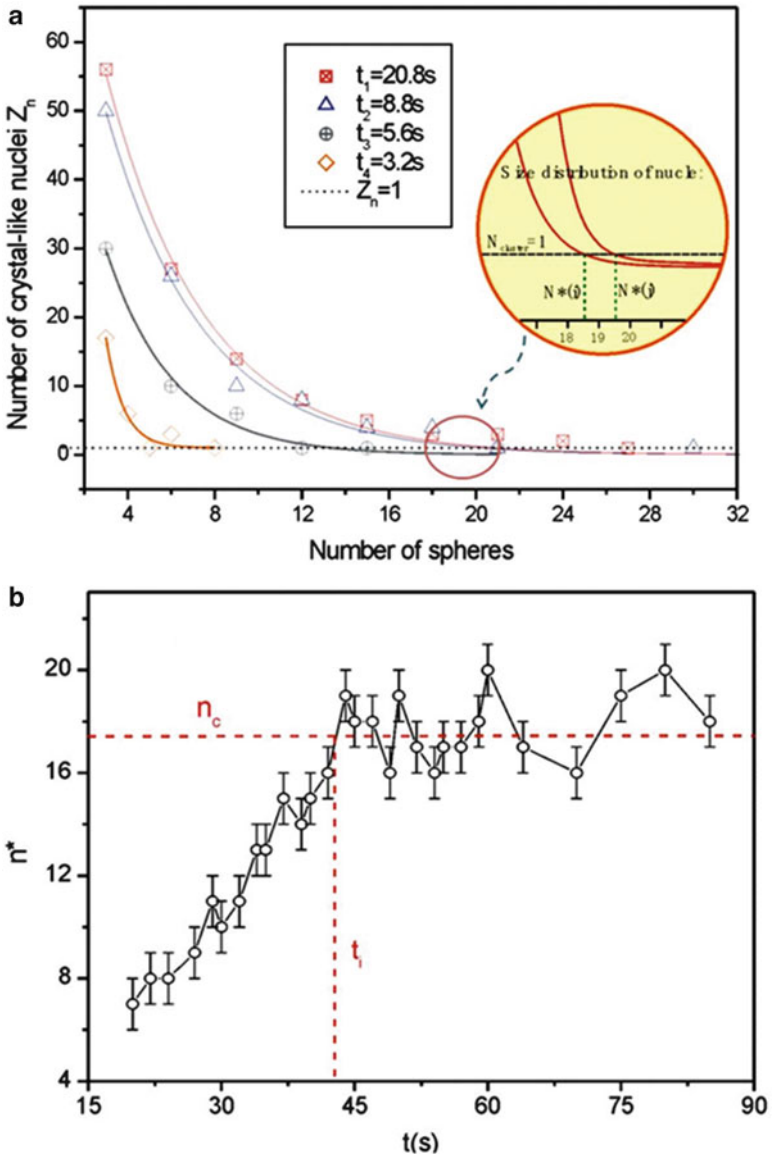

Fig. 7.5 Measurement of nucleation kinetics parameters. (**a**) The typical size distribution of subcritical nuclei versus time ($\sigma_E = 2.6\times10^4$ V/m, $f = 600$ Hz.). (**b**) $n^*(t)$ versus time. After the induction time, $n^*(t)$ becomes stable. The critical size can be determined. (**c**) The number of nuclei for which the size is larger than the critical size in different time. We can measure the nucleation rate in the unit area according to the slope of linear fitting of this *curve*. (**d**) The nucleation rate under the different supersaturation (driving force). The *straight line* fitting is based on (7.39). From (7.39), we also can get the line tension of interface. The value of γ_{step} is $0.50kT/a$ (a is the diameter of colloidal particles), which is in agreement with the measurements. For more details, see Ref. [15]. Reprinted with permission from Ref. [13] © 2004 Nature Publishing Group

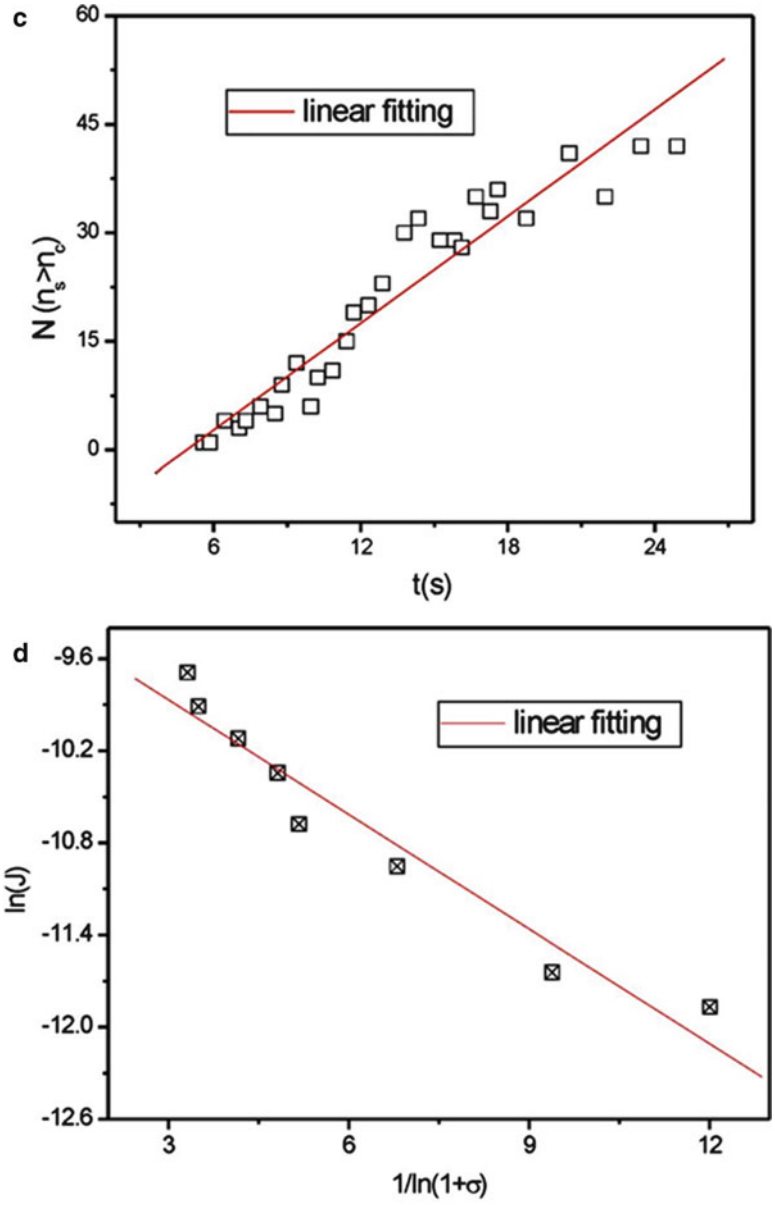

Fig. 7.5 (continued)

To identify the crystalline-like particles from the liquid-like particles in 2D crystal nuclei, a local 2D bond-order parameter is defined as follows [37–41]:

$$\psi_6(r_i) = M^{-1}\left|\sum\nolimits_j e^{i6\theta_{ij}}\right| \tag{7.40}$$

where r_i is the center of particle i, and θ_{ij} is the angle subtended between the vector from particle i to its jth nearest neighbor and the arbitrarily chosen x axis. M is the number of nearest neighbors of particle i. The mean value of $\psi_6(r_i)$ for crystalline structures obtained from the experiments is 0.8, which is taken as the criterion for a crystal-like particle.

Figure 7.6a reveals that at relatively low supersaturations, the structure of crystalline clusters is a bit fluid-like and more disordered at the beginning and gradually approaches to the ordered structure in the bulk crystalline phase at a size close to the critical size of nuclei. The transition from the initial metastable structure to the final stable structure is a continuous process.

On the other hand, at high supersaturations (decreasing frequency gives rise to the increase in supersaturation) [60], Fig. 7.6b shows the structural transition occurring under conditions of $f = 3{,}000$ Hz and $V_{pp} = 2.5$ V. Different from the behavior of $\langle\psi_6\rangle$ in Fig. 7.6(a), $\langle\psi_6\rangle$ can be as high as 0.8 instantaneously even before it reaches its transition size (30) (in Fig. 7.6b(i)). This implies that the nucleus can have a crystalline structure even before it becomes stable in structure. Nevertheless, the crystalline structure of the precritical nuclei is transient and fluctuated. In Fig. 7.6b(ii) and (iv), the structure of the nucleus is ordered. In the subsequent seconds, as shown in Fig. 7.6b(iii) and (v), it becomes disordered again. Only when the size is beyond the critical size 30, the crystalline structure becomes stable. As the supersaturation is increased further by decreasing frequency, $\langle\psi_6\rangle$ remains more or less 0.8 in the whole growth process from the beginning, and crystal nuclei are initially created with a crystalline structure as suggested by CNT [44].

The results in Fig. 7.6 indicate that the initial structure of crystal nuclei and the structural evolution of crystal nuclei are *supersaturation-dependent*. At low supersaturations, a metastable liquid-like structure is likely to occur first. This is

Fig. 7.6 (continued) a critical size. (*iv*) $\langle\psi_6\rangle$ is a function of nuclei size N. Monodisperse colloidal particles (polystyrene spheres of diameter 0.99 mm, polydispersity <5%, Bangs Laboratories) were dispersed uniformly in deionized water. The colloidal suspension was then sealed between two parallel horizontal conducting glass plates coated with indium tin oxide (*ITO*).The gap between the two glass plates is $H = 120 \pm 5$ mm. The dynamic process is recorded by a digital camera (*CCD*) for analysis. *AEF* alternating electric field. (**b**) Phase diagram of the system when the concentration of Na_2SO_4 is 2×10^{-4} M. V_{pp}, peak-to-peak voltage. Due to the nature of 2D crystals, $\langle\psi_6\rangle$ for a perfect 2D crystal is 0.8. (**b**) Transient crystalline structure of nuclei under condition of $V_{pp} = 2.5$ V, $f = 3{,}000$ Hz. (*i*) Fluctuation of order parameter during the growth. (*ii*, *iii*) Due to the structural fluctuation, nuclei can have a transient crystalline structure. (*iv*, *v*) Liquid-like structure displayed by precritical nuclei. Reprinted with permission from Ref. [44] © 2008 Wiley-VCH Verlag GmbH & Co

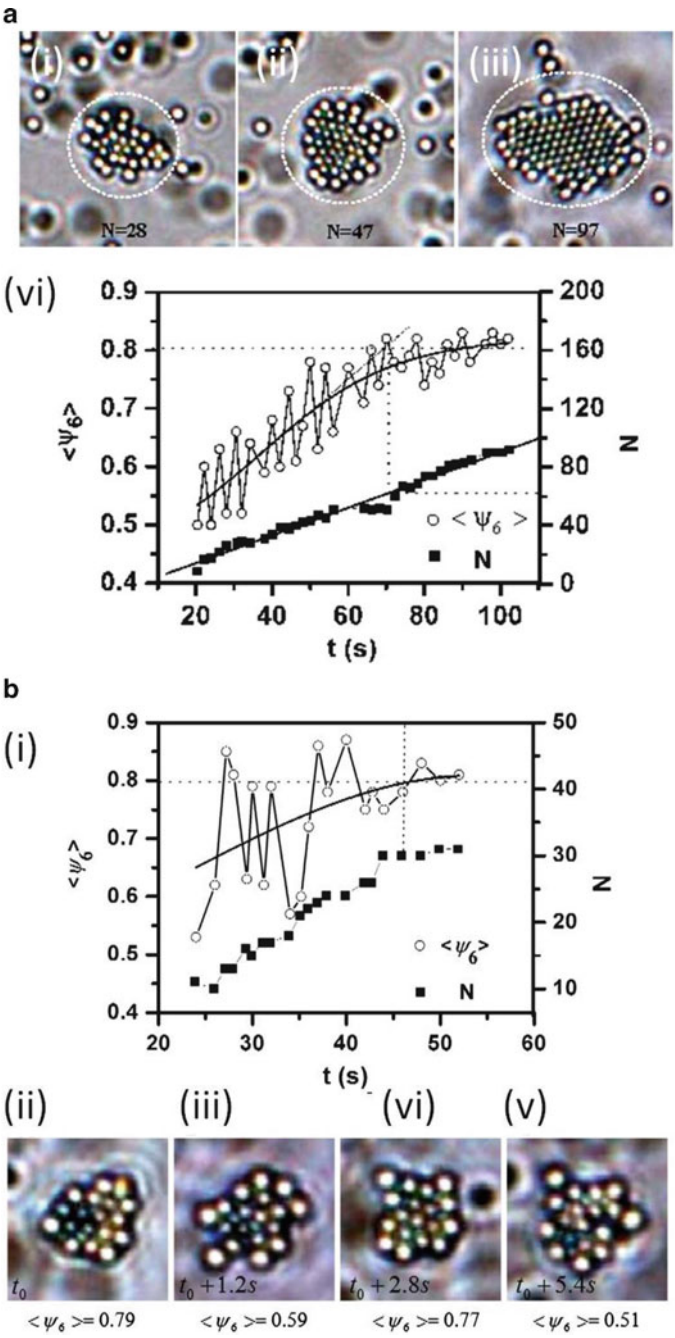

Fig. 7.6 (**a**) Structural evolution of nuclei under conditions of $V_{pp} = 2.5$ V, $f = 5{,}000$ Hz. (*i*) Initial structure of nuclei is liquid-like. (*ii*) As the nucleus grows, its core first becomes ordered with the exterior layer remaining liquid-like. (*iii*) The nuclei become completely ordered after they exceed

because the nucleation barrier is very high at low supersaturations (cf. (7.16) and (7.21)). The occurrence of the metastable structure at the nuclei may help to reduce the nucleation barrier [61, 62]; therefore, it is kinetically more favorable. On the other hand, the nucleation barrier becomes much lower at higher supersaturations (cf. (7.16) and (7.21)), and the structural relaxation of nuclei is not kinetically very favorable. Therefore, the structure of pre-nucleation clusters can be as ordered as that of the bulk crystalline phase.

The analyses on the kinetic data [34, 36, 44] confirm that, at low supersaturations, the evolution of nuclei from a liquid-like structure to a crystal-like structure will effectively reduce nucleation barrier and facilitate the nucleation dynamics. In other words, at low supersaturations, the CNTs overestimate the nucleation barrier. At high supersaturations, as the nucleation barrier decreases substantially. Adopting the structure of the bulk crystals during nucleation need not be energetically unfavorable. Therefore, the dynamic behavior predicted by the CNTs becomes valid.

7.3.4 Multistep Nucleation/Crystallization in Biomineralization

In the case of biomineralization, it is often found that the most thermodynamically stable calcium phosphate phase, hydroxyapatite ($Ca_{10}(PO_4)_6(OH)_2$ or $Ca_5(PO_4)_3(OH)$, HAP), does not occur first. Instead, the least stable phase, the amorphous calcium phosphate (ACP) phase, occurs at the beginning and then transforms into more thermodynamically stable phases in solutions. Pan and Liu [63] applied the combined in situ UV–vis extinction detection and ex situ electronic microscopy to examine the formation of ACP and the evolution to HAP under the physiological pH and ionic strength condition in a simulated body fluid. The UV–vis extinction spectroscopy was applied to monitor the mineralization process (Fig. 7.7).

According to the UV–vis extinction curves, the mineralization process can be divided into four stages (Fig. 7.7b). In stage I, after the mixing of a calcium solution and a phosphate solution, ACP occurs, and the solution becomes turbid. In stage II, the extinction of the solution arises and gradually reaches a plateau. In this stage, the aggregation of ACP occurred (Fig. 7.8a). In stage III, an abrupt decrease in the extinction is observed, corresponding to the transformation of ACP mineral to HAP crystallites (Fig. 7.8b, e–g) [64, 65].

Afterward, the crystallites undergo further growth, ripening and aggregation in stage IV. The final products are some spherulites, composed of platelet crystallites organized in the radial orientation (Fig. 7.8c,i). The characteristic four stages in the UV–vis extinction curves can be found from the solutions of different calcium and phosphate concentrations [63]. The details of the morphological change and phase evolution of ACP were captured by ex situ EM. The spherical-liked minerals (215 ± 29 nm) were first formed (within 3 min, Fig. 7.8a,d). The selected area

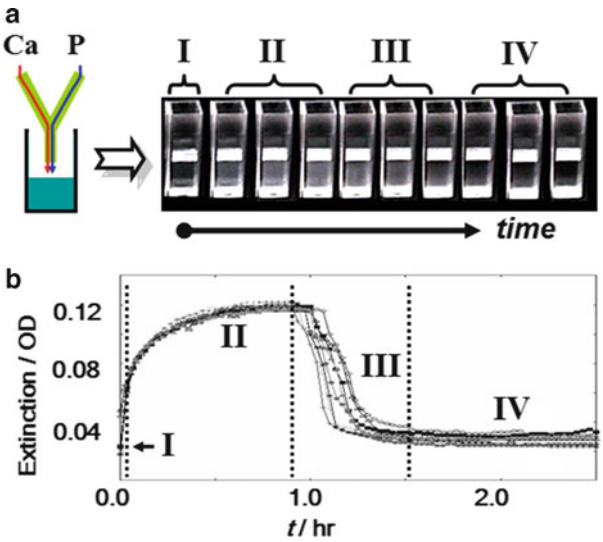

Fig. 7.7 The evolution of calcium phosphate solution. After the mixing of a calcium solution with a phosphate solution (with final concentration: 4 mM $CaCl_2$, 6 mM K_2HPO_4, 150 mM NaCl, pH 7.40, i.e., the saturation indices (log (*IAP*) - log (K_{sp}), where *IAP* is the ionic activity product of precipitation; K_{sp} is the solubility product constant) of initial solution were 0.25 (for ACP, $Ca_9(PO_4)_6$), 25.8 (for HAP), 23.1 (after the precipitation of ACP), the solution became turbid gradually. In about 1 h, the suspension suddenly became clear, accompanied with visible sedimentations formed simultaneously (see (**a**)). The entire mineralization process can be monitored by the extinction curves (the optical difference of 405 nm and 550 nm). (**a**) Photographs of the suspensions. The solution became turbid, then clear again accompanied with the sediment of minerals. (**b**) The extinction curves of calcium phosphate solutions. Reproduced with permission from Ref. [63] © The Royal Society of Chemistry 2010

election diffraction (SAED) patterns of diffusive rings indicate that the spheres are amorphous (Fig. 7.8a). The initially round-shaped ACP particles indicate the occurrence of fluid-like structure at the beginning. The sintering of the submicro-sized ACP droplets in solutions leads to the further aggregation of these spheres (Fig. 7.8a). The ACP aggregate partially merged as showed in Fig. 7.8d. After the formation of ACP, the particles remained in amorphous state for about 1 h before the transformation took place.

Concerning the transformation of ACP spheres, at first, the boundary of ACP spheres became polygonal-like (Figs. 7.8b,e and 7.9a; 67 min). Some condensed rings or dots appear in the SAED patterns (Fig. 7.8b), indicating the formation of crystalline materials. The bright dots in the dark-field TEM images (DF-TEM) (Fig. 7.9b) indicate the occurrence of crystallized minerals. The high-resolution TEM images (HR-TEM) (Fig. 7.9c) directly show that the crystallization happens at the surface of the ACP spheres, while the main portion of the sphere remains amorphous (i.e., fast Furrier transform (FFT) patterns of selected region in Fig. 7.9c, region 3).

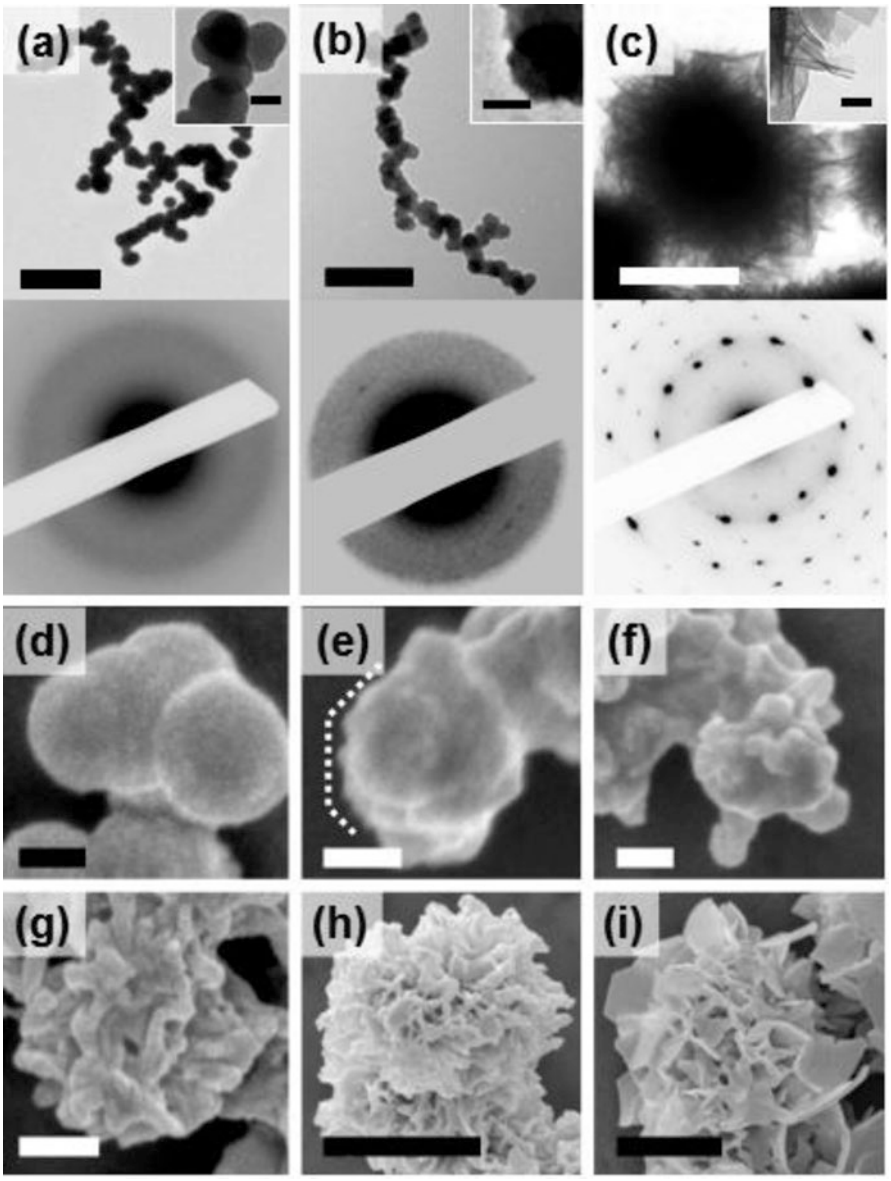

Fig. 7.8 Phase and morphology evolution of calcium phosphate minerals. (**a**–**c**) TEM images and SAED patterns of the precipitates. (**a**) Initially formed ACP spheres. Bar: 1 μm and 100 nm (subimage). (**b**) Intermediate state of ACP. Bar: 1 μm and 100 nm (subimage). (**c**) Final spherulite HAP. Bar: 1 μm and 200 nm (subimage). (**d**–**i**) SEM images of the evolution of ACP. (**d**) 3 min. (**e**–**g**) 67–73 min. (**h**) 90 min. (*i*) 7 h. Bar: (**d**–**f**) 100 nm; (**g**) 200 nm; (**h**–**i**) 1 μm. The selected area diffraction (*SAED*) study together with XRD examination indicates that the mineral phase is HAP, and each platelet in a spherulite arm is a single crystallite (see (**c**)). Reproduced with permission from Ref. [63] © The Royal Society of Chemistry 2010

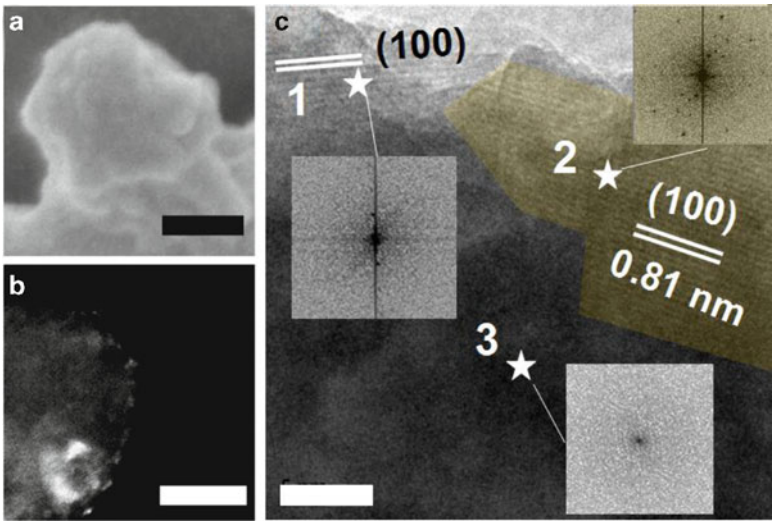

Fig. 7.9 Initial phase transformation stage of ACP particles. (**a**) SEM image (**b**) DF-TEM image. (**c**) HR-TEM image, and the fast Fourier transform (*FFT*) patterns of crystallized regions (*1*, *2*) and the amorphous region (*3*). Bar: (**a**) 100 nm; (**b**) 50 nm; (**c**) 10 nm. Reproduced with permission from Ref. [63] © The Royal Society of Chemistry 2010

The above results indicate that at the initial stage of biomineralization in a simulated body fluid solution, ACP spheres occur soon after mixing the two reactants. The transformation from ACP to HAP takes place in about 1 h. During the transformation, the nucleation occurs preferably at the surface of ACP spheres. The embedded/adhered crystallites on the ACP surface would not allow the crystallites to rotate their orientations and/or relocate from their relative positions. This gives rise to the formation of the HAP spherulites.

The process outlined above is a typical stepwise crystallization, the so-called two-step crystallization (TSC) [66]. It is one way to facilitate the nucleation kinetics and often observed during protein crystallization [10, 67–69], biomineralization, etc. According to TSC, dense amorphous droplets are first formed from the mother phase; crystalline nuclei are then created from the droplets. For instance, during the formation of calcite in sea urchin larvae, a transient amorphous phase is formed first, before the final crystal phase is reached [70, 71]. Similarly, a transient amorphous phase is also identified during the formation of aragonite controlled by mollusk bivalve larvae [72]. Recently, the similar process has also been observed for the HAP formation from a simulated body fluid [73]. It is widely believed that in biological systems, the development of crystalline structures characterized by well-defined shape and size is essentially facilitated by the occurrence of transient amorphous phases [64, 71, 72]. In fact, recent studies indicated that TSC may be a mechanism underlying most crystallization occurring in typical atomic systems [62, 73, 74].

Although the TSC can be captured by Ostwald's rule· [17], the detailed understanding has not been acquired till recently. In this regard, the controlled colloidal assembly can be applied to examine the mechanism. MSC has attracted much attention in the past decade due to its importance in both scientific and technological points of view. However, the understanding of TSC remains to be insufficient. A key challenge is that the kinetics creating the initial crystalline nuclei from the dense droplets is unclear and thus it is no way to predict the overall nucleation rate J_c of crystals. In the following, we will recap the multistep crystallization (MSC) in the colloidal model system. The kinetics of MSC is discussed and a mathematical method is developed to address the local nucleation rate j_c of crystal in the droplets.

A typical process of MSC, observed under conditions of $V_{pp} = 2.0$ V and $f = 800$ Hz, is presented in Fig. 7.10. Colloidal particles in the initial mother solution are uniformly distributed in the solution (i.e., Fig. 7.10a).

When an AEF is applied to the system, colloidal particles are transported onto the glass surface where they first form dense droplets (Fig. 7.10b). Subsequently, a few subcrystal nuclei are created from the droplets as illustrated in Fig. 7.10c. These subnuclei are not stable and will dissolve soon after they are created. Experimentally, it is found that the crystalline nuclei in the droplets have to acquire a critical size N^*_{cry} before they can grow stably in the droplets as shown in Fig. 7.7d. In the experiments, every droplet can produce only one stable crystal. Moreover, to form a stable crystal beyond N^*_{cry}, the droplets have to first acquire a critical size N^*. It is found that although, at an early stage, many small dense droplets are created, only 3 or 4 out of 20 droplets can reach the critical size N^* and develop successfully into a stable crystal. This is consistent with previous observations in protein crystallization [75, 76]. However, it is contradicting with the assumption by Kashchiev et al. [77]. A detailed analysis on the overall nucleation rate J_c of MSC, determined by the local rate j_c in the individual dense droplets, is given in Ref. [52].

In general, the MSC in a colloidal model system indicates that amorphous dense droplets first nucleate from the mother phase. Subsequently, a few unstable subcrystalline nuclei can be created simultaneously by fluctuation from the tiny dense droplets, which is different from previous theoretical predictions. Notice that it is necessary for these crystalline nuclei to reach a critical size N_{cry} to become stable. However, in contrast to subcrystalline nuclei, a stable mature crystalline nucleus is not created by fluctuation but by coalescence of subcrystalline nuclei, which is unexpected. To accommodate a mature crystalline nucleus larger than the critical size N_{cry}, the dense droplets have to first acquire a critical size N^*. This implies that only a fraction of amorphous dense droplets can serve as a precursor of crystal nucleation. As an outcome, the overall nucleation rate of the crystalline phase is, to a large extent, determined by the nucleation rate of crystals in the dense droplets, which is much lower than the previous theoretical expectation. The calculations indicate that the MSC is indeed kinetically more favorable than one-step crystallization under the given conditions [41].

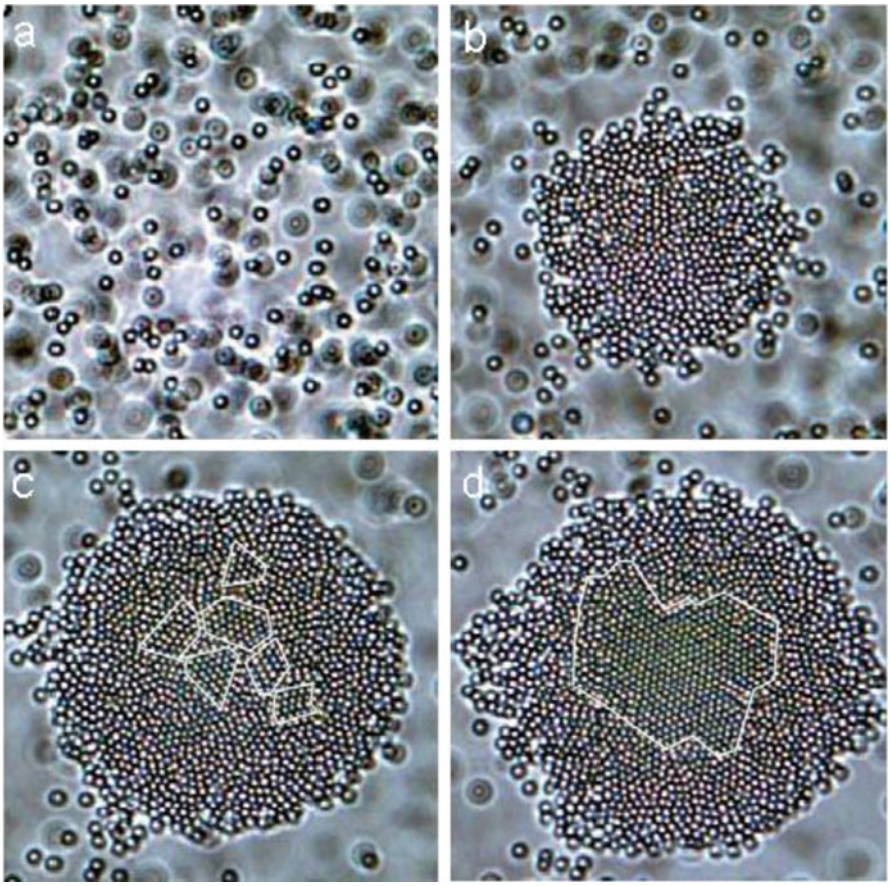

Fig. 7.10 Multistep crystallization: (**a**) Initial dilute liquid phase. (**b**) Amorphous dense droplets are first created from the mother phase. (**c**) A few subcrystal nuclei are created from the amorphous phase. (**d**) A stable crystal is formed from the dense droplets. Colloidal suspension is sealed between two pieces of ITO-coated conducting glass plates separated by insulating spacers. The gap between the two glass plates is $H = 120 \pm 5$ μm. The dynamic process is recorded by a digital camera for analysis. (**b**) Phase diagram of the colloidal suspension. Monodisperse colloidal particles (polystyrene spheres of diameter 0.99 μm, polydispersity < 5%, Bangs Laboratories) are dispersed uniformly in deionized water. In the case, the volume fraction 0.03% of colloidal solid is chosen, and the surface potential of the colloidal spheres is adjusted to -72 mV by Na_2SO_4 (10^{-4} M). The pH of the suspension is measured at 6.35. Monodisperse colloidal particles are dispersed uniformly in deionized water. Reproduced with permission from Ref. [40] ©2003 American Chemical Society

7.3.5 *Formation of Ordered and Disordered Structures in Biominerals*

Many living organisms rely on hard tissues, which are composed of biominerals and protein matrices with exquisite microarchitectures, for support, protection, and defense [78–80]. Natural composite materials such as teeth, bones, and shells represent intriguing and diverse design paradigms for exploring the relationships between structure and mechanical properties such as fracture toughness, stiffness, and hardness[81]. Despite the variety of these complex hierarchical architectures, biominerals are generally organized in a certain order to harden or stiffen tissues in living organisms. Although it is quite clear that the composite character of these materials plays an important role, some important questions need to be addressed. For example, how can the self-assembled nanocomposites exhibit superior mechanical characteristics? What are the key structural factors leading to the superior strength of hard tissues? Although the mechanical properties of hard tissues can be affected by the factors, cf. the type of minerals, the degree of mineralization, and size of mineral particles, there is still a striking variation in mechanical properties even when the components of the composites are similar [82, 83]. Combined with nanoindentation, Jiang and Liu [83] applied the position-resolved small-angle X-ray scattering and electron microscopy to examine the correlation between the microstructure of the enamels of human teeth and the mechanical properties.

The human tooth enamels can be roughly regarded as a bundle of nano HAP crystallite needles (94%) that sandwiched some proteins and water. It follows the experiments [83] that the degree of ordering of the biominerals varies strikingly within the dental sample, showing that both the hardness H and the elastic modulus E increase predominantly with the ordering of the biomineral crystallites [83] (see Fig. 7.11).

The mechanism concerning the toughness enhancement of hard tissues *vs* the improvement of the crystallite alignment are not entirely clear. Nevertheless, the following so-called crack stopper model may provide some physical insight into this matter. As indicated in Fig. 7.12, normally, crystals are never perfect. Instead, many defect lines or more seriously many grain boundaries may occur in crystals. The letter can even form the mosaic structure, composed of micro-crystallite grains that are misfit to a small degree with respect to each other (Fig. 7.12a). At collision, the crack may occur at the surface and easily propagate across the crystals along the defect lines or the grain boundaries (Fig. 7.12a). This results in the breakage of the crystals. On the other hand, for a block of crystallite assembly in which lamella or needle-like nano crystallites are packed in parallel to the surface (see Fig. 7.12b), a serious collision will also cause a crack at the surface of the block. Nevertheless, the propagation of the crack along the defect lines, or the grain boundaries at the surface, will be stopped at the interface between the parallel packed crystallites, preventing the crack propagating across the block (see Fig. 7.12b). In other words, this parallel packing structure in a crystallite assembly will prevent the breakage versus the penetration of the crack lines across the crystallite assemblies.

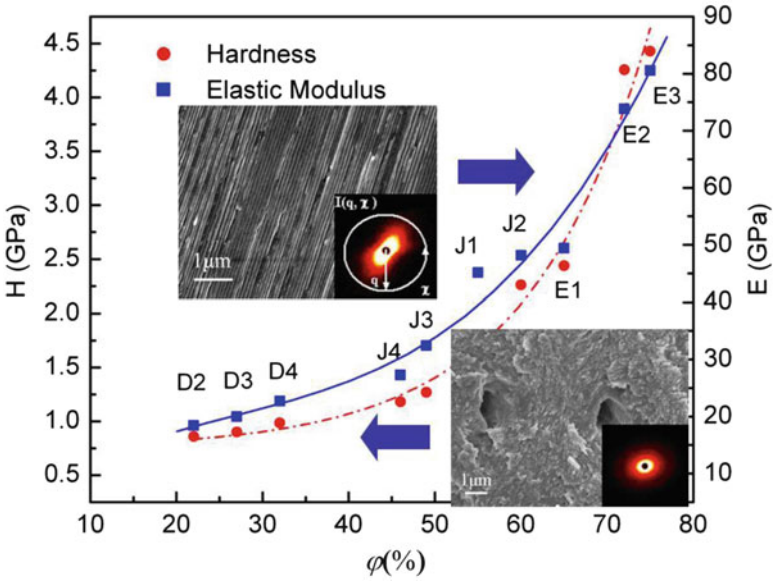

Fig. 7.11 Quantitative correlation between mechanical properties and local alignment of minerals within the dental sample. Hardness versus alignment. Elastic modulus versus alignment. The *solid circles* and the *hollow circles* represent data measured from dental enamel and dentin, respectively. φ is an ordering parameter measured by small angle X-ray scattering. For a completely aligned assembly of crystallites, $\varphi = 100\%$, while for a completely disordered assembly, $\varphi = 0$. Reproduced with permission from Ref. [83] ©2005 American Institute of Physics

Now, the key question to be addressed is how this parallel packing structure in the bundle of crystallites occurs. One of the well-accepted interpretation is *the self-epitaxial nucleation-induced assembly* and the *supersaturation-driven interfacial structural mismatch* [9, 76, 84–86].

A typical example of *the self-epitaxial nucleation-induced assembly* and the *supersaturation-driven interfacial structural mismatch* is illustrated in Fig. 7.13a. As shown, in a solution growth, calcite crystals evolve from single crystals to polycrystals with supersaturation. At relatively low supersaturations, the polycrystals are well aligned with each other. The polycrystallites altogether form a well-aligned crystallites assembly. This is the so-called *self-epitaxial nucleation-induced assembly*. As with further increase in supersaturation, the structural match between the adjacent crystallites in the assembly is lost, giving rise to the *supersaturation-driven interfacial structural mismatch* (Fig. 7.13a).

Before going into the details of the model, let us first review the relevant nucleation processes. Kinetically, the occurrence of substrates in heterogeneous nucleation will on one hand lower the nucleation barrier thus leading to an increase in the nucleation rate, but on the other hand it will exert a negative impact on the surface integration. Nucleation on a substrate will reduce the effective collision of structural units to the surface of clusters (cf. Fig. 7.3c), where the structural

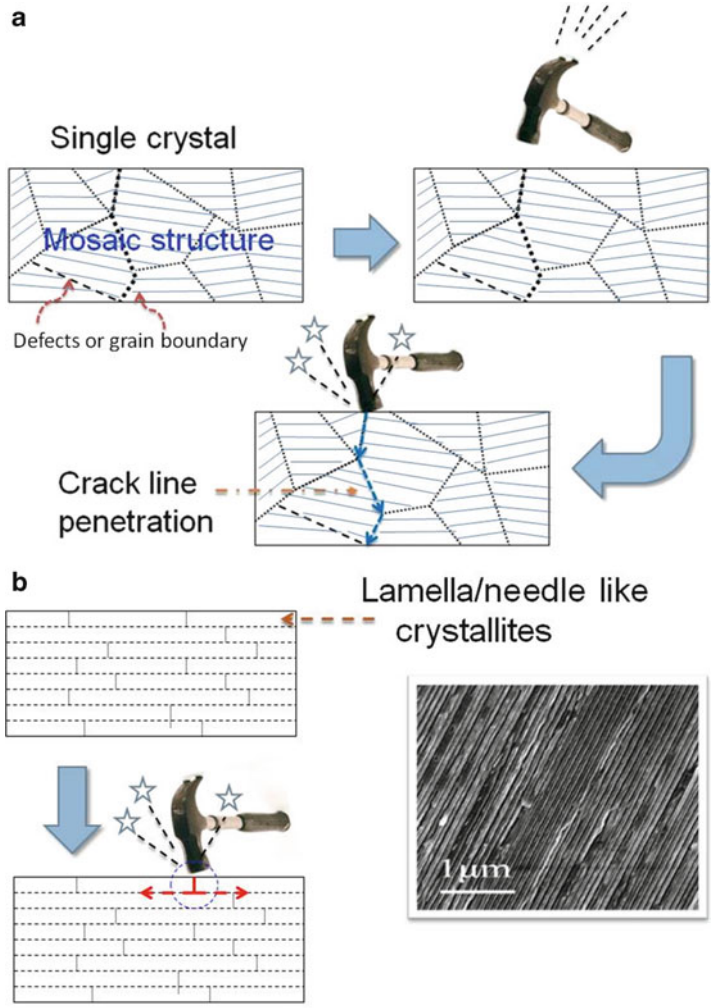

Fig. 7.12 The crack stopper. Parallel packing of lamella or needle-like crystals will stop the crack line to penetrate the bundled crystallites. (**a**) The mosaic structure of a crystal causes the propagation of crack line, leading to the breakage of the crystal. (**b**) The parallel packing of lamella or needle-like crystallites in a crystallites assembly will stop the propagation of the crack line from one crystallite to the adjacent crystallites

units are incorporated into the crystal phase. This will slow down the nucleation kinetics, whose effect is contrary to the effect of lowering the nucleation barrier. As mentioned above, the latter effect, the so-called *shadow effect* of the substrate, is reflected in the appearance of $f''(m)$ and $f(m)$ in the pre exponential term of (7.32).

These two controversial effects play different roles in different regimes. At low supersaturations, the nucleation barrier is very high (cf. (7.33) and (7.34)). The

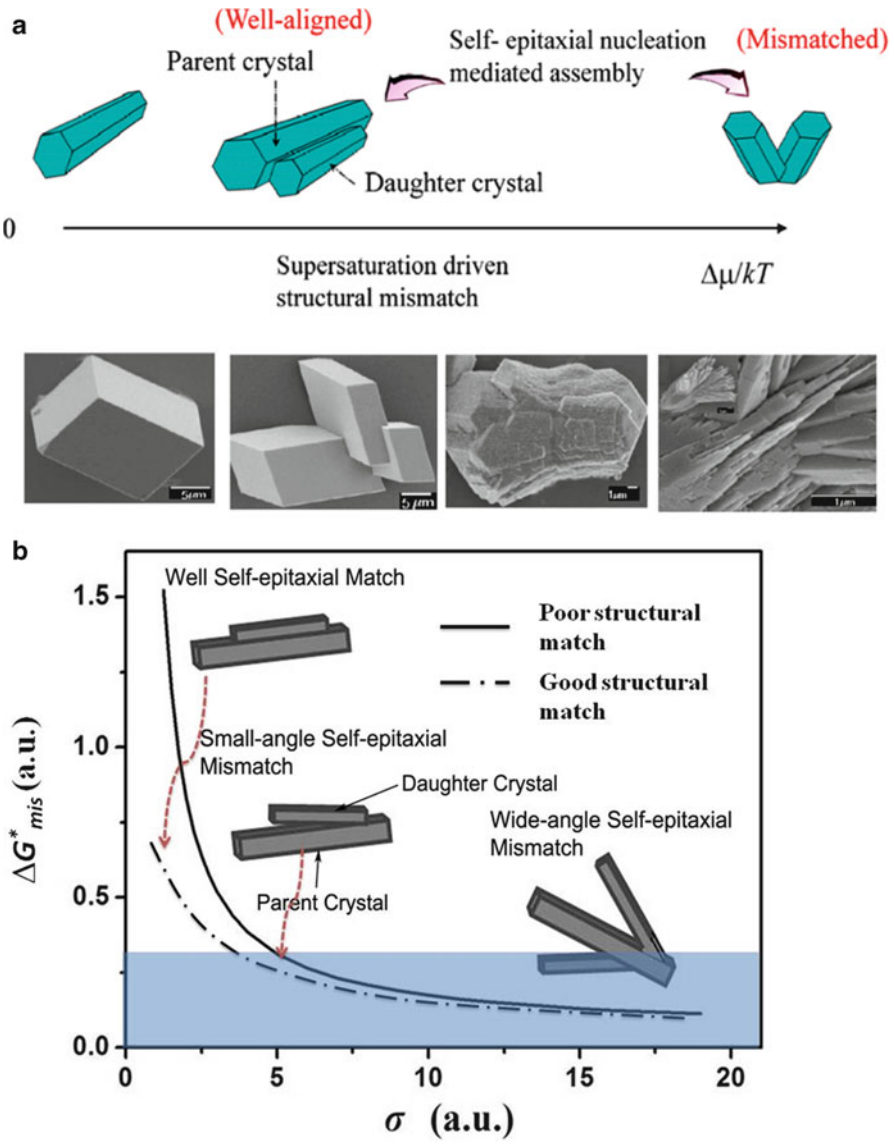

Fig. 7.13 (**a**) Self-epitaxial nucleation induced assembly and supersaturation-driven interfacial structure mismatch nucleation: the structural match between the daughter crystals and the parent crystal will become poor as supersaturation increases. An example in calcite crystallization is demonstrated. (**b**) The change of the mismatch nucleation barrier ΔG^*_{mis} with supersaturation (cf. (7.16)). (**c**) The plot of $\ln t_s$ versus $1/[\ln(1+\sigma)]^2$ for $CaCO_3$ (calcite) nucleation. Within the range of supersaturations where experiments were carried out, three straight lines with different slopes intercept one another, dividing the space into three regimes. (**d**) Supersaturation-driven interfacial structural mismatch: with the increase in the supersaturation, the interfacial correlation factor $f(m)$ will increase abruptly at a certain supersaturation, such as A, B, . . . , corresponding to the transition from an ordered and structurally matched to a less ordered and structurally mismatched

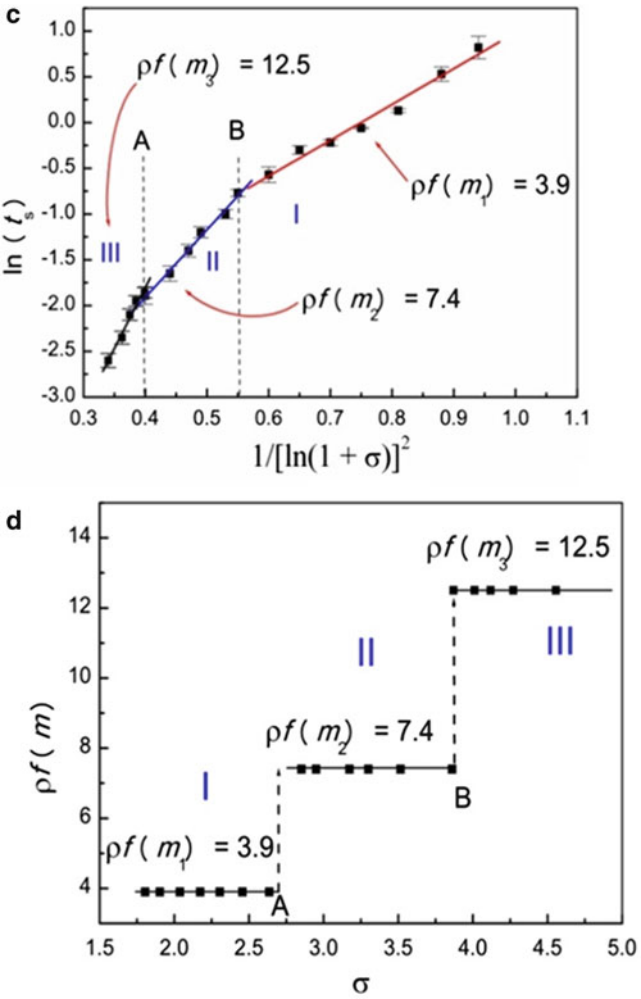

Fig. 7.13 (continued) biomineral/substrate interface. (**a**) Reprinted with permission from Ref. [30] © 2008 Wiley-VCH Verlag GmbH & Co. (**c**, **d**) Reproduced with permission from Ref. [84] ©2003 American Chemical Society

nucleation rate will be substantially enhanced if the nucleation barrier is suppressed effectively ($f(m) \to 0$). Therefore, heterogeneous nucleation with a strong interaction and optimal structural match between the substrate and the nucleating phase will be kinetically favored. In this case, the nucleation of crystalline materials will be best templated by substrates capable of providing the excellent structural correlation with the crystalline phase. The structural synergy between the nucleating phase and the substrate will be optimal under this condition [84, 87].

The observation in Fig.7.13a can be understood as follows: the occurrence of daughter crystals on the parent crystals is via self-epitaxial nucleation. This belongs to a special type of 3D nucleation, and there is a 3D nucleation barrier (ΔG^*_{mis}) associated with it. For such a process, suppose there are two events of *the self-epitaxial nucleation* occurring at the same site, one with a poor structural match (ΔG^*_{mis}) and the other with a good structural match ($\Delta G^{*\prime}_{\text{mis}} = f_{\text{match}}(m)\Delta G^*_{\text{mis}},\ f_{\text{match}}(m) \ll 1$) as shown in Fig. 7.13b. Due to the high nucleation barrier at low supersaturations, it is very difficult for the mismatch epitaxial nucleation to occur as ΔG^*_{mis} is very high (i.e., (7.16) and Fig. 7.13b). Under such conditions, only the epitaxial nucleation with a good structural match may occur, as the good structural match substantially lowers the nucleation barrier (i.e., $f_{\text{match}}(m) \ll 1$, Fig. 7.13b). One has the formation of the ordered calcite crystallite assembly observed in Fig. 7.13a. As the supersaturation increases, the nucleation barrier for mismatch epitaxial nucleation ΔG^*_{mis} drops rapidly (Fig. 7.13b). At relatively high supersaturations, the requirement of adopting the good structural match between the daughter crystals and the substrates becomes less demanded, in the view of a low nucleation barrier ΔG^*_{mis}. Due to the shadow effect, the mismatch self-epitaxial nucleation becomes kinetically more favorable. The shadow region in Fig. 7.13b illustrates the region the mismatch self-epitaxial nucleation may occur. This facilitates self-epitaxial nucleation leading to formation of the assembly of HAP crystallites with small mismatch (see Fig. 7.13a,b). As the supersaturation increases further, the nucleation barrier for mismatch epitaxial nucleation totally collapses. Self-epitaxial nucleation occurs much more easily, resulting in a severe interfacial structural mismatch. In this case, the crystallite assembly will often be randomly and highly branched (see Fig. 7.13a,b). This causes the *supersaturation-driven interfacial structural mismatch*.

As indicated above, as σ progressively increases from low supersaturations to high supersaturations, the self-epitaxial nucleation will be governed by a sequence of progressive heterogeneous processes associated with increasing $f(m)$. In analogy with the above analysis, the biomineralization of HAP in simulated body fluids was carried out [84]. Correspondingly, we should obtain a set of pairwise intersecting straight lines if $\ln t_s$ is plotted against $1/[\ln(1+\sigma)]^2$ (t_s: induction time; cf. Fig. 7.13c,d). Since for the crystalline phase, m, and $f(m)$ take on only those values that correspond to some crystallographically preferential orientations, $f(m)$ or the slope of the straight lines will take on discrete values, and $f(m)$ will increase as σ increases.

As shown in Fig. 7.13c and d, the interfacial correlation factor $f(m,R')$ subsequently increases from $3.9/\rho$ to $12.5/\rho$, as supersaturation increases from 1.5 to 5. This result unambiguously confirms that the increase in supersaturation will drive the substrates/biominerals from an interfacial structural match state (a lower $f(m)$) to an interfacial structure mismatch state (a higher $f(m)$). The abrupt changes from one state to the other at certain supersaturations (such as A, B, . . . in Fig. 7.13d) are due to the anisotropy of the crystalline phase.

To explore the effects of *the self-epitaxial nucleation-induced assembly* and the *supersaturation-driven interfacial structural mismatch* at the single particle

level, controlled heterogeneous 2D colloidal crystallization experiments by the AE field can be applied again. The pre-defined 1D colloidal lines or lithographically templated electrodes (Fig. 7.14a) can be utilized to site-specifically initiate the 2D colloidal nucleation and control the crystal orientation, wherein controlling an external AEF (thermodynamic driving force) allows us to precisely and conveniently manipulate the kinetic process of the crystal growth. Here, the epitaxial assembly method based on the crystallization of 2D colloidal crystals under an AEF can be applicable to investigate this matter (Fig. 7.14).

To examine the ordering of the colloidal crystals at the template, the orientational order parameter $S = \frac{1}{2}\langle 3\cos^2\theta - 1\rangle$ [88] is applied to characterize the uniaxial ordering of the colloidal assembly. θ is the misfit angle of the crystal domain with respect to the epitaxial colloidal line, as shown in the right inset in Fig. 7.14b. The brackets denote an average over all of the particles in the assembly. When colloidal particles are perfectly oriented parallel to the epitaxial template, one has $S = 1$. Figure 7.14b shows the frequency dependence of the orientation order parameter of the colloidal crystals. The perfectly oriented single colloidal crystals are obtained in the low-frequency range (400–800 Hz, low-driving force regime). When the frequency increases to the high-frequency range (1,000–2,000 Hz, high-driving force regime), the degree of perfection gradually decreases [33, 35, 37, 39]. For 1.8 μm PS particles, the interparticle separation r_{eq} among the assembly decreases with increasing frequency from 400 to 1,000 Hz and then reaches its minimum in the frequency range of 1,000–2,000 Hz, as shown in Fig. 7.14c. This suggests that the attractive forces among the particles become more dominant with increasing frequency and are much stronger than the repulsive ones in the frequency range of 1,000–2,000 Hz. In the high-frequency range, the homogeneous nuclei are very tightly assembled. Hence, the conformations and orientations of the homogeneous nuclei are difficult to be rearranged by the attractions from the template when they approach the template. Therefore, the degree of perfection of the colloidal crystals decreases in the frequency range of 1,000–2,000 Hz. On the other hand, the nucleation rate, in the bulk fluid phase, is large because of the increased attractive forces in the high-frequency range (Fig. 7.14c). Due to the increase in the homogeneous nucleation rate, the entropy effect and the transport will result in a certain degree of randomness [88]. This will lead to a reduction of interfacial correlation between the template and the incoming growth units and, thus, a decrease in the degree of perfection of the colloidal crystals and the mismatch with the template, which can be considered as the verification of the *supersaturation-driven interfacial structural mismatch* effect.

Note that the self-epitaxial nucleation-induced assembly and the supersaturation-driven interfacial structural mismatch will explain not only the pattern formation in biomineralization, but also the influence of F^- in the hard tissue formation [86]. In the field of materials engineering, by carefully adjusting these two effects, one can engineer and fabricate the complex structures of functional materials at the micro/nanostructural level.

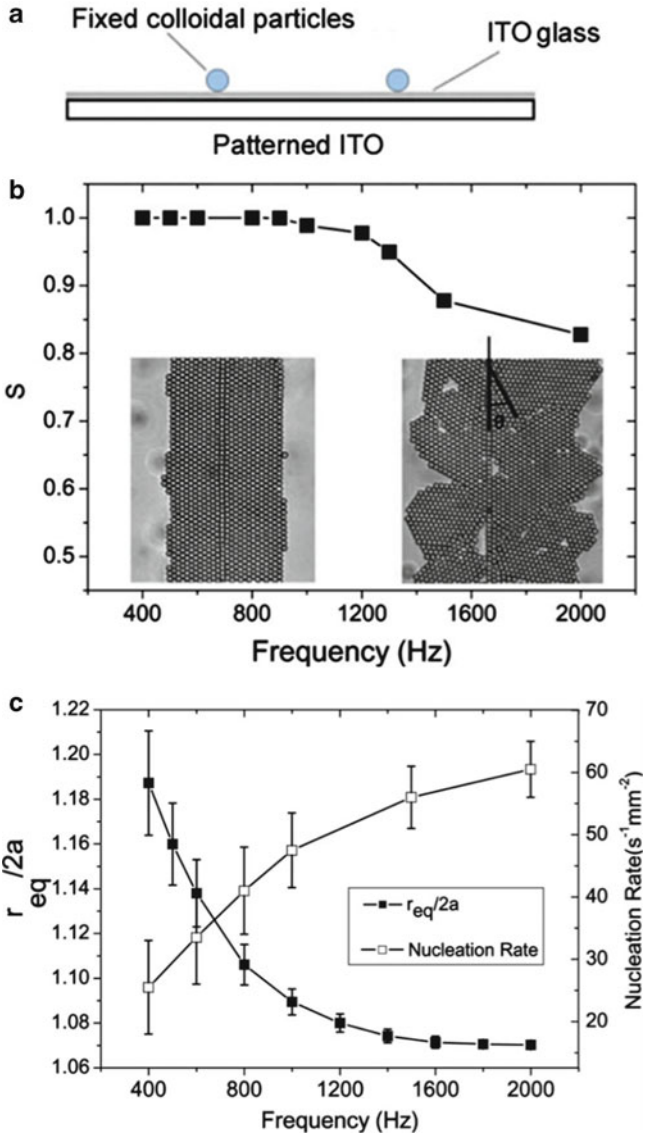

Fig. 7.14 (**a**) Schematic illustration of experimental setup for heterogeneous 2D colloidal crystallization experiments under an AEF. Refs. [39–42]. (**b**) Frequency dependence of the orientational order parameter S under an AEF. Also shown are the optical images of a perfectly oriented colloidal crystal (*left* inset, $S = 1$) and a roughly oriented colloidal crystal (*right* inset, $S = 0.83$), assembled at 800 Hz and 2,000 Hz for 10 min, respectively. (**c**) Variation of $r_{eq}/2a$ and nucleation rate in the bulk fluid phase with frequency for 1.8 μm PS particles. Reproduced with permission from Ref. [31] ©2009 American Chemical Society

7.4 Photonic Crystals and Biomimetics of Butterflies' Wings Crystals

Apart from the advancing of our knowledge in crystallization, colloidal crystallization has a wide range of applications in different areas. Among these, fabricating photonic crystals is one of the most important applications. The periodic modulation of the refractive index in a dielectric material creates a forbidden gap in the photonic band structure, which is not allowed in the existence of optical modes within a specific range of frequencies. Such photonic band-gap materials, known as photonic crystals, are attractive optical materials for controlling and manipulating light. In the last decades, a number of methods have been developed to fabricate photonic crystals at various length scales, including layer-by-layer stacking techniques using microfabrication tools [89–91], electrochemical etching [92, 93], laser-beam-scanning chemical vapor deposition [94], and holographic lithography [95, 96]. Colloidal crystal, in which the periodic modulation of the dielectric constant is realized by self-assembling monodisperse colloidal objects such as silica (SiO_2) or polystyrene (PS) microspheres into ordered arrays, turns out to be an effective approach to photonic crystal preparation [97–100]. The resulting photonic properties are determined by the symmetry and lattice constant of the crystal and the refractive index contrast between the colloids and the surrounding medium. The sizes of colloids are typically in the range of 100 nm to several micrometers. The self-assembly and fabrication of 2D/3D colloidal crystals have attracted broad interest because of their wide applications in photonic crystals [26, 101–103], chemical and biochemical sensors [28, 104], optoelectronic devices [105, 106], and templates for colloidal nanolithography [107].

7.4.1 Fabrication of 2D Colloidal Crystals and Templating

The commonly used methods to fabricate self-assemble monodispersed colloidal particles into ordered 2D arrays are based on the lateral capillary interaction, which originates from the deformation of the liquid surface [108–111]. The colloidal particles are typically assembled at the air–liquid interface or in a thin liquid layer supported on a flat, clean, and chemically homogeneous solid substrate in terms of the surface pressure and convection [112–117]. Another method to create 2D arrays is electrophoretic deposition, which applies a strong electric field to assemble colloidal dispersions confined between two parallel solid electrodes as outlined above [31, 37–46].

To achieve practical applications, two major obstacles need to be overcome in fabricating 2D colloidal crystal. First, many applications for colloidal crystals require samples that are free from defects over large length scales. However, most self-assembly systems suffer from disorders resulting from homogeneous nucleation and uncontrollable crystal growth. Second, the introduction of well-defined artificial

defects within colloidal crystals is another prerequisite for some practical applications [118]. Linear defects, for instance, could be used as photonic waveguides and point defects as microcavities [105]. However, this cannot be achieved through conventional self-assembly methods alone, as the intentionally added defects will substantially frustrate the crystal growth and locally induce disordering in colloidal crystals [119]. Experimentally, a key challenging of controlling colloidal crystals is lack of reliable methods to control colloidal crystallization of large and perfect single crystals with predefined orientations, artificial defects, and patterns over fast time scales. Obviously, the electrically controlled 2D colloidal crystallization is one of the most promising technologies to acquire large and perfect 2D crystals based on the principles outlined in Sect. 7.3.5.

7.4.2 Fabrication of 3D Photonic Crystals

The technologies adopted to fabricate the 2D colloidal crystals can be extended to fabricate 3D colloidal crystals with some modifications. Several other methods have also been widely employed to assemble highly ordered 3D crystals with large domain size, including sedimentation, repulsive electrostatic interactions, and physical confinement. Among these, sedimentation in a gravitational field seems to be the simplest approach for building 3D colloidal crystals [120]. A number of parameters must be carefully controlled to grow colloidal crystals of high quality. These parameters include the size, uniformity, and density of the colloids, as well as the rate of sedimentation. The main disadvantages of this method are the poor control over the structure and the thickness of the crystalline arrays, the long preparation time, and the polycrystalline nature of the products. Highly charged colloidal particles suspended in a solution can spontaneously self-organize into ordered structures, driven by the minimization of electrostatic repulsive interactions [121–125]. The colloidal crystals prepared using this method are typically non-close-packed, because the repulsive electrostatic interactions keep the particles away from each other. This method has very strict requirements regarding the experimental conditions such as the surface charge density, the colloidal concentration, and the ionic strength. By leaving the colloidal suspension to a physical confinement, it would self-assemble into long-range-ordered crystalline structures [126–128]. Colloidal crystals with domain sizes of square centimeters could be fabricated by using a specially designed packing cell [129–131]. This method is relatively fast, and it also provides tight control over the structures and the thickness of the 3D colloidal crystals.

7.4.3 Biomimetics of Structural Color

Color production in the animal kingdom normally takes advantage of either pigmentation or structural coloration. Color produced from pigmentation is also called chemical color, which comes from the selective absorption of the incident light and the reflection from the remaining spectra of the light by pigments. Structural color, also called physical color, is caused by complicated interaction between light and microstructures with featured sizes comparable to the visible wavelengths [132]. In this case, fundamental optical processes such as reflection, refraction, interference, diffraction, and scattering are the basic physical origination of structural color. Comparing with the colors arising from pigments, structural colors possess many interesting features since it is produced structurally. Generally, structural color is of high brightness and saturation and is hence sometimes called metallic color. It may display iridescence [133], i.e., a color change with perspective. The variations of structures or contrast of refractive indices may alter structural color, which can be achieved by applying pressure or infiltrating liquids in air voids. In contrast to pigmentary coloration, structural color never fade away provided that the corresponding photonic structure retains unchanged.

In recent years, structural color and relevant photonic structure have been subjected to extensive studies because of their scientific and practical importance [132–139]. The study of structural color may render tremendous important information related from evolution, biological functions, structural formation, to strategies of light steering. On the other hand, structural color may have potential applications in a variety of industries including photonics, display, painting, and textile. Natural photonic structures and the ingenious ways of light steering may have been a great source of inspiration in our design and fabrication of new optical materials and devices for future technological applications.

A wide variety of structural colors can be found in nature, among which the most famous examples are vivid colors of some breeds of butterfly wings and peacock feathers [140–144]. Metallic reflection from the elytra of beetles and iridescent stripes in some kinds of fish are also typical natural structural colors [145–147]. As illustrated in Fig. 7.10a, the 2D photonic crystals in the cortex of different colored barbules are responsible for the coloration of peacock feather [140, 144], while the multilayer structures of wing scales produce the structural coloration of some breeds of butterflies [148].

7.4.3.1 Applications of Colloidal Crystals in Mimicking of Structural Color

During the last two decades, much effort has been devoted to mimicking natural structural color, although to obtain the dedicated structures with the structural color as seen in animal kingdom (Fig. 7.15a) remains to be a big challenge. One way to acquire structural color was to adopt the nature structural color materials as

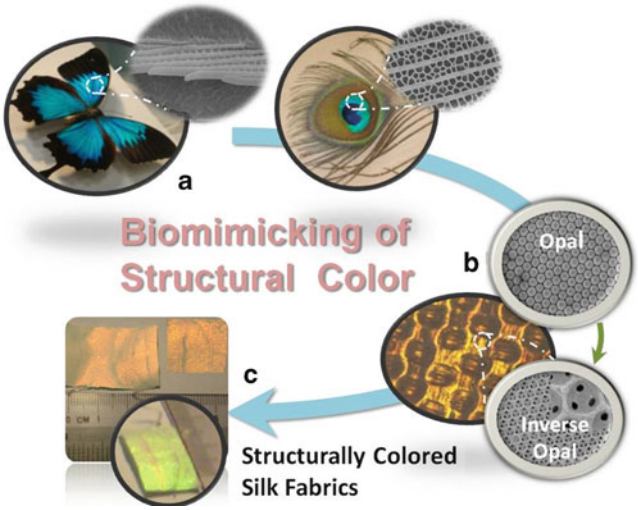

Fig. 7.15 Biomimetics of structural colors on silk fabrics. (**a**) The structural colors of butterfly (*Papilio ullysess* butterfly) and peacock feather. (**b**) Fabrication of opal and inverse opal on silk fabrics. Refer to Ref. [140] for the details of fabrication. (**c**) Structurally colored silk fabrics. Reprinted with permission from Ref. [30] © 2012 Wiley-VCH Verlag GmbH & Co

templates to replicate the nanostructures so as to obtain the optical properties. Wang *et al.* examined the fine structure of the wing scale of a *Morpho peleides* butterfly and replicated the entire configuration by a uniform Al_2O_3 coating through a low-temperature atomic layer deposition (ALD) process [149]. An inverted structure was achieved by removing the butterfly wing template at high temperature, forming a polycrystalline Al_2O_3 shell structure with precisely controlled thickness. Other than the copy of the morphology of the structure, the optical property, such as the existence of photonic band gap (PBG), was also inherited by the alumina replica. Other replicating methods have also been employed to replicate the structures of natural photonic materials, including conformal-evaporated-film-by-rotation technique and soft lithography technique [150, 151].

3D colloidal crystals with a PBG lying in the visible range are another option for mimicking natural structural color. Inspired by natural photonic crystals (Fig. 7.15), researchers have fabricated colloidal crystals with tunable structural colors [152–158]. One of the most commonly used techniques to fabricate colloidal crystals is the evaporation-induced self-assemble method, which enables the rapid production of highly ordered 3D colloidal crystals with face-center cubic structure. In connection with this technology, the wettability can be adjusted by the intrinsic roughness of colloidal crystals in combination with the tunable chemical composition of latex surfaces while the band gaps can be tuned by changing the size of the colloidal spheres.

Although colloidal crystals can be fabricated easily and are of wide potential applications, they are weak in the mechanical properties and dispersible in water.

Practically, the applications require colloidal crystals to be either fixed or replicated by other more robust materials [158–163]. Alternatively, one can replicate the colloidal crystal structure using a durable material, creating an inverse opal structure. In this regard, colloidal crystals serve as the templates, with the voids infiltrated by a material that solidifies in place without disrupting the order of the crystals. The original colloidal particles are subsequently removed, leaving behind an inverted structure of the colloidal crystals. The method has by now been used to make highly ordered porous materials from a wide variety of precursors and templates. By adjusting the dimension of the pores, as well as the refractive index of the material, PBG of the inverse opal structure can be tuned accordingly.

Another important property that can be seen in nature is tunable structural color, such as the color change that can be seen on the surface of a damselfish [164]. In order to mimic such color change, several methods have been developed to create tunable structural color films. Responsive photonic crystals (RPCs) are materials with photonic band-gap properties that can be tuned by external stimuli. To create such materials, a stimulus–response mechanism needs to be coupled with the photonic crystal structure [165]. There are generally two approaches to introduce such responsive materials. In the first case, the responsive materials are directly prepared in the form of building blocks that can be used for constructing photonic crystals. A typical example is the 1D Bragg stacks formed by self-assembly of block copolymers that contain segments that can expand when exposed to certain solvents. In the second case, the periodic structures are defined first, and then the responsive materials are filled into the interstitial space to form a composite material that is optically tunable and mechanically stable [166–171]. If the responsive material cannot provide enough mechanical strength, an inverse opal structure will be formed by first infiltrating an inert material into the interstitial space of the periodic structure to form a robust framework and then removing the original periodic template through calcination or chemical etching. Finally, the responsive materials are filled into the porous structure of the inverse opals. In the second case, the responsibility of nature structural color was mimicked by fabricating various RPCs (thermal, chemical, optical) based on colloidal crystals and templating.

To create structural colors on fabrics is extremely important, practically, but remains as a challenging task. As color fading caused by leaching or oxidation/bleaching is a key issue in fabric care, producing with vivid and durable structural colors on fabrics by fabricating the 3D colloidal crystals onto the surface of fabrics will revolutionize textile and fashion industries [158]. If the physical structure of photonic crystals on the fabrics is strong enough, the colors will last forever. Recently, a combined surface treatment technology [158] allows us to create opal and/or inverse opal structures on silk fabrics (cf Fig. 7.15). In producing structural colors on silk fabrics, polystyrene spheres with different diameters were assembled on the surface of silk fabrics. Silk fibroin was dispersed on the colloidal crystals as binding materials (Fig. 7.15b). Thus, silk fabrics with different reflection peaks ranging from ultraviolet to near-infrared can be obtained. It follows that the colors (the reflected wave lengths) can be created by tuning the lattice constant of

the inverse opal, a, according to $\lambda = va$ (v: a function of the refractive index of the material) [152–158].

Furthermore, multifunctional silk fabrics may also be obtained by controlling the band gaps of the photonic crystals. For example, one can acquire the UV protective clothing by creating photonic crystals or inverse capable of reflecting UV light. On one hand, the thermal insulating performance due to a reflection peak in the IR range will create cooling textiles in a hot summer. On the other hand, it will preserve to some extent our body heat in a cold winter if the IR reflecting structure is generated in the inner layer of textiles.

7.4.3.2 Double Reflection of Structural Color by Surface Structural Engineering

Although great accomplishment has been made, the structural colors produced by the animal kingdom are much richer and more effective than what we can produce so far. Furthermore, it is especially difficult to mimic some unique optical properties of natural structural color, such as polarization, colors mixing, etc. In the following, we will describe the double reflection and polarization effect produced by *Papilio* butterfly and a method utilizing a combined colloidal crystal and surface deposition technique to mimic these effects.

Apart from the iridescent visibility, nature structural color produced by some animals also gives rise to additional unique optical properties and benefits. For instance, the brown barbules in male peacock tail feathers adopt mixed structural coloration [140], Some breeds of *Papilio* butterflies reveal the double reflection effect [141, 172].

The color mixing mentioned above is created by in nature in different ways [173]. Figure 7.16a depicts the double reflection and iridescent visibility created by the blue wing scales of *Papilio ulysses*. The surface of its wings is composed of millions of scales. The scales of *P. ulysses* are of a size around 150 μm × 90 μm and consist of a fairly regular array of concavities. Under optical microscope, the concavities reveal a green reflection light (Fig. 7.11a(i)). When illuminated and observed at normal incident light, the concavities in *P. ulysses* appear to be green (Fig. 7.16a(i,ii)). However, upon crossing an input linear polarizer with an exit analyzer, the green reflected light in *P. ulysses* almost disappear while the deep purple (near-UV) color reflected by ridges in *P. ulysses* reflect back (Fig. 7.16a(iii) & (iv)). This implies that the purple reflected light is not altered by the polarizers. By further characterization of the microstructures of the wing scales, it was found that the profile of the concavities was almost flat, the ridges run through the full length of the scales with a periodicity of 4–5 μm (Fig. 7.16a(iv)). The configuration of the ridges is a 2D array of 70 nm×100 nm rectangular air squares surrounded by organic cuticle layers (the main and sub-ribs) with a periodicity of 140 nm ($D_1 + d_1$) along its length direction and 160 nm ($D_2 + d_2$) along the main ribs. This long-range ordered structure with a very small periodicity can be considered to be a 2D photonic crystal slab tilt about 30° with respect to the surface of the scales.

As shown in Fig. 7.16a(v), the transverse cross section of the wing scales consists of 21 alternative cuticle and air layers, which share almost the same thickness (95 nm). The multilayer structure of the concavities (Fig. 7.16a(iii)) produces the green reflection light and gives rise to a main reflection peak at 550 nm for normal incident light. The 2D photonic crystal slab of the ridges tilts 30° to the surface of scales, interacting with the normal incident light at 60° and producing a small reflection located at 380 nm. Under 45° incident light, the main reflection peak produced by concavity blue-shifts to 350 nm; the ridges interact with the incident light at 15° and give rise to the small reflection peak at 550 nm. Therefore, the two spectra peaks originating from the concavities and the ridges could be observed for both normal and 45° incident light. The shifting of peaks suggests the iridescent property of structural color for *P. ulysses*. These two reflection peaks mix to the blue color perceived by human eyes.

The bright green-colored wings of *P. blumei* (Fig. 7.16b, another breed of *Papilio* butterfly) result from a juxtaposition of blue and yellow-green light reflected from different microscopic regions on the wing scales. Optical microscopy reveals that these regions are the centers (yellow) (Fig. 7.16b(ii)) and the edges (blue) of concavities (Fig. 7.16b(iii)). Unlike *P. ulysses*, the concavities of *P. blumei* are cap shaped, of 4–6 μm in diameter (Fig. 7.11b(vi)). The profile is much deeper than *P. ulysses*. The inclined sides of each concavity tilt 45° with respect to the horizontal surface, and the opposites of each concavity are perpendicular to each other. The ridges run through the full length of each scale with a periodicity of 7–8 μm. The transverse cross section of the concavities also consists of 21 alternative cuticle and air layers with a thickness around 110 nm (Fig. 7.16b(v)). For the normal incident light, theoretical calculation predicts that the reflection peak resulted from the flat portions locates at 600 nm, in agreement with the yellow color observed under optical microscopy, while the light incident on the edges of concavities with an angle 45°, producing a reflection peak at 450 nm, in accordance with the blue color observed under optical microscope. The light incident on one side of the concavity, reflected from one 45° side, travels across the concavity to the opposite orthogonal side and then reflects backward in parallel to the original incident direction. Through this double reflection process, the blue reflected light undergoes a polarization conversion. As a result, it survives upon the crossed polarizers. Under 45° incident light, the reflection peak arising from the flat portions is 450 nm (blue color) (Fig. 7.16b(iii), right), while the light is incident normally on the inclined sides and gives rise to a reflection peak located at 600 nm (yellow color) (Fig. 7.16b(ii), left). Therefore, for normal and 45° incident light, the cap-shaped concavities produce both yellow and blue colors. These two colors mix up to the green coloration caught by human eyes. It follows that the two breeds of butterfly take advantage of the color-mixing strategy. The blue color of *P. ulysses* is mixed by the green and deep purple colors reflected by concavities and ridges, respectively. The green color seen from *P. blumei* is a mixture of yellow and blue colors reflected by the flat portions and inclined sides of concavities, respectively. We notice that many studies show that the eyes of the butterflies have a duplicated gene, allowing them to see ultraviolet colors and distinguish the spectral properties and spatial

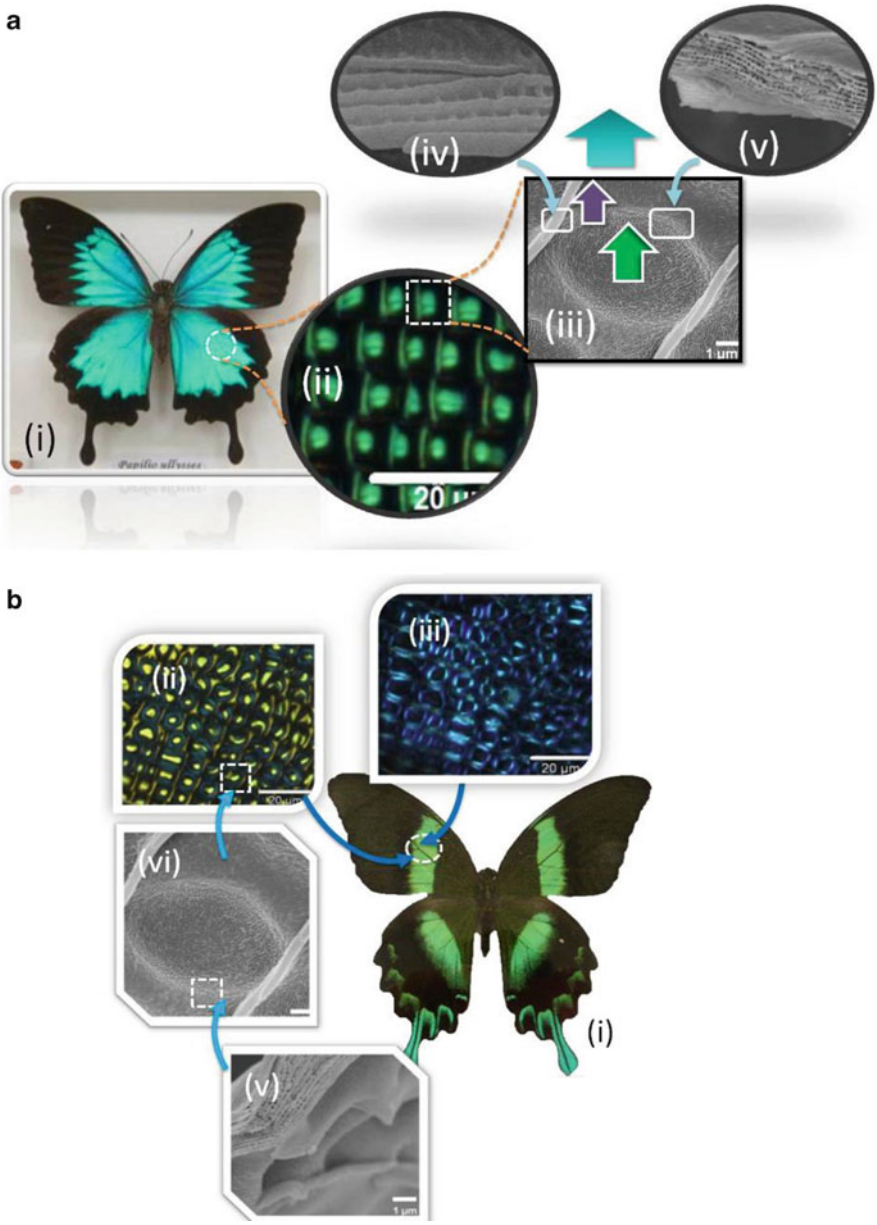

Fig. 7.16 Biomimetics of structural colors by structural engineering. (**a**) Nature photonic structure, *Papilio ulysses* butterfly. (*i*) The *bright blue* wings of *P. ulysses* butterfly resulted from the mixed colors from different regions of the scales. (*ii*, *iii*) Optical and scanning electronic micrographs (scale bar: 20 μm) showing that the surface of a wing scale of a fairly regular array of concavities and ridges (*iv*). The concavities reflect *green color* light. (*iv*) UV light reflected from the ridges. (*v*) The transverse cross section of concavities of 21 alternative cuticle and air layers with a thickness of 95 nm, which reflect green light consistently (Ref. [148]).

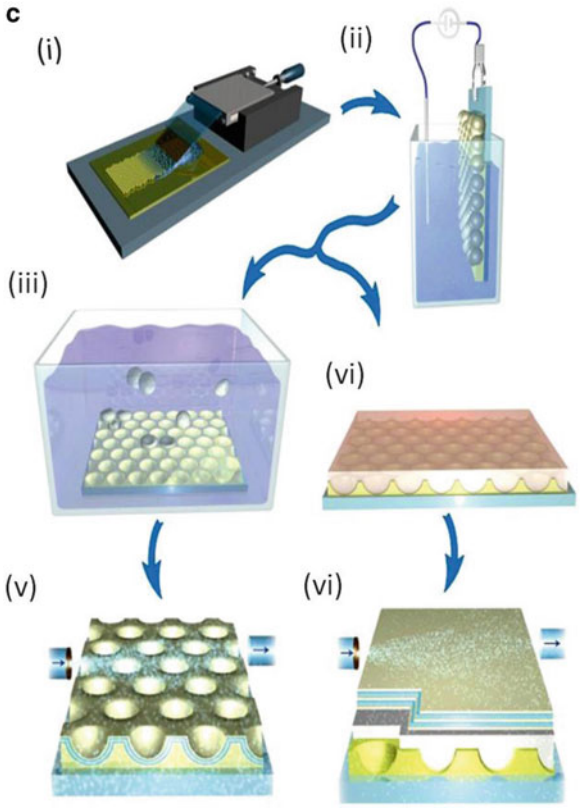

Fig. 7.16 (continued) (**b**) Natural photonic structure, *Papilio blumei* butterfly. (*i*) The bright green wings of the *P. blumei* butterfly resulted from the mixing of the different *colors* of light from different regions of the wing scales. (*ii*, *iii*), Optical micrographs (scale bar: 20 μm) showing that the concavities reflect *yellow* and *blue colors* under normal incident light. (*vi*) Scanning electron micrograph showing that the surface of a wing scale is covered with concavities (diameter ≈ 5–10 μm). (*v*) The transverse cross section of concavities consists of 21 alternative cuticle and air layers with a thickness of 120 nm. Reflectance spectra under normally incident light and 45° incident light, and the overlapping of the spectra confirm the non-iridescent property of the green wing scales of *P. blumei* (From [148]). (**c**) Mimicking by surface structural engineering. (*i*) Deposition of polystyrene colloids on a gold-coated silicon substrate. (*ii*) Growth of platinum or gold in the interstices of the colloidal array by electroplating. The metal deposition is terminated when the thickness of the deposited film equals the microsphere radius. (*iii*) Removal of the polystyrene spheres from the substrate by ultrasonication in acetone. (*iv*) Sputtering of a thin carbon film and ALD of a stack of 11 alternating TiO_2 and Al_2O_3 layers (*arrows* indicate the precursor gas flow). (**e**, **f**) In a second route, the colloids are molten to cover the cavities with a homogeneous film, (*v*) which is covered by a TiO_2–Al_2O_3 multilayer [141] (*vi*). (**a**, **b**) Reprinted with permission from [30] © 2012 Wiley-VCH Verlag GmbH & Co. (**c**) Reprinted with permission from [172] ©2010, Nature publishing group

distribution of the visual colors [174]. And also, they are sensitive to the polarized light. Therefore, the knowledge on the structural origination of the two reflection peaks and polarization property of butterfly wings would have broad biological implications [175, 176]. Furthermore, with the understanding of the correlation between the optical properties and the corresponding structures, researchers could be able to find a way to mimic natural structural colors with designated properties. Evidently, the ability to mimic the structural color with its spectacular function will broaden the biomimicry field in the design of structural color materials targeted for ultra and smart performance.

Kolle et al. adopted the combined techniques of colloidal crystal self-assembly, sputtering, and ALD to fabricate photonic structures that mimic the color mixing and polarization effect found on the colored wing scales of *P. blumei* [172]. They demonstrated the replication of the periodically shaped multilayer structure of the *Papilio* butterfly scale in five steps (Fig. 7.16c). Polystyrene colloids with a diameter of 5 μm were assembled on a gold-coated silicon substrate to create regularly arranged concavities. A layer of platinum or gold with thickness 2.5 μm was then electrochemically grown into the interstitial space between the colloids, creating a negative replica [177–179]. Ultrasonication of the sample in dimethylformamide or acetone removed the colloids, resulting in a template of hexagonally arranged metal concavities. An 20-nm-thick carbon film was sputtered onto the gold surface. Finally, a conformal multilayer of thin quarter-wave titania and alumina films was grown by ALD [180]. The carbon layer between the gold (or platinum) and the multilayer stack adsorbs light passing through the multilayer stack, reducing specular reflections and unwanted destructive interferences that would otherwise severely limit the optical performance.

During the fabrication process, the diameter and the height of the concavities for the artificial mimic were well controlled by the size of colloidal spheres and thickness of platinum or gold layer. The number of the alternating titania and alumina layers, as well as their thicknesses, could be carefully controlled during the ALD process. By choosing proper thicknesses of the titania and alumina layers, the stop-band center wavelength for the artificial multilayer structure could locate 550 nm, matching the reflectance band of the natural *P. blumei* structure closely. Due to the concave structure, the center of the concavities exhibit yellow-green reflection (550 nm), while the reflection light from the four segments of the concavities blue-shifts to blue color. The observation of the artificial mimic between crossed polarizers leads to a similar effect as described for the *P. blumei* structure. Only light incident onto four segments of the concavity edges is detected. The local surface normal of 45° gives rise to a double reflection at the opposing cavity walls, causing a polarization rotation. The artificial mimic therefore displays the same optical characteristics as the natural *P. blumei* wing scale structure.

Nevertheless, this approach described above needs to fabricate complex nanostructures, wherein the two reflections come from different parts of the structure. This technique is costly and difficult to obtain different properties by tuning the structure. In this regard, the key challenges in future work to biomimic natural structural color turn out to be how to design and fabricate photonic crystals with the

unique optical properties of natural structural color through a simple process. One promising way is to construct photonic crystals with two PBGs to get the desired double reflection. On the other hand, the growing demand for optical interfaces and sensors for biomedical applications is a motivating research toward realizing biocompatible photonic components that offer a seamless interface between the optical and biological worlds. Therefore, another key issue in this field is how to mimic the double reflection effect using biocompatible and biodegradable materials.

We notice that the double reflection has its biological function. For instance, there are three major photoreceptors in the compound eyes of *Heliconius erato* with spectral sensitivity peaks at 370, 470, and 560–570 nm, allowing the detection of ultraviolet colors, and they distinguish the spectral properties of visible light [175]. It follows that the double reflection of butterfly wings giving rise to both visible and UV reflections may serve for communication and mating signals in butterfly kingdom [174–176]. Thus, investigating the correlation between the optical properties and the structures may help to explain the innate behaviors of the butterfly kingdom. Investigating the coloration mechanisms of these optical properties and the corresponding structures also has crucial implications for biomimicry, including color-stimulus synthesis, display technologies, and various polarization applications [116, 181].

7.5 Conclusive Remarks

As can be seen from the results presented in this chapter, almost all fundamental aspects of crystallization in biomineralization can be examined in terms of the AEF-controlled 2D colloidal crystallization system. For instance, the initial stage of nucleation may not be exactly the same as we expected. Unlike the assumption that both the embryos and the bulk crystals share the same structure, the structures of the embryos are supersaturation dependent. Such a deviation would be beneficial in lowering the nucleation barrier and then facilitating the nucleation kinetics at low supersaturations. From the point of view of solid–fluid interface, the above "experimental modeling" can also provide some unique and extremely relevant information, which is capable of updating our knowledge in crystallization in general. Notice that the effect of supersaturation-driven structure mismatch has been put forward, but never been visualized directly before. The templated 2D colloidal nucleation provides the first observation of this effect. Such an experimental modeling system has been successfully applied to examine many other crystallization processes, i.e., MSC, roughening transition, adatomic step integration, defects generation and migration kinetics, etc., which have never been examined quantitatively before at the single particle level. Note that the key advantage of the experimental modeling system is the combination of the visualization and the quantitative treatment, which can transfer our knowledge to a new phase. As the colloidal crystallization system displays the phase behaviors similar to normal crystalline materials, and the crystallization condition can be controlled easily and precisely, it can be foreseen that this approach will become a powerful tool to study the science and technology

of crystallization. In the area of application, apart from the fabrication of photonic devices, sensor, and tunable lasers, colloidal crystallization has been now applied to mimic the structural colors and double reflection on silk fabrics, which will exert a significant impact on textile, personal care, and fashion industries.

Acknowledgements The authors acknowledge the supports from Singapore ARC funding (Project No. T13-0602-P10).

References

1. Gibbs, J.W.: Collected Works. Thermodynamics, vol. I. Longmans and Green, New York (1928)
2. Votmer, M., Weber, A.: Keimbildung in übersättigten Gebilden. Z. Phys. Chem. **119**, 277 (1926)
3. Farkas, L.: The speed of germinitive formation in over saturated vapours. Z. Phys. Chem. **125**, 236–242 (1926)
4. Kaischew, R., Stranski, I.: On the kinetic deflection rate of germ formation. Z. Phys. Chem. B **26**, 317–326 (1934)
5. Becker, R., Doering, W.: Kinetic treatment of germ formation in supersaturated vapour. Ann. Phys. **24**, 719–752 (1935)
6. Zeldovich, J.B.: On the theory of new phase formation, cavitation. Acta Physicochim. U.R.S.S. **18**, 1–22 (1943)
7. Hirth, J.P., Pound, G.M.: Progress in Materials Science: Condensation and Evaporation, vol. 2. Pergamon, Oxford (1963)
8. Nielsen, A.E.: Kinetics of Precipitation. Pergamon, Oxford (1964)
9. Liu, X.Y.: From molecular structure of solid-liquid interfaces to nucleation kinetics: implications for nanostructure engineering. In: Liu, X.Y., De Yoreo, J.J. (eds.) Nanoscale Structure and Assembly at Solid-Fluid Interfaces, vol. 2, pp. 109–176. Springer, London (2004)
10. Vekilov, P.G., Galkin, O.: Fundamental aspects of nucleation theory revealed in experiments with protein solid phases (Chp 5). In: Liu, X.Y., De Yoreo, J.J. (eds.) Nanoscale Structure and Assembly at Solid-Fluid Interfaces, vol. 1, pp. 105–144. Springer, London (2004)
11. Gasser, U., Weeks, E.R., Schofield, A., Pusey, P.N., Weitz, D.A.: Real-space imaging of nucleation and growth in colloidal crystallization. Science **292**, 258 (2001)
12. Philpott, M.R.: Atomic scale modelling of the solid-liquid interface (Chp 1). In: Liu, X.Y., De Yoreo, J.J. (eds.) Nanoscale Structure and Assembly at Solid-Fluid Interfaces, vol. 1, pp. 1–55. Springer, London (2004)
13. Zhang, K.Q., Liu, X.Y.: In situ observation of colloidal monolayer nucleation driven by an alternating electric field. Nature **429**, 739–743 (2004)
14. Hirtzel, C.S., Rajagopalan, R.: Invited review stability of colloidal dispersions. Chem. Eng. Commun. **33**, 301–324 (1985)
15. Evans, D.F., Wenneerstrom, H.: The Colloidal Domain: Where Physics, Chemistry, Biology, and Technology Meet. Wiley-VCH, Weinheim (1984)
16. Bradley, J.S.: The chemistry of transition metal colloids (Chp 6). In: Schmid, G. (ed.) Clusters and Colloids, pp. 459–537. Wiley-VCH, Weinheim (1994)
17. Ostwald, W.: Studien uber die Bildung und Umwandlung fester Korper. Z. Phys. Chem. **22**, 289 (1897)
18. ten Wolde, P.R., Frenkel, D.: Homogeneous nucleation and the Ostwald step rule. Phys. Chem. Chem. Phys. **1**, 2191–2196 (1999)
19. Poon, W.: Colloids as big atoms. Science **2004**(304), 830–831 (2004)
20. Frenkel, D.: Playing tricks with designer "Atoms". Science **2002**(296), 65–66 (2002)

21. Anderson, V.J., Lekkerkerker, H.N.W.: Insights into phase transition kinetics from colloid science. Nature **416**, 811–815 (2002)
22. Nadal, F., Argoul, F., Hanusse, P., Pouligny, B., Ajdari, A.: Electrically induced interactions between colloidal particles in the vicinity of a conducting plane. Phys. Rev. E **65**, 061409 (2002)
23. Grier, D.G., Murray, C.A.: The microscopic dynamics of freezing in supercooled colloidal fluids. J. Chem. Phys. **100**, 9088–9095 (1994)
24. van Blaaderen, A., Wiltzius, P.: Real-space structure of colloidal hard-sphere glasses. Science **1995**(270), 1177–1179 (1995)
25. Kegel, W.K., van Blaaderen, A.: Direct observation of dynamical heterogeneities in colloidal hard-sphere suspensions. Science **2000**(287), 290–293 (2000)
26. Vlasov, Y.A., Bo, X.Z., Sturm, J.C., Norris, D.J.: On-chip natural assembly of silicon photonic bandgap crystals. Nature **414**, 289–293 (2001)
27. Cheng, W., Wang, J., Jonas, U., Fytas, G., Stefanou, N.: Observation and tuning of hypersonic bandgaps in colloidal crystals. Nat. Mater. **5**, 830–836 (2006)
28. Holtz, J., Asher, S.A.: Polymerized colloidal crystal hydrogel films as intelligent chemical sensing materials. Nature **389**, 829–832 (1997)
29. Lawrence, J.R., Ying, Y., Jiang, P., Foulger, S.H.: Dynamic tuning of organic lasers with colloidal crystals. Adv. Mater. **18**, 300–303 (2006)
30. Diao, Y.Y., Liu, X.Y.: Controlled colloidal assembly: Experimental modeling of general crystallization and biomimicking of structural color. Adv. Func. Mater. **22**, 1354–1375 (2012)
31. Xie, R.G., Liu, X.Y.: Controllable epitaxial crystallization and reversible oriented patterning of two-dimensional colloidal crystals. J. Am. Chem. Soc. **131**, 4976–4982 (2009)
32. Everett, D.H.: Basic Principles of Colloidal Science. The Royal Society of Chemistry, Cambridge (1998)
33. Liu, Y., Narayanan, J., Liu, X.Y.: Colloidal phase transition driven by alternating electric field. J. Chem. Phys. **124**, 124906–124911 (2006)
34. Zhang, T.H., Liu, X.Y.: Configurations and diffusion of point defects in two-dimensional colloidal crystals. Appl. Phys. Lett. **89**, 261914 (2006)
35. Liu, Y., Liu, X.Y., Narayanan, J.: Kinetics and equilibrium distribution of colloidal assembly under an alternating electric field and correlation to degree of perfection of colloidal crystals. J. Phys. Chem. C **111**, 995 (2007)
36. Zhang, T.H., Liu, X.Y.: Effect of long-range attraction on growth model. J. Phys. Chem. C **111**, 1342–1346 (2007)
37. Zhang, K.Q., Liu, X.Y.: Size-dependent planar colloidal crystals guided by alternating electric field. Appl. Phys. Lett. **90**, 111911 (2007)
38. Zhang, K.Q., Liu, X.Y.: Two scenarios of the colloidal phase transitions. Phys. Rev. Lett. **96**, 105701–105704 (2006)
39. Liu, Y., Xie, R.G., Liu, X.Y.: Fine tuning of equilibrium distance of two-dimensional colloidal assembly under an electric field. Appl. Phys. Lett. **90**, 063105 (2007)
40. Zhang, T.H., Liu, X.Y.: How does transient amorphous precursor template crystallization. J. Am. Chem. Soc. **129**, 13520–13526 (2007)
41. Zhang, T.H., Liu, X.Y.: Multistep crystal nucleation: a kinetic study based on colloidal crystallization. J. Phys. Chem. B **111**, 14001–14005 (2007)
42. Xie, R.G., Liu, X.Y.: Electrically directed on-chip reversible patterning of two-dimensional tunable colloidal structures. Adv. Funct. Mat. **18**, 802–809 (2008)
43. Xie, R.G., Liu, X.Y.: Epitaxial assembly and ordering of two-dimensional colloidal crystals. Appl. Phys. Lett. **92**, 083106 (2008)
44. Zhang, T.H., Liu, X.Y.: Nucleation: what happens at the initial stage? Angew. Chem. Int. Ed. **48**, 1308–1312 (2009)
45. Zhang, K.Q., Liu, X.Y.: Controlled formation of colloidal structures by an alternating electric field and its mechanisms. J. Chem. Phys. **130**, 184901–7 (2009)
46. Zhang, K.Q., Liu, X.Y.: Determination of elastic constants of two-dimensional close-packed colloidal crystals. Langmuir **25**, 5432–5436 (2009)

47. Trau, M., Saville, D.A., Aksay, I.A.: Field-induced layering of colloidal crystals. Science **272**, 706–709 (1996). Trau, M., Saville, D.A., Aksay, I.A.: Assembly of colloidal crystals at electrode interfaces. Langmuir **13** 6375–6381 (1997).
48. Yeh, S.R., Seul, M., Shraiman, B.I.: Assembly of ordered colloidal aggregates by electric-field-induced fluid flow. Nature **386**, 57–59 (1997)
49. Liu, X.Y.: Gleation with small molecules: from formation mechanism to nanostructure architecture. In: Sato, K., Nakajima, K., Furukawa, Y. (eds.) Advances in Crystal Growth Research, pp. 42–61. Elsevier Science B.V., Amsterdam (2001)
50. Liu, X.Y.: From template nucleation to functional materials engineering. In: Skowronski, M., DeYoreo, J.J., Wang, C.A. (eds.) Perspectives on Inorganic, Organic and Biological Crystal Growth: From Fundamentals to Applications, pp. 439–465. American Institute of Physics, Park City, Utah (2007)
51. Li, J.-L., Liu, X.Y. Architecture of supramolecular soft functional materials: from understanding to micro/nano engineering. Adv. Fun. Mat. **20** 3196–3216 (2010). Liu, X.Y.: Chapter 1. In: Frédéric, F. (ed.) Low Molecular Mass Gelators: Design, Self-Assembly, Function. Topics in Current Chemistry. Springer, Berlin, pp. 1–37 (2005).
52. Fowler, R., Giggenhein, E.A.: Statistical Thermodynamics. Cambridge University, London (2005)
53. Mutaftschiev, B.: Nucleation theory. In: Hurle, D.T.J. (ed.) Handbook on Crystal Growth, pp. 189–245. North-Holland, Amsterdam (1993)
54. Liu, X.Y.: Simulating 'atomic' processes of crystallization via controlled colloidal assembly. In Wang, M., Tsukamoto, K., Wu, D. (eds.) Selected Topics on Crystal Growth: 14th International Summer School on Crystal Growth. American Institute of Physics, Dalian, pp. 173–220 (2010). Chernov, A.A. Modern Crystallography III—Crystal Growth. Springer-Verlag, Berlin (1984).
55. Liu, X.Y., Du, N.: Zero-sized effect of nano-particles and inverse homogeneous-like nucleation: principles of freezing and antifreeze. J. Biol. Chem. **279**, 6124–6131 (2004)
56. Liu, X.Y.: A new kinetic model for 3D heterogeneous nucleation. J. Chem. Phys. **111** 1628 (1999). Liu, X.Y.: Heterogeneous nucleation or homogeneous nucleation? J. Chem. Phys. **112**, 9949–9955 (2000). Liu, X.Y., Maiwa, K., Tsukamoto, K.: Two-dimensional heterogeneous nucleation and the growth kinetics. J. Chem. Phys. **106** 1870 (1997)
57. Santana-Solano, J., Wu, D.T., Marr, D.W.M.: Direct measurement of colloidal particle rotation and field dependence in alternating current electrohydrodynamic flows. Langmuir **22**, 5932–5396 (2006)
58. Zettlemoyer, A.C.: Nucleation. Dekker, New York (1969)
59. Kashchiev, D.: The kinetic approach to nucleation. Cryst. Res. Technol. **19**, 1413–1423 (1984)
60. Lewis, B., Andersen, J.C.: Nucleation and Growth of Thin Films. Academic, New York (1978)
61. Lutsko, J.F., Nicolis, G.: Theoretical evidence for a dense fluid precursor to crystallization. Phys. Rev. Lett. **96**, 046102 (2006)
62. Navrotsky, A.: Energetic clues to pathways to biomineralization: Precursors, clusters, and nanoparticles. Proc. Natl. Acad. Sci. **101**, 12096–12101 (2004)
63. Pan, H., Liu, X.Y., Tang, R., Xu, H.: Mystery of the transformation from amorphous calcium phosphate to hydroxyapatite. Chem. Commun. **46**, 7415–7417 (2010)
64. Termine, J.D., Eanes, E.D.: Comparative chemistry of amorphous and apatitic calcium phosphate preparations. Calcif. Tissue Int. **10**, 171 (1972)
65. Bradt, J.H., Mertig, M., Teresiak, A., Pompe, W.: Biomimetic mineralization of collagen by combined fibril assembly and calcium phosphate formation. Chem. Mater. **11**, 2694–2701 (1999)
66. ten Wolde, P.R., Frenkel, D.: Enhancement of protein crystal nucleation by critical density fluctuations. Science **277**, 1975–1978 (1997)
67. Zhang, J., Liu, X.Y.: Effect of protein-protein interactions on protein aggregation kinetics. J. Chem. Phys. **119** 10972 (2003). Narayanan, J., Liu, X.Y.: Protein interactions in undersatu-

rated and supersaturated solutions: a study using light and X-ray scattering. Biophys. J. **84**, 523–532 (2003). Chow, P.S., Liu, X.Y., Zhang, J., Tan, R.B.H.: Spherulitic Growth Kinetics of Protein Crystals. Appl. Phys. Lett. **81**, 1995–1997 (2002)
68. Jia, Y.W., Liu, X.Y. Self-assembly of protein at aqueous solution surface in correlation to protein crystallization. Appl. Phy. Lett. **86**, 023903 (2005). Jia, Y.W., Narayanan, J., Liu, X. Y., Liu, Y.: Investigation of the mechanism of crystallization of soluble protein in the presence of nonionic surfactant. Biophys. J. **89** 4245–4251 (2005)
69. Wang, L., Liu, X.Y.: Kinetic analysis of protein nucleation in gel matrix. Biophys. J. **95**, 5931–5940 (2008)
70. Haas, C., Drenth, J.: The interface between a protein and an aqueous solution and its effects on nucleation and crystal growth. J. Phys. Chem. B **104**, 368–377 (2000)
71. Beniash, E., Aizenberg, J., Addadi, L., Weiner, S.: Amorphous calcium carbonate transforms into calcite during sea urchin larval spicule growth. Proc. R. Soc. Lond. Ser. B **264**, 461–465 (1997)
72. Addadi, L., Raz, S., Weiner, S.: Taking advantage of disorder: amorphous calcium carbonate and its roles in biomineralization. Adv. Mater. **15**, 959–970 (2003)
73. Chen, X., Samia, A.C.S., Lou, Y., Burda, C.: Investigation of the crystallization process in 2 nm CdSe quantum dots. J. Am. Chem. Soc. **127**, 4372–4375 (2005)
74. Kashchiev, D., Vekilov, P.G., Kolomeisky, A.B.: Kinetics of two-step nucleation of crystals. J. Chem. Phys. **122**, 244706 (2005)
75. Kuznetsov, Y.G., Malkin, A.J., McPherson, A.: The liquid protein phase in crystallization: a case study-intact immunoglobulins. J. Cryst. Growth **232**, 30–39 (2001)
76. Auer, S., Frenkel, D.: Line tension controls wall-induced crystal nucleation in hard-sphere colloids. Phys. Rev. Lett. **91**, 015703 (2003). Liu, X.Y., Bennema, P., van der eerden, J.P.: The rough-flat-rough transition at crystal surfaces. Nature **356**, 778 (1992)
77. Vekilov, P.G.: Dense liquid precursor for the nucleation of ordered solid phases from solution. Cryst. Growth Des. **4**, 671–685 (2004)
78. Kamat, S., Su, X., Ballarini, R., Heuer, A.H.: Structural basis for the fracture toughness of the shell of the conch Strombus gigas. Nature **405**, 1036–40 (2000)
79. Li, X., Chang, W.C., Chao, Y.J., Wang, R., Chang, M.: Nanoscale structural and mechanical characterization of a natural nanocomposite material: the shell of red abalone. Nano Lett. **4**, 613–617 (2004)
80. Weiner, S., Wagner, H.D.: The material bone: structure-mechanical function relations. Annu. Rev. Mater. Sci. **28**, 271–298 (1998)
81. Birchall, J.D.: In: Mann, S., Webb, J., Williams, R.J.P. (eds.) Biomineralization: Chemical and Biochemical Perspectives, p. 491. VCH, Weinheim (1989)
82. Gao, H., Ji, B., Jager, I.L., Arzt, E., Fratzl, P.: Materials become insensitive to flaws at nanoscale: Lessons from nature. Proc. Natl. Acad. Sci. U.S.A. **100**, 5597–5600 (2003)
83. Jiang, H.D., Liu, X.Y., Lim, C.T., Hsu, C.Y.: Ordering of self-assembled nanobiominerals in correlation to mechanical properties of hard tissues. Appl. Phys. Lett. **86**, 16391 (2005)
84. Liu, X.Y., Lim, S.W.: Templating and supersaturation driven anti-templating: principles of biominerals architecture. J. Am. Chem. Soc. **125**, 888–995 (2003). Liu, X.Y.: Effect of microgravity on Ca mineral crystallization and implications for osteoporosis in space. Appl. Phys. Lett. **79**, 3539–3541 (2001)
85. Jiang, H.D., Liu, X.Y.: Principles of mimicking and engineering the self-organized structure of hard tissues. J. Biol. Chem. **279**, 41286–41293 (2004)
86. Wang, Z.Q., Ma, G.B., Liu, X.Y.: Will fluoride toughen or weaken our teeth? J. Phys. Chem. B **113**, 16393–16399 (2009)
87. Liu, X.Y.: Interfacial effect of molecules on nucleation kinetics. J. Phys. Chem. B **105**, 11550–11558 (2001)
88. Liu, X.Y.: A new kinetic model for 3D heterogeneous nucleation. J. Chem. Phys. **111**, 1628 (1999)
89. Lin, S.Y., Fleming, J.G., Hetherington, D.L., Smith, B.K., Biswas, R., Ho, K.M., Sigalas, M.M., Zubrzycki, W., Kurtz, S.R., Bur, J.: A three-dimensional photonic crystal operating at infrared wavelengths. Nature **394**, 251–253 (1998)

90. Fleming, J.G., Lin, S.Y.: Three-dimensional photonic crystal with a stop band from 1.35 to 1.95 μm. Opt. Lett. **24**, 49–51 (1999)
91. Noda, S., Tomoda, K., Yamamoto, N., Chutinan, A.: Full three dimensional photonic bandgap crystals at near-infrared wavelengths. Science **289**, 604–606 (2000)
92. Birner, A., Wehrspohn, R.B., Gsele, U.M., Busch, K.: Silicon-based photonic crystals. Adv. Mater. **13**, 377–388 (2001)
93. Masuda, H., Ohya, M., Asoh, H., Nakao, M., Nohtomi, M., Tamamura, T.: Photonic crystal using anodic porous alumina. Jpn. J. Appl. Phys. **38**, L1403–L1405 (1999)
94. Wanke, M.C., Lehmann, O., Mller, K., Wen, Q.Z., Stuke, M.: Science **275**, 1284–1286 (1997)
95. Campbell, M., Sharp, D.N., Harrison, M.T., Denning, R.G., Turberfield, A.J.: Fabrication of photonic crystals for the visible spectrum by holographic lithography. Nature **404**, 53–56 (2000)
96. Shoji, S., Kawata, S.: Photofabrication of three-dimensional photonic crystals by multibeam laser interference into photopolymerizable resin. Appl. Phys. Lett. **76**, 2668 (2000)
97. Xia, Y., Gates, B., Yin, Y., Lu, Y.: Monodispersed colloidal spheres: old materials with new applications. Adv. Mater. **12**, 693–713 (2000)
98. Schroden, R.C., Al-Daous, M., Blanford, C.F., Stein, A.: Optical properties of inverse opal photonic crystals. Chem. Mater. **14**, 3305–3315 (2002)
99. Lpez, C.: Three-dimensional photonic bandgap materials: semiconductors for light. J. Opt. A **8**, R1 (2006)
100. Halaoui, L.I., Abrams, N.M., Mallouk, T.E.: Increasing the conversion efficiency of dye-sensitized TiO_2 photoelectrochemical cells by coupling to photonic crystals. J. Phys. Chem. B **109**, 6334–6342 (2005)
101. Judith, J.E.G., Vos, W.L.: Preparation of photonic crystals made of sir spheres in titania. Science **281**, 802–804 (1998)
102. Norris, D.J., Vlasov, Y.A.: Chemical approaches to three-dimensional semiconductor photonic crystals. Adv. Mater. **13**, 371–376 (2001)
103. Hynninen, A.P., Thijssen, J.H.J., Vermolen, E.C.M., Dijkstra, M., van Blaaderen, A.: Self-assembly route for photonic crystals with a bandgap in the visible region. Nat. Mater. **6**, 202–205 (2007)
104. Velev, O.D.E., Kaler, W.: In situ assembly of colloidal particles into miniaturized biosensors. Langmuir **15**, 3693–3698 (1999)
105. Joannopoulos, J.D., Villeneuve, P.R., Fan, S.: Photonic crystals: putting a new twist on light. Nature **386**, 143–149 (1997)
106. Yamasaki, T., Tsutsui, T.: Spontaneous emission from fluorescent molecules embedded in photonic crystals consisting of polystyrene microspheres. Appl. Phys. Lett. **72**, 1957 (1998)
107. Yang, S.M., Jang, S.G., Choi, D.G., Kim, S., Yu, H.K.: Nanomachining by colloidal lithography. Small **2**, 458–475 (2006)
108. Murray, C.A., VanWinkle, D.H.: Experimental observation of two-stage melting in a classical two-dimensional screened coulomb system. Phys. Rev. Lett. **58**, 1200–1203 (1987)
109. Bowen, W.R., Sharif, A.O.: Long-range electrostatic attraction between like-charge spheres in a charged pore. Nature **393**, 663–665 (1998)
110. Kralchevsky, P.A., Denkov, N.D.: Capillary forces and structuring in layers of colloidal particles. Curr. Opin. Colloid Interface Sci. **6**, 383–401 (2001)
111. Danov, K.D., Pouligny, B., Kralchevsky, P.A.: Capillary forces between colloidal particles confined in a liquid film: the finite-meniscus problem. Langmuir **17**, 6599–6609 (2001)
112. Hurd, A.J., Schaefer, D.W.: Diffusion-limited aggregation in two dimensions. Phys. Rev. Lett. **54**, 1043–1046 (1985)
113. Burmeister, F., Schafle, C., Matthes, T., Bohmisch, M., Boneberg, J., Leiderer, P.: Colloid monolayers as versatile lithographic masks. Langmuir **13**, 2983–2987 (1997)
114. Wickman, H.H., Korley, J.N.: Colloid crystal self-organization and dynamics at air/water interface. Nature **393**, 445–447 (1998)
115. Paunov, V.N., Kralchevsky, P.A., Denkov, N.D., Nagayama, K.: Lateral capillary forces between floating submillimeter particles. J. Colloid Interface Sci. **157**, 100–112 (1993)

116. Dimitrov, A.S., Miwa, T., Nagayama, K.: A comparison between the optical properties of amorphous and crystalline monolayers of silica particles. Langmuir **15**, 5257–5264 (1999)
117. Kralchevsky, P.A., Nagayama, K.: Capillary forces between colloidal particles. Langmuir **10**, 23–26 (1994)
118. Arsenault, A., Fleischhaker, F., von Freymann, G., Kitaev, V., Miguez, H., Mihi, A., Te´treault, N., Vekris, E., Manners, I., Aitchison, S., Perovic, D., Ozin, G.A.: Perfecting imperfection—designer defects in colloidal photonic crystals. Adv. Mater. **18**, 2779–2785 (2006)
119. de Villeneuve, V.W.A., Dullens, R.P.A., Aarts, D.G.A.L., Groeneveld, E., Scherff, J.H., Kegel, W.K., Lekkerkerker, H.N.W.: Colloidal hard-sphere crystal growth frustrated by large spherical impurities. Science **309**, 1231–1233 (2005)
120. Arora, A.K., Tata, B.V.R.: Ordering and Phase Transitions in Colloidal Systems. VCH, Weinheim (1996)
121. Pieranski, P.: Colloidal crystals. Contemp. Phys. **24**, 25–73 (1983)
122. van Negen, W., Shook, I.: Equilibrium properties of suspensions. Adv. Colloid Interface Sci. **21**, 119–194 (1984)
123. Asher, S.A., Flaugh, P.L., Washinger, G.: Crystalline colloidal Bragg diffraction devices: the basis for a new generation of Raman instrumentation. Spectroscopy **1**, 26–31 (1986)
124. Flaugh, P.L., Donnell, S.E.O., Asher, S.A.: Development of a new optical wavelength rejection filter: development of its utility in Raman spectroscopy. Appl. Spectrosc. **38**, 847–850 (1984)
125. Carlson, R.J., Asher, S.A.: Characterization of optical diffraction and crystal structure in monodisperse polystyrene colloids. Appl. Spectrosc. **38**, 297–304 (1984)
126. VanWinkle, D.H., Murray, C.A.: Layering transitions in colloidal crystals as observed by diffraction and direct-lattice imaging. Phys. Rev. A **34**, 562–573 (1986)
127. Pieranski, P., Strzelecki, L., Pansu, B.: Thin colloidal crystals. Phys. Rev. Lett. **50**, 900–903 (1983)
128. Neser, S., Bechinger, C., Leiderer, P., Palberg, T.: Finite-size effects on the closest of hard spheres. Phys. Rev. Lett. **79**, 2348–2351 (1997)
129. Park, S.H., Qin, D., Xia, Y.: Crystallization of meso-scale particles over large areas. Adv. Mater. **10**, 1028–1031 (1998)
130. Park, S.H., Xia, Y.: Crystallization of meso-scale particles over large areas and its application in fabricating tunable optical filters. Langmuir **15**, 266–273 (1999)
131. Park, S.H., Gates, B., Qin, D., Xia, Y.: A three-dimensional photonic crystal operating in the visible. Adv. Mater. **11**, 462–466 (1999)
132. Berthier, S.: Iridescence. The Physical Colours of Insets. Springer (2007)
133. Fox, D.L.: Animal Biochromes and Structural Colors. University of California, Berkely (1976)
134. Ghiradella, H.: Light and color on the wing—structural colors in butterflies and moths. Appl. Opt. **30**, 3492–3500 (1991)
135. Kinoshita, S., Yoshioka, S., Miyazaki, J.: Physics of structural colors. Rep. Prog. Phys. **71**, 076401 (2008)
136. Parker, A.R.: 515 million years of structural color. J. Opt. A Pure Appl. Opt. **2**, R15–R28 (2000)
137. Parker, A.R.: Bird Coloration, vol. 1. Mechanism and Measurements, vol 2. Function and Evolution. Tls-Times Lit Suppl, 4–4 (2006)
138. Srinivasarao, M.: Nano-optics in the biological world: beetles, butterflies, birds, and moths. Chem. Rev. **99**, 1935–1961 (1999)
139. Vukusic, P., Sambles, J.R.: Photonic structures in biology. Nature **424**, 852–855 (2003)
140. Li, Y.Z., et al.: Structural origin of the brown color of barbules in male peacock tail feathers. Phys. Rev. E **72**, 010902 (2005)
141. Vukusic, P., Sambles, J.R., Lawrence, C.R.: Structural color—color mixing in wing scales of a butterfly. Nature **404**, 457–457 (2000)
142. Vukusic, P., Sambles, R., Lawrence, C., Wakely, G.: Sculpted-multilayer optical effects in two species of Papilio butterfly. Appl. Opt. **40**, 1116–1125 (2001)

143. Wong, T.H., Gupta, M.C., Robins, B., Levendusky, T.L.: Color generation in butterfly wings and fabrication of such structures. Opt. Lett. **28**, 2342–2344 (2003)
144. Zi, J., et al.: Coloration strategies in peacock feathers. Proc. Natl. Acad. Sci. U.S.A. **100**, 12576–12578 (2003)
145. Liu, F., Dong, B.Q., Liu, X.H., Zheng, Y.M., Zi, J.: Structural color change in longhorn beetles Tmesisternus isabellae. Opt. Express **17**, 16183–16191 (2009)
146. Vukusic, P.: Evolutionary photonics with a twist. Science **325**, 398–399 (2009)
147. Liu, F., et al.: Inconspicuous structural coloration in the elytra of beetles Chlorophila obscuripennis (Coleoptera). Phys. Rev. E **77**, 012901 (2008)
148. Kinoshita, S.: Structural Colors in the Realm of Nature. World Scientific Publishing Co., Singapore (2008)
149. Chen, Y., Gu, J.J., Zhu, S.M., Fan, T.X., Zhang, D., Guo, Q.X.: Iridescent large-area ZrO_2 photonic crystals using butterfly as templates. Appl. Phys. Lett. **94**, 053901 (2009)
150. Ge, H.L., Song, Y.L., Jiang, L., Zhu, D.B.: One-step preparation of polystyrene colloidal crystal films with structural colors and high hydrophobicity. Thin Solid Films **515**, 1539–1543 (2006)
151. Wang, J.X., Wen, Y.Q., Ge, H.L., Sun, Z.W., Zheng, Y.M., Song, Y.L., Jiang, L.: Simple fabrication of full color colloidal crystal films with tough mechanical strength. Macromol. Chem. Phys. **207**, 596–604 (2006)
152. You, B., Wen, N.G., Shi, L., Wu, L.M., Zi, J.: Facile fabrication of a three-dimensional colloidal crystal film with large-area and robust mechanical properties. J. Mater. Chem. **2009**(19), 3594–3597 (2009)
153. Wang, J.X., Wen, Y.Q., Hu, J.P., Song, Y.L., Jiang, L.: Fine control of the wettability transition temperature of colloidal-crystal films: from superhydrophilic to superhydrophobic. Adv. Funct. Mater. **17**, 219–225 (2007)
154. Wang, J.X., Wen, Y.Q., Hu, J.P., Song, Y.L., Jiang, L.: Control over the wettability of colloidal crystal films by assembly temperature. Macromol. Rapid Commun. **27**, 188–192 (2006)
155. Wang, J.X., Wen, Y.Q., Hu, J.P., Song, Y.L., Jiang, L.: Bioinspired colloidal photonic crystals with controllable wettability. Acc. Chem. Res. **44**, 405–415 (2011)
156. Fudouzi, H., Xia, Y.N.: Colloidal crystals with tunable colors and their use as photonic papers. Langmuir **19**, 9653–9660 (2003)
157. Sato, O., Kubo, S., Gu, Z.Z.: Structural color films with lotus effects, superhydrophilicity, and tunable stop-bands. Acc. Chem. Res. **42**, 1–10 (2009)
158. Liu, X.Y., Diao, Y.Y.: Light reflective structures and methods for their manufacture and use. PCT/SG2011/000075 (2011)
159. Velev, O.D., Kaler, E.W.: Structured porous materials via colloidal crystal templating: from inorganic oxides to metals. Adv. Mater. **12**, 531–534 (2000)
160. Holland, B.T., Blanford, C.F., Do, T., Stein, A.: Synthesis of highly ordered, three-dimensional, macroporous structures of amorphous or crystalline inorganic oxides, phosphates, and hybrid composites. Chem. Mater. **11**, 795–805 (1999)
161. Holland, B.T., Blanford, C.F., Stein, A.: Synthesis of macroporous minerals with highly ordered three-dimensional arrays of spheroidal voids. Science **281**, 538–540 (1998)
162. Holland, B.T., Abrams, L., Stein, A.: Dual templating of macroporous silicates with zeolitic microporous frameworks. J. Am. Chem. Soc. **121**, 4308–4309 (1999)
163. Johnson, S.A., Ollivier, P.J., Mallouk, T.E.: Ordered mesoporous polymers of tunable pore size from colloidal silica templates. Science **283**, 963–965 (1999)
164. Wang, J.X., Zhang, Y.Z., Wang, S.T., Song, Y.L., Jiang, L.: Bioinspired colloidal photonic crystals with controllable wettability. Acc. Chem. Res. **44**, 405–415 (2011)
165. Ge, J., Yin, Y.: Responsive photonic crystals. Angew. Chem. Int. Ed. **50**, 1492–1522 (2011)
166. Ge, J., Hu, Y., Yin, Y.: Highly tunable superparamagnetic colloidal photonic crystals. Angew. Chem. **119**, 7572–7575 (2007)
167. Saito, H., Takeoka, Y., Watanabe, M.: Simple and precision design of porous gel as a visible indicator for ionic species and concentration. Chem. Commun. 2126–2127 (2003)

168. Takeoka, Y., Watanabe, M.: Tuning structural color changes of porous thermosensitive gels through quantitative adjustment of the cross-linker in pre-gel solutions. Langmuir **19**, 9104–9106 (2003)
169. Sharma, A.C., Jana, T., Kesavamoorthy, R., Shi, L.J., Virji, M.A., Finegold, D.N., Asher, S.A.: A general photonic crystal sensing motif: creatinine in bodily fluids. J. Am. Chem. Soc. **2004**(126), 2971–2977 (2004)
170. Puzzo, D.P., Arsenault, A.C., Manners, I., Ozin, G.A.: Electroactive inverse opal: a single material for all colors. Angew. Chem. Int. Ed. **48**, 943–947 (2009)
171. Ozaki, M., Shimoda, Y., Kasano, M., Yoshino, K.: Electric field tuning of the stop band in a liquid-crystal-infiltrated polymer inverse opal. Adv. Mater. **14**, 514–518 (2002)
172. Kolle, M., Salgard-Cunha, P.M., Scherer, M.R.J., Huang, F.M., Vukusic, P., Mahajan, S., Baumberg, J.J., Steiner, U.: Mimicking the colourful wing scale structure of the Papilio blumei butterfly. Nat. Nanotechnol. **5**, 511–515 (2010)
173. Diao, Y.Y., Liu, X.Y.: Mysterious coloring: structural origin of color mixing for two breeds of Papilio butterflies. Opt. Express **2011**(19), 9232–9241 (2011)
174. Lim, M.L.M., Land, M.F., Li, D.Q.: Sex-specific UV and fluorescence signals in jumping spiders. Science **315**, 481 (2007)
175. Briscoe, A.D., Bybee, S.M., Bernard, G.D., Yuan, F.R., Sison-Mangus, M.P., Reed, R.D., Warren, A.D., Llorente-Bousquets, J., Chiao, C.C.: Reply to Nozawa et al. Complementary statistical methods support positive selection of a duplicated UV opsin gene in Heliconius. Proc. Natl. Acad. Sci. **107**, 3628–3633 (2010)
176. Takeuchi, Y., Arikawa, K., Kinoshita, M.: Color discrimination at the spatial resolution limit in a swallowtail butterfly, Papilio xuthus. J. Exp. Biol. **209**, 2873–2879 (2006)
177. Bartlett, P.N., Birkin, P.R., Ghanem, M.A.: Electrochemical deposition of macroporous platinum, palladium and cobalt films using polystyrene latex sphere templates. Chem. Commun. **17**, 1671–1672 (2001)
178. Braun, P.V., Wiltzius, P.C.O.: Macroporous materials—electrochemically grown photonic crystals. Curr. Opin. Colloid Interface Sci. **7**, 116–123 (2002)
179. Wijnhoven, J.E.G.J., Zevenhuizen, S.J.M., Hendriks, M.A., Vanmaekelbergh, D., Kelly, J.J., Vos, W.L.: Electrochemical assembly of ordered macropores in gold. Adv. Mater. **12**, 888–890 (2000)
180. Puurunen, R.L.: Surface chemistry of atomic layer deposition: a case study for the trimethylaluminum/water process. J. Appl. Phys. **97**, 121301 (2005)
181. Labhart, T., Baumann, F., Bernard, G.D.: Specialized ommatidia of the polarization-sensitive dorsal rim area in the eye of monarch butterflies have non-functional reflecting tapeta. Cell Tissue Res. **338**, 391–400 (2009)

Chapter 8
Photonic Structures for Coloration in the Biological World

Jian Zi, Biqin Dong, Tianrong Zhan, and Xiaohan Liu

Abstract In the biological world the living organisms have exploited photonic structures to produce striking structural coloration since the Cambrian period. In recent years, structural colors and associated photonic structures have received increasing attention from scientists in a wide variety of disciplines ranging from physics, biology, and chemistry to material science. Revealed natural photonic structures are diverse, delicate, and multifunctional as well. Natural photonic structures and their ingenious ways of light steering could be a great source of inspiration, invaluable to our bio-inspired technologies. In this chapter, we will give a review on natural photonic structures and their coloration. A historical survey is given in Sect. 8.2. In Sect. 8.3, we discuss the mechanisms of structural coloration, including interference, diffraction, scattering, or their combination. Experimental and theoretical methods for studying natural photonic structures are briefly reviewed in Sect. 8.4. In Sect. 8.5, we present some typical photonic structures occurring in the biological world, such as thin films, multilayers, diffraction gratings, photonic crystals, and amorphous photonic structures, and also discuss their coloration mechanisms. An outlook is given in the last section.

8.1 Introduction

In the biological world, the evolution of coloration stems from the fact that light could be a significant selection pressure for certain life forms. As a result, colors and also color patterns may have important biological, physical, and even physiological

J. Zi (✉) • B. Dong • T. Zhan • X. Liu
Department of Physics, Key Laboratory of Micro and Nano Photonic Structures (Ministry of Education), and Key Laboratory of Surface Physics, Fudan University, Shanghai 200433, China
e-mail: jzi@fudan.edu.cn; dong_bq@hotmail.com; 071019035@fudan.edu.cn; liuxh@fudan.edu.cn

X.Y. Liu (ed.), *Bioinspiration: From Nano to Micro Scales*, Biological and Medical Physics, Biomedical Engineering, DOI 10.1007/978-1-4614-5372-8_8,

significance. It is thus not surprising that the study of the mechanisms of color production in the biological world attracted the attention of scientific giants like Newton, Michelson, and Lord Rayleigh.

There are several ways to produce coloration in the biological world. The most general cause of coloration is the presence of pigments. Pigments can selectively absorb certain wavelengths of light and reflect or scatter others. Fireflies and many marine organisms can produce coloration by bioluminescence. In bioluminescence, energy will be released in the form of "cold light" emission via chemical reactions. Fluorescence can also generate coloration for materials containing fluorescent molecules when illuminated by ultraviolet (UV) light.

Another important category of color production is structural coloration. Distinctly different from other categories, structural colors are of structural origin, namely, from the interaction of natural light with photonic structures whose feature sizes are comparable to the visible wavelengths. Structural coloration is thus purely produced by physical means via optical phenomena such as interference, diffraction, scattering, or their combination.

Structural colors possess many interesting features that are distinct from pigmentary colors since they are produced structurally. Generally, structural colors are bright and highly saturated, and are hereby called "metallic colors" sometimes. They may display iridescence,[1] i.e., a color change with perspective. Variations in structures or contrast of refractive indices may alter or even destroy structural colors, for instance, by applying pressure or infiltrating liquids into air voids. In contrast to pigmentary colors, structural colors would not fade provided that the associated photonic structures retain unchanged.

In recent years, structural colors and associated photonic structures have been subjected to extensive studies because of their scientific and practical importance [1–9]. Studies of structural colors could offer important information related to their evolution, biological functions, structural formation, and strategies of light steering. On the other hand, structural colors may have potential applications in a variety of industries such as photonics, display, painting, and textile. Natural photonic structures and their ingenious ways of light steering could be a great source of inspiration in our design and fabrication of new optical materials and devices for future technological applications.

8.2 Historical Survey

Historically, Hooke and Newton might be the first ones to give a scientific description of structural colors. In his book *Micrographia* published in 1665, Hooke described his microscopic observations on the feathers of peacock and duck, and

[1]The terms *structural color* and *iridescent color* are sometimes used indiscriminately to name colors produced structurally. An iridescent color is certainly a structural color. But a structural color may not display iridescence.

other feathers of changeable colors. Newton described in his book *Opticks* published in 1704 that the color production mechanism for the finely colored feathers of birds and particularly those of peacock tails is after the same manner of thin films. Both Hooke and Newton attributed feather colors to the thin films of the transparent parts of feathers, but the true physical mechanism was still unanswered.

We now know that the correct mechanisms of structural coloration rely on the wave nature of light, resulting from the interaction of natural light with photonic structures. But quantitative descriptions of reflection, refraction, interference, diffraction, and scattering had to wait until the establishment of the electromagnetic theory by Maxwell in 1873, known as Maxwell's equations.

Ever since the distinction of pigmentary and structural colors, there existed a big debate on the cause of structural coloration in the early twentieth century. Michelson [10] supported strongly the claim proposed by Walter [11] that structural colors are *surface colors* caused from a thin layer of pigments by selective reflection, similar to those from metallic surfaces. The conclusion was based on the similar behavior of polarized light when reflected from iridescent structures and from thin films of aniline dyes. So satisfied with his opinion, he even wrote [10] "it is somewhat surprising to find that the contrary view is still hold by eminent naturalists, and it is hoped that the further evidence here presented may serve to emphasis the distinction between 'metallic' or 'surface' colours and the remaining classes of colours (due to pigment, interference, and diffraction)."

On the opposite side, Lord Rayleigh [12] believed that iridescent colors such as those of peacocks and insects are interference colors from thin films. Many experimental results defied Michelson's suggestion. For example, in *Micrographia* Hooke described the observation that the iridescent colors of peacock feathers would be destroyed by water wetting, and "the colours again appear in their former lustre" by continuous evaporations. Biedermann [13] also noticed that the colors of all iridescent scales of beetles would change after their immersion in liquids, and if the refractive index of a liquid approaches that of chitin, the colors would vanish completely. Besides color changes by liquid infiltrations, Mollock [14] even found that the structural colors of scales or feathers could be destroyed by applying pressure. Merritt [15] might be the first to use spectroscopy to characterize structural colors optically. He measured reflection spectra of pigeon feathers and butterfly wings under different incident angles, and found that reflection minima shifted to a short wavelength with increasing incident angles, which could be explained by thin-film interference. Onslow [16] and Mason [17–21] conducted a multitude of microscopic observations on insect scales and bird feathers, and supported the interference origin of iridescent colors. With convincing arguments, the opinion that iridescent colors are of structural origin prevails eventually.

It is known that the spatial resolution of optical microscopes should be smaller than a half of the visible wavelengths owing to the diffraction limit. As a result, the relations between structural colors and detailed structural features could be determined after the invention of electron microscopy in 1930s since many photonic structures for coloration have submicron feature sizes. With electron microscopy, Frank and Ruska [22] made the first structural observation for the blue feathers of

Pitta maxima, and revealed a spongy structure of keratin in the barbs. Conventionally, two kinds of electron microscopy are frequently used in the characterizations of natural photonic structures: one is scanning electron microscopy (SEM) and the other is transmission electron microscopy (TEM). With the powerful image resolution of SEM and TEM, a wide variety of natural photonic structures have been identified, including single thin films, multilayers, diffraction gratings, two-dimensional (2D) and 3D periodical photonic structures, amorphous photonic structures with only short-range order, or their composites [1–9].

As for the physical mechanisms of structural coloration, early understandings were almost all attributed to the interference of thin films or multilayers due to the lack of structural information. With the development of both structural characterizations and computation algorithms, interesting mechanisms have been uncovered. Structural coloration can thus be understood by interference, diffraction, scattering, or their combination, depending on detailed structural configurations. Despite the great progress in understanding of the mechanisms, there remain still many important questions to be answered in a quantitative way owing to the diversity and complexity of natural photonic structures.

8.3 Mechanisms for Structural Coloration

Different from pigmentary coloration, structural coloration is purely of structural origin, produced by the interaction of natural light with photonic structures via optical phenomena. These optical effects include interference, diffraction, scattering, or their combination.

8.3.1 Interference

The simplest way of structural coloration is thin-film interference [23], as shown schematically in Fig. 8.1a. A soap bubble in sunlight is a known example. As a light beam is incident upon a thin film, it will be reflected and transmitted (refracted) at the upper surface. The transmitted beam at the upper surface will once again be reflected and transmitted when reaching the lower surface. The reflected beam at the lower surface will also encounter reflection and transmission at the upper surface. Due to the different optical path, the reflected light beams at the upper surface possess different phases, eventually leading to interference. The optical path difference between the reflected light beams depends on the refracted angle θ, and the thickness d and refractive index n of the film, given by $2nd\cos\theta$. In calculating the optical path difference, one should consider an abrupt phase change of π when a light beam gets reflected from a low-refractive-index medium to a high-refractive-index medium. This will give rise to an extra contribution $\lambda/2$ to the optical path difference.

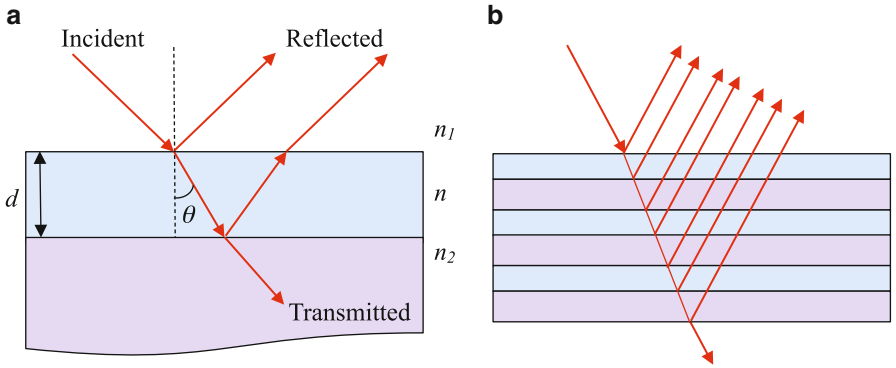

Fig. 8.1 (**a**) Thin-film interference. A thin film with a thickness d and refractive index n is sandwiched between an upper medium with a refractive index n_1 and a lower medium with a refractive index n_2. The refracted angle with respect to the surface normal in the thin film is denoted by θ. (**b**) Interference in a multilayer

Constructive interference occurs when the optical path difference is an integral number of wavelength. On the other hand, destructive interference happens when the optical path difference is a half integral number of wavelength. Considering the possible phase change upon reflection at both the upper and lower surfaces, the condition for constructive interference for $n_1 < n < n_2$ or $n_1 > n > n_2$ is given by

$$2nd\cos\theta = m\lambda, \tag{8.1}$$

where λ is the wavelength in vacuum and m is an integer. For $n_1 < n > n_2$ or $n_1 > n < n_2$, e.g., a free-standing thin film, the condition for constructive interference becomes

$$2nd\cos\theta = \left(m - \frac{1}{2}\right)\lambda. \tag{8.2}$$

For a thin film, its reflection reaches maxima at the wavelengths that satisfy the constructive interference condition, giving rise to structural coloration. It is obvious that the optical path difference increases with increasing incident angle. As a result, reflection peaks undergo a blue shift in wavelength with increasing incident angle, leading to iridescence. Similar to that in thin films, multiple interference occurs also in multilayers, as shown schematically in Fig. 8.1b, since successively reflected light from each interface can interfere with each other.

8.3.2 Diffraction

When light interacts with a periodically structured surface such as a grating shown in Fig. 8.2, diffraction is expected [23]. This is because the scattered light beams by neighboring corrugations possess a constant optical path difference

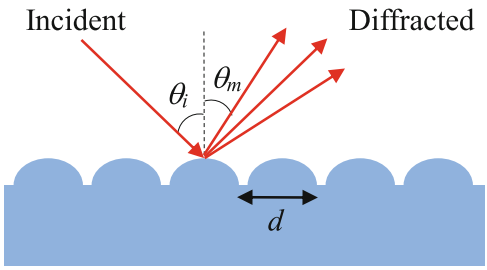

Fig. 8.2 Diffraction by a grating consisting of a periodically corrugated surface. The incident angle is θ_i, the diffracted angle is θ_m, and the grating period is d

$d(\sin\theta_i + \sin\theta_m)$. When this optical path difference is an integral number of wavelengths, i.e., satisfying the following grating equation, diffraction occurs due to the constructive interference of the scattered light beams, namely,

$$d(\sin\theta_i + \sin\theta_m) = m\lambda. \tag{8.3}$$

Here, m is an integer which can be positive or negative, representing the order of diffraction. The zero-order diffraction ($m = 0$) corresponds to the specular reflection. In general, the intensity of nonzero order ($m \neq 0$) diffraction is much smaller than that of the specular reflection.

For a fixed wavelength, diffraction occurs at certain diffracted angles that satisfy the grating equation. For a fixed incident angle, different wavelengths will be diffracted at differently diffracted angles with each order forming a spectrum, leading to structural coloration. For 2D diffraction gratings, structural coloration is also expected due to diffraction, although the grating equation is different from that for 1D gratings.

8.3.3 Scattering

Light will be scattered when encountering irregularities (scatters), e.g., particles. Light scattering depends strongly on light wavelength and scatter geometry and arrangement. In general, light scattering can be classified into incoherent or coherent scattering.

Rayleigh scattering [24] and Tyndall scattering [25] are typical incoherent scattering by single particles. Rayleigh scattering is the light scattering by molecules or particles whose sizes are much smaller than light wavelengths. In Rayleigh scattering, the intensity of scattered light varies inversely as the fourth power of wavelength and shows a strong angle dependence as $(1 + \cos^2\theta)$, where θ is the scattering angle. The blue color of sky is caused by Rayleigh scattering from molecules since short-wavelength light such as violet and blue is scattered much more than long-wavelength light such as yellow and red.

For particle sizes comparable to light wavelengths, it belongs to Tyndall scattering which is much more intense than Rayleigh scattering. Unlike Rayleigh

scattering, there are no simple mathematic formulae for Tyndall scattering. But for spherical particles, light scattering can be mathematically treated by Mie theory [26]. Light scattering by spherical particles is commonly called Mie scattering.

Whether light scattering is coherence or incoherence depends on the coherent length of illumination light and the scatter arrangement as well. For natural light such as sunlight, its coherent length is about a few microns. When the separations of scatters are larger than the coherent length, it can be considered as incoherent scattering. In contrast, if the separations of scatters are smaller than the coherent length, light scattering is coherent since scattered light may interfere with each other.

8.3.4 The Combination

For thin films, multilayers, and diffraction gratings, their coloration can be understood simply by interference or diffraction. In the biological world, there exist many nontrivial photonic structures, e.g., 2D and 3D periodic photonic structures [1–9]. Their structural coloration cannot be simply interpreted by interference, diffraction, or scattering alone. Instead, it results from the combination of interference, diffraction, and scattering.

Periodic photonic structures, those with a spatially periodical variation of refractive index, are also called photonic crystals [27–29]. For light interactions with photonic crystals, there may exist scattering by constituent units, diffraction due to the periodic arrangement, and interference among scattered or diffracted light, leading to complicated photonic band structures [29], analogous to those for electrons propagating in crystalline solids. Between photonic bands, there may exist a partial (along a certain direction) or complete (along all directions) photonic bandgap.[2]

For complicated or composite photonic structures, their color production can be generally interpreted by the combination of interference, diffraction, and scattering. The understandings are usually conceptual. This is because the interplay among interference, diffraction, and scattering may considerably complicate our quantitative analyses. It may even result in new optical phenomena. To understand in a quantitative way, numerical simulations by solving Maxwell's equations are needed.

8.4 Methodology for Studying Natural Photonic Structures

Optical, spectral, and structural information are vital for our understandings of structural coloration. Consequently, both macroscopic and microscopic observations on structural colors are essential. To establish the relations between structural

[2] In natural photonic structures, there exist only partial photonic band gaps because refractive-index contrasts among constituent materials are not big enough to open up complete photonic band gaps.

colors and associated microstructures, structural characterizations at the submicron level are needed. To explore the ultimate mechanisms of structural coloration in a quantitative way, numerical simulations are of great importance.

8.4.1 Optical Observations

With a specimen, the first thing is to determine whether a color is a structural color or not. If iridescence is observed, it should be a structural color. But this method cannot be applied to non-iridescent structural colors. Another way is to immerse the specimen into a liquid aiming to observe the change in color. Commonly used liquids include water, ethanol, and glycerin. If a color change occurs, the color should be a structural color. This is because structural coloration is determined by the spatial arrangement of refractive index. Liquid infiltrations into air voids may change this arrangement, leading to a change in color. On the contrary, pigmentary colors do not alter their hue by liquid infiltrations. Structural coloration has an interesting feature that the reflected and transmitted colors are *complementary* provided that the constituents are transparent. This feature can also be adopted to distinguish structural and pigmentary coloration.

Optical characterizations of structural colors are conventionally conducted by optical microscopy under different magnifications. This is because the colored bodies are sometimes too small to be resolved by our naked eye. In some cases, a color perceived by us is a mixed color, resulting from differently colored small bodies which may be resolved with optical microscopy.

For conventional observations, unpolarized light is used. We may also use polarized light to obtain information on polarization effects. For a photonic structure covered with an uneven cortex, glares caused by surface reflection and scattering may hinder our observations. To reduce the glare disturbances, an oil immersion objective can be used. This is because the oil immersion can reduce or even eliminate the refractive-index contrast between oil and specimen, as well as unwanted glares. For certain samples, dark-field microscopy can be used to enhance the topographic contrast of samples.

8.4.2 Spectral Measurements

Spectral characteristics of natural photonic structures can offer important optical information on their structural colors. For spectral measurements, angle-resolved optical spectroscopy is commonly used to obtain angle-dependent reflection, scattering, and even transmission spectra. A typical angle-resolved spectrometer is schematically shown in Fig. 8.3.

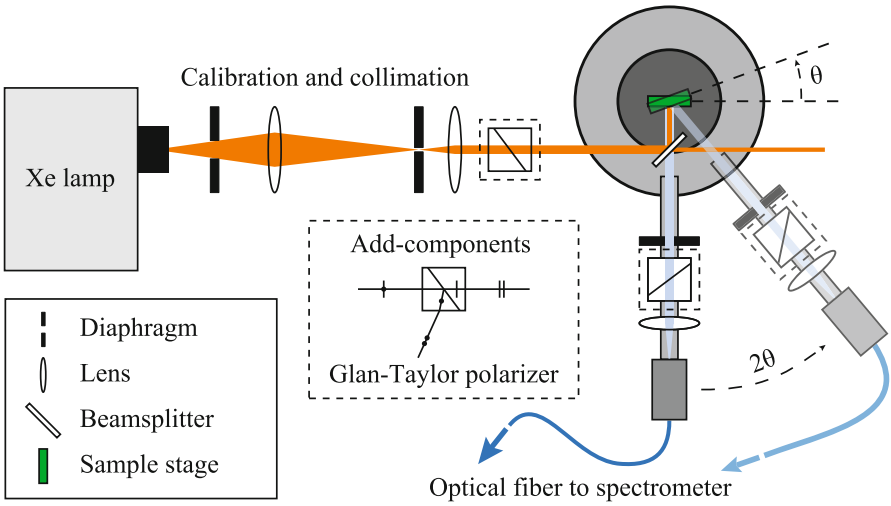

Fig. 8.3 Schematic of a home-built angle-resolved optical spectroscopy at Fudan University. The light source is a Xenon lamp which covers a wavelength range from 250 to 800 nm. Diaphragms are used to control the beam size. A beamsplitter is used to split light beams (50R/50T). Two coaxial motorized rotary stages are used to control the incident and detecting angles. The rotating angles of the upper (*dark gray disk*) and lower (*light gray disk*) stages can be adjusted independently. Samples are placed on the center of the upper stage. An optical fiber is put on the detection arm which is fixed on the lower stage. A high-resolution spectrometer is connected to the fiber. Two Glan–Tailor polarizers can be added in if measurements with polarized light are needed

In this angle-resolved spectrometer, the incident angle θ can be adjusted by rotating the detection arm fixed on the lower stage. Different spectra such as specular reflection (incidence at θ and detection at $-\theta$), scattering (incidence at θ and detection at other angles), backscattering (incidence and detection at the same θ), and transmission can be obtained. Two polarizers can be added in if polarized spectra are to be measured. In measurements of absolute reflectance, a reference standard, e.g., diffuse white, should be used in order to remove the influence of the characteristic wavelength dependence of light sources.

Structurally colored parts of biological samples, e.g., scales of insects and barbules of bird feathers, are usually very small. A single part may even display different structural colors. Under the circumstances, microscopic spectral detections are necessary. A typical microspectrometer that can detect spectra of microscopic regions is schematically shown in Fig. 8.4.

Total reflection, transmission, and absorption spectra can provide important information for structural colors, which can be measured with integrating spheres, as shown in Fig. 8.5. An integrating sphere is a hollow spherical cavity with a diffuse high reflectivity coating on its inner surface, and also with small holes for light entrance and exit. Samples are placed in close proximity to the exit port. Incident light can be introduced, e.g., through an optical fiber. It will bounce around the inner surface and finally impinge the detector.

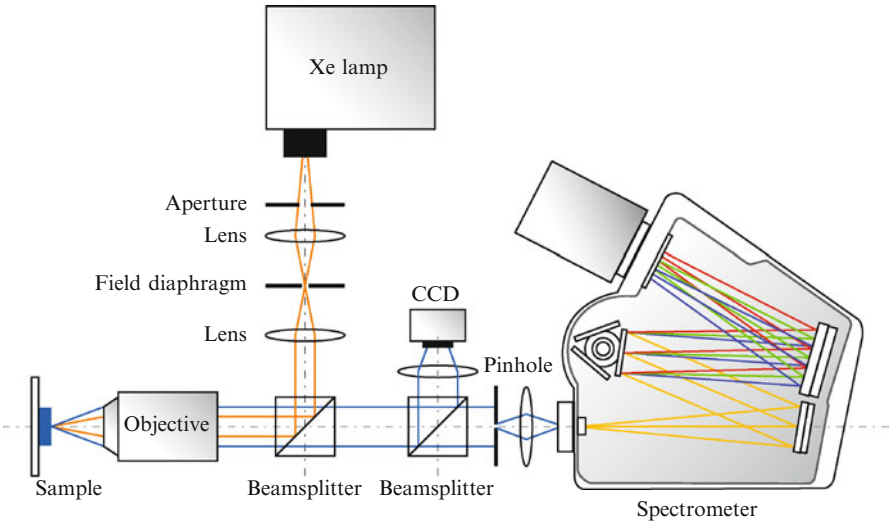

Fig. 8.4 Schematic of a home-built microspectrometer at Fudan University that enables spectral detections of microscopic regions. It is based on an optical microscope with the beam size controlled by the field diaphragm and pinhole

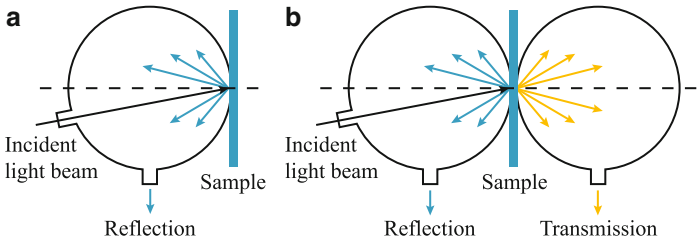

Fig. 8.5 (**a**) Schematic of an integrating sphere for reflection measurements. (**b**) Schematic of a double-integrating sphere for transmission measurements

Transmission measurements require two integrating spheres: one serves as a uniform light source and the other is used to collect transmitted light. Absorptance A can also be obtained, from the formula $A = 1 - R - T$, where R is reflectance and T is transmittance.

8.4.3 Color Specifications

Any possible color can be specified according to their hue, saturation, and brightness. The hue of a color can be considered as the peak wavelength in its reflection spectrum. Saturation tells the purity of the color, characterized by the peak width.

The narrower the peak width is, the higher the saturation is. Brightness renders the relative intensity of the reflection spectrum, strongly related to the response of our vision system.

Practically, colors are specified in color spaces. Commonly used color spaces include CIE XYZ and xyZ color spaces.[3] For the human eye, there are three color-sensitive photoreceptors with sensitivity peaks located in short (420–440 nm), middle (530–540 nm), and long (560–580 nm) wavelengths. Three tristimulus values are thus needed to describe a color since color spaces are 3D.

In the CIE XYZ color space, the tristimulus values are a set of values called X, Y, and Z. For a given illuminating source $D(\lambda)$ and the resulting reflection spectrum $R(\lambda)$ of a color, they can be calculated by

$$\begin{aligned} X &= \frac{1}{k}\int_0^\infty D(\lambda)R(\lambda)\overline{x}(\lambda)\mathrm{d}\lambda, \\ Y &= \frac{1}{k}\int_0^\infty D(\lambda)R(\lambda)\overline{y}(\lambda)\mathrm{d}\lambda, \\ Z &= \frac{1}{k}\int_0^\infty D(\lambda)R(\lambda)\overline{z}(\lambda)\mathrm{d}\lambda, \end{aligned} \tag{8.4}$$

where $\overline{x}(\lambda)$, $\overline{y}(\lambda)$, and $\overline{z}(\lambda)$ are three CIE color matching functions [30] shown in Fig. 8.6a, and $k = \int_0^\infty D(\lambda)\overline{y}(\lambda)\mathrm{d}\lambda$ is a normalization factor which ensures that an object with $R(\lambda) = 1$ yields the component $Y = 1$. In practical calculations, CIE Illuminant D65 [30] is often used as the illuminating source $D(\lambda)$, which matches closely that of the sky daylight.

The CIE 1931 XYZ is at the root of all colorimetry. In the CIE XYZ color space, the Y parameter was deliberately designed as a measure of the brightness of a color. The chromaticity of a color can thus be represented by the two derived parameters x and y, defined by

$$x = \frac{X}{X+Y+Z}, \qquad y = \frac{Y}{X+Y+Z}, \tag{8.5}$$

and derived parameter z can be obtained from $z = Z/(X+Y+Z) = 1-x-y$. The derived color space specified by x, y, and Y is known as the CIE xyY color space which is widely used in practice for color specification. In the CIE xyY color space, the brightness of a color is given by Y, while x and y specify the color chromaticity which can be obtained from the CIE color chromaticity diagram shown in Fig. 8.6b.

[3]The CIE XYZ color space was one of the first mathematically defined color spaces created, according to the human visual system, by Commission Internationale de l'Eclairage (CIE) in 1931.

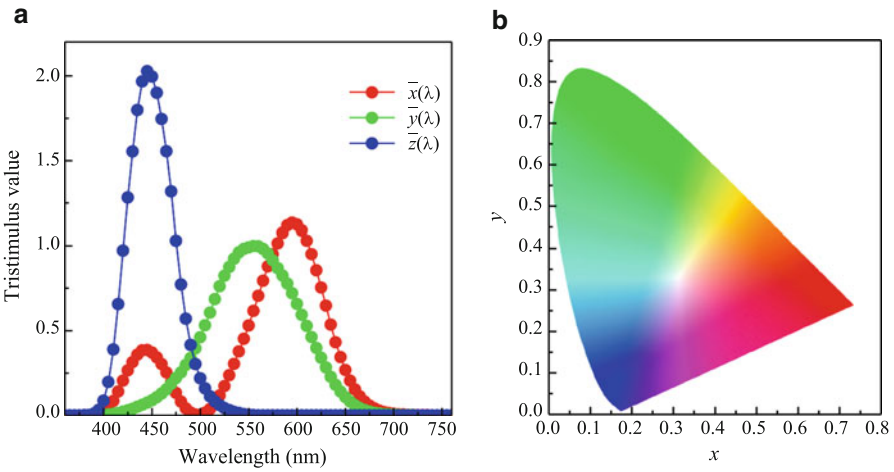

Fig. 8.6 (**a**) CIE 1964 10° color matching functions. (**b**) CIE 1931 2° color space chromaticity diagram. The outer curved boundary is the spectral locus which corresponds to monochromatic light. The straight edge at the lower part represents the line of purples which have no counterparts in monochromatic light. Mixed or less saturated colors appear in the interior with white at the point $(x, y) = (1/3, 1/3)$

8.4.4 Structural Characterizations

Electron microscopes are indispensable tools for structural characterizations because they have a much higher resolving power than optical microscopes. This is due to the fact that electrons have wavelengths much shorter than those of visible light. SEM and TEM are two types of electron microscopes commonly used to characterize natural photonic structures. TEM may have a resolution of atomic level, while the resolution of SEM is poorer by about an order of magnitude than that of TEM.

SEM can image the surface topography of a sample by scanning the surface with a fine high-energy electron beam and measuring reflected electrons. For many samples, structural information on the substructure is needed. This can be done by sectioning the samples. In SEM observations, a thin conductive layer of a few nanometers (gold, platinum, tungsten, or graphite) is usually introduced on sample surfaces in order to produce high topographic contrast and resolution.

Unlike SEM, TEM images samples by taking advantage of transmitted electrons. This means that samples should be ultrathin in order to allow the transmission of electrons. The ultrastructure or even the composition of samples may be distinguished from the intensity of transmitted electrons.

Atomic force microscopy (AFM) can have a spatial resolution at the nanometer scale and can also be used to scan the surface of a sample. AFM relies on a cantilever with a sharp tip and a feedback mechanism that adjusts the tip-to-sample distance

in order to maintain a constant force between the tip and the sample. Due to its working mechanism, AFM has a limited applicability in natural photonic structures as the structural information beneath the sample surface cannot be probed.

8.4.5 Theoretical Treatments

For natural photonic structures, analytical treatments are only possible for some particular cases, e.g., thin films [23]. To give a quantitative description of the optical properties for nontrivial natural photonic structures, numerical simulations are needed. Analytical and numerical results can provide reflection, scattering, transmission, and absorption spectra which can be directly compared with experimental results. Other optical quantities, such as photonic band structures and photon density of states, can be also obtained. With these results, we may uncover interesting mechanisms of structural coloration, light steering strategies, and even new optical phenomena.

With the development of computational algorithms and computer itself, various computational methods have been proposed and implemented to solve Maxwell's equations numerically. Commonly used methods include transfer matrix method (TMM) [31–33], finite-difference time-domain (FDTD) method [34, 35], and plane-wave expansion (PWE) method [29].

TMM was originally developed for multilayers. In TMM, the fields of the adjacent layers are related by a transfer matrix that is composed of two matrices: one is to propagate the fields in a distance in the uniform medium and the other is to make the fields from one side of an interface to the other. From the total transfer matrix, the fields at one side of a multilayer can be related to those at the other side. TMM can be extended to deal with photonic structures of higher dimensions [32, 33].

FDTD is a popular tool which is widely used for electromagnetic computations [35]. The central idea of FDTD is to solve Maxwell's equations based on discretizing time and space into finite grids. The electric and magnetic fields at all points within the computational domain can be calculated. FDTD is a versatile and powerful technique which can be applied to complicated photonic structures. But the spatial grid discretizations must be sufficiently fine, which will increase the computational time and computer memory.

For periodic photonic structures, i.e., photonic crystals, their photonic band structures can offer important information in understanding the optical response. PWE is widely used for calculating photonic band structures [29]. Within the framework of PWE, the electric and magnetic fields are expanded by plane waves, and Maxwell's equations are then cast into eigen-problems. By imposing the Bloch theorem, photonic band structures can be obtained by solving eigen-equations. Photonic band structures can also be calculated by other methods such as TMM and FDTD provided that the Bloch theorem is imposed.

In principle, TMM, FDTD, and PWE are applicable to arbitrary photonic structures. For some special cases, e.g., photonic structures consisting of spheres or spherical cylinders, the scattering matrix method based on Korringa–Kohn–Rostoker techniques is much more efficient [36].

8.5 Photonic Structures Occurring in the Biological World

Color-producing photonic structures are widely spread in the biological world [1–9]. With the advancement of characterization tools, more and more interesting natural photonic structures have been revealed, including thin films, multilayers, diffraction gratings, photonic crystals, amorphous photonic structures, and even composite structures. These photonic structures show a great diversity of construction and topology, leading to optical effects that may implement vital biological functions.

8.5.1 Single Thin Film

A single thin film is the simplest structure that can produce structural coloration via thin-film interference. Perceived structural colors are due to the constructive interference of reflected light from the upper and lower surfaces. Thin-film interference will produce a series of harmonic reflection peaks with equal intensity and frequency interval if the refractive index of a thin film is wavelength independent. However, the intensity of the reflection peaks is rather low. For example, for a thin film with a refractive index of 1.5 its maximal reflectance is less than 20% at normal incidence. In contrast, a multilayer can achieve a very high peak reflectance, ideally as high as 100% in principle.

The wings of most insects are mainly composed of two integument layers apposed closely to form a thin membrane. It was found more than 50 years ago that the transparent wings of some houseflies can produce structural colors via thin-film interference [37]. However, the biological significance of the structural colors as well as color patterns caused by reflecting insect wings has been largely disregarded. This might be due to the fact that these colors are simply produced by thin-film interference like soap bubbles, and imaginarily supposed to flash randomly over the wing surfaces.

In a recent paper [38], the structural-color patterns in the transparent wings of small Hymenoptera and Diptera were studied. These extremely thin wings reflect vivid structural-color patterns caused by the wing membranes. The visibility of these color patterns depends strongly on backgrounds, as shown in Fig. 8.7. In a white background, the reflected structural colors and resulting color patterns are faint or even invisible. This is due to the transparency of the wings. Background light can transmit the wings which will overpower the interference colors. In contrast, these colors and color patterns can be easily perceived by any animal with color vision in a

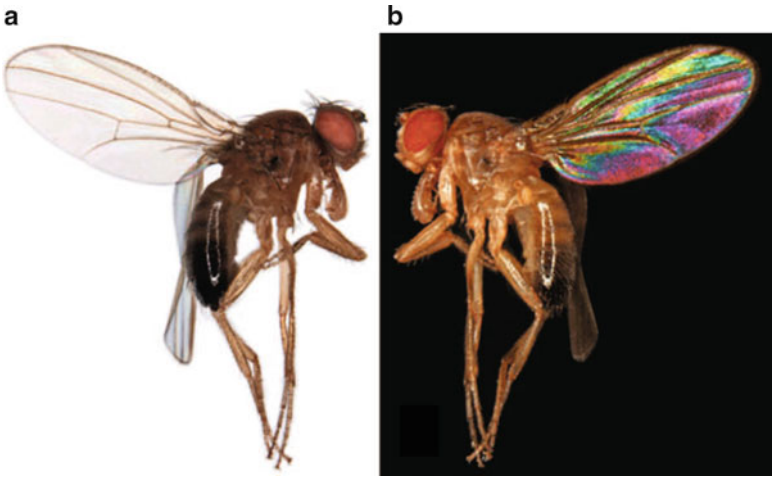

Fig. 8.7 Male *Drosophila melanogaster* on *white* (**a**) and *black* (**b**) backgrounds. (Reproduced from [38])

black background (eliminating the disturbance of reflected light from backgrounds) since about 20% of incoming light can be reflected by the wing membranes. The thickness of the wing membranes is about several hundred nanometers, ideal for thin-film interference, and varies with wing positions. As a result, positions with different thicknesses produce different structural colors, giving rise to specific structural-color patterns. The visibility of these color patterns is affected by the way the insects display their wings against backgrounds.

Interestingly, the wings of small Hymenoptera and Diptera almost universally display stable and non-iridescent structural-color patterns that are often taxon-specific [38], as shown in Fig. 8.8. In other words, these color patterns are visible as well as stable over a wide range of perspective angles. The non-iridescence of the wing structural colors can be understood by the surface morphology of the wing membrane. The membrane surface is uneven with corrugations and dense setae. The corrugations and setae may reduce or even eliminate the iridescence. This is because the existence of the corrugations and setae could cause random scattering, leading to non-iridescence over a wide range of viewing angles.

Another example of structural coloration caused by a single thin film is the iridescent neck feathers of domestic pigeons (*Columba livia domestica*). In spite of a long study history [15,39,40], the detailed origin of their structural coloration was uncovered until recently [41–43]. Basically, there are two kinds of iridescent neck feathers: one is green and the other is purple under normal perspective, as shown in Fig. 8.9. Like many other bird feathers, each iridescent neck feather consists of a central rachis with an array of barbs projecting on both sides. On each side of a barb there is an array of barbules. Each barbule is composed of successively connected segments. The perceived iridescent green and purple colors arise from barbules. Barbs do not possess any iridescent color.

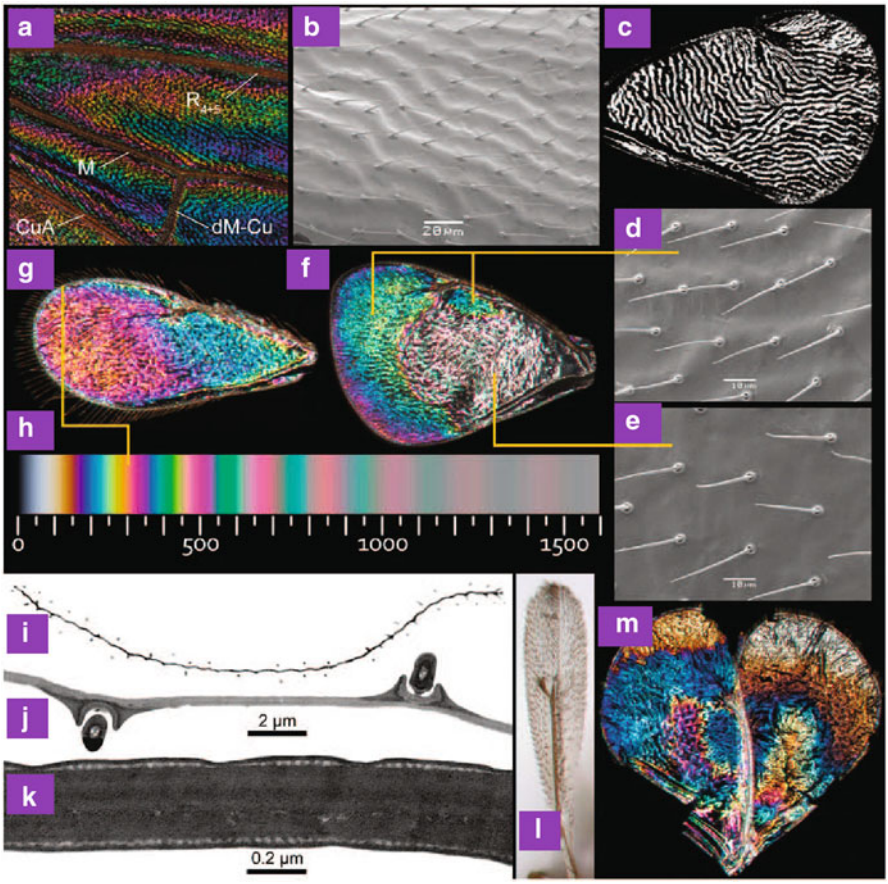

Fig. 8.8 Color and structural features of the wings in small chalcidoid wasps and *Drosophila* showing strong non-iridescent structural-color patterns. (**a**) Midsection of the wing of *D. melanogaster*. (**b**) SEM image of the forewing of *Chrysocharis* sp. (**c**) Duotone image of (**b**). (**d**)–(**f**) Forewing of a male *Achrysocharoides latreillei*. SEM images of corrugated parts and smooth central parts are shown in (**d**) and (**e**), respectively. Resulting structural-color patterns are indicated in (**f**). (**g**) Color pattern of female *Asecodes congruens*. (**h**) Calculated structural colors for a thin film with a refractive index of 1.57 in air under normal incidence with scales indicating its thickness in nanometers. (**i**) Composite duotone image of a whole apical cross-section of the forewing of *Achrysocharoides atys*. (**j**) and (**k**) TEM images of cross-sections of the apical part of a forewing from the same species as in (**g**). (**l**) Left "balloon" forewing of male *Omphale* sp. in frontal view. (**m**) Unequal organization of dorsal (*left*) and ventral (*right*) membranes of an opened left forewing of a male *Achrysocharoides platanoidae* (Reproduced from [38])

SEM characterizations revealed that all iridescent barbules are composed of a central medullary layer surrounded by an outer keratin cortex layer. The barbules are about 2∼4 μm in thickness, while the thickness of the medullary layer varies from 1 to 3 μm. The medulla consists of randomly dispersed melanin granules in

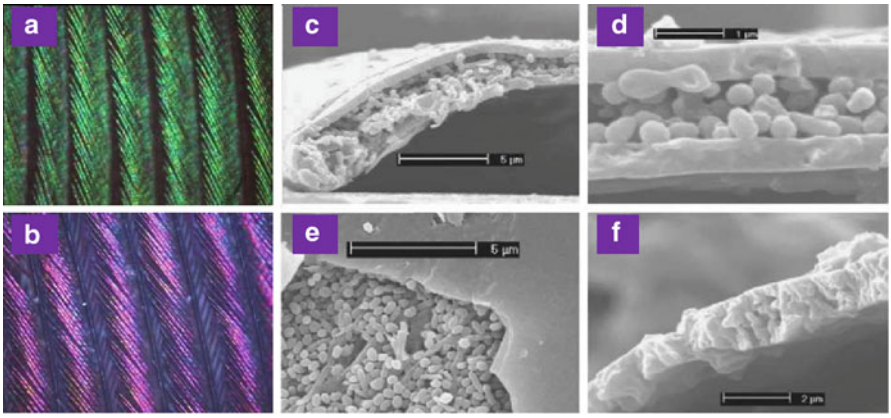

Fig. 8.9 (**a**) and (**b**) Optical microscopic images of iridescent green and purple neck feathers of domestic pigeons under 100× magnification, respectively. (**c**)–(**f**) SEM images of iridescent barbules. (**c**) Perspective view of the cross-section of a green barbule. (**d**) Transverse cross-section of a purple barbule. (**e**) Perspective top view of a green barbule with the top keratin cortex layer removed (lower left corner). (**f**) Perspective view of the cross-section of a gray barbule. Scale bars: (**c**) and (**e**) 5 μm; (**d**) 1 μm; and (**f**) 2 μm (Reproduced from [41])

shapes of spheres, ellipses, and rods, and also a small amount of randomly dispersed keratin. The outer surface of the keratin cortex is rather smooth. Green and purple barbules show different thicknesses. For green barbules, the mean thickness is about 595 nm, while it is about 530 nm for purple barbules. Different from the iridescent barbules, gray barbules are a single uneven layer composed of randomly dispersed keratin and melanin granules, leading to gray colors.

The iridescent neck feathers of domestic pigeons display interesting *opposite* iridescence. Namely, green feathers become purple with the observing angle varying from normal to oblique, while simultaneously purple feathers become green. This can be clearly seen from the measured reflection spectra for iridescent neck feathers at different incident angles, shown in Fig. 8.10. Under normal incidence, iridescent green feathers display a series of harmonic reflection peaks, positioned at about 415, 530, and 730 nm, corresponding to violet, green, and red colors, respectively. With increasing incident angle, all reflection peaks show a blue shift to a shorter wavelength. The violet reflection peak at normal incidence shifts to UV, the green reflection peak to blue, and the red reflection peak to orange. These harmonic reflection peaks can be easily understood by thin-film interference. Although there are two cortex layers, only the dorsal cortex layer gives rise to structural coloration. This is due to the fact that the central layer sandwiched by the two cortex layers is composed of randomly dispersed melanin particles such that light will be absorbed or randomly scattered by this layer. It can also be confirmed by the fact that no colors can be seen if the dorsal cortex layer is removed. Therefore, the central layer

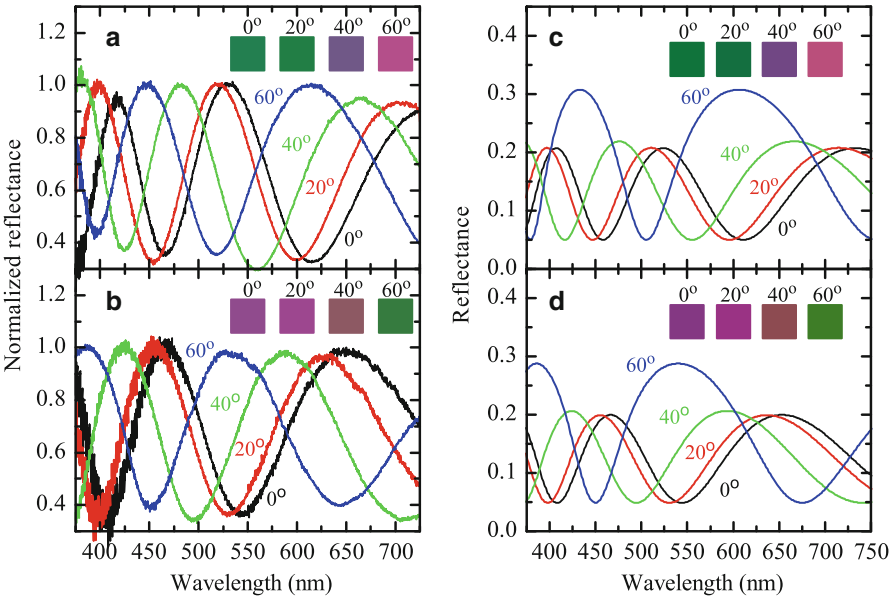

Fig. 8.10 Measured and predicted reflection spectra of iridescent neck feathers of domestic pigeons for unpolarized light at different incident angles. (**a**) and (**b**) Normalized measured results for green and purple feathers, respectively. (**c**) and (**d**) Predicted results for a thin film with a thickness of 595 and 530 nm mimicking green and purple barbules, respectively. The converted RGB colors from the reflection spectra at different incident angles are shown in insets (Reproduced from [41])

plays a role of a poor mirror.[4] As a result, the observed reflectance R should result from the interference in the dorsal cortex layer combined with the reflection from the poor mirror, namely,

$$R = R_1 + (1 - R_1)R_2(1 - R_1), \tag{8.6}$$

where R_1 is the reflectance of the dorsal cortex alone and R_2 is the reflectance of the poor mirror. From experiments, we can determine $R_2 \sim 5\%$ by measuring the region in a barbule where the dorsal cortex layer is removed.

For a thin film in air, its reflectance is given by [23]

$$R_1 = \frac{4r^2 \sin^2\left(2\pi d\sqrt{n^2 - \sin^2\theta}/\lambda\right)}{(1 - r^2)^2 + 4r^2 \sin^2\left(2\pi d\sqrt{n^2 - \sin^2\theta}/\lambda\right)}, \tag{8.7}$$

[4]The central layer may not completely absorb impinging light, and thus acts as a poor mirror with a very low reflectivity.

where λ is wavelength in vacuum, θ is the incident angle, d and n are the thickness and refractive index of the thin film, respectively, and r is the reflection coefficient. For s and p polarizations, the reflection coefficients r are different, given by

$$r_s = \frac{\cos\theta - \sqrt{n^2 - \sin^2\theta}}{\cos\theta + \sqrt{n^2 - \sin^2\theta}}, \qquad r_p = \frac{n^2\cos\theta - \sqrt{n^2 - \sin^2\theta}}{n^2\cos\theta + \sqrt{n^2 - \sin^2\theta}}. \tag{8.8}$$

For unpolarized light, the reflectance of a thin film is the superposition of those from both s and p polarizations, namely, $R_1 = (R_{1s} + R_{1p})/2$, where R_{1s} and R_{1p} are the reflectance for s and p polarizations, respectively.

For a keratin thin film with a refractive index of 1.54 and a thickness of 595 and 530 nm, mimicking respectively the green and purple barbules, the calculated reflection spectra for unpolarized light at different incident angles, obtained from the above equations, are in good agreement with the measured ones. The converted RGB colors from the measured and calculated reflection spectra, shown in the insets of Fig. 8.10, can well reproduce the observed opposite iridescence: green feathers change their coloration from green to purple with the viewing angle varying from normal to oblique, while purple feathers alter their coloration in an opposite way, i.e., from purple to green. This is rather meaningful for color vision since both green and purple colors can be perceived no matter what the perspective angle is, or how the green and purple feathers are arranged. This strategy of opposite iridescence may provide an optimal way for signalling and communication. For multilayers, however, it is difficult to achieve such opposite iridescence. It can thus be concluded that the exploitation of a single thin film for iridescent coloration in neck feathers of domestic pigeons might not be accidental.

Another interesting feature is the optical function of the poor mirror. Without the poor mirror underneath, the peak reflectance of the keratin thin film is less than 17%, and the reflection minimum is zero [41]. With the introduction of the poor mirror, the peak reflectance increases to 20%, and the reflection minimum also increases to about 5%. The poor mirror can thus raise the overall reflectance. Without this poor mirror it is difficult to perceive the iridescent colors in a white background, similar to the case for insect wings [38]. With the poor mirror the color visibility can be largely enhanced since the poor mirror acts also as a black background.

8.5.2 Multilayer

Multilayers are those consisting of alternating layers of materials with different refractive indices. For multilayers, the mechanism of structural coloration is basically similar to that for single thin films, namely, thin-film interference. In general, structural colors produced by multilayers are much brighter than those by single thin films. This is due to multiple interference from the successive interfaces. Multilayers are the most common form of structural coloration in the biological world, appearing, e.g., in insects, fishes, and even plants [7–9, 44–46].

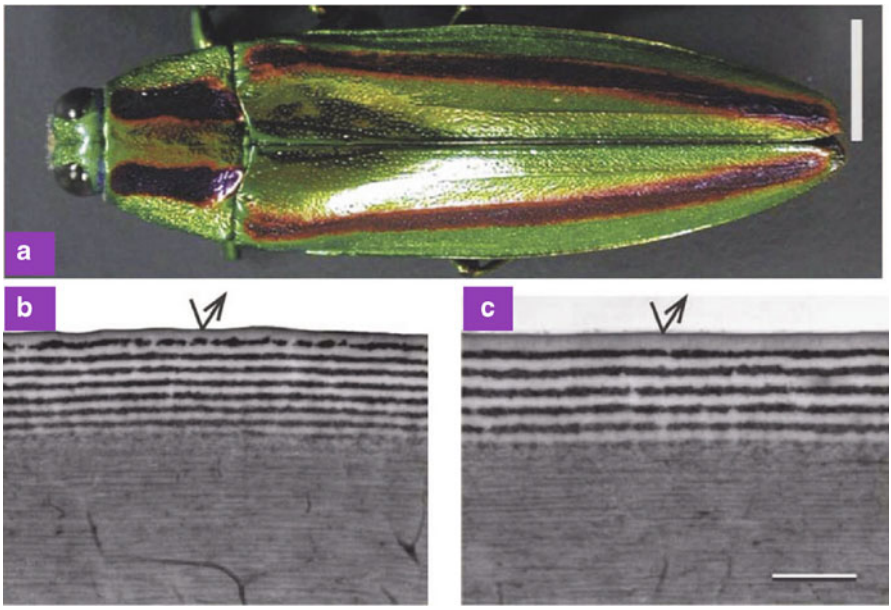

Fig. 8.11 (**a**) Dorsal view of a female Japanese jewel beetle *C. fulgidissima*. (**b**) and (**c**) TEM images of green and purple sections of the beetle elytra, respectively. Scale bars: (**a**) 0.5 cm; and (**b**) and (**c**) 1 μm (Reproduced from [50])

The elytra of some beetles, e.g., the jewel beetles [21], display brilliant, metallic structural colors which are caused by a multilayer in the cuticle. For the buprestid beetle *Euchroma gigantea*, Durrer and Villinger [47] examined its elytra by TEM and revealed an epicuticle multilayer consisting of five melanin layers with a thickness of 60–80 nm embedded in chitin at a regular distance of 60 nm. This multilayer was found to be the basis of color production of the elytra. Similar multilayers were also found in other Buprestidae, e.g., the jewel beetles *Chrysochroa vittata* [48, 49], *Chrysochroa fulgidissima* [8, 50], and *Chrysochroa raja* [51].

Figure 8.11 shows the Japanese jewel beetle *C. fulgidissima* [50]. The elytra of this beetle are metallic green marked with longitudinal purple stripes. Because of the striking iridescence and beautiful luster, this jewel beetle was used as ornament in ancient Japanese times. TEM characterizations revealed that the epicuticle of the green and purple areas consists of stacks of 16 and 12 layers, respectively. The corresponding period for green and purple areas are 160 and 205 nm, respectively. Simulations revealed that both green and purple colors are created by a multilayer with a surprisingly small gradient refractive-index range of 1.6–1.7. The multilayer in the cuticle exhibits both strong angle and polarization iridescence, which is a known optical property for multilayers. The angle dependence can be understood by the fact that the optical path difference between reflected light at successive interfaces differs at different incident angles, which leads to iridescence.

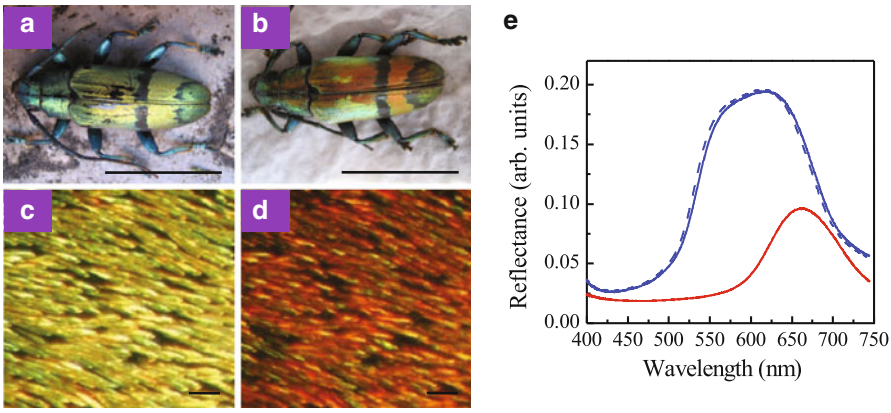

Fig. 8.12 Optical images of the beetle *T. isabellae* in the dry (**a**) and wet (**b**) states. The iridescent golden color in the dry state is able to change to red in the wet state. (**c**) Close-up image of the golden colored region of the elytra in the dry state. In the colored region the elytral surface is densely imbricated with colored scales. (**d**) Same as (**c**) but in the wet state. The color of the scales becomes red. (**e**) Measured reflection spectra of the colored region of the elytra in the dry (*solid blue line*) and fully wet (*solid red line*) under normal incidence. The spectrum for the redried elytra is shown by a *dashed blue line*. Scale bars: (**a**) and (**b**) 10 mm; and (**c**) and (**d**) 100 μm (Reproduced from [53])

Polarization effects, on the other side, can be understood by the fact that *s*- and *p*-polarized light undergoes different reflection and refraction at each interface. Specifically, there exists a brewster's angle for *p* polarization at which reflection is zero.

In addition to cuticles, multilayers also exist in the scales on the elytra of some beetles, e.g., the chaffer beetle *Hoplia coerulea* (Coleoptera) [52]. This beetle belongs to the large family of *Scarabaeidae*. The elytra of the male beetle display a spectacular iridescent blue–violet color. This blue–violet iridescent coloration was found to originate from a multilayer structure in the scales on the elytra. The structure consists of a stack of planar sheets separated by a well-organized network of spacers. It can be approximately viewed as a multilayer. Another example was found in the scale of the beetle *Tmesisternus isabellae* with interesting tunable structural coloration [53].

The beetle *T. isabellae* belong to a large family of longhorn beetles. The colored region of the elytra displays an iridescent golden color in the dry state, as shown in Fig. 8.12. With water dropped onto, the golden color can turn into red within a few minutes. The colored region can recover the golden color by returning to the dry state through evaporation. The colored region of the elytra is composed of long and flat scales, responsible for the metallic golden color. In the dry state the measured reflection spectrum of the colored region is characterized by a broad peak positioned at about 600 nm, showing a golden color. In the wet state, however, the reflection peak is shifted to 662 nm, showing a red color.

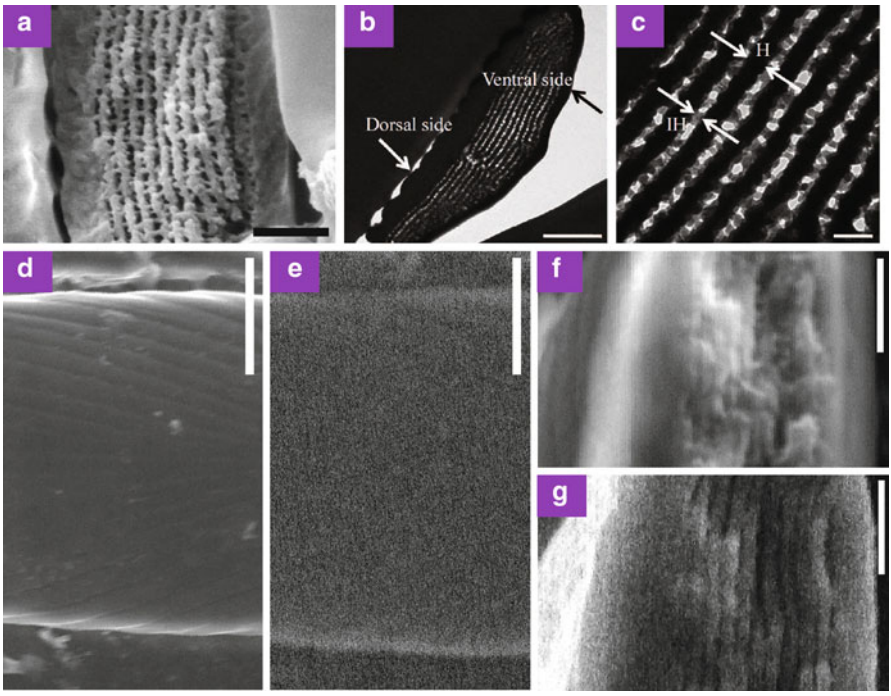

Fig. 8.13 (**a**) Cross-sectional SEM image of a scale of the beetle *T. isabellae* in the dry state. (**b**) and (**c**) Cross-sectional TEM images of a scale in the dry state. (**d**)–(**g**) ESEM images of a scale. (**d**) Top view of the dorsal side in the dry state. (**e**) Top view of the dorsal side in the fully wet state. (**f**) and (**g**) Transverse cross-sections in the dry and fully wet states, respectively. Scale bars: (**a**) 1 μm; (**b**) 2 μm; (**c**) 0.5 μm; (**d**) and (**e**) 5 μm; and (**f**) and (**g**) 1 μm (Reproduced from [53])

The microstructures of the scales in the dry state were characterized by SEM and TEM, as shown in Fig. 8.13a–c. Cross-sectional SEM images revealed a multilayer structure in the interior of the scales. The thickness of the scales is about 3 μm. As seen from both SEM and TEM images, the multilayer is composed of two alternating layers. The first one is a homogeneous layer (dark layers in TEM images) and the second one is an inhomogeneous layer. The inhomogeneous layer consists of nanoparticles (gray areas in TEM images) and air voids (bright areas in TEM images). The number of periods of the multilayer in different regions is different. In the central region of a scale, it is about 10. The thickness of the homogeneous layers is about 105 nm while it is about 70 nm for the inhomogeneous layers.

In order to get insight into the color change of the scales, environmental SEM (ESEM) was used to measure the change in the microstructure of the scales in the wet state, shown in Fig. 8.13d–g. Scales swell noticeably after water absorption. Close-up images show that both the cortex and the multilayer swell in the wet state. The swelling of both the cortex and multilayer is due to the water absorption. The period of the multilayer swells from about 175 nm in the dry state to about 190 nm

in the fully wet state. From cross-sectional ESEM images we can determine that the thickness of the homogeneous layers in the fully wet state swells to about 120 nm, while the thickness of the inhomogeneous layers remains nearly unchanged. The swelling of the period of the multilayer can cause a color change from golden in the dry state to red in the wet state. Furthermore, it could be proved from calculated reflection spectra that the air voids in the wet state are filled with water, since the intensity of reflection in the wet state is much smaller than that in the dry state.

In the biological world, many animals can change their coloration in response to environmental stimuli. The adaptive values of color changes are usually regarded as camouflage, signal communication, conspecific recognition, and reproductive behavior. In principle, color changes can occur via the change in pigment, microstructure, or their combination. Although the precise functionality of the tunable structural coloration in the beetle *T. isabellae* is not clear, the reversible structural color change may certainly render more options for both adaption and function. Owing to its unique properties, tunable structural colors could open new avenue to the applications in display and imaging technology, printing and painting, textile industry, sensing, and photonic devices [54, 55].

In butterflies, there exist also structures closely similar to multilayers which give rise to structural colors. The most significant example may be the *Morpho* butterflies, one of the most representative animals that display brilliant structural colors. In most of the *Morpho* butterflies, the dorsal wings of the male display a brilliant blue color, while their ventral side is usually dark brown in color. Along the direction perpendicular to the wing veins, the blue color shows a weak viewing-angle dependence. Only at large oblique viewing angles the blue color will change rather abruptly to dark blue or violet. Along the direction of the wing veins, however, the blue color will disappear abruptly with increasing viewing angles. This fascinating iridescence in the *Morpho* butterflies has drawn considerable attention of scientists [10, 11, 16, 20, 56–65].

The wings of the *Morpho* butterflies are covered with rows of partially overlapping scales. Various forms of scales are present depending on the species and the wing positions. In the blue iridescent region of the wings, there exist usually two kinds of scales: cover scales (glass scales) and ground scales (basal scales) that lie beneath cover scales. Typical ground scales are rectangular and their dimensions are of the order of 0.1×0.2 mm^2. Figure 8.14 shows a *Morpho* butterfly, *Morpho rhetenor*, its scales, and scale microstructures [60]. The wings of *M. rhetenor* have one layer of highly iridescent ground scales on its dorsal wing surface. The top surface of the ground scales exhibits periodic rows of ridges that extend longitudinally from one end of the scale to the other. Each ridge contains a bookshelf-like multilayer, responsible for the blue structural color. Structural coloration in the wings is determined by many factors such as the geometrical structure of the discrete multilayer and the arrangement of the ridges. The discrete multilayer can produce interference while the ridges and the discrete multilayer itself can give rise to diffraction. As a result, the blue structural color in the *Morpho* butterflies stems from the interplay of interference and diffraction. The parallel ridges can offer a strong anisotropic reflection, while the irregularity in the ridge

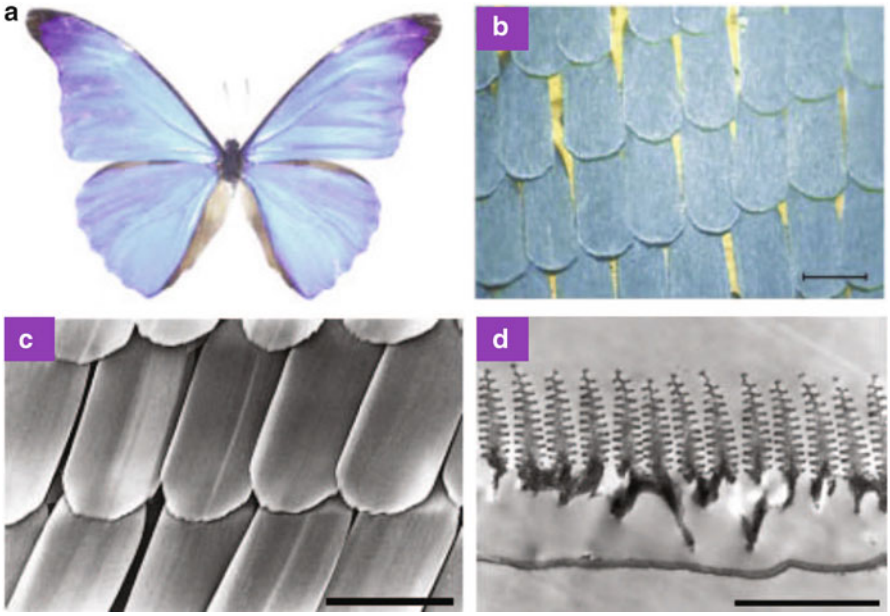

Fig. 8.14 (**a**) Optical image of the butterfly *M. rhetenor*. (**b**) Optical microscopic image of the dorsal wing showing the ordered arrangement of a single layer of ground scales. (**c**) SEM image of the scales. (**d**) Cross-sectional TEM image of an iridescent ground scale. Scale bars: (**b**) 100 μm; (**c**) 120 μm; and (**d**) 3 μm (Reproduced from [60])

height and the small ridge width can eliminate the interference between scattered light from the neighboring ridges, leading to a weak viewing-angle dependence for the blue structural color.

In other butterfly species, e.g., *Ancyluris meliboeus*, similar discrete multilayers were also found, responsible for the wing coloration [66]. These multilayers are highly titled to the base of scales, leading to a strong color flicker contrast from minimal wing movement.

In addition to insects, multilayer structures are also present in spiders. The jumping spider *Cosmophasis umbratica* is a highly ornamented species from Singapore, as shown in Fig. 8.15. Many parts of the male's body are covered with green-orange scales. These scales possess a chitin–air–chitin sandwich structure, which can reflect both the visible and UV light [67]. This spider has an intriguing sexual recognition system that involves the use of UV light. During courtship, the males display their reflecting parts in front of the females. The females tend to accept those males who can reflect more UV light [68].

Although rare, multilayer structures exist also in plants [69–76]. Blue-green iridescent leaves can be usually found in certain understory plants growing in moist and low light environments of tropical rainforests. The first example of a multilayer in plants was found in the leaves of the lycophyte *Selaginella willdenowii* [69, 70].

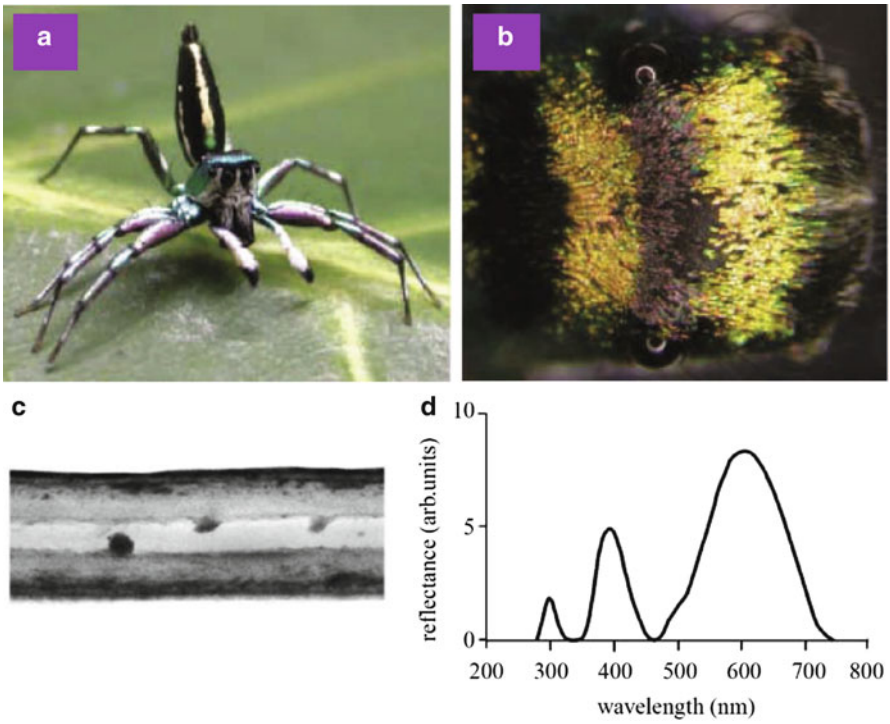

Fig. 8.15 (**a**) Male jumping spider *C. umbratica*. (**b**) Dorsal view of the cephalothorax, showing two bars of green-orange reflecting scales. (**c**) Cross-sectional TEM image of a colored scale, showing a sandwich structure. (**d**) Measured reflection spectrum of the colored scales (Reproduced from [67])

The multilayer in *S. willdenowii* consists of two alternating layers with a period of about 80 nm at the outer cell wall of the adaxial epidermis, producing blue structural coloration. Similar multilayers exist also in the leaves of the Malaysian rain forest understory plants *Diplazium tomentosum*, *Lindsaea lucida*, *Begonia pavonina*, and *Phyllagathis rotundifolia* [72], as shown in Fig. 8.16a–c. Iridescent leaves were also found in the ferns *Danaea nodosa* and *Trichomanes elegans* [71], as well as in the angiosperms *Phyllagathis rotundifolia* and *Begonia pavonina* [72]. In *D. nodosa* there exists a multilayer of cellulose microfibrils in the adaxial cell walls of the adaxial epidermis. In *T. elegans* the blue-green coloration is caused by a multilayer with a remarkably uniform thickness and arrangement of grana in specialized chloroplasts adjacent to the adaxial wall of the adaxial epidermis. In both *B. pavonina* and *P. rotundifolia* the blue-green coloration is caused by a multilayer of parallel lamellae in specialized plastids adjacent to the abaxial wall of the adaxial epidermis.

Multilayer structures were also found in the fruits of *Elaeocarpus angustifolius* and *Delarbrea michiana*, as shown in Fig. 8.16d, producing brilliant blue coloration

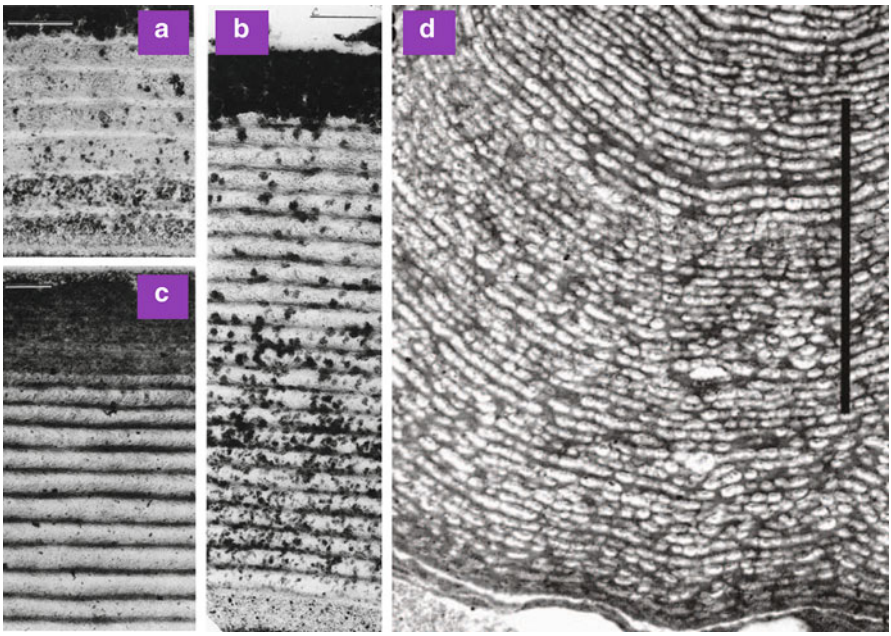

Fig. 8.16 TEM transverse section through helicoidal cell wall in adaxial epidermis of an iridescent green leaf (**a**) and an iridescent blue leaf (**b**) from *D. tomentosu*. (**c**) TEM transverse section through helicoidal cell wall in adaxial epidermis of an iridescent blue-green leaf from *L. lucida*. (**d**) TEM image of the iridisome in the fruits of *D. michieana*, showing an iridescent blue color. Scale bars: (**a**)–(**c**) 0.5 μm; and (**d**) 2 μm ((**a**)–(**c**) Reproduced from [72] and (**d**) from [75])

[74, 75]. The multilayers are so-called "iridisomes" which are within the epidermal cells. The molecular basis of iridosome is primarily cellulose, forming a layered structure that can cause structural coloration via interference.

Structural coloration in plants may have some adaptive benefit, similar to that in animals. Blue coloration in plant leaves may increase the capture of photosynthetically important wavelengths, and may also be exploited as a visual defence against herbivores or as a photoprotective mechanism to protect shade-adapted plants against sun-flecks and other potentially damaging [70]. On the other side, such structural coloration in fruits may aid in attracting mammals and large frugivorous birds, and may also allow ripe fruits to continue photosynthetic carbon assimilation [75].

In addition to simple periodic multilayers in the biological world, there also exist modified multilayers. These modified multilayers include chirped [77–81], chiral [10, 71–73, 82–92], and sculpted multilayers[93–96], which can produce interesting structural coloration and may possess some intriguing selective advantages.

A periodic multilayer is a structure consisting of alternating layers of low- and high-refractive indices (bilayers) with an identical bilayer thickness. In contrast, the bilayer thickness in a chirped multilayer changes progressively with depth.

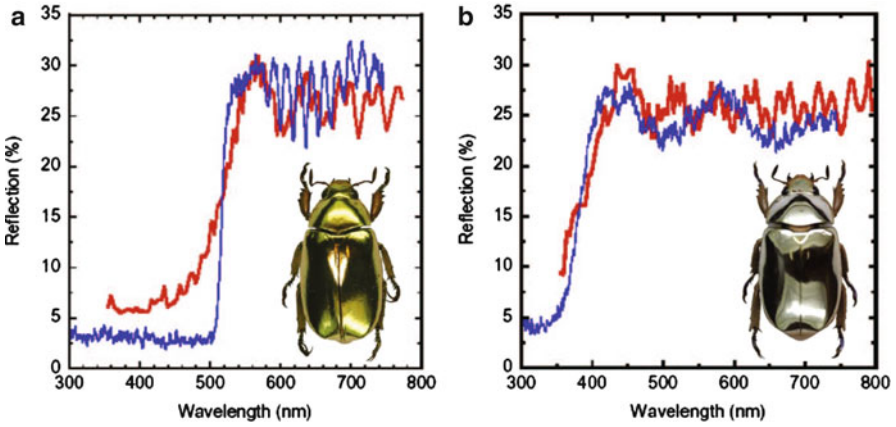

Fig. 8.17 Measured (*blue lines*) and calculated (*red lines*) reflection spectra for *C. aurigans* (**a**) and *C. limbata* (**b**). Calculated results are based on chirped multilayers with linearly decreasing values in the thickness of the sequence of layers (Reproduced from [81])

A periodic multilayer can produce high reflections over a narrow wavelength range.[5] However, a chirped multilayer produces wide-band reflections. This is because for different wavelengths constructive interference occurs for the layers with different *correct* thicknesses, which can result in silvery or golden coloration. For example, certain scarabaeid and tortoise beetles, and lepidopteran larvae and pupae exhibit silvery or golden hues which are caused by chirped multilayers [77].

In the pupaes of the butterflies *Amauris ochlea* and *Euplorea core*, most of their cuticles display a strong metallic golden or silvery luster. Electron microscopic observations revealed a chirped multilayer consisting of up to 250 pairs of bilayers in the exocuticle [78, 79]. The most striking example of metallic golden or silvery coloration may be given by the Coleoptera *Chrysina aurigans* and *Chrysina limbata* [81]. *C. aurigans* displays a brilliant golden color, while *C. limbata* shows a brilliant silvery color, as shown in Fig. 8.17. Chirped multilayers with linearly decreasing values in the thickness of the sequence of layers were assumed, which could result in reflection spectra in good agreement with the measured ones. Metallic silvery coloration is due to a chirped multilayer with constituent layers that can reflect all visible wavelengths. However, in a chirped multilayer without suitable constituent layers that can reflect blue and violet light, metallic golden coloration can be achieved.

Conventional photonic media do not produce circular dichroism. In other words, there is no distinction between left- and right-handed circular polarizations. In contrast, there may exist strong circular dichroism in chiral media. It was shown for the first time by Michelson in 1911 that some scarab beetles can differentially

[5] In other words, the resulting structural color is bright and highly saturated.

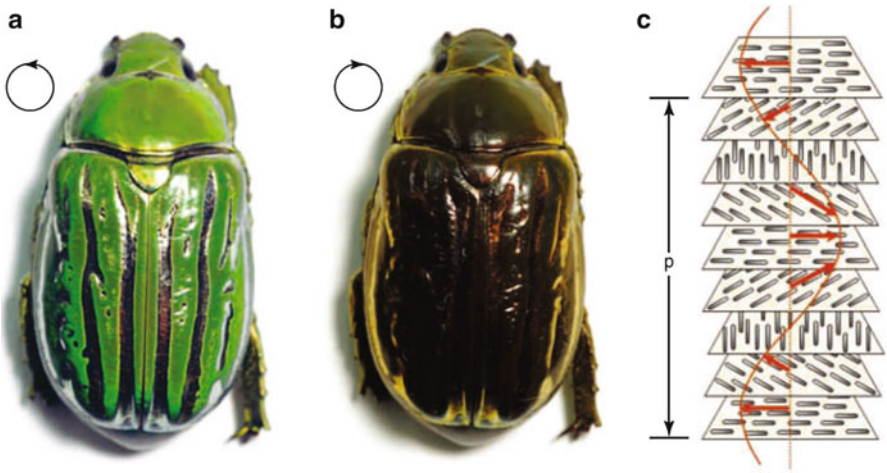

Fig. 8.18 Beetle *C. gloriosa* seen under unpolarized light or with a left-handed circular polarizer (**a**) and with a right-handed circular polarizer (**b**). In (**a**) the bright green color with silvery stripes can be seen. In (**b**) the green color is mostly lost. (**c**) Schematic representation of twisted arrangement of a chiral multilayer structure (Reproduced from [92])

reflect circularly polarized light [10]. The ability to reflect circularly polarized light in certain beetles has attracted considerable attention for nearly a century [82–92]. Ellipsometric measurements confirmed that scarab beetles can reflect predominately the left-handed circular polarization at visible wavelengths. In some cases, however, there is a tendency to reflect the elliptical or right-handed circular polarization at red and near infrared wavelengths [90].

The jeweled beetle *Chrysina gloriosa* possesses a brilliant metallic green color and can reflect selectively the left-handed circularly polarized light [92], as shown in Fig. 8.18. The exocuticle of the beetle consists of many layers of microfibrils aligned parallel with each other, causing a preference for light polarized along the direction of the fibers. Each layer is rotated slightly relative to the layer above, forming a helicoidal stack twisting in the left handedness. This alignment of the layers enables the reflection of the left-handed circularly polarized light, a phenomenon similar to that in cholesteric liquid crystals.

This circularly polarized reflection was also found in some plant species [71–73]. The multilayers found in the outer epidermal cell walls of some iridescent plants produce more elaborate structures, alternating with arcs of cellulose microfibrils. The angle of the cellulose microfibrils changes gradually through the alternating layers up to a total of 180° rotation. The resulting helicoidal structure is remarkably similar to the helical stack of chitin microfibrils, and may be an example of convergent evolution [73].

Most of the multilayers in the biological world take the form of flat layers to produce structural coloration. In flat multilayers, the resulting structural colors are usually very conspicuous and strongly iridescent. However, there exists also a

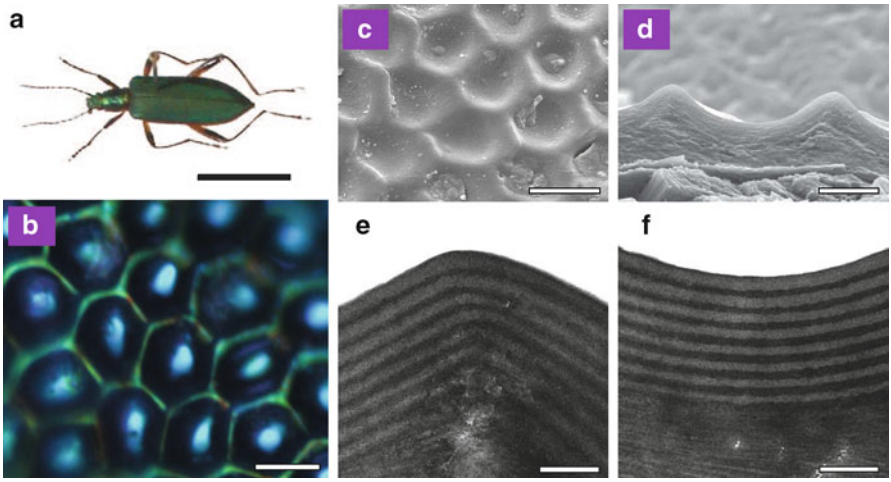

Fig. 8.19 (**a**) Optical image of a male beetle *C. obscuripennis*. Its elytra display an inconspicuous iridescent blueish green color. (**b**) Optical microscopic image of an elytron under 1,000× magnification. (**c**) SEM top view of the outer elytral surface. The elytral surface is composed of an array of hexagonal pits. (**d**) Transverse SEM cross-section of the outermost elytra surface. (**e**) and (**f**) Transverse TEM cross-sections of the ridge and basin regions, respectively. Scale bars: (**a**) 1 cm; (**b**) 5 μm; (**c**) 10 μm; (**d**) 5 μm; and (**e**) and (**f**) 0.5 μm (Reproduced from [96])

special form of multilayers in the biological world, sculpted multilayers [93–95] that can produce structural colors different in many ways from those in flat multilayers, e.g., inconspicuous structural coloration. The adoption of an inconspicuous green color by sculpted multilayers may be more advantageous for camouflage against green backgrounds [94, 95], especially on diffuse leafy surfaces.

Sculpted multilayers found for the first time might be those in the elytra of tiger beetles (Carabidae: Cicindelinae) [93]. The elytral surfaces are in the form of a hexagonal array of pits, and the multilayer in the elytra conforms with the profile of the pits in a sculpted way. The reflecting sculpted multilayer at the basins and ridges possesses different periods and hence cause different structural colors, leading to "pointillistic" color mixing.

A similar sculpted multilayer occurs also in the beetle *Chlorophila obscuripennis* (Coleoptera) [96], as shown in Fig. 8.19. Unlike other beetles, this beetle shows a very inconspicuous iridescent blueish green color. The SEM top-view image shows that the outer surface of the elytra is not flat; instead, it comprises an array of hexagonal pits. Compared with the optical microscopic images, there exists an exact correspondence between the surface morphology and the observed color pattern: the pit ridges produce a green color, the basins a cyan color, and the inclined sides a dull blue color. All these colors change with the viewing angle. From the transverse cross-sectional images, the pits are about 11 μm in size and about 2.8 μm in depth. From TEM images, the sculpted multilayer consists of about 16 thin layers with alternating low and high electron densities, which are the cause of

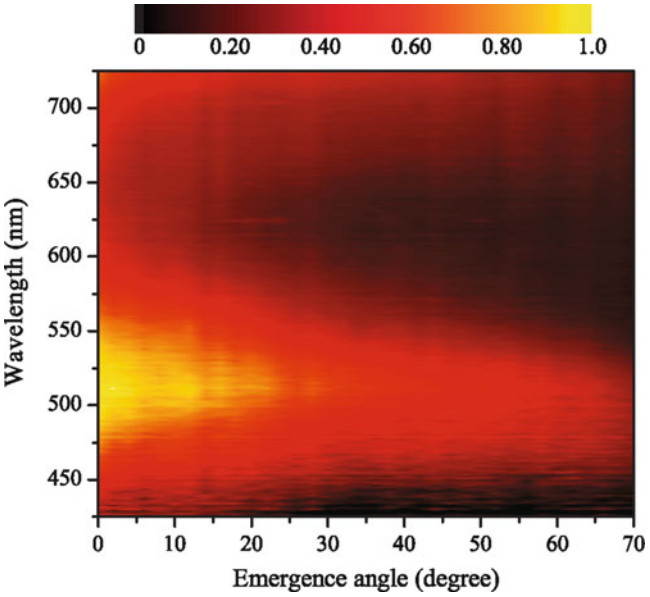

Fig. 8.20 Measured relative emergence intensity for an elytron of the male beetle *C. obscuripennis* as a function of wavelength and emergence angle at normal incidence. The emergence angle is defined as the angle of reflected light with respect to the elytral surface normal. The intensity of non-specular reflection is smaller than that of specular reflection. For normal incidence, non-specular reflection occurs mainly at emergence angles that are smaller than 20°. The intensity of non-specular reflection decreases with increasing emergence angle. At small emergence angles, non-specular reflection is dominant at wavelengths around 520 nm, but at large emergence angels it is dominant at slightly lower wavelengths (Reproduced from [96])

the elytral structural coloration. The layer with low electron density is chitin. By chemical treatments [93], the layer with high electron density was determined to be melanoprotein. The average thickness of both chitin and melanoprotein layers shows distinct differences in different regions. The average thickness of the chitin layer is about 90, 85, and 78 nm at the ridge, the inclined side, and the basin, respectively. For the melanoprotein layer its average thickness in different regions is nearly the same, about 66 nm.

Sculpted multilayers can produce optical effects different from flat ones. In flat multilayers, only specular reflection is expected, leading to conspicuous structural coloration. In contrast, both specular and non-specular reflections exist in sculpted multilayers. Owing to the surface profile, the effective area for specular reflection in a sculpted multilayer is much smaller than that in a flat multilayer. This will lead to inconspicuous structural coloration. In addition to specular reflection, a sculpted multilayer can also render non-specular reflection, giving rise to light emergence at directions of non-specular reflection, as shown in Fig. 8.20. A resulting consequence is that structural coloration can be perceived in a much wider range of viewing angles. This feature may be of significance in signal communication and conspecific recognition.

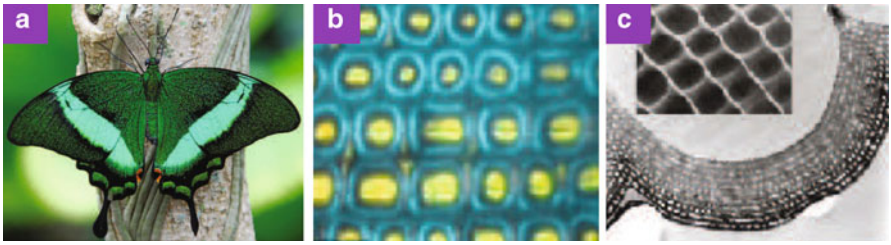

Fig. 8.21 (**a**) Indonesian male butterfly *P. palinurus*. (**b**) Close-up optical image of the surface of a *P. palinurus* iridescent scale, showing the dual-color nature. (**c**) Cross-sectional TEM image showing one concavity on a *P. palinurus* iridescent scale. The inset is the SEM image of the surface of an iridescent scale (Reproduced from [97])

In the wing scales of the Indonesian male butterfly *Papilio palinurus* [97], there also exits a sculpted multilayer, as shown in Fig. 8.21. The bright green coloration of the wing scales is caused by this ingeniously designed sculpted multilayer, which enables the reflection of yellow light at normal incidence from the base of each concavity and blue light through a double reflection from the opposite and perpendicularly inclined sides of each pit, producing a blue annulus with a yellow center. In the beetle *C. obscuripennis* shown in Fig. 8.19, however, the inclined sides produce a dull blue, giving a minor contribution to color mixing. The production of a blue color at the inclined sides in the *P. palinurus* butterfly lies in the double reflection by a pair of orthogonal surfaces inclined about 45° to the scale surface. At normal incidence, reflected light from one inclined surface is directed across to its adjacent inclined side, where it is reflected back to the incident direction. In the beetle *C. obscuripennis*, the inclined angle is, however, much smaller than 45°. Moreover, the pits in the beetle *C. obscuripennis* is hexagonal rather than square in the butterfly *P. palinurus*. As a result, at normal incidence double reflection cannot cause light emergence back to the incidence direction. Nevertheless, at oblique incidence we may still observe a dull structural color produced by the inclined sides (see Fig. 8.19b).

In the Madagascan sunset moth *Chrysiridia rhipheus*, curved multilayers were found showing interesting features [20, 98, 99]. The wings of *C. rhipheus* exhibit a striking iridescent pattern from the arranged scales, as shown in Fig. 8.22. The scales consist of a stack of three to six thin layers and are highly curved from the root to the distal end. Owing to this strong curvature, a valley-like deep grooved structure is present between adjacent two rows of the regularly arranged scales. The combination of the grooved structure and the multilayer gives rise to two different colors: one is the direct reflection from the top flat part of the scales, and the other is the dual reflection between adjacent scales. This color mixing is also strongly polarization-sensitive even under unpolarized illumination, because the reflectivity is naturally different for *s* and *p* polarizations.

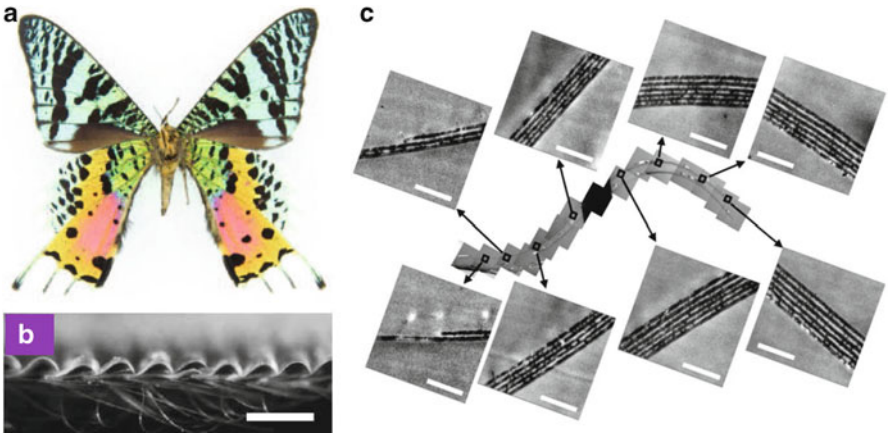

Fig. 8.22 (**a**) Ventral side of a Madagascan sunset moth *C. rhipheus*. (**b**) SEM image of a longitudinal cross-section of the hind wing. (**c**) Cross-sectional TEM image of a cover scale in the longitudinal direction. The enlarged views at various positions are given in the insets. Scale bars: (**b**) 300 μm and (**c**) 2 μm (Reproduced from [98])

8.5.3 Diffraction Grating

Diffraction gratings can generate structural colors by diffraction. In addition to the specular reflection (zero-order diffraction), light can be diffracted at non-specular angles. For natural light, the zero-order diffracted light should be white in color. For a fixed observing angle that differs from the specular one, diffracted light with wavelengths that satisfy the grating equation (8.3) can be perceived. By varying the observing angle, color changes can be seen, leading to iridescence. The ability to disperse spectral light spatially renders diffraction gratings as an indispensable optical element [100]. Diffractive colors and their intensity and spatial distributions depend on many parameters such as the grating period, grating morphology, and refractive index of the grating.

The first revealed biological diffraction grating was probably the one found in 1942 by Anderson and Richards [56] on the elytra of the scarab beetle *Serica sericea*. This dark brown beetle possesses line gratings on its elytra with a period of 800 nm, which can produce brilliant iridescent colors. A taxa list of beetles with cuticular diffraction gratings was described later by Hinton and Gibbs [101–107]. Diffraction gratings are widespread in beetles in 1D as well as 2D forms [46, 108, 109], as shown in Fig. 8.23.

The beetle *Sphaeridiinae gen.* sp. (Hydrophilidae) displays bright diffractive colors caused by an ordered diffraction grating on its elytral surface, as shown in Fig. 8.23a. Up to the third-order diffraction can be clearly seen. The zero-order diffraction is just the specular reflection, showing a bright white appearance. Higher-order diffraction creates interesting rainbow-like spectral colors. Unlike that in the beetle *Sphaeridiinae gen.* sp., the cuticular diffraction grating in the

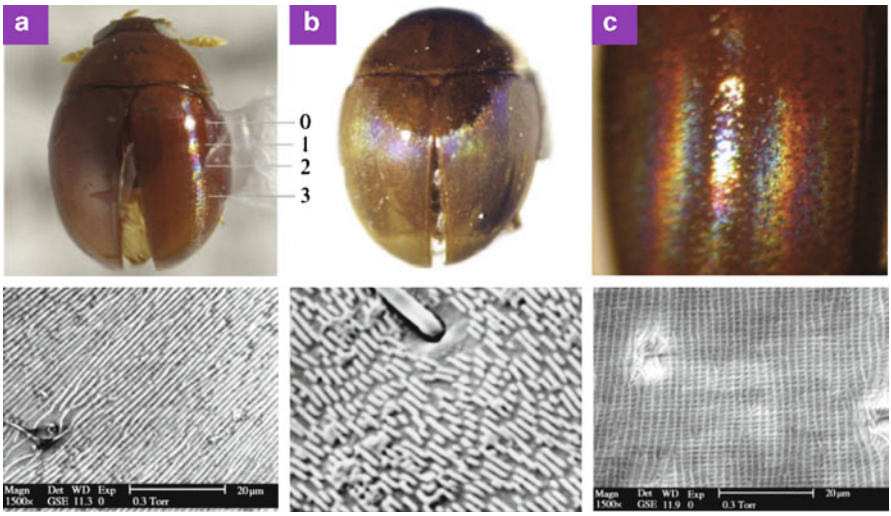

Fig. 8.23 Beetles showing diffractive structural colors (*upper panels*) and corresponding nanostructures of diffraction gratings (*lower panels*). (**a**) Beetle *Sphaeridiinae gen.* sp. and SEM image of the cuticular diffraction grating. Labels indicate the zero-, first-, second-, and third-order diffractive colors. (**b**) Beetle *A. tumerus* and SEM image of the quasi-ordered, discontinuous cuticular diffraction grating. (**c**) Beetle *Pallodes* sp. and SEM image of the 2D cuticular diffraction grating (Reproduced from [46])

beetle *Aglyptinus tumerus* (Leiodidae: Leiodinae) is not very ordered, as shown in Fig. 8.23b. It consists of weakly parallel, discontinuous ridges, but still can diffract incident light and produce structural colors.

In addition to 1D gratings, there also exist 2D diffraction gratings. In a 1D diffraction grating, it cannot diffract light along the direction perpendicular to the grating. In contrast, 2D diffraction gratings can diffract light in all azimuth angles. The beetle *Pallodes* sp. displays a spectral "halo" on its elytra around the point of the specular reflection, which is caused by a 2D cuticular diffraction grating, as shown in Fig. 8.23c.

Some marine animals also use diffraction gratings to produce iridescent colors. One example is the halophores (hairs) on the first antenna of the seed-shrimp *Azygocypridina lowryi* (ostracod) [110], as shown in Fig. 8.24. The halophores possess a diffraction grating with a period of about 600 nm on the surface. The colors on the halophores are caused by this diffraction grating. Different diffraction colors are due to the different orientations of the halophores.

In addition to animals, diffraction gratings also exist in plants, e.g., on the petals of the flowers *Tulipa* sp., *Hibiscus trionum*, and *Mentzelia lindleyi* [111, 112], as shown in Fig. 8.25. In these species, the petal epidermal cells are elongated and flat. In white epidermis, the epidermal cell surface is smooth. In contrast, the pigmented (dark) epidermal cell surface is microscopically uneven, marked with microscopic striations. These striations are nearly periodically arranged, acting as a diffraction

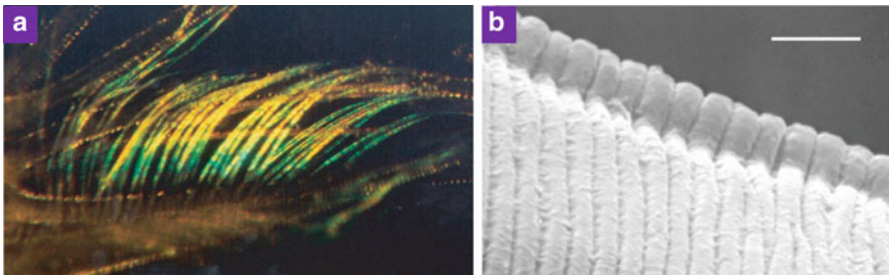

Fig. 8.24 (**a**) Halophores (hairs) on the first antenna of seed-shrimp *A. lowryi* (ostracod). (**b**) SEM image of a diffraction grating on a halophore. Scale bar: (**b**) 2 μm (Reproduced from [4])

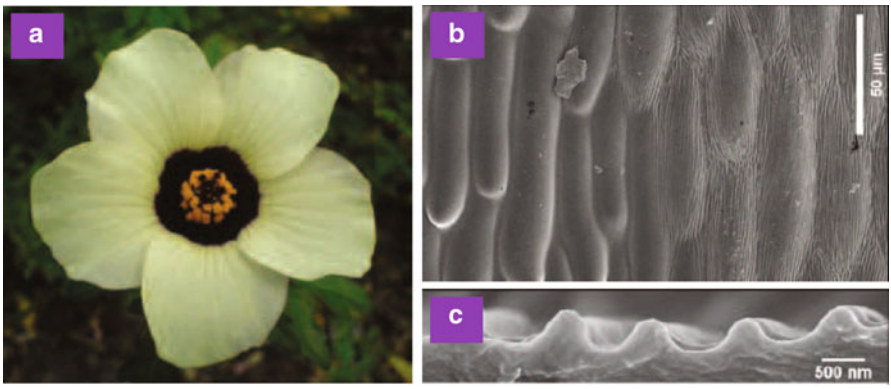

Fig. 8.25 (**a**) Flower *H. trionum*. (**b**) Top-view SEM image of the petal of the flower *H. trionum*. The left-half image corresponds to white epidermis with smooth cells, and the right-half image to dark epidermis (pigmented) with microscopic striations marked on the cell surface. (**c**) Transverse cross-sectional SEM image of the dark epidermis of the flower *T. kolpakowskiana*. The period of the microscopic striations is about 1.2 μm (Reproduced from [111])

grating. These diffraction gratings can diffract light predominantly in UV, which is of great significance for attracting pollinators such as bees and birds.

Another grating structure in plants was found in the edelweiss *Leontopodium nivale* [113]. The whole plane including stems, leaves, and bracts is covered with white hairs consisting of transparent hollow filaments. On the surface of the filaments there exists an array of parallel ridges with a period of about 420 nm. The ridges are about 410 nm in height. This curved diffraction grating can block UV light to reach the cellular tissues underneath since UV light can be strongly absorbed by the filaments, owing to the interplay of diffraction caused by the grating and guiding by the ridges.

Structural coloration produced by diffraction gratings requires that the grating period is comparable to light wavelengths. For wavelengths much larger than the grating period, only zero-order diffraction (specular reflection) exists. These sub-wavelength diffraction gratings can be used as antireflective structures. For example,

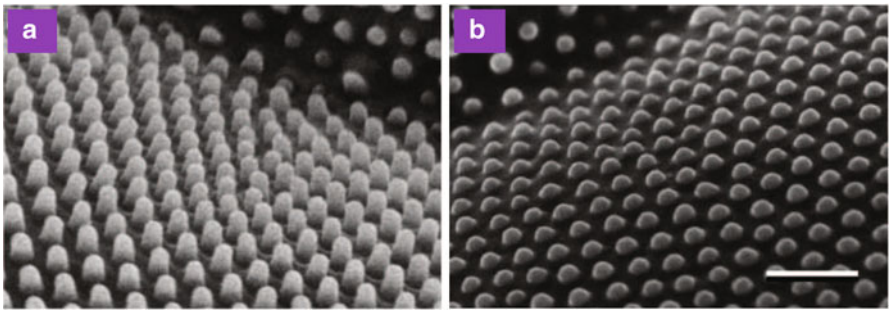

Fig. 8.26 SEM images of the corneal nipple arrays in the nymphalid *Pseudozizeeria maha* (**a**) and the lycaenid *Pseudozizeeria maha* (**b**), showing differences in nipple height and shape. Scale bar: 500 nm (Reproduced from [117])

corneal nipple arrays on the corneal surface of eyes in certain insects function as an antireflective layer [114–116], as shown in Fig. 8.26. Similar structures were also found on the transparent wings of certain insects [117–119], which can increase the transparency of the wings and hence reduce visibility.

8.5.4 Photonic Crystal

Photonic crystals are composite structures with a spatially periodic variation of refractive index [27–29]. As discussed above, light interactions with photonic crystals involve scattering by the constituent units, diffraction by the periodic arrangement of the units, and interference among scattered or diffracted light. Due to the introduced periodicity, light propagation in photonic crystals is strongly modified by the multiple Bragg scattering. As a result, the dispersion relation is characterized by complicated photonic band structures displaying photonic bands and even bandgaps (stop bands). For frequency within photonic bands, light propagation is allowed. For frequency within photonic bandgaps, however, the propagation of light is forbidden. There may exist a complete photonic bandgap for frequency within which light propagations are forbidden for all directions. These interesting features render the control of light propagation by photonic crystals possible, potentially leading to revolutionary approaches in photonics [29].

According to the periodicity in different dimensions, photonic crystals can be classified into 1D, 2D, and 3D. Periodic multilayers are 1D photonic crystals which are already discussed in the previous subsection. Here, our discussions will focus on 2D and 3D photonic crystals in the biological world. As aforementioned, there is no complete photonic bandgap in natural photonic crystals due to the fact that the refractive-index contrast among the constituent materials is not big enough. Only partial photonic bandgaps exist along certain directions. For a photonic crystal with a partial photonic bandgap along a certain direction, light cannot propagate

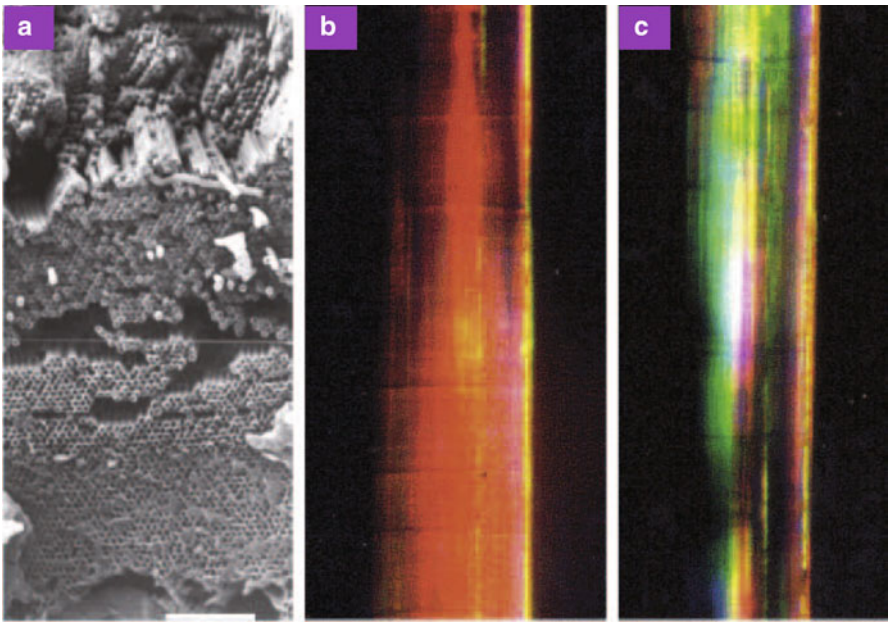

Fig. 8.27 (**a**) Cross-sectional SEM image of the wall region of a spine in the sea mouse *Aphrodita* sp. (**b**) and (**c**) Optical images of a spine showing the color change when the orientation in the horizontal plane varies (by 90°) with respect to the direction of the light source. Scale bar: (**a**) 8 μm (Reproduced from [45])

along this direction. As a result, strong reflection for frequency within this partial bandgap is expected, leading to iridescent structural coloration. Iridescence can be understood by the fact that partial photonic bandgaps are direction dependent.

8.5.4.1 2D Photonic Crystal

The spines of the sea mouse *Aphrodita* sp. (Polychaeta: Aphroditidae) display spectacular iridescence. A spine appears normally dull red in color. However, if illuminated perpendicularly to its axis, different colors can be seen as stripes running parallel to the axis, as shown in Fig. 8.27. SEM characterizations revealed that the spines consist of a wall and a hollow center [120]. The wall region is composed of hollow cylinders, made of pure α-chitin, along the spine axis. The hollow cylinders are close-packed hexagonally, forming a 2D photonic-crystal structure. The cylinders have thicker walls near the spine edge, but after a few layers the wall thickness slightly decreases to a constant value. The spacing of adjacent layers of cylinders is about 0.51 μm and remains constant throughout the wall cross-section. From the calculated photonic band structure of the 2D photonic crystal, there exists a partial photonic bandgap along the $\Gamma - M$ direction, responsible for the observed structural coloration and iridescence.

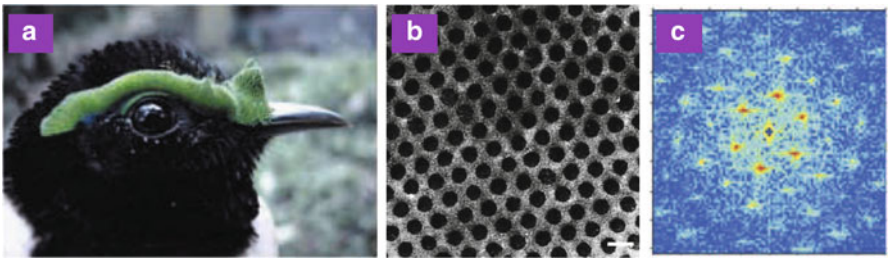

Fig. 8.28 (**a**) Optical image of *P. castanea*. (**b**) TEM image of the nanostructured arrays of the dermal collagen fibers. (**c**) 2D Fourier power spectrum of the TEM image showing discrete bright points of spatial frequency. Scale bar: (**b**) 200 nm (Reproduced from [121])

Structural blue and green colors occur in the skin of a broad diversity of birds from many avian orders and families. Structural characterizations with electron microscopy revealed that the dermal collagen layer contains quasi-ordered or ordered arrays of parallel collagen fibers [121], which are responsible for the skin coloration. The arrays of collagen fibers in the skin of most birds are quasi-ordered, but in *Philepitta castanea* (Eurylaimidae) the collagen fibers are exceptionally ordered, arranged in a hexagonal array, as shown in Fig. 8.28. This ordered arrangement of the collagen fibers manifests a 2D hexagonal photonic crystal, confirmed by a hexagonal pattern of spatial frequency peaks in the power spectrum, obtained from a 2D Fourier analysis.

The most remarkable example of 2D photonic crystals in the biological world resides in peacock feathers [122–125]. Over the centuries, humanity has been impressed by the splendor of the colors of peacocks. The coloration of peacock feathers had puzzled scientists for a long time. More than 300 years ago, Hook and Newton studied peacock feathers by optical observations and suggested that their colors were produced by thin films. The ultimate physical mechanism of the color production was, however, uncovered only recently [124, 125].

The male peacock tail contains spectacular beauty because of the brilliant, iridescent, diversified colors, and the intricate, colorful eye patterns. In the eye pattern of a tail feather of a male green peacock (*Pavo muticus*), blue, green, yellow, and brown feathers can be found, as shown in Fig. 8.29. A typical peacock tail feather possesses a central stem with an array of barbs on each side. Barbs are colorless. On each side of a barb there is an array of flat barbules. Perceived feather colors are from barbules. Each barbule has connected round indentations of typically about 20–30 μm. The round indentations have a smoothly curved crescent-like profile in transverse cross-section. From transverse cross-sectional SEM images, a barbule consists of a medullary core of about 3 μm enclosed by a cortex layer. The medulla consists of randomly dispersed keratin and melanin. In contrast, the cortex layer displays a regular structure. The outer surface of the cortex is a thin layer of keratin. Beneath the surface keratin layer, there is a 2D photonic-crystal structure, made up of an array of melanin rods connected by keratin. The remaining hollows

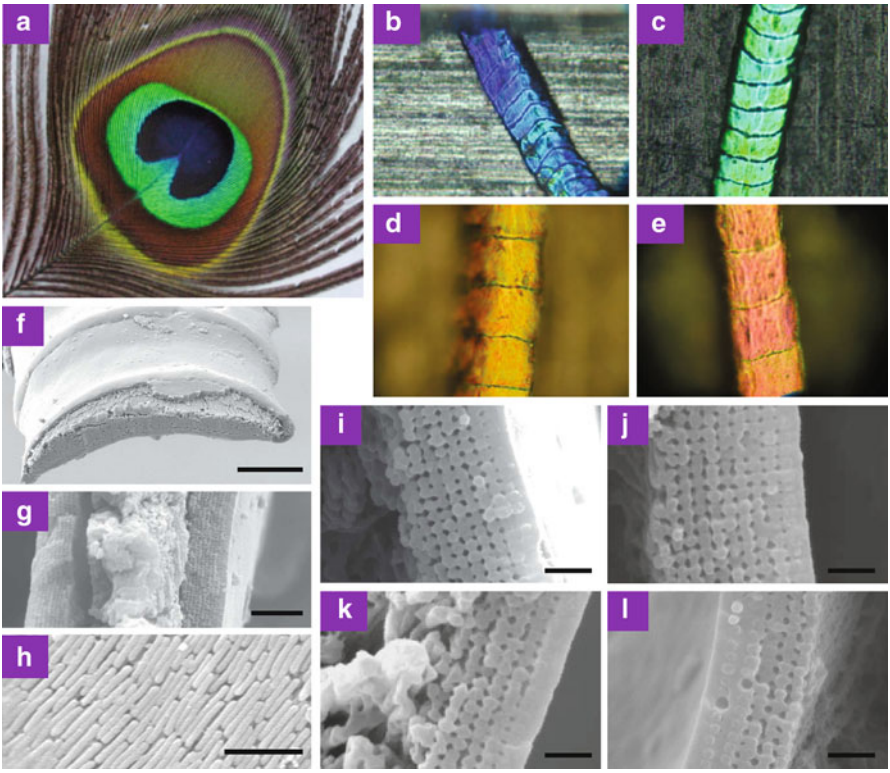

Fig. 8.29 (**a**) Eye pattern of a tail feather of a male green peacock *P. muticus*. (**b**)–(**e**) Optical microscopic images of *blue* (**b**), *green* (**c**), *yellow* (**d**), and *brown* (**e**) barbules. (**f**)–(**l**) SEM images of barbules. (**f**) Perspective view of a sectioned yellow barbule. (**g**) Transverse cross-section of a green barbule. (**h**) Longitudinal cross-section of a green barbule with the surface keratin layer removed. Melanin rods can be clearly seen. (**i**)–(**l**) Transverse cross-sectional images of *blue* (**i**), *green* (**j**), *yellow* (**k**), and *brown* (**l**) barbules. Scale bars: (**f**) 10 μm; (**g**) 2 μm; (**h**) 1 μm; and (**i**)–(**l**) 500 nm

are air holes. Melanin rods are parallel to the cortex surface, running along the axis of a barbule. Photonic-crystal structures in all differently colored barbules are quite similar. In the blue, green, and yellow barbules, the lattice structure is a square lattice, whereas in the brown barbule it is a rectangular lattice. The only differences are the lattice constant (rod spacing) and the number of periods (melanin rod layers) along the direction normal to the cortex surface. The lattice constant for the blue, green, and yellow barbules is 140, 150, and 165 nm, respectively. In the brown barbule, the lattice constant is 150 and 185 nm along the directions parallel and perpendicular to the cortex surface, respectively. The number of periods is 9–12 for the blue and green barbules, and about 6 for the yellow barbules. The brown barbules have the least number of periods, about 4. These differences in the lattice constant and number of periods in differently colored barbules can give rise to diversified coloration.

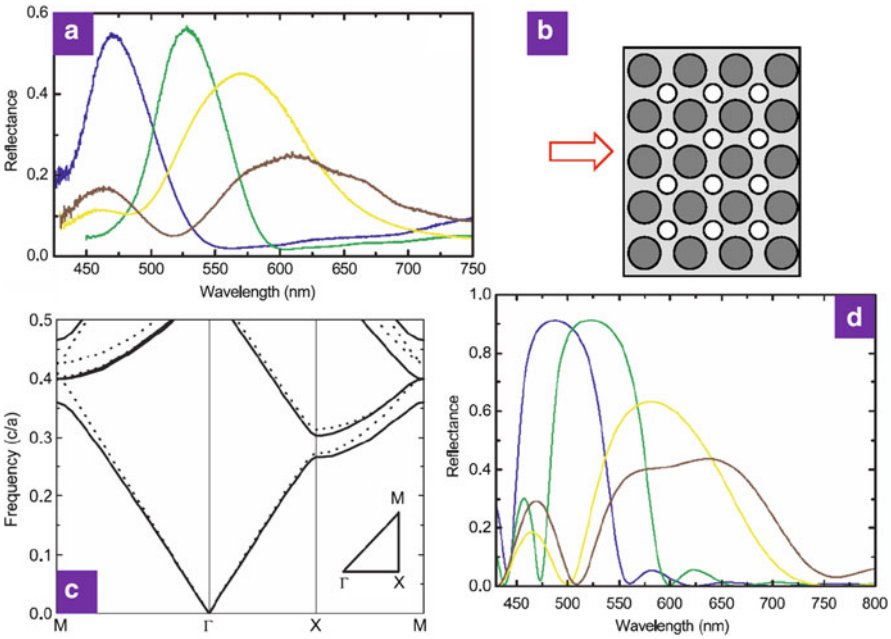

Fig. 8.30 (**a**) Measured reflection spectra of differently colored barbules of the male *P. muticus* under normal incidence. *Blue, green, yellow, and brown lines* represent the results for blue, green, yellow, and brown barbules, respectively. (**b**) Schematic of a 2D photonic crystal used in simulations. *Light gray area, dark gray dot, and white dot* indicate keratin matrix, melanin rod, and air hole, respectively. The *red arrow* indicates the direction perpendicular to the cortex surface. (**c**) Calculated photonic band structure for the electric vector parallel (*solid lines*) and perpendicular (*dashed lines*) to the melanin rods. Frequency is in units of c/a, where c is the light speed in vacuum and a is the lattice constant. The *inset* shows the irreducible Brillouin zone with Γ, X, and M representing its center, edge center, and corner, respectively. Note that the $\Gamma - X$ direction is along the direction normal to the cortex surface. (**d**) Calculated reflection spectra under normal incidence for generic 2D photonic crystals with a finite number of periods. *Blue, green, yellow, and brown lines* represent the results for blue, green, yellow, and brown barbules, respectively, and the corresponding number of periods is 10, 10, 6, and 4, respectively (Reproduced from [124])

Measured reflection spectra for differently colored barbules with a microspectrophotometer under normal incidence are shown in Fig. 8.30. The blue and green barbules display a single reflection peak, while the yellow and brown barbules show two reflection peaks. For the blue and green barbules, their reflection peaks are located into blue and green wavelengths, respectively. For the yellow barbule, the main peak ranges from green to orange wavelengths, indicating that the yellow color is a mixed color. The intensity of the secondary peak at blue wavelengths is too small to contribute to coloration. For the brown barbule, however, the peak at blue wavelengths has a intensity comparable to the broad reflection peak ranging from green, yellow, orange to red wavelengths.

To explore the origin of coloration in the feather barbules, the photonic band structure of an infinite 2D photonic crystal was calculated by a PWE method, shown in Fig. 8.30c. The structural parameters for this photonic crystal were taken from the measurements, i.e., $r_{\text{rod}}/a = 0.4$ and $r_{\text{air}}/a = 0.25$, where r_{rod} and r_{air} are the radii of the melanin rods and air holes, respectively, and a is the lattice constant. The refractive indices of keratin and melanin were taken to be 1.54 and 2.0, respectively. This 2D photonic crystal does not exhibit a complete photonic bandgap. However, a partial photonic bandgap for both polarizations exists along the $\Gamma - X$ direction. It is noted that the photonic band structure for the two polarizations shows a small difference at low frequencies (corresponding to the visible wavelengths), and it differs at high frequencies (corresponding to the UV wavelengths or below). The difference between the midgap frequencies for the two polarizations is rather small. This indicates that the peacock feather barbules exhibit small polarization effects in coloration. Strong reflections are expected for frequencies within the partial photonic bandgap along the $\Gamma - X$ direction, responsible for barbule coloration. It should be mentioned that the partial photonic bandgap shifts to a higher frequency range with the increasing angle of incidence, leading to iridescence.

For blue, green, and yellow barbules, their colors stem from the partial photonic bandgap of the 2D photonic crystal in the cortex. This can be confirmed by the calculated reflection spectra of generic 2D photonic crystals with a finite number of periods by a TMM, shown in Fig. 8.30d. The calculated reflection spectra correctly reproduce the main features of the experiments.

Note that brown is a mixed color. The partial photonic bandgap can only cause a reflection peak covering green, yellow, orange to red wavelengths. Simulations [124, 125] revealed that the Fabry–Perot interference plays an important role in the color production of brown barbules. For any finite photonic crystal, Fabry–Perot interference should exist owing to the interference from their two surfaces, leading to oscillating side peaks on the two sides of the reflection peak produced by the partial photonic bandgap. For a finite photonic crystal with a large number of periods, the reflection peak produced by the partial photonic bandgap is dominant, while the contribution of the side peaks to coloration by Fabry–Perot interference is negligible. However, with the decreasing number of periods, side peaks also play a role in coloration, giving rise to an additional color. For brown barbules, the number of periods is the least. As a result, the Fabry–Perot interference leads to an additional blue reflection peak which is comparable to the main peak from the partial photonic bandgap, eventually giving rise to a structural brown color by color mixing. It was found [125] that other factors such as the interdistance and missing air holes between the two melanin layers nearest to the cortex surface are important in the production of the structural brown color.

Peacock feathers take advantage of a 2D photonic crystal in the barbule cortex for coloration. The strategies for diversified color production are very ingenious and rather simple, i.e., by means of the variation of the lattice constant and the number of periods. Varying the lattice constant will shift the midgap frequency of the partial photonic bandgap, leading to different colors. The reduction in the number of periods may cause an additional color, resulting in mixed coloration. By the two strategies, diversified structural colors can be produced.

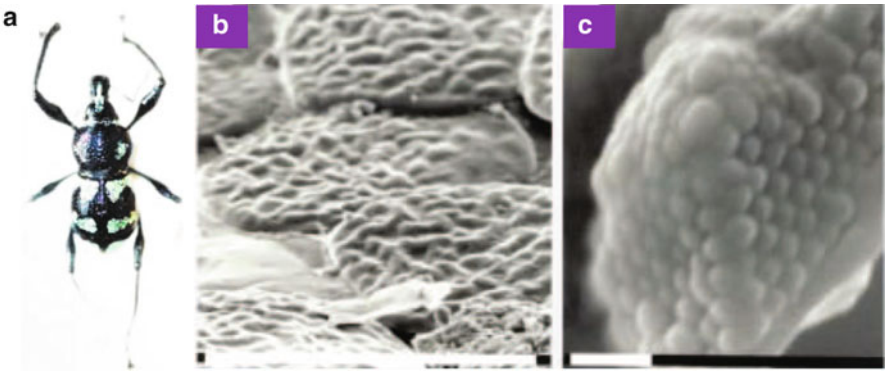

Fig. 8.31 (**a**) Photograph of the weevil *P. argus*. (**b**) SEM image showing several partially overlapping scales. (**c**) Cross-sectional SEM image of a region of a scale. Scale bars: (**b**) 100 μm and (**c**) 1 μm (Reproduced from [126])

8.5.4.2 3D Photonic Crystal

In addition to 2D photonic crystals, 3D photonic crystals that are periodic in three dimensions are also present in the biological world. Revealed 3D photonic crystals display various forms exhibiting different optical effects. Unlike 1D and 2D photonic structures, the determination of the detailed structural configurations for 3D photonic structures is rather difficult and challenging, especially for those with complicated connectivity and topology. This is because commonly used electron microscopy such as SEM and TEM can only offer 2D structural information for certain sectioned orientations. Electron tomography could be very helpful in the reconstructions of 3D photonic structures. The correct determination of complex 3D photonic structures are, however, still a difficult task even with electron tomography. As a result, one has to be very careful in the recognition and reconstruction when based on a few 2D SEM or TEM sectioned images.

The first 3D photonic crystal revealed in the biological world might be the one in the scales of the weevil *Pachyrhynchus argus* [126], as shown in Fig. 8.31. The weevil displays a metallic color coming from the scales, about 0.1 mm in diameter, occurring in the patches on the top and sides of its body. The scales are flat, lying parallel to the body. The colored scales show a yellow-green color in reflected light and a complementary purple color in transmitted light from most directions. These colored scales consist of an outer shell and an inner part. The inner part is an array of transparent spheres, each with a diameter of 250 nm, arranged in the close-packing order. This arrangement is similar to that in opal, i.e., spheres that are arranged in a face-centered cubic lattice. The invariant yellow-green color perceived is a result of global averaging of different domains since the scales contain differently oriented domains of opal-like structures. Moreover, iridescence is absent due to the averaging effects, leading to nearly the same bright coloration from every direction. This could be useful for interspecific color or pattern recognition.

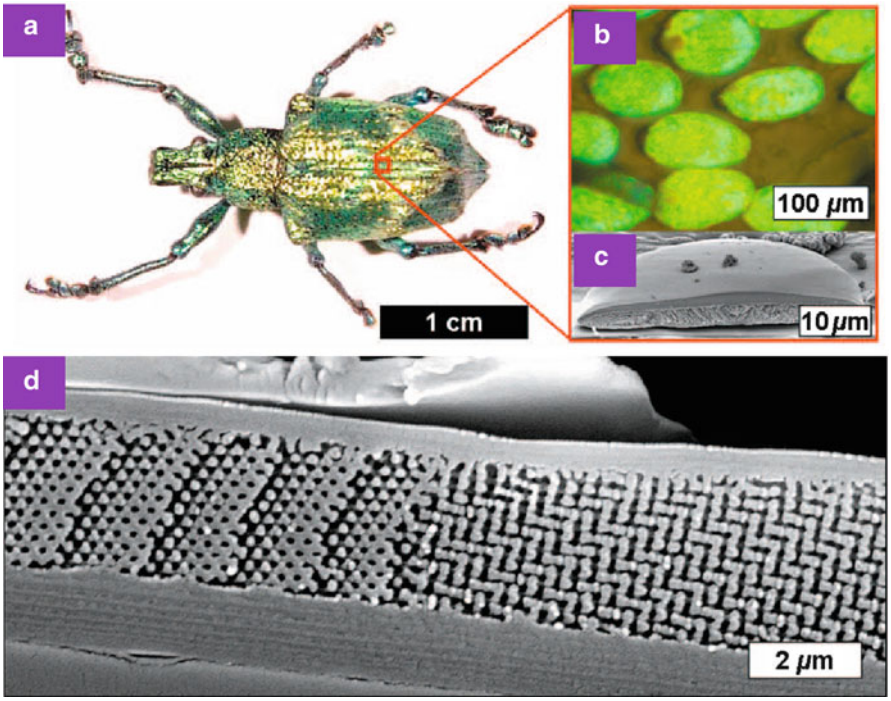

Fig. 8.32 (**a**) Optical image of the weevil *L. augustus*. (**b**) Optical microscopic image of individual scales attached to the exoskeleton. (**c**) Cross-sectional SEM image of a scale. (**d**) Close-up cross-sectional SEM image of a region of a scale (Reproduced from [128])

Among various 3D photonic structures, photonic crystals with a diamond lattice are the "champion" structures because they may create the largest complete photonic bandgaps [127], but the artificial fabrication of such photonic structures at the visible regime is still very challenging. This diamond-based photonic crystal was, however, found in the weevil *Lamprocyphus augustus* [128], as shown in Fig. 8.32. The weevil shows bright green coloration that is nearly angle-independent. The green coloration derives from leaf-like cuticle scales attached to the weevil's exoskeleton. By combining a high-resolution structure analysis technique based on sequential focused ion beam milling and SEM imaging, a 3D photonic-crystal structure with a diamond-based lattice was revealed in the scale interior. The measured average lattice constant is about 450 nm. Within individual scales, the diamond-based photonic-crystal structures are assembled in the form of differently oriented single-crystalline micrometer-sized domains with only selected lattice planes facing the top surface of the scales. Simulations revealed that partial photonic bandgaps exist along different directions with different midgap frequencies, yielding different coloration. The nearly angle-independent green coloration in the scales is thus a combination of all contributions from the differently oriented diamond-based photonic-crystal structures.

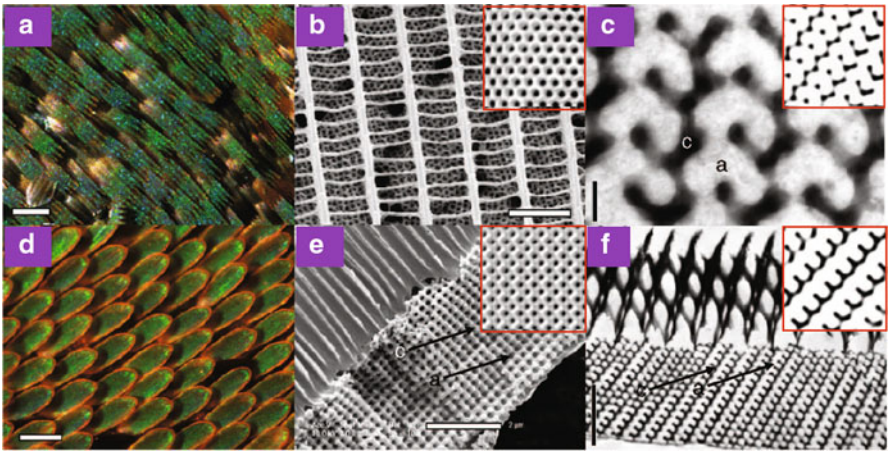

Fig. 8.33 Nanostructures for structural coloration in the scales of lycaenid and papilionid butterflies. (**a**) Optical microscopic image of the ventral wing cover scales of *C. gryneus*. (**b**) SEM image of the dorsal surface of a *C. gryneus* scale showing disjoint crystallites beneath windows created by a network of parallel, longitudinal ridges and slender, spaced cross-ribs. The inset shows the simulated SEM (111) projection from a thick slab of a level set single gyroid nanostructure. (**c**) TEM image of the *C. gryneus* nanostructure showing a distinctive motif, uniquely characteristic of the (310) plane of the gyroid morphology. The inset shows a matching simulated (310) TEM section of a level set single gyroid model. (**d**) Optical microscopic image of the dorsal wing cover scales of *P. sesostris*. (**e**) SEM image of the lateral surface of the wing scale nanostructure of *P. sesostris* showing fused polycrystalline domains beneath columnar windows created by a network of ridges and spaced cross-ribs. The fractured face features a square lattice of air holes in chitin. The inset shows the simulated SEM (100) projection from a thick slab of a level set single gyroid nanostructure. (**f**) TEM image of the *P. sesostris* nanostructure showing a distinctive motif, uniquely characteristic of the (211) plane of the gyroid morphology. The inset shows a matching simulated (211) TEM section of a level set single gyroid model. The labels *c* and *a* in (**c**), (**e**), and (**f**) indicate chitin and air void, respectively. Scale bars: (**a**) and (**d**) 100 μm; (**b**) 2.5 μm; (**c**) 200 nm; and (**e**) and (**f**) 2 μm (Reproduced from [137])

In additional to multilayers, 3D photonic crystals are also exploited in butterflies for structural coloration, e.g., in papilionid and lycaenid butterfly scales [129–137]. Revealed 3D photonic structures exhibit various forms and complexity, attributed to simple cubic [129] and face-centered cubic [130] structures, and gyroid structures [135–137].

The wings of the butterflies *Callophrys gryneus* (Lycaenidae) and *Parides sesostris* (Papilionidae) display vivid structural colors. Structural characterizations based on electron microscopy and small angle X-ray scattering [137] show that these wing colors are caused by a gyroid (I_4132) photonic crystal in the scales, a bicontinuous triply periodic structure of the network of chitin and air, as shown in Fig. 8.33. The measured lattice parameter is about 306 nm for *C. gryneus* and about 288 nm for *P. sesostris*. The estimated filling fraction is about 0.34 and 0.3 for *C. gryneus* and *P. sesostris*, respectively. Photonic band structure calculations revealed

that there exist three relatively closely spaced partial photonic bandgaps along the (110), (111), and (200) directions for the butterfly gyroid photonic crystal, which are the origin of the structural coloration of the wings.

8.5.5 Amorphous Photonic Structure

According to their arrangements, photonic structures can be classified into three classes: ordered structures with both short- and long-range order, quasi-ordered or amorphous structures with only short-range order, and random structures with neither short- nor long-range order. These three classes of photonic structures have different optical response, leading to structural coloration with distinctive features. For ordered photonic structures, they can produce iridescent structural coloration. The iridescence of ordered photonic structures stems from long-range order. On the other hand, quasi-ordered or amorphous photonic structures can cause angle-independent structural coloration, i.e., non-iridescent structural coloration. Random photonic structures that lack both short- and long-range order may only produce white colors.[6]

In addition to ordered categories in the biological world, there also exist quasi-ordered or amorphous photonic structures that possess only short-range order, giving rise to non-iridescent structural coloration. The most known example is the spongy structure of keratin in the feather barbs of many birds. These non-iridescent colors were hypothesized over 100 years ago to be produced by incoherent scattering from individual scatters, namely, individual air vacuoles [1, 17, 138, 139], where phase relations among scattered light are random. Two types of incoherent scattering mechanisms were proposed: one is Rayleigh scattering [138] and the other is Tyndall or Mie scattering [1, 17, 139].

In 1934 Raman opposed this incoherent-scattering hypothesis with the thorough observations of the feathers of the bird *Coracias Indica* which displays a non-iridescent blue color under natural light [140]. He concluded that incoherent scattering such as a Tyndall effect was definitely insufficient to explain the observations, and suggested that the diffraction by the air cavities and the interference from the surfaces of minute films were responsible for the non-iridescent blue feather barb coloration.

In 1970s Dyck challenged the Rayleigh model for the blue coloration of feather barbs [141, 142]. He noticed that the reflection spectra of many bird feathers display discrete peaks, which is inconsistent with the prediction of a continued scattering efficiency that is inversely proportional to the fourth power of wavelength by the Rayleigh law. Dyck hypothesized that coherent light scattering by the ordered matrix of air vacuoles and keratin was the cause of the blue coloration.

[6] White colors are always of structural origins.

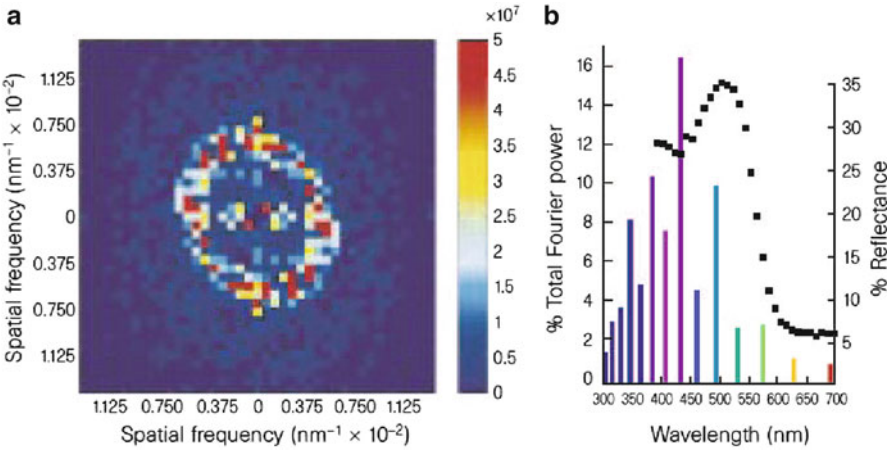

Fig. 8.34 (**a**) 2D Fourier power spectrum of the spongy keratin matrix in a blue feather barb of *Cotinga maynana*. (**b**) Observed reflection spectrum of a blue feather barb (*black squares*, right axis) and predicted reflection spectrum (*bars*, left axis) based on the 2D Fourier power spectrum in (**a**) (Reproduced from [143])

In late 1990s Prum and coworkers demonstrated ambiguously by structural analyses in the reciprocal space that the blue coloration of feather barbs is indeed produced by coherent light scattering [143, 144]. They performed 2D Fourier analyses for cross-sectional TEM images of the spongy keratin layer in the blue feather barbs of some birds, and revealed a nearly circular ring around the origin in 2D Fourier power spectra, as shown in Fig. 8.34. The existence of a ring in 2D Fourier power spectra indicates that the spongy keratin has only short-range order, which will lead to coherent light scattering and hence cause the non-iridescent blue coloration. Recently, they employed small-angel X-ray scattering to characterize the nanostructures of the blue feather barbs of some birds [145, 146], as shown in Fig. 8.35. Clearly, the scattering spectra exhibit rings, implying again that these nanostructures possess only short-range order, resulting in non-iridescent coloration via coherent light scattering.

To compare with measurements quantitatively, a simply theory has been frequently used [6, 143–146], namely, simply translating 2D Fourier power spectra or small-angle X-ray scattering spectra into reflection spectra by imposing a Bragg-like condition

$$\frac{2\pi}{\lambda}\tilde{n} = \frac{k_{\max}}{2}, \tag{8.9}$$

where $\tilde{n}$ is the averaged refractive index of a nanostructure and $k_{\max}$ is the peak value of the spatial frequencies. It should be mentioned that this simply theory is valid only for very weak scattering. The application to amorphous photonic structures seems problematic.

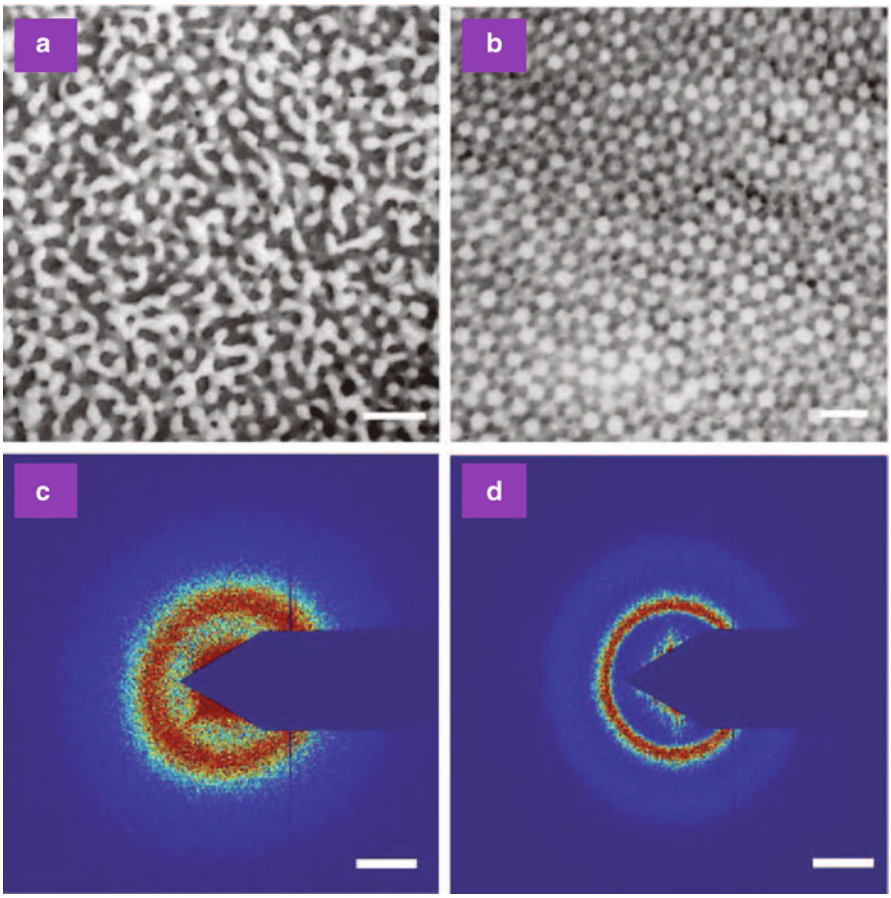

Fig. 8.35 (**a**) and (**b**) Cross-sectional TEM images of the nanostructures from back contour feather barbs of *Sialia sialis* and *C. maynana*, respectively. (**c**) and (**d**) Small-angle X-ray scattering data for feather barbs of *S. sialis* and *C. maynana*, respectively. Scale bars: (**a**) and (**b**) 500 nm; and (**c**) and (**d**) 0.025 nm^{-1} of spatial frequency (Reproduced from [145])

Coherent light scattering is conceptually the correct understanding for the non-iridescent structural coloration produced by amorphous photonic structures [6, 141–147], but it is not the ultimate physical mechanism. Moreover, the simple translation of Fourier power spectra into reflection spectra by using the Bragg-like condition could be problematic since the Bragg condition is only valid for very weak scattering or dilute scatters. This is because for amorphous photonic structures light scattering is far from weak owing to the short-range order. On the other side, the translation procedure relies solely on the structural information, i.e., the structure factor. As is known, reflection is related not only to the structure factor but also to the detailed spatial distribution of refractive index.

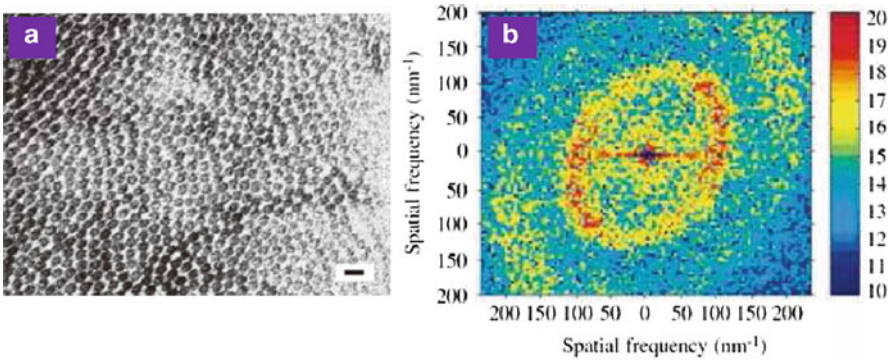

Fig. 8.36 (**a**) TEM image of a collagen array from dark blue caruncle tissue of *Neodrepanis hypoxantha*. (**b**) 2D Fourier power spectrum of the tissue. Scale bar: (**a**) 200 nm (Reproduced from [150])

Recently, the optical response of amorphous photonic structures was studied numerically by the authors with rigorous methods to solve Maxwell's equations [148, 149]. From the calculated photon density of states (PDOS) for amorphous photonic structures, there exist angle-independent (isotropic) *photonic pseudogaps* due to coherent light scattering from short-range order. Unlike photonic bandgaps in photonic crystals within which the PDOS is zero, photonic pseudogaps show nonzero dips in the PDOS. Our results indicate unambiguously that photonic pseudogaps are the ultimate physical origin for the non-iridescent structural coloration of amorphous photonic structures. Non-iridescence can be understood by the fact that light is scattered evenly in all directions since there is no preferred orientation in amorphous photonic structures due to the lack of long-orange order.

In feather barbs, the amorphous photonic structures responsible for the blue coloration are mostly a keratin network in the spongy medullary layer [143–147], with keratin bars and air channels in tortuous and twisting forms, as shown in Fig. 8.35a. These nanostructures possess only short-range order and are responsible for the iridescent structural coloration. Another kind of nanostructure was found in the blue back plumage of the Eastern Bluebird (*S. sialis*) where the air cavities are nearly spherical and close-packed [146], as shown in Fig. 8.35b. The nanostructure of spherical air cavities also exhibits short-range order.

Amorphous photonic structures were also found in the structurally colored skin of some birds [121, 150]. The dermis of structurally colored skin consists of a thick (100–500 μm) layer of collagen. TEM characterizations revealed that most of the color producing dermal collagen layers consist of a quasi-ordered array of parallel collagen fibers as shown in Fig. 8.36. 2D Fourier analyses showed that the array of collagen fibers has short-range order, indicating that the collagen fibers are arranged in the form of 2D amorphous photonic structures. The dermal colors are determined by the nanostructure of the collagen arrays via coherent light scattering.

In addition to birds, amorphous photonic structures are also present in beetles [148, 149, 151, 152]. For example, the scales of the longhorn beetle *Anoplophora graafi* contain a random-close-packing photonic structure of chitin nanoparticles [148], while the scales of the longhorn beetle *Sphingnotus mirabilis* possess a disordered bi-continuous photonic structure of chitin [149]. Both photonic structures have only short-range order and are responsible for the non-iridescent structural coloration of the scales.

As shown in Fig. 8.37, the beetle *A. graafi* has a dull metallic blue or green color on its elytra marked with brilliant greenish white lateral stripes. Under optical microscopy, these stripes are composed of differently colored scales which are seed-like, about 50 μm long and 20 μm wide. Each scale has a distinct non-iridescent color and the scale color can cover almost the whole visible range. The perceived greenish white is thus a mixed color resulting from differently colored scales in a pointillistic way. Cross-sectional SEM images revealed that the interior of scales is an array of chitin nanoparticles in a form of random close-packing (RCP), confirmed by comparing with the generated RCP structure. The 2D radial distribution function indicates that the RCP photonic structure in the scale interior possesses only short-range order.

To get insight into the coloration mechanism of RCP photonic structures, the PDOS of model RCP photonic structures were calculated, as shown in Fig. 8.38. Two prominent dips (photonic pseudogaps) appear in the calculated PDOS. Compared with the PDOS, the calculated reflection peaks and photonic pseudogaps show a one-to-one correspondence. This indicates that photonic pseudogaps are the ultimate cause of the non-iridescent structural coloration of RCP photonic structures.

8.6 Outlook

Photonic structures occurring in the biological world show striking diversity, complexity, and delicacy. They have received increasing research interest from a variety of fields ranging from physics, biology, and chemistry to material science due to their fundamental and application-oriented significance. The studies of natural photonic structures and resultant structural colors may not only provide insights into our understanding of their biological and physical aspects but also offer valuable inspirations. Despite considerable advances made especially in recent years, there exist still many important questions and challenging problems to be answered. Interesting topics related to photonic structures in the biological world include their evolution, structural formation, function, structural characterization, material determination, mechanism, and bio-inspired design and fabrication.

The evolution of natural photonic structures, a fundamental problem, is poorly researched. Although some progress has been made in recent years, there remain a number of interesting and challenging problems [2, 58, 59, 145, 153–156] such as the evolution mechanism, how natural photonic structures develop and form during individual growth, and the underling genetic mechanisms that determine phenotype.

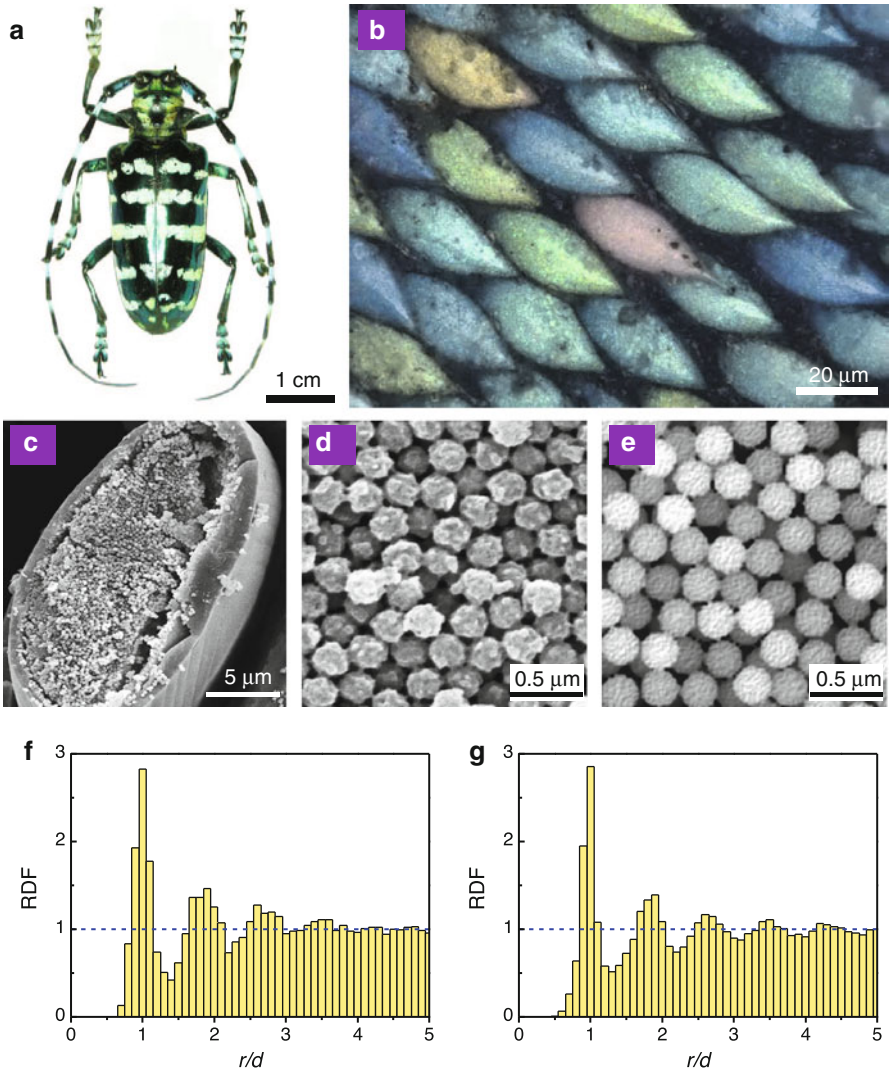

Fig. 8.37 (**a**) Optical image of *A. graafi*. (**b**) Optical microscopic image of a greenish white stripe under 500× magnification. (**c**) Cross-sectional SEM image of a green scale. (**d**) Close-up cross-sectional SEM image of the interior of a green scale. (**e**) Cross-section of a generated RCP structure of equal spheres with surfaces roughened arbitrarily. (**f**) and (**g**) Histogram of the 2D radial distribution function with (**f**) for the RCP structure in the green scale and (**g**) for the generated one, where d is the diameter of nanoparticles (Reproduced from [148])

The functions of natural photonic structures are closely related to their evolution. Structural coloration in animals often serves primarily as intraspecific communication such as species recognition, mate choice, and intrasexual competition, and also as interspecific interactions such as predator avoidance by using aposematic

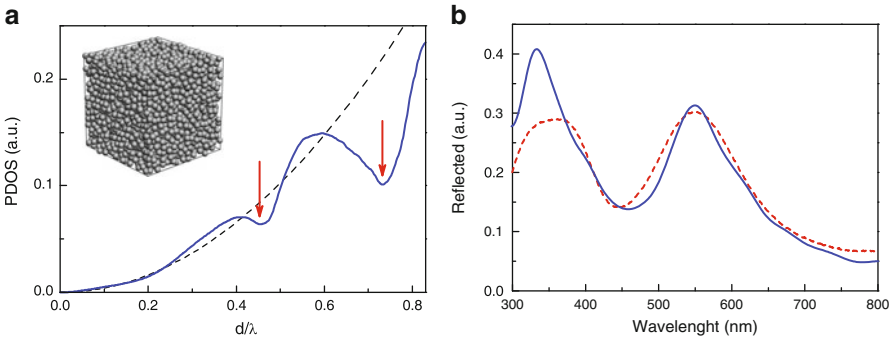

Fig. 8.38 (**a**) Calculated PDOS of a model RCP photonic structure (*inset*) as a function of reduced frequency d/λ, where d is the diameter of the nanoparticles and λ is the wavelength in vacuum. The PDOS of a homogeneous medium with a refractive index of 1.38 (*dashed red line*) is given for comparison. Photonic pseudogaps are indicated by *arrows*. (**b**) Calculated (*solid line*) and measured (*dashed line*) reflection spectra. Measured reflection spectrum for green scales was obtained by macro-optical spectroscopy. In the calculations, the nanospheres take a refractive index of 1.56, a typical value for chitin, and their diameter is assumed to be 240 nm, a typical value for the chitin nanoparticles in green scales (Reproduced from [148])

and cryptic coloration [157]. Noncommunicative functions of natural photonic structures have also been proposed such as thermoregulation [158], structural support and strengthening [159, 160], friction reduction [161], and photoprotection and visual enhancement [162]. Most of the biological, physical, and physiological functions are hypothetical, and more research efforts are hence needed.

Structural determinations are essential in understanding structural coloration. For simple natural photonic structures such as thin films, multilayers, and 2D photonic crystals, they can be explored by SEM and TEM. As aforementioned, however, structural determinations are sometimes extremely difficult especially for natural photonic structures with complex building units or connectivity, e.g., nontrivial 3D photonic structures, since frequently used tools such as SEM and TEM can only offer 2D structural information in certain orientations. Combinational, correlational, and advanced tools are highly desired in order to get correct structures.

Another important and also less known and researched problem is about the constituent materials and their distribution in natural photonic structures, particularly with refractive index (both real and imaginary components) and dispersion across the relevant wavelength range. Additionally, surrounding materials are sometimes also important in determining the optical response of natural photonic structures. The structural and optical properties of surrounding materials ought to be studied in detail.

Among the relatively better understood aspects of natural photonic structures are the mechanisms of their structural color production. Generally, structural coloration can be understood in terms of interference, diffraction, and scattering. As is shown, natural photonic structures exhibit astonishing diversity and complexity. For complicated photonic structures with architectures of different levels, their color

production may be the interplay among interference, diffraction, and scattering, which could obstacle considerably the finding of ultimate physical mechanisms. Moreover, the combination of these optical effects may even lead to new optical phenomena. For example, complicated photonic band structures occurring in photonic crystals are due to the combination of these optical effects. The ultimate physical cause of iridescent structural coloration in photonic crystals is direction-dependent partial photonic band gaps [124, 126, 128, 137]. In amorphous photonic crystals, on the other side, isotropic photonic pseudogaps are the ultimate physical cause of non-iridescent structural coloration [148, 149].

Nature usually takes the strategy of maximal achievement at minimal cost. As a result of evolution, photonic structures exploited in the biological world may be optimal in the sense of their biological, physical, or even physiological functions. Natural photonic structures in step with their coloration strategies are a valuable source of inspiration. In recent years, there has been a growing interest in biomimetic and bio-inspired design [163–166]. The use of structural color is environmentally promising since it bypasses the need for chemical pigments, which are often toxic. Bio-inspired photonic structures and structural colors may have potential applications in a variety of industries such as photonics, display, painting, and textile. Natural photonic structures and the ingenious ways of light steering may have been a great source of inspiration in our design and fabrication of new optical materials and devices for future technological applications.

References

1. Fox, D.L.: Animal Biochromes and Structural Colours. University of California Press, Berkeley (1976)
2. Ghiradella, H.: Appl. Opt. **30**, 3492 (1991)
3. Srinivasarao, M.: Chem. Rev. **99**, 1935 (1999)
4. Parker, A.R.: J. Opt. A Pure Appl. Opt. **2**, R15 (2000)
5. Vukusic, P., Sambles, J.R.: Nature (London) **424**, 852 (2003)
6. Prum, R.O.: In: Hill, G.E., McGraw, K.J. (eds.) Bird Coloration, vol. 1, p. 295. Harvard University Press, Cambridge, MA (2006)
7. Berthier, S.: Iridescences: The Physical Colors of Insects. Springer, New York (2007)
8. Kinoshita, S., Yoshioka, S., Miyazaki, J.: Rep. Prog. Phys. **71**, 076401 (2008)
9. Vigneron, J.P., Simonis, P.: Adv. Insect Physiol. **38**, 181 (2010)
10. Michelson, A.A.: Phil. Mag. **21**, 554 (1911)
11. Walter, B.: Die Oberflöchen- orde Schillerfarben. Vieweg, Braunschweig (1895)
12. Rayleigh, L.: Phil. Mag. **37**, 98 (1919)
13. Biedermann, W.: Festschrift Zum Siebzigsten Geburtstage von Haeckel, p. 215. Denschriften Med. Naturwiss. Ges., Jena (1904)
14. Mallock, A.: Proc. R. Soc. Lond. A **85**, 598 (1911)
15. Merritt, E.: J. Opt. Soc. Am. Rev. Sci. Instrum. **11** 93 (1925)
16. Onslow, H.: Phil. Trans. **211**, 1 (1923)
17. Mason, C.W.: J. Phys. Chem. **27**, 201 (1923)
18. Mason, C.W.: J. Phys. Chem. **27**, 401 (1923)
19. Mason, C.W.: J. Phys. Chem. **30**, 383 (1926)

20. Mason, C.W.: J. Phys. Chem. **31**, 321 (1927)
21. Mason, C.W.: J. Phys. Chem. **31**, 1856 (1927)
22. Frank, F., Ruska, H.: Naturwiss **27**, 229 (1939)
23. Born, M., Wolf, E.: Principles of Optics. Cambridge University Press, Cambridge (1999)
24. Rayleigh, L.: Philos. Mag. **41**, 107, 274 (1871)
25. Tyndall, J.: Philos. Mag. **37**, 384 (1869)
26. van de Hulst, H.C.: Light Scattering by Small Particles. Dover, New York (1981)
27. Yablonovitch, E.: Phys. Rev. Lett. **58**, 2059 (1987)
28. John, S.: Phys. Rev. Lett. **58**, 2486 (1987)
29. Joannopoulos, J.D., Johnson, S.G., Winn, J.N., Meade, R.D.: Photonic Crystals: Molding The Flow of Light, 2nd edn. Princeton University Press, Princeton (2008)
30. CVRL Color & Vision database, http://www.cvrl.org/
31. Yeh, P.: Optical Waves in Periodic Media. Wiley, New York (1988)
32. Pendry, J.B., Mackinnon, A.: Phys. Rev. Lett. **69**, 2772 (1992)
33. Bell, P.M., Pendry, J.B., Moreno, L.M., Ward, A.J.: Comput. Phys. Commun. **85**, 306 (1995)
34. Yee, K.S.: IEEE Trans. Antennas Propag. **14**, 302 (1966)
35. Taflove, A., Hagness, S.C.: Computational Electrodynamics: The Finite-Difference Time-Domain Method. Artech House, Norwood, MA (2000)
36. Stefanou, N., Yannopapas, V., Modinos, A.: Comput. Phys. Commun. **132**, 189 (2000)
37. Fox, H.M., Vevers, G.: The Nature of Animal Colours. Sidgwick and Jackson, London (1960)
38. Shevtsova, E., Hansson, C., Janzen, D.H., Kjærandsen, J.L Proc. Natl. Acad. Sci. USA **108**, 668 (2011)
39. Dyck, J.: Biol. Skr. (Copenhagen) **30**, 2 (1987)
40. McGraw, K.J.: Naturwissenschaften **91**, 125 (2004)
41. Yin, H., Shi, L., Sha, J., Li, Y., Qin, Y., Dong, B., Meyer, S., Liu, X., Zhao, L., Zi, J.: Phys. Rev. E **74**, 051916 (2006)
42. Yoshioka, S., Nakamura, E., Kinoshita, S.: J. Phys. Soc. Jpn. **76**, 013801 (2007)
43. Nakamura, E., Yoshioka, S., Kinoshita, S.: J. Phys. Soc. Jpn. **77**, 124801 (2008)
44. Land, M.F.: Prog. Biophys. Mol. Biol. **24**, 75 (1972)
45. Parker, A.R.: J. Roc. Soc. Interface **2**, 1 (2005)
46. Seago, A.E., Brady, P., Vigneron, J.P., Schultz, T.D.: J. Roc. Soc. Interface **6**, S165 (2009)
47. Durrer, H., Villiger, W.: Int. J. Insect Morphol. Embryol. **1**, 233 (1972)
48. Deparis, O., Vandenbem, C., Rassart, M., Welch, V.L., Vigneron, J.P.: Opt. Express **14**, 3547 (2006)
49. Vigneron, J.P., Rassart, M., Vandenbem, C., Lousse, V., Deparis, O., Biro, L.P., Dedouaire, D., Cornet, A., Defrance, P.: Phys. Rev. E **73**, 041905 (2006)
50. Stavenga, D.G., Wilts, B.D., Leertouwer, H.L., Hariyama, T.: Phil. Trans. R. Soc. B **366**, 709 (2011)
51. Noyes, J.A., Vukusic, P., Hooper, I.R.: Opt. Express **15**, 4351 (2007)
52. Vigneron, J.P., Colomer, J.F., Vigneron, N., Lousse, V.: Phy. Rev. E **72**, 061904 (2005)
53. Liu, F., Dong, B.Q., Liu, X.H., Zheng, Y.M., Zi, J.: Opt. Express **17**, 16183 (2009)
54. Arsenault, A.C., Clark, T.J., Von Freymann, G., Cademartiri, L., Sapienza, R., Bertolotti, J., Vekris, E., Wong, S., Kitaev, V., Manners, I., Wang, R.Z., John, S., Wiersma, D., Ozin, G.A.: Nat. Mater. **5**, 179 (2006)
55. Walish, J.J., Kang, Y., Mickiewicz, R.A., Thomas, E.L.: Adv. Mater. **21**, 1 (2009)
56. Anderson, T., Richards Jr., A.: J. Appl. Phys. **13**, 748 (1942)
57. Gentil, K.: Z. Morph. Ökol. Tiere **38**, 344 (1942)
58. Ghiradella, H.: Ann. Entomol. Soc. Am. **77**, 637 (1984); ibid., **78**, 252 (1984)
59. Ghiradella, H.: Microsc. Res. Tech. **27**, 429 (1994)
60. Vukusic, P., Sambles, J.R., Lawrence, C.R., Wootton, R.J.: Proc. R. Soc. Lond. B **266**, 1403 (1999)
61. Gralak, B., Tayeb, G., Enoch, S.: Opt. Express **9**, 567 (2001)
62. Kinoshita, S., Yoshioka, S., Kawagoe, K.: Proc. R. Soc. Lond. B **269**, 1417 (2002)
63. Yoshioka, S., Kinoshita, S.: Proc. R. Soc. Lond. B **271**, 581 (2004)

64. Yoshioka, S., Kinoshita, S.: Proc. R. Soc. Lond. B **273**, 129 (2006)
65. Berthier, S., Charron, E., Boulenguez, J.: Insect Sci. **13**, 145 (2006)
66. Vukusic, P., Sambles, J.R., Lawrence, C.R., Wootton, R.J.: Nature **410**, 36 (2001)
67. Land, M.F., Horwood, J., Lim, M.L.M., Li, D.Q.: Proc. R. Soc. Lond. B **274**, 1583 (2007)
68. Lim, M.L.M., Land, M.F., Li, D.Q.: Science **315**, 481 (2007)
69. Hébant, C., Lee, D.W.: Am. J. Bot. **71**, 216 (1984)
70. Thomas, K.R., Kolle, M., Whitney, H.M., Glover, B.J., Steiner, U.: J. Roc. Soc. Interface **7**, 1699 (2010)
71. Graham, R.M., Lee, D.W., Norstog, K.: Am. J. Bot. **80**, 198 (1993)
72. Gould, K.S., Lee, D.W.: Am. J. Bot. **83**, 45 (1996)
73. Lee, D.W.: Nature's Palette, the Science of Plant Colour. The University of Chicago Press, Chicago (2007)
74. Lee, D.W.: Nature **349**, 260 (1991)
75. Lee, D.W., Taylor, G.T., Irvine, A.K.: Int. J. Plant Sci. **161**, 297 (2000)
76. Richards, P.W.: The Tropical Rainforest, 2nd edn. Cambridge University Press, London (1994)
77. Neville, A.C.: J. Insect Physiol. **23**, 1267 (1977)
78. Steinbrecht, R.A., Mohren, W., Pulker, H.K., Schneider, D.: Proc. R. Soc. Lond. B **226**, 367 (1985)
79. Steinbrecht, R.A.: Tissue Cell **17**, 745 (1985)
80. Parker, A.R.: J. Exp. Biol. **201**, 2343 (1998)
81. Campos-Fernández, C., Azofeifa, D.E., Hernández-Jiménez, M., Ruiz-Ruiz, A., Vargas, W.E.: Opt. Mater. Express **1**, 85 (2011)
82. Bouligand, Y.: C. R. Acad. Sci. Paris **261**, 4864 (1965)
83. Neville, A.C., Caveney, S.: Biol. Rev. Cambridge Philos. Soc. **44**, 531 (1969)
84. Caveney, S.: Proc. R. Soc. Lond. B **178**, 205 (1971)
85. Neville, A.C.: Biology of the Arthropod Cuticle. Springer, Berlin (1975)
86. Neville, A.C., Parry, D.A.D., Woodhead-Galloway, J.: J. Cell Sci. **21**, 73 (1976)
87. Bouligand, Y.: In: Bruter, C.P., Arangol, A., Lichenrowicz, A. (eds.) Bifurcation Theory, Mechanics, and Physics. Riedel, Dordecht (1983)
88. Neville, A.C.: Biology of Fibrous Composites Development Beyond the Membrane. Cambridge University Press, Cambridge (1993)
89. Osorio, D., Ham, A.D.: J. Exp. Biol. **205**, 2017 (2002)
90. Goldstein, D.H.: Appl. Opt. **45**, 7944 (2006).
91. Bouligand, Y.: C. R. Chim. **11**, 281 (2008)
92. Sharma, V., Crne, M., Park, J.O., Srinivasarao, M.: Science **325**, 449 (2009)
93. Schultz, T.D., Rankin, M.A.: J. Exp. Biol. **117**, 87 (1985)
94. Schultz, T.D.: Bull. Entomol. Soc. Am. **32**, 142 (1986)
95. Schultz, T.D., Bernard, G.D.: Nature **337**, 72 (1989)
96. Liu, F., Yin, H.W., Dong, B.Q., Qing, Y.H., Zhao, L., Meyer, S., Liu, X.H., Zi, J., Chen, B.: Phys. Rev. E **77**, 012901 (2008)
97. Vukusic, P., Sambles, J.R., Lawrence, C.R.: Nature (London) **404**, 457 (2000)
98. Yoshioka, S., Kinoshita, S.: Opt. Express **15**, 2691 (2007)
99. Yoshioka, S., Kinoshita, S.: J. R. Soc. Interface **5**, 457 (2007)
100. Loewen, E.G., Popov, E.: Diffraction Gratings and Applications. Marcel Dekker, New York (1997)
101. Hinton, H.E.: Entomologist **102**, 185 (1969)
102. Hinton, H.E., Gibbs, D.: Nature **221**, 953 (1969)
103. Hinton, H.E., Gibbs, D.: J. Insect Physiol. **15**, 959 (1969)
104. Hinton, H.E., Gibbs, D.: J. Insect Physiol. **17**, 1023 (1971)
105. Hinton, H.E.: Some little known surface structures. In: Neville, A.C. (ed.) Insect Ultrastructure, pp. 41–58. Royal Entomological Society, London (1973)
106. Hinton, H.E.: Natural deception. In: Gregory, R.L., Gombrich, E.H. (eds.) Illusion in Nature and Art, pp. 97–159. Duckworth, London (1973)

107. Hinton, H.E.: Proc. Br. Ent. Nat. Hist. Soc. **6**, 43 (1973)
108. Seago, A.E., Wheeler, Q.D.: Coleopterists Bull. **58**, 235 (2004)
109. Ingram, A.L., Lousse, V., Parker, A.R., Vigneron, J.P.: J. Roc. Soc. Interface **5**, 1387 (2008)
110. Parker, A.R.: Proc. Roc. Soc. Lond. B **262**, 349 (1995)
111. Whitney, H.M., Kolle, M., Andrew, P., Chittka, L., Steiner, U., Glover, B.J.: Science **323**, 130 (2009)
112. Whitney, H.M., Kolle, M., Alvarez-Fernandez, R., Steiner, U., Glover, B.J.: Communicative Integr. Biol. **2**, 230 (2009)
113. Vigneron, J.P., Rassart, M., Vertesy, Z., Kertesz, K., Sarrazin, M.L., Biro, L.P., Ertz, D., Lousse, V.: Phys. Rev. E **71**, 011906 (2005)
114. Miller, W.H., Moller, A.R., Bernhard, C.G.: The corneal nipple array. In: Bernhard, C.G. (ed.) The Functional Organisation of the Compound Eye, p. 21. Pergamon, Oxford (1966)
115. Miller, W.H., Bernard, G.D., Allen, J.L.: Science **162**, 760 (1968)
116. Parker, A.R., Hegedus, Z., Watts, R.A.: Proc. Roc. Soc. Lond. B **265**, 811 (1998)
117. Stavenga, D.G., Foletti, S., Palasantzas, G., Arikawa, K.: Proc. Roc. Soc. Lond. B **273**, 661 (2006)
118. Yoshida, A., Motoyama, M., Kosaku, A., Miyamoto, K.: Zool. Sci. **13**, 525 (1996)
119. Binetti, V.R., Schiffman, J.D., Leaffer, O.D., Spanier, J.E., Schauer, C.L.: Integr. Biol. **1**, 324 (2009)
120. Parker, A.R., McPhedran, R.C., McKenzie, D.R., Botten, L.C., Nicorovici, N.A.: Nature **409**, 36 (2001)
121. Prum, R.O., Torres, R.: J. Exp. Biol. **206**, 2409 (2003)
122. Durrer, H.: Verhand. Naturforsch. Ges. Basel **73**, 204 (1962)
123. Yoshioka, S., Kinoshita, S.: Forma **17**, 169 (2002)
124. Zi, J., Yu, X.D., Li, Y.Z., Hu, X.H., Xu, C., Wang, X.J., Liu, X.H., Fu, R.T.: Proc. Natl. Acad. Sci. USA **100**, 12576 (2003)
125. Li, Y.Z., Lu, Z.H., Yin, H.W., Yu, X.D., Liu, X.H., Zi, J.: Phys. Rev. E **72**, 010902(R) (2005)
126. Parker, A.R., Welch, V.L., Driver, D., Martini, N.: Nature **426**, 786 (2003)
127. Maldovan, M., Thomas, E.L.: Nat. Mater. **3**, 593 (2004)
128. Galusha, J.W., Richey, L.R., Gardner, J.S., Cha, J.N., Bartl, M.H.: Phys. Rev. E **77**, 050904(R) (2008)
129. Morris, R.B.: J. Entomol. A **49**, 149 (1975)
130. Ghiradella, H., Radigan, W.: J. Morphol. **150**, 279 (1976)
131. Ghiradella, H.: J. Morphol. **202**, 69 (1989)
132. Argyros, A., Large, M.C.J., McKenzie, D.R., Cox G.C., Dwarte, D.M.: Micron **33**, 483 (2002)
133. Prum, R.O., Quinn, T., Torres, R.H.: J. Exp. Biol. **209**, 748 (2006)
134. Kertész, K., Bálint, Z., Vértesy, Z., Márk, G.I., Lousse, V., Vigneron, J.P., Rassart, M., Biró, L.P.: Phys. Rev. E **74**, 021922 (2006)
135. Michielsen, K., Stavenga, D.G.: J. R. Soc. Interface **5**, 85 (2008)
136. Michielsen, K., De Raedt, H., Stavenga, D.G.: J. R. Soc. Interface **7**, 765 (2010)
137. Saranathan, V., Osuji, C.O., Mochrie, S.G.J., Noh, H., Narayanan, S., Sandy, A., Dufresne, E.R., Prum, R.O.: Proc. Natl. Acad. Sci. USA **107**, 11676 (2010)
138. Häcker, V., Meyer, G.: Zool. Jb. Abt. Syst. Geog. Biol. Tiere **15**, 267 (1902)
139. Finger, E.: Naturwissenschaften **82**, 570 (1995)
140. Raman, C.V.: Proc. Ind. Acad. Sci. A **1**, 1 (1934)
141. Dyck, J.: Z. Zellforsch. **115**, 17 (1971)
142. Dyck, J.: In: Proc. Int. Orthnithol. Congr., vol. 16, p. 426. Australian Acad. Sci., Canberra (1976)
143. Prum, R.O., Torres, R.H., Williamson, S., Dyck, J.: Nature **396**, 28 (1998)
144. Prum, R.O., Torres, R., Williamson, S., Dyck, J.: Proc. R. Soc. Lond. B **266**, 13 (1999)
145. Dufresne, E.R., Noh, H., Saranathan, V., Mochrie, S.G.J., Cao, H., Prum, R.O.: Soft Matter **5**, 1792 (2009)
146. Noh, H., Liew, S.F., Saranathan, V., Mochrie, S.G.J., Prum, R.O., Dufresne, E.R., Cao, H.: Adv. Mater. **22**, 2871 (2010)

147. Shawkey, M.D., Estes, A.M., Siefferman, L.M., Hill, G.E.: Proc. R. Soc. Lond. B **270**, 1455 (2003)
148. Dong, B.Q., Liu, X.H., Zhan, T.R., Jiang, L.P., Yin, H.W., Liu, F., Zi, J.: Opt. Express **18**, 14430 (2010)
149. Dong, B.Q., Zhan, T.R., Liu, X.H., Jiang, L.P., Liu, F., Hu, X.H., Zi, J.: Phys. Rev. E **84**, 011915 (2011)
150. Prum, R.O., Torres, R., Kovach, C., Williamson, S., Goodman, S.M.: J. Exp. Biol. **202**, 3507 (1999)
151. Galusha, J.W., Richey, L.R., Jorgensen, M.R., Gardner, J.S., Bartl, M.H.: J. Mater. Chem. **20**, 1277 (2010)
152. Lafait, J., Andraud, C., Berthier, S., Boulenguez, J., Callet, P., Dumazet, S., Rassart, M., Vigneron, J.-P.: Mater. Sci. Eng. B **169**, 16 (2010)
153. Doucet, S.M., Shawkey, M.D., Rathburn, M.K., Mays Jr., H.L., Montgomerie, R.: Proc. R. Soc. Lond. B **271**, 1663 (2004)
154. Wickham, S., Large, M.C.J., Poladian, L., Jermiin, L.S.: J. R. Soc. Interface **3**, 99 (2006)
155. Parker, A.R.: Phil. Trans. R. Soc. B **363**, 2465 (2008)
156. Hubbard, J.K., Uy, J.A.C., Hauber, M.E., Hoekstra, H.E., Safran, R.J.: Trends Genet. **26**, 231 (2010)
157. Doucet, S.M., Meadows, M.G.: J. R. Soc. Interface **6**, S115 (2009)
158. Biró, L.P., Bálint, Zs., Kertész, K., Vértesy, Z., Márk, G.I., Horváth, Z.E., Balázs, J., Méhn, D., Kiricsi, I., Lousse, V., Vigneron, J.P.: Phys. Rev. E **67**, 021907 (2003)
159. Jackson, A.P., Vincent, J.F.V., Turner, R.M.: Proc. R. Soc. Lond. B **234**, 415 (1988)
160. Butler, M.W., Johnson, A.S.: J. Exp. Biol. **207**, 285 (2004)
161. Gower, D.J.: J. Morphol. **258**, 249 (2003)
162. Douglas, R.H., Marshall, N.J.: In: Archer, S.N., Djamgoz, M.B.A., Loew, E.R., Partridge, J.C., Vallerga, S. (eds.) Adaptive Mechanisms in the Ecology of Vision, p. 95. Springer, New York (1999)
163. Parker, A.R.: Phil. Trans. R. Soc. A **364**, 1759 (2009)
164. Vukusic, P.: Contact Lens Spectrum **25**, 6 (2010)
165. Biró, L.P., Vigneron, J.P.: Laser Photon. Rev. **5**, 27 (2011).
166. Liu, K.S., Jiang, L.: Nano Today **6**, 155 (2011)

Chapter 9
Superhydrophobic Surfaces: Beyond Lotus Effect

X.D. Zhao, G.Q. Xu, and X.Y. Liu

Abstract The term of lotus effect represents the superhydrophobic property of lotus leaves. The super water repellency endows self-cleaning function to lotus leaves, on which dirt particles are easily removed by raindrops. This phenomenon generates increasing interest for both fundamental research and practical applications. Integrated with up-to-date science and technology, superhydrophobic surfaces have been widely applied in industrial innovation and microengineering. In this review, after a brief overview on basic characterization of the superhydrophobic surface, the principle of its fabrication method and varied preparing technologies are introduced. Then, beyond the lotus effect, we will discuss the techniques applied on the modification of wetting behavior on superhydrophobic surface as well as multifunctional superhydrophobic surfaces derived from conventional ones.

9.1 Introduction

Wettability of solid is important for both fundamental researches and technical applications, ranging from industrial coating to microfluidic engineering. Specifically, non-wettable surfaces with high contact angles and small sliding angles, called superhydrophobic or ultrahydrophobic, have received a large amount of attention in recent years. Water drops that come into contact with superhydrophobic surfaces remaining a nearly spherical shape, with contact angle close to 180°, have

X.D. Zhao • G.Q. Xu • X.Y. Liu (✉)
College of Materials, Xiamen University, 422 Si Ming Nan Road, Xiamen, 361005, P.R. China

Department of Physics and Department of Chemistry, Faculty of Science, National University of Singapore, 2 Science Drive 3 117542, Singapore
e-mail: phyliuxy@nus.edu.sg

X.Y. Liu (ed.), *Bioinspiration: From Nano to Micro Scales*, Biological and Medical Physics, Biomedical Engineering, DOI 10.1007/978-1-4614-5372-7_9,

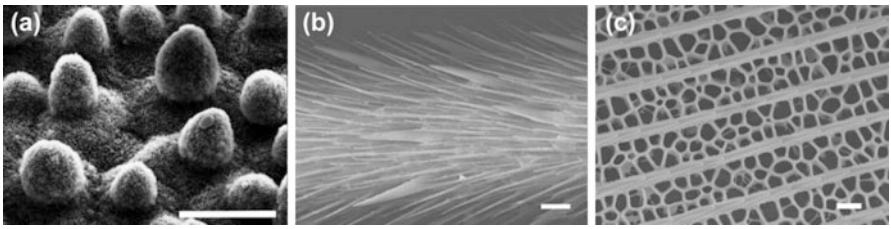

Fig. 9.1 SEM image of (**a**) *Nelumbo nucifera* surface which is characterized by microsized papillae, (**b**) a water strider leg showing numerous oriented spindly microsetae, (**c**) hollow and bridges structures of *Papilio ulysses* wings. Scale bars: (**a**) and (**b**) 20 μm, (**c**) 1 μm. Reprinted with permission from ref. [10]. Copyright (2004) Nature Publishing Group

been reported. These surfaces are of practical interest due to their water-repellent, antisticking, and self-cleaning properties. These properties are desirable for many application, including raindrop self-cleaning [1], oil spill cleanup [2], water-capture devices [3], laboratory-on-a-chip devices [4], bioinspired geckos/mussels feet [5], and functional interface for cell and tissue engineering [6].

In nature, various species exhibit impressive water-repellent property and one prominent example is the lotus leaf. Lotus leaf is well known for its self-clean feature removing dust and mud by water droplets rolling off surfaces and is regarded as a traditional symbol of purity in Buddhist societies. In 1997, Barthlott et al. [7] have revealed for the first time the interdependence between the surface roughness and the water-repellent property as well as dust particles adhesion. By comparing and summarizing the surface structures and their wetting properties of different plant leaves, the author found those with microsized papillae all exhibit contact angles (CAs) larger than 150°. Figure 9.1(a) shows the SEM image of lotus leaf (*Nelumbo nucifera*), from which fine-branched nanostructures on top of microsized papillae can be observed. Following researchers have found that such dual-scale structure surfaces combined with low-surface energy are crucial to design superhydrophobic surfaces with large CA and small sliding angle (SA) [8, 9]. Barthlott et al. also coined the term "lotus effect" for the demonstrable superhydrophobic property and since then researches on superhydrophobic surfaces have been activated to mimic the nature.

Since functionally optimized surface structures are one of the key innovations in the more than 400 million years of evolution of species, much more superhydrophobic surfaces with particular functions in wildlife have been explored. The water strider's legs are structured with numerous superhydrophobic nanohairs, which provide the impressive supporting force on water surface. The micrographs (Fig. 9.1(b)) revealed numerous oriented setae on the legs. These needle-shaped setae endow a single leg with maximal supporting force about 15 times the total body weight of the insect [10]. The secret of the *Stenocara* beetle surviving in extremely arid habitat is due to its structured superhydrophobic back which is able to collect water from the fog-laden wind in the morning [3]. The wings of many

butterflies are endowed with superhydrophobic feature to prevent capillary forces sticking them together [11]. The fine structure of butterfly (*Papilio ulysses*) wings is shown in Fig. 9.1(c). Inspired by these observations in nature, increasing endeavors from chemistry, material science, physics, and biology have been made to mimic those structures for varied functional concern.

The process for fabrication of a superhydrophobic surface via altering the surface energy and roughening of the surface has been well accepted. Since Kao et al. [12] have demonstrated the artificial superhydrophobic fractal surface made of alkylketene dimer and reemphasized the importance of geometrical structure in surface wettability, an increasing number of ways to fabricate superhydrophobic surfaces have been reported, either by introducing roughness into a low-surface-energy material and modifying a rough surface with low-surface-energy materials. Among those, multifunctional superhydrophobic surfaces have attracted a greater attention. The conventional super water repellent surfaces are integrated with various features of transparency, structure color, reversibility, anti-reflectivity, breathability, and other properties [13–18].

For structured surfaces, seeking to understand the relationship between surface roughness and its wetting property, Wenzel's [19] and Cassie's [20] theories are the most applied. Essentially, these two theories describe different superhydrophobic states: the former is complete wetting and the latter is when water droplets sit on a composite surface with air pockets trapped underneath. Besides, some other researchers [21–24] have argued that it is the three-interface contact line (TCL) that determines the contact angle behavior including advancing, receding, and hysteresis angles rather than the interfacial area within the perimeter. Even though conceptual problems may exist within Wenzel's and Cassie's theories, they still have merits to be applied at certain situations as advocated by their critics [22–24]. It is fairly straightforward to use them to characterize two distinguishable superhydrophobic states: the "slippy" Cassie state and the "sticky" Wenzel state. In general, water droplets adhere more strongly to the textured surface in the Wenzel state than in the Cassie state, causing stronger contact angle hysteresis (the difference between advancing and receding angle). In many cases, water droplets on structured surfaces are in the metastable Cassie state and the transition from Cassie to Wenzel state can be induced by external stimuli, such as pressure, electric voltage, or vibration.

In this review, we are not intended to provide an in-depth overview of the vast body of literatures; rather we want to summarize some selected aspects of superhydrophobic surfaces with their wetting properties and look ahead to future developments. The major objective of this chapter is (a) to introduce theoretical background charactering the lotus effect and the mechanism of wettability, (b) to review the most recent progress in the fabrication methods of superhydrophobic

surfaces in a systematic way, (c) to illustrate different superhydrophobic states and how to control the state transition, and (d) to address the multifunction of superhydrophobic surfaces and their potential applications.

9.2 Theoretical Background and Mechanism of Wettability

9.2.1 Ideal Surfaces

The wetting angle of a water droplet on an ideal surface is determined by the Young's law [25] and is based on the assumption of the balance among the cohesive forces acting in the TCL shown in Fig. 9.2(a) (see 9.1).

$$F_{SV} = F_{LV} \cos\theta_Y + F_{SL} \tag{9.1}$$

For many years, this equation has been reinterpreted in a way of thermodynamic equilibrium by substituting forces by surface tension:

$$\cos\theta_Y = \frac{\gamma_{SV} - \gamma_{SL}}{\gamma_{LV}} \tag{9.2}$$

where γ_{SL}, γ_{SV}, and γ_{LV} refer to the interfacial energy in the solid–liquid, solid–vapor, and liquid–vapor interface, respectively. Young's theory provides a very simple description of the different wetting scenarios on flat surfaces with varied surface energy. When the solid–vapor interface exhibits a high-surface energy, theoretically the addition of γ_{SV} and γ_{SL} equals γ_{LV}, and then the drop wets completely the surface, reaching a superhydrophilic state. In the case of surfaces with low surface tension, the water contact angle (WCA) increases. WCAs on surfaces higher than 90° are commonly defined as hydrophobic state, while WCAs higher than 150° are referred to as superhydrophobic state.

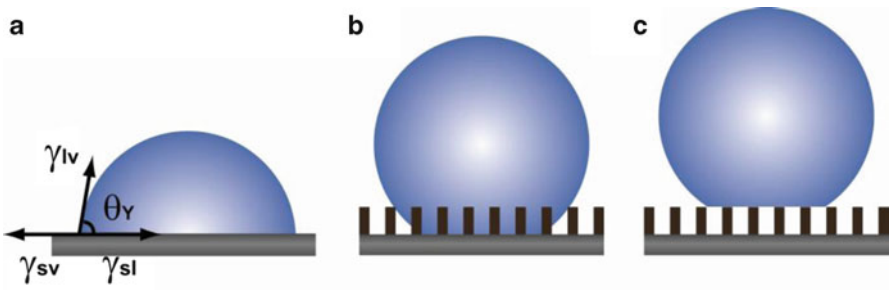

Fig. 9.2 Schematic illustration of wetting state: (**a**) drop on an ideal surface with contact angle θ and γ_{ij} indicated. (**b**) Wenzel state. (**c**) Cassie–Baxter state

9.2.2 *Non-ideal Surfaces*

It was found at an early stage that surface roughness and morphological heterogeneities may lead to a deviation of contact angle (CA) from the value predicted by Young's equation [19, 20]. To correlate the CA of real surfaces, two models are commonly applied.

9.2.2.1 Wenzel Model

Wenzel [19] introduced non-dimensional surface roughness r to address the roughness-amplified wetting properties of the smooth surface. r is the ratio of the actual area of liquid–solid contact to the projected area on the horizontal plane (Fig. 9.2(b)). In this case, the actual area of the drop's solid–liquid interface is enlarging a factor r. It follows that the contact angle on the rough surface, θ_W, is expressed as

$$\cos\theta_W = r\cos\theta_Y \tag{9.3}$$

Equation (9.3) implies that a flat hydrophobic surface with $\theta_Y > 90°$ becomes more hydrophobic via increasing the surface roughness. Similarly a flat hydrophilic surface with $\theta_Y < 90°$ becomes more hydrophilic if the roughness is introduced. Meanwhile, if the r reaches a critical value as $1/\cos\theta_Y$, the CA turns to 0° (complete wetting or superwetting).

9.2.2.2 Cassie/Baxter Model

Cassie and Baxter consider the effect of chemical heterogeneities of the surface on the measured apparent contact angle [20]. In their model, the total surface energy is considered as the average of respective component surface energy in the equilibrium state (Fig. 9.2(c)). It follows that the contact angle θ_C on the heterogeneous surface is expressed as

$$\cos\theta_C = \sum_i \phi_i \cos\theta_i \tag{9.4}$$

where Φ_i is the area fraction of component surface and θ_i is the angle corresponding to area fraction i ($\sum \phi_i = 1$).

On rough materials characterized by very hydrophobic surface chemistries and/or pronounced degrees of roughness, drops often prefer to rest on top of the roughness features, with air trapped underneath (Fig. 9.2(c)) [7,26,27]. In this case, the heterogeneous surface can be simplified as a composited surface composed of solid and air, where the air parts of the interface are considered as perfect non-wetting. It follows that the measured contact angle becomes $\cos\theta = \phi(\cos\theta_Y + 1) - 1$, where ϕ is the fraction of solid in contact with the liquid.

Equations (9.3) and (9.4) have sometimes been combined to a more general form: [28]

$$\cos\theta_C = r\phi\cos\theta_Y + \phi - 1 \tag{9.5}$$

where θ_C is the apparent contact angle on the rough surface and r characterizes to the degree of roughness of the solid area that contacts with liquid.

9.2.3 Dynamic Wetting Behavior

Both Wenzel's and Cassie–Baxter's theories predict the apparent CA in the equilibrium state, describing the static behavior of a liquid drop. In order to characterize the dynamic wetting behavior, advancing/receding angles and sliding angle (SA) are measured to evaluate the repellency of a surface. By definition, the maximum/minimum values of CAs for a drop front which has been advanced/receded over a surface are termed the advancing/receding angles; the difference between advancing angle and receding angle renders the contact angle hysteresis. SA can be measured as an inclined plate tilts at a critical angle, beyond which a liquid drop will rolling off or sliding down the plate surface. The quantitative relationship between the CA hysteresis and SA is provided by (9.6) [29]:

$$mg(\sin\alpha)/w = \gamma_{LV}(\cos\theta_R - \cos\theta_A) \tag{9.6}$$

where θ_A and θ_R are the advancing and receding angles, respectively, g is the gravity force, and m and w represent the mass and width of the drop, respectively. Equation 9.8 shows that small CA hysteresis results in small SA, indicating liquid drop rolling off or sliding down surfaces effortlessly. This equation also interprets one of the mechanisms of *Stenocara* beetle's back. Condensed water droplets roll off easily to be collected due to small SA on superhydrophobic surfaces.

9.2.4 Three-Interface Contact Line-Related Wetting Behavior

As discussed above, even though Wenzel's and Cassie's theories achieve great agreement with experimental results in many areas, unfortunately they make no statement about hysteresis. In the case of Cassie's theory, it simply describes an increasing "most stable" (in Marmur's notation) [30] contact angle in an equilibrium state with decreasing solid fraction ϕ. However, many experimental results show that drops may behave quite differently on two patterned surfaces of identical ϕ [31]; thus, the solid fraction should not be the only parameter determining the contact angle hysteresis. Chen et al. suggested that the topology of rough surfaces plays an important role in determining the contact angle hysteresis [32]. They concluded that

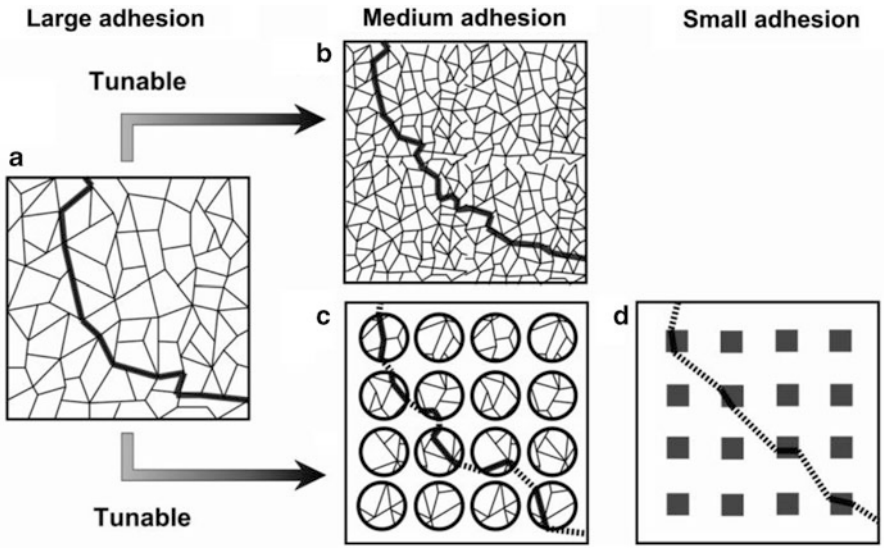

Fig. 9.3 Schematic illustration of TCL on MnO_2 films with different patterns. The solid lines demonstrate the possible solid–liquid–air interface contact line, and the dash lines demonstrate the liquid–air boundary for a droplet. (**a**) Formation of a continuous contact line on the L-MLS, which exhibits large adhesion. (**b**) TCL on S-MLS. (**c**) Formation of a dash-line-like TCL forms on BCS. (**d**) Formation of a highly discontinuous dotlike TCL forms on TNS, which exhibits extremely small adhesion. Reprinted with permission from ref. [33]. Copyright (2011) American Chemical Society

the contact angle hysteresis correlates to the continuity of TCL formed differently on varied patterns. When drops are in contact with a mesh-like porous structure, the TCL is continuous contact with the roughness features and large contact angle hysteresis is found. Comparatively, for a surface consisting of isolated roughness features, like posts shown in the literature, they assumed that the energy barriers decreased between metastable states, giving rise to a lowered contact angle hysteresis. Öner and McCarthy followed the same principle, highlighting the significance of "destabilizing the contact line" in a way to obtain superhydrophobic materials [33].

Recently, Zhao et al. [34] have proposed two strategies for controlling the TCL continuity adopted to tune the adhesion on MnO_2 films. The surface topography and patterns of MnO_2 films were simplified according to the high-contrast black and white SEM images shown in Fig. 9.3. The solid lines describe the possible TCL for a droplet in contact with these patterns, showing different continuity [32, 35]. When a droplet is placed on most surfaces, it will come to rest at a local energy minimum. The contact line will be pinned at a metastable state, and there will be an energy barrier for any advancing or receding of the water droplet on the surface [32, 36]. This kinetic barrier difference in the advancing and the receding modes gives rise to the CA hysteresis, leading to the adhesive force. As for a mesh-like structured (MLS) film, continuous linelike TCL is formed on the top of nanowall

sheets schemed in Fig. 9.3(a). Because of the large energy barrier between the two metastable pinning states, the film with large-sized MSL (L-MLS) generates a high CA hysteresis and thus a very high adhesive force. With decreasing the mesh size, the energy barrier decreases as well. Consequently, the adhesive force is reduced as the mesh size shrinks (Fig. 9.3(b)). Unlike MLS structure, a highly discontinuous dotlike TCL forms on the tilted nanorod structured (TNS) film (Fig. 9.3(d)). Herein, the energy barrier between the metastable pinning states is negligible. As a result, the TNS film is nonadhesive, and water droplets roll off effortlessly even when the surface tilts slightly. Furthermore, an intermediate state between these two distinct TCL modes can be obtained by mixing the patterns (linelike and dotlike TCL, Fig. 9.3(c)). On the hierarchical ball cactus-like structured (BCS) film, the contact line is a combination of continuous linelike and discontinuous dotlike TCL, illustrated as a separated dash-linelike TCL. Correspondingly, medium CA hysteresis and adhesive force are observed on this pattern.

9.2.5 Wetting Transitions

On some rough surfaces, drops can coexist in both Wenzel and Cassie states, depending on the way how the respective drop was deposited [37–42]. From theoretical prediction, the Wenzel state is energetically favored for a given r and ϕ, if the contact angle on a smooth material θ_Y is below a critical value θ_{Crit}. θ_{Crit} can be obtained by equating the Wenzel and the Cassie equation [(9.2) and (9.4)]: [43, 44]

$$r\cos\theta_{Crit} = \phi\cos\theta_{Crit} + \phi - 1 \tag{9.7}$$

In reality, kinetic barriers may stabilize drops in a metastable state instead of the minimum-energy state [42, 45–48]. Consequently, drops in both Cassie and Wenzel wetting states may appear on the same material. Theoretically, Patankar derive a model on a post array to study the Cassie to Wenzel transition [45]. For a hydrophobic surface (i.e., $\theta_Y > 90°$), the initial impalement of a drop on the post array is found to be correlated with an increase in interfacial energy. Energy was then recovered when the drop was in contact with the bottom of the post surface and liquid–air interface was replaced by liquid–solid interface. Following similar line of thought, Nosonovsky and Bhushan provide an energy diagram of the Cassie-to-Wenzel transition, illustrating both states separated by an energy barrier [48].

Varied external stimuli have been applied to introduce a transition of drops from the Cassie to the Wenzel state including pressure [38–40, 44], vibrating [49], electrical voltage [50, 51], and evaporate [48, 52]. In principle, the driving force for the transition can be ascribed to the increased Laplace pressure ΔP across the drops' liquid–air interfaces [53]. The pressure difference ΔP can be calculated by Laplace equation, which correlates surface tension γ_{lg}, and the radius of the meniscus:

$$\Delta P = \frac{2\gamma_{lg}}{R} \tag{9.8}$$

Theoretically, Bartolo et al. modeled the critical Cassie and Wenzel transition in "touching" and "sliding" scenario based on the vertical aligned pillars.

A Cassie and Wenzel transition takes place once the meniscus is so intensively curved that either direct contact with the bottom of the surface or the local advancing angle, which is defined as the advancing angle on the sidewalls of the roughness structure, is reached, so that the meniscus can slide down to bottom. In drop impact experiments, the energy necessary for inducing a Cassie-to-Wenzel transition as a function of the post height was measured on the structured post array [54]. For a transition to occur, Bartolo et al. found an approximately linear increase in the energy barrier with increasing post height and reach maximum above a critical post height. This trend suggests at the beginning the "touching" mechanism determines the Cassie-to-Wenzel transition, and "sliding" scenario occurs after the critical post height. This model has been further proved in his following research by investigating the shape of the drop footprint during the Cassie-to-Wenzel transition [52]. For a similar post-type structure, Zheng et al. simulated the hydraulic pressure at which a transition begins, ΔP_{Crit}, as: [55]

$$\Delta P_{\text{Crit}} = \frac{\gamma_{lg}\phi\cos\theta_Y}{(1-\theta)\lambda} \tag{9.9}$$

where λ is the cross-sectional area of a post divided by its perimeter. In contrast, Extrand's results suggested that ΔP_{Crit} increases with an increase in the λ_P-parameter [56]. Furthermore, Liu and Lange simulated the critical pressure on a surface composed of regularly arranged, microscale spheres [57]. Bormashenko et al. revealed that a critical threshold parameter responsible for the Cassie-to-Wenzel transition depends on the force per unit length of the triple line instead of pressure [49].

Moreover, some recent experimental studies and simulations suggest that the transition from the Cassie to the Wenzel state start from one or more nucleation sites instead of over the entire drop footprint at once [58–61]. How the transition proceeds is then determined by how easily the meniscus can move within the surface structure.

Compared to the Cassie-to-Wenzel transition, the Wenzel-to-Cassie transition has received much less attention, and it is mainly due to rare observation. The Cassie-to-Wenzel transition is generally considered as an irreversible process for the case where the Wenzel state is at the absolute energy minimum [46, 47, 62]. However, recent studies on condensation of water on microstructure indicate that Wenzel-to-Cassie transitions are possible when the Wenzel state is metastable, and the Cassie state stay within lower energy state [42]. The solid experimental results show that Wenzel, Cassie, and mixed Wenzel–Cassie drops co-exist when water was condensed onto microscale post-type surfaces [41, 42]. In one series of experiments,

it was found that Wenzel drops could sometimes make a transition to the Cassie state either entirely or over part of their footprint area through coalescence during the condensation process [42]. The authors suggest that the calescence of two drops eliminates liquid–air interfacial area, and then enough energy is brought into the system for this energy barrier to be overcome.

9.3 Biomimicking Technologies

It is found that suitable roughness combined with low-surface energy are essential to obtain superhydrophobic surfaces no matter what material is used (organic or inorganic) and what kind of structure formed on the surface (particles, rod arrays, or pores). As a result, roughening the surface followed by hydrophobization or transforming low-surface-energy materials into rough surfaces are common procedures to produce superhydrophobic surfaces.

The most used substrates for fundamental research on superhydrophobic surfaces involve rigid solid substrates such as silicon wafers, glass slides, and metal surfaces, which might limit the practical applications and the large-scale production of superhydrophobic surfaces [63]. Flexible substrates such as polymer films and fibrous substrates outperform the rigid substrates for superhydrophobic surfaces in industrial applications. The rough surfaces could be cast, spray coated, or post treated on polymer films with intrinsic low-surface energy or imparted by hydrophobization. Fibrous substrates include woven or nonwoven textiles with natural or synthetic microfibers.

Practically, the methods for superhydrophobic surface preparation can be generally ascribed into three categories: top-down, bottom-up, and combination of bottom-up with top-down approaches. Top-down approaches involve lithographic and template-based techniques [64], as well as surface plasma treatment [65–72]. Bottom-up approaches encompass mostly self-assembly and self-organization [65–72], such as chemical deposition [73–77], layer-by-layer (LBL) deposition [77–81], hydrogen bonding [73, 77, 78], and colloidal assemblies [82]. Methods combining bottom-up with top-down approaches contain casting of polymer solution, phase separation [64, 76, 83–85], and electrospinning [86]. In the subsequent section, different approaches are illustrated in detail.

9.3.1 Top-Down Approaches

The top-down approach is a general term referring to the manufacture of materials and devices by carving, molding, or machining bulk materials with tools and lasers in microelectronics, including technologies such as templation [79, 87, 88] and lithographic approaches [39, 89], micromachining [8, 33, 45, 90–92], and plasma treatments. The technologies are frequently combined in order to produce

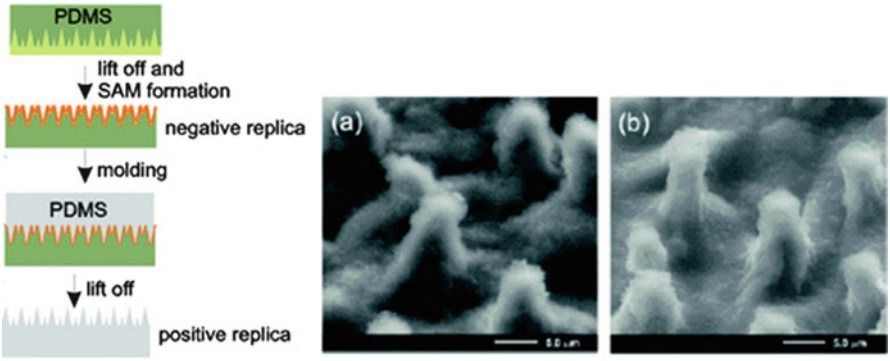

Fig. 9.4 Schematic illustration of nanocasting and SEM images of (**a**) a natural lotus leaf and (**b**) its positive PDMS replica. (Images reprinted with permission from Sun et al. [100] Copyright 2005, American Chemical Society)

surfaces with desired features. For example, the surfaces produced by lithographic approaches and micromachining can be used as a replicating template.

Template methods involve molding and replication steps with the template removed by lifting off [93], dissolution [39, 89], or even sublimation as the following steps [94] in order to replicate the desired features. In the lithographic approaches, irradiation of light through a mask with designed features onto the substrates with a photoresist is followed by the etching steps, generating the desired patterned surfaces which correspond to the feature of mask. Silanization is subsequently used to make these surfaces hydrophobic [95, 96]. In micromachining, surfaces are diced into the anticipated texture [8, 33, 45, 90–92]. In the plasma treatments, surfaces are etched anisotropically, hence yielding rough surfaces. For instance, plasma treatment of poly(ethylene terephthalate) [70, 71], poly(tetrafluoroethylene) (PTFE) [97], and polyethylene (PE) [68]. Pulse-laser treatments of poly(dimethylsiloxane) (PDMS) for the fabrication of superhydrophobic surfaces have also been developed [98, 99].

9.3.1.1 Templating

In principle, either 2D or 3D pattern or shape can be replicated via a templating method. Template methods involve molding and replication steps with the template removed by lifting off [93], dissolution [39, 89], or even sublimation as the following steps [94] in order to replicate the desired features. Templation is a useful technique to prepare polymeric superhydrophobic surfaces, with a wide range of materials used as a template containing natural lotus leaves [100], a master produced by lithographic processes as well as commercial inorganic membranes.

Sun et al. [100] have obtained a negative replication of the lotus leaf structure through nanocasting replication process with lotus leaf as the template and PDMS as the replication media (Fig. 9.4). This negative template was further applied as

a master for preparing a positive replica of the lotus leaf, which has nearly the same surface morphology as the natural lotus leaf on both the micro- and nanoscale. Small papillae hills with an average distance of 6 μm and even the intricate nano textures between the hills and in the valleys were successfully replicated in the positive replica as shown in the SEM images (Fig. 9.4, SEM images). The positive replica also exhibits the same superhydrophobic property as the natural counterpart with a contact angle of 160° while the negative replica of the lotus leaf displays hydrophobic properties with a contact angle of 110°.

Master prepared by macromachining can also be used as template to fabricate superhydrophobic substrates. In He et al.'s work [39], substrates contain squared posts of 25 μm wide, 30 μm deep, 8–80 μm between the posts. A water drop can both suspend on top of the posts and wet the posts determined by how the water drop is attached. Gentle deposition causes a suspension of the water drop, with the measured contact angle following the Cassie's theory prediction. While dropping the water from some height induces a wetting of the gaps between the posts, with the contact angle satisfying the Wenzel's theory.

Nanoimprint lithography is another kind of replication process with the pattern replication achieved by heat- and pressure-driven process, and a hard master pushed firmly onto a thermoplastic polymer layer whose temperature is above its glass transition temperature [101]. And then the master is cooled and removed to acquire a negative replica of the template. Impressively, nanoimprint lithography is able to make very small features even down to a few nanometers based on the master design. Take the work of Lee et al. [102], for example, nanoimprint lithography is harnessed for the preparation of polystyrene substrates with disparate nanostructures. In the nanoimprinting process, textured aluminum sheets and anodic aluminum oxide (AAO) membranes were used as replication templates and the master were pressed onto polystyrene (PS) polymer substrates with the temperature raised simultaneously. After a temperature cooling down and pressure release process, the replication template was eliminated from the polymer substrate by dissolving with saturated $HgCl_2$ solution, achieving the successful replication outcome, the large area, nanostructured PS surface. The diameters of PS nanofibers were controlled by changing the pore diameter of the AAO replication templates, which was adjusted as desired through wet-chemical etching. On the other hand, the length of PS nanofibers could be tuned by appropriately varying the thickness of the AAO template. Unlike imprint nanolithography using a hard master, capillary force lithography utilizes a patterned elastomeric mold, which is directly laid onto a spin-coated polymer film (Fig. 9.5). In order to obtain the negative replica of the mold, the temperature is raised above the polymer's glass transition temperature after solvent evaporation, known as temperature-induced capillarity; or by direct molding prior to solvent evaporation, known as solvent induced capillarity.

Similar to this, alumina membrane was exploited as the mold to facilitate aligned PS nanotubes, as demonstrated by Jin et al. [94]. The membrane was brought into contact with the PS solution which was previously cast on glass. After capillary molding, the membrane was dissolved in NaOH to achieve aligned PS nanotubes. The surface is superhydrophobic but very sticky, with the water droplet on it not

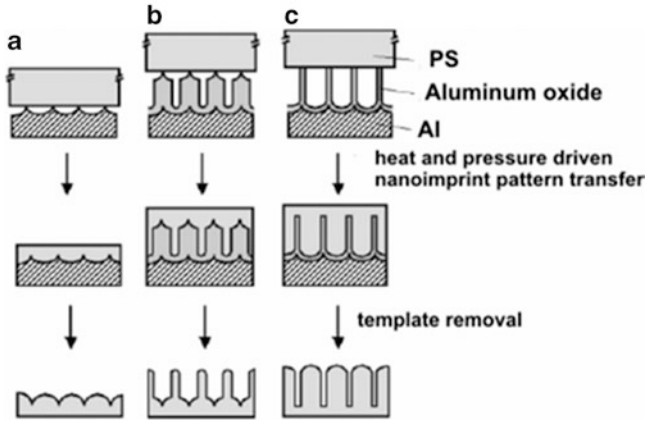

Fig. 9.5 Schematic outline of the heat- and pressure-driven nanoimprint pattern transfer process for nanofabricating the surface of the thick polymer substrate with (**a**) aligned nanoemboss, (**b**) nanopost array with embossed base, and (**c**) aligned nanofibers. (Images reprinted with permission from Lee et al. [102] Copyright 2004, American Chemical Society)

rolling off even it is upside down. This super sticky effect is attributed to the van der Waals' forces between the water molecules and the highly dense nanotubes, generating a strong adhesion in similar principle with the gecko's mechanism [103]. Such a sticky surface is applied as a mechanical hand to transfer a water droplet.

Through extrusion with AAO membranes with pores of average diameter of 68.7 nm [104], the researchers have successfully accomplished the fabrication of superhydrophobic poly(vinyl alcohol) (PVA) nanofibers. Although PVA is a hydrophilic material, the produced nanofibers exhibited superhydrophobicity with WCA of 171°, mainly due to the orientation of the PVA molecules that leads to hydrophobic backbones exposed to the surface as verified by angle dependent X-ray photoelectron spectroscopy study.

As shown above, templation is a useful technique in preparing superhydrophobic surfaces with tunable surface morphology. Hence, many features can be fabricated depending on the type of templates. Furthermore, the diverse polymeric materials available have endowed templation a versatile approach. However, the attainable geometry is limited by the available templates and not every material is suitable for the templation approach.

9.3.1.2 Photo Lithography

In photolithographic approaches, light is radiated through a mask with required features to the substrates such as silicon with a photoresist. Succeeding developing and etching steps generate the desired patterned surfaces. There are two kinds of photolithography, X-ray lithography and E-beam lithography, depending on the

light source, either radiation or electrons. An additional surface treatment procedure is demanded to render the surface's superhydrophobicity. Structures prepared by photolithography can be easily characterized and they are frequently applied in the surface modeling.

For instance, Furstner et al. [90] fabricated silicon wafers with ordered patterns of spikes by X-ray lithography. Subsequent sputtering of a layer of gold and immersion into a hexadecanethiol solution make the wafer hydrophobic. The spikes have a width (d) of 1 or 2 μm, the distance between the spikes (a) range from 1 to 5 μm, and the height of the spikes (h) was also different, from 1 to 4 μm. CA of the surfaces ranged from 113 to 161° determined by the pillar size, the clearance as well as the height of the spikes. And the best self-cleaning surface was found with $d/a = 2$ and $h/d = 4$, while the self-cleaning property of the specimen was measured by applying an artificial fog.

Martines et al. [92] have produced nanopillars and nanopits on silicon wafers by E-beam lithography. The center-to-center distance among pitches is kept in a constant value at 300 nm. The diameter (d) and height (h) of the pillars and pits are varied for different samples. The hydrophobic nanopatterns were obtained by silanization, covering of a surface through self-assembly with silane-like molecules, the octadecyltrichlorosilane. All treated surfaces exhibit improved hydrophobicity in contrast to the flat control surface. The contact angle behavior of samples with nanopits falls in the Wenzel regime. Samples with pillars are found in Wenzel and Cassie–Baxter states, being ascribed to the differences in aspect ratio (h/d). They displayed that a given spacing with increasing aspect ratio can remarkably stabilize the Cassie–Baxter regimes.

9.3.1.3 Plasma Treatment of Surfaces

Plasma treatment on surfaces involves plasma etching, a dry etching technique where reactive atoms or ions (such as oxygen, chlorine, and fluorine) are engendered in a gas discharge. The ions are expedited in the border layer between plasma and substrate with high directionality. They are thus capable of creating deep grooves with steep walls to yield reactive ion etching. Due to this anisotropic etching of the surface layers, plasma treatment can induce a considerable change in the surface structure.

Fresnais et al. [68] treated low-density polyethylene (LDPE) with plasma etching. The surfaces were treated by LDPE with oxygen and subsequent CF_4 plasma, then surfaces with CA of 170° and low hysteresis less than 5° and with the roughness within the range of 20–400 nm were fabricated [68].

Minko et al. [97] fabricated self-adaptive surfaces using oxygen plasma treatment of PTFE. The resulting plasma-etched PTFE exhibited a water CA about 160° and was observed with CA hysteresis. The superhydrophobic PTFE surfaces then undergo sequent treatment of ammonia plasma and a mixed polymer brush consisting of two carboxyl terminated incompatible polymers: carboxyl-terminated poly(styrene-*co*-2,3,4,5,6-pentafluorostyrene) (PSF-COOH)

and carboxyl-terminated poly(2-vinylpyridine) (PVP-COOH). The wettability of the grafted surface can be switchable by controlling through soaking in different solvents. This phenomenon was ascribed to the favored component attached on the surface of the substrate and the other component collapsing into the interior of the polymeric film.

Apart from the examples shown above, more examples [70, 71, 105–107] demonstrate that plasma treatment is a dry etching technique for the preparation of superhydrophobic surfaces. Furthermore, different elements providing additional functions can be readily introduced in the surface depending on the type of gas, tetrafluoromethane, ammonia, argon, or oxygen,

9.3.2 Bottom-Up Approaches

Opposite from the top-down approach, bottom-up methods refer to the building of larger, more complex objects by integrating smaller building units or components. The bottom-up approach in nanofabrication normally involves self-assembly and self-organization. Self-assembly and self-organization are normally used interchangeably. To be specific, self-organization is a nonequilibrium process while self-assembly is an integration process leading to equilibrium in which components assemble spontaneously in solution or the gas phase until they reach a stable structure with minimum energy. Bottom-up approaches utilized in the preparation of superhydrophobic surfaces cover chemical deposition methods such as chemical bath deposition (CBD) [72, 79–81], chemical vapor deposition (CVD) [79, 80], and electrochemical deposition [77, 78, 108], LBL deposition via electrostatic assembly [73], colloidal assembly [76, 85], sol–gel methods [83, 85, 109–117], hydrogen bonding [82], and chemical synthesis [118]. Some important examples will be introduced and discussed in detail in the following sections.

9.3.2.1 Chemical Deposition

Chemical deposition is generally used for generating thin films of crystalline inorganic materials, such as ZnS, CuSe, InS, CdS, MnO_2, etc., with the material self-assembling and depositing on some appropriate substrates. The chemical deposition encompasses different methods such as CBD, CVD, and electrochemical deposition, in regard to corresponding deposition conditions. Various surface morphologies can be obtained from nanopins, nanotubes to nanorods, by changing the material and tuning the deposition conditions.

CBD is implemented to create a nanopin film from a solution of $CoCl_2$ and NH_2CO in water by Hosono et al. [81]. The nanopin film with the top of the needle being sharp (a diameter of 6.5 nm) was deposited on borosilicate glass slides in an autoclave. Besides, the nanopin exhibits single crystalline-like structures because each metal complex in the solution is singly deposited on the surface owing to

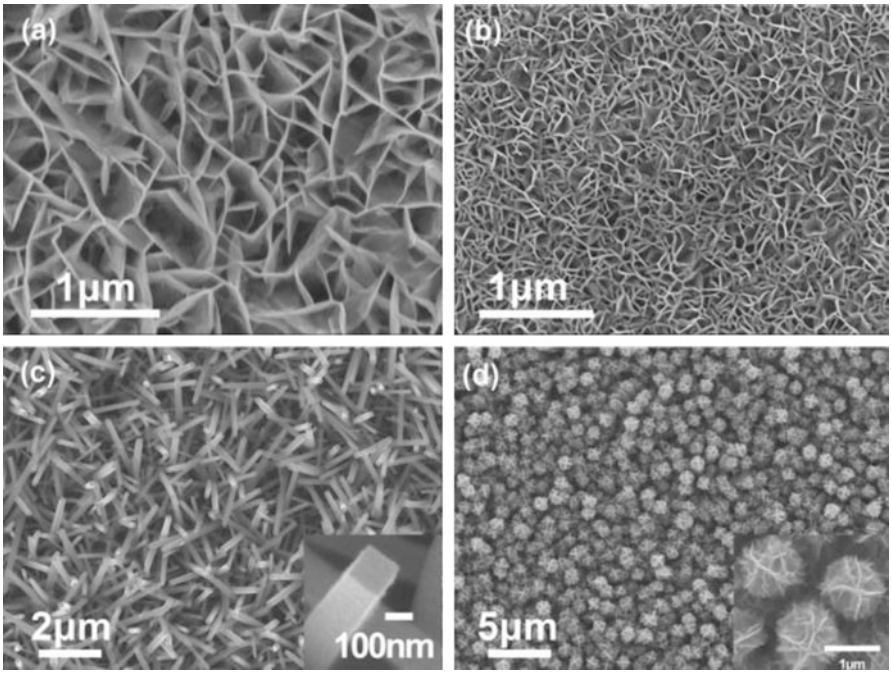

Fig. 9.6 (**a**–**d**) SEM images of MnO_2 MLS, TNS, and BCS films. (**a**–**b**) Large and small mesh size MLS. (**c**) TNS film. (**d**) BCS film. Reprinted with permission from ref. [34]. Copyright (2011) American Chemical Society

thermodynamic equilibrium conditions. Subsequently, the nanopin was treated with lauric acid (with $\theta = 75.1$) to acquire a superhydrophobic surface, of which the measured water CA is 178°.

Wu et al. [119] also used CBD to prepare uniform and dense superhydrophobic surfaces of zinc oxide (ZnO) nanorods with diameters ranging from 400 to 600 nm glass slides as substrate, using a solution mixture of $Zn(NO_3)_2$, NH_4Cl, urea, and ammonia. Surface modification with SAMs of alkanoic acids of different chain length generate substrates with high advancing contact angle (>150°), and different receding angles determined by the chain length of the alkanoic acids.

Zhao et al. [50] have prepared the MnO_2 nanotube array (MTA) membrane by the simple and low-cost hydrothermal treatment of a solution of KMnO4 and HCl. The open end and the square cross-section of the nanotubes can be clearly observed. The average length of MnO2 nanotube is 2 μm and outer diameter and wall thickness are 103 nm and 23 nm, respectively. The density of the MAT membrane is about 2.38 tubes μm^2. The as-prepared MTA membrane was nearly superhydrophilic with a CA of 6°. It was further treated by stearic acid sodium to achieve superhydrophobicity with a CA of 160.9° and a small slide angle (<5°).

To acquire diverse adhesive property on superhydrophobic surfaces, Zhao et al. [34] later prepared different patterns of MnO_2 films: a MLS, a BCS, and a TNS (Fig. 9.6) were synthesized on the basis of the hydrothermal method. In a typical

experimental procedure, 2.5 mM $KMnO_4$ and 10 mM concentrated HCl were added to 45 mL deionized water to form a precursor solution, which was then transferred into a teflon-lined stainless steel autoclave with a capacity of 100 mL. Two types of Si wafers (1×3 cm^2) with and without Pt coating were used as the substrates to grow high-oriented MLS films with different mesh sizes. The autoclave was sealed and treated hydrothermally at 140°C for 50 min to obtain MnO_2 MLS films. The TNS films were synthesized by extending the reaction time to 135 min to form the α-MnO_2 layer. By employing the TNS films as the substrate, BCS films were obtained via the same procedures as MLS. All the as-fabricated films were rinsed with deionized water and dried in air overnight. To achieve surface superhydrophobicity, the as-prepared MnO_2 films were immersed into methanol solution of hydrolyzed 1 wt% PFOTES (1H,1H,2H,2H-perfluorooctyltriethoxysilane ($CF_3(CF_2)_5CH_2CH_2Si(OCH_2CH_3)_3$)) for 1 h at room temperature. The samples were rinsed with ethanol and subsequently heated to 140°C for 1 h to remove nonbonded PFOTES molecules.

In addition, Huang et al. [120] have used CVD to prepare aligned carbon nanotubes (ACNTs) on Fe–N-coated silicon substrates. The substrates deposited by a ZnO layer showed water CA of 159°, where the wettability is tunable and the property can be utilized in the application in microfluidic devices. Specifically, the superhydrophobic surface can be turned into hydrophilic after a long period of exposure to UV illumination. And the hydrophobicity of the surface can be recovered after storage in the darkness.

Besides, electrochemical deposition of the zinc oxide [108], gold clusters [121], or silver aggregates together with the further modification with SAMs has been used to fabricate superhydrophobic surfaces [77].

9.3.2.2 Colloidal Assemblies

The close-packed particle assemblies formed by monodispersed particles owing to van der Waals' interactions impart roughness to the underlying substrates. This roughness can be further improved by the subsequent treatment such as plasma etching [122]. Various colloidal particles ranging from polymer beads to inorganic spheres can be used in the assembly. Colloidal assembly is widely used in laboratory research because it is an economic way compared with expensive lithographic technique and it is easy to master.

Spin coating is a way to assemble monodispersed polystyrene (PS) beads to closely packed structure [122], with the solid–air fraction of these nanostructures tuned by oxygen plasma etching which can reduce the sizes of beads by controlling the etching conditions. The surfaces were then coated with a layer of gold and a layer of octadecanethiol SAM in order to make the surfaces superhydrophobic.

Zhang et al. [76] have used binary colloidal assemblies for the production of superhydrophobic surfaces. $CaCO_3$-loaded hydrogel spheres were assembled on silicon substrates using dip-coating, serving as templates for the subsequent self-assembly of silica nanoparticles or polystyrene beads. The hydrophilicity is

different between silicon wafers and $CaCO_3$-loaded hydrogel spheres. Hence, the silica or polystyrene spheres localize in selective regions, leading to irregular binary structures possessing a hierarchical roughness. The substrate can also be tuned to superhydrophobic surface by depositing gold and SAM formation.

9.3.2.3 Layer-by-Layer Deposition

The LBL technique is easy to perform where the thickness of the resulting layer can be controlled with molecular precision, utilizing the electrostatic charge interactions between the different layers such as polyanion and polycation. Incorporating nanoparticles into the multilayer system and additional treatment can be used to enhance the roughness, rendering multilayer films the hydrophobicity,

Zhai et al. [123] have acquired superhydrophobic silicon surfaces with poly(allylamine hydrochloride) (PAH)/poly(acrylic acid) (PAA) multilayers via LBL deposition. Acidic treatments generate pores on the order of 10 μm and a microscopic honeycomb-like structure was formed on the PAH/PAA films. Further coating of silica nanoparticles and a semifluorinated silane leads to the stable superhydrophobic substrate, with the stability tested by extended immersion in water. In general, the acid treatments create microstructure and the deposition of silica nanoparticles induces nanostructure. Both the procedures are important in creating stable superhydrophobic surfaces.

Another approach for the incorporation of particles in the LBL assembly has been performed by Han et al. [73] in order to prepare superhydrophobic surfaces. PAA-coated ZrO_2 particles and PAH take turns to be deposited on clean silicon substrates. Through 20 deposition cycles, the surface displays WCA of 139° with a PAH exposed as the outermost layer and a huge hysteresis (±40°), which are remarkable since PAH is rather hydrophilic (±60°). Further deposition of silica nanoparticles and perfluorinated dodecyltrichlorosilane reduced the contact angle hysteresis of 2° and enhanced the superhydrophobicity of a WCA of 170° significantly. Amidation through thermal treatment of substrates at an increased temperature of 220°C render the film additional stability.

The LBL technique is facile to implement and control the film thickness with molecular precision. However, a hydrophobization is often necessary since polyelectrolytes are hydrophilic. In addition, some additional steps such as the incorporating nanoparticles are required to generate rough surfaces, thus making it a less direct and immediate way in preparing superhydrophobic surfaces.

9.3.2.4 Sol–Gel Methods

Hydrolysis of the corresponding oxide in the presence of solvent produces sol. Gel is formed when a large amount of solvent are also congested in the network during the network formation process. The sol can be used either straight way or

combined with filling such as silica nanoparticles. The surface property depends on the preparing process of the sol and surface functional groups of the outcome gel [83, 85, 109–115, 117, 124].

Sol–gel processing and self-assembly have been utilized by Shang et al. [125] to prepare transparent superhydrophobic films. And the surface roughness was tuned through the microstructures of the sol–gels by controlling hydrolysis and condensation reactions of varied silica precursors over the sol–gel processing, while introducing a monolayer through surface condensation reaction to modify surface chemistry. The resulting silica-based coatings by direct dip-coating demonstrated optical transparency higher than 90%. The advancing and receding WCAs were about 165 and 115°, correspondingly, thus a relatively large contact angle hysteresis of 50°.

Hikita et al. [83] have used the sol–gel method to fabricate super liquid repellent surfaces, where colloidal silica particles and fluoroalkylsilane are used to control the surface energy and roughness. The surfaces can exhibit repellency to both water and oil, when films have optimal ratio between colloidal silica and fluoroalkylsilane.

Doshi et al. [126] used silica sol–gel to prepare 50-nm-thick surfaces with switchable properties from superhydrophobic to superhydrophilic. A rough and highly porous organosilica aerogel-like film was achieved through a low-temperature, low-pressure technique, where coatings of mixed alkoxides 3,3,3-trifluoropropyltrimethoxysilane and tetramethylorthosilicate make the substrate superhydrophobic. CA reached 155–160°, and angles up to 170° was observed. UV/ozone treatments were used to modulate the surface coverage of hydrophobic organic ligands on the silica framework, adjusting the CA continuously varying from superhydrophobic of 160° with the presence of organic ligands, to hydrophilic less than 10° after removal of the organic ligands.

The merits of the bottom-up approach are the molecular precision in controlling the chemistry composition and the thickness of the products. The weakness of this method lies in the difficulty to anticipate the hydrophobic properties unless it is fully completed.

9.3.3 Combination of Bottom-Up and Top-Down Approaches

The combination of bottom-up and top-down approaches is especially useful for creating substrates with a two-scale roughness, similar to the structure of the lotus leaf. The combination methods typically consist of two stages: the top-down approach creating a rough surface and the subsequent bottom-up process producing fine roughness. However, combination methods do not necessarily require a distinct two-stage process. Take phase separation, for example; it involves casting of thin film and succeeding phase separation by adjusting the environmental conditions.

9.3.3.1 Combination Methods Based on Chemical Vapor Deposition

Sun et al. [127] have utilized CVD to fabricate superhydrophobic film with anisotropically ACNTs with uniform tube length on quadrate micropillar arrays silicon substrates produced by photolithography. Due to the anisotropic nature of the carbon nanotube (CNT) arrays, both hydrophobic and hydrophilic surfaces coexist depending on the spacing between the pillar arrays. However, after further coating with a fluorinated SAM of (2-(perfluorooctyl)ethyl)trimethoxysilane, all surfaces turned to be superhydrophobic without the spacing effects.

Zhu et al. [128] also used CVD to grow CNT arrays on micro-patterned silicon wafers and nanoscaled CNT films, creating surfaces with two-scale roughness, to compare the wetting properties. As for the CNT arrays on CNT films, the size, pitch, and height are varied to explore their effects on the hydrophobicity of the surfaces. The results suggest that the micro-scale roughness determines the WCA since the nanoscale roughness does not significantly increase the WCA compared to micro-patterned silicon surfaces with similar geometrical sizes. However, the nanoscale roughness can lower the contact angle hysteresis to less than 1° and refine the stability of the superhydrophobic surfaces.

9.3.3.2 Combination Methods Based on Membrane Casting

Most porous polymer membranes are produced by casting polymer solution through an appropriate template, with microscopic structures formed by phase separation, which occurs when the polymer solution approaching the cloud point is immersed in nonsolvents or experiences heat treatments. The nucleation of polymer results in rich poor phases of polymer due to the interaction of solvent and nonsolvents with macromolecules. The macromolecules nucleate and the networks form in the polymer-rich phase whereas pores form after the solvent removal in the polymer-poor phase [129].

Erbil et al. [130] have used isotactic polypropylene (i-PP) to prepare superhydrophobic surfaces by changing solvents, nonsolvents, solute concentration as well as drying temperature. The results show that decreasing the drying temperature promotes a loose network formation and methyl ethyl ketone is the best nonsolvent, generating a surface with contact angle of 160°.

Based on the above work, Lu et al. [131] used LDPE to prepare superhydrophobic surfaces through thermally induced phase separation. The structure and thus the wettability of the ultimate film can be controlled by changing the endurance time of heat treatment.

Super-amphiphobic surfaces are achieved by Xie et al. [132] with coating by two polymeric materials: poly(methyl methacrylate) (PMMA) and fluorine-end-capped polyurethane (FPU). Films containing only PMMA exhibit water CA of 145° and rough structures with micropapillae. Films with the mixture of PMMA and FPU

possess both micro- and nanopapillae with water CA of 166°. In addition to the low-surface energy of the FPU, the high CA and low sliding angle of the surface was also due to the lotus-like micro–nano binary structure.

Yabu and Shimonura [133] have cast block copolymers consisting of equimolar fluorinated acrylate and methyl methacrylate monomers on a substrate by a blade to prepare superhydrophobic surfaces. A honeycomb film is eventually achieved through the control of the condensation of water droplets as well as ultimate evaporation of the solvent and water. After peeling off the top layer of the honeycomb film, pin cushion structures can be acquired, where the sizes of both the honeycomb and pincushion structures can be readily adjusted by tuning the volume of casting polymer solution. The pincushion surface deriving from honeycomb films with 1.6 μm pores exhibits superhydrophobicity with the contact angle maximizing at 170°.

Wessling's group has fabricated superhydrophobic surfaces possessing two-scale roughness by membrane casting with Hyflon AD solution on a silicon template patterned by photolithography [134], denoted as the phase separation micromolding (PSμM). This method supplies the surface with roughness on both the microstructure level originating from the template and pore-size level arising from the phase inversion, which can be controlled independently.

In conclusion, membrane casting is comparatively easy to perform and the roughness can be controlled during the film formation process, by tuning parameters such as the choice of solvents, nonsolvents, the concentration of the solution, and the environmental conditions for membrane casting. Nevertheless, membrane casting with the PSμM [134] stands as promising technique in preparing superhydrophobic surfaces.

9.3.3.3 Micelles

Micelles are termed as the aggregates of colloidal dimensions formed by the association colloids which are in equilibrium with molecules or ions. Micelles are formed by the microscale phase separation. Block copolymers form micelles due to the different solubility of the blocks in the particular solvent [135, 136]. The cast micelles formed by block polymer will generate films with different morphologies when exposed to environments with varied relative humidity.

Micelle solutions stemming from PS-*b*-PDMS block copolymer were used in preparing superhydrophobic surface through phase separation induced by vapor [135]. Surfaces with different wetting properties are generated according to different solvents and environment humidity. Enrichment of PDMS block in the outmost surface shows superhydrophobicity with CA of 163°, owing to the rearrangement of PDMS block to the surface in the period of phase separation process.

Block copolymer of PtBA-*b*-PDMS-*b*-ptBA micelle solution was used by Han et al. [137] to produce superhydrophobic surfaces with WCA reaching 163°. When incorporating silica nanoparticles into the micelle solution, the surface will exhibit a contact angle of 170° and a sliding angle less than 2°.

Superhydrophobic films based on micelles depend on the selection of solvents and the block copolymers, the casting methods, relative humidity of the environment. Thanks to the diversity of available polymer materials, superhydrophobic surfaces with different structures can be fabricated by this method [136, 137].

9.3.3.4 Electrospinning

Electrospinning is normally a process extruding polymer nanofibers from the extrusion nozzle to a grounded collection plate where an electrical bias is applied [138]. A continuous, nonwoven web of electrospun fibers forms films, along the trajectory of the extruded polymer fiber, where most of the solvents evaporate. The film properties can also be modified by introducing chemical modification such as fluorine [88].

Electrospinning independently [88, 139] or in combination with other methods, such as CVD [92], have been used in preparing superhydrophobic films of polymers. The morphology of the electrospun film varies from mostly beads to solely fibers when the viscosity of the polymer solution is increased [88], thus changing the final wetting behavior. It is observed that surfaces containing beads are more hydrophobic compared with those with only nanofibers. Therefore, polymers with lower molecular weight were used to obtain surfaces with higher WCAs due to the results that more beads can be formed by lower molecular weight polymers, with the CA reaching as high as167°.

Combination of electrospinning of poly(caprolectone) (PCL) with initiated CVD (i-CVD) of polymerized perfluoroalkyl ethyl methacrylate were used to fabricate superhydrophobic surfaces by Ma et al. [79]. The inherent hierarchical surface roughness of the PCL films gained through electrospinning and the considerably low surface free energy of the coating layer through i-CVD contributes to the remarkably stable superhydrophobicity with a water CA of 175° and a threshold sliding angle less than 2.5°.

9.4 Control Wettability on Superhydrophobic Surfaces via External Stimuli

Increasing attention is paid on the way of manipulating wetting behaviors on superhydrophobic surfaces. Reversible superhydrophobic and superhydrophilic state transitions controlled by varied external stimuli have been reported. These studies have revealed that micro/nanostructures of superhydrophobic surfaces and chemical composition are the key parameters to control wetting behaviors. These superhydrophobic surfaces with controllable wettability are of great importance for both fundamental researches and practical applications

9.4.1 Light Illumination as External Stimulus

Light is one of the most important external stimuli [140]. A variety of photo-responsive inorganic oxides and organic polymers undergo the transition from larger CAs to relatively lower CAs upon ultraviolet (UV) illumination, reverting to the original states with larger CAs after the UV-irradiated films are placed in the dark or exposed to visible (Vis) illumination. This alternating transition can repeat for several cycles under this environment.

TiO_2 is one of the most studied and widely applied photo-sensitive semiconductors, because of its impressive self-cleaning property under sunlight and natural rainfall. The mechanism of self-clean can be ascribed to the intrinsic photocatalytic and photo-stimulated properties. In 1997, Fujishima et al. [141] have found reversible wetting behavior on anatase TiO_2 polycrystalline films upon UV illumination. In his report, the CAs on TiO_2 polycrystalline films change between $72 \pm 1°$ and $0 \pm 1°$. Therefore, based on the principle of roughness-induced superhydrophobicity, there is increasing attention on the introduction of fine surface textures to TiO_2 films to prepare superhydrophobic TiO_2 films. Tadanaga et al. [142] have prepared a rough TiO_2 gel layer on flowerlike Al_2O_3 film modified with hydrolyzed fluoroalkylsilane. By combining microstructure and chemical modification, CA larger than 150° was achieved on such surfaces. In addition, wetting transition from superhydrophobicity to superhydrophilic was realized after exposure to UV irradiation. Similar result has been reported on superhydrophobic TiO_2 nanorod films with dual-scale hierarchical structures. The CA modulation range is from $154 \pm 1.3°$ to about 0° and this process can be repeated several cycles before and after UV irradiation (Fig. 9.7) [143]. Fujishima et al. have reported another simple and reproducible method to roughen TiO_2 surfaces by adopting a CF_4 plasma etching technique [144, 145]. The discontinuous TiO_2 wedge-like microtextural films were formed via plasma etching for 30 s, after that the surface was coated with an octadodecyl phosphonic acid monolayer to exhibit superhydrophobicity. The sample originally showed water CAs larger than 165° and were converted to superhydrophilic ones with CA about 0° upon UV irradiation for 1 h.

ZnO is another prominent photo-responsive inorganic oxide that possesses several favorable properties on optical, electronic, and acoustic. It has been found a similar wetting behavior and converting mechanism as the TiO_2 surface [146, 147]. On a flat ZnO substrate, the maximum water CA is only 109°. Considering the roughness enhanced on superhydrophilicity/superhydrophobicity, a large amount of efforts have been devoted to fabricate ZnO film with varied micro/nanostructures, including nanoporous ZnO films [108], aligned ZnO nanorod array [148] to nanocolumnar ZnO surfaces [149], and to hierarchically structured ZnO film [80] and nanoprotrusions [150], and so on. Combining these structured surfaces with low-surface-energy materials, switchable superhydrophobic and superhydrophilic wetting states can be achieved on ZnO-based film upon alternating UV irradiation and storage in the dark. Besides, much more photo-responsive inorganic oxide

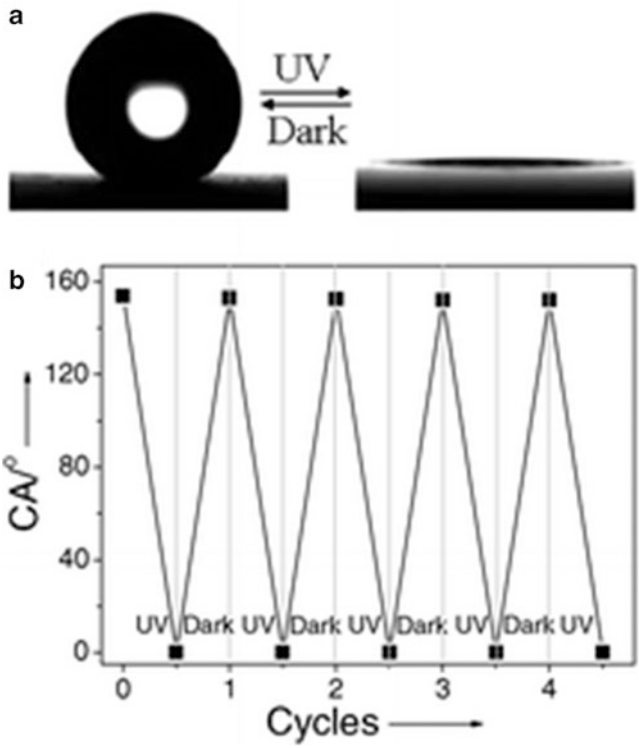

Fig. 9.7 (**a**) Photographs of a spherical water droplet with a CA of $154 \pm 1.3°$ (left) and a flat water film with a CA of 0° (right) before and after the films were exposed to UV illumination, respectively [143]. (**b**) Cycles of reversible superhydrophobicity/superhydrophilicity transformation of the films by alternating between UV irradiation and storage in the dark [143]

materials such as WO_3 [151], V_2O_5 [152], SnO_2 [153], and some metal alloys [154] have been explored. Reversible wetting states (hydrophilicity/hydrophobicity) transition has been observed under the amplifying effect of roughness.

In addition to semiconductor inorganic oxides, some organic materials containing photochromic functional groups are able to reversibly change conformations of two chemical species triggered by UV/visible irradiation [155–160]. Therefore, they are expected to be used in superhydrophobic coatings to reversibly control wetting transition by UV/visible irradiation. For instance, azobenzene layers transform from *trans* isomer to *cis* isomers upon UV irradiation and this process is reversed by visible irradiation. Meanwhile, the wetting behavior of azobenzene layers change depending on different irradiations, because the *trans* isomer has a smaller dipole moment exhibiting a higher water CA, while the *cis* form has a higher dipole moment showing lower water CA. Usually, the change of water CA on flat azobenzene surface is less than 10° upon alternating UV and visible irradiation [161]. To amplify the wetting transition, Jiang et al. [162] have prepared a self-assembly azobenzene

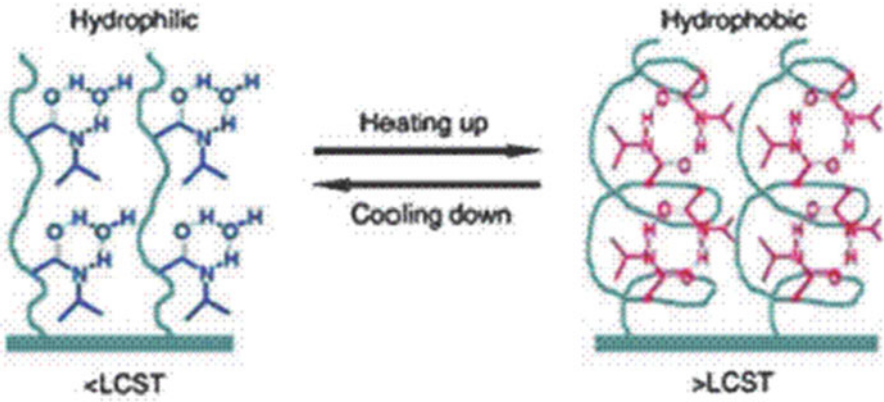

Fig. 9.8 The effect of temperature on the changing in hydrogen bonding and corresponding conformation of PNIPAAm [169]

monolayer on patterned silicon wafer composed of square pillars. Different wetting behaviors related to the pillar spacing on the silicon are reveal and the maximum CA change was only about 66° based on 40 μm spacing.

Alternatively, spiropyran is another kind of photochromic organic molecule. Its closed nonpolar form with hydrophobicity and its highly polar open type—merocyanine isomers with hydrophilicity can be reversibly tuned upon UV and Vis irradiation by properly choosing photon energy. The process is reversible upon green laser irradiation, and it possesses a light-switchable wetting property [156, 163]. Obviously, the light-switchable wettability of films modified by spiropyrans can be further amplified by introducing surface roughness [164].

9.4.2 Temperature and Dual Temperature/PH as External Stimuli

Thermo-sensitive compounds, changing chemical compositions and/or surface roughness under different temperature, have been considered as other promising external stimuli to manipulate the surface wettability. Poly(*N*-isopropylacrylamide) (PNIPAAm) is an prominent thermal responsive polymer favored by a lower critical solution temperature (LCST) of about 32–33°C [165–168]. Below the LCST, the intermolecular hydrogen bonding between PNIPAAm chains and water molecules are predominant, resulting in an extended brush structure with hydrophilic ends. Above the LCST, intramolecular hydrogen bonding in the PNIPAAm chains leads to a compact and collapsed conformation showing hydrophobicity (Fig. 9.8). By introducing the roughness into the surface, reversible switching between superhydrophobicity and superhydrophilicity has been achieve in a narrow temperature range of about 10°C [169].

In addition, temperature/PH dual responsive surfaces with tunable wettability have been investigated by introduction of multi-responsive functional groups. For instance, integrating NIPAAm films with the pH-dependent component acrylic acid (AAc) leads to temperature/pH dual-stimulated P(NIPAAm-*co*-AAc) copolymer films. Jiang et al. [170] have demonstrated wetting behavior is controlled simultaneously by temperature and pH in a wide range. Figure 9.9 shows the wetting behavior on these films becomes more hydrophobic as temperatures increases when the pH is fixed, and becomes more hydrophilic as pH value increases at certain temperature. The extreme hydrophobic state with water CA 148.8° is found when the temperature is at 45°C and pH value is 2. While the extreme hydrophilic state with water CA 7.6° is obtained when the temperature is at 21°C and pH value is 11.

9.4.3 Electrical Potential as External Stimulus

Electrical potential as another attractive external stimulus is able to control the surface chemistry and/or morphology in a few seconds or less. Hence, electrowetting is expected as an effective and versatile method to manipulate surface wettability [171–173]. Electrocapillarity, the basis of modern electrowetting, was first described in detail in 1875 by Gabriel Lippmann [174]. Recently, Berge [175] has developed the idea to isolate the conductive liquid from the substrate using a dielectric layer in order to eliminate the problem of electrolysis. This concept has also become known as electrowetting on dielectric as shown in Fig. 9.10. Basically, the application of an external electrical bias across the solid/liquid interface leads charges to build up both at the liquid side and at the solid electrode, while decreasing the solid/liquid interfacial tension. Consequently, wetting behavior can be tuned to become more hydrophilic without changing the surface morphology and composition.

Even though studies on electrowetting have been conducted for decades, researches are limited on superhydrophobic surfaces. In 2004, Krupenkin et al. [176] had demonstrated dynamic electrical control of the wetting behavior of liquids on designed nanostructured silicon wafer surfaces. For the first time, over the entire possible range from superhydrophobicity to superhydrophilicity was achieved based on electro-wetting with a small electrical bias. Since then electrowetting studies on superhydrophobic surfaces have been increasingly investigated on varied materials, such as CNTs [177–181], ZnO [182], and MnO_2 [50]. Wang et al. [181] have demonstrated that water can be efficiently wet and pumped through superhydrophobic aligned multiwalled CNTs membranes via electrowetting. The CNTs membranes were found be strong polarity-dependent and an abrupt transition from superhydrophobicity to hydrophilicity was observed at a critical bias (1.7 V), with the membrane connecting to anode. Zhao et al. [50] have demonstrated electrowetting on a superhydrophobic membrane of MTAs. In particular, the electro-driven adhesion was enhanced on the superhydrophobic surfaces, on which a water droplet can be immobilized by application of a small DC bias, despite of its large contact angle. For a 3-μL water droplet, the measured adhesive force increases

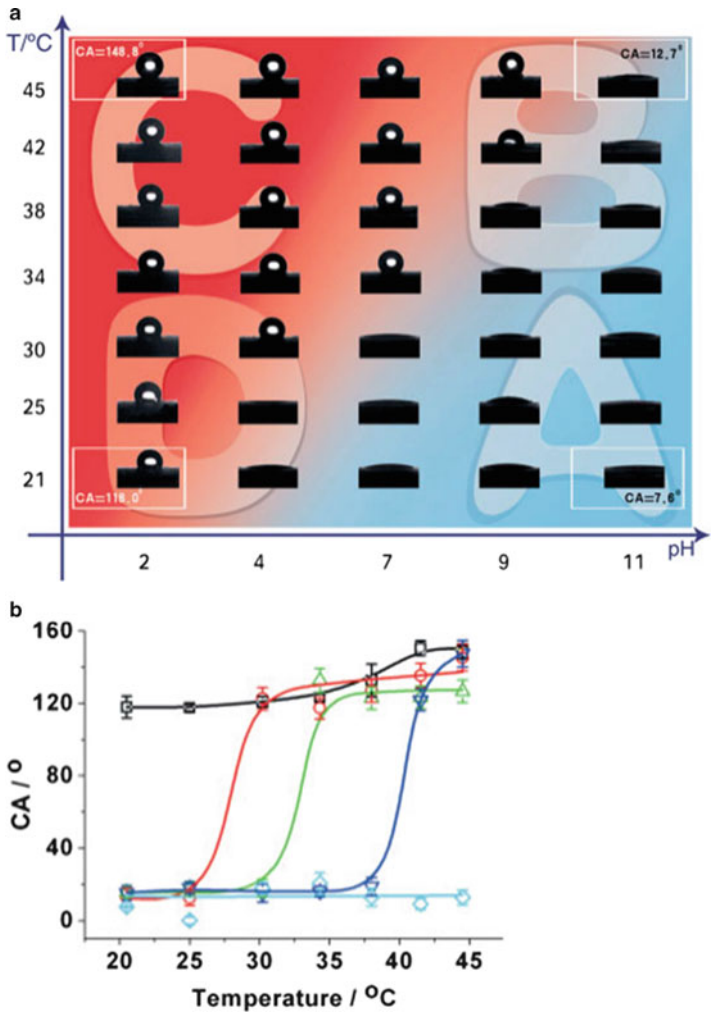

Fig. 9.9 (**a**) When the pH and/or temperature is varied, the CAs reversibly change. (**b**) Temperature and pH dependence of water CAs for P(NIPAAm-co-AAc) thin films. Water CAs change at different temperatures for a modified substrate at pH values of 2 (□), 4 (○), 7 (▲), 9 () and 11 (◇), respectively. Reprinted with permission from [170]. Copyright Wiley-VCH Verlag GmbH & Co. KGaA

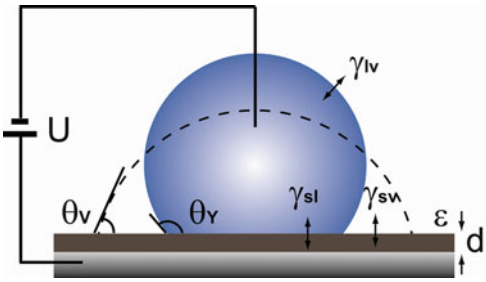

Fig. 9.10 Schematic illustration of electrowetting set-up. Partially wetting liquid droplet at zero voltage (dashed) and at high voltage (solid). See the text for details. Reprinted with permission from ref. [50]. Copyright (2011) Wiley-VCH

monotonically with increasing negative voltage, reaching a maximum of 130 μN at 22 V, 25 times higher than the original value. It follows that the nearly spherical water droplet can be controllably pinned on the substrate, even if the substrate is turned upside down. Moreover, the electrically adjustable adhesion is strongly polarity-dependent; only a fivefold increase is found when a positive bias of 22 V is applied. This remarkable electrically controlled adhesive property is ascribed to the change of contact geometries between the water droplet and MTAs, on which water droplets exhibit different continuities of TCL.

Alternatively, self-assembled conducting polymers with different wettability conformations are found to be used to control the wetting behavior on the surfaces by electrical potential. Choi [183] has found that (16-mercapto)hexadecanoic acid molecules undergo transition of conformation between straight and bent by applying an electrical potential. In the straight conformation, the molecules exhibit hydrophilic feature due to the carboxylate anion on the topmost layer, while the conformation re-orientating to bent state, they display hydrophobicity because of the exposure of the hydrophobic tails of the molecules outwards. Hence, by controlling these two inverse conformations, surface wettability changes within the range of CA from 20 to 30°. To amplifying the range of wettability switching, Xu et al. [184] have demonstrated a simple facile electropolymerization of superhydrophobic polypyrrole (PPy) films and the reversible transition of the PPy films between superhydrophobicity and superhydrophilicity. The PPy films are endowed with a unique porous structure, on which the reversible superhydrophobic-to-superhydrophilic switching is achieved by simply adjusting the electrical potential.

9.5 Superhydrophobic Surfaces for Various Functional Applications

The research on superhydrophobic surfaces is driven by various functional applications. We will discuss below not only how superhydrophobic coatings are used to improve the performance of conventional materials by surface modification, but also how superhydrophobic modification brings about new functions which are not available for the materials themselves.

9.5.1 Transparent and Antireflective Superhydrophobic Coatings

Transparent superhydrophobic coatings behave intensively applied in various application including architecture or automobile windows, eyeglasses, optical windows for electronic devices, etc.

The comment microstructured surfaces are, however, not transparent due to Mie scattering [185] from their rough surfaces. The Mie scattering occurs whenever the surface structures larger than the visible light wavelength. In this case, the wide range of irradiated light is scattered by the structured surface depending upon the size of surface structures, incident angles of light, and differences of refractive indices between the air and materials.

To make superhydrophobic surfaces transparency, the dimensions of roughness should be lower than the wavelength of visible light (ca. 380–760 nm) [186]. According to this criterion, several superhydrophobic coatings techniques have been developed to achieve the integration of superhydrophobicity and transparency. For the applicable concern, Nakajima et al. have prepared hard superhydrophobic thin films by a phase separation method to avoid abrasion and contamination. The hardness of the fabricated film is almost at the same level as normal silica-based hard coatings, meanwhile the transmittance of the film is high in the visible wavelength range [95]. Moreover, Nakajima et al. endows the superhydrophobic transparent film with self-cleaning properties by introducing TiO_2 photocatalyst. Only 2% of TiO_2 was added into the superhydrophobic coating, and the self-cleaning is activated by photo-decomposition of organic contaminants under sunlight irradiation [187]. It was found that the photo-decomposition rate of the fluorinated silane hydrophobic outermost layer was very low due to the high stability of C–F bonds, while stains were photo-decomposed relatively much faster.

While the technique of inorganic coatings has been gaining rapid development, the study of organic transparent superhydrophobic coatings is still in its early stages. Compared to inorganic coating, organic coating structures are more flexible, easier to fabricate, and comparatively not fragile. Till now, a few endeavors have been made to fabricate organic transparent superhydrophobic coatings. Fresnais et al. used O_2–CF_4 double plasma modification of LDPE for a transparent superhydrophobic surface coating [188]. In Teshima et al. work, low-temperature CVD or plasma-enhanced CVD was adopted for hydrophobic coating [70]. Yabu et al. used block copolymers containing equimolar fluorinated acrylate and methyl methacrylate monomers to the fabrication of superhydrophobic surfaces. Through careful controlling the condensation of water droplets and final evaporation of the solvent and water, a honeycomb film with around 300 nm was obtained [133].

Meanwhile, the antireflective properties of superhydrophobic coatings have been developed to enhance their transparency. Xu et al. have reported the fabrication of simultaneous superhydrophobic and antireflective coatings on the basis of silica colloidal suspension sol–gel methods and the lowest reflectivity on one-sided film reached 0.03% [14]. Bravo et al. utilized a LBL process to make a transparent

superhydrophobic coating. In order to achieve superhydrophobic behavior with limited light scattering, they optimized the level of surface roughness by controlling the placement and level of aggregation of differently sized nanoparticles within the multilayer thin film. It follows that optical transmission levels above 90% throughout most of the visible region of the spectrum were achieved in optimized coatings [13].

As an important aspect, some experimental studies show that antireflective superhydrophobic coatings on uneven solar cell surfaces can increase the performance of solar cells. Prevo et al. assembled silica nanoparticles into antireflective coatings on the rough uneven surfaces of polycrystalline silicon solar cells by controlling the evaporation process.

The nanocoatings reduce the reflectance of the solar cells by approximately 10% across the UV to near IR range, providing a 17% increase in the output power. Furthermore, the superhydrophobic coating can help to decrease water uptake which improve maintenance of the performance in the antireflective properties [189].

9.5.2 Structural Color and Iridescence

The vivid color and special wetting features of butterfly wings have attracted increasing attention, because of their potential applications in the external decoration of architectures, where both esthetic and self-cleaning are required. Gu et al. [190] have presented uniform inverse opal film to mimic the colored superhydrophobic property of butterfly wings by a convenient dipping method shown in Fig. 9.11. To exhibit both structural color and superhydrophobicity, colloidal particles with two different sizes were utilized to deposit on glass in a long-range order structure.

Iridescence is generally known as the change in color with different observation angles or lamp flounce, and there are rare studies reporting on artificial superhydrophobic surfaces endowed with such vivid color. Wu et al. employed lithography to fabricate regular micro-needle arrays and further implanted nanometal protrusions on its surface via electroless plating to achieve hierarchical structure. The as-prepared sample exhibited both the superhydrophobic ability and iridescence feature [16]. Alternatively, optical feature can be imparted to the superhydrophobic materials by the inclusion of quantum dots or organic dyes. Hong et al. demonstrated multifunction thin films by incorporating CdSe@ZnS quantum dots (QD) and organic dye into the polystyrene (PS) cores of charged block copolymer micelles [15].

9.5.3 Air-Retaining Property and Fluidic Drag Reduction and Water Support Force

Whereas large amount of superhydrophobic materials have been functionalized in the ambient state, little attention was given to their air-retaining feature when they

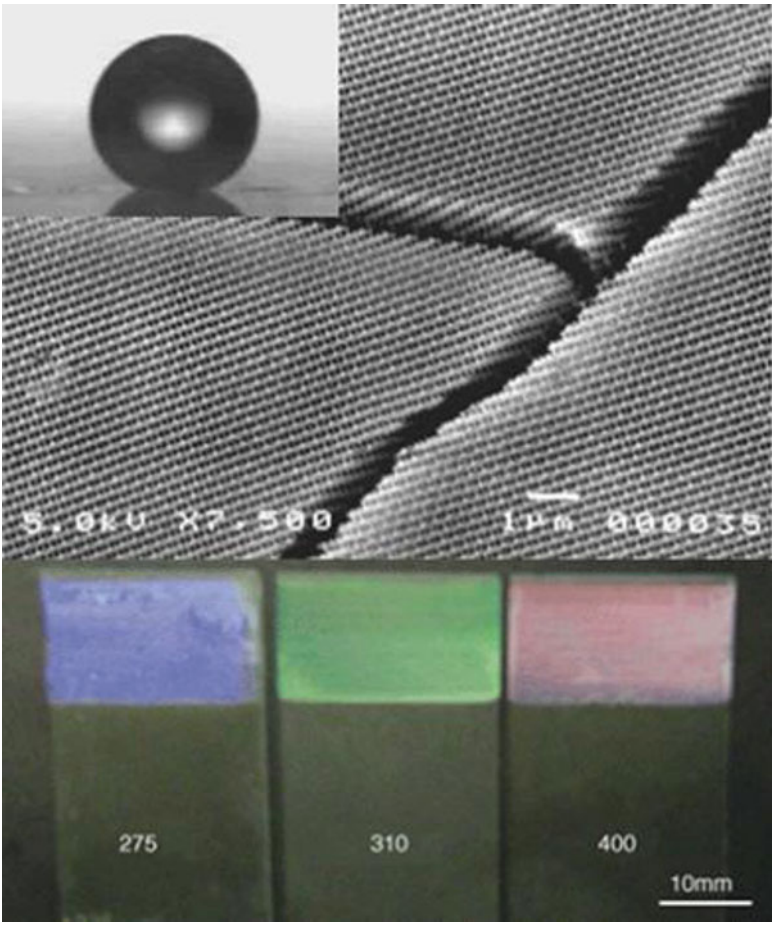

Fig. 9.11 SEM image of the superhydrophobic coating with structural colors (cross-sectional view) and their different colors due to the different sizes of the opals used in the fabrication procedure of the coatings. Reprinted with permission from [190]. Copyright 2003 by Wiley-VCH

are immersed under water. Air-retaining surfaces are of great interest in fundamental studies and economic and ecological applications, for example, for low friction fluid transport, drag-reducing ship coating, extra water support force. Barthlott et al. studied the floating water fern Salvinia revealing a novel mechanism for long-term air-retention property. It was found the hierarchical architecture of the leaf surface composed of superhydrophobic eggbeater-shaped hairs and evenly distributed hydrophilic patches. The author concluded that the unique combination of hydrophilic patches on an otherwise superhydrophobic surface help to stabilize the air–water interface at a predefined level at the top of the hair [191]. The stability

of the thin air layer covering superhydrophobic surfaces under water has been studied by Poetes et al. experimentally. Their results reveal the stability of the air layer depending to the immersion depth: the deeper depth, the faster decay of the air layer [192].

One of the benefits from air-retaining property under water is the fluidic drag reduction. Truesdell et al. provided an experimental result to conclude that the structured superhydrophobic surface reduces the fluidic drag reduction by decreasing the water/solid contact area and forming of a thin layer of air. The thin layer of air establishes an new boundary condition from no slip to limited slip [193]. Watanabe et al. were among the first to report the laminar flow drag reduction phenomenon of superhydrophobic coatings for Newtonian fluids [194]. Recently, the theoretical and experimental details of the fluidic drag reduction of superhydrophobic surfaces in laminar flow were studied thoroughly. According to Ou et al. [195, 196] experimental results, superhydrophobic surface reduces pressure drop of over 40% and results in apparent slip lengths exceeding 20 mm. More importantly, no drag reduction is observed for smooth hydrophobic surfaces. Through detailed velocity measurements, the author demonstrated that slip along the shear-free air–water interface trapped within microstructure is the primary mechanism responsible for the drag reduction phenomenon [195, 196]. Alternatively, Shi et al. have compared superhydrophobic and hydrophobic coating on gold threads confirming that for the first time that a superhydrophobic coating can effectively reduce the fluidic drag for objects moving in water Experimental results show that with the same initial propulsion the velocity of a superhydrophobic-coated gold thread is as much as 1.7 times as that of a normal hydrophobic-modified gold thread [197].

9.5.4 Enhancing Water Supporting Force

As an another important aspect of air-retaining property, researchers found that superhydrophobic coatings can provide extra supporting force for floating objects on the water surface and for objects immersed underwater, like impressive supporting force of water striders' legs [197]. Shi et al. mimic the strider's leg by gold threads and have presented experimental data of a maximum upward forces per centimeter of gold threads with superhydrophobic coating (contact angle 156°) and hydrophobic coating (contact angle 110°). The results show that the thread with superhydrophobic coating overall provides 0.4 mN supporting force per centimeter more than the one with hydrophobic coating. The authors concluded that the air trapped in the cavities of superhydrophobic surfaces providing extra buoyancy forces, which can reduce the apparent density of a water strider to 0.71 $\mathrm{g\,cm^{-3}}$ in water [10, 78, 197].

9.5.5 *Fluidic Transportation*

There are two basic paradigms in microfluidics: one is continuous flow in microchannels and the other is droplet microfluidics without channel, the so-called digital microfluidics. In either paradigm, superhydrophobic coatings have been widely applied for fluidic transportation. Washizu [198] have reported that water droplets can be transported in a controlled manner on a superhydrophobic surface with electrostatic methods. The surface is constructed by arrays of microelectrodes and actuation was achieved by sequentially applying voltages to the electrodes. The author also demonstrated that deflection of a droplet in either of the bifurcating paths, and the mixing of two droplets serving as droplet reactor. The driving force in this system was proposed as to field lines connecting the energized electrode resulting in Maxwell stress by induced charge. This prototype device may find various applications in microfluidic transportation, chemical analyses, and lab-on-chip devices. Alternatively, rapid manipulation of discrete microdroplets was demonstrated on a microactuator composed by two sets of opposing planar electrodes. Pollack et al. [199] demonstrated droplet transportation over 1,000's cycles at switching rates up to 20 Hz. The average droplet velocity is 3.0 cm/s, which is nearly 100 times faster than a previously report for electrical manipulation of droplets. Furthermore, Takeda et al. [200] have investigated the effect of vertical electric field on the movement of water droplets on a superhydrophobic surface. It was found that a water droplet can jump up from the superhydrophobic surface without splitting itself. However, to obtain the jump of a 5 mg water droplet without splitting, precise control of Coulomb force and high voltage of 9.0 KV DC were required. Therefore, further investigation and new design of electrode are desired for the practical application of fluidic transportation.

Since high voltage and electric heating may limit the applications in bioactive component detection, researchers have found that magnetic fields can be an alternative candidate for activation source to control the fluidic transportation. For instance, Garcia et al. [201] have demonstrated magnetic fields controlled movement of aqueous drops on non-patterned, silicon nanowire superhydrophobic surfaces by introducing magnetizable carbonyl iron microparticles into the liquid. Standard key operations of movement, coalescence, and splitting of biological fluid drops were presented. Such droplet-based digital magnetofluidics system further demonstrated the ability to performance reliable electrochemical measurements [202]. The advantage of this method is that droplets are moved in air without needing for a water-immiscible carrier fluid. Meanwhile, the lack of oil facilitates electrochemical measurement by minimizing electrode fouling and viscous drag.

Another way of water droplets transportation is conducted from one surface to another according to the different wetting performance of water droplets on special surfaces under varied wetting conditions. Jin et al. [94] have reported a special superhydrophobic-like surface composed of greater than 6 million aligned polystyrene (PS) nanotubes per square millimeter. Contrary to normal superhydrophobic surfaces with large contact angle and small adhesion, this

Fig. 9.12 Controllable pinning and transport of a nearly spherical water droplet between two superhydrophobic MTA membranes. Reprinted with permission from ref. [50]. Copyright (2011) Wiley-VCH

superhydrophobic-like surface has a large adhesive force which can hold water droplets even when the substrate is turned upside down. This kind of surface can be used as a "mechanical had" to transfer a water droplet from a normal superhydrophobic surface to a hydrophilic one. By using the electric field to control the adhesion on the superhydrophobic surfaces, transporting a water droplet can be achieved between the same kinds of substrates. Zhao et al. [50] have demonstrated a continuously transportation a small water droplet from one MTA membrane to another by controlling electrode polarity and magnitude of the applied voltage. As shown in Fig. 9.12, a water droplet was first placed on an MTA membrane (M1) with no voltage applied. Next, another MTA membrane (M2), adopted as a cathode, was slowly moved toward M1 to make contact and adhere the water droplet by application of 5 V voltage, as shown in the left side of Fig. 9.7(b). Then, M2 was moved away from M1 and the water droplet was completely transferred from M1 to M2. Following the same procedure, this water droplet can be transferred back to M1 by switching the electrode polarity and applying a 15 V voltage. The final CA of the water droplet was still higher than 150°. This water transport process has been repeated more than 30 times in one day using the same MTA membranes, indicating good durability of the MTA membrane.

9.5.6 Battery and Fuel Cell Application

Superhydrophobic materials have shed light on battery system to solve the problems in their duration and efficiency. Based on superhydrophobic nanostructured materials, Lifton et al. have developed a novel battery architecture to extend the shelf life of the battery [203]. In principle, they modified both electrodes of a battery with superhydrophobic materials to separate the liquid electrolyte from the active electrode materials in order to prevent the reaction happen. To initial the battery reaction, the electrowetting principle will lead to change the wetting feature of the liquid electrolyte on the superhydrophobic treated electrodes, and therefore, liquid electrolyte will penetrate into the electrode. Consequently, the battery is activated to produce power. The electrowetting phenomenon can be defined as the change of the solid–electrolyte contact angle due to the applied potential difference between the solid and the electrolyte. It can be understood in terms of the tendency of the solid–electrolyte thermodynamic system to minimize energy by changing the

solid–electrolyte capacitor. The superhydrophobic materials can also improve the mass transport in the fuel cell system by optimize water repellency of the electrode, because this will promote the removal of water produced during electrode reaction. Li et al. have prepared partially oriented superhydrophobic CNTs film catalyzed with Pt nanoparticles (30 wt%) and they found the superhydrophobic film can moderate the mass transport difficulty [204].

9.5.7 Oil–Water Separation and Oil Absorption

Porous materials that are superhydrophobic but superoleophilic can be applied for oil–water separation. In the study by Feng et al., a copper mesh coated with PTFE is used to demonstrate oil–water separation [205]. It has been recorded that a falling water droplet was stopped by the mesh due to the surface superhydrophobicity; while an oil drop can easily pass through the mesh within 240 ms. Alternatively, a membrane combining both the superhydrophobic and superoleophilic properties can be used for selective absorption. Yuan et al. [2] have fabricated nanoporous membranes which can selectively absorb oils up to 20 times the material's weight in preference to water. This superwetting membrane can also be used to separate one solvent from a mixture of solvents of very similar polarity. The technique mechanism is similar to thin layer chromatography.

9.5.8 Microcondensation

Microcondensation of water on patterned superhydrophobic surfaces can be utilized in water collection system. An intriguing example is provided by Namib desert *Stenocara* beetle's back [3], on which micrometer-sized patterns of hydrophobic and hydrophilic region are able to capture water from humid air. The hydrophilic region promotes water condensation from the fogs in the desert atmosphere and the hydrophobic region results in water falling down to the beetle's mouth. To mimic the micro-structures of the beetle's back, Rubner et al. [206] have fabricated superhydrophobic/hydrophilic patterned surfaces via PAH/PAA/silica nanoparticles. Water sprayed on the patterned surface only adhered to the hydrophilic region and grew to spherical water droplet which is easier to fall off. Garrod et al. [207] have applied a simple two-step plasma chemical methodology to fabricate a microcondensor surface on which hydrophilic polymer array was deposited on the superhydrophobic background. In a series of experiments, the author concluded that patterned hydrophilic–hydrophobic surfaces were the most efficient for water microcondensation and these results are compared to the hydrophilic–hydrophobic pattern on the Namib Desert *Stenocara* beetle's back. Another water-collecting example in nature is the capture silk of the cribellate spider *Uloborus walckenaerius*. Zheng et al. [208] have found that the wet-rebuilt periodic spindle-knots structure

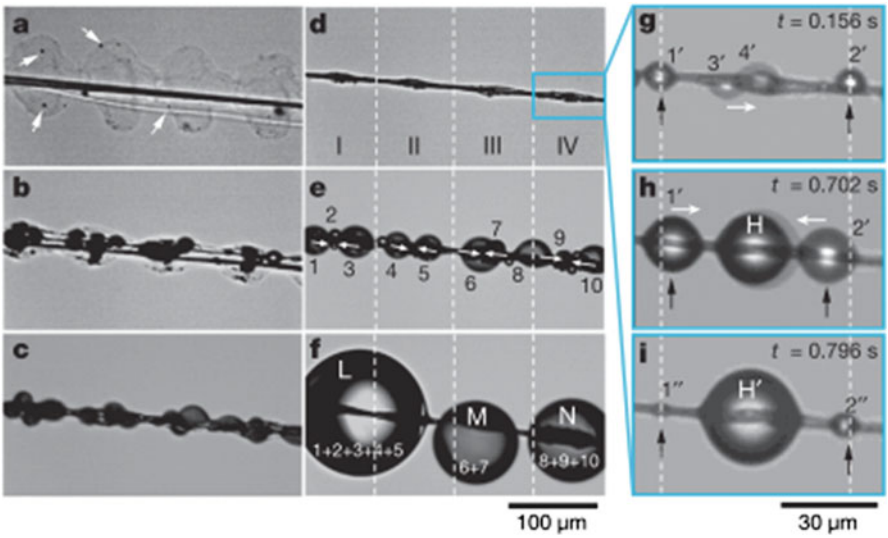

Fig. 9.13 In situ optical microscopic observation of directional water collection on spider silk in mist. Reprinted with permission from [208]

of the spider silk leading to periodic surface energy gradient and difference in Laplace pressure, both of which result in continuous condensation and directional collection of water droplets (shown in Fig. 9.13). Inspired by the special wet-rebuilt structure of spider silk, they achieved to fabricate artificial fiber to mimic the periodic structure and its directional water collection capability. According to the above studies, superhydrophobic/hydrophilic patterned coatings are expected to find wide applications in practical water harvest, microfluidics, and lab-on-chip devices.

9.5.9 Bio-engineering

For various biomedical applications such as biosensors, protenmics, drug screening, and immunoassays, a large amount of interest have been attracted to the development of novel nano/micropatterning techniques, which are utilized to design and fabricate arrays of functional biomolecules for miniaturized assays. Wang et al. [209] have demonstrated cell patterning experiment on hydrophilic–superhydrophobic patterned surface. The patterned surface was designed as an array of pedestals composed of SU-8 on glass substrates, and then coated with a hydrophobic silane. Upon addition of protein solutions to the patterned surface, a layer of air was trapped within the hydrophobic cavities between the pedestals. The author claimed that the trapped air formed a "virtual wall" blocking access to these cavities. Therefore, cells cultured on the patterned surface were forced to grow

only on the hydrophilic pedestals' top forming separated regions. Shiu et al. [210] have reported nanostructured switchable superhydrophobic surfaces allowing fast and addressable protein deposition. The wettability of the superhydrophobic surface was controlled by electrowetting, which converted a water-repellent superhydrophobic surface into a wettable one. A novel multicomponent protein-patterning technique has also been integrated on these switchable superhydrophobic surfaces and 100×100 protein spots with 10 μm resolution can be created within one second. In addition, much effort has been endeavored to improve the cell adhesion, transfection efficiency, and colony separation in cell microarrays application. Shiu et al. [211] have found that cells attached preferentially on the roughened area of patterned superhydrophobic surfaces allowing the formation of cell microarrays. The great improvement of transfection efficiencies of the CHO cells and NIH 3T3 cells was observed on the superhydrophobic surfaces. The author concluded that the patterned superhydrophobic surfaces could be used as cell microarrays with the advantages of enhanced cell adhesion natural separation of colonies and improved transfection efficiency.

Platelet adhesion and activation on material surfaces may cause blood coagulation and thrombosis, which impede the function of artificial manmade blood vessels, organ implantations, and other blood-contacting medical devices. Therefore, it is desired to fabricate more blood-compatible materials. Due to the anti-cell adsorption properties of superhydrophobic surfaces, they may find potential application in clinical therapy and biomedical research. Sun et al. [212] have examined platelet adherence property on partly fluorinated poly(carbonate urethane) (PCU) superhydrophobic surface compared with a flat PCU surface. The results showed that significant platelet adherence is observed on the flat PCU surface and almost no adhered platelet found on the superhydrophobic one. The flow cytometry analysis and immunofluorescence experiments were also executed on these surfaces, indicating their good biocompatibility.

9.5.10 From Microdevices to Marina Industry

Superhydrophobic coatings have excellent water repellency, and they may find applications electronic devices coating and marina technology. Samuel et al. [213] have reported that the waterproof coating can be securing some moisture-sensitive electronic devices. In his report, thin fluoropolymer superhydrophobic coatings were applied on the surfaces of field effect transistor devices via violet photochemical process. It has been found that even at high relative humidity the superhydrophobic coating can eliminate the surface discharge caused by the leakage current. Microwave telecommunication antennae also utilize superhydrophobic coating to reduce water and ice accumulation on its surface, because they can impede the telecommunication and weaken the signals. In the Yamauchi et al. study [214], PTFE was coated on the surfaces of microwave antennae as an ice-proof layer. The authors have found effective prevention of snow or ice accumulation on the

antenna comparing with non-superhydrophobic coating sample. Superhydrophobic surfaces have been found to be candidate of anti-biofouling coatings materials, which can remove the undesirable adherence of microorganisms, plants, algae, and animals on submerged surfaces, for example, ships' hulls. Traditional anti-biofouling coatings on the hulls of ships and other marine-based architectures contain poisons to kill the adhered marine organisms. And this solution is not environment-friendly. Zhang et al. [215] have investigated superhydrophobic materials as anti-biofouling coating. Compared with non-treated substrates exhibiting fouling within a day, the superhydrophobic one can keep the surface clean in the first weeks of immersion. Then the superhydrophobic surface lost its function due to gradually deterioration of the coating. This study indicates that robust superhydrophobic surfaces that can sustain in real marine environment are desired in marine technology. Another related research is that optimizing superhydrophobic coatings on metal surface to moderate corrosion process. Liu et al. [216] have fabricated copper cluster superhydrophobic surfaces by immersing polished fresh copper surfaces into *n*-tetradecanoic acid ethanol solution. The strong bound between copper and *n*-tetradecanoic acid makes the superhydrophobic-modified copper remain intact in seawater for 1 month.

9.6 Outlook

We have tried our best to provide a balanced review of the combination of surface roughness and low-surface-energy coatings for superhydrophobicity. Although the superhydrophobic coating is the focus of many practical applications, and some commercial products have appeared, for example, non-stick pans, superhydrophobic textiles, and self-cleaning coatings, there are still lots of questions that need to be addressed. For example, the contact angle hysteresis is a key factor for the application of superhydrophobic coatings; however, its origin is still not fully understood. There is a need to establish the relationship between contact angle hysteresis and the surface structures and compositions. Many types of methods have been developed to fabricate superhydrophobic surfaces, but most of them are limited to laboratory research and are not suitable for industrial scale production. One-step fabrication or other simple techniques are greatly needed to easily fabricate superhydrophobic surfaces of large scale and good homogeneity. Stability is another important issue we need to be concerned with in view of practical applications. Superhydrophobic coatings cannot find practical use without sufficient stability including mechanical and thermal stability. The stimuli-responsive superhydrophobic surfaces have been discussed, and these studies are certainly a new direction in this field and may provide interesting functional surfaces. In summary, the study of superhydrophobic surfaces originates from mimicking nature, but it has been extended to create new surface materials beyond those found in nature. Therefore, it is a multidisciplinary field interfacing with surface chemistry and physics, nanomaterials, biosurface, mechanics, and so on, where researchers can make full use of their imagination.

References

1. Li, Y., Zhang, J., Zhu, S., Dong, H., Jia, F., Wang, Z., Sun, Z., Zhang, L., Li, Y., Li, H., Xu, W., Yang, B.: Biomimetic surfaces for high-performance optics. Adv. Mater. **21**(46), 4731–4734 (2009)
2. Yuan, J.K., Liu, X.G., Akbulut, O., Hu, J.Q., Suib, S.L., Kong, J., Stellacci, F.: Superwetting nanowire membranes for selective absorption. Nat. Nanotechnol. **3**(6), 332–336 (2008)
3. Parker, A.R., Lawrence, C.R.: Water capture by a desert beetle. Nature **414**(6859), 33–34 (2001)
4. Dorvee, J.R., Derfus, A.M., Bhatia, S.N., Sailor, M.J.: Manipulation of liquid droplets using amphiphilic, magnetic one-dimensional photonic crystal chaperones. Nat. Mater. **3**(12), 896–899 (2004)
5. Lee, H., Lee, B.P., Messersmith, P.B.: A reversible wet/dry adhesive inspired by mussels and geckos. Nature **448**(7151), 338–341 (2007). U4
6. Suh, K.-Y., Park, M.C., Kim, P.: Capillary force lithography: a versatile tool for structured biomaterials interface towards cell and tissue engineering. Adv. Funct. Mater. **19**(17), 2699–2712 (2009)
7. Barthlott, W., Neinhuis, C.: Purity of the sacred lotus, or escape from contamination in biological surfaces. Planta **202**(1), 1–8 (1997)
8. Patankar, N.A.: Mimicking the lotus effect: influence of double roughness structures and slender pillars. Langmuir **20**(19), 8209–8213 (2004)
9. Gao, L.C., McCarthy, T.J.: The "lotus effect" explained: two reasons why two length scales of topography are important. Langmuir **22**(7), 2966–2967 (2006)
10. Gao, X., Jiang, L.: Biophysics: water-repellent legs of water striders. Nature **432**(7013), 36 (2004). 36
11. Cong, Q., Chen, G.H., Fang, Y., Ren, L.Q.: Study on the super-hydrophobic characteristic of butterfly wing surface. J. Bionics Eng. **1**, 249 (2004)
12. Shibuichi, S., Onda, T., Satoh, N., Tsujii, K.: Super water-repellent surfaces resulting from fractal structure. J. Phys. Chem. **100**(50), 19512–19517 (1996)
13. Bravo, J., Zhai, L., Wu, Z., Cohen, R.E., Rubner, M.F.: Transparent superhydrophobic films based on silica nanoparticles. Langmuir **23**(13), 7293–7298 (2007)
14. Xu, Y., Fan, W.H., Li, Z.H., Wu, D., Sun, Y.H.: Antireflective silica thin films with super water repellence via a solgel process. Appl. Opt. **42**(1), 108–112 (2003)
15. Hong, J., Bae, W.K., Lee, H., Oh, S., Char, K., Caruso, F., Cho, J.: Tunable superhydrophobic and optical properties of colloidal films coated with block-copolymer-micelles/micelle-multilayers. Adv. Mater. **19**(24), 4364–4369 (2007)
16. Wu, D., Chen, Q.-D., Xia, H., Jiao, J., Xu, B.-B., Lin, X.-F., Xu, Y., Sun, H.-B.: A facile approach for artificial biomimetic surfaces with both superhydrophobicity and iridescence. Soft Matter **6**(2), 263–267 (2010)
17. Wang, T., Hu, X., Dong, S.: A general route to transform normal hydrophilic cloths into superhydrophobic surfaces. Chem. Commun. **18**, 1849–1851 (2007)
18. Shirtcliffe, N.J., McHale, G., Newton, M.I., Perry, C.C., Pyatt, F.B.: Plastron properties of a superhydrophobic surface. Appl. Phys. Lett. **89**(10), 104106 (2006). 2
19. Wenzel, R.N.: Resistance of solid surfaces to wetting by water. Ind. Eng. Chem. **28**(8), 988–994 (1936)
20. Cassie, A.B.D., Baxter, S.: Wettability of porous surfaces. Trans. Faraday Soc. **40**, 0546–0550 (1944)
21. Pease, D.C.: The significance of the contact angle in relation to the solid surface. J. Phys. Chem. **49**(2), 107–110 (1945)
22. Gao, L., McCarthy, T.J.: How Wenzel and Cassie were wrong. Langmuir **23**(7), 3762–3765 (2007)
23. Gao, L., McCarthy, T.J.: Wetting 101°†. Langmuir **25**(24), 14105–14115 (2009)

24. Gao, L., McCarthy, T.J.: An attempt to correct the faulty intuition perpetuated by the Wenzel and Cassie "laws". Langmuir **25**(13), 7249–7255 (2009)
25. Young, T.: An essay on the cohesion of fluids. Phil. Trans. R. Soc. Lond. **95**, 23 (1805)
26. Quere, D.: Non-sticking drops. Rep. Prog. Phys. **68**(11), 2495–2532 (2005)
27. Herminghaus, S.: Roughness-induced non-wetting. Europhys. Lett. **52**(2), 165 (2000)
28. Marmur, A.: Wetting on hydrophobic rough surfaces: to be heterogeneous or not to be? Langmuir **19**(20), 8343–8348 (2003)
29. Furmidge, C.G.L.: Studies at phase interfaces. I. The sliding of liquid drops on solid surfaces and a theory for spray retention. J. Colloid Sci. **17**(4), 309–324 (1962)
30. Marmur, A.: Soft contact: measurement and interpretation of contact angles. Soft Matter **2**(1), 12–17 (2006)
31. Dorrer, C., Rühe, J.: Advancing and receding motion of droplets on ultrahydrophobic post surfaces. Langmuir **22**(18), 7652–7657 (2006)
32. Chen, W., Fadeev, A.Y., Hsieh, M.C., Oner, D., Youngblood, J., McCarthy, T.J.: Ultrahydrophobic and ultralyophobic surfaces: some comments and examples. Langmuir **15**(10), 3395–3399 (1999)
33. Öner, D., McCarthy, T.J.: Ultrahydrophobic surfaces. Effects of topography length scales on wettability. Langmuir **16**(20), 7777–7782 (2000)
34. Zhao, X.D., Fan, H.M., Liu, X.Y., Pan, H., Xu, H.Y.: Pattern-dependent tunable adhesion of superhydrophobic MnO2 nanostructured film. Langmuir **27**(7), 3224–3228 (2011)
35. Bormashenko, E.: Why does the Cassie-Baxter equation apply? Colloids Surf. A **324**(1–3), 47–50 (2008)
36. Chung, J.Y., Youngblood, J.P., Stafford, C.M.: Anisotropic wetting on tunable micro-wrinkled surfaces. Soft Matter **3**(9), 1163–1169 (2007)
37. Callies, M., Quere, D.: On water repellency. Soft Matter **1**(1), 55–61 (2005)
38. Bico, J., Marzolin, C., Quere, D.: Pearl drops (vol 47, pg 220, 1999). Europhys. Lett. **47**(6), 743–744 (1999)
39. He, B., Patankar, N.A., Lee, J.: Multiple equilibrium droplet shapes and design criterion for rough hydrophobic surfaces. Langmuir **19**(12), 4999–5003 (2003)
40. Lafuma, A., Quere, D.: Superhydrophobic states. Nat. Mater. **2**(7), 457–460 (2003)
41. Wier, K.A., McCarthy, T.J.: Condensation on ultrahydrophobic surfaces and its effect on droplet mobility: ultrahydrophobic surfaces are not always water repellant. Langmuir **22**(6), 2433–2436 (2006)
42. Dorrer, C., Rühe, J.: Condensation and wetting transitions on microstructured ultrahydrophobic surfaces. Langmuir **23**(7), 3820–3824 (2007)
43. Bico, J., Thiele, U., Quéré, D.: Wetting of textured surfaces. Colloids Surf. A Physicochem. Eng. Asp. **206**(1–3), 41–46 (2002)
44. Quéré, D., et al.: Slippy and sticky microtextured solids. Nanotechnology **14**(10), 1109 (2003)
45. Patankar, N.A.: Transition between superhydrophobic states on rough surfaces. Langmuir **20**(17), 7097–7102 (2004)
46. Ishino, C., Okumura, K., Quere, D.: Wetting transitions on rough surfaces. Europhys. Lett. **68**(3), 419–425 (2004)
47. Barbieri, L., Wagner, E., Hoffmann, P.: Water wetting transition parameters of perfluorinated substrates with periodically distributed flat-top microscale obstacles. Langmuir **23**(4), 1723–1734 (2007)
48. Nosonovsky, M., Bhushan, B.: Biomimetic superhydrophobic surfaces: multiscale approach. Nano Lett. **7**(9), 2633–2637 (2007)
49. Bormashenko, E., Pogreb, R., Whyman, G., Erlich, M.: Cassie-Wenzel wetting transition in vibrating drops deposited on rough surfaces: is the dynamic Cassie-Wenzel wetting transition a 2D or 1D affair? Langmuir **23**(12), 6501–6503 (2007)
50. Zhao, X.-D., Fan, H.-M., Luo, J., Ding, J., Liu, X.-Y., Zou, B.-S., Feng, Y.-P.: Electrically adjustable, super adhesive force of a superhydrophobic aligned MnO2 nanotube membrane. Adv. Funct. Mater. **21**(1), 184–190 (2011)

51. Krupenkin, T., Taylor, J.A., Kolodner, P., Hodes, M.: Electrically tunable superhydrophobic nanostructured surfaces. Bell Labs Tech. J. **10**(3), 161–170 (2005)
52. Moulinet, S., Bartolo, D.: Life and death of a fakir droplet: impalement transitions on superhydrophobic surfaces. Eur. Phys. J. E Soft Matter **24**(3), 251–260 (2007)
53. Reyssat, M., et al.: Impalement of fakir drops. Europhys. Lett. **81**(2), 26006 (2008)
54. Bartolo, D., Bouamrirene, F., Verneuil, E., Buguin, A., Silberzan, P., Moulinet, S.: Bouncing or sticky droplets: impalement transitions on superhydrophobic micropatterned surfaces. Europhys. Lett. **74**(2), 299–305 (2006)
55. Zheng, Q.S., Yu, Y., Zhao, Z.H.: Effects of hydraulic pressure on the stability and transition of wetting modes of superhydrophobic surfaces. Langmuir **21**(26), 12207–12212 (2005)
56. Extrand, C.W.: Designing for optimum liquid repellency. Langmuir **22**(4), 1711–1714 (2006)
57. Liu, B., Lange, F.F.: Pressure induced transition between superhydrophobic states: configuration diagrams and effect of surface feature size. J. Colloid Interf. Sci. **298**(2), 899–909 (2006)
58. Schwartz, L.W., Garoff, S.: Contact angle hysteresis on heterogeneous surfaces. Langmuir **1**(2), 219–230 (1985)
59. Chatain, D., Lewis, D., Baland, J.-P., Carter, W.C.: Numerical analysis of the shapes and energies of droplets on micropatterned substrates. Langmuir **22**(9), 4237–4243 (2006)
60. Ishino, C., Okumura, K.: Nucleation scenarios for wetting transition on textured surfaces: the effect of contact angle hysteresis. Europhys. Lett. **76**(3), 464 (2006)
61. Sbragaglia, M., Peters, A.M., Pirat, C., Borkent, B.M., Lammertink, R.G.H., Wessling, M., Lohse, D.: Spontaneous breakdown of superhydrophobicity. Phys. Rev. Lett. **99**(15), 156001 (2007)
62. Zhang, J., Kwok, D.Y.: Contact line and contact angle dynamics in superhydrophobic channels. Langmuir **22**(11), 4998–5004 (2006)
63. Xue, C.H., Jia, S.T., Zhang, J., Tian, L.Q.: Superhydrophobic surfaces on cotton textiles by complex coating of silica nanoparticles and hydrophobization. Thin Solid Films **517**(16), 4593–4598 (2009)
64. Li, J., Fu, J., Cong, Y., Wu, Y., Xue, L., Han, Y.: Macroporous fluoropolymeric films templated by silica colloidal assembly: a possible route to super-hydrophobic surfaces. Appl. Surf. Sci. **252**(6), 2229–2234 (2006)
65. Stelmashuk, V., Biederman, H., Slavínská, D., Zemek, J., Trchová, M.: Plasma polymer films rf sputtered from PTFE under various argon pressures. Vacuum **77**(2), 131–137 (2005)
66. Kim, S.H., Kim, J.-H., Kang, B.-K., Uhm, H.S.: Superhydrophobic CFx coating via in-line atmospheric RF plasma of He−CF4−H2. Langmuir **21**(26), 12213–12217 (2005)
67. Carpentier, J., Grundmeier, G.: Chemical structure and morphology of thin bilayer and composite organosilicon and fluorocarbon microwave plasma polymer films. Surf. Coat.Technol. **192**(2–3), 189–198 (2005)
68. Fresnais, J., Benyahia, L., Poncin-Epaillard, F.: Dynamic (de)wetting properties of superhydrophobic plasma-treated polyethylene surfaces. Surf. Interface Anal. **38**(3), 144–149 (2006)
69. Kiuru, M., Alakoski, E.: Low sliding angles in hydrophobic and oleophobic coatings prepared with plasma discharge method. Mater. Lett. **58**(16), 2213–2216 (2004)
70. Teshima, K., Sugimura, H., Inoue, Y., Takai, O., Takano, A.: Transparent ultra water-repellent poly(ethylene terephthalate) substrates fabricated by oxygen plasma treatment and subsequent hydrophobic coating. Appl. Surf. Sci. **244**(1–4), 619–622 (2005)
71. Teshima, K., Sugimura, H., Inoue, Y., Takai, O., Takano, A.: Wettablity of poly(ethylene terephthalate) substrates modified by a two-step plasma process: ultra water repellent surface fabrication. Chem. Vapor Depos. **10**(6), 295–297 (2004)
72. Wu, Y., Bekke, M., Inoue, Y., Sugimura, H., Kitaguchi, H., Liu, C., Takai, O.: Mechanical durability of ultra-water-repellent thin film by microwave plasma-enhanced CVD. Thin Solid Films **457**(1), 122–127 (2004)
73. Han, J.T., Zheng, Y., Cho, J.H., Xu, X., Cho, K.: Stable superhydrophobic organic−inorganic hybrid films by electrostatic self-assembly. J. Phys. Chem. B **109**(44), 20773–20778 (2005)

74. Schondelmaier, D., Cramm, S., Klingeler, R., Morenzin, J., Zilkens, C., Eberhardt, W.: Orientation and self-assembly of hydrophobic fluoroalkylsilanes. Langmuir **18**(16), 6242–6245 (2002)
75. Song, X., Zhai, J., Wang, Y., Jiang, L.: Fabrication of superhydrophobic surfaces by self-assembly and their water-adhesion properties. J. Phys. Chem. B **109**(9), 4048–4052 (2005)
76. Zhang, G., Wang, D., Gu, Z.-Z., Möhwald, H.: Fabrication of superhydrophobic surfaces from binary colloidal assembly. Langmuir **21**(20), 9143–9148 (2005)
77. Zhao, N., Shi, F., Wang, Z., Zhang, X.: Combining layer-by-layer assembly with electrodeposition of silver aggregates for fabricating superhydrophobic surfaces. Langmuir **21**(10), 4713–4716 (2005)
78. Shi, F., Wang, Z., Zhang, X.: Combining a layer-by-layer assembling technique with electrochemical deposition of gold aggregates to mimic the legs of water striders. Adv. Mater. **17**(8), 1005–1009 (2005)
79. Ma, M., Mao, Y., Gupta, M., Gleason, K.K., Rutledge, G.C.: Superhydrophobic fabrics produced by electrospinning and chemical vapor deposition. Macromolecules **38**(23), 9742–9748 (2005)
80. Liu, H., Feng, L., Zhai, J., Jiang, L., Zhu, D.B.: Reversible wettability of a chemical vapor deposition prepared ZnO film between superhydrophobicity and superhydrophilicity. Langmuir **20**(14), 5659–5661 (2004)
81. Hosono, E., Fujihara, S., Honma, I., Zhou, H.S.: Superhydrophobic perpendicular nanopin film by the bottom-up process. J. Am. Chem. Soc. **127**(39), 13458–13459 (2005)
82. Han, J.T., Lee, D.H., Ryu, C.Y., Cho, K.: Fabrication of superhydrophobic surface from a supramolecular organosilane with quadruple hydrogen bonding. J. Am. Chem. Soc. **126**(15), 4796–4797 (2004)
83. Hikita, M., Tanaka, K., Nakamura, T., Kajiyama, T., Takahara, A.: Super-liquid-repellent surfaces prepared by colloidal silica nanoparticles covered with fluoroalkyl groups. Langmuir **21**(16), 7299–7302 (2005)
84. Li, Y., Cai, W., Cao, B., Duan, G., Sun, F.: Fabrication of the periodic nanopillar arrays by heat-induced deformation of 2D polymer colloidal monolayer. Polymer **46**(26), 12033–12036 (2005)
85. Nakajima, A., Saiki, C., Hashimoto, K., Watanabe, T.: Processing of roughened silica film by coagulated colloidal silica for super-hydrophobic coating. J. Mater. Sci. Lett. **20**(21), 1975–1977 (2001)
86. Jiang, L., Zhao, Y., Zhai, J.: A lotus-leaf-like superhydrophobic surface: a porous microsphere/nanofiber composite film prepared by electrohydrodynamics. Angew. Chem. Int. Ed. **43**(33), 4338–4341 (2004)
87. Singh, A., Steely, L., Allcock, H.R.: Poly[bis(2,2,2-trifluoroethoxy)phosphazene] superhydrophobic nanofibers. Langmuir **21**(25), 11604–11607 (2005)
88. Acatay, K., Simsek, E., Ow-Yang, C., Menceloglu, Y.Z.: Tunable, superhydrophobically stable polymeric surfaces by electrospinning. Angew. Chem. Int. Ed. **43**(39), 5210–5213 (2004)
89. Suh, K.Y., Jon, S.: Control over wettability of polyethylene glycol surfaces using capillary lithography. Langmuir **21**(15), 6836–6841 (2005)
90. Fürstner, R., Barthlott, W., Neinhuis, C., Walzel, P.: Wetting and self-cleaning properties of artificial superhydrophobic surfaces. Langmuir **21**(3), 956–961 (2005)
91. Patankar, N.A.: On the modeling of hydrophobic contact angles on rough surfaces. Langmuir **19**(4), 1249–1253 (2003)
92. Martines, E., Seunarine, K., Morgan, H., Gadegaard, N., Wilkinson, C.D.W., Riehle, M.O.: Superhydrophobicity and superhydrophilicity of regular nanopatterns. Nano Lett. **5**(10), 2097–2103 (2005)
93. Yoshimitsu, Z., Nakajima, A., Watanabe, T., Hashimoto, K.: Effects of surface structure on the hydrophobicity and sliding behavior of water droplets. Langmuir **18**(15), 5818–5822 (2002)

94. Jin, M.H., Feng, X.J., Feng, L., Sun, T.L., Zhai, J., Li, T.J., Jiang, L.: Superhydrophobic aligned polystyrene nanotube films with high adhesive force. Adv. Mater. **17**(16), 1977–1981 (2005)
95. Nakajima, A., Abe, K., Hashimoto, K., Watanabe, T.: Preparation of hard super-hydrophobic films with visible light transmission. Thin Solid Films **376**(1–2), 140–143 (2000)
96. Nakajima, A., Fujishima, A., Hashimoto, K., Watanabe, T.: Preparation of transparent superhydrophobic boehmite and silica films by sublimation of aluminum acetylacetonate. Adv. Mater. **11**(16), 1365–1368 (1999)
97. Minko, S., Müller, M., Motornov, M., Nitschke, M., Grundke, K., Stamm, M.: Two-level structured self-adaptive surfaces with reversibly tunable properties. J. Am. Chem. Soc. **125**(13), 3896–3900 (2003)
98. Khorasani, M.T., Mirzadeh, H.: In vitro blood compatibility of modified PDMS surfaces as superhydrophobic and superhydrophilic materials. J. Appl. Polym. Sci. **91**(3), 2042–2047 (2004)
99. Khorasani, M.T., Mirzadeh, H., Kermani, Z.: Wettability of porous polydimethylsiloxane surface: morphology study. Appl. Surf. Sci. **242**(3–4), 339–345 (2005)
100. Sun, M., Luo, C., Xu, L., Ji, H., Ouyang, Q., Yu, D., Chen, Y.: Artificial lotus leaf by nanocasting. Langmuir **21**(19), 8978–8981 (2005)
101. Guo, L.J.: Recent progress in nanoimprint technology and its applications. J. Phys. D: Appl. Phys. **37**(11), R123 (2004)
102. Lee, W., Jin, M.-K., Yoo, W.-C., Lee, J.-K.: Nanostructuring of a polymeric substrate with well-defined nanometer-scale topography and tailored surface wettability. Langmuir **20**(18), 7665–7669 (2004)
103. Autumn, K., Liang, Y.A., Hsieh, S.T., Zesch, W., Chan, W.P., Kenny, T.W., Fearing, R., Full, R.J.: Adhesive force of a single gecko foot-hair. Nature **405**(6787), 681–685 (2000)
104. Feng, L., Song, Y., Zhai, J., Liu, B., Xu, J., Jiang, L., Zhu, D.: Creation of a superhydrophobic surface from an amphiphilic polymer. Angew. Chem. Int. Ed. **42**(7), 800–802 (2003)
105. Cicala, G., Milella, A., Palumbo, F., Favia, P., D'Agostino, R.: Morphological and structural study of plasma deposited fluorocarbon films at different thicknesses. Diam. Relat. Mater. **12**(10-11), 2020–2025 (2003)
106. Wu, Y., Kuroda, M., Sugimura, H., Inoue, Y., Takai, O.: Nanotextures fabricated by microwave plasma CVD: application to ultra water-repellent surface. Surf. Coat.Technol. **174–175**, 867–871 (2003)
107. Wu, Y., Sugimura, H., Inoue, Y., Takai, O.: Preparation of hard and ultra water-repellent silicon oxide films by microwave plasma-enhanced CVD at low substrate temperatures. Thin Solid Films **435**(1–2), 161–164 (2003)
108. Li, M., Zhai, J., Liu, H., Song, Y., Jiang, L., Zhu, D.: Electrochemical deposition of conductive superhydrophobic zinc oxide thin films. J. Phys. Chem. B **107**(37), 9954–9957 (2003)
109. Daoud, W.A., Xin, J.H., Tao, X.: Superhydrophobic silica nanocomposite coating by a low-temperature process. J. Am. Ceram. Soc. **87**(9), 1782–1784 (2004)
110. Jung, D.-H., Park, I.J., Choi, Y.K., Lee, S.-B., Park, H.S., Rühe, J.: Perfluorinated polymer monolayers on porous silica for materials with super liquid repellent properties. Langmuir **18**(16), 6133–6139 (2002)
111. Li, X.H., Cao, Z., Liu, F., Zhang, Z.J., Dang, H.X.: A novel method of preparation of superhydrophobic nanosilica in aqueous solution. Chem. Lett. **35**(1), 94–95 (2006)
112. Mahltig, B., Böttcher, H.: Modified silica sol coatings for water-repellent textiles. J. Sol-gel Sci. Technol. **27**(1), 43–52 (2003)
113. Nakagawa, T., Soga, M.: A new method for fabricating water repellent silica films having high heat-resistance using the sol-gel method. J. Non-Cryst. Solids **260**(3), 167–174 (1999)
114. Venkateswara Rao, A., Kulkarni, M.M., Amalnerkar, D.P., Seth, T.: Superhydrophobic silica aerogels based on methyltrimethoxysilane precursor. J. Non-Cryst. Solids **330**(1–3), 187–195 (2003)

115. Rao, A.V., Pajonk, G.M., Bhagat, S.D., Barboux, P.: Comparative studies on the surface chemical modification of silica aerogels based on various organosilane compounds of the type RnSiX4-n. J. Non-Cryst. Solids **350**, 216–223 (2004)
116. Roig, A., Molins, E., Rodriguez, E., Martinez, S., Moreno-Manas, M., Vallribera, A.: Superhydrophobic silica aerogels by fluorination at the gel stage. Chem. Commun. **20**, 2316–2317 (2004)
117. Shirtcliffe, N.J., McHale, G., Newton, M.I., Perry, C.C.: Intrinsically superhydrophobic organosilica sol–gel foams. Langmuir **19**(14), 5626–5631 (2003)
118. Ming, W., Wu, D., van Benthem, R., de With, G.: Superhydrophobic films from raspberry-like particles. Nano Lett. **5**(11), 2298–2301 (2005)
119. Wu, X., Zheng, L., Wu, D.: Fabrication of superhydrophobic surfaces from microstructured ZnO-based surfaces via a wet-chemical route. Langmuir **21**(7), 2665–2667 (2005)
120. Huang, L., Lau, S.P., Yang, H.Y., Leong, E.S.P., Yu, S.F., Prawer, S.: Stable superhydrophobic surface via carbon nanotubes coated with a ZnO thin film. J. Phys. Chem. B **109**(16), 7746–7748 (2005)
121. Zhang, X., Shi, F., Yu, X., Liu, H., Fu, Y., Wang, Z., Jiang, L., Li, X.: Polyelectrolyte multilayer as matrix for electrochemical deposition of gold clusters: toward super-hydrophobic surface. J. Am. Chem. Soc. **126**(10), 3064–3065 (2004)
122. Shiu, J.-Y., Kuo, C.-W., Chen, P., Mou, C.-Y.: Fabrication of tunable superhydrophobic surfaces by nanosphere lithography. Chem. Mater. **16**(4), 561–564 (2004)
123. Zhai, L., Cebeci, F.Ç., Cohen, R.E., Rubner, M.F.: Stable superhydrophobic coatings from polyelectrolyte multilayers. Nano Lett. **4**(7), 1349–1353 (2004)
124. Gu, G., Dang, H., Zhang, Z., Wu, Z.: Fabrication and characterization of transparent superhydrophobic thin films based on silica nanoparticles. Appl. Phys. Mater. Sci. Process. **83**(1), 131–132 (2006)
125. Shang, H.M., Wang, Y., Limmer, S.J., Chou, T.P., Takahashi, K., Cao, G.Z.: Optically transparent superhydrophobic silica-based films. Thin Solid Films **472**(1–2), 37–43 (2005)
126. Doshi, D.A., Shah, P.B., Singh, S., Branson, E.D., Malanoski, A.P., Watkins, E.B., Majewski, J., van Swol, F., Brinker, C.J.: Investigating the interface of superhydrophobic surfaces in contact with water. Langmuir **21**(17), 7805–7811 (2005)
127. Sun, T., Wang, G., Liu, H., Feng, L., Jiang, L., Zhu, D.: Control over the wettability of an aligned carbon nanotube film. J. Am. Chem. Soc. **125**(49), 14996–14997 (2003)
128. Zhu, L., Xiu, Y., Xu, J., Tamirisa, P.A., Hess, D.W., Wong, C.-P.: Superhydrophobicity on two-tier rough surfaces fabricated by controlled growth of aligned carbon nanotube arrays coated with fluorocarbon. Langmuir **21**(24), 11208–11212 (2005)
129. Mulder, M.: Basic Principles of Membrane Technology. Kluwer, Dordrecht (1991)
130. Erbil, H.Y., Demirel, A.L., Avcı, Y., Mert, O.: Transformation of a simple plastic into a superhydrophobic surface. Science **299**(5611), 1377–1380 (2003)
131. Lu, X., Zhang, J., Zhang, C., Han, Y.: Low-density polyethylene (LDPE) surface with a wettability gradient by tuning its microstructures. Macromol. Rapid Commun. **26**(8), 637–642 (2005)
132. Xie, Q., Xu, J., Feng, L., Jiang, L., Tang, W., Luo, X., Han, C.C.: Facile creation of a super-amphiphobic coating surface with bionic microstructure. Adv. Mater. **16**(4), 302–305 (2004)
133. Yabu, H., Shimomura, M.: Single-step fabrication of transparent superhydrophobic porous polymer films. Chem. Mater. **17**(21), 5231–5234 (2005)
134. Vogelaar, L., Lammertink, R.G.H., Wessling, M.: Superhydrophobic surfaces having two-fold adjustable roughness prepared in a single step. Langmuir **22**(7), 3125–3130 (2006)
135. Zhao, N., Xie, Q., Weng, L., Wang, S., Zhang, X., Xu, J.: Superhydrophobic surface from vapor-induced phase separation of copolymer micellar solution. Macromolecules **38**(22), 8996–8999 (2005)
136. Xie, Q., Fan, G., Zhao, N., Guo, X., Xu, J., Dong, J., Zhang, L., Zhang, Y.: Facile creation of a bionic super-hydrophobic block copolymer surface. Adv. Mater. **16**(20), 1830–1833 (2004)
137. Han, J.T., Xu, X., Cho, K.: Diverse access to artificial superhydrophobic surfaces using block copolymers. Langmuir **21**(15), 6662–6665 (2005)

138. Huang, Z.-M., Zhang, Y.Z., Kotaki, M., Ramakrishna, S.: A review on polymer nanofibers by electrospinning and their applications in nanocomposites. Compos. Sci. Technol. **63**(15), 2223–2253 (2003)
139. Ma, M., Hill, R.M., Lowery, J.L., Fridrikh, S.V., Rutledge, G.C.: Electrospun poly(styrene-block-dimethylsiloxane) block copolymer fibers exhibiting superhydrophobicity. Langmuir **21**(12), 5549–5554 (2005)
140. Wang, S., Song, Y., Jiang, L.: Photoresponsive surfaces with controllable wettability. J. Photochem. and Photobio. C: Photochem. Rev. **8**(1), 18–29 (2007)
141. Wang, R., Hashimoto, K., Fujishima, A., Chikuni, M., Kojima, E., Kitamura, A., Shimohigoshi, M., Watanabe, T.: Light-induced amphiphilic surfaces. Nature **388**(6641), 431–432 (1997)
142. Tadanaga, K., Morinaga, J., Matsuda, A., Minami, T.: Superhydrophobic–superhydrophilic micropatterning on flowerlike alumina coating film by the sol–gel method. Chem. Mater. **12**(3), 590–592 (2000)
143. Feng, X., Zhai, J., Jiang, L.: The fabrication and switchable superhydrophobicity of TiO2 nanorod films. Angew. Chem. Int. Ed. **44**(32), 5115–5118 (2005)
144. Zhang, X., Jin, M., Liu, Z., Nishimoto, S., Saito, H., Murakami, T., Fujishima, A.: Preparation and photocatalytic wettability conversion of TiO2-based superhydrophobic surfaces. Langmuir **22**(23), 9477–9479 (2006)
145. Zhang, X., Jin, M., Liu, Z., Tryk, D.A., Nishimoto, S., Murakami, T., Fujishima, A.: Superhydrophobic TiO2 surfaces: preparation, photocatalytic wettability conversion, and superhydrophobic–superhydrophilic patterning. J. Phys. Chem. C **111**(39), 14521–14529 (2007)
146. Sun, R.-D., Nakajima, A., Fujishima, A., Watanabe, T., Hashimoto, K.: Photoinduced surface wettability conversion of ZnO and TiO2 thin films. J. Phys. Chem. B **105**(10), 1984–1990 (2001)
147. Miyauchi, M., Shimai, A., Tsuru, Y.: Photoinduced hydrophilicity of heteroepitaxially grown ZnO thin films. J. Phys. Chem. B **109**(27), 13307–13311 (2005)
148. Feng, X., Feng, L., Jin, M., Zhai, J., Jiang, L., Zhu, D.: Reversible super-hydrophobicity to super-hydrophilicity transition of aligned ZnO nanorod films. J. Am. Chem. Soc. **126**(1), 62–63 (2003)
149. Zhang, X.-T., Sato, O., Fujishima, A.: Water ultrarepellency induced by nanocolumnar ZnO surface. Langmuir **20**(14), 6065–6067 (2004)
150. Papadopoulou, E.L., Barberoglou, M., Zorba, V., Manousaki, A., Pagkozidis, A., Stratakis, E., Fotakis, C.: Reversible photoinduced wettability transition of hierarchical ZnO structures. J. Phys. Chem. C **113**(7), 2891–2895 (2009)
151. Wang, S., Feng, X., Yao, J., Jiang, L.: Controlling wettability and photochromism in a dual-responsive tungsten oxide film. Angew. Chem. Int. Ed. **45**(8), 1264–1267 (2006)
152. Lim, H.S., Kwak, D., Lee, D.Y., Lee, S.G., Cho, K.: UV-driven reversible switching of a roselike vanadium oxide film between superhydrophobicity and superhydrophilicity. J. Am. Chem. Soc. **129**(14), 4128–4129 (2007)
153. Zhu, W., Feng, X., Feng, L., Jiang, L.: UV-Manipulated wettability between superhydrophobicity and superhydrophilicity on a transparent and conductive SnO2 nanorod film. Chem. Commun. **26**, 2753–2755 (2006)
154. Kietzig, A.-M., Hatzikiriakos, S.G., Englezos, P.: Patterned superhydrophobic metallic surfaces. Langmuir **25**(8), 4821–4827 (2009)
155. Delorme, N., Bardeau, J.F., Bulou, A., Poncin-Epaillard, F.: Azobenzene-containing monolayer with photoswitchable wettability. Langmuir **21**(26), 12278–12282 (2005)
156. Rosario, R., Gust, D., Hayes, M., Jahnke, F., Springer, J., Garcia, A.A.: Photon-modulated wettability changes on spiropyran-coated surfaces. Langmuir **18**(21), 8062–8069 (2002)
157. Cooper, C.G.F., MacDonald, J.C., Soto, E., McGimpsey, W.G.: Non-covalent assembly of a photoswitchable surface. J. Am. Chem. Soc. **126**(4), 1032–1033 (2004)

158. Driscoll, P.F., Purohit, N., Wanichacheva, N., Lambert, C.R., McGimpsey, W.G.: Reversible photoswitchable wettability in noncovalently assembled multilayered films. Langmuir **23**(26), 13181–13187 (2007)
159. Abbott, S., Ralston, J., Reynolds, G., Hayes, R.: Reversible wettability of photoresponsive pyrimidine-coated surfaces. Langmuir **15**(26), 8923–8928 (1999)
160. Ichimura, K., Oh, S.-K., Nakagawa, M.: Light-driven motion of liquids on a photoresponsive surface. Science **288**(5471), 1624–1626 (2000)
161. Siewierski, L.M., Brittain, W.J., Petrash, S., Foster, M.D.: Photoresponsive monolayers containing in-chain azobenzene. Langmuir **12**(24), 5838–5844 (1996)
162. Jiang, W., Wang, G., He, Y., Wang, X., An, Y., Song, Y., Jiang, L.: Photo-switched wettability on an electrostatic self-assembly azobenzene monolayer. Chem. Commun. **28**, 3550–3552 (2005)
163. Rosario, R., Gust, D., Garcia, A.A., Hayes, M., Taraci, J.L., Clement, T., Dailey, J.W., Picraux, S.T.: Lotus effect amplifies light-induced contact angle switching. J. Phys. Chem. B **108**(34), 12640–12642 (2004)
164. Athanassiou, A., Lygeraki, M.I., Pisignano, D., Lakiotaki, K., Varda, M., Mele, E., Fotakis, C., Cingolani, R., Anastasiadis, S.H.: Photocontrolled variations in the wetting capability of photochromic polymers enhanced by surface nanostructuring. Langmuir **22**(5), 2329–2333 (2006)
165. Liang, L., Feng, X., Liu, J., Rieke, P.C., Fryxell, G.E.: Reversible surface properties of glass plate and capillary tube grafted by photopolymerization of N-isopropylacrylamide. Macromolecules **31**(22), 7845–7850 (1998)
166. Yim, H., Kent, M.S., Mendez, S., Balamurugan, S.S., Balamurugan, S., Lopez, G.P., Satija, S.: Temperature-dependent conformational change of PNIPAM grafted chains at high surface density in water. Macromolecules **37**(5), 1994–1997 (2004)
167. Yim, H., Kent, M.S., Huber, D.L., Satija, S., Majewski, J., Smith, G.S.: Conformation of end-tethered PNIPAM chains in water and in acetone by neutron reflectivity. Macromolecules **36**(14), 5244–5251 (2003)
168. Kidoaki, S., Ohya, S., Nakayama, Y., Matsuda, T.: Thermoresponsive structural change of a poly(N-isopropylacrylamide) graft layer measured with an atomic force microscope. Langmuir **17**(8), 2402–2407 (2001)
169. Sun, T., Wang, G., Feng, L., Liu, B., Ma, Y., Jiang, L., Zhu, D.: Reversible Switching between Superhydrophilicity and Superhydrophobicity. Angew. Chem. Int. Ed. **43**(3), 357–360 (2004)
170. Xia, F., Feng, L., Wang, S., Sun, T., Song, W., Jiang, W., Jiang, L.: Dual-responsive surfaces that switch between superhydrophilicity and superhydrophobicity. Adv. Mater. **18**(4), 432–436 (2006)
171. Isaksson, J., Tengstedt, C., Fahlman, M., Robinson, N., Berggren, M.: A solid-state organic electronic wettability switch. Adv. Mater. **16**(4), 316–320 (2004)
172. Hayes, R.A., Feenstra, B.J.: Video-speed electronic paper based on electrowetting. Nature **425**(6956), 383–385 (2003)
173. Jones, T.B.: On the relationship of dielectrophoresis and electrowetting. Langmuir **18**(11), 4437–4443 (2002)
174. Lippmann, G.: Relations entre les ph´enom‘enes ´electriques et capillaires. Ann. Chim. Phys. **5**, 494 (1875)
175. Berge, B.: Electrocapillarite et mouillage de films isolants par l'eau. C. R. Acad. Sci. II **317**, 157 (1993)
176. Krupenkin, T.N., Taylor, J.A., Schneider, T.M., Yang, S.: From rolling ball to complete wetting: the dynamic tuning of liquids on nanostructured surfaces. Langmuir **20**(10), 3824–3827 (2004)
177. Han, Z.J., Tay, B., Tan, C.M., Shakerzadeh, M., Ostrikov, K.: Electrowetting control of Cassie-to-Wenzel transitions in superhydrophobic carbon nanotube-based nanocomposites. ACS Nano **3**(10), 3031–3036 (2009)

178. Kakade, B., Mehta, R., Durge, A., Kulkarni, S., Pillai, V.: Electric field induced, superhydrophobic to superhydrophilic switching in multiwalled carbon nanotube papers. Nano Lett. **8**(9), 2693–2696 (2008)
179. Chen, J.Y., Kutana, A., Collier, C.P., Giapis, K.P.: Electrowetting in carbon nanotubes. Science **310**(5753), 1480–1483 (2005)
180. Zhu, L.B., Xu, J.W., Xiu, Y.H., Sun, Y.Y., Hess, D.W., Wong, C.P.: Electrowetting of aligned carbon nanotube films. J. Phys. Chem. B **110**(32), 15945–15950 (2006)
181. Wang, Z.K., Ci, L.J., Chen, L., Nayak, S., Ajayan, P.M., Koratkar, N.: Polarity-dependent electrochemically controlled transport of water through carbon nanotube membranes. Nano Lett. **7**(3), 697–702 (2007)
182. Bodre, C., Pauporte, T.: Nanostructured ZnO-Based Surface with Reversible Electrochemically Adjustable Wettability. Adv. Mater. **21**(6), 697 (2009)
183. Lahann, J., Mitragotri, S., Tran, T.N., Kaido, H., Sundaram, J., Choi, I.S., Hoffer, S., Somorjai, G.A., Langer, R.: A reversibly switching surface. Science **299**(5605), 371–374 (2003)
184. Xu, L.B., Chen, W., Mulchandani, A., Yan, Y.S.: Reversible conversion of conducting polymer films from superhydrophobic to superhydrophilic. Angew. Chem. Int. Ed. **44**(37), 6009–6012 (2005)
185. Mie, G.: Ultra Water-Repellent Surface Resulting from Complicated Microstructure of SiO2 nano particles Ann. Phys. 25, 377 (1908)
186. Soeno, T., Inokuchi, K., Shiratori, S.: Trans. Mater. Res. Soc. Jpn 28 (2003)
187. Nakajima, A., Hashimoto, K., Watanabe, T., Takai, K., Yamauchi, G., Fujishima, A.: Transparent superhydrophobic thin films with self-cleaning properties. Langmuir **16**(17), 7044–7047 (2000)
188. Fresnais, J., Chapel, J.P., Poncin-Epaillard, F.: Synthesis of transparent superhydrophobic polyethylene surfaces. Surf. Coat.Technol. **200**(18–19), 5296–5305 (2006)
189. Prevo, B.G., Hon, E.W., Velev, O.D.: Assembly and characterization of colloid-based antireflective coatings on multicrystalline silicon solar cells. J. Mater. Chem. **17**(8), 791–799 (2007)
190. Gu, Z.-Z., Uetsuka, H., Takahashi, K., Nakajima, R., Onishi, H., Fujishima, A., Sato, O.: Structural color and the lotus effect. Angew. Chem. Int. Ed. **42**(8), 894–897 (2003)
191. Barthlott, W., Schimmel, T., Wiersch, S., Koch, K., Brede, M., Barczewski, M., Walheim, S., Weis, A., Kaltenmaier, A., Leder, A., Bohn, H.F.: The salvinia paradox: superhydrophobic surfaces with hydrophilic pins for air retention under water. Adv. Mater. **22**(21), 2325–2328 (2010)
192. Poetes, R., Holtzmann, K., Franze, K., Steiner, U.: Metastable underwater superhydrophobicity. Phys. Rev. Lett. **105**(16), 166104 (2010)
193. Truesdell, R., Mammoli, A., Vorobieff, P., van Swol, F., Brinker, C.J.: Drag reduction on a patterned superhydrophobic surface. Phys. Rev. Lett. **97**(4), 044504 (2006)
194. Watanabe, K., Udagawa, Y., Udagawa, H.: Drag reduction of Newtonian fluid in a circular pipe with a highly water-repellent wall. J. Fluid Mech. **381**, 225–238 (1999)
195. Ou, J., Perot, B., Rothstein, J.P.: Laminar drag reduction in microchannels using ultrahydrophobic surfaces. Phys. Fluids **16**(12), 4635–4643 (2004)
196. Ou, J., Rothstein, J.P.: Direct velocity measurements of the flow past drag-reducing ultrahydrophobic surfaces. Phys. Fluids **17**(10), 103606–103610 (2005)
197. Shi, F., Niu, J., Liu, J., Liu, F., Wang, Z., Feng, X.Q., Zhang, X.: Towards understanding why a superhydrophobic coating is needed by water striders. Adv. Mater. **19**(17), 2257–2261 (2007)
198. Washizu, M.: Electrostatic actuation of liquid droplets for micro-reactor applications. IEEE Trans. Ind. Appl. **34**(4), 732–737 (1998)
199. Pollack, M.G., Fair, R.B., Shenderov, A.D.: Electrowetting-based actuation of liquid droplets for microfluidic applications. Appl. Phys. Lett. **77**(11), 1725–1726 (2000)
200. Takeda, K., Nakajima, A., Hashimoto, K., Watanabe, T.: Jump of water droplet from a superhydrophobic film by vertical electric field. Surf. Sci. **519**(1–2), L589–L592 (2002)

201. García, A.A., Egatz-Gómez, A., Lindsay, S.A., Domínguez-García, P., Melle, S., Marquez, M., Rubio, M.A., Picraux, S.T., Yang, D., Aella, P., Hayes, M.A., Gust, D., Loyprasert, S., Vazquez-Alvarez, T., Wang, J.: Magnetic movement of biological fluid droplets. J. Magn. Magn. Mater. **311**(1), 238–243 (2007)
202. Lindsay, S., Vazquez, T., Egatz-Gomez, A., Loyprasert, S., Garcia, A.A., Wang, J.: Discrete microfluidics with electrochemical detection. Analyst **132**(5), 412–416 (2007)
203. Lifton, V.A., Simon, S., Frahm, R.E.: Reserve battery architecture based on superhydrophobic nanostructured surfaces. Bell Labs Tech. J. **10**(3), 81–85 (2005)
204. Li, W., Wang, X., Chen, Z., Waje, M., Yan, Y.: Carbon nanotube film by filtration as cathode catalyst support for proton-exchange membrane fuel cell. Langmuir **21**(21), 9386–9389 (2005)
205. Feng, L., Zhang, Z., Mai, Z., Ma, Y., Liu, B., Jiang, L., Zhu, D.: A super-hydrophobic and super-oleophilic coating mesh film for the separation of oil and water. Angew. Chem. Int. Ed. **43**(15), 2012–2014 (2004)
206. Zhai, L., Berg, M.C., Cebeci, F.Ç., Kim, Y., Milwid, J.M., Rubner, M.F., Cohen, R.E.: Patterned superhydrophobic surfaces: toward a synthetic mimic of the Namib Desert beetle. Nano Lett. **6**(6), 1213–1217 (2006)
207. Garrod, R.P., Harris, L.G., Schofield, W.C.E., McGettrick, J., Ward, L.J., Teare, D.O.H., Badyal, J.P.S.: Mimicking a Stenocara beetle's back for microcondensation using plasma-chemical patterned superhydrophobic–superhydrophilic surfaces. Langmuir **23**(2), 689–693 (2006)
208. Zheng, Y., Bai, H., Huang, Z., Tian, X., Nie, F.-Q., Zhao, Y., Zhai, J., Jiang, L.: Directional water collection on wetted spider silk. Nature **463**(7281), 640–643 (2010)
209. Wang, Y., Sims, C.E., Marc, P., Bachman, M., Li, G.P., Allbritton, N.L.: Micropatterning of living cells on a heterogeneously wetted surface. Langmuir **22**(19), 8257–8262 (2006)
210. Shiu, J.Y., Chen, P.L.: Addressable protein patterning via switchable superhydrophobic microarrays. Adv. Funct. Mater. **17**(15), 2680–2686 (2007)
211. Shiu, J.-Y., Kuo, C.-W., Whang, W.-T., Chen, P.: Observation of enhanced cell adhesion and transfection efficiency on superhydrophobic surfaces. Lab Chip **10**(5), 556–558 (2010)
212. Sun, T., Tan, H., Han, D., Fu, Q., Jiang, L.: No platelet can adhere—largely improved blood compatibility on nanostructured superhydrophobic surfaces. Small **1**(10), 959–963 (2005)
213. Samuel, J.D.J.S., Ruther, P., Frerichs, H.P., Lehmann, M., Paul, O., Rühe, J.: A simple route towards the reduction of surface conductivity in gas sensor devices. Sens. Actuators B Chem **110**(2), 218–224 (2005)
214. Yamauchi, G., Takai, K., Saito, H.: PTEE based water repellent coating for telecommunication antennas. IEICE T. Electron. **E83C**(7), 1139–1141 (2000)
215. Zhang, H., et al.: Engineering nanoscale roughness on hydrophobic surface—preliminary assessment of fouling behaviour. Sci. Technol. Adv. Mater. **6**(3–4), 236 (2005)
216. Liu, T., Yin, Y., Chen, S., Chang, X., Cheng, S.: Super-hydrophobic surfaces improve corrosion resistance of copper in seawater. Electrochim. Acta **52**(11), 3709–3713 (2007)

Index

X.Y. Liu (ed.), *Bioinspiration: From Nano to Micro Scales*, Biological and Medical Physics, Biomedical Engineering, DOI 10.1007/978-1-4614-5372-8,